UC Riverside

UC Riverside Electronic Theses and Dissertations

Title

Diboraanthracene-Based Platforms for the Redox Activation of Small Molecules

Permalink

https://escholarship.org/uc/item/30k0731j

Author

Taylor, Jordan Wayne

Publication Date

2019

Copyright Information

This work is made available under the terms of a Creative Commons Attribution-NonCommercial-NoDerivatives License, availalbe at https://creativecommons.org/licenses/by-nc-nd/4.0/

Peer reviewed|Thesis/dissertation

eScholarship.org Powered by the California Digital Library
University of California

UNIVERSITY OF CALIFORNIA
RIVERSIDE

Diboraanthracene-Based Platforms for the Redox Activation of Small Molecules

A Dissertation submitted in partial satisfaction
of the requirements for the degree of

Doctor of Philosophy

in

Chemistry

by

Jordan Wayne Taylor

June 2019

Dissertation Committee:
Dr. W. Hill Harman, Chairperson
Dr. Catharine H. Larsen
Dr. De-en Jiang

Copyright by
Jordan Wayne Taylor
2019

The Dissertation of Jordan Wayne Taylor is approved:

_____

_____

_____

Committee Chairperson

University of California, Riverside

Acknowledgments

The number of people that have helped me make forward progress during my Ph.D. is staggering. Foremost, I would like to start by thanking Hill (and potentially a greater cosmic force) for guiding me to Riverside and somehow being exactly the sort of graduate mentor I needed. Having never seen a glovebox or Schlenk line, Hill's patience with me slowing learning the "air-sensitive ropes" was absolutely necessary and fortunately, paid off. The ability to fairly assess, digest and be creative with research are a few of the most important qualities I gleaned from him during my time at Riverside. I didn't expect this process to amount to as much self-discovery as it did and can't thank Hill enough for hanging in there with me. Maybe now he will go mountain biking with me.

At Riverside, I had the opportunity to meet some life-long friends and top-notch chemists. If Hill helped me understand the why, our wily Australian post-doc Alex McSkimming, who I had the pleasure to work with for 2 years, showed me the how. I can't thank Alex enough for the time he took to show me techniques or for thickening my "science-skin". He and his wife Jaime are truly friends and I am looking forward to our next karaoke rendition of "Miami" and "Kiss from a Rose". My fellow lab mates and inaugural Harman Lab members Amy Bartrom and Marissa Barrientos are acknowledged for navigating graduate school with me and, despite quarrelling like siblings at times, ultimately being

there for one another. I sincerely wish them success and happiness in their future endeavors. Dr. Fook Tham, the crystallographer for the first 5 years of my Ph.D., was a wonderful person to get to know. I am deeply grateful and privileged to have been let in on the wealth of crystallography knowledge he possesses. Here's to enjoying your retirement Fook! Our spectroscopy guru Dan Borchardt is thanked for having nearly infinite patience for questions, for bearing with me when I accidentally turned off the spectrometer with my knee and for being, in general, a super cool guy. Additionally, Prisciliano Saavedra is thanked for delivering and shipping countless packages of compounds and cookies during my time at Riverside.

To my family, the boundless support and care you showed for me is humbling. Thank you Grandma Taylor, for always thinking about your grandson and helping me escape college debt free. Thank you Grandma and Grandpa Baumgarten and Grandpa Taylor for somehow letting me know you are with me despite your passing. Thank you Mom, for weathering the limited amount of trips the distance of Riverside to Baraboo allowed for and for constantly reminding me how deeply you love me. Thank you Jim, for loving and supporting Mom during the hard times and being an active proponent of carrot cake during the good times. Thank you Zach, for being a fiercely loyal big brother and for setting such a high bar for personal achievement. It may not seem like it, but I have always looked up to you. Thank you Anita and Web, for caring about me like a son and

for being so encouraging and excitable about what I do. Lastly, thank you Dad. Our cross-country trip to Riverside 6 years ago feels so long ago but still means such a great deal to me. Throughout our shared trials and tribulations, your wisdom, guidance and love has been unwavering and paramount to my successes in life.

Finally, to Laura, my love, lab mate and soon-to-be wife, thank you. Having someone that truly understands the joy of my successes and the pain of my failures has facilitated an inner-peace that I wasn't aware existed before meeting you.

The text, figures, and schemes for the following chapters have been reproduced, in part, from the following published manuscripts.

Chapter 2:
Taylor, J. W.; McSkimming, A.; Guzman, C. F.; Harman, W. H. N-Heterocyclic Carbene-Stabilized Boranthrene as a Metal-Free Platform for the Activation of Small Molecules. *J. Am. Chem. Soc.* **2017**, *139* (32), 11032.

Chapter 3, Section 1:
Taylor, J. W.; McSkimming, A.; Moret, M.-E.; Harman, W. H. A Molecular Boroauride: A Donor-Acceptor Complex of Anionic Gold. *Angew. Chem. Int. Ed.* **2017**, *56* (35), 10413.

Chapter 3, Section 2:
Taylor, J. W.; McSkimming, A.; Essex, L.A.; Harman, W. H. CO_2 Reduction with Protons and Electrons at a Boron-Based Reaction Center. *Submitted*.

Chapter 4:
Taylor, J. W.; McSkimming, A.; Moret, M.-E.; Harman, W. H. *Inorg. Chem.* **2018**, *57* (24), 15406.

Chapter 6:
McSkimming, A.; Harman, W. H. A Terminal N_2 Complex of High-Spin Iron(I) in a Weak, Trigonal Ligand Field. *J. Am. Chem. Soc.* **2015**, *137* (28), 8940.

Appendices:
Essex, L. A.; Taylor, J. W.; Harman, W. H. Nickel Complexes of Phosphine-appended Benzannulated Boron Heterocycles *Tetrahedron* **2019**, *75* (15), 2255.

ABSTRACT OF THE DISSERTATION

Diboraanthracene-Based Platforms for the Redox Activation of Small Molecules

by

Jordan Wayne Taylor

Doctor of Philosophy, Graduate Program in Chemistry
University of California, Riverside, June 2019
Dr. Hill Harman, Chairperson

The efficient multielectron reduction of small molecules (e.g. CO_2, N_2) is a key step in the renewable synthesis of both fuels and fertilizers. Due to their intrinsic redox activity and reactivity, transition metals have been targetted as catalysts for these processes. Recently, p-block systems have been developed that affect the activation of small molecules however the limited redox activity of these systems limits their use as catalysts. To address this challenge, we have targeted the 9,10-dihydro-9,10-diboraanthracene (DBA) framework, due to its synthetic modularity and reversible two-electron redox activity. Conventional derivatives of the DBA scaffold require very negative potentials to access their two-electron reduced states (ca. –2.4 V vs Fc/Fc^+), limiting their prospects as efficient electrocatalysts. We have targeted two approaches to modulate the redox potentials and facilitate small molecule activation chemistry at DBA derivatives:

1) N-heterocyclic carbene (NHC) stabilization; 2) transition metal coordination via tethered phosphine ligands.

The use of NHCs enables the reduction of DBA at potentials over a volt positive of DBA derivatives with aryl substitution (–1.07 and –1.40 V vs Fc/Fc^+). The reduced species is a rare example of a 1,4-diboron analogue of a parent acene and is capable of binding CO_2, ethylene, and O_2 via apparent [4+2] cycloaddition reactions across the two boron atoms. This platform captures key features of transition metal complexes despite being comprised exclusively of light elements. Complimentary to the NHC system, we developed a novel diphosphine tethered diboraanthracene ligand (B_2P_2) and explored the redox chemistry of its transition metal complexes. In the course of these studies, we synthesized the first molecular complex of anionic gold (auride). The auride-B_2P_2 complex was accessed at modest potentials for a DBA-containing molecule (–2.05 V vs. Fc/Fc^+) and was found capable of activating a range of small molecules including CO_2, H_2, H_2O, formaldehyde, benzaldehyde, and acetone. Furthermore, the copper-, silver-, iron-, cobalt- and nickel-B_2P_2 complexes were synthesized, revealing multiple coordination modes and varying electron-accepting properties of the B_2P_2 ligand. Collectively, these studies establish the feasibility of redox small molecule activation at conjugated boranes.

Table of Contents

List of Figures

List of Schemes

List of Tables

Chapter 1) Introduction

1.1) The Beginnings of 1,4-disposed Diboron Rings

Of the multitude types of compounds boron can form, its incorporation into ring systems has captured the interest of the chemistry community for decades. The fundamental interest for incorporating boron into rings systems relies on boron having a $[He]2s^2 2p^1$ electronic configuration that results in boron traditionally forming three covalent bonds while possessing an unoccupied π-orbital. When replacing carbon with boron in conjugated ring systems, the ring becomes electron deficient and the unoccupied π-orbital on boron effectively lowers the energy of the HOMO-LUMO gap of the resulting boron-doped π-conjugated cyclic molecule. This HOMO-LUMO modulation allows for synthetic

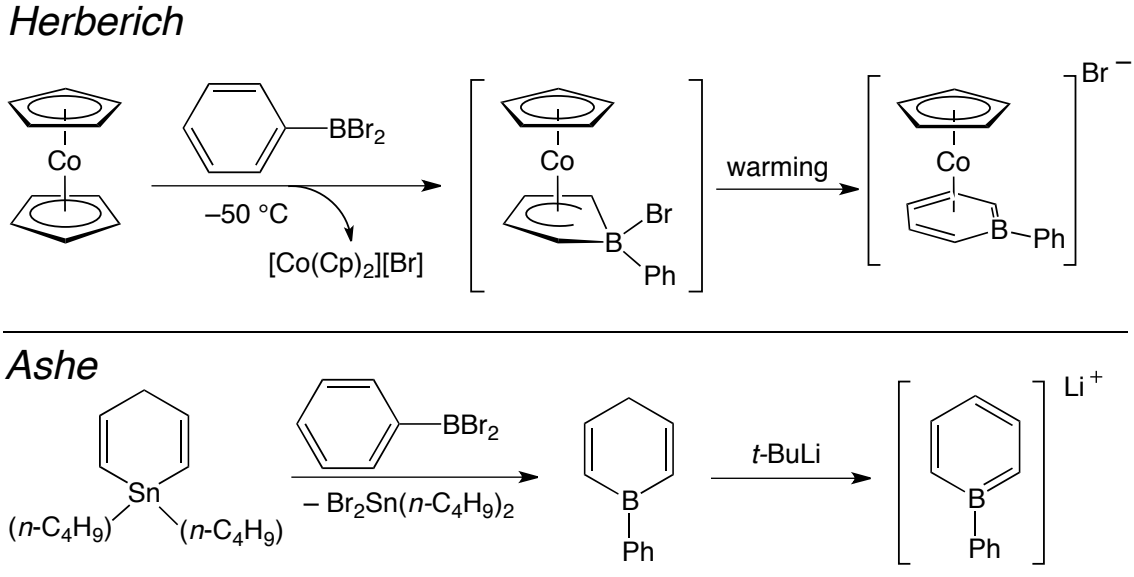

Figure 1.1. Synthesis of 1-phenylboratabenzene in situ (top) and directly (bottom)

control over the redox and optoelectronic properties of the resulting heterocycle, and it is this fundamental property that chemists have been exploiting for applications spanning catalysis, optoelectronics, semiconductors and more. The simplest boron containing heterocycle, where a single carbon in benzene is replaced by a boron atom, was first reported by Herberich[1] in 1970 who used the electron rich Co(Cp) fragment to stabilize the *in situ* generated 1-phenylborabenzene anion that was isolated as the parent anion by Ashe[2] a year later, Figure 1.1. Around this time, incorporation of a second boron atom into a six-membered ring system to generate 1,4-disposed diboron heterocycles was also being investigated. The 9,10-dihydro-9,10-diboraanthracene (9,10-dihydro-DBA) class of molecules was first synthesized in 1965 by Clement[3] through the reaction of the highly toxic diphenylenedimercury with BCl_3 or $BBr_2(NMe_2)$ to afford 9,10-dichloro-DBA and 9,10-dimethylamino-DBA, respectively, Scheme 1.1.

Scheme 1.1. First synthesis of 9,10-dichloro-DBA

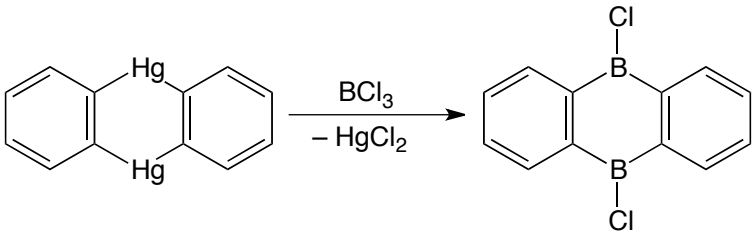

This finding proved serendipitous as benzannulated 1,4-diboron rings are more synthetically accessible and chemically robust than their non-benzannulated, 1,4-dibora-2,5-cyclohexadiene analogs. Efforts to produce 1,4-

diboraabenzenes was originally carried out by Timms[4,5] in 1968 who reacted elemental boron with BF_3 at 2000 °C to produce boron monofluoride prior to the addition of acetylene, Scheme 1.2. Through painstaking hydrolysis experiments and characterization of the byproducts by mass spectrometry the heterocyclic

Scheme 1.2. Synthesis 1,4-difluoro-1,4-dibora-2,5-cyclohexadiene

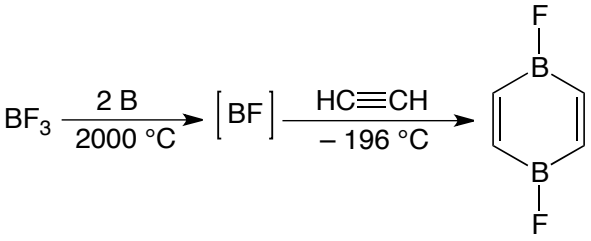

nature of the predominant product, 1,4-dibora-2,5-cyclohexadiene, was correctly inferred with experiments in 1975[6] confirming its assignment. The extreme conditions utilized in these experiments were not adopted by the general academic community however and further studies by Herberich and Hessner[7] in 1978 on the formation of 1,4-dibora-2,5-cyclohexadienes initially produced these rings via transmetallation with 1,1,4,4-tetramethyl-1,4-distanna-2,5-cyclohexadiene and alkyldihaloboranes at low temperature, Scheme 1.3.

Scheme 1.3. Synthesis of 1,4-dibora-2,5-cyclohexadienes using alkyldihaloboranes

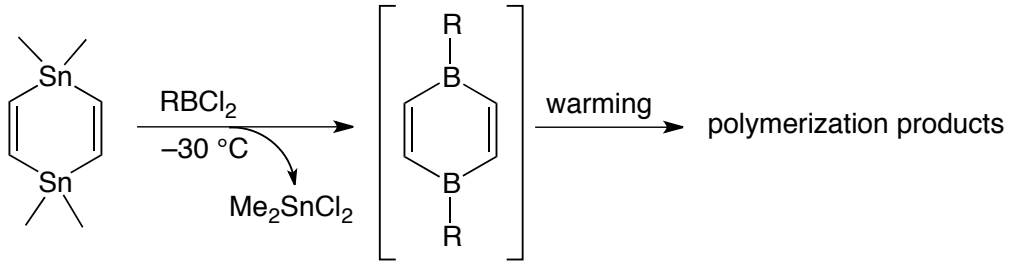

However, these reaction mixtures displayed a propensity for intermolecular rearrangements and an updated method employing ferrocenyldibromoborane produced monomeric, 1,4-bis(ferrocenyl)-1,4-dibora-2,5-cyclohexadiene that could be converted to 1,4-methoxy-1,4-dibora-2,5-cyclohexadiene with MeOH, Scheme 1.4. Overall, the reactivity and arduous synthesis of 1,4-dibora-2,5-cyclohexadienes resulted in 9,10-dihydro-DBA molecules being the most investigated 1,4-disposed diboron ring system to date. Additionally, recent breakthroughs in the synthesis of 9,10-dihydro-DBA derivatives by Wagner[8] and Luliński and Durka[9] have made access to large amounts of these materials possible for the first time.

Ultimately, while the synthesis of many of the fundamental boron-doped ring structures have been known for 50+ years, current societal problems including energy production, energy storage and the need for improved conducting and optic materials for devices has launched a renaissance in the chemistry of boron-doped ring systems.

Scheme 1.4. Synthesis of 1,4-dibora-2,5-cyclohexadienes using ferrocenylboranes

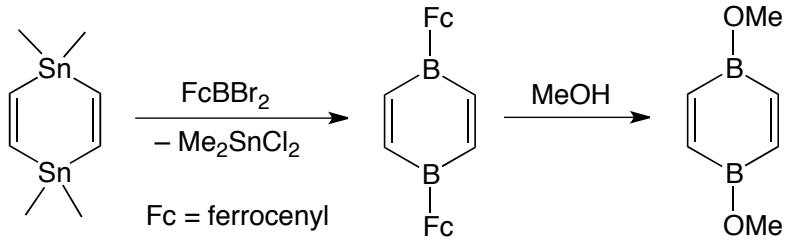

1.2) Synthesis of Diboraanthracene Molecules

The 9,10-dihydro-DBA molecule is formally anti-aromatic with 12 pi-electrons. The naming formalism of DBA molecules is based on carbonaceous

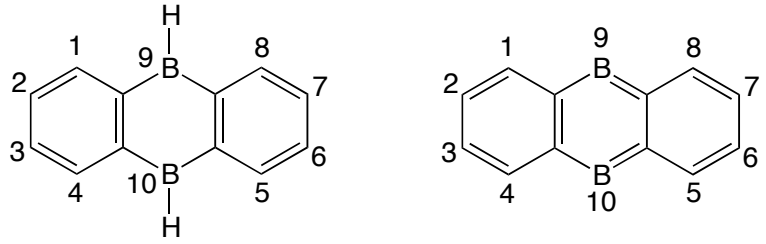

Figure 1.2. Nomenclature and counting formalisms for DBA molecules

anthracene and is outlined in Figure 1.2. By addition of two electrons to these systems, formally Hückel aromatic 14 pi-electron species are obtained. These systems are rare examples of main-group only molecules that undergo multiple reversible redox events at reasonably mild potentials (< 3 V). DBA-based molecules have garnered interest as components in organic optoelectronics and have thus been the subject of extensive studies on their synthesis and physical properties, including their redox chemistry. Following the original synthesis of 9,10-dihydro-DBA by Clement,[3] various synthetic approaches have appeared over the years with two main procedures being utilized currently.

The first method, and perhaps best for large-scale production, is the cyclocondensation of 1,2-bistrimethylsilyl benzene with BX_3 in *n*-alkane solvents at 120 °C to afford 9,10-dihalo-DBAs.[9] This method is general for symmetric 1,2-bis(trimethylsilyl)benzene derivatives however late-stage modification of the

phenylene units (C1-C8) has not been realized and functionalized 1,2-bis(trimethylsilyl)benzenes are required. The haloborane unit at each boron site in 9,10-dihalo-DBA is easily interchanged by nucleophilic substitution with organolithium or Grignard reagents. Alternatively, addition of $HSiEt_3$ exchanges Br for H, producing the parent 9,10-dihydro-DBA that can then perform hydroboration chemistry to enable further organic substitution at the 9,10-positions.

The other method to produce 9,10-DBAs is the double-nucelophilic substitution method.[10] Here, lithium-halogen exchange with *t*BuLi at –78 °C produces an ortho-lithiated phenylboronic acid that upon warming to room temperature dimerizes in a head-to-tail arrangement thereby forming two new B-

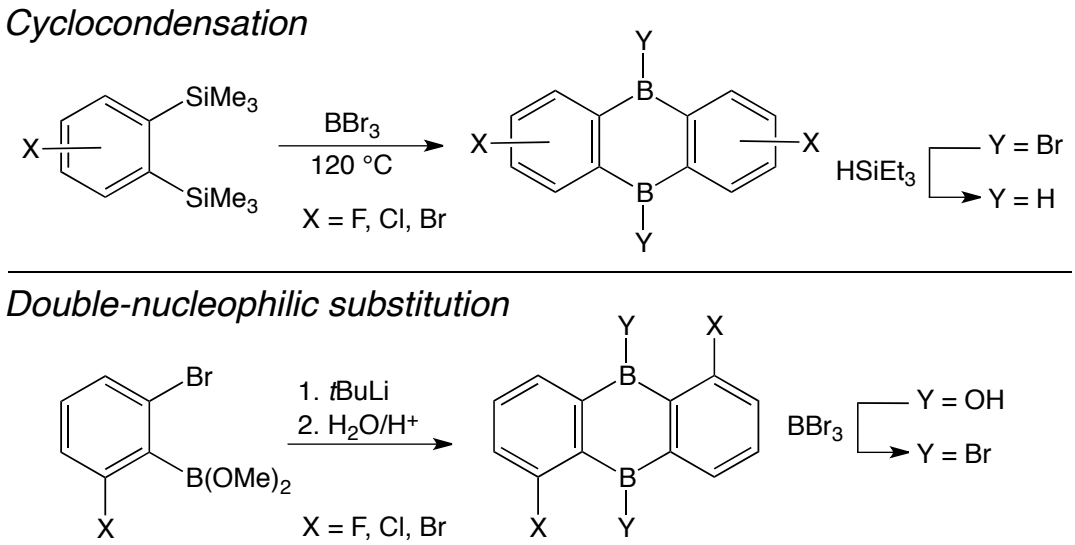

Figure 1.3. Methods to synthesis 9,10-DBA molecules

C bonds. Acidic, aqueous workup produces 9,10-dihydroxy-DBA derivatives that can undergo reaction with BX_3 to produce 9,10-dihalo-DBAs. This method

alleviates the need for symmetric 1,2-bis(trimethylsilyl)benzenes and allows additional organic functionalities to be introduced at the C1-C8 positions. Both synthetic methods are outlined in in Figure 1.3.

1.3) Properties of Diboraanthracene Molecules

Synthetic control over the optoelectronic properties and redox chemistry of DBA molecules has been achieved by either direct modification of the atoms bound to boron or through extension, by modification of the π-conjugated network the boron atoms reside in. Both of these methods seek to either enhance the Lewis acidity of the C_4B_2 core (i.e. ring halogenation) or extend the conjugated π-system the C_4B_2 heterocycle resides in (i.e. annulation, acene substitution). Efforts in both of these veins have mostly come from Wagner and coworkers however a critical discovery by Kawashima[11] that enabled the proliferation of DBA chemistry was that by attaching phenyl substituents to boron that possess *o*-steric bulk, the π-orbitals of the C_4B_2 core become effectively shielded from attack by water and oxygen, thus yielding these derivatives benchtop stable. Without *o*-flanking substituents on the phenyl substituent attached to boron, DBA derivatives are exceedingly air and moisture sensitive, rapidly decomposing when removed from an inert atmosphere.

The optoelectronic properties of DBA molecules were originally presented in 2009 by Wagner through the formation of polymeric DBA-containing

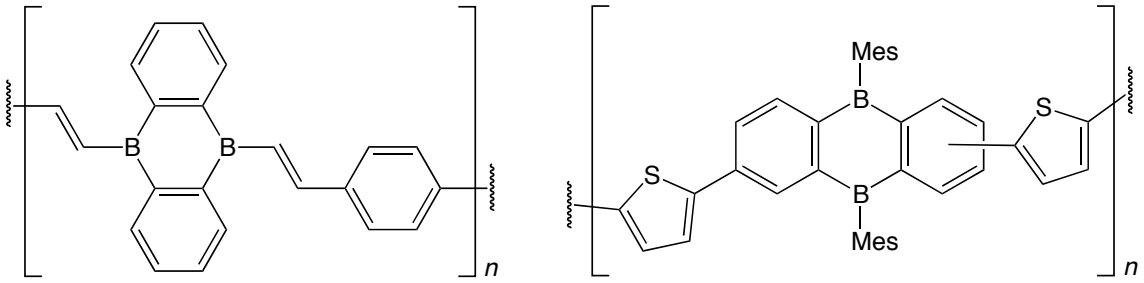

Figure 1.4. Select Examples of Polymeric DBA molecules

materials.[11] Hydroboration of 1,4-diethynylbenzenes with 9,10-dihydro-DBA produced polymeric materials (Figure 1.4, left) that displayed solid-state luminescence with a concomitant bathochromic shift of emission with increasing solvent polarity, suggesting a significant polarization of the excited state. Additionally, methods to produce symmetric[12] and asymmetric[13] polymeric DBAs have been presented that allow for fine tuning of the material's luminescent properties, with more conjugated and strained materials displaying enhanced absorbance and fluorescence at longer wavelengths. DBA containing oligomers with thiophene linkers (Figure 1.4, right) have also been prepared that display the maximum effective conjugation length (the lower limit of the HOMO-LUMO band gap) and exhibit dark orange fluorescence in both solution and as thin films.[14]

The redox chemistry of DBA derivatives often displays two reversible redox events assigned to the radical anion and dianions, respectively. While initial studies of DBA molecules featured 9,10-dimethyl-DBA,[15] the 9,10-Mes_2-

DBA molecule has served as a proxy for the "free" DBA core amongst the DBA research community given its enhanced air-stability. 9,10-Mes_2-DBA features two reversible redox events at $E_{1/2}$ = –1.82 and –2.78 V (vs. Fc/Fc^+, THF, 100 mV/s, [$n$$Bu_4N$][$ClO_4$]) in its cyclic voltammogram,[11] with each member of the redox series being isolated by Wagner.[16] Since report of 9,10-dimethyl- and 9,10-Mes_2-DBA, derivatives possessing extended π-conjugated substituents including napthyl and anthracenyl groups have been synthesized.[17,18] The incorporation of π-conjugated substituents (Figure 1.5, left) has a modest effect on the redox chemistry of the DBA molecule however, as the orthogonal binding nature of the aryl substituent to the B atom limits the effective π-overlap with the DBA framework.

Investigation into direct changes to the DBA heterocycle framework have also been investigated by the incorporation of halogens, heterocycles and expanding the anthracene framework in efforts to further delocalize the electron density of the DBA core. Towards this end, chloride, bromide, fluoride, thiophene,

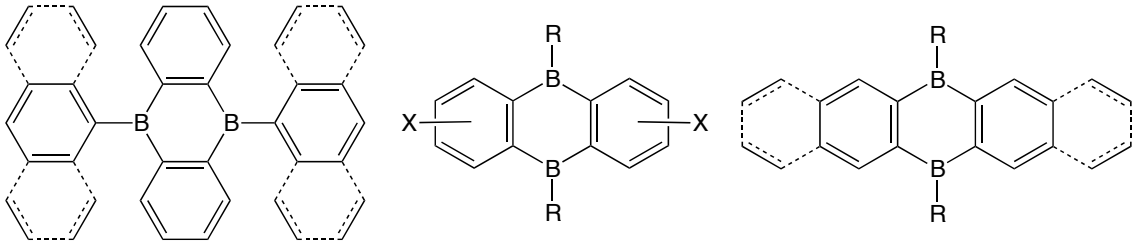

π-conjugation *ring substitution* *annulation*

Figure 1.5. Established methods to manipulate DBA redox

aniline and ferrocenyl substituted DBAs have been prepared (Figure 1.5, middle), each with reported redox chemistry.[19] Halide incorporation into the DBA heterocycle shifts the 1st reduction potential anodically, however irreversibility of the 2nd redox process is often observed, likely representing a competing reductive coupling reaction. The largest effect on DBA redox chemistry using this technique was octafluorination of the C_4B_2 flanking phenylene groups, resulting in ~ 600 m/V positive shift of the first reduction event. Incorporation of thiophenes has a modest effect on DBA redox events as sequential thiophene addition results in an anodic shift of ~ 5-10 mV per thiophene unit. Additionally, ferrocenyl substituted DBA molecules feature an additional redox event representing the Fc/Fc^+ couple however the DBA redox events remain largely unaffected.

Finally, annulation (Figure 1.5, right) is a method for tuning the redox chemistry of DBA derivatives. The first annulated derivative of DBA was prepared by Ashe[20] as the 6,13-dihydro-6,13-diboraapentacene with later results from Yamaguchi[21] assembling an extended boron-doped graphene flake through intramolecular dehydrogenative coupling of a 6,13-dianthryl-6,13-dihydro-6,13-diborapentacene. Most recently, Wagner presented an improved synthesis for the pentacene DBA derivative along with napthyl and biphenylene annulated molecules.[22] Electrochemistry was performed on each member of the annulated series and, while two-reversible redox events were observed for each molecule, the biphenylene DBA derivative featured the most positive redox potentials. *A*

priori, this result was counterintuitive as the most π-conjugated DBA molecule did *not* possess the most energetically accessible LUMO. The effective Lewis acidity of each member of the acene system was also probed by Lewis base titration experiments. Here it was found that the biphenylene DBA molecule possesses a greater affinity to complex a host of Lewis bases, including MeCN, DMF and F^- and collectively these findings suggest the Lewis acidity of the boron heterocycle is perhaps a more significant measure for its redox chemistry than extensive π-conjugation.[23]

1.4) References

[1] Herberich, G. E.; Greiss, G.; Heil, H. F. *Angew. Chem. Int. Ed.* **1970**, 9 (10), 805.

[2] Ashe, A. J.; Shu, P. *J. Am. Chem. Soc.* **1971**, 93 (7), 1804.

[3] Clement, R. *Acad. Sci., Ser. C.* **1965**, 261*,* 4436.

[4] Timms, P. L. *J. Am. Chem. Soc.* **1968**, 90 (17), 4585.

[5] Timms, P. L. *J. Am. Chem. Soc.* **1967**, 89 (7), 1629.

[6] Maddren, P. S., Modinos, A., Timms, P. L., Woodward, P. *J. Chem. Soc., Dalton Trans.* **1975**, 13, 1272.

[7] a) Herberich, G.E., Hessner, B. *J. Organomet. Chem.* **1978**, 161, 36; b) Herberich, G.E., Hessner, B. *Z. Naturforsch. B.* **1978**, 33, 180.

[8] Reus, C., Weidlich, S., Bolte, M, Lerner, H.-W., Wagner, M. *J. Am. Chem. Soc.* **2013**, 135, 12892–12907.

[9] Luliński, S.; Smętek, J.; Durka, K.; Serwatowski, J. *Eur. J. Org. Chem.* **2013**, 36, 8315.

[10] Agou, T.; Sekine, M.; Kawashima, T. *Tet. Lett.* **2010**, 38, 5013.

[11] a) Lorbach, A.; Bolte, M.; Li, H.; Lerner, H.-W.; Holthausen, M. C.; Jäkle, F.; Wagner, M. *Angew. Chem. Int. Ed.* **2009**, *48* (25), 4584.; b) Chai, J.; Wang, C.; Jia, L.; Pang, Y.; Graham, M.; Cheng, S. Z. D. *Synth. Met.* **2009**, *159* (14), 1443.

[12] Januszewski, E.; Bolte, M.; Lerner, H.-W.; Wagner, M. *Organometallics* **2012**, *31* (23), 8420.

[13] Januszewski, E.; Lorbach, A.; Grewal, R.; Bolte, M.; Bats, J. W.; Lerner, H.-W.; Wagner, M. *Chem. Eur. J.* **2011**, *17* (45), 12696.

[14] Reus, C.; Guo, F.; John, A.; Winhold, M.; Lerner, H.-W.; Jäkle, F.; Wagner, M. *Macromolecules* **2014**, 11, 3727.

[15] a) Müller, P.; Pritzkow, H.; Siebert, W. *J. Organomet. Chem.* **1996**, 524, 41.; b) Müller, P., Huck, S., Köppel, H., Pritzkow, H., Siebert, W. *Z. Naturforsch B.* **1995**, 10, 1476-1484.

[16] Hoffend, C.; Diefenbach, M.; Januszewski, E.; Bolte, M.; Lerner, H.-W.; Holthausen, M. C.; Wagner, M. *Dalton Trans.* **2013**, *42* (38), 13826.

[17] a) Hoffend, C.; Schödel, F.; Bolte, M.; Lerner, H.-W.; Wagner, M. *Chem. Eur. J.* **2012**, *18* (48), 15394.; b) Hoffend, C.; Diefenbach, M.; Januszewski, E.; Bolte, M.; Lerner, H.-W.; Holthausen, M. C.; Wagner, M. *Dalton Trans.* **2013**, *42* (38), 13826.

[18] a) Hoffend, C.; Schickedanz, K.; Bolte, M.; Lerner, H.-W.; Wagner, M. *Tetrahedron* **2013**, *69* (34), 7073.; b) Dou, C.; Saito, S.; Yamaguchi, S. *J. Am. Chem. Soc.* **2013**, *135* (25), 9346.

[19] a) Brend'amour, S.; Gilmer, J.; Bolte, M.; Lerner, H.-W.; Wagner, M. *Chem. Eur. J.* **2018**, *24* (63), 16910.; b) Reus, C.; Weidlich, S.; Bolte, M.; Lerner, H.-W.; Wagner, M. *J. Am. Chem. Soc.* **2013**, *135* (34), 12892.; c) Pakkirisamy T.; Venkatasubbaiah K.; Kassel, W. S.; Rheingold, A. L.; Jäkle F. *Organometallics* **2008**, 27, 3056–3064.

[20] Chen, J.; Kampf, J. W.; Ashe, A. J. *Organometallics* **2008**, *27* (15), 3639.

[21] a) Dou, C.; Saito, S.; Matsuo, K.; Hisaki, I.; Yamaguchi, S. *Angew. Chem. Int. Ed.* **2012**, *51* (49), 12206.; b) Kawai, S.; Saito, S.; Osumi, S.; Yamaguchi, S.; Foster, A. S.; Spijker, P.; Meyer, E. *Nat. Comm.* **2015**, *6* (1), 8098.

[22] Kirschner, S.; Mewes, J.-M.; Bolte, M.; Lerner, H.-W.; Dreuw, A.; Wagner, M. *Chem. Eur. J.* **2017**, *23* (21), 5104.

[23] Blagg, R. J.; Simmons, T. R.; Hatton, G. R.; Courtney, J. M.; Bennett, E. L.; Lawrence, E. J.; Wildgoos, G. G. *Dalton Trans.* 2016, **45**, 6032–6043.

Chapter 2) NHC-Stabilized Boranthrene as a Metal-Free Platform for the Activation of Small Molecules

2.1) Introduction

The storage of renewable electricity in the form of chemical fuels is a promising strategy for scalable carbon-neutral energy production.[1] This approach requires catalysts capable of efficiently coupling multiple electron transfers to the formation and cleavage of chemical bonds in energy conversion reactions.[2] Owing to their intrinsic re-dox activity, flexible coordination sphere, and ability to activate small molecules of energy consequence, transition metals have long been targeted in this role (Figure 2.1, top).[3] More recently, approaches to multi-

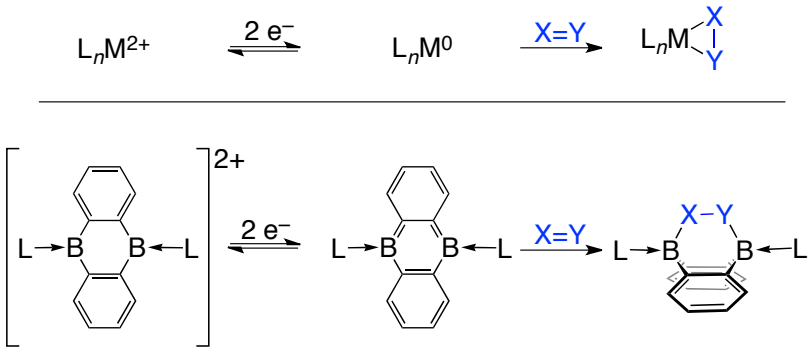

Figure 2.1. Small-molecule activation with transition metals (top) and ligand supported boranthrene (bottom)

electron small-molecule activation that forego transition metals have emerged,[4] including frustrated Lewis pairs (FLPs),[5] unsaturated main-group centers such as carbenes[6] and related species,[7] and weak element-element multiple bonds.[8] As they lack the empty d-orbitals of the transition metals, one challenge for these

main group systems is their limited redox activity. Redox-active ligands provide one way of addressing this issue on main-group metals.[9]

Inspired by reports that materials based on graphitic (sp^2) carbon, often doped with other light atoms, can serve as electrocatalysts for energy conversion reactions,[10] we have been exploring molecular platforms based on carbon and other *2p* elements that attain redox activity via extended conjugation. We were drawn to the 9,10-diboraanthracene skeleton due to its synthetic tractability[11] and precedent for reversible two-electron redox chemistry.[12] Furthermore, boron-containing heteroarenes have been shown to undergo reactions with small molecules of interest such as O_2, CO_2, H_2, and organic substrates.[13]

Unfortunately, very negative potentials are required to access the two-electron reduced states of 9,10-dihydrocarbyl-DBA scaffolds (ca. –2.4 V vs. Fc/Fc^+), limiting their prospects as efficient electrocatalysts. Given the widespread success of N-heterocyclic carbenes (NHCs) in stabilizing reactive main-group species[14] (including those containing boron[15]), we reasoned that neutral boranthrene[16] (BA; 9,10-diboraanthracene, $C_{12}H_8B_2$) supported by NHCs might be accessed at relatively positive potentials and react readily with small molecules—key criteria for the development of potential electrocatalysts (Figure 2.1, bottom). Herein, we report the synthesis of NHC-stabilized boranthrene, its one- and two-electron oxidized congeners, as well as its reactivity with CO_2, C_2H_4, and O_2. These results demonstrate that molecular compounds based on

aromatic hydrocarbons can exhibit many of the desirable features of transition metal complexes, including reversible ligand binding, multielectron redox chemistry at mild potentials, and the ability to activate small molecules of energy consequence.

2.2) Results and Discussion

The synthesis of NHC-stabilized BA is shown in Scheme 2.1. Bis-NHC adduct IPr2(BA)Br_2 (**1**) was accessed by the addition of two equivalents of 1,3-bis(2,6-diisopropylphenyl)imidazol-2-ylidene (IPr) to 9,10-Br_2-DBA. Dissolution of **1** in acetonitrile induces bromide dissociation allowing the isolation of the

Scheme 2.1. Synthesis of NHC-Stabilized Boranthrene

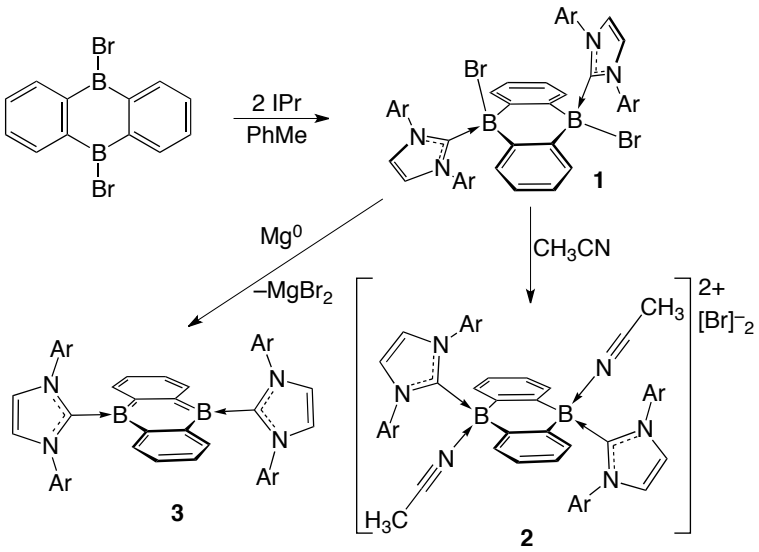

acetonitrile-ligated diborenium dication $[IPr_2(BA)(CH_3CN)_2]^{2+}$ with outer-sphere bromide counteranions (**2**). The solid-state structures of **1** and **2** were determined by single crystal X-ray diffraction (XRD, Figures 2.2a and 2.2b).

Although both **1** and **2** have similar connectivities, they exhibit significant structural differences. Crystallized from THF, **1** retains its B–Br linkages and features approximate *Cs* symmetry. The puckered C_4B_2 ring exhibits a pseudo-boat configuration with trans-disposed bromines and nearly orthogonal IPr ligands. Low-temperature ^{1}H and ^{13}C NMR spectra (–50 ºC, THF-d_8) of **1** are consistent with the preservation of this structure in solution. Although **2** possesses a similar trans orientation of the boron-bound substituents, its diboraanthracene core is nearly planar, with approximate overall C_{2h} symmetry. Efforts to isolate an unligated form of $[\mathbf{2}]^{2+}$ using noncoordinating counterions and/or solvents have been unsuccessful, presumably due to the extreme Lewis acidity of the targeted species. Compound **2** is itself very hydrolytically sensitive and must be handled under rigorously anhydrous conditions.

Magnesium reduction of **1** in diethyl ether affords the dark green, NHC-stabilized boranthrene $IPr_2(BA)$ (**3**). This reduction is accompanied by a dramatic

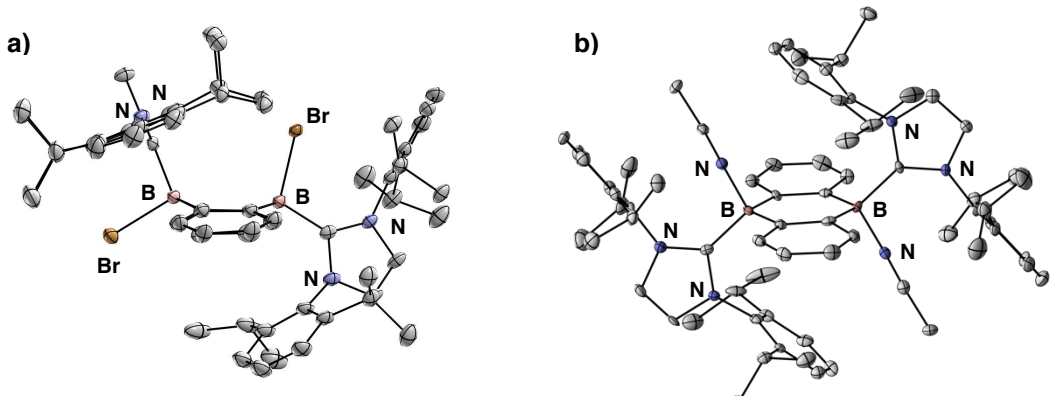

Figure 2.2. Thermal ellipsoid plots (30% probability) of (a) $IPr_2(BA)Br_2$ (1) and (b) $[IPr_2(BA)(CH_3CN)_2][Br]_2$ (2) (bromide counterions not shown)

Scheme 2.2. Synthesis of [IPr$_2$(BA)][Br] (4)

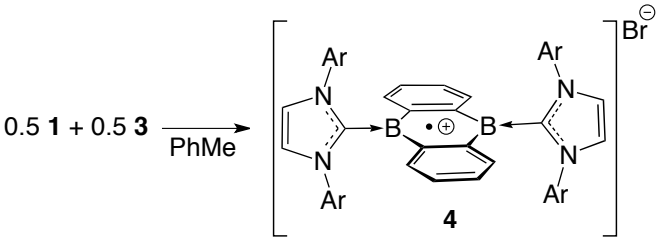

downfield shift in the ^{11}B NMR resonance of 3 to 20.1 ppm, compared to –3.6 ppm in **1**, consistent with equivalent, three-coordinate boron centers. The solid-state structure of **3** confirms this geometry and reveals an approximately planar DBA core (Figures 2.3a). Although the ^{1}H NMR spectrum of **2** in C_6D_6 is broadened due to fluxionality at room temperature, both the low (–50 ºC) and high (80 ºC) temperature ^{1}H NMR spectra in toluene-d_8 are consistent with D_{2h} symmetry in solution. After Braunschweig's CAAC-stabilized 1,4-diborabenzene, **3** is only the second example of a neutral 1,4-diboron acene homologue.

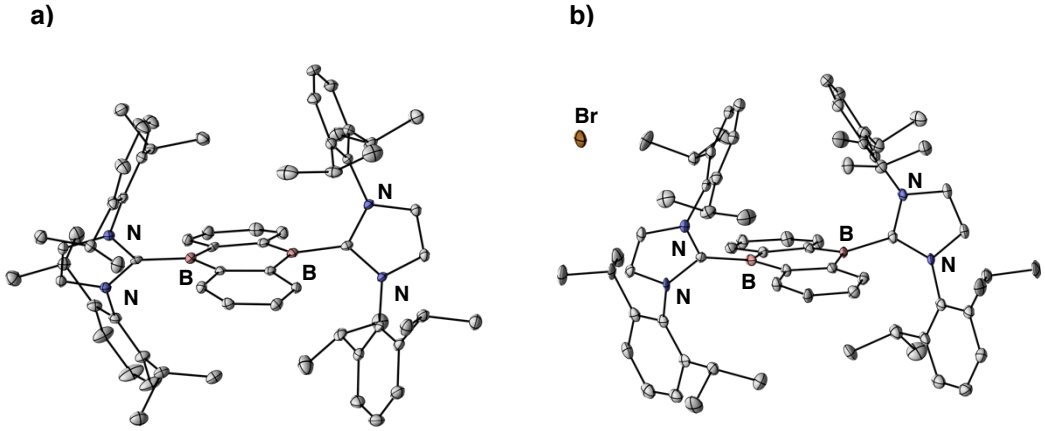

Figure 2.3. Thermal ellipsoid plots (30% probability) of (a) IPr$_2$(BA) (3) and (b) [IPr$_2$(BA)][Br] (4)

To complete the three-membered redox series, we targeted the radical cation $[IPr_2(BA)]^{\bullet+}$. Comproportionation of **1** and **3** provides ready access to this compound as the bromide salt $[IPr_2(BA)][Br]$ (**4**) (Scheme 2.2). In the solid state (Figure 2.3b), **4** features a planar DBA core with three-coordinate boron centers very similar to **3** and an outer sphere bromide counteranion. Electron paramagnetic resonance (EPR) studies are consistent with a symmetric, ionized structure for **4** in solution. At room temperature in a 1:1 mixture of CH_2Cl_2/toluene, the X-band EPR spectrum of **4** shows a broad singlet centered at

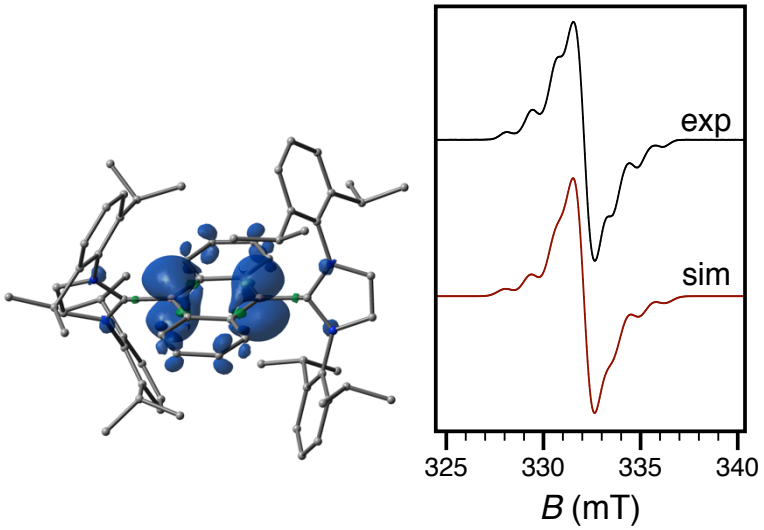

Figure 2.4. Left: Spin density isosurface (isovalue = 0.003) calculated for $[IPr_2(BA)]^{\bullet+}$ by DFT at the M06L//TZV(2d) (H)/TZV(2d) (B, C, and N) Right: Experimental and simulated X-band EPR spectra of 4 collected in a 1:1 toluene/CH_2Cl_2 glass at 107 K. Simulation parameters are g = [2.0034, 2.0015, 2.0002]; $A(^{11}B, 80.1\%)$ = [3, 32, 0] MHz; $A(^{10}B, 19.9\%)$ = [1, 11, 0] MHz (for two B nuclei).

g = 2.00 with no resolved hyperfine interactions (Figure 2.5.36). When the same solution is frozen, a seven-line hyperfine structure is resolved that is well-simulated by strongly axial interactions with two equivalent boron nuclei such that

$A(^{11}B)$ = [3, 32, 0] MHz (Figure 2.4, right). The highly anisotropic boron hyperfine interactions suggest a SOMO with predominant boron *p*-character, and the spin density map computed via density functional theory (DFT) for **4** (Figure 2.4, left) supports this description. Isolable cationic boron-centered radicals are rare, with carbene-supported diborene[17] and borylene radical cations being two noteworthy examples.

Cyclic voltammetry performed on **2** (0.1 M [^{n}Bu$_4$N][Br] in CH_3CN), revealed an initial broad reduction with $E_{1/2}$ = –1.07 V corresponding to the reduction of [**2**]$^{2+}$ to [**4**]$^+$ followed by a fully reversible redox event at $E_{1/2}$ = –1.40 V assigned to the [**4**]$^+$/**3** redox couple (Figure 2.5). The oxidative event at $E_{1/2}$ = –0.76 V corresponds to the oxidation of [**4**]$^+$. The electrochemical irreversibility of the first reduction process is likely a result of the dissociation of the two coordinated acetonitrile ligands that occurs upon one-electron reduction of [**2**]$^{2+}$ (*vide supra*).

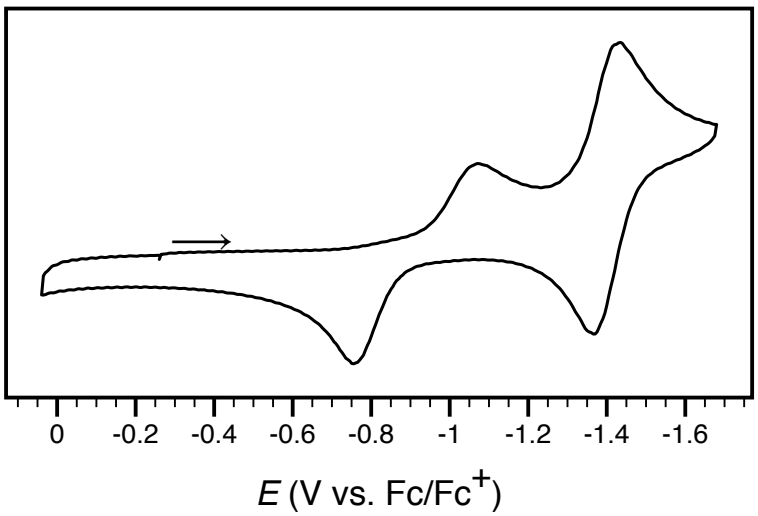

Figure 2.5. Cyclic voltammogram of 1 in CH_3CN with 0.1 M [^{n}Bu$_4$N][Br] at a scan rate of 100 mV/s.

These redox potentials are remarkably positive for a DBA-derived molecule. For example, under similar conditions, the one- and two-electron reductions of 9,10-Mes_2-DBA occur at –1.62 and –2.48 V, respectively.[18] This anodic shift (ca. 1 V) highlights the profound effect of NHC coordination in stabilizing the reduced forms of [IPr_2(BA)] (**3** and **4**).

Having characterized the redox chemistry of the [IPr_2(BA)]^n system, we explored its ability to activate small molecules in the reduced state (**3**). Exposure of a benzene solution of **3** to an atmosphere of dry air results in the rapid formation of IPr_2(BA)(O_2) (**5**) via the formal cycloaddition of O_2 across the central

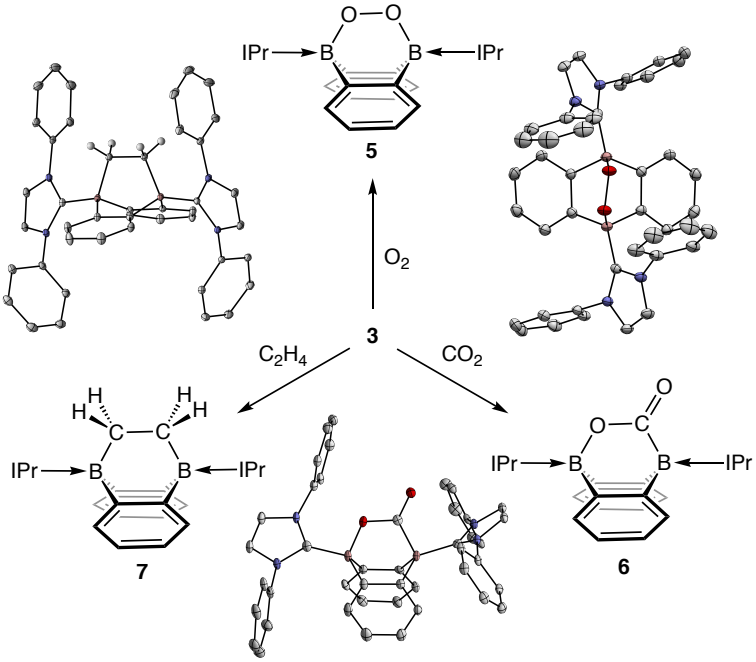

Figure 2.6. Reaction of IPr_2(BA) with O_2, CO_2, and C_2H_4. Thermal ellipsoid plots (30% probability) are shown clockwise from the respective line drawing with grey, red, pink, and blue ellipsoids corresponding to carbon, oxygen, boron, and nitrogen, respectively. Isopropyl groups, molecules of solvation, and most hydrogens have been omitted for clarity.

ring of the boranthrene core (Figure 2.6). The ^{11}B NMR spectrum of **5** features a single resonance at 4.9 ppm, shifted over 15 ppm upfield of that for **3**. Single-crystal XRD confirmed the structure of **5** as possessing an endoperoxide core (d_{OO} = 1.4733(14) Å) similar to the NHC-stabilized boraanthracene endoperoxide reported by Piers. Analogous reactivity is observed for both CO_2 and ethylene (Figure 2.6), although these reactions are significantly slower. The CO_2 adduct $IPr_2(BA)(CO_2)$ (**6**) forms over the course of hours at 60 ºC and features ^{11}B NMR resonances at 0.95 and –8.17 corresponding to the O- and C-bound sites, respectively. The XRD structure of **6** reveals a long C–O bond (d_{CO} = 1.342(2) Å) spanning the two B atoms with a shorter, terminal C=O bond of 1.229(2) Å.[19] In contrast to **5**, the IPr coordinated to the C-bound B center is approximately orthogonal to the CO_2 moiety, presumably to accommodate the larger three-atom substrate. The isotopically enriched compound $IPr_2(BA)(^{13}CO_2)$ (**6**-^{13}C) was synthesized from $^{13}CO_2$ and confirmed the ^{13}C chemical shift of the bound CO_2 unit at 198.4 ppm in C_6D_6 (Figure 2.5.18). Formation of the ethylene adduct $IPr_2(BA)(C_2H_4)$ (**7**) is complete after 20 hours at 70 ºC under 1 atm of ethylene. The boron-bound C_2H_4 unit of **7** exhibits an upfield ^{1}H singlet at –0.81 ppm which was correlated via [^{1}H–^{13}C] HSQC experiment to a ^{13}C resonance at 17.6 ppm (Figure 2.5.27). Degassed solutions of **5**, **6**, and **7** proved stable to extended heating in contrast to the reversible binding of both CO_2 and ethylene to related diazaborinine derivatives reported by Kinjo.

The rapid rate of formation of **5** compared to **6** and **7** warrants some comment. As O_2 is smaller than both CO_2 and ethylene, a steric component may contribute to the more rapid reactivity of **3** with O_2. However, O_2 is reduced to O_2^- in acetonitrile at $E_{½}$ = –1.29 V vs. Fc/Fc^{+}[20] and is thus susceptible to outer-sphere reduction by **3** ($E_{½}$ = –1.4 V vs. Fc/Fc^{+}). Electron transfer may therefore play a role in the formation of **5**. As neither CO_2 nor ethylene are able to oxidize **3**, concerted cycloaddition mechanisms are likely to be operative in the formation of **6** and **7**.

2.3) Concluding Remarks

In conclusion, we have prepared an NHC-stabilized boranthrene (**3**) and its one- and two-electron oxidized congeners. Boranthrene **3** reacts with a range of unsaturated molecules including O_2, CO_2, and ethylene via formal [4+2] cycloaddition to the diborabutadiene core. Although [IPr_2(BA)] is composed entirely of light elements, it features many of the properties of transition metal complexes that make them attractive targets for small molecule activation: multi-electron redox chemistry at mild potentials, reversible ligand binding, and reactivity with important small molecule substrates. B-doped graphene (BDG) has shown great promise for electrochemical energy storage.[21] As a molecular analogue of BDG or "nanographene,"[22] the chemistry [IPr_2(BA)]^n and related

systems may provide insight the operation and design of boron-doped planar carbon materials.

2.4) Experimental Section

2.4.1) General Considerations

Unless otherwise noted, all manipulations were carried out using standard Schlenk or glovebox techniques under a N_2 atmosphere. Hexanes, benzene, toluene, and acetonitrile were dried and deoxygenated by argon sparge followed by passage through activated alumina in a solvent purification system from JC Meyer Solvent Systems followed by storage over 4 Å molecular sieves. THF and Et_2O were distilled from sodium-benzophenone ketyl under N_2 followed by storage over 4Å molecular sieves for at least 24 hours prior to use. Non-halogenated and non-nitrile containing solvents were tested with a standard purple solution of sodium benzophenone ketyl in THF to confirm effective oxygen and moisture removal prior to use. Hexamethyldisiloxane (HMDSO) was distilled from sodium metal and stored over 4Å molecular sieves for 24 hours prior to use. All reagents were purchased from commercial suppliers and used without further purification unless otherwise noted. 9,10-dibromo-9,10-diboraanthracene (9,10-Br_2-DBA),[23] 1,3-bis(2,6-diisopropylphenyl)imidazol-2-ylidene (IPr),[24] and Rieke magnesium[25] were synthesized according to literature procedures. Elemental analyses were performed by Midwest Microlab, LLC, Indianapolis, IN. Deuterated

solvents were purchased from Cambridge Isotope Laboratories Inc., degassed, and dried over activated 3Å molecular sieves for at least 24 h prior to use. Dry air used for the synthesis of **5** was generated by passage of air through a sulfuric acid bubbler followed by passage through a drying tube packed with P_2O_5. NMR spectra were recorded on Varian Inova 500 MHz, Bruker Avance 600 MHz, and Bruker Avance 700 MHz spectrometers. ^{1}H and ^{13}C chemical shifts are reported in ppm relative to tetramethylsilane using residual solvent as an internal standard. ^{11}B chemical shifts are reported in ppm relative to $BF_3 \cdot Et_2O$. Original ^{11}B NMR spectra were processed using MestReNova 10.0.2 with a backwards-linear prediction applied to eliminate background signal from the borosilicate NMR tube.[26] For ^{11}B NMR spectra with peaks overlapping the borosilicate signal, a manual baseline correction was applied. EPR X-band spectra were obtained on a Bruker EMX spectrometer with the aid of Bruker Win-EPR software suite version 3.0. EPR spectral simulations were performed using the Easyspin software suite.[27] UV-Vis spectra were recorded using a Cary Bio 500 spectrometer using a 1 cm path length quartz cuvette with a solvent background subtraction applied. IR spectra were recorded using a Bruker Alpha FT-IR with a universal sampling module collecting at 4 cm^{-1} resolution with 32 scans. X-ray diffraction studies were performed using a Bruker-AXS diffractometer. Cyclic Voltammetry (CV) experiments were performed using a Pine AFP1 potentiostat. The cell consisted of a glassy carbon working electrode, a Pt wire auxiliary

electrode and a Pt wire pseudo-reference electrode. All potentials are referenced vs. the Fc/Fc^+ couple measured as an internal standard.

2.4.2) $IPr_2(BA)Br_2$ (1).

IPr (0.885 g, 2.28 mmol) and Br_2-DBA (0.362 g, 1.09 mmol) were added as solids to a 20 mL vial and placed in a liquid nitrogen cooled bath. Toluene (8 mL) was cooled to –78 °C and added to the vial containing the two solids. The mixture was allowed to warm to room temperature and stirred for 2 hours during which time a microcrystalline, colorless solid separated. Hexane (2 mL) was added to aid precipitation and stirring continued for several more minutes. The product was collected by filtration and quickly washed with toluene (2 mL) then Et_2O (5 mL) and dried in vacuo. Overall yield: 0.819 g, 68%. X-ray quality crystals of **1** were grown by layering a concentrated THF solution with Et_2O and letting stand at –15 °C. X-ray quality crystals of the acetonitrile adduct $[IPr_2(BA)(CH_3CN)_2][Br]_2$ (**2**) were grown by dissolving **1** in minimal MeCN (ca. 1 mL/0.05g) and cooling to –15 °C overnight. ^1H NMR (600 MHz, THF-d_8, –50 °C) δ 7.73 (s, 1H), 7.67 (s, 1H), 7.43 (t, J = 7.5 Hz, 1H), 7.31 (d, J = 7.7 Hz, 2H), 7.27 (s, 4H), 7.25 (s, 2H), 7.03 (d, J = 7.6 Hz, 2H), 6.84 (d, J = 6.8 Hz, 2H), 6.78 (t, J = 7.6 Hz, 1H), 6.69 (dd, J = 6.4, 1.9 Hz, 2H), 6.64 (d, J = 7.7 Hz, 2H), 6.27 (t, J = 6.9 Hz, 2H), 5.71 (t, J = 7.3 Hz, 2H), 3.62 (dq, J = 13.0, 6.5 Hz, 2H), 3.28 (dq, J = 13.2, 6.7 Hz, 2H), 2.66 (dq, J = 13.0, 6.3 Hz, 2H), 1.77 (dq, J = 13.4, 6.4 Hz, 2H), 1.59 (d, J = 6.1 Hz, 2H), 1.54 (d, J = 6.2 Hz, 2H), 1.22 (d, J = 5.9 Hz, 2H), 1.06 (d, J = 6.6 Hz,

2H), 0.85 (d, J = 5.8 Hz, 2H), 0.66 (d, J = 6.3 Hz, 2H), 0.55 (d, J = 6.7 Hz, 2H), 0.48 (d, J = 5.8 Hz, 2H). $^{11}B\{^1H\}$ (192 MHz, THF-d_8, –50 °C) δ –3.58 (bs). $^{13}C\{^1H\}$ NMR (151 MHz, THF-d_8, –50 °C) δ 170.5, 165.0, 152.4, 148.4, 146.8 (d, J = 78.9 Hz), 146.2 (d, J = 75.6 Hz), 139.5, 138.6, 138.3 (d, J = 40.2 Hz), 132.8, 130.6, 130.2, 129.9, 129.2, 128.9, 126.6, 126.3, 124.3 (d, J = 32.7 Hz), 124.2, 124.1 (d, J = 52.0 Hz), 122.0, 35.6, 33.1, 31.2, 31.0, 30.3, 29.7, 29.3, 28.6, 27.1, 26.9, 26.4, 26.1, 24.5, 24.0, 23.4, 22.4, 21.8, 15.0. Anal. Calcd. for $C_{66}H_{80}B_2Br_2N_4$: C, 71.36 H, 7.26 N, 5.04. Found: C, 71.55 H, 7.36 N, 4.95.

2.4.3) IPr_2(BA) (3).

A single portion of Rieke magnesium (0.097 g, 10 mol. eq.) was added to a slurry of **1** (0.441 g, 0.397 mmol) in Et_2O (7 mL). The mixture was stirred vigorously for 5 hours during which time the reaction became dark black-green. The mixture was filtered through a pad of celite and the solvent removed *in vacuo.* The residue was extracted with benzene (2 x 4 mL), filtered again through a celite pad and diluted with half a volume of acetonitrile. The solution was concentrated to ca. 3 mL *in vacuo* and the resulting crystalline precipitate collected by filtration, washed with acetonitrile (1 mL) and dried *in vacuo*. Several additional crops were obtained by concentrating the mother liquor *in vacuo*. Overall yield: 0.357 g, 94%. X-ray quality crystals were grown by layering a concentrated benzene solution with HMDSO. ^1H NMR (600 MHz, toluene-d_8, –50 °C) δ 7.71 (s, 4H), 7.04 (t, *J* = 7.5 Hz, 4H), 6.96 (s, 4H), 6.81 (d, *J* = 7.7 Hz, 8H), 6.70 (s, 4H), 3.38 (sept, *J* =

6.3, Hz, 8H), 1.00 (d, J = 6.2 Hz, 24H), 0.80 (d, J = 5.9 Hz, 24H). $^{11}B\{^1H\}$ (160 MHz, C_6D_6, 25 °C) δ 20.1 (bs). $^{13}C\{^1H\}$ (125 MHz, C_6D_6, 25 °C) δ 145.6, 145.4, 135.0, 133.1, 128.9, 124.1, 122.8, 116.4, 29.1, 26.6, 22.2. UV-vis (THF): λ_{max} (nm) (ε_{max} ($M^{-1}cm^{-1}$)) 314 (sh, 8.3 x 10^4), 417 (sh, 1.1 x 10^5), 450 (1.2 x 10^5), 517 (sh, 1.4 x 10^5), 680 (1.8 x 10^5), 727 (1.9 x 10^5), 865 (2.3 x 10^5), 910 (2.4 x 10^5). Anal. Calcd. for $C_{66}H_{80}B_2N_4$ (2 x MeCN): C, 81.28 H, 8.39 N, 8.13. Found: C, 80.93 H, 8.62 N, 8.01.

2.4.4) [IPr_2(BA)][Br] (4).

To a slurry of **1** (0.049 g, 0.044 mmol) in toluene (1 mL) was added a solution of **3** (0.042 g, 1 mol.eq.) in toluene (1 mL). The mixture was stirred for 1 hour during which time a golden-brown crystalline solid separated. The solvent was decanted and the golden/brown solid rinsed with toluene (2 mL) before being dried *in vacuo*. The solid was dissolved in the minimum CH_2Cl_2 (ca. 2 mL), filtered through a pad of celite, then diluted with toluene (6 mL). Concentration of the solution to ca. 5 mL *in vacuo* caused the product to crystallize. The toluene was decanted, the golden crystals rinsed with toluene (1 mL) and dried *in vacuo*. Yield: 0.074 g, 81%. X-ray quality crystals were grown by layering a concentrated THF solution with toluene at –15 °C. UV-vis (THF): λ_{max} (nm) (ε_{max} ($M^{-1}cm^{-1}$)) 315 (sh, 1.2 x 10^5), 363 (sh, 1.4 x 10^5), 393 (1.5 x 10^5), 412 (1.6 x 10^5), 515 (sh, 2.0 x 10^5), 645 (sh, 2.5 x 10^5), 708 (sh, 2.7 x 10^5), 765 (2.9 x 10^5), 864 (3.3 x

10^5). Anal. Calcd. for $C_{66}H_{80}B_2BrN_4$: C, 76.90 H, 7.82 N, 5.43. Found: C, 77.15 H, 7.91 N, 5.12.

2.4.5) $IPr_2(BA)(O_2)$ (5).

A solution of **3** (0.050 g, 0.053 mmol) in benzene (10 mL) was subjected to three freeze-pump-thaw cycles before adding 1 atm. of dry air (*vide supra*). After 5 minutes volatiles were removed *in vacuo* to afford the product as a pale-yellow solid. Yield: 0.47 g, 92%. Recrystallization from THF/HMDSO gave an analytical sample. X-ray quality crystals were grown by slow evaporation of a hexanes:HMDSO (1:10) solution. ^{1}H NMR (500 MHz, C_6D_6) δ 7.25 (t, J = 7.7 Hz, 4H), 7.06 (d, J = 7.6 Hz, 8H,), 6.75 (dd, J = 4.6 Hz, 4H), 6.34 (s, 4H), 6.12 (bs, 4H), 2.92 (bs, 8H), 1.07 (d, J = 5.2 Hz, 24H) 0.82 (d, J = 7.1 Hz, 24H). ^{11}B{^{1}H} (160 MHz, C_6D_6) δ 4.93. ^{13}C{^{1}H} NMR (176 MHz, C_6D_6) 146.0, 137.9, 129.5, 128.6, 126.8, 124.6, 124.1, 121.3, 29.0, 25.4, 24.0. UV-vis (THF): λ_{max} (nm) (ε_{max} ($M^{-1}cm^{-1}$)) 330 (1.0 x 10^5), 380 (sh, 1.2 x 10^5), 912 (2.8 x 10^5). Anal. Calcd. for $C_{66}H_{80}B_2N_4O_2 \cdot C_4H_8O$: C, 79.68 H, 8.41 N, 5.31. Found: C, 80.03 H, 8.38 N, 5.56.

2.4.6) $IPr_2(BA)(CO_2)$ (6).

A solution of **3** (0.050 g, 0.053 mmol) in toluene (10 mL) was subjected to three freeze-pump-thaw cycles before adding 1 atm. CO_2. The reaction was heated at 60 °C for 8 hours during which time the reaction became colorless. Volatiles were removed *in vacuo* to afford the product as a colorless solid. Yield: 0.048 g, 92 %.

X-ray quality crystals were grown by layering a concentrated THF solution with HMDSO. ^{1}H NMR (500 MHz, C_6D_6, 25 °C) δ 7.26 (t, *J* = 7.6 Hz, 2H), 7.18 (t, *J* = 7.6 Hz, 2H), 7.11 (d, *J* = 7.1 Hz, 4H), 7.00 (bs, 4H), 6.48 (s, 2H), 6.45 (t, *J* = 7.4 Hz, 2H), 6.40 (s, 4H), 6.39 (s, 2H), 6.34 (t, *J* = 7.4 Hz, 2H), 6.02 (bs, 2H), 3.75 (bs, 2H), 3.06 (bs, 4H), 2.77 (bs, 2H), 1.04 (dd, *J* = 7.2 Hz, 42H), 0.74 (bs, 6H). ^{11}B{^{1}H} (160 MHz, C_6D_6) δ 0.95, –8.17. ^{13}C{^{1}H} NMR (151 MHz, C_6D_6) 198.4, 175.6, 174.0, 156.7, 148.2, 146.1, 138.4, 137.4, 130.2 (d, J = 20 Hz), 129.0 (d, J = 15 Hz), 126.9 (d, J = 17 Hz), 125.5 (d, J = 14 Hz), 125.2 (d, J =19 Hz), 124.6 (d, J =16 Hz), 123.4, 120.2, 116.1, 29.1, 27.9, 26.3, 25.5, 24.0, 23.4. FTIR: ν_{max} (cm^{-1}) 1655 (C=O). Anal. Calcd. for $C_{67}H_{80}B_2N_4O_2 \cdot C_7H_8$: C, 81.76 H, 8.16 N, 5.15. Found: C, 81.82 H, 8.24 N, 5.00.

2.4.7) IPr$_2$(BA)(^{13}CO$_2$) (6-^{13}C).

The ^{13}C-labeled compound was synthesized similarly to **6** using $^{13}CO_2$. ^{1}H and ^{11}B NMR data was identical to **6**. No ^{13}C-^{11}B coupling could be resolved in the ^{11}B NMR spectrum at 25 °C, likely due to the broadness of the ^{11}B resonances (See Figure 2.6.17). The isotopically enriched carbon appears at 198.4 ppm in the ^{13}C NMR spectrum.

2.4.8) IPr2(BA)(C2H4) (7).

A solution of **3** (0.050 g, 0.053 mmol) in benzene (10 mL) was subjected to three freeze-pump-thaw cycles before adding 1 atm. of ethylene. The reaction was heated at 70 °C for 20 hours during which time the reaction became colorless.

Volatiles were removed *in vacuo* to afford the product as a colorless solid. Yield: 0.045 g, 88 %. X-ray quality crystals were grown by layering a concentrated THF solution with HMDSO. ^{1}H NMR (600 MHz, C_6D_6) δ 7.11–6.63 (bs, 12H), 6.83 (dd, J = 5.0, 3.4 Hz, 4H), 6.76 (dd, J = 5.0, 3.4 Hz, 4H), 6.63–6.31 (bs, 4H), 3.31 (bs, 8H), 1.03 (d, J = 6.8 Hz, 4H), 0.91 (bs, 24H), –0.81 (s, 4H). ^{11}B{^{1}H} (160 MHz, C_6D_6) δ –9.80 (bs). ^{13}C{^{1}H} NMR (176 MHz, C_6D_6) 183.6, 159.0, 147.0, 145.4, 137.2, 129.8, 127.7, 125.8, 124.0, 122.8, 119.9, 29.3, 27.3, 26.2, 23.4, 22.0, 17.7. Anal. Calcd. for $C_{68}H_{84}B_2N_4$: C, 83.42 H, 8.65 N, 5.72. Found: C, 83.32 H, 8.73 N, 5.64.

2.5) Spectroscopic Data

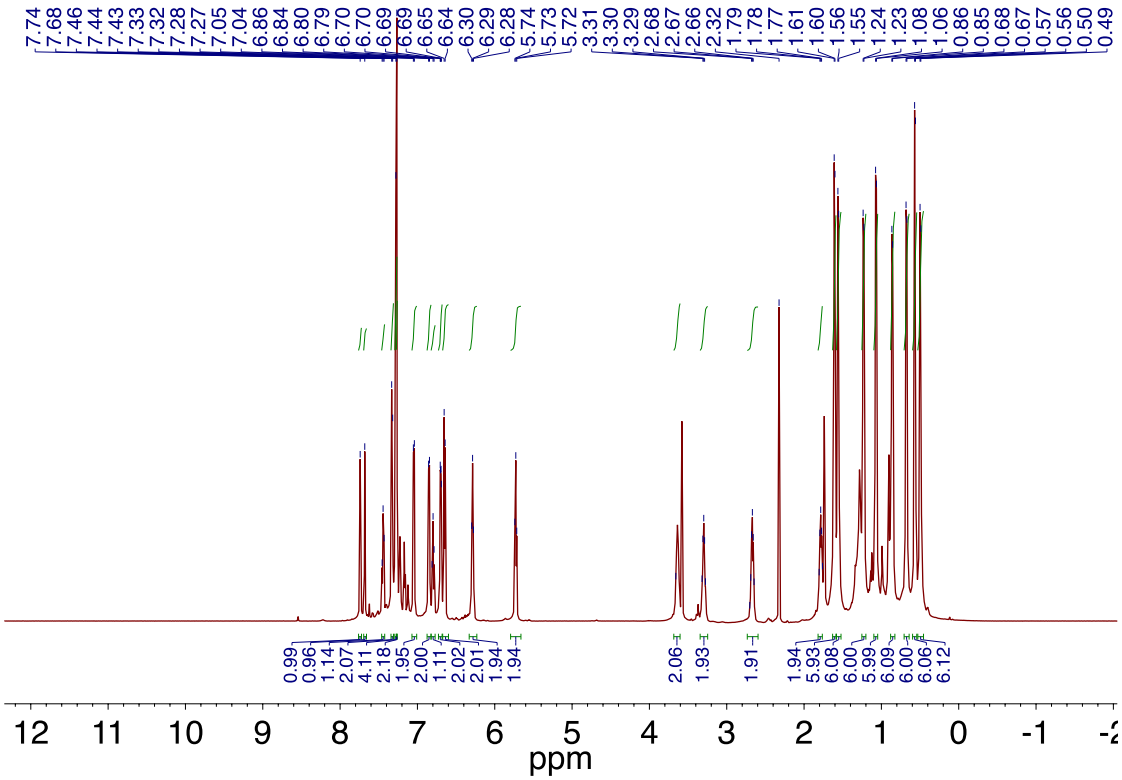

Figure 2.5.1. ^{1}H NMR spectrum of **$IPr_2(BA)Br_2$** recorded at 600 MHz in THF-d_8 at –50 °C.

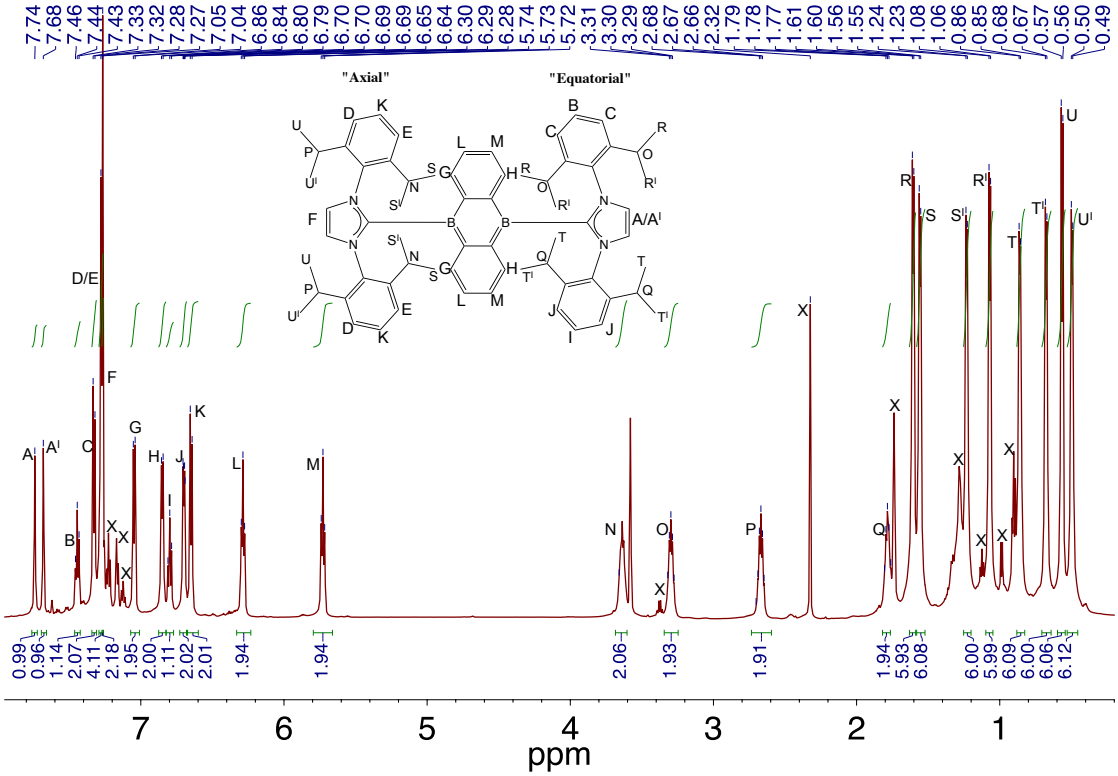

Figure 2.5.2. ^{1}H NMR spectrum of **IPr$_2$(BA)Br$_2$** recorded at 600 MHz in THF-d_8 at –50 °C. Letter-labels, "A–U", denote unique protons in the molecule as labeled. Prime labels denote protons that are chemically similar but were unable to be unambiguously assigned. Peaks labeled "X" denote residual solvent. The bromine atoms attached to each boron have been excluded in the inlayed diagram for clarity.

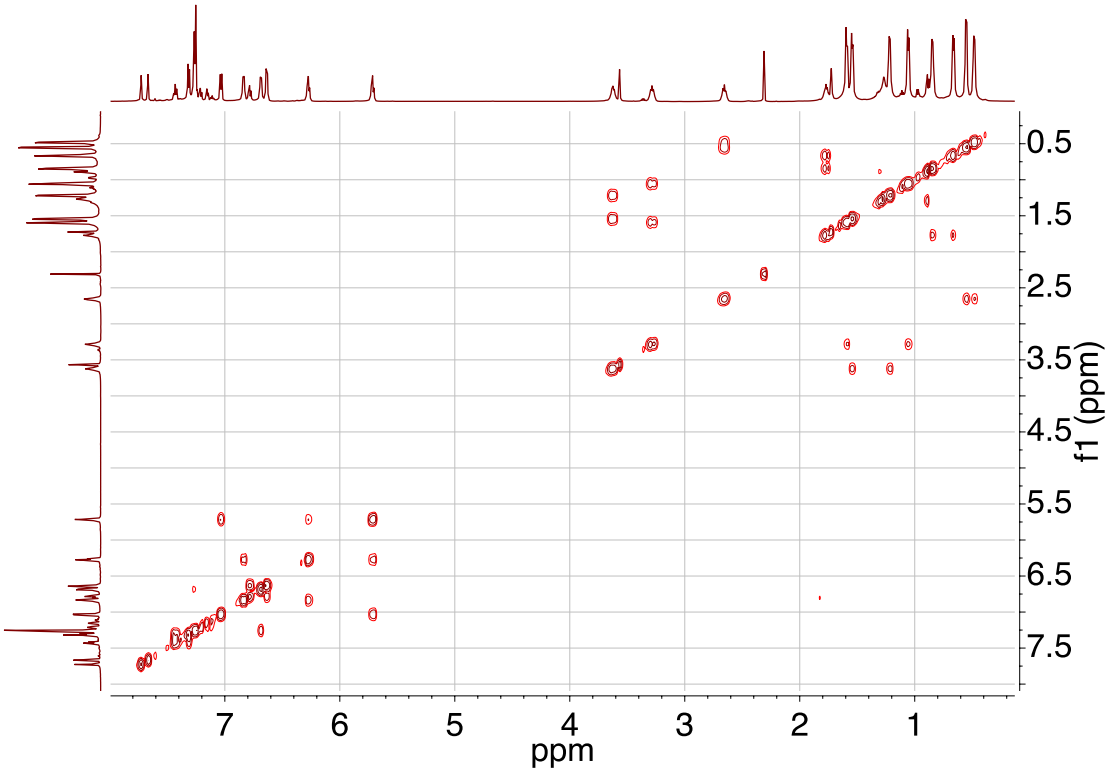

Figure 2.5.3. ^{2}D[^{1}H-^{1}H]-COSY spectrum of **IPr$_2$(BA)Br$_2$** recorded at 600 MHz in THF-d_8 at –50 °C.

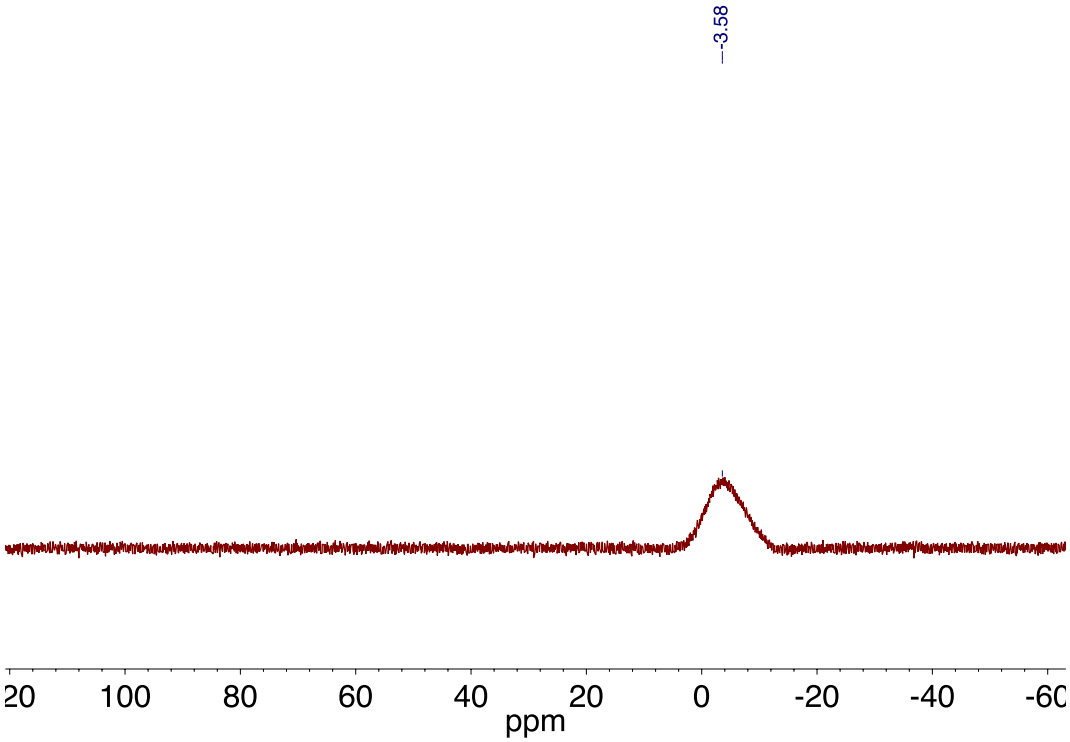

Figure 2.5.4. ^{11}B NMR spectrum of **IPr$_2$(BA)Br$_2$** recorded at 193 MHz in THF-d_8 at –50 °C.

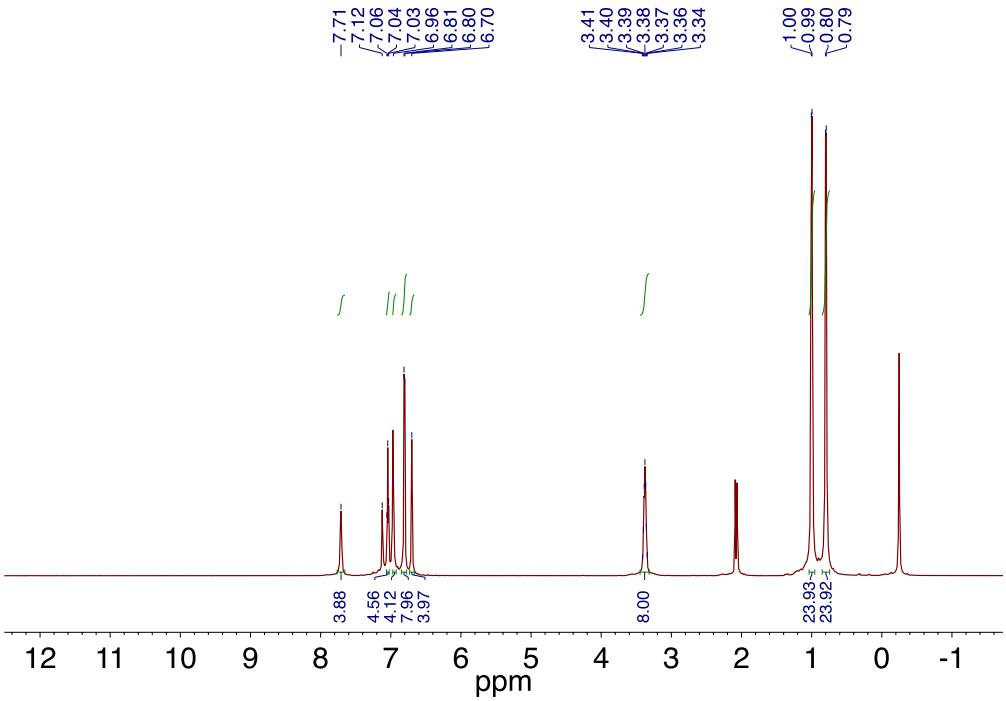

Figure 2.5.5. ^{1}H NMR spectrum of **IPr$_2$(BA)** recorded at 600 MHz in toluene-d_8 at –50 °C.

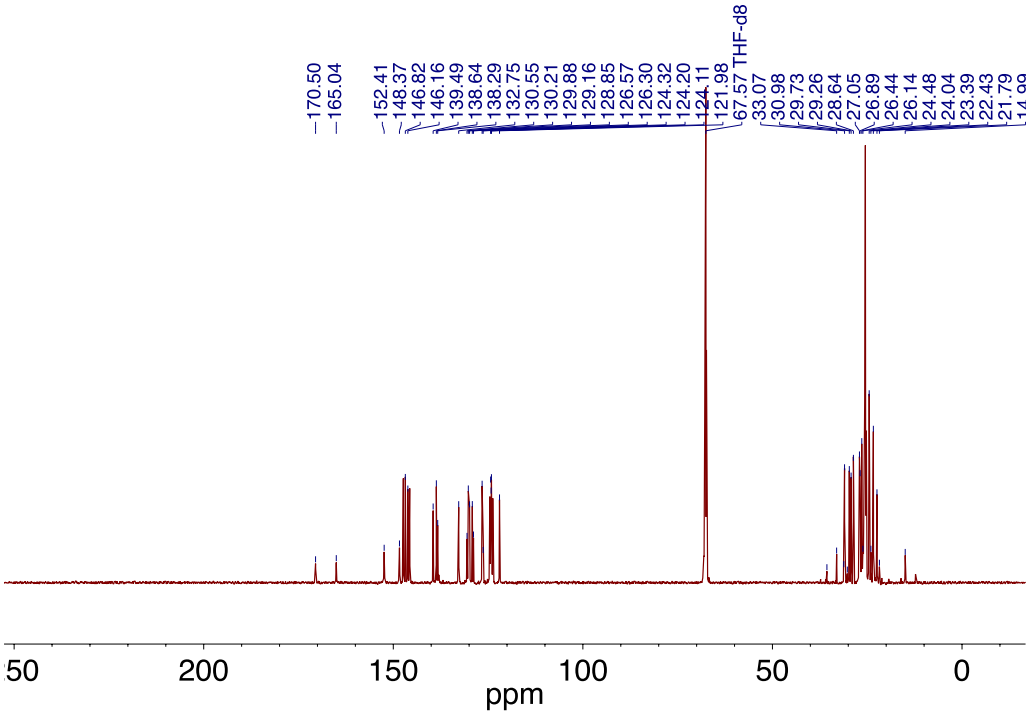

Figure 2.5.6. ^{13}C NMR spectrum of **IPr$_2$(BA)Br$_2$** recorded at 151 MHz in THF-d_8 at –50 °C.

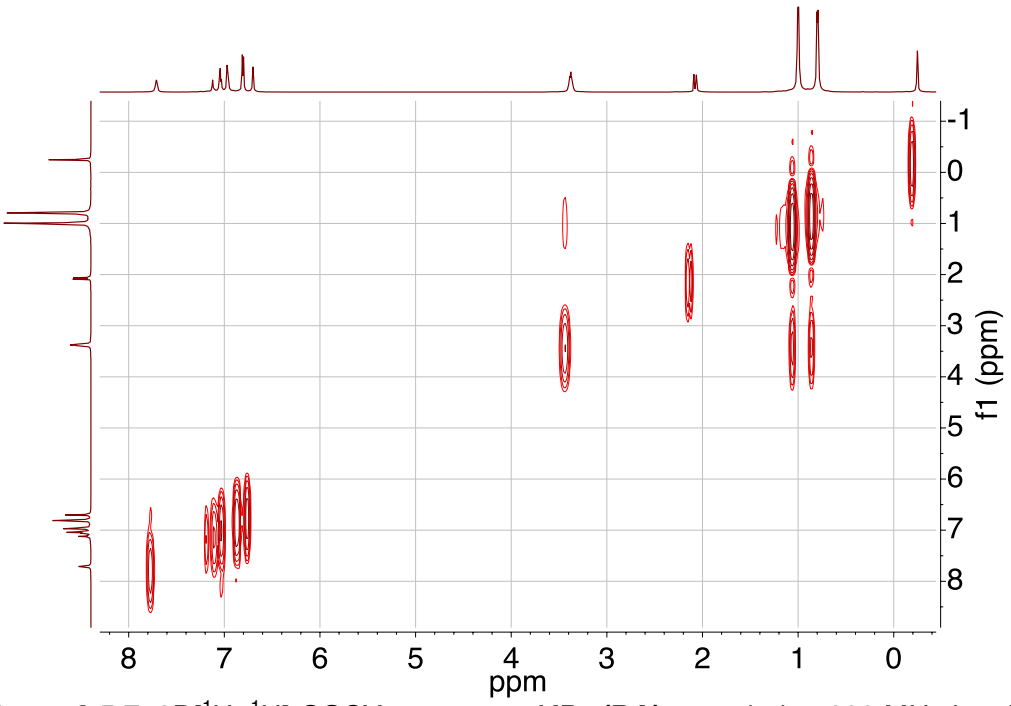

Figure 2.5.7. 2D[^{1}H–^{1}H]-COSY spectrum of **IPr$_2$(BA)** recorded at 600 MHz in toluene-d_8 at –50 °C.

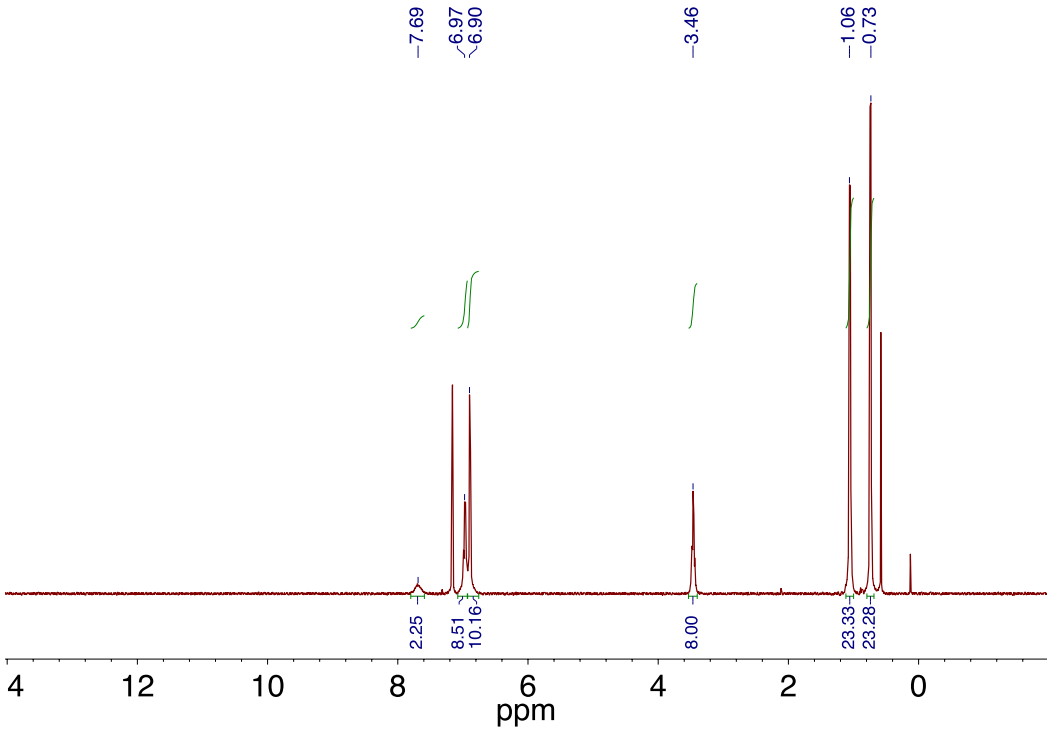

Figure 2.5.8. ^{1}H NMR spectrum of **IPr$_2$(BA)** recorded at 500 MHz in C_6D_6 at 25 °C.

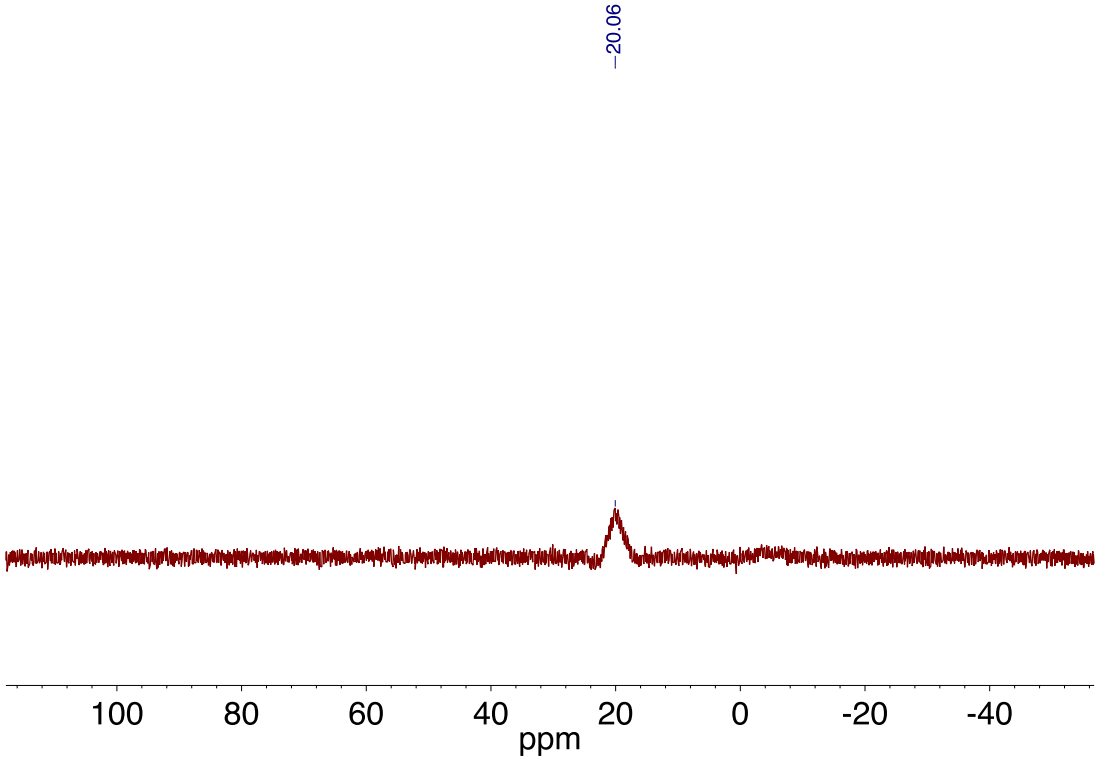

Figure 2.5.9. ^{11}B NMR spectrum of **IPr$_2$(BA)** recorded at 160 MHz in C_6D_6 at 25 °C.

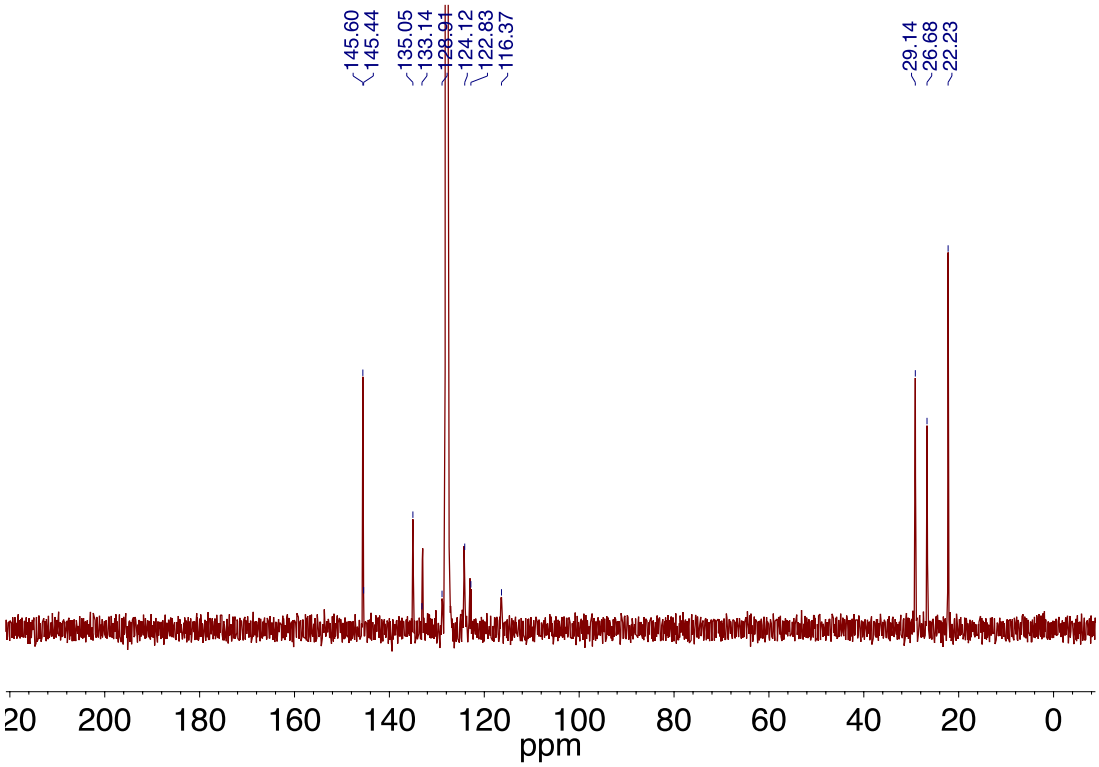

Figure 2.5.10. ^{13}C NMR spectrum of **IPr_2(BA)** recorded at 176 MHz in C_6D_6 at 25 °C.

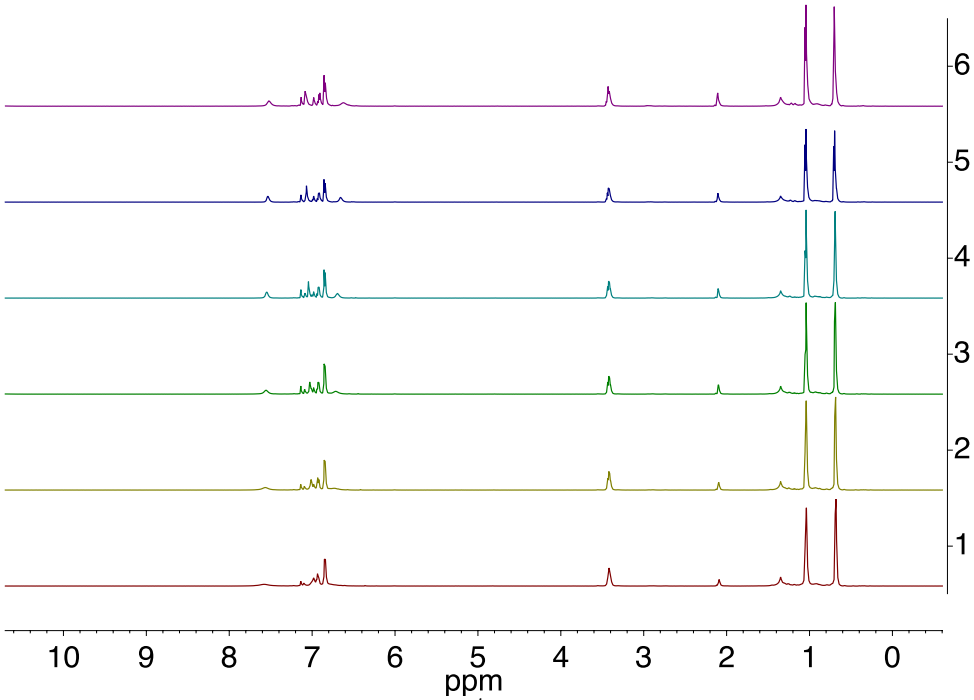

Figure 2.5.11. Variable Temperature ^1H NMR spectrum of **IPr_2(BA)** recorded at 600 MHz in toluene-d_8. Spectra 1–6 were collected at 25, 40, 60, 80, and 100 °C, respectively.

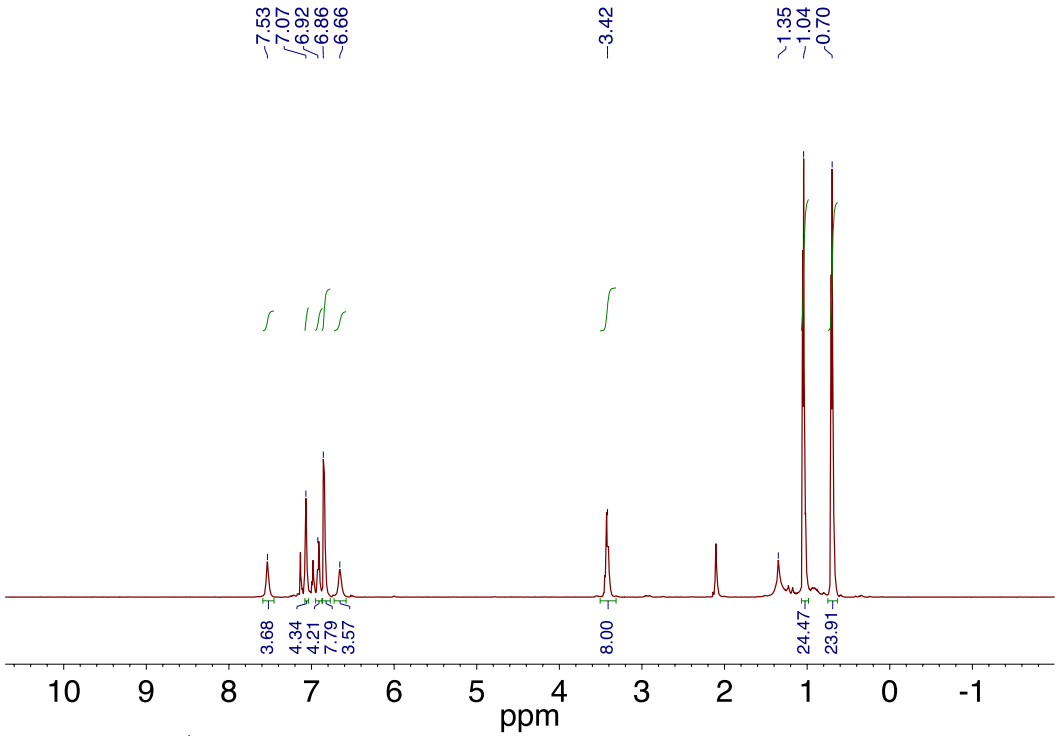

Figure 2.5.12. ^{1}H NMR spectrum of **IPr_2(BA)** recorded at 600 MHz in toluene-d_8 at 80 °C.

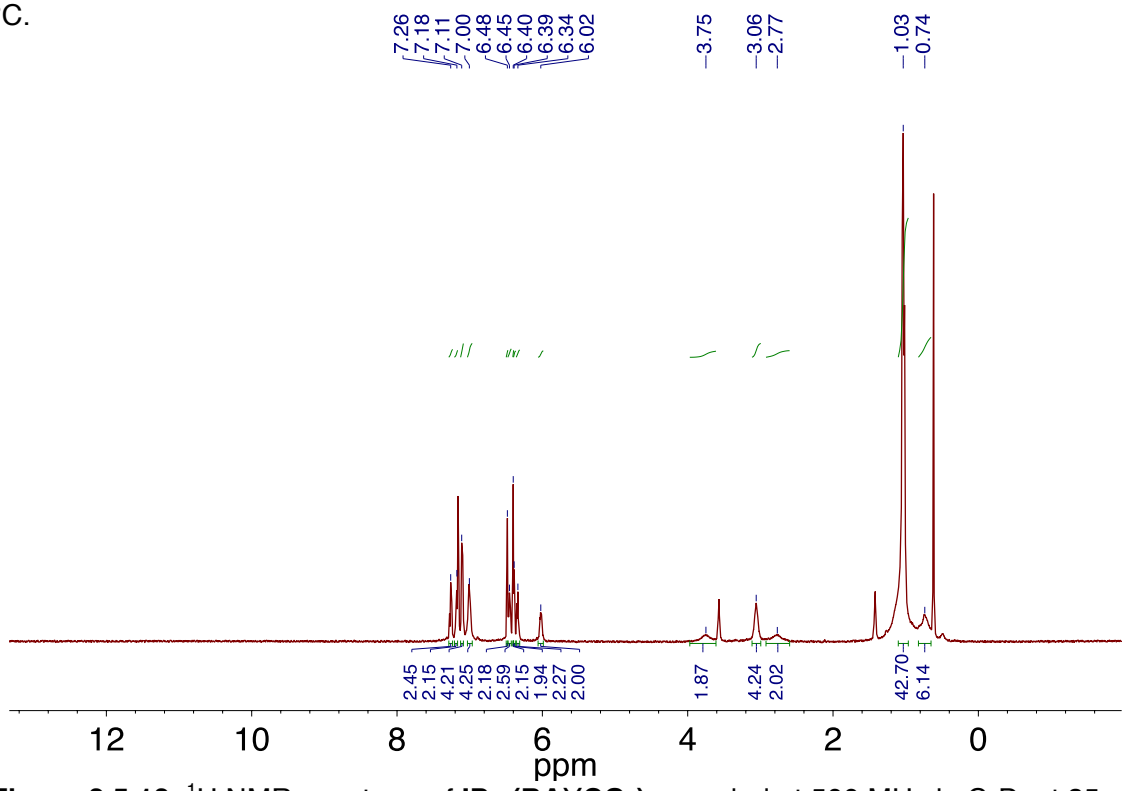

Figure 2.5.13. ^{1}H NMR spectrum of **IPr_2(BA)(CO_2)** recorded at 500 MHz in C_6D_6 at 25 °C.

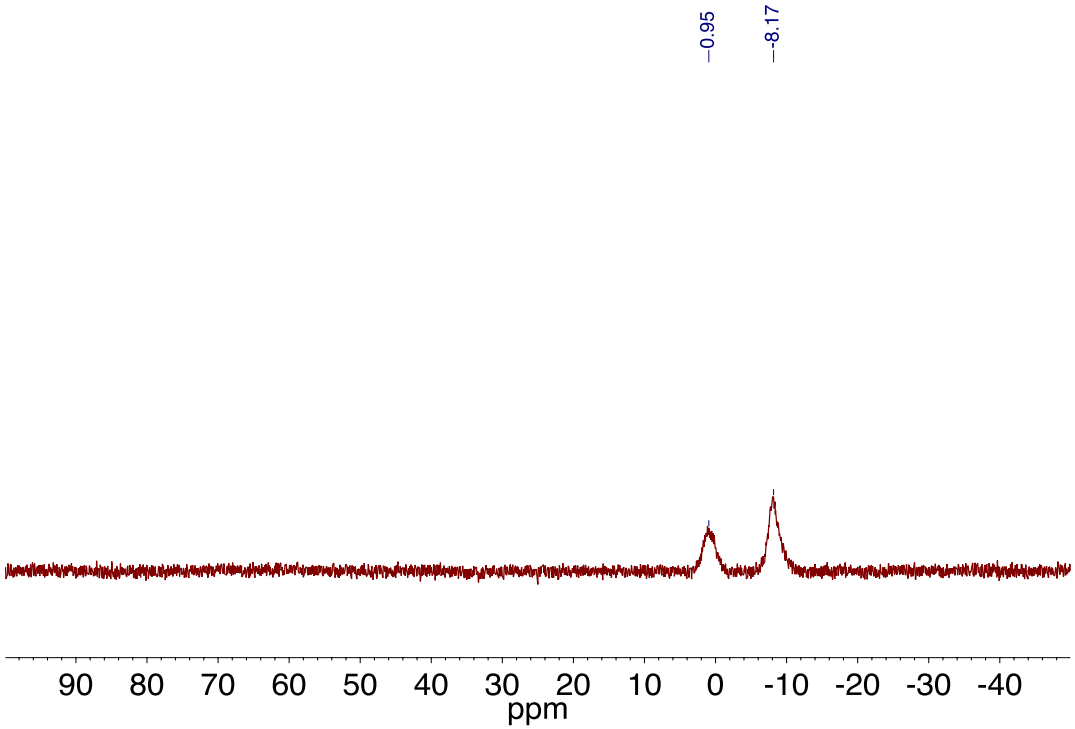

Figure 2.5.14. ^{11}B NMR spectrum of **$IPr_2(BA)(CO_2)$** recorded at 160 MHz in C_6D_6 at 25 °C.

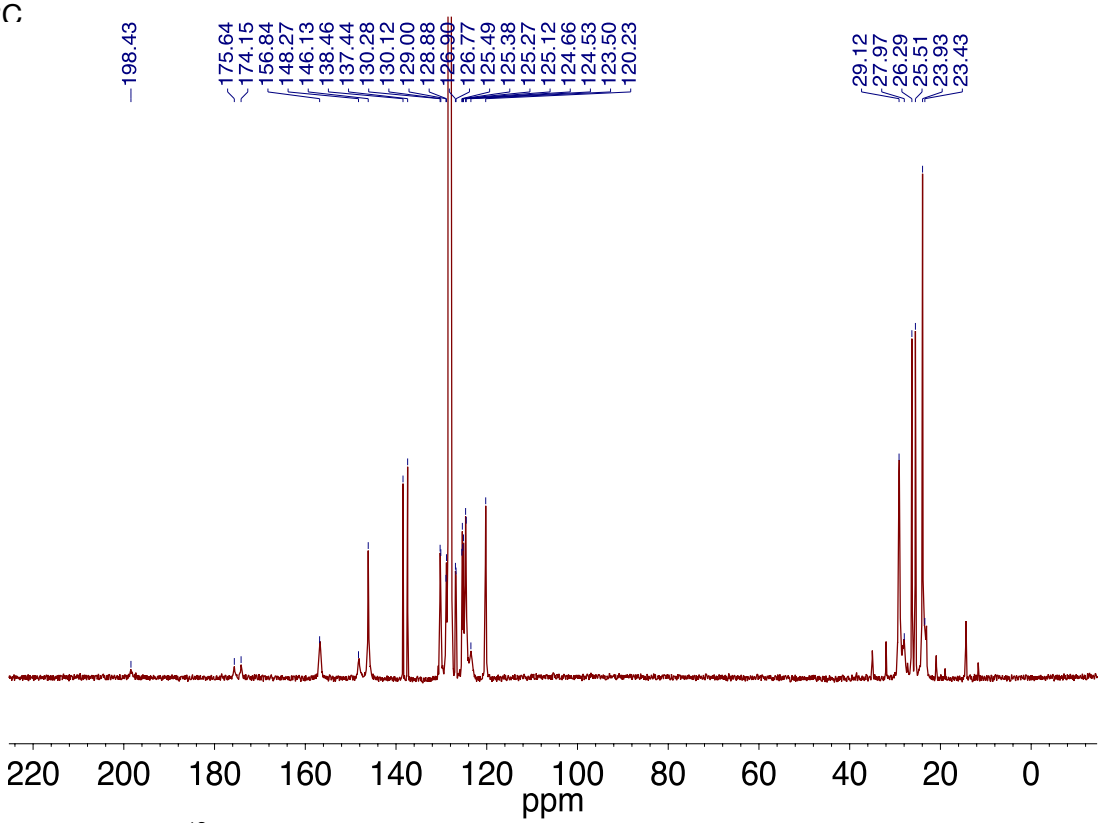

Figure 2.5.15. ^{13}C NMR spectrum of **$IPr_2(BA)(CO_2)$** recorded at 176 MHz in C_6D_6 at 25 °C.

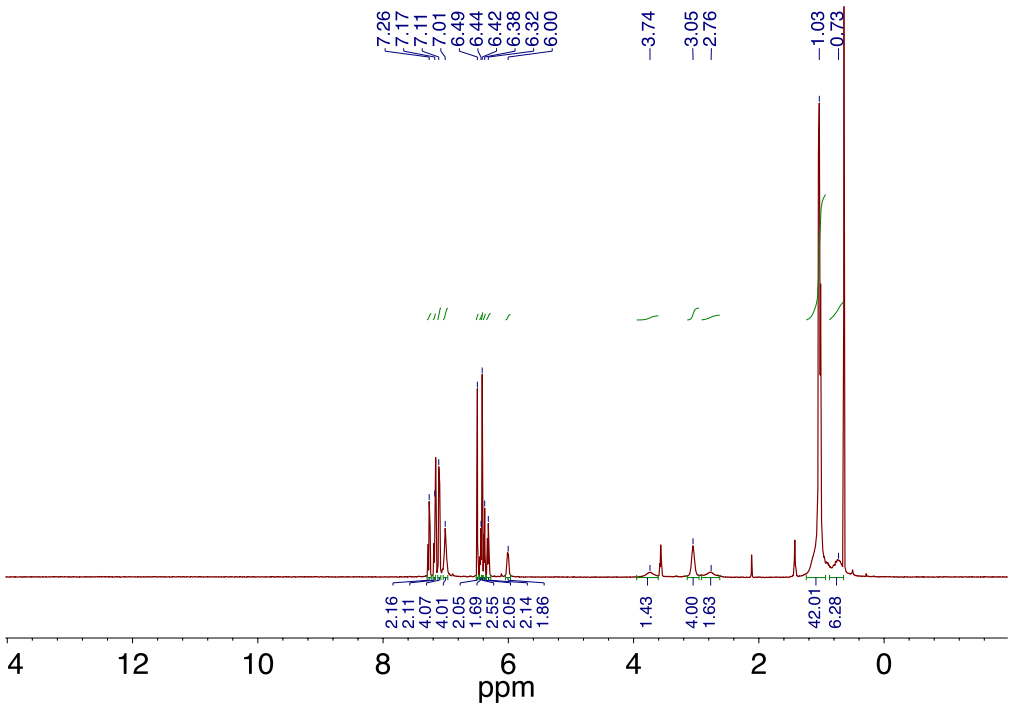

Figure 2.5.16. ^{1}H NMR spectrum of **IPr$_2$(BA)(^{13}CO$_2$)** recorded at 500 MHz in C_6D_6 at 25 °C.

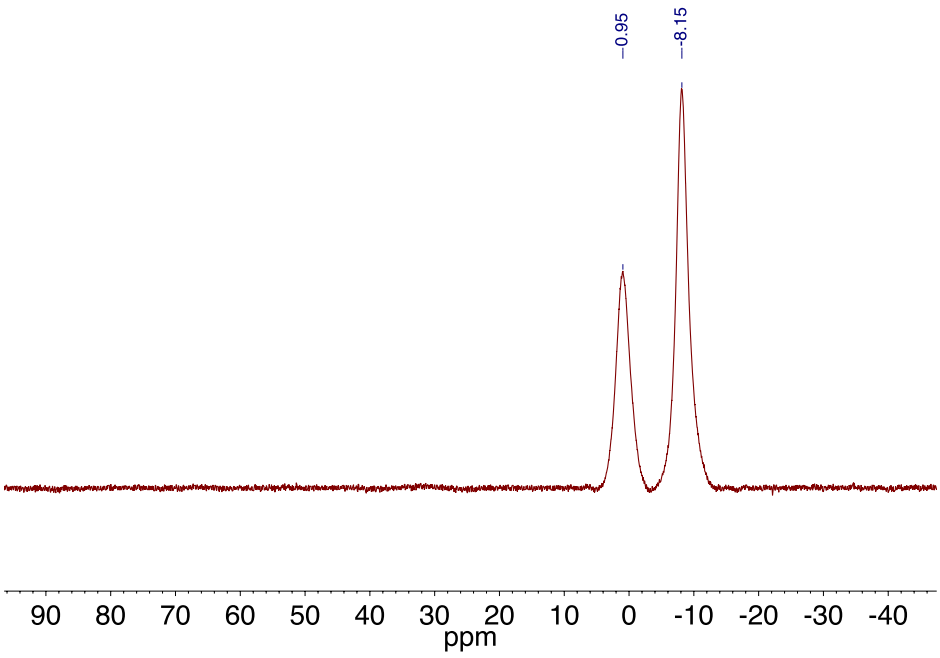

Figure 2.5.17. ^{11}B NMR spectrum of **IPr$_2$(BA)(^{13}CO$_2$)** recorded at 160 MHz in C_6D_6 at 25 °C.

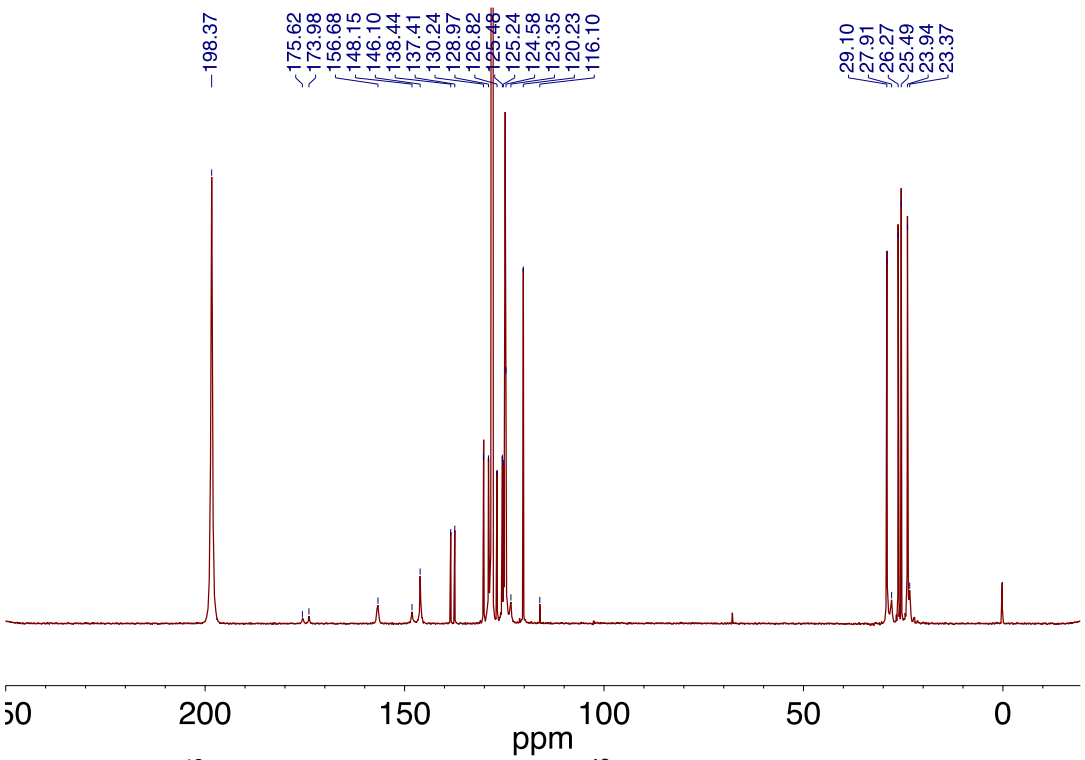

Figure 2.5.18. ^{13}C NMR spectrum of **IPr$_2$(BA)(^{13}CO$_2$)** recorded at 151 MHz in C_6D_6 at 25 °C.

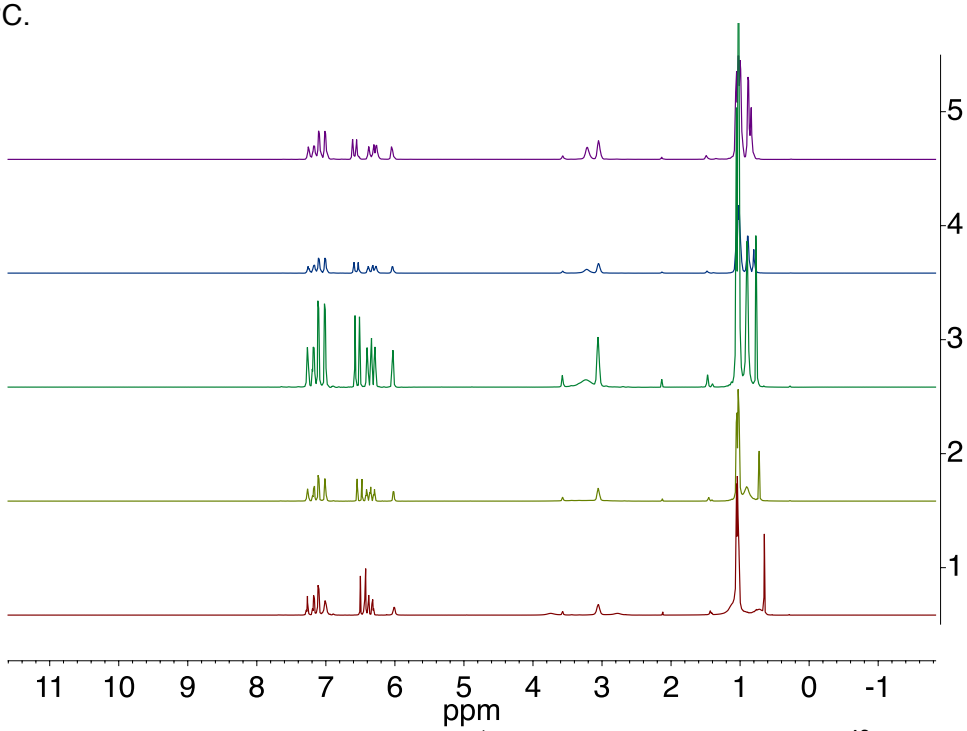

Figure 2.5.19. Variable Temperature ^{1}H NMR spectra of **IPr$_2$(BA)(^{13}CO$_2$)** recorded at 600 MHz in C_6D_6. Spectra 1–5 were collected at 25, 40, 50, 60, and 70 °C, respectively.

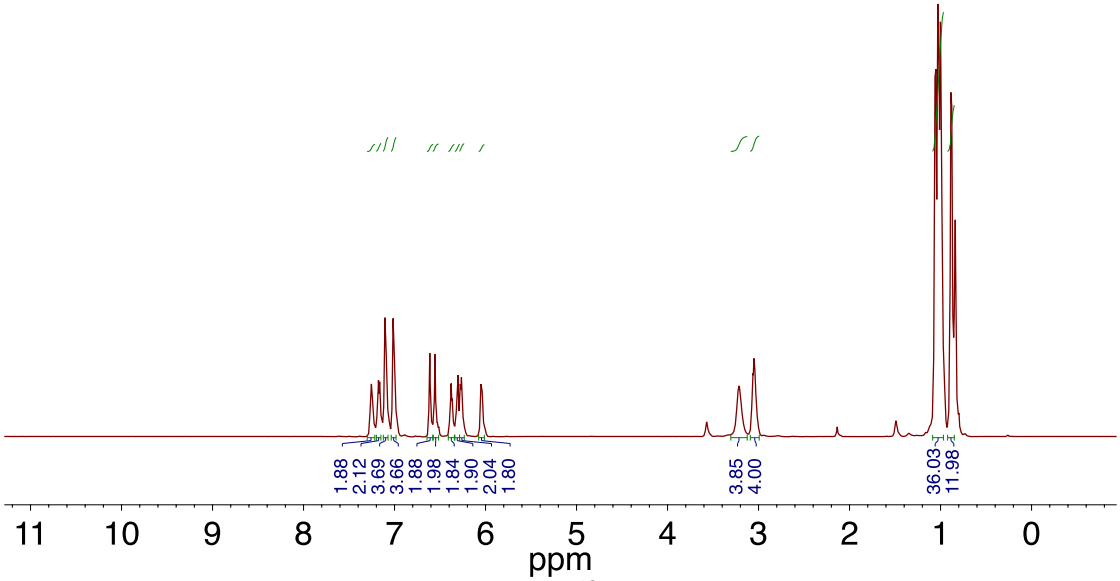

Figure 2.5.20. ^{1}H NMR spectrum of **$IPr_2(BA)(^{13}CO_2)$** recorded at 600 MHz in C_6D_6 at 70 °C.

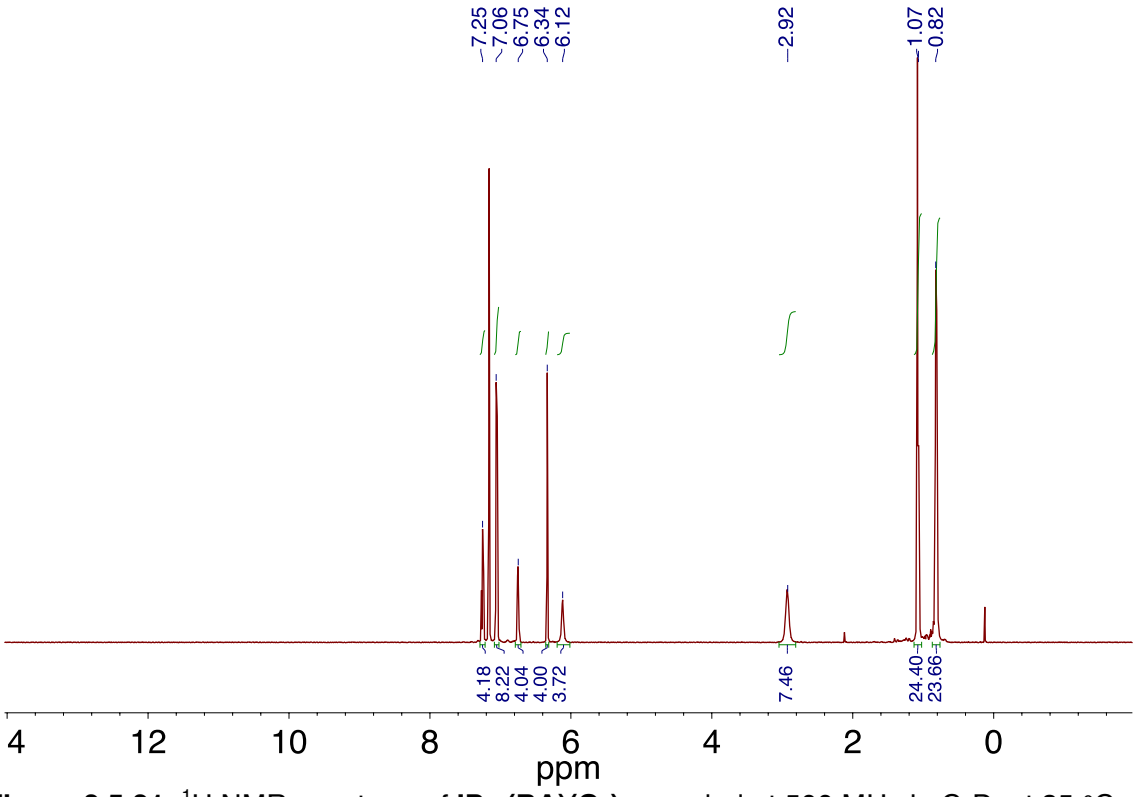

Figure 2.5.21. ^{1}H NMR spectrum of **$IPr_2(BA)(O_2)$** recorded at 500 MHz in C_6D_6 at 25 °C.

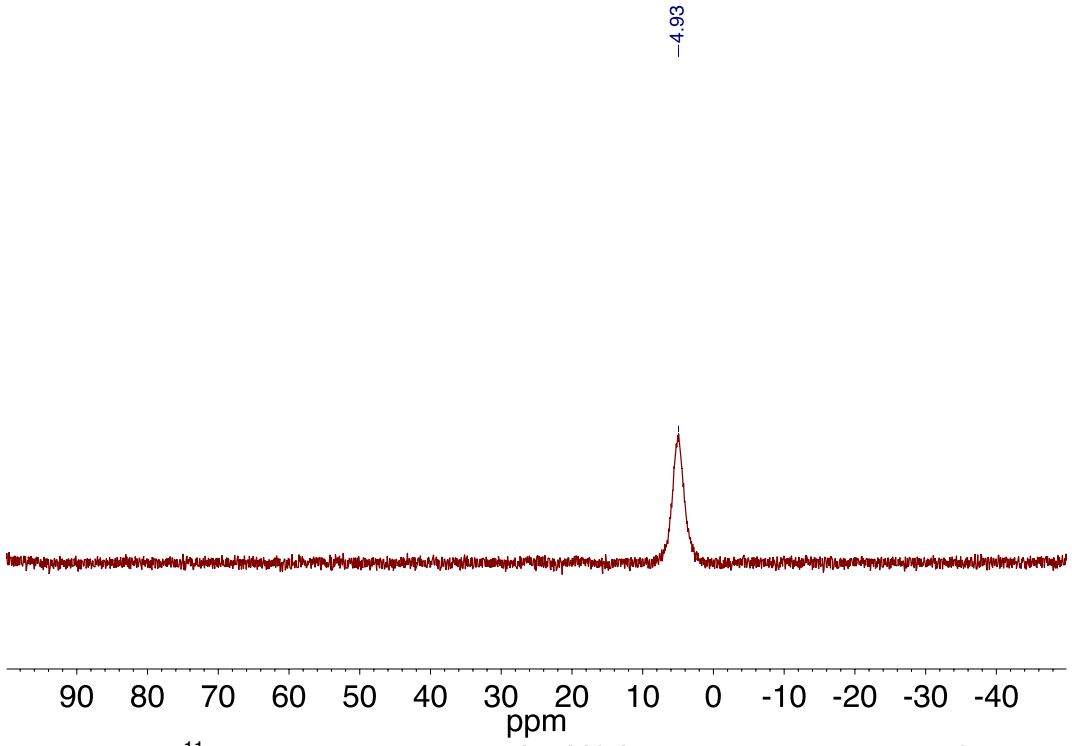

Figure 2.5.22. ^{11}B NMR spectrum of **IPr$_2$(BA)(O$_2$)** recorded at 160 MHz in C_6D_6 at 25 °C.

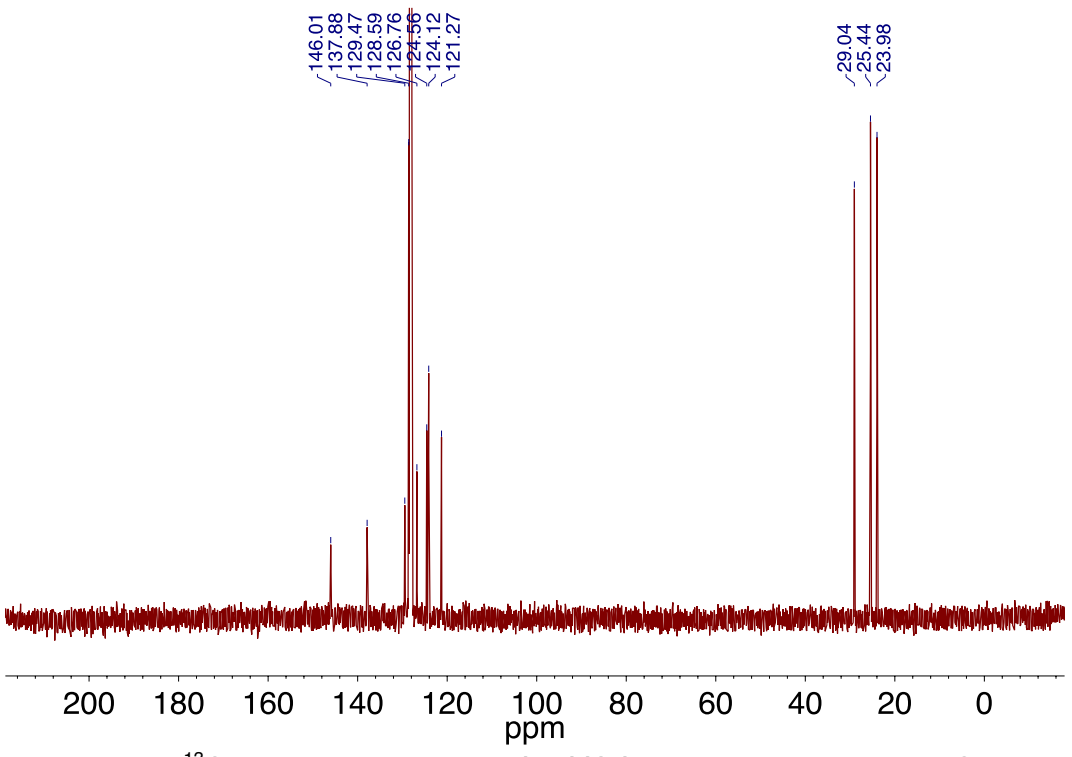

Figure 2.5.23. ^{13}C NMR spectrum of **IPr$_2$(BA)(O$_2$)** recorded at 176 MHz in C_6D_6 at 25 °C.

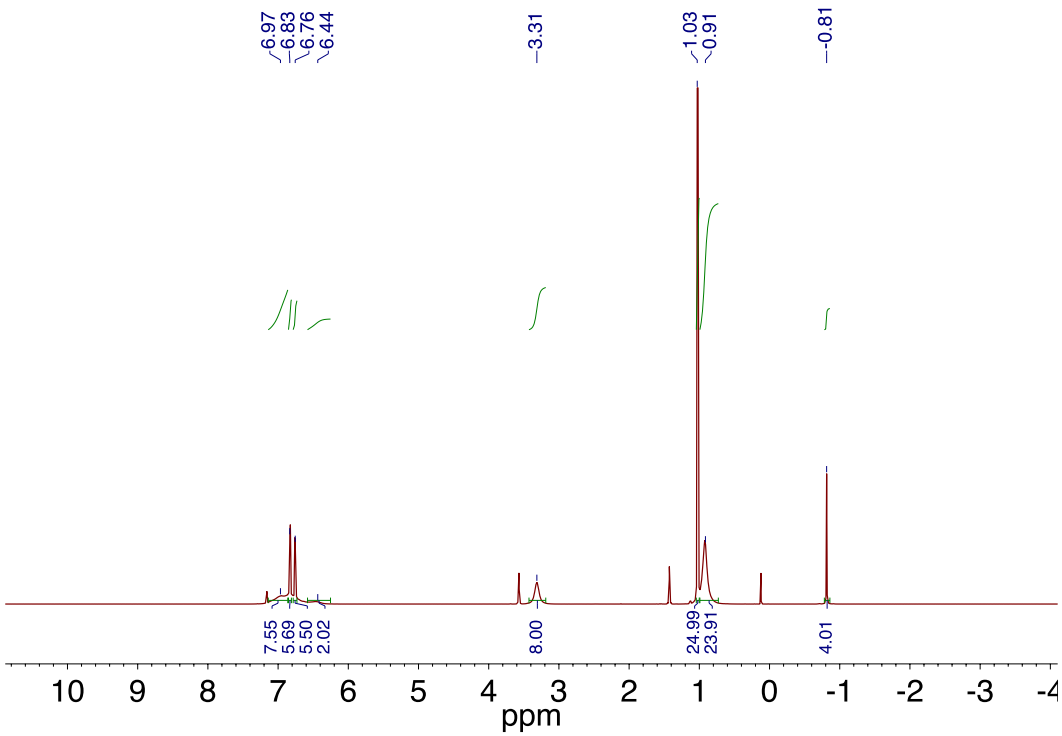

Figure 2.5.24. ^{1}H NMR spectrum of **$IPr_2(BA)(C_2H_4)$** recorded at 600 MHz in C_6D_6 at 25 °C.

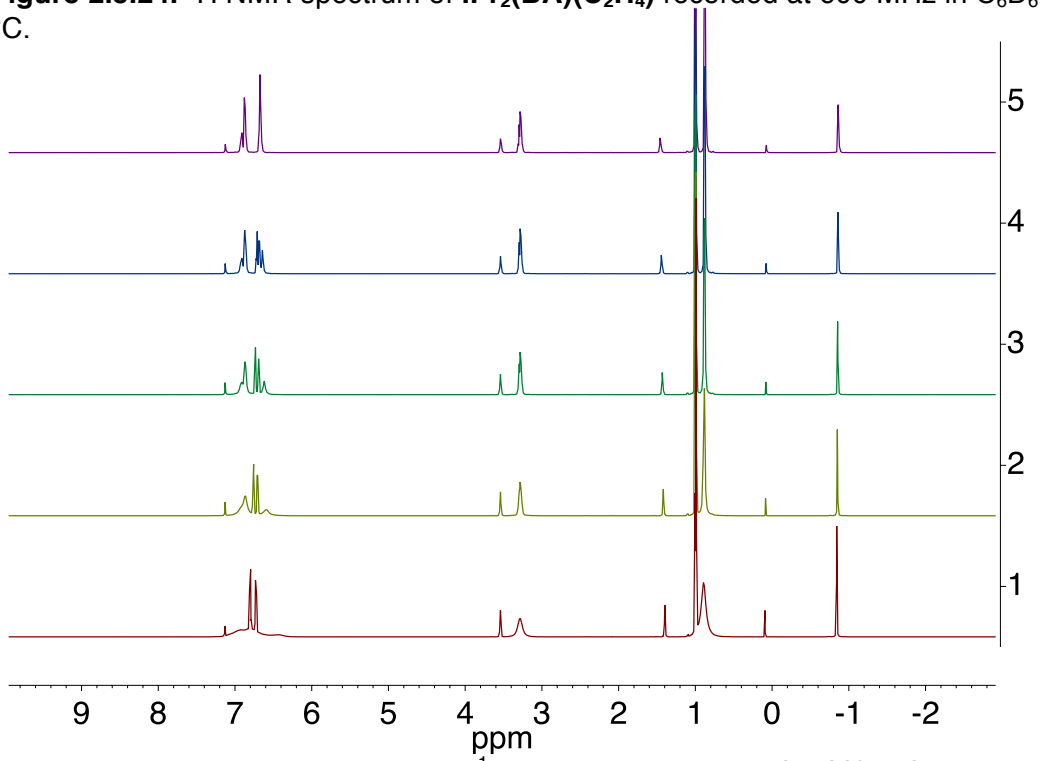

Figure 2.5.25. Variable Temperature ^{1}H NMR spectra of **$IPr_2(BA)(C_2H_4)$** recorded at 600 MHz in C_6D_6. Spectra 1–5 were collected at 25, 40, 50, 60, and 70 °C, respectively.

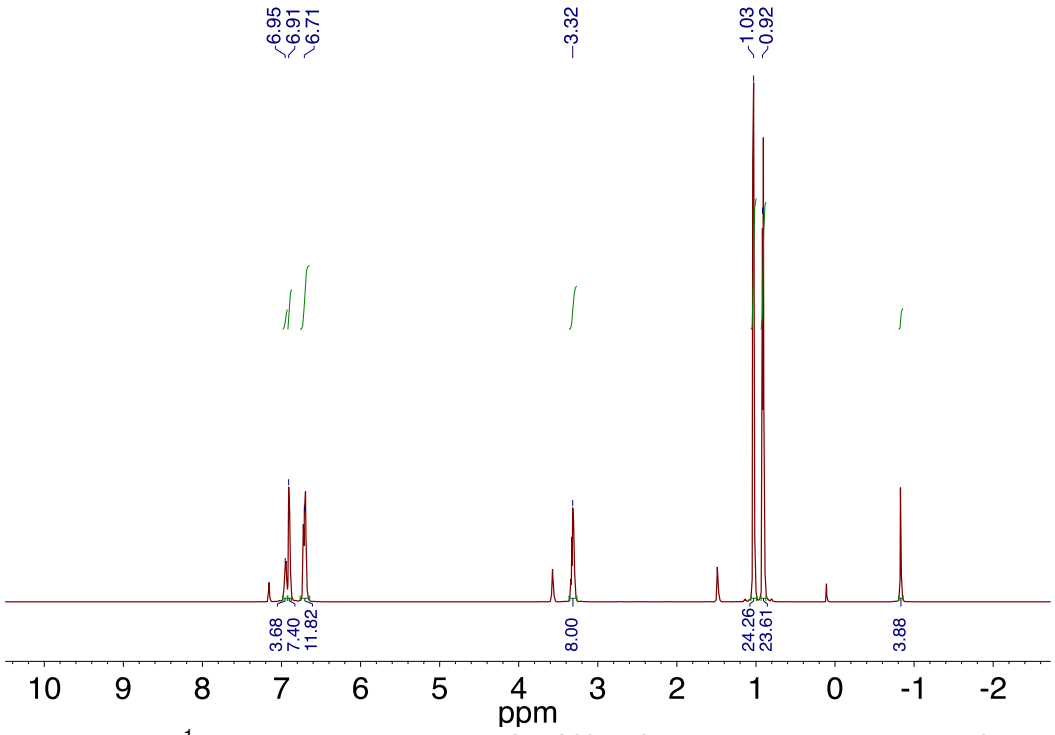

Figure 2.5.26. ^{1}H NMR spectrum of **$IPr_2(BA)(C_2H_4)$** recorded at 600 MHz in C_6D_6 at 70 °C.

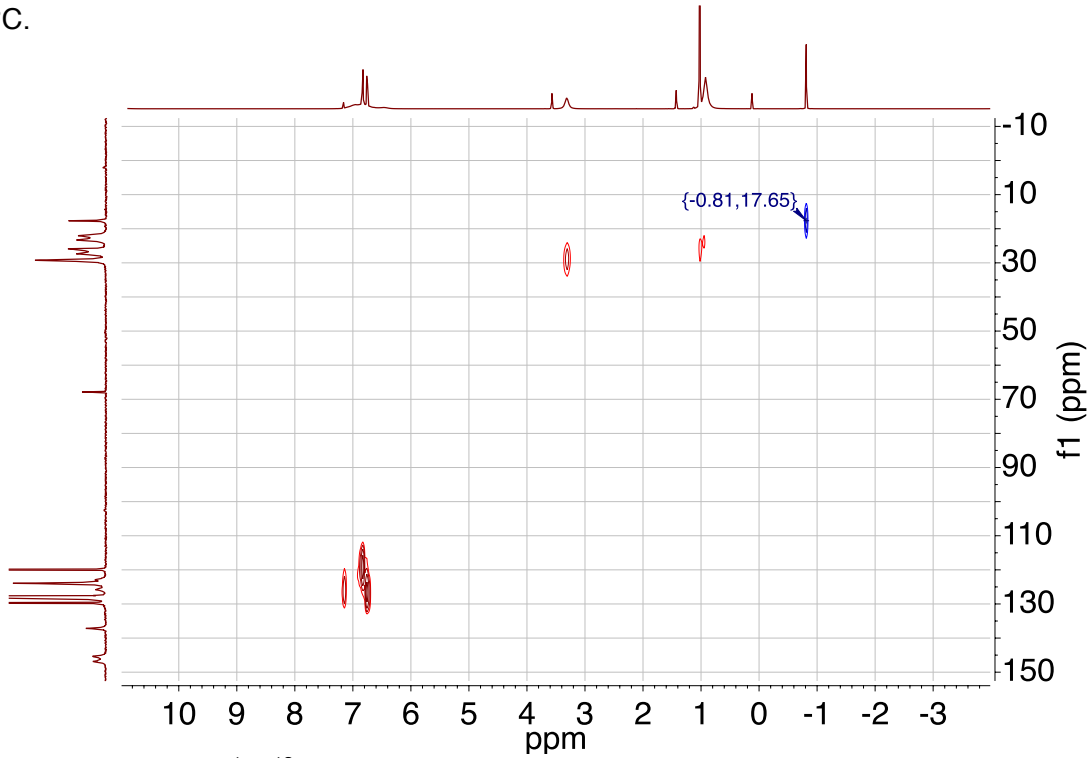

Figure 2.5.27. 2D[^{1}H-^{13}C]-HSQC spectrum of **$IPr_2(BA)(C_2H_4)$** recorded at 600 MHz in C_6D_6 at 25 °C.

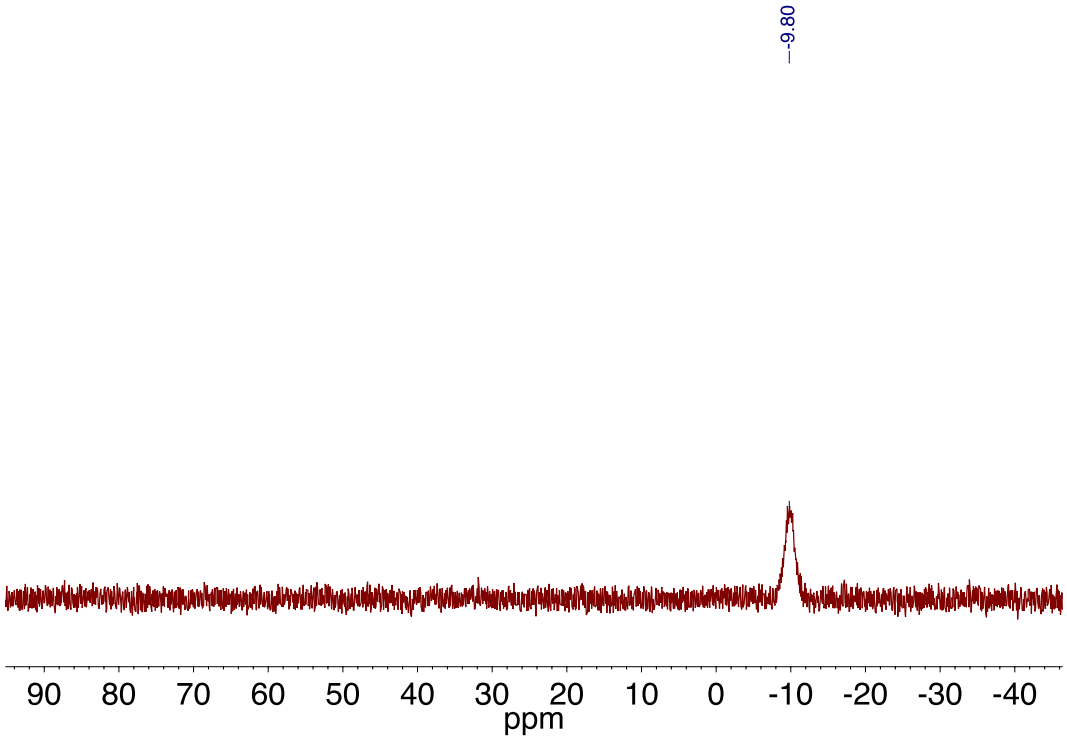

Figure 2.5.28. ^{11}B NMR spectrum of **$IPr_2(BA)(C_2H_4)$** recorded at 160 MHz in C_6D_6 at 25 °C.

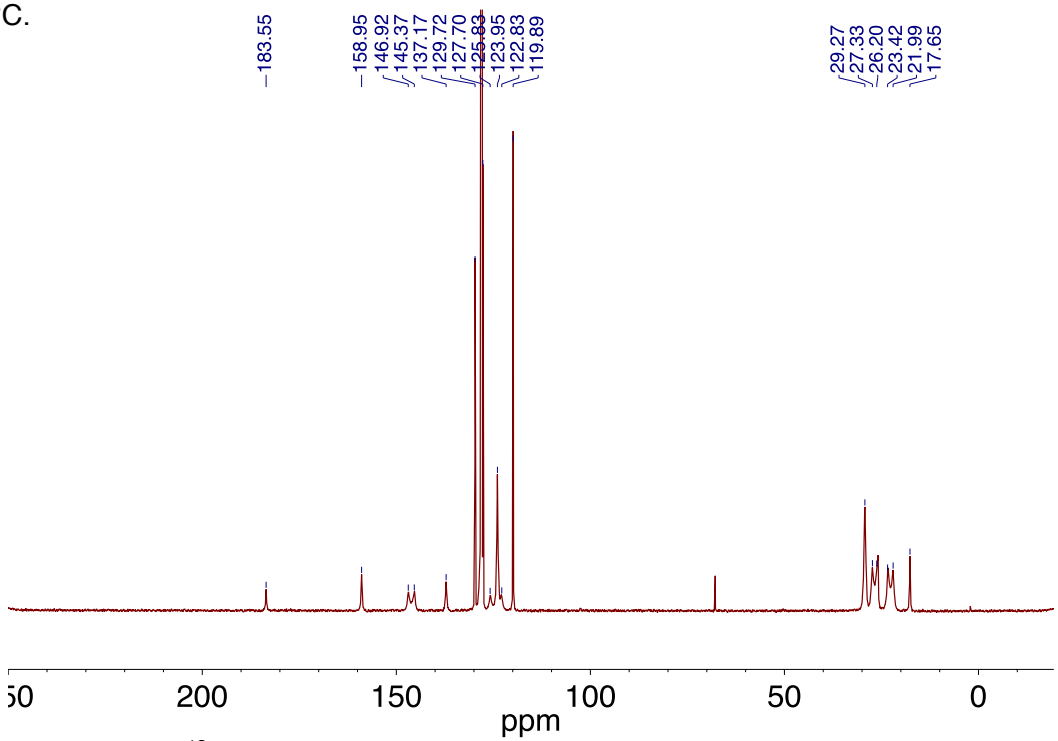

Figure 2.5.29. ^{13}C NMR spectrum of **$IPr_2(BA)(C_2H_4)$** recorded at 176 MHz in C_6D_6 at 25 °C.

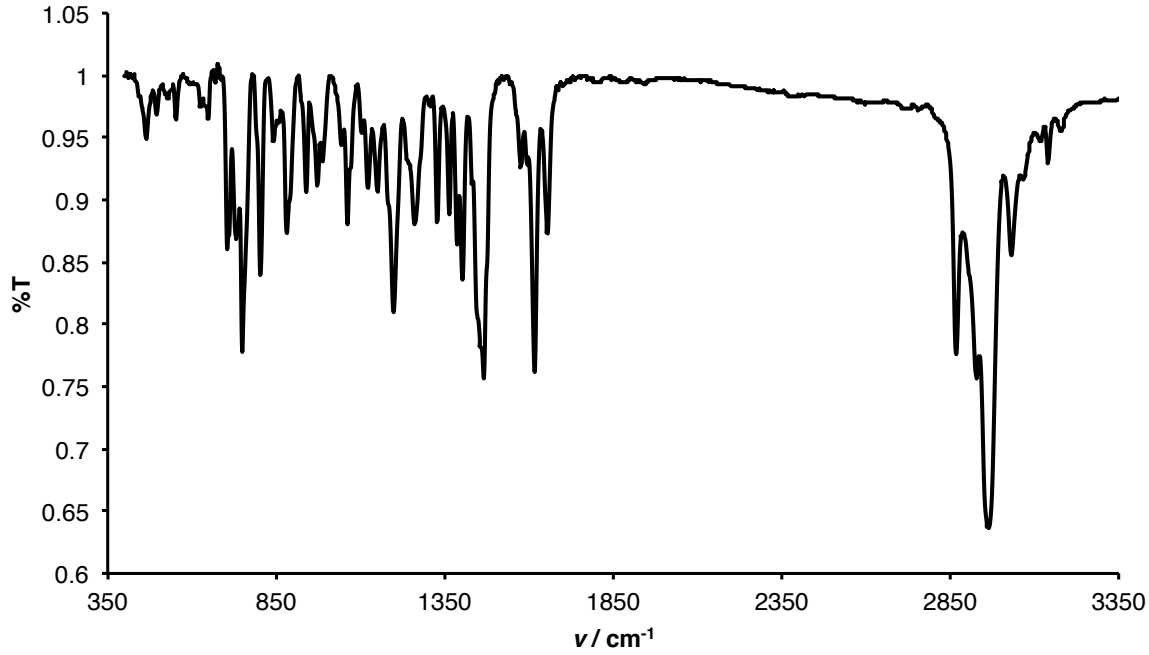

Figure 2.5.30. FT-IR spectrum of **$IPr_2(BA)(CO_2)$**.

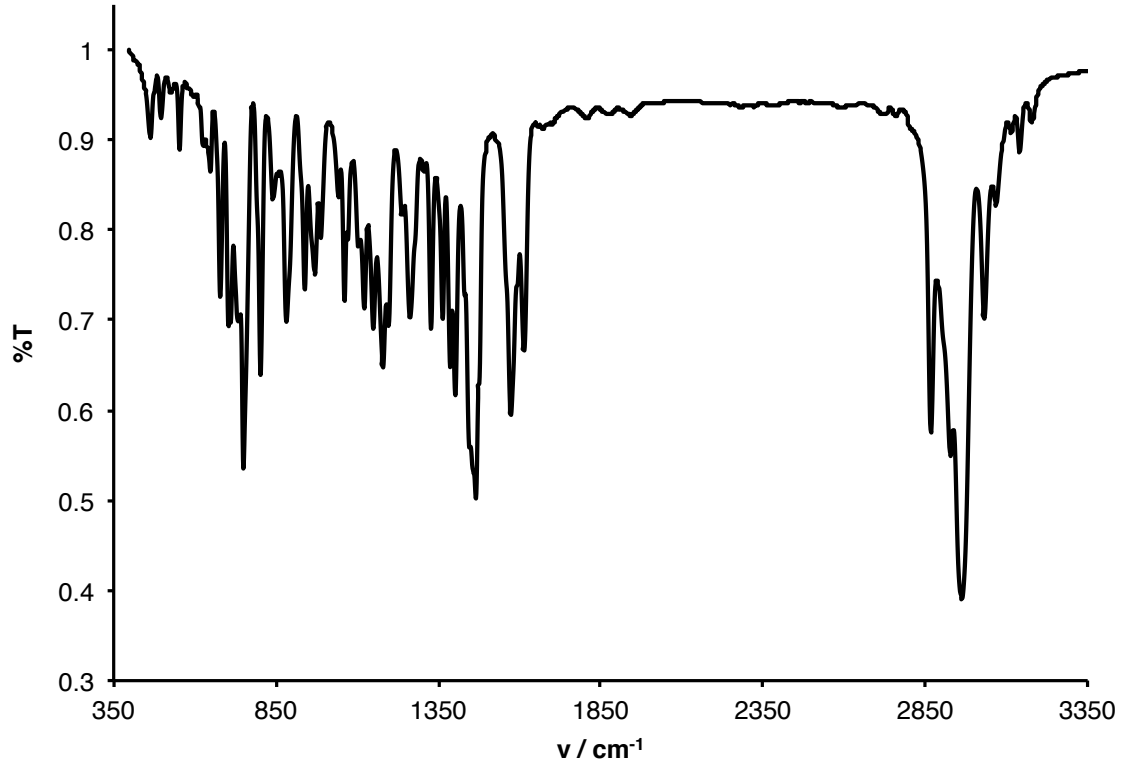

Figure 2.5.31. FT-IR spectrum of **$IPr_2(BA)(^{13}CO_2)$**.

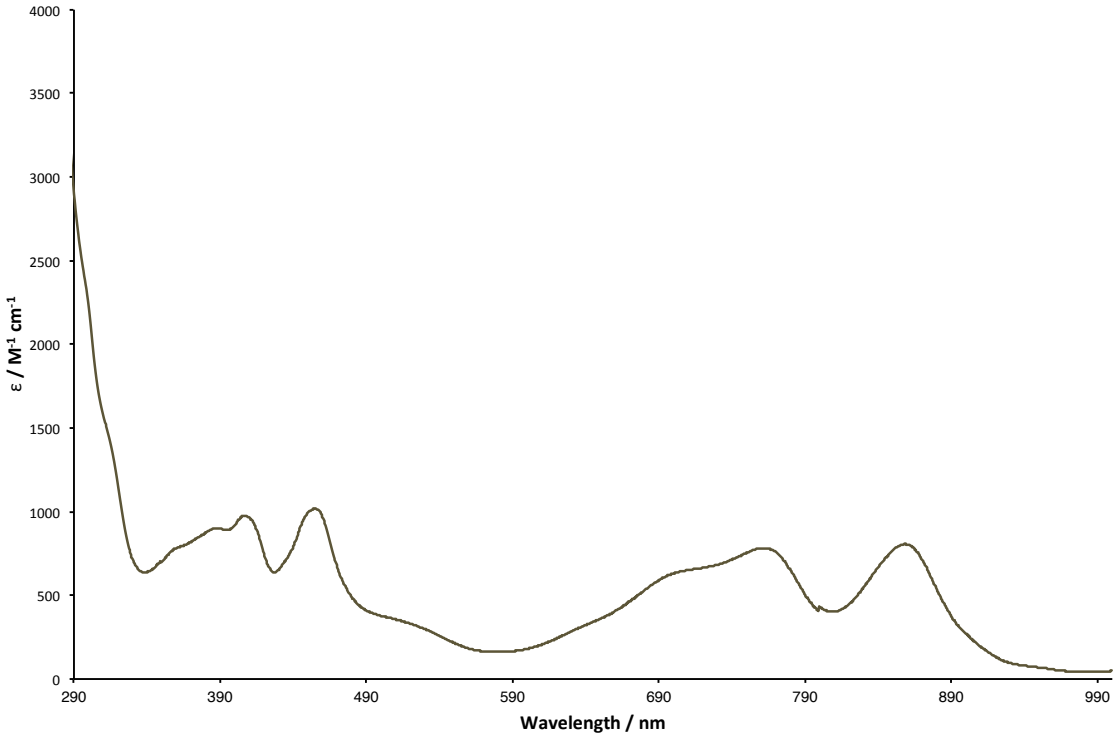

Figure 2.5.32. UV-Vis spectrum of **[IPr$_2$(BA)][Br]** in THF.

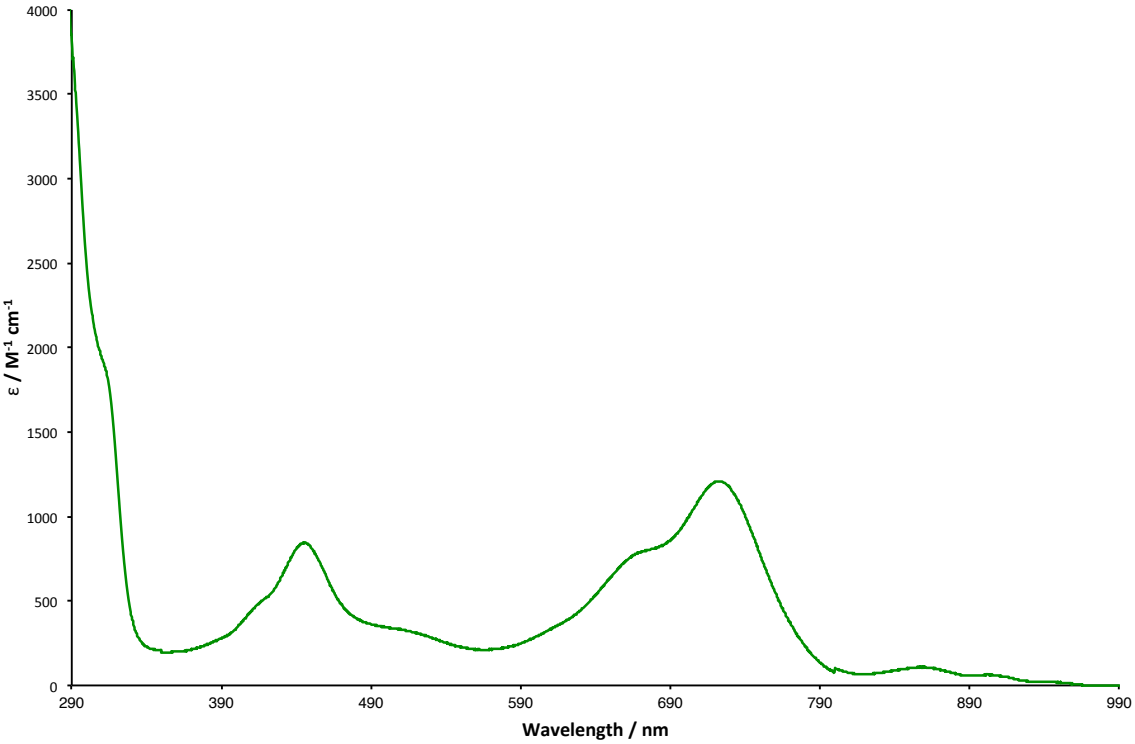

Figure 2.5.33. UV-Vis spectrum of **IPr$_2$(BA)** in THF.

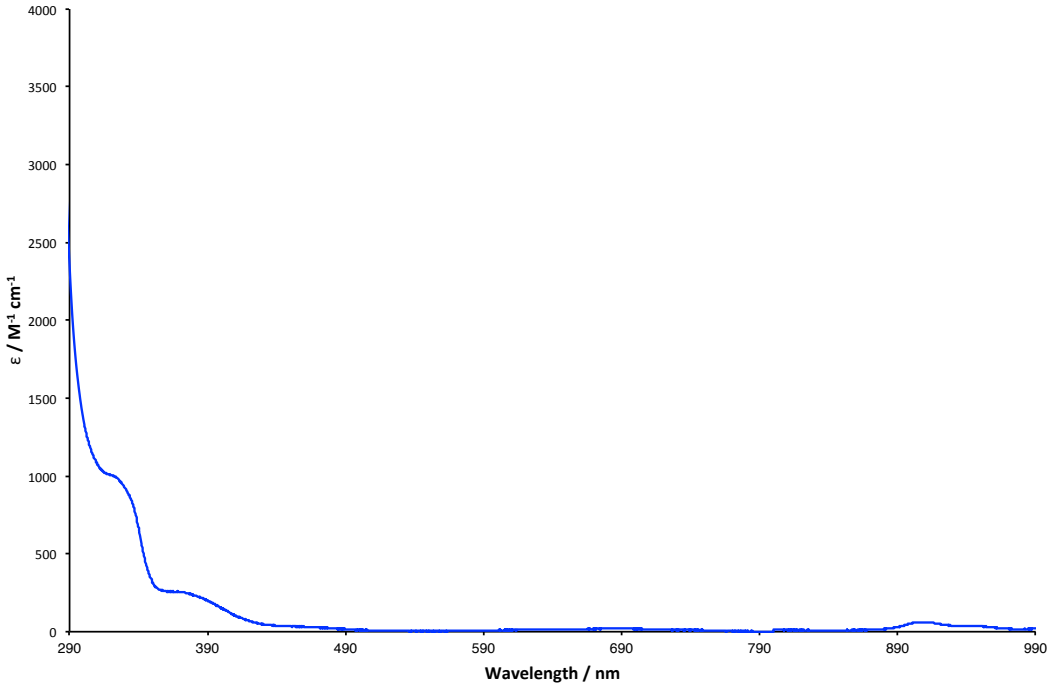

Figure 2.5.34. UV-Vis spectrum of **$IPr_2(BA)(O_2)$** in THF.

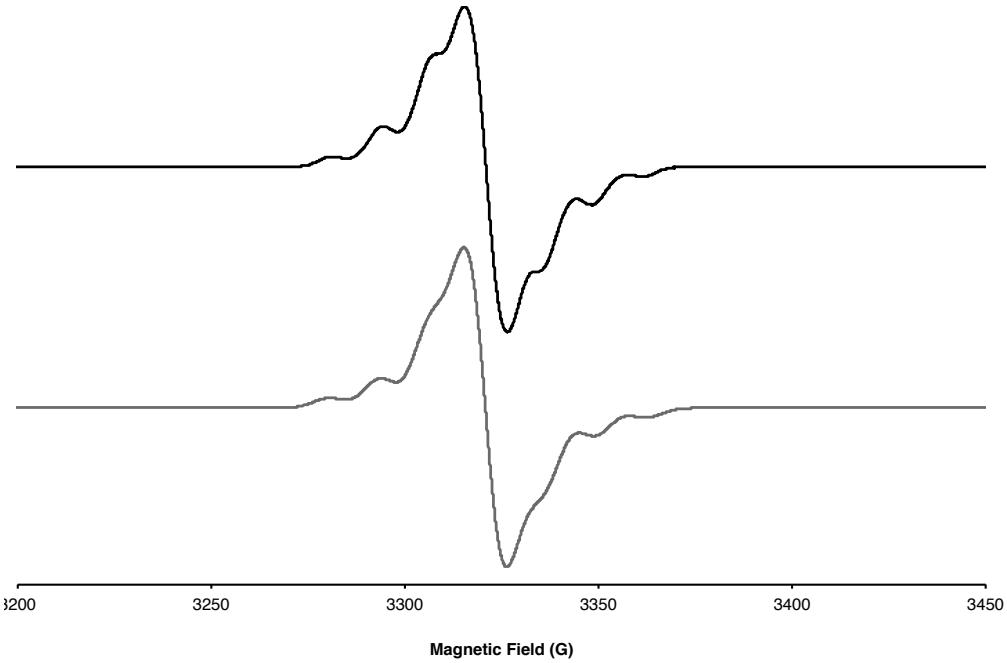

Figure 2.5.35. X-band EPR spectrum (9.314 GHz) of **$[IPr_2(BA)][Br]$** in DCM:toluene (1:1) at 107 K with a field modulation of 0.9 G (black) and its simulated spectrum (gray). Simulation parameters: g_1 = 2.0034, g_2 = 2.0015, g_3 = 2.0002; A_1[B] = 3 MHz, A_2[B] = 32 MHz, A_3[B] = 0 MHz; A_1[B] = 3 MHz, A_2[B] = 32 MHz, A_3[B] = 0 MHz; $HStrain_1$ = 5.0229, $HStrain_2$ = 7.6138, $HStrain_3$ = 20.69; lw = 0.7.

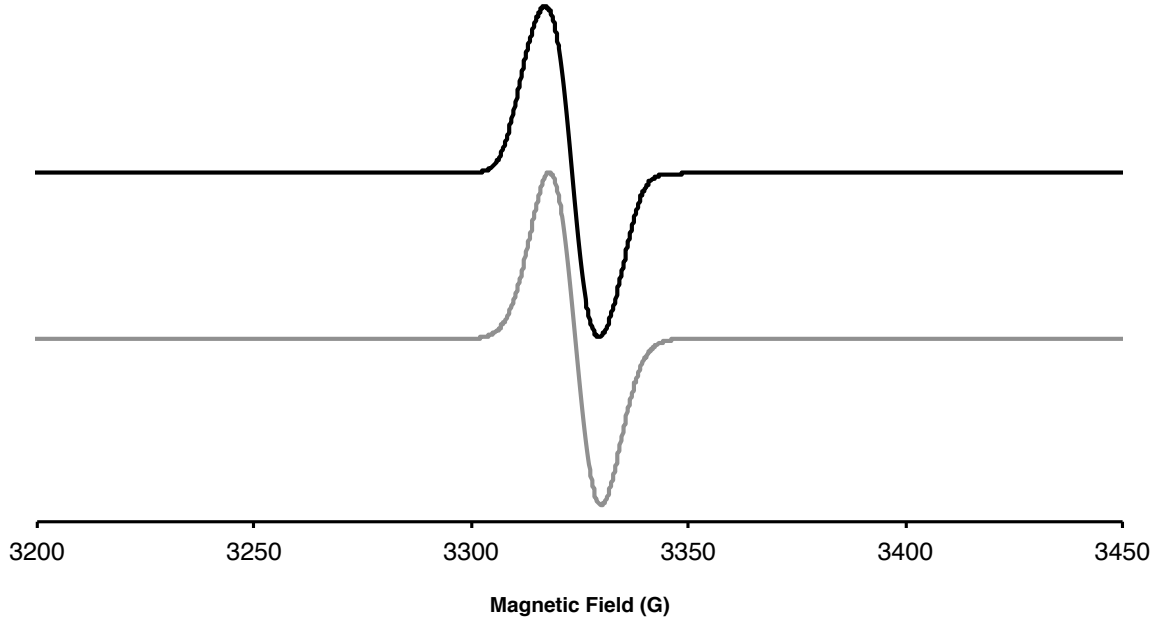

Figure 2.5.36. X-band EPR spectrum (9.314 GHz) of **[IPr$_2$(BA)][Br]** in DCM:toluene (1:1) at 298 K with a field modulation of 0.5 G (black) and its simulated spectrum (gray). Simulation parameters: g = 2.0014; A[B] = 4 MHz, lw = 1.1.

2.6) X-Ray Crystallography

2.6.1) General Considerations

Single crystals were coated with paratone oil and mounted on cryo-loop glass fibers. X-ray intensity data were collected at 100(2) K on a Bruker APEX2[28] platform-CCD X-ray diffractometer system using fine-focus Mo K_α radiation (λ = 0.71073 Å, 50kV/30mA power). The CCD detector was placed at 5.0600 cm from the crystal. Frames were integrated using the Bruker SAINT software package[29] and using a narrow-frame integration algorithm. Absorption corrections were applied to the raw intensity data using the SADABS program.[30] The Bruker SHELXTL software package[31] was used for phase determination and structure

refinement. Atomic coordinates, isotropic and anisotropic displacement parameters of all the non-hydrogen atoms were refined by means of a full matrix least-squares procedure on F^2. The H-atoms were included in the refinement in calculated positions riding on the atoms to which they were attached. Relevant details for individual data collections are reported in Tables 2.6.1–2.6.7.

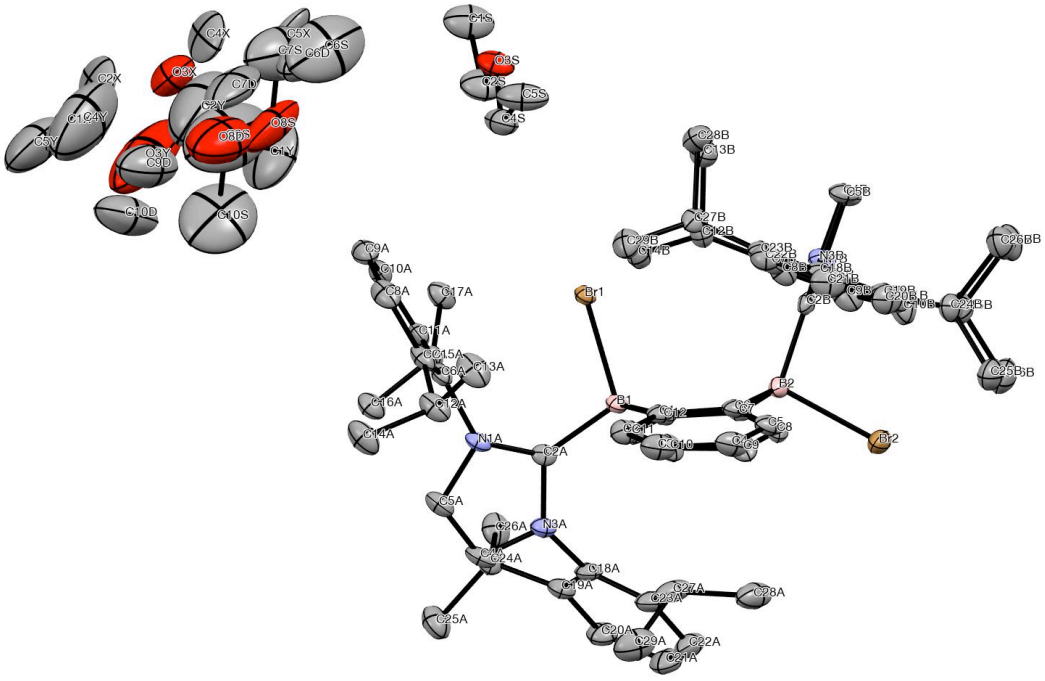

Figure 2.6.1. Labelled thermal ellipsoid plot (50%) for **IPr$_2$(BA)Br$_2$**.

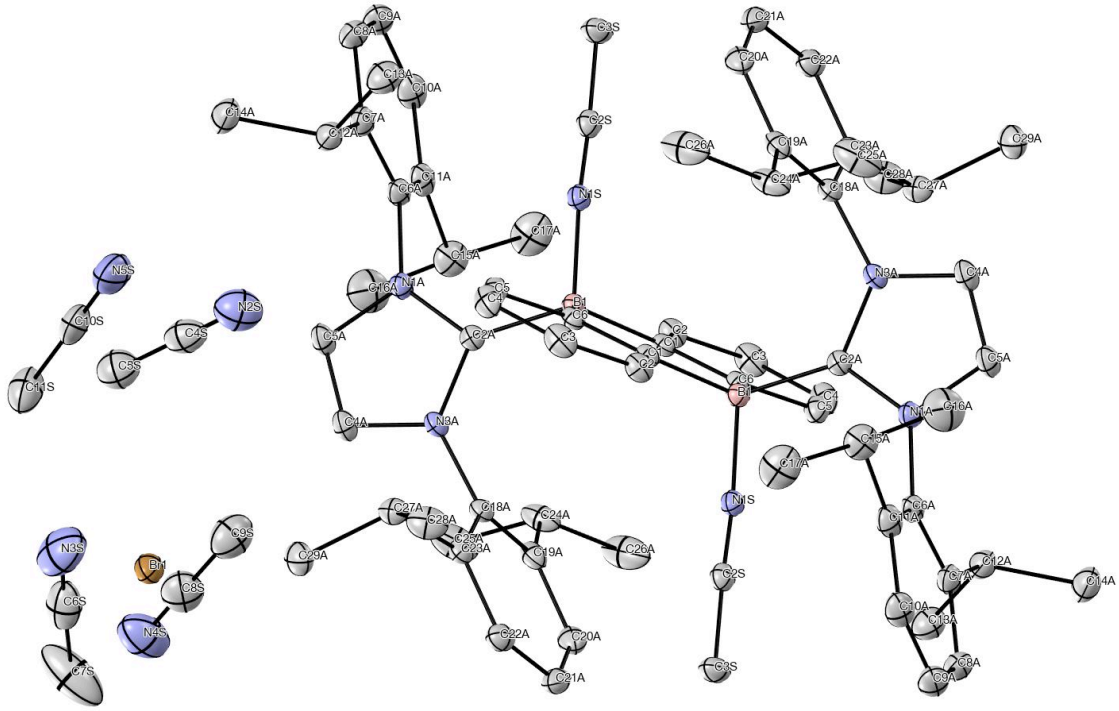

Figure 2.6.2. Labelled thermal ellipsoid plot (50%) for **[IPr$_2$(BA)(CH$_3$CN)$_2$][Br]$_2$**. The second bromide is generated by a crystallographic symmetry operation.

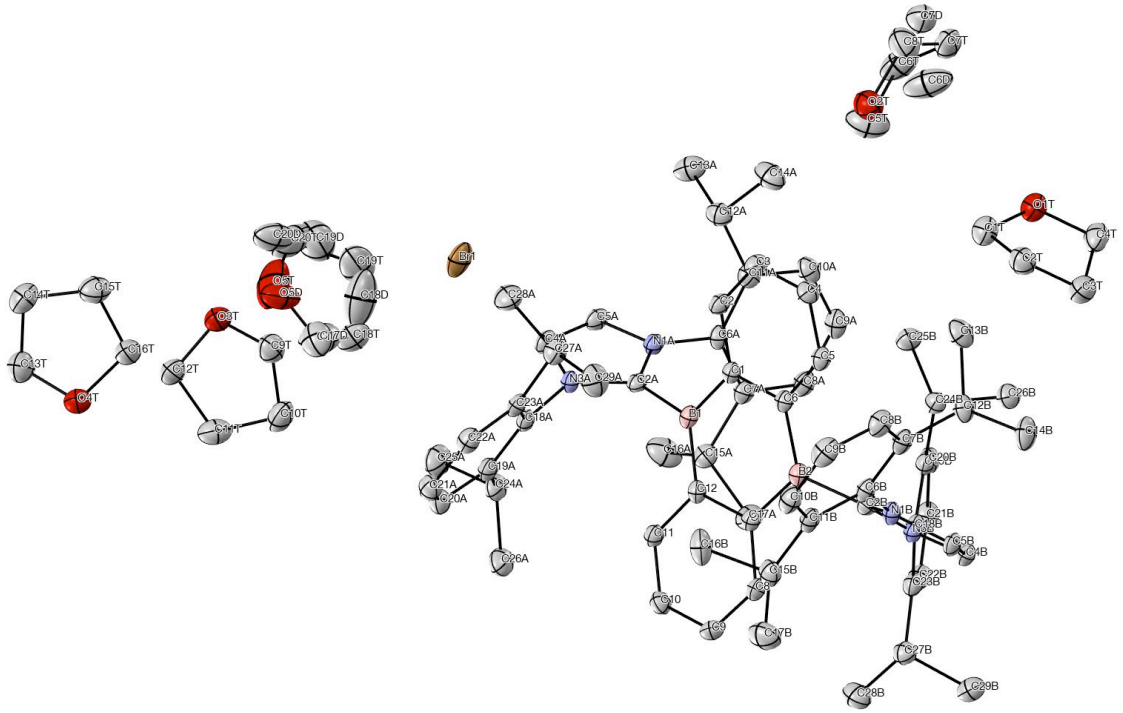

Figure 2.6.3. Labelled thermal ellipsoid plot (50%) for **[IPr$_2$(BA)][Br].**

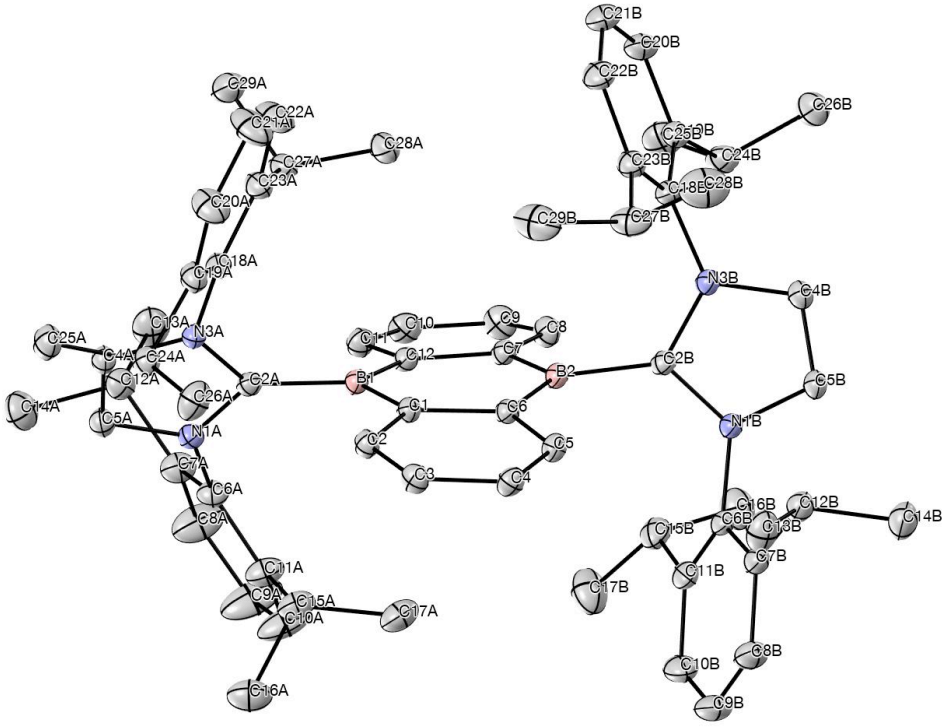

Figure 2.6.4. Labelled thermal ellipsoid plot (50%) for **IPr$_2$(BA).**

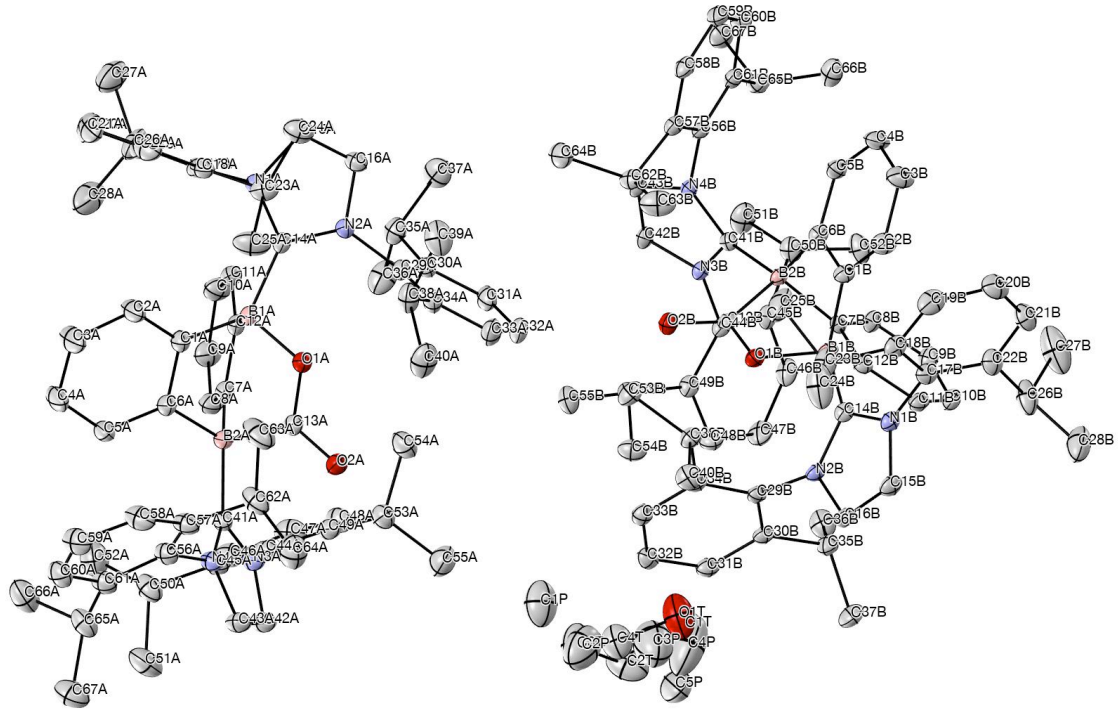

Figure 2.6.5. Labelled thermal ellipsoid plot (50%) for **IPr$_2$(BA)(CO$_2$)**.

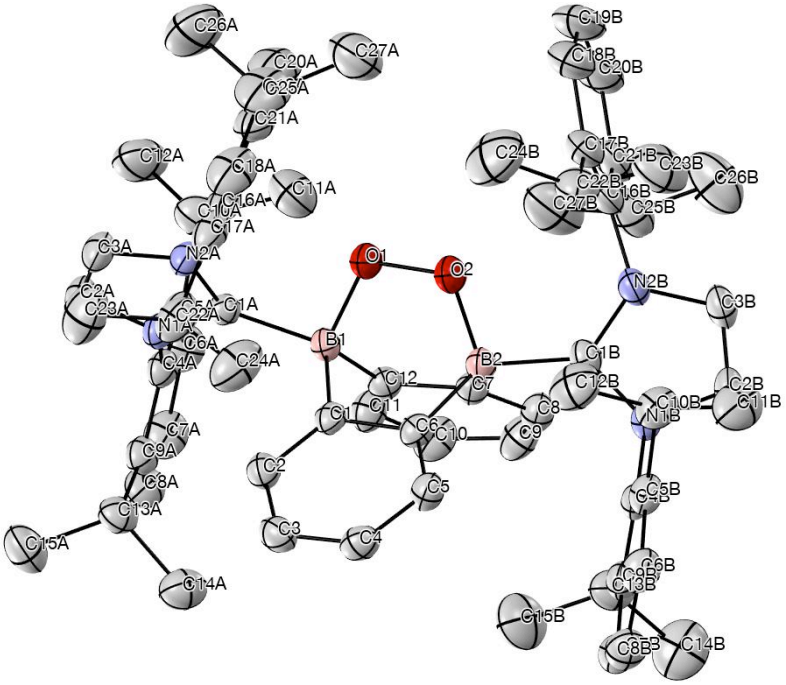

Figure 2.6.6. Labelled thermal ellipsoid plot (50%) for **IPr$_2$(BA)(O$_2$)**.

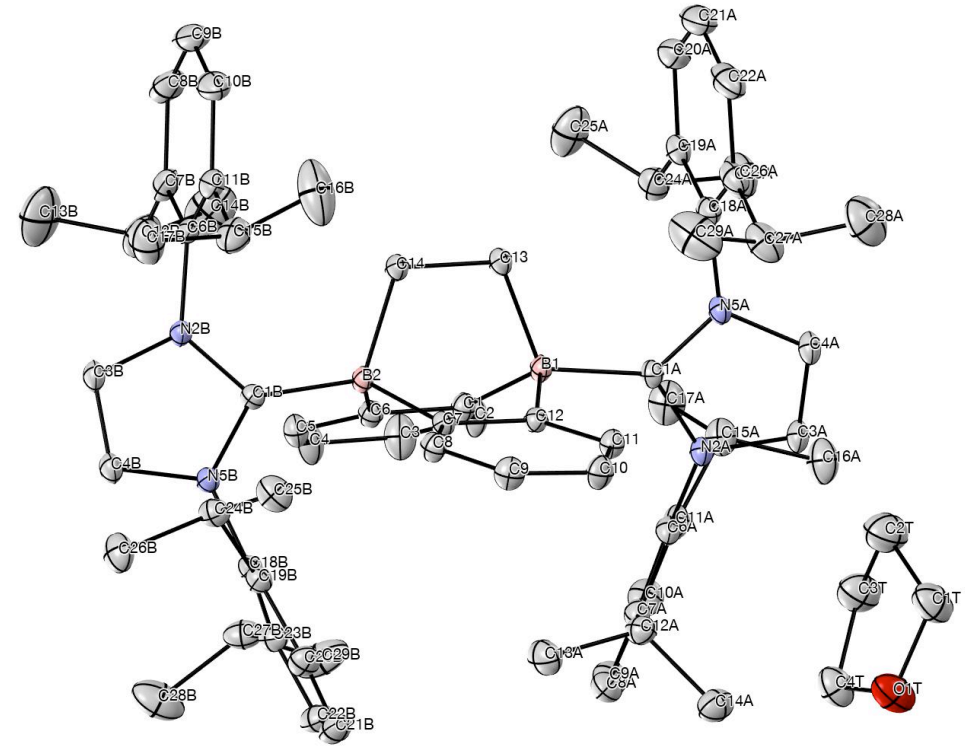

Figure 2.6.7. Labelled thermal ellipsoid plot (50%) for **IPr$_2$(BA)(C$_2$H$_4$)**.

Table 2.6.1. Crystal data and structure refinement for **$IPr_2(BA)Br_2$**.

Identification code	hh168JT81_0m-5
Empirical formula	$C_{77}H_{107.50}B_2Br_2N_4O_{2.75}$
Formula weight	1314.60 g/mol
Temperature	100(2) K
Wavelength	0.71073 Å
Crystal system	Triclinic
Space group	P –1
Unit cell dimensions	a = 14.0685(10) Å α = 90.7365(11)°. b = 15.0125(10) Å β =106.7863(11)°. c = 17.8170(12) Å γ = 95.7848(11)°.
Volume	3580.8(4) $Å^3$
Z	2
Density (calculated)	1.219 mg/m^3
Absorption coefficient	1.180 mm^{-1}
F(000)	1399
Crystal size	0.506 x 0.104 x 0.058 mm^3
θ range for data collection	1.521 to 26.372°.
Index ranges	$-17 \le h \le 16$, $-18 \le k \le 18$, $0 \le l \le 22$
Reflections collected	32577
Independent reflections	14607 [R_{int} = 0.0297]
Completeness to θ = 25.242°	100.0 %
Absorption correction	Semi-empirical from equivalents
Refinement method	Full-matrix least-squares on F^2
Data / restraints / parameters	14607 / 260 / 903
Goodness-of-fit on F^2	1.016
Final R indices [$I > 2\sigma_I$]	R_1 = 0.0436, wR_2 = 0.0955
R indices (all data)	R_1 = 0.0606, wR_2 = 0.1024
Largest diff. peak and hole	0.840 and –0.851 e/$Å^3$

Note: The Bruker CELL_NOW[32] program was used to obtain the two different orientation matrices of the rotational twin components (the twin law is 180° rotation about the 001 reciprocal axis). The absorption correction was applied with TWINABS.[33] There was one molecule of $IPr_2(BA)Br_2$ and 2.75 molecules of THF solvent present in the asymmetric unit of the unit cell. Two of the three solvent molecules were modeled with disorder where one was located at the inversion center (disordered site occupancy ratios were 59%/41% and 50%/25%). The major/minor component twin ratio was 92%/8%.

Table 2.6.2. Crystal data and structure refinement for **[IPr_2(BA)(CH_3CN)$_2$][Br]$_2$**.

Identification code	hh168JT81r_0m	
Empirical formula	$C_{86}H_{110}B_2Br_2N_{14}$	
Formula weight	1521.31g/mol	
Temperature	100(2) K	
Wavelength	0.71073 Å	
Crystal system	Triclinic	
Space group	P –1	
Unit cell dimensions	a = 10.9914(4) Å	α = 90.8263(5)°.
	b = 12.4217(4) Å	β = 105.4512(5)°.
	c = 16.6359(6) Å	γ = 100.8307(5)°.
Volume	2145.25(13) Å^3	
Z	1	
Density (calculated)	1.178 mg/m^3	
Absorption coefficient	0.995 mm^{-1}	
F(000)	804	
Crystal size	0.487 x 0.456 x 0.179 mm^3	
θ range for data collection	1.673 to 28.282°	
Index ranges	$-14 \le h \le 14$, $-16 \le k \le 16$, $-22 \le l \le 22$	
Reflections collected	54967	
Independent reflections	10640 [R_{int} = 0.0292]	
Completeness to θ = 25.242°	99.9 %	
Absorption correction	Semi-empirical from equivalents	
Refinement method	Full-matrix least-squares on F^2	
Data / restraints / parameters	10640 / 0 / 482	
Goodness-of-fit on F^2	1.032	
Final R indices [$I > 2\sigma_I$]	R_1 = 0.0319, wR_2 = 0.0790	
R indices (all data)	R_1 = 0.0377, wR_2 = 0.0817	
Largest diff. peak and hole	0.801 and –0.328 e/Å^3	

Table 2.6.3. Crystal data and structure refinement for **[IPr$_2$(BA)][Br].**

Identification code	hh183JT90r_0m
Empirical formula	$C_{86}H_{120}B_2BrN_4O_5$
Formula weight	1391.38 g/mol
Temperature	100(2) K
Wavelength	0.71073 Å
Crystal system	Monoclinic
Space group	P 21/c
Unit cell dimensions	a = 13.9529(12) Å α = 90°. b = 36.527(3) Å β =113.4464(12)°. c = 16.6593(14) Å γ = 90°.
Volume	7789.5(12) Å^3
Z	4
Density (calculated)	1.186 mg/m^3
Absorption coefficient	0.581 mm^{-1}
F(000)	2996
Crystal size	0.425 x 0.257 x 0.177 mm^3
θ range for data collection	1.591 to 27.484°.
Index ranges	$-18 \le h \le 18$, $-47 \le k \le 47$, $-21 \le l \le 21$
Reflections collected	98746
Independent reflections	17851 [R_{int} = 0.0617]
Completeness to θ = 25.242°	100.0 %
Absorption correction	Semi-empirical from equivalents
Refinement method	Full-matrix least-squares on F^2
Data / restraints / parameters	17851 / 198 / 964
Goodness-of-fit on F^2	1.038
Final R indices [$I > 2\sigma_I$]	R_1 = 0.0481, wR_2 = 0.0931
R indices (all data)	R_1 = 0.0829, wR_2 = 0.1034
Largest diff. peak and hole	0.536 and –0.591 e/Å^3

Note: There are five molecules of THF present in the asymmetric unit of the unit cell. Two of the five solvent molecules of THF were modeled with disorder (disordered site occupancy factor ratios were 56%/44% and 57%/43%).

Table 2.6.4. Crystal data and structure refinement for **IPr_2(BA).**

Identification code	hh146JT67_0m
Empirical formula	$C_{66}H_{80}B_2N_4$
Formula weight	950.96 g/mol
Temperature	100(2) K
Wavelength	0.71073 Å
Crystal system	Orthorhombic
Space group	P 21 21 21
Unit cell dimensions	a = 12.2145(7) Å α = 90°. b = 19.8453(11) Å β = 90°. c = 23.3976(13) Å γ = 90°.
Volume	5671.6(6) Å^3
Z	4
Density (calculated)	1.114 mg/m^3
Absorption coefficient	0.064 mm^{-1}
F(000)	2056
Crystal size	0.620 x 0.558 x 0.505 mm^3
θ range for data collection	1.741 to 30.507°.
Index ranges	$-17 \le h \le 17$, $-28 \le k \le 28$, $-33 \le l \le 33$
Reflections collected	135830
Independent reflections	17325 [R_{int} = 0.0347]
Completeness to θ = 25.242°	100.0 %
Absorption correction	Semi-empirical from equivalents
Refinement method	Full-matrix least-squares on F^2
Data / restraints / parameters	17325 / 0 / 656
Goodness-of-fit on F^2	1.047
Final R indices [$I > 2\sigma_I$]	R_1 = 0.0369, wR_2 = 0.0956
R indices (all data)	R_1 = 0.0424, wR_2 = 0.0999
Absolute structure parameter	–0.4(3)
Largest diff. peak and hole	0.349 and –0.151 e/Å^3

Table 2.6.5. Crystal data and structure refinement for **$IPr_2(BA)(O_2)$.**

Identification code	hh153JT72_0m	
Empirical formula	$C_{66}H_{80}B_2N_4O_2$	
Formula weight	982.96 g/mol	
Temperature	200(2) K	
Wavelength	0.71073 Å	
Crystal system	Triclinic	
Space group	P –1	
Unit cell dimensions	a = 12.2955(9) Å	α = 99.6469(13)°.
	b = 13.3751(10) Å	β = 93.4959(13)°.
	c = 20.8112(15) Å	γ = 117.3094(12)°.
Volume	2960.6(4) $Å^3$	
Z	2	
Density (calculated)	1.103 mg/m^3	
Absorption coefficient	0.065 mm^{-1}	
F(000)	1060	
Crystal size	0.253 x 0.237 x 0.179 mm^3	
θ range for data collection	1.757 to 26.372°.	
Index ranges	$-15 \le h \le 15$, $-16 \le k \le 16$, $-26 \le l \le 26$	
Reflections collected	54175	
Independent reflections	12119 [R_{int} = 0.0396]	
Completeness to θ = 25.242°	100.0 %	
Absorption correction	Semi-empirical from equivalents	
Refinement method	Full-matrix least-squares on F^2	
Data / restraints / parameters	12119 / 0 / 683	
Goodness-of-fit on F^2	1.028	
Final R indices [$I > 2\sigma_I$]	R_1 = 0.0467, wR_2 = 0.1099	
R indices (all data)	R_1 = 0.0703, wR_2 = 0.1223	
Largest diff. peak and hole	0.471 and –0.198 e/$Å^3$	

Note: Crystals of $IPr_2(BA)(O_2)$ crack when cooled to 100 K. As a result, data was collected at 200 K. The large solvent accessible voids (ca. 80 $Å^3$) are likely related to the onset of this phase transition at 200 K.

Table 2.6.6. Crystal data and structure refinement for **$IPr_2(BA)(CO_2)$.**

Identification code	hh181JT89_0m	
Empirical formula	$C_{69}H_{84.49}B_2N_4O_{2.38}$	
Formula weight	1031.02 g/mol	
Temperature	100(2) K	
Wavelength	0.71073 Å	
Crystal system	Monoclinic	
Space group	P 21/c	
Unit cell dimensions	a = 37.9259(11) Å	α = 90°.
	b = 12.4199(3) Å	β = 93.9393(5)°.
	c = 25.2260(7) Å	γ = 90°.
Volume	11854.3(6) $Å^3$	
Z	8	
Density (calculated)	1.155 mg/m^3	
Absorption coefficient	0.069 mm^{-1}	
F(000)	4450	
Crystal size	0.424 x 0.224 x 0.157 mm^3	
θ range for data collection	1.618 to 28.282°.	
Index ranges	$-50 \le h \le 50$, $-16 \le k \le 16$, $-33 \le l \le 33$	
Reflections collected	202788	
Independent reflections	29428 [R_{int} = 0.0492]	
Completeness to θ = 25.242°	100.0 %	
Absorption correction	Semi-empirical from equivalents	
Refinement method	Full-matrix least-squares on F^2	
Data / restraints / parameters	29428 / 162 / 1470	
Goodness-of-fit on F^2	1.024	
Final R indices [$I > 2\sigma_I$]	R_1 = 0.0510, wR_2 = 0.1194	
R indices (all data)	R_1 = 0.0704, wR_2 = 0.1297	
Largest diff. peak and hole	0.416 and –0.452 e/$Å^3$	

Note: There is one disordered THF/pentane solvent combination (disordered THF/pentane site occupancy ratio was 75%/25%). The Level B checkcif alert is a result of this disorder.

Table 2.6.7. Crystal data and structure refinement for **$IPr_2(BA)(C_2H_4)$.**

Identification code	hh174JT83_0m	
Empirical formula	$C_{72}H_{92}B_2N_4O$	
Formula weight	1051.11 g/mol	
Temperature	100(2) K	
Wavelength	0.71073 Å	
Crystal system	Monoclinic	
Space group	P 21/c	
Unit cell dimensions	a = 13.8441(5) Å	α = 90°.
	b = 40.4583(14) Å	β = 114.3143(5)°.
	c = 12.3400(4) Å	γ = 90°.
Volume	6298.7(4) $Å^3$	
Z	4	
Density (calculated)	1.108 mg/m^3	
Absorption coefficient	0.064 mm^{-1}	
F(000)	2280	
Crystal size	0.526 x 0.438 x 0.396 mm^3	
θ range for data collection	1.614 to 30.507°.	
Index ranges	$-19 \le h \le 19$, $-57 \le k \le 57$, $-17 \le l \le 17$	
Reflections collected	151735	
Independent reflections	19235 [R_{int} = 0.0364]	
Completeness to θ = 25.242°	100.0 %	
Absorption correction	Semi-empirical from equivalents	
Refinement method	Full-matrix least-squares on F^2	
Data / restraints / parameters	19235 / 0 / 728	
Goodness-of-fit on F^2	1.069	
Final R indices [$I > 2\sigma_I$]	R_1 = 0.0511, wR_2 = 0.1276	
R indices (all data)	R_1 = 0.0617, wR_2 = 0.1348	
Largest diff. peak and hole	0.703 and −0.272 e/$Å^3$	

2.7) Computational Procedures

2.7.1) General Considerations

Density functional theory calculations were performed on $[IPr_2(BA)]^+$ using the M06L[34] functional as implemented in the ORCA 3.0 computational chemistry package[35] with a custom Alrichs-type[36] basis set (DefBas4): for H atoms, TZV(p); for B, C, and N atoms, TZV(2d). The solid-state X-ray structure coordinates of **4** were used as a starting point. Successful optimization to a minimum was confirmed by the absence of imaginary frequencies in a subsequent frequency calculation.

Table 2.7.1. Optimized geometry of $IPr_2(BA)$ ($S = ½$).

#	atom	*x*	*y*	*z*
1	B	2.605761	10.390916	2.979626
2	C	1.188419	10.335639	3.557099
3	C	0.418714	9.156668	3.565501
4	H	0.831286	8.251918	3.128101
5	C	-0.836212	9.098673	4.131055
6	H	-1.39659	8.172188	4.136239
7	C	-1.385578	10.244619	4.707638
8	H	-2.383205	10.210767	5.127279
9	C	-0.652578	11.4109	4.732934
10	H	-1.099664	12.293032	5.182592
11	C	0.639279	11.501923	4.180533
12	B	1.439711	12.807705	4.164176
13	C	2.828956	12.877122	3.528551
14	C	3.578787	14.068368	3.473382
15	H	3.144223	14.983247	3.863809

16	C	4.854209	14.113077	2.956547
17	H	5.407548	15.043871	2.933591
18	C	5.442135	12.94365	2.468363
19	H	6.443956	12.976421	2.057777
20	C	4.736069	11.761851	2.502833
21	H	5.202437	10.866312	2.103645
22	C	3.426778	11.680772	3.016732
23	N	4.29297	8.362899	2.776255
24	C	3.228472	9.079738	2.330636
25	N	2.788607	8.431127	1.220746
26	C	3.573739	7.321565	0.980115
27	H	3.401963	6.680031	0.135379
28	C	4.501626	7.270734	1.957938
29	H	5.286728	6.563157	2.150578
30	C	5.130523	8.673278	3.920426
31	C	6.484024	8.967695	3.68237
32	C	7.272041	9.25758	4.791798
33	H	8.319283	9.489998	4.646001
34	C	6.745486	9.258125	6.070077
35	H	7.379833	9.492528	6.915511
36	C	5.415145	8.944396	6.269322
37	H	5.015111	8.923271	7.275768
38	C	4.571585	8.635699	5.204876
39	C	7.130793	8.956286	2.307075
40	H	6.341079	8.97709	1.548427
41	C	8.022576	10.173825	2.070053
42	H	7.509034	11.105233	2.298366
43	H	8.34681	10.206334	1.030312
44	H	8.922195	10.134374	2.684125
45	C	7.953617	7.681095	2.106808
46	H	7.370819	6.772685	2.254836
47	H	8.780613	7.648881	2.817329
48	H	8.377726	7.648626	1.10324
49	C	3.149658	8.204257	5.502858
50	H	2.591893	8.160055	4.567731
51	C	3.141437	6.79637	6.09958
52	H	3.61027	6.072961	5.431584
53	H	2.11906	6.467944	6.288463
54	H	3.680186	6.767634	7.047797
55	C	2.432419	9.192252	6.42008
56	H	2.485933	10.213647	6.039665
57	H	2.861235	9.186746	7.423407

58	H	1.377253	8.933019	6.513981
59	C	1.697273	8.843416	0.355985
60	C	0.583413	7.996705	0.24207
61	C	-0.447635	8.416183	-0.593504
62	H	-1.324654	7.790642	-0.700202
63	C	-0.372771	9.608721	-1.288044
64	H	-1.190769	9.914013	-1.928312
65	C	0.755156	10.399526	-1.182798
66	H	0.821723	11.315213	-1.757253
67	C	1.824061	10.039007	-0.366527
68	C	0.467759	6.64574	0.924666
69	H	1.216162	6.590658	1.721259
70	C	0.747184	5.517852	-0.072057
71	H	1.717932	5.612637	-0.557867
72	H	-0.005701	5.514976	-0.861282
73	H	0.712178	4.547424	0.422897
74	C	-0.902931	6.430014	1.562148
75	H	-1.197728	7.27491	2.180264
76	H	-0.895757	5.533364	2.181207
77	H	-1.67501	6.288731	0.805681
78	C	3.080323	10.887303	-0.391993
79	H	3.725326	10.585069	0.433133
80	C	2.784004	12.374289	-0.217699
81	H	2.20854	12.568479	0.688426
82	H	2.223816	12.773333	-1.06477
83	H	3.71265	12.94057	-0.145466
84	C	3.853517	10.631046	-1.687003
85	H	4.107039	9.576718	-1.804341
86	H	4.780942	11.204531	-1.697753
87	H	3.26896	10.928525	-2.558859
88	N	0.517603	14.272447	6.154219
89	C	0.813456	14.104503	4.838518
90	N	0.441973	15.260051	4.228703
91	C	-0.093813	16.131196	5.155886
92	H	-0.466316	17.097925	4.871461
93	C	-0.033793	15.521574	6.357936
94	H	-0.323845	15.85781	7.33636
95	C	0.794004	13.332119	7.226158
96	C	-0.290263	12.801211	7.942254
97	C	0.005162	11.901271	8.962688
98	H	-0.806844	11.468335	9.532879
99	C	1.308569	11.554659	9.263013

100	H	1.51083	10.848029	10.058018
101	C	2.354047	12.126536	8.563907
102	H	3.374134	11.875879	8.827719
103	C	2.130487	13.03691	7.534617
104	C	-1.737701	13.196297	7.712928
105	H	-1.815982	13.692956	6.740989
106	C	-2.675671	11.991641	7.694937
107	H	-2.314331	11.209406	7.031172
108	H	-3.670979	12.291418	7.368433
109	H	-2.783881	11.558105	8.689148
110	C	-2.196325	14.181494	8.791461
111	H	-1.566794	15.069119	8.848696
112	H	-2.169212	13.707226	9.773341
113	H	-3.220554	14.506316	8.608596
114	C	3.320286	13.727652	6.897386
115	H	2.992031	14.219389	5.981679
116	C	3.844881	14.818922	7.832869
117	H	3.071056	15.547924	8.077056
118	H	4.675946	15.3521	7.369836
119	H	4.204173	14.392942	8.770787
120	C	4.431656	12.753211	6.516403
121	H	4.065391	11.94503	5.881273
122	H	4.892978	12.305505	7.397919
123	H	5.217858	13.271884	5.968146
124	C	0.591945	15.58496	2.821393
125	C	1.450661	16.644127	2.479761
126	C	1.5798	16.940778	1.126613
127	H	2.233212	17.749847	0.825717
128	C	0.896271	16.223741	0.162395
129	H	1.019117	16.472504	-0.884036
130	C	0.044417	15.202558	0.535358
131	H	-0.507479	14.662403	-0.223974
132	C	-0.140603	14.859402	1.872548
133	C	2.206637	17.490614	3.490735
134	H	2.21155	16.967419	4.453106
135	C	3.662843	17.720424	3.090307
136	H	4.171033	16.789016	2.850019
137	H	4.203633	18.207347	3.901149
138	H	3.739234	18.371494	2.219691
139	C	1.517441	18.843446	3.684632
140	H	0.474046	18.748861	3.983207
141	H	1.533319	19.412655	2.754402

142	H	2.031807	19.433158	4.443304
143	C	-1.17091	13.802731	2.217984
144	H	-1.072517	13.546283	3.272769
145	C	-2.580227	14.361965	2.01852
146	H	-2.749663	15.252454	2.625153
147	H	-3.328812	13.618582	2.293543
148	H	-2.751308	14.635743	0.976365
149	C	-0.969948	12.520406	1.414243
150	H	0.047247	12.138008	1.509722
151	H	-1.170821	12.678844	0.35354
152	H	-1.647317	11.739886	1.762465

Final Energy: -2832.37967003 E_h

2.8) References

[1] Bolton, J. R. *Science* **1978**, *202*, 705.

[2] Lewis, N. S.; Nocera, D. G. *Proc. Natl. Acad. Sci. U.S.A.* **2006**, *103*, 15729.

[3] Cook, T. R.; Dogutan, D. K.; Reece, S. Y.; Surendranath, Y.; Teets, T. S.; Nocera, D. G. *Chem. Rev.* **2010**, *110*, 6474.

[4] a) Power, P. P. *Nature* **2010**, *463*, 171. b) Martin, D.; Soleilhavoup, M.; Bertrand, G. *Chem. Sci.* **2011**, *2* (3), 389.

[5] Stephan, D. W. *Science* **2016**, *354*, 1248.

[6] Melaimi, M.; Jazzar, R.; Soleilhavoup, M.; Bertrand, G. *Angew. Chem. Int. Ed.* **2017**, *56* (34), 10046.

[7] a) Mizuhata, Y.; Sasamori, T.; Tokitoh, N. *Chem. Rev.* **2009**, *109*, 3479. b) Dunn, N. L.; Ha, M.; Radosevich, A. T. *J. Am. Chem. Soc.* **2012**, *134*, 11330. c) Chong, C. C.; Hirao, H.; Kinjo, R. *Angew. Chem. Int. Ed.* **2014**, *53*, 3342.

[8] Fischer, R. C.; Power, P. P. *Chem. Rev.* **2010**, *110*, 3877.

[9] a) Myers, T. W.; Berben, L. A. *J. Am. Chem. Soc.* **2011**, *133* (31), 11865. b) Myers, T. W.; Kazem, N.; Stoll, S.; Britt, R. D.; Shanmugam, M.; Berben, L. A. *J. Am. Chem. Soc.* **2011**, *133* (22), 8662.

[10] Duan, J.; Chen, S.; Jaroniec, M.; Qiao, S. Z. *ACS Catal.* **2015**, *5*, 5207.

[11] a) Müller, P.; Huck, S.; Köppel, H.; Pritzkow, H.; Siebert, W. *Z. Naturforsch. B Chem. Sci.* **1995**, *50*, 1476. b) Agou, T.; Sekine, M.; Kawashima, T. *Tet. Lett.* **2010**, *51*, 5013. c) Reus, C.; Weidlich, S.; Bolte, M.; Lerner, H.-W.; Wagner, M. *J. Am. Chem. Soc.* **2013**, *135*, 12892.

[12] Hoffend, C.; Diefenbach, M.; Januszewski, E.; Bolte, M.; Lerner, H.-W.; Holthausen, M. C.; Wagner, M. *Dalton Trans.* **2013**, *42*, 13826.

[13] a) Wood, T. K.; Piers, W. E.; Keay, B. A.; Parvez, M. *Org. Lett.* **2006**, *8*, 2875. b) Wood, T. K.; Piers, W. E.; Keay, B. A.; Parvez, M. *Chem. Eur. J.* **2010**, *16*, 12199. c) Lorbach, A.; Bolte, M.; Lerner, H.-W.; Wagner, M. *Organometallics* **2010**, *29*, 5762. d) Di Wu; Kong, L.; Li, Y.; Ganguly, R.; Kinjo, R. *Nat. Commun.* **2015**, *6*, 1. e) Di Wu; Ganguly, R.; Li, Y.; Hoo, S. N.; Hirao, H.; Kinjo, R. *Chem. Sci.* **2015**, *6*, 7150. f) Wang, B.; Li, Y.; Ganguly, R.; Hirao, H.; Kinjo, R. *Nat. Commun.* **2016**, *7*, 1. g) Grotthuss, von, E.; Diefenbach, M.; Bolte, M.; Lerner, H.-W.; Holthausen, M. C.; Wagner, M. *Angew. Chem. Int. Ed.* **2016**, *55*, 14067.

[14] Masuda, J. D.; Schoeller, W. W.; Donnadieu, B.; Bertrand, G. *J. Am. Chem. Soc.* **2007**, *129*, 14180. b) Wang, Y.; Robinson, G. H. *Inorg. Chem.* **2011**, *50*, 12326. c) Wang, Y.; Robinson, G. H. *Dalton Trans.* **2012**, *41*, 337. d) Martin, C. D.; Soleilhavoup, M.; Bertrand, G. *Chem. Sci.* **2013**, *4*, 3020.

[15] a) Wang, Y.; Quillian, B.; Wei, P.; Wannere, C. S.; Xie, Y.; King, R. B.; Schaefer, H. F.; Schleyer, P. V. R.; Robinson, G. H. *J. Am. Chem. Soc.* **2007**, *129*, 12412. b) Matsumoto, T.; Gabbaï, F. P. *Organometallics* **2009**, *28* (15), 4252. c) Kinjo, R.; Donnadieu, B.; Celik, M. A.; Frenking, G.; Bertrand, G. *Science* **2011**, *333*, 610. d) Braunschweig, H.; Dewhurst, R. D.; Hammond, K.; Mies, J.; Radacki, K.; Vargas, A. *Science* **2012**, *336*, 1420. e) Braunschweig, H.; Dewhurst, R. D. *Organometallics* **2014**, *33*, 6271. f) Arrowsmith, M.; Böhnke, J.; Braunschweig, H.; Celik, M. A.; Claes, C.; Ewing, W. C.; Krummenacher, I.; Lubitz, K.; Schneider, C. *Angew. Chem. Int. Ed.* **2016**, *55*, 11271.

[16] Bünzli-Trepp, U. Systematic Nomenclature of Organic, Organometallic and Coordination Chemistry: Chemical-Abstracts Guidelines with IUPAC

Recommendations and Many Trivial Names; EPFL Press: Lausanne, Switzerland, 2007; p. 91.

[17]a) Ruiz, D. A.; Melaimi, M.; Bertrand, G. *Chem. Commun.* **2014**, *50*, 7837. b) Bissinger, P.; Braunschweig, H.; Damme, A.; Hörl, C.; Krummenacher, I.; Kupfer, T. *Angew. Chem. Int. Ed.* **2015**, *54*, 359. c) Wang, H.; Zhang, J.; Lin, Z.; Xie, Z. *Organometallics* **2016**, *35*, 2579.

[18] Taylor, J. W.; McSkimming, A.; Moret, M.-E.; Harman, W. H. *Angew. Chem. Int. Ed.* **2017**, *Early View*, doi:10.1002/anie.201703235.

[19] Metrical parameters reported for **6** are an average of the two chemically equivalent but crystallographically distinct molecules present in the asymmetric unit.

[20] Singh, P. S.; Evans, D. H. *J. Phys. Chem. B* **2006**, *110* (1), 637.

[21] Agnoli, S.; Favaro, M. *J. Mater. Chem. A* **2016**, 4, 5002.

[22] Osumi, S.; Saito, S.; Dou, C.; Matsuo, K.; Kume, K.; Yoshikawa, H.; Awaga, K.; Yamaguchi, S. *Chem. Sci.* **2015**, *00* (1), 1.

[23] Bieller, S.; Zhang, F.; Bolte, M.; Bats, J. W.; Lerner, H.-W.; Wagner, M. *Organometallics,* **2004**, *23*, 2107–2113.

[24] Fujimoto, T.; Ritter, T. *Org. Lett.,* **2015**, *17*, 544–547.

[25] Scott T.; Ooro B.; Collins D.; Shatruk M., Yakovenko A., Dunbar K., Zhou H.-C. *Chem Comm.*, **2008**, 65.

[26] J. J. Led and H. Gesmar. *Chem. Rev.*, **1991**, *91*, 1413-1426.

[27] Stoll, S.; Schweiger, A. *J. Magn. Reson.,* **2006**, *178*, 42-55.

[28] *APEX 2,* version 2014.1-1, Bruker (2014), Bruker AXS Inc., Madison, Wisconsin, USA.

[29] *SAINT,* version V8.34A, Bruker (2012), Bruker AXS Inc., Madison, Wisconsin, USA.

[30] *SADABS,* version 2012/1, Bruker (2012), Bruker AXS Inc., Madison, Wisconsin, USA.

[31] *SHELXTL,* version 2013/4, Bruker (2013), Bruker AXS Inc., Madison, Wisconsin, USA.

[32] *CELL_NOW*, version 2008/4, Bruker (2012), Bruker AXS Inc., Madison, Wisconsin, USA.

[33] *TWINABS*, version 2012/1, Bruker (2012), Bruker AXS Inc., Madison, Wisconsin, USA.

[34] Zhao, Y.; Truhlar, D. G. *J. Chem. Phys.*, **2006**, *125*, 194101-1.

[35] Neese, F. *Wiley Interdiscip. Rev.: Comput. Mol. Sci.* **2012**, *2*, 73.

[36] Weigend, F.; Ahlrichs, R. *Phys. Chem. Chem. Phys.* **2005**, *7*, 3297.

Chapter 3) Au Complexes of a Diphosphine-Diboraanthracene Ligand: A Versatile Platform for Redox Transformations of Small Molecules

3.1) A Molecular Boroauride: A Donor-Acceptor Complex of Anionic Gold

3.1.1.) Introduction

The ability to adopt multiple d-electron configurations (and hence oxidation states) is a hallmark of the transition metals,[1] and much of the chemistry associated with transition metal complexes, including electron transfer, oxidative addition/reductive elimination, and atom transfer, depends on this phenomenon.[2] While the transition metals are typically regarded as cation-forming elements, complexes with d-electron counts (d^5–d^{10}) corresponding to apparent negative oxidation states can be stabilized by electron-accepting ligands such as carbon monoxide and arenes.[3] In this context, the chemistry of gold is remarkable, as it alone among transition metals is stable as an isolated anion in the condensed phase.[4] The stability of the 12-valence-electron auride anion (Au^-), such as in the salt [NMe_4][Au],[5] thus highlights the unusual properties of Au in the context of transition metal chemistry more generally. Owing in part to the relativistic stabilization of the 6s orbital, the electron affinity of Au (2.3 eV)[6] is significantly larger than most transition metals and rivals that of the halogens.[7] Unfortunately, Au^- is only accessible by the direct reaction of metallic Au with elemental alkali

metals such as Cs and Rb, and the solution chemistry of auride compounds is restricted to liquid ammonia.[8] Furthermore, the intermediacy of Au(0) and its propensity to aggregate into metallic gold[9] complicates the electrochemical conversion of Au^- to more well-known monometallic gold complexes in positive oxidation states. As a result, a molecular system capable of reversible interconversion between Au(I) and Au(–I) states is unknown.

Intrigued by the possibility of accessing redox chemistry associated with the auride anion in a molecular setting, we began to explore ligand scaffolds capable of circumventing two central problems with a hypothetically reversible Au(I)/Au(–I) system: 1) the potential intermediacy of Au(0) that could lead to the precipitation of elemental gold and 2) the electronically saturated and highly reducing Au(–I) state, which should require strong acceptor interactions[10] for stability within a molecular framework. By utilizing concepts including ligand redox-activity and hemilability, respectively, we designed the ligand B_2P_2 (**1**, Scheme 3.2.1) to overcome these challenges, which features *trans*-disposed phosphine donors straddling a 9,10-dihydro-9,10-diboraanthracene (DBA) core. Agapie, et al. have recently used metal complexes of related noninnocent terphenyl diphosphines for the activation of small molecules, including CO[11] and O_2.[12] The phosphine donors are poised to stabilize a linear Au(I) cation, while the intrinsic redox activity and Lewis acidity of the DBA core give it the ability to both serve as an electron reservoir and engage in acceptor interactions with a highly

reduced metal atom as needed. Herein, we report the synthesis and reversible redox chemistry of $[Au(B_2P_2)]^n$ (**2**^{n}, $n = -1, 0, +1$), which is isolable in three states of charge. Both the cationic and neutral forms of this molecule possess Au(I) centers, with the first reduction event taking place at the DBA core. The anionic form, however, is best described as a bridging boroauride featuring a three-center, two-electron (3c-2e) B–Au–B interaction. Taken together, these results detail a strategy for accessing an unprecedented reversible Au(I)/Au(–I) redox couple in a molecular system

3.1.2) Results and Discussion

The diphosphine-DBA ligand **1** is accessed by the addition of two equivalents of 2-diisopropylphosphinophenyllithium to 9,10-dibromo-DBA in toluene. Metallation of **1** with $(Me_2S)AuCl$ in CH_2Cl_2 affords a complex with the stoichiometry $[Au(B_2P_2)]Cl$ (**2-Cl**) in 89% yield. Single crystal X-ray diffraction (XRD) reveals **2-Cl** to be zwitterionic in the solid state with the chloride anion bound to a tetrahedral boron center (Figure 3.1.1, left).[13] The geometry at the *pseudo*-two-coordinate Au(I) center is modestly bent ($\angle$P–Au–P = 153.7°) with an intermediate length contact with the second planar, three-coordinate boron atom ($d_{Au–B}$ = 2.5645(16) Å). In a 3:1 mixture of THF:benzene, **2-Cl** exhibits a pair of inequivalent and strongly coupled ^{31}P resonances by NMR at 57.3 and 53.9 ppm ($^2J_{P\text{-}P}$ = 240 Hz, Figure 3.1.5.6), consistent with the preservation of the

zwitterionic form in solution. In $CDCl_3$, however, a single ^{31}P resonance is

Scheme 3.1.1. Synthesis of the ligand B_2P_2 and its Au complexes.

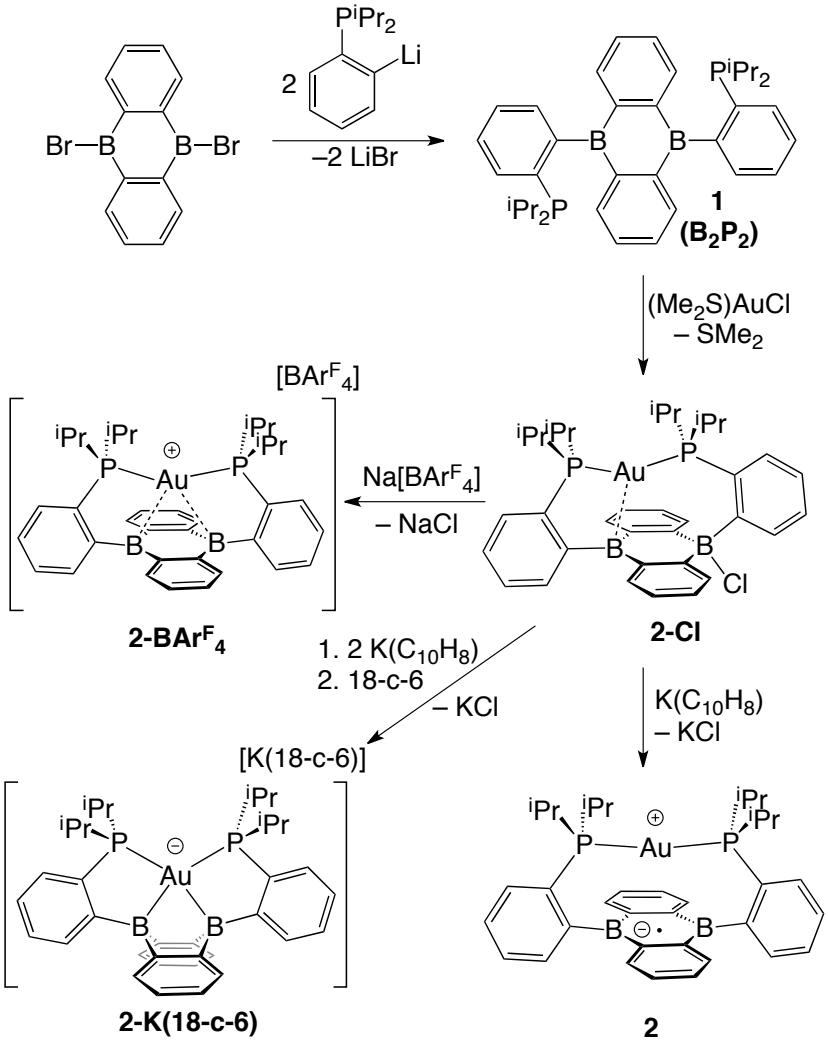

observed for **2-Cl** at 57.1 ppm (Figure 3.1.5.5), suggesting either complete chloride dissociation or its rapid exchange between the two boron sites.

Anion metathesis of **2-Cl** with $Na[BAr^F_4]$ (Ar^F = 3,5-bis(trifluoromethyl)phenyl) gives the complex salt $[Au(B_2P_2)][BAr^F_4]$ (**2-BAr$^F_4$**) (Scheme 3.1.1). The single-crystal XRD structure of **2-BAr$^F_4$** reveals a

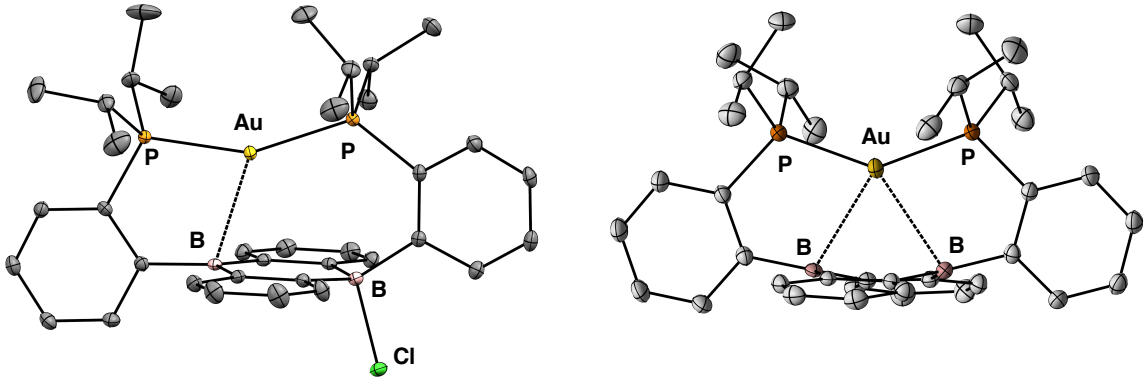

Figure 3.1.1. Thermal ellipsoid plots (50%) of $[Au(B_2P_2)]Cl$ (2-Cl, left) and the cation in $[(AuB_2P_2)][BAr^F{}_4]$ (2-$BAr^F{}_4$, right).

symmetrical $[Au(B_2P_2)]^+$ cation ([**2**]$^+$) with a significantly bent P–Au–P linkage ($\angle$P–Au–P = 141.6^o) that situates the gold center within 2.7 Å of each boron atom (d_{Au-B} = 2.6101(17), 2.6785(18) Å) (Figure 3.1.1, right). While long, these Au–B distances are consistent with those observed in related Au(I) borane complexes for which weak donor acceptor interactions are thought to exist.[14] Given the electron deficiency of the central C_4B_2 ring of the DBA core, this interaction in [**2**]$^+$ can be viewed as an inverse cation-π interaction, wherein an electron-rich cation interacts with an electron deficient π-system.

Cyclic voltammetry performed on **2-BAr$^F{}_4$** (0.1 M $[NBu_4][PF_6]$ in CH_3CN, 100 mV/s scan rate) revealed two reversible redox processes at –1.60 and –2.05 V versus Fc/Fc^+ (Fc = $(C_5H_5)_2Fe$, Figure 3.1.2). By comparison, the gold-free DBA derivative 9,10-Mes_2-DBA (Mes = 2,4,6-trimethylphenyl),[15] a proxy for the DBA core in [**2**]$^+$, undergoes reversible reduction events at –1.62 and –2.48 V versus Fc/Fc^+ under these conditions.[16] While the first reduction of [**2**]$^+$ occurs at

a potential comparable to that of its gold-free analogue, the second reduction is positively shifted by over 400 mV relative to 9,10-Mes_2-DBA. These data imply a crucial role for Au in the observed redox chemistry of the [Au(B_2P_2)] platform.

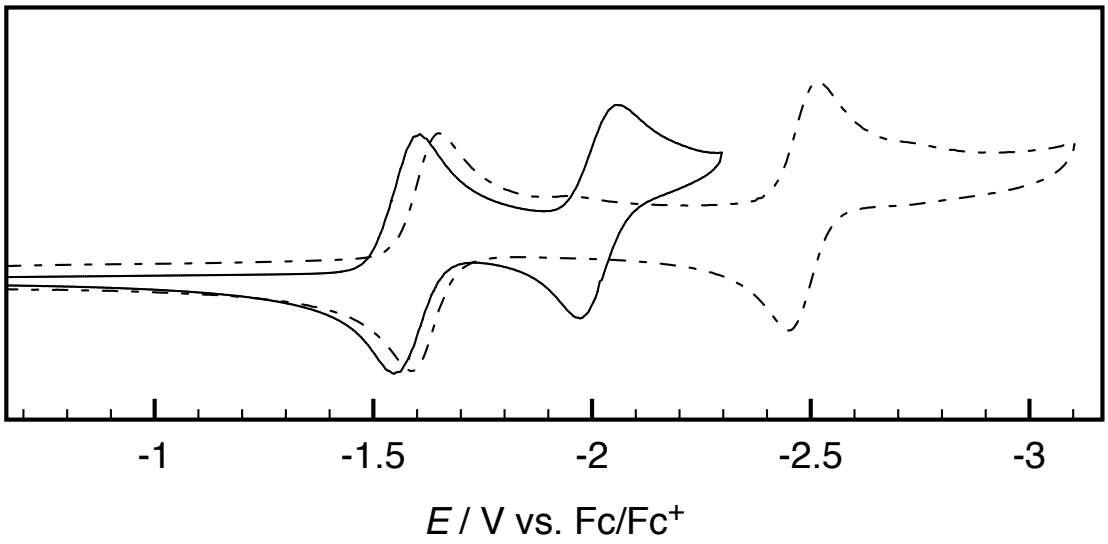

Figure 3.1.2. Normalized cyclic voltammograms of [Au(B_2P_2)][BAr^F_4] (solid) and 9,10-Mes_2-DBA (dashed)

To understand roles of both the Au center and the DBA core in the redox chemistry of [Au(B_2P_2)], especially the remarkable anodic shift in the second reduction event, we sought to isolate and characterize the one- and two-electron reduced products. Chemical reduction of **2-Cl** with 1 equivalent of K($C_{10}H_8$) in THF gives the neutral radical Au(B_2P_2) (**2**) as a purple crystalline solid (Scheme 3.1.1). The solid-state structure of **2** was determined by XRD and features a slightly bent diphosphine-gold moiety (∠P–Au–P = 158.97(2)°) spanning a planar DBA core (Figure 3.1.3, left). In contrast to [**2**]$^+$, the Au–B interactions in **2** are lengthened substantially (d_{Au-B} = 3.013(2) and 3.084(3) Å). The ^{1}H NMR spectra of **2** are consistent with paramagnetism (Figure 3.1.5.11), and the X-band

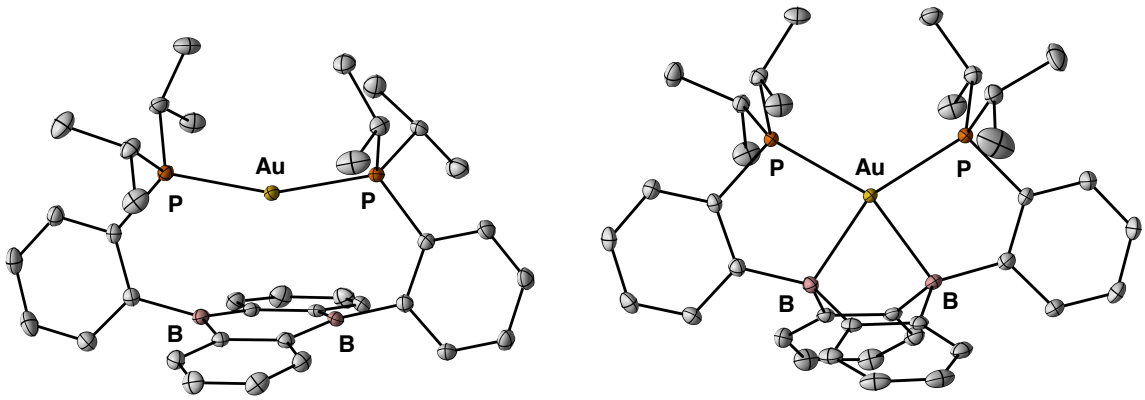

Figure 3.1.3. Thermal ellipsoid plots (50%) of $Au(B_2P_2)$ (**2**, left), and the anion in $[Au(B_2P_2)][K(18\text{-c-}6)]$ (**[2]–**, right).

electron paramagnetic resonance (EPR) spectrum of **2** in fluid 2-methyltetrahydrofuran (2-MeTHF) reveals a broad triplet centered at $g = 1.99$ (Figure 3.1.4, left). The observed feature is consistent with hyperfine interactions with two equivalent ^{31}P nuclei ($I = 1/2$, $A_{iso}(^{31}P) = 55$ MHz), and while this signal broadens upon cooling to 100 K, no additional fine structure was resolved (Figure 3.1.5.22). Although the ^{31}P hyperfine interactions in **2** could be taken to indicate significant spin density (and hence reduction) at Au, the established redox chemistry of DBA derivatives and lack of precedent for authentic coordination complexes of Au(0)[17] suggest that **2** is best formulated as a zwitterion containing a Au(I) cation linked to a DBA radical anion. Indeed, DFT calculations performed on a slightly truncated[18] model suggest that the spin-density of **2** is localized

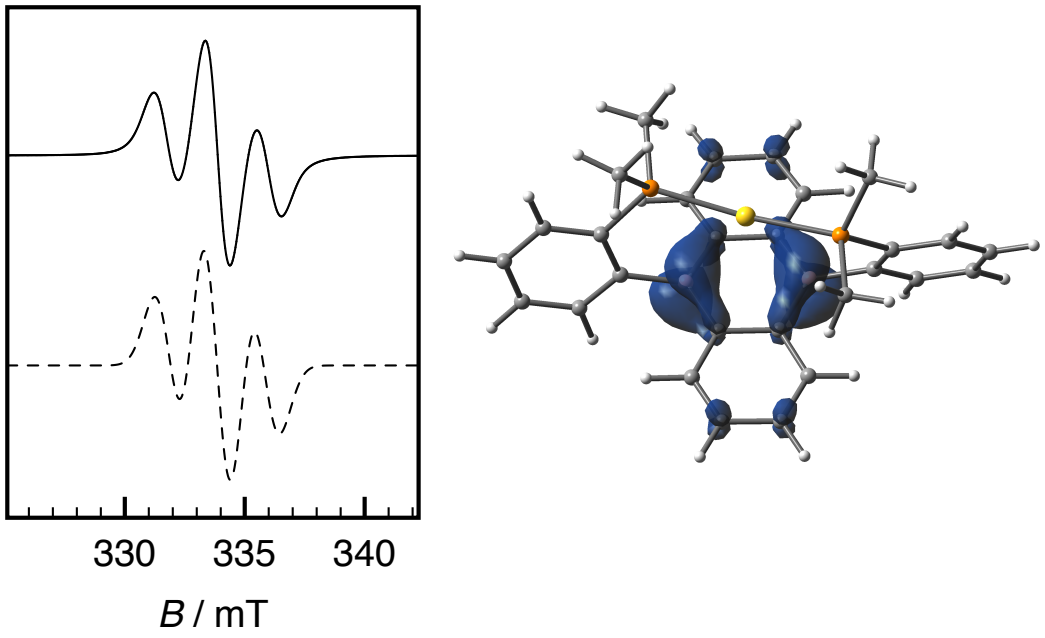

Figure 3.1.4. Left: X-band EPR spectrum (9.309 GHz) of $(B_2P_2)Au$ collected in 2-MeTHF solution at 298 K (solid) along with its simulation (dashed). Simulation parameters are g = 1.99215 and $A_{iso}(^{31}P)$ = [56.5, 56.5] MHz with a linewidth of 1.54 mT. Right: spin-density plot for a truncated model of **2** calculated by DFT (see Computational Procedures for details).

primarily on the DBA core (Figure 3.1.4, right), with natural spin populations of 0.26 e^- on each boron and most of the remaining spin delocalized over the carbons of the DBA unit (See Computational Procedures). This electronic structure nonetheless gives rise to a significant calculated hyperfine interaction (via the IGLO method, see Computational Procedures for details)[19] with the ^{31}P nuclear spins (calc. $A_{iso}(^{31}P)$ = 37.0 MHz) and much smaller boron hyperfine interactions (calc. $A_{iso}(^{11}B)$ = 9.7 MHz) in qualitative agreement with the experimental spectrum. The large, isotropic ^{31}P hyperfine interaction is presumably mediated by hyperconjugation[20] either through the phenylene linker or the Au center. In either case, very small spin densities at ^{31}P can lead to large EPR hyperfine interactions so long as there is significant involvement of the 3s

orbital on P.[21] To wit, the natural spin density at each P atom is calculated to be ca. 0.005 e^- for **2**, 43% of which is hosted in the 3s orbital. From a structural perspective, the lengthening of the Au–B distances in **2** is consistent with the population of the DBA-based orbital that served as the acceptor for the weak interaction observed in [**2**]$^+$ (*vide supra*).

Reduction of **2-Cl** with 2 equivalents of K($C_{10}H_8$) gives the diamagnetic crimson anion [Au(B_2P_2)]$^-$ ([**2**]$^-$), which features a sharp singlet in its ^{11}B NMR spectrum at 11.1 ppm, a significant upfield shift relative to the broad feature at 32.0 ppm observed for [**2**]$^+$. Addition of 18-crown-6 (18-c-6) to the reaction mixture affords crystals of the complex salt [Au(B_2P_2)][K(18-c-6)] (**2-K(18-c-6)**). Single crystal XRD on this material reveals a dramatic rearrangement of the AuB_2P_2 core, with very short Au–B distances ($d_{Au–B}$ = 2.241(2), 2.237(2) Å) and pyramidalized boron centers ($\sum\angle$C-B-C = 343.8°, 343.9°) (Figure 3.1.3, right). Although complexes with gold-borane donor-acceptor interactions have been reported, they typically feature a Au(I) donor to a single borane acceptor and longer Au–B distances in the range of 2.3–2.9 Å. In contrast, [**2**]$^-$ is formally composed of an auride anion interacting with two *cis*-disposed borane ligands and is the only example of a mononuclear transition metal complex featuring two such short metal-organoborane (BR_3) interactions. The short Au–B distances in [**2**]$^-$ are comparable to those found in gold complexes featuring base-stabilized

boryl[22] and borylene[23] ligands, multimetallic boride complexes,[24] as well as metallaborane cluster compounds.[25]

There are in principle two qualitative descriptions of the B–Au–B bonding in [**2**]$^-$, either as two, two-center, two-electron (2c-2e) bonds or a single three-center, two-electron (3c-2e) bond. Given the well-established isolobal relationship between gold and hydrogen[26] we favor the latter description wherein [**2**]$^-$ is understood as a donor-acceptor complex between an auride anion and DBA. Thus [**2**]$^-$ is analogous to a borohydride, and would therefore be described as a bridging boroauride ($[R_3B(\mu\text{-}Au)BR_3]^-$). We stress the plausibility of the auridic description of the gold center in [**2**]$^-$ by emphasizing that Au is stable in anionic form (*vide supra*) and significantly more electronegative than hydrogen (χ_{Au} = 2.54 and χ_H = 2.20 on the Pauling Scale). In fact, the Au atom is the most electronegative atom in [**2**]$^-$. We also highlight that the tetraauridoborate anion ($[BAu_4]^-$) has been explored computationally and found to exhibit significant similarities with the tetrahydridoborate anion ($[BH_4]^-$).[27]

Further insight into this question was provided by DFT calculations on a model of [**2**]$^-$. [18] A Quantum Theory of Atoms In Molecules (QTAIM)[28] analysis of the calculated electron density reveals a straight bond path connecting the Au center to each B atom (Figure 3.1.5A). Interestingly, the corresponding bond critical point (BCP) is found in a negative region of the Laplacian, i.e. a region with local accumulation of electron density, indicative of a strongly covalent

interaction, which sets it apart from typical coordination bonds such as the P–Au interaction in the same compound. In addition, a natural bond orbital (NBO)[29] analysis reveals that the Au atom and the two B atoms engage in a 3c-2e bond, akin to that found in hydride-bridged boranes such as B_2H_6, which is described by one filled (τ) and two empty ($\tau^{*(\pi)}$ and $\tau^{*(\Delta)}$) orbitals formed by linear combinations of the 6s(Au) with two boron-centered hybrid orbitals of mostly p character ($sp^{9.3}$: 90.3% p, 9.7% s) (Figure 3.1.5B).The filled τ orbital arises from a fully in-phase combination (37.6 % Au, 2 × 31.2% B); the $\tau^{*(\pi)}$ orbital has a nodal plane containing the Au atom and is purely boron-centered, while the $\tau^{*(\Delta)}$ orbital has a nodal surface containing both boron atoms and consists of 62.4% 6s(Au) and 2 × 18.8% $sp^{9.3}$(B). Two main delocalization effects are identified by second-order perturbation theory. First, a strong donation from P-centered lone pairs into the $\tau^{*(\Delta)}$ orbital (57.1 kcal/mol) describes the expected P⟶Au dative bonds. Second, the in-plane d-orbital of Au is somewhat delocalized into the $\tau^{*(\pi)}$ orbital (31.4 kcal/mol). Taken together, these data support the description of [**2**]$^-$ as a boroauride compound.

Interestingly, the covalent bonding picture of the [B–Au–B]$^-$ linkage arising from NBO analysis contrasts with the more ionic description obtained for the [B–Cu]$^-$ unit in the related [(TPB)Cu]$^-$ anion (TPB = tris[2-(diispropylphosphino)phenyl]borane).[30,31] There, the bonding electron pair principally resides on the boron atom and engages in a dative bond with the

copper center, and the compound is best described as a boron(I) dianion stabilized by coordination to a Cu(I) center rather than an authentic cupride. This is likely a consequence of the comparatively higher electronegativity (χ_{Au} = 2.54; χ_{Cu} = 1.9) and electron affinity (EA_{Au} = 2.3 eV; EA_{Cu} = 1.2 eV)[32] of gold, highlighting its unique ability among transition metals to afford a molecular complex derived from an $d^{10}s^2$ electronic configuration.

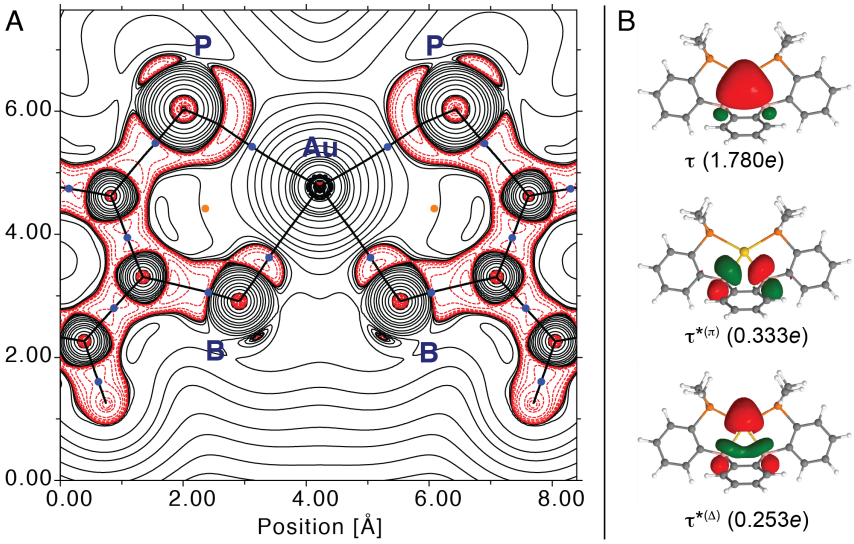

Figure 3.1.5. Computational analysis of the Au–B interaction. (A) Contour map (negative values in dashed red) of the Laplacian distribution $\nabla^2\rho(r)$ in the B–Au–B plane. Bond paths are depicted as black lines, bond (BCP) and ring (RCP) critical points as blue and orange circles, respectively. (B) Natural bonding orbitals (NBOs) describing the B–Au–B 3-center/2-electrons bond and their electronic population (in parenthesis).

3.1.3) Concluding Remarks

In conclusion, through the use of a ligand capable of both redox activity and strong acceptor interactions, we have synthesized a coordination complex of the auride anion and demonstrated its reversible interconversion between Au(I) and Au(–I) states. The strategy outlined herein provides a blueprint for unlocking

the redox chemistry of auride in mild solution-based processes. Access to an auride equivalent under such conditions may have significant implications for both molecular catalysis and nanotechnology, given the importance of gold chemistry to both fields and ongoing studies are aimed at realizing these goals.

3.1.4) Experimental Section

3.1.4.1) General Considerations

Unless otherwise noted, all manipulations were carried out using standard Schlenk or glovebox techniques under a purified dinitrogen atmosphere. Tetrahydrofuran (THF), dichloromethane (DCM), diethyl ether, toluene, benzene, and *n*-hexane were dried and deoxygenated by sparging with argon and passage through activated alumina in a solvent purification system from JC Meyer Solvent Systems. Hexamethyldisiloxane (HMDSO) was distilled from sodium metal and stored over 4Å molecular sieves for 24 hours prior to use. 2-Methyltetrahydrofuran(2-MeTHF) was distilled from purple sodium benzophenone ketyl and stored over 4Å molecular sieves for at least 24 hr prior to use. Non-halogenated solvents were tested with a standard purple solution of sodium benzophenone ketyl in tetrahydrofuran to confirm effective oxygen and moisture removal. All reagents were purchased from commercial suppliers and used without further purification unless otherwise noted. (2-bromophenyl)diisopropylphosphine[33] (9,10-dibromo-9,10-diboraanthracene, [34]

sodium tetrakis[3,5-bis(trifluoromethyl)phenyl]borate ($NaBAr^F_4$)[35] and $K(C_{10}H_{10})(THF)_{0.5}$ [36] were synthesized according to literature procedures. Elemental analyses were performed by Midwest Microlab, LLC, Indianapolis, IN. Deuterated solvents were purchased from Cambridge Isotope Laboratories Inc., degassed, and dried over activated 4Å molecular sieves for at least 24 hr prior to use. NMR spectra were recorded on Varian Inova 500MHz and Bruker Avance 600MHz spectrometers. ^1H chemical shifts are reported in ppm relative to tetramethylsilane using residual solvent as internal standards. ^{31}P and ^{11}B chemical shifts are reported in ppm relative to 85% aqueous H_3PO_4 and $BF_3{\cdot}Et_2O$, respectively. ^{11}B NMR spectra were manipulated with MestReNova 10.0.2. and had a backwards LP applied to eliminate background signal from the borosilicate NMR tube.[37] NMR spectral resonances are assigned as Ar^P and DBA for those in the phosphino-phenyl and diboraanthracene ring systems, respectively. EPR X-band spectra were obtained on a Bruker EMX spectrometer controlled by Bruker Win-EPR software suite version 3.0. Simulations were performed using the Easyspin software suite.[38] UV-Vis spectra were recorded using a Cary Bio 500 spectrometer using a 1 cm path length quartz cuvette with a solvent background subtraction applied. Mass spectra were recorded using a Waters GCT high-resolution mass spectrometer operating in liquid injected field desorption ionization (LIFDI) mode. X-ray diffraction studies were performed using a Bruker-AXS diffractometer. Cyclic Voltammetry (CV) experiments were

performed using a Pine AFP1 potentiostat. The cell consisted of a glassy carbon working electrode, a Pt wire auxiliary electrode and a Pt wire pseudo-reference electrode. All potentials are referenced vs. the Fc/Fc^+ couple measured as an internal standard.

3.1.4.2) 9,10-bis(2-(diisopropylphosphino)phenyl)-9,10-dihydro-9,10 diboraanthracene (B_2P_2) (1).

A solution of (2-bromophenyl)diisopropylphosphine (18.01 g, 65.93 mmol) in ether (50 mL) was cooled to –78 ºC and ^{n}BuLi (41.2 mL of a 1.6 M solution in hexanes, 66 mmol) added drop-wise with stirring. The resulting pale-orange solution was warmed slowly to room temperature and the solvent removed *in vacuo*. The residue was re-dissolved in toluene (30 mL) and added dropwise to a cooled (–78ºC) solution of 9,10-dibromo-9,10-diboraanthracene (10.00 g, 29.97 mmol) in toluene (20 mL). The resulting suspension was allowed to warm to room temperature overnight and filtered. The solvent was removed *in vacuo* and the crude solid dissolved in the minimum pentane (*ca.* 100 mL). Addition of HMDSO (10 mL) caused a small amount of amorphous solid to precipitate that was removed by filtration through celite. Concentration of the solution *in vacuo* caused the product to precipitate as a pale-yellow solid which was collected by filtration and washed once with HMDSO (5 mL). Concentration of the mother liquor yielded an additional crop of material that was sufficiently pure for the synthesis of metal complexes. Overall yield: 9.85 g, 59%. ^{1}H NMR (500 MHz, C_6D_6) δ 7.68 (ddd, *J* = 8.5, 3.7, 1.4 Hz, 4H, 4x 2-DBA*H*), 7.50 (d, *J* = 7.3 Hz, 2H,

2x 6-Ar^P*H*), 7.40 (t, *J* = 7.3 Hz, 2H, 2x 5-Ar^P*H*), 7.39 (d, *J* = 7.5 Hz, 2H, 2x 3-Ar^P*H*), 7.28 (t, *J* = 7.5 Hz, 2H, 2x 4-Ar^P*H*), 7.21 (ddd, *J* = 1.3, 5.5, 8.5 Hz, 4H, 4x 1-DBA*H*), 1.99 (sept, *J* = 7.0 Hz, 4H, 4x C*H*(Me)$_2$), 0.88 (d, *J* = 7.0 Hz, 12H, 4x CH(*Me*)), 0.86 (d, *J* = 7.0 Hz, 12H, 4x CH(*Me*)). ^{13}C{^{1}H} (125.7 MHz, C_6D_6) δ 162.6 (d, J_{CP} = 38.7 Hz), 152.6, 137.4 (d, J_{CP} = 20.1 Hz), 136.9, 131.8 (d, J_{CP} = 30.6 Hz), 130.5 (d, J_{CP} = 16.2 Hz), 126.8, 24.8, 19.9, 19.8. ^{31}P{^{1}H} NMR (202 MHz, C_6D_6) δ 18.40 (s). ^{11}B{^{1}H} (160 MHz, C_6D_6) δ 34.13 (s). LIFDI MS: *m/z* Found: 560.3124; Calc. for $[B_2P_2]^+$: 560.3104.

3.1.4.3) Au(B_2P_2)Cl (2-Cl).

B_2P_2 (0.100 g, 0.179 mmol) in DCM (5 mL) was added dropwise to a cooled (–15 °C) slurry of $AuClSMe_2$ (0.053 g, 0.180 mmol) in DCM (3 mL) with stirring. The mixture was stirred at –15 °C for 30 mins before being allowed to warm slowly to room temperature. After stirring an additional 1-hour, the mixture was filtered and diluted with toluene (8 mL). Concentration *in vacuo* caused the product to crystallize. The solid was collected by filtration and washed with a small portion of benzene (1 mL) and diethyl ether (2 mL). Yield: 0.126 g, 89%. X-ray quality crystals were grown by layering a concentrated THF solution with toluene. ^{1}H NMR (500 MHz, $CDCl_3$) δ 8.52 (bs, 2H, 2x 6-Ar^P*H*), 7.64 (t, *J* = 7.0 Hz, 2H, 2x 4/5-Ar^P*H*), 7.52 (td, *J* = 4.0, 7.5 Hz, 2H, 2x 3-Ar^P*H*), 7.43 (t, *J* = 7.5 Hz, 2H, 2x 4/5-Ar^P*H*), 7.23 (dd, *J* = 4.5, 6.0 Hz, 4H, 2x 1-DBA*H*), 7.09 (dd, *J* = 3.0, 6.0 Hz, 4H, 2x 2-DBA*H*), 2.41 (m, 4H, 4x C*H*(Me)$_2$), 0.96 (d, *J* = 8.5 Hz, 6H, 2x CH(*Me*)),

0.94 (d, *J* = 8.5 Hz, 6H, 2x CH(*Me*)), 0.83 (d, *J* = 7.5 Hz, 6H, 2x CH(*Me*)), 0.81 (d, *J* = 7.5 Hz, 6H, 2x CH(*Me*)). $^{31}P\{^{1}H\}$ NMR (202 MHz, $CDCl_3$) δ 57.08 (s). $^{31}P\{^{1}H\}$ NMR (243 MHz, THF:Benzene, 3:1) δ 57.33 (d, $J_{P\text{-}P}$ = 239.4 Hz), 53.94 (d, $J_{P\text{-}P}$ = 240 Hz). $^{11}B\{^{1}H\}$ (193 MHz, THF:Benzene, 3:1) δ 0.10 (s). Anal. Calcd for $C_{36}H_{44}AuB_2ClP_2$(1x $CDCl_3$): C, 48.67 H, 5.08. Found: C, 48.47 H, 5.26.

3.1.4.4) [Au(B_2P_2)][BAr^F_4] (2-BAr^F_4).

To a solution of **2-Cl** (0.050 g, 0.065 mmol) in THF (4 mL) was added Na[BAr^F_4] (0.055 g, 0.065 mmol) in Et_2O (2 mL) and the mixture stirred for 30 minutes. Precipitated NaCl was removed via filtration and volatiles removed *in vacuo*. The solid residue was re-dissolved in the minimum THF (*ca.* 8 mL) and diluted with an equal volume of hexane. Concentration of the solution *in vacuo* caused the product to crystallize. The solid was collected by filtration and washed with a small amount of cold Et_2O (*ca.* 0.5 mL). Yield: 0.016 g, 79%. X-ray quality crystals were grown by layering a concentrated THF solution with hexanes. ^{1}H NMR (500 MHz, $CDCl_3$) δ 7.83 (m, 4H, 4x DBA*H*), 7.70 (m, br, 8H, 8x BAr^F_4H), 7.59–7.68 (m, 4H, 4x Ar^PH), 7.51 (s, br 4H, 4x BAr^F_4H), 7.47 (m, 8H, 4x DBA*H* + 4x Ar^PH), 2.43 (m, 4H, 4x C*H*$(Me)_2$), 0.76–0.94 (m, br, 24H, 8x CH(*Me*)). $^{31}P\{^{1}H\}$ NMR (202 MHz, $CDCl_3$) δ 58.75 (s). $^{11}B\{^{1}H\}$ (193 MHz, $CDCl_3$) δ 32.00 (DBA*B*), –6.69 (*B*Ar^F_4). LIFDI MS: *m/z* Found: 757.2765; Calc. for $[AuB_2P_2]^+$: 757.2770. Anal. Calcd for $C_{68}H_{56}AuB_3F_{24}P_2$: C, 50.40 H, 3.48. Found: C, 50.41 H, 3.38.

3.1.4.5) Au(B_2P_2) (2).

$K(C_{10}H_{10})(THF)_{0.5}$ (7.7 mg, 0.038 mmol) in THF (4 mL) was added dropwise to a

slurry of **2-Cl** (0.030 g, 0.038 mmol) in benzene (2 mL) with stirring. The resulting dark purple mixture was stirred for 10 minutes before volatiles were removed *in vacuo*. The solid residue was washed with several portions of hexane, re-dissolved in benzene (5 mL) and filtered through celite. Removal of all volatiles *in vacuo* gave the pure compound as a purple crystalline solid. Yield: 0.020 g (70%). X-Ray quality crystals were grown by layering a concentrated toluene solution of the compound with HMDSO. ^{1}H NMR (500 MHz, C_6D_6) δ 6.37, 1.20, 1.14. UV-vis (THF): λ_{max} (nm) (ε_{max} (M^{-1} cm^{-1})) 375 (sh, 8.1 x 10^3), 446 (3.2 x 10^3), 473 (3.4 x 10^3), 569 (4.4 x 10^3). As a result of its extreme sensitivity and despite multiple attempts, good elemental analysis of this compound was not obtained.

3.1.4.6) [Au(B_2P_2)][K(18-c-6)] (2-K(18-c-6)).

$K(C_{10}H_{10})(THF)_{0.5}$ (18.7 mg, 0.092 mmol) in THF (2 mL) was added dropwise to a slurry of Au(B_2P_2Cl) (0.037g, 0.046 mmol) in benzene (5 mL). The resulting crimson mixture was stirred 30 minutes before volatiles were removed *in vacuo.* The solid was washed with several portions of hexane, re-dissolved in the minimum benzene (*ca.* 4 mL) and filtered through celite. A solution of 18-crown-6 (0.013 g, 0.049 mmol) in hexane (8 mL) was then added. Storage at –15 ^{o}C overnight gave dark red crystals, which were collected by filtration and washed with hexane (1 mL). Yield (0.036 g, 74%). X-Ray quality crystals were grown by layering a concentrated benzene solution with HMDSO. ^{1}H NMR (500 MHz,

C_6D_6) 8.14 (d, J = 7.2 Hz, 2H, 2x Ar^P*H*), 7.73 (t, J = 6.6 Hz, 2H, 2x Ar^P*H*), 7.61 (d, br, J = 6.0 Hz, 2H, 2x Ar^P*H*), 7.43 (t, J = 7.4 Hz, 2H, 2x Ar^P*H*), 7.02 (m, br, 4H, 4x DBA*H*), 6.64 (m, br, 4H, 4x DBA*H*), 3.05 (s, br, 24H, 18-c-6), 2.44 (m, br, 4x C*H*$(Me)_2$), 1.13 (d, J = 7.0 Hz, 6H, 4x CH(*Me*)), 1.09 (d, J = 7.4 Hz, 6H, 4x CH(*Me*)), 1.03 (d, J = 6.9 Hz, 6H, 4x CH(*Me*)), 1.01 (d, J = 6.8 Hz, 6H, 4x CH(*Me*)). ^{13}C NMR (126 MHz, C_6D_6) δ 170.45 (br), 139.11 (br), 134.09, 131.45, 127.85, 122.89, 121.20 (br), 120.27, 69.98 (18-c-6), 26.41, 20.04, 19.07. $^{31}P\{^1H\}$ NMR (121 MHz, C_6D_6) δ 85.30 (s). $^{11}B\{^1H\}$ (193 MHz, C_6D_6) δ 11.09 (s). UV-vis (THF): λ_{max} (nm) (ε_{max} ($M^{-1}cm^{-1}$)) 370 (sh, 6.8 x 10^3), 485 (2.5 x 10^3), 550 (sh, 1.8 x 10^3). Anal. Calcd for $C_{48}H_{68}AuB_2P_2KO_6$: C, 54.35 H, 6.46. Found: C, 53.95 H, 6.49.

3.1.5) Spectroscopic Data

.

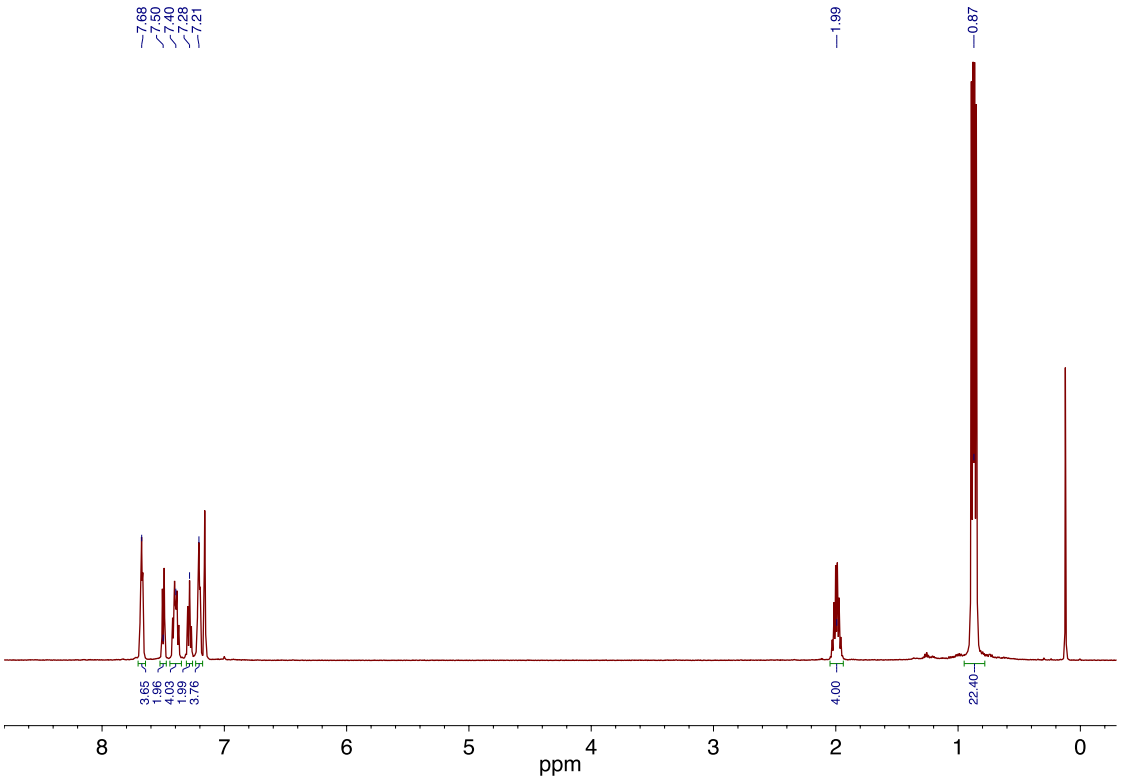

Figure 3.1.5.1. ^{1}H NMR spectrum of **B_2P_2** recorded at 500 MHz in C_6D_6.

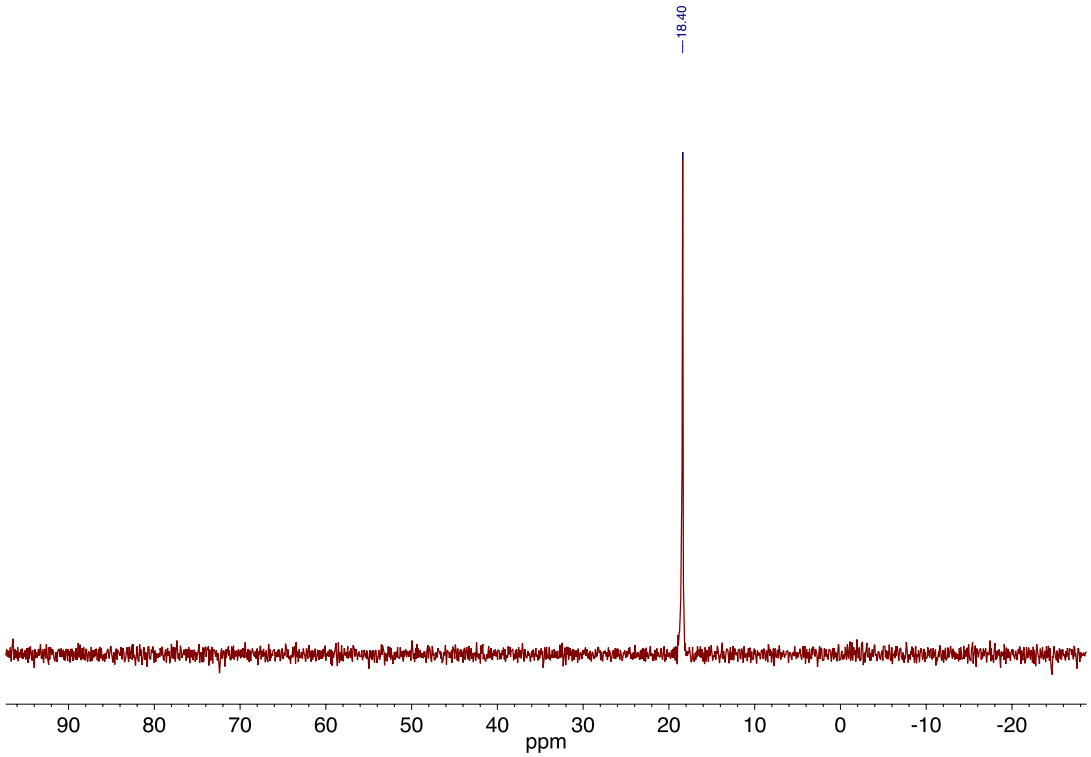

Figure 3.1.5.2. ^{31}P NMR spectrum of $\mathbf{B_2P_2}$ recorded at 202 MHz in C_6D_6.

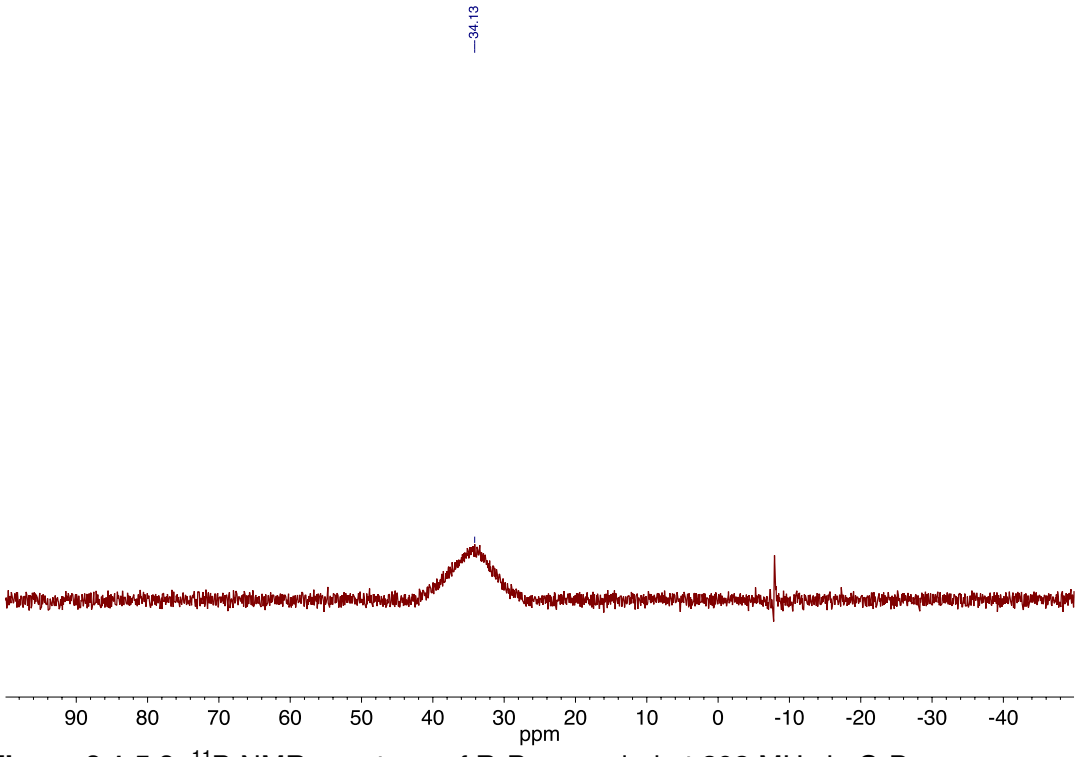

Figure 3.1.5.3. ^{11}B NMR spectrum of $\mathbf{B_2P_2}$ recorded at 202 MHz in C_6D_6.

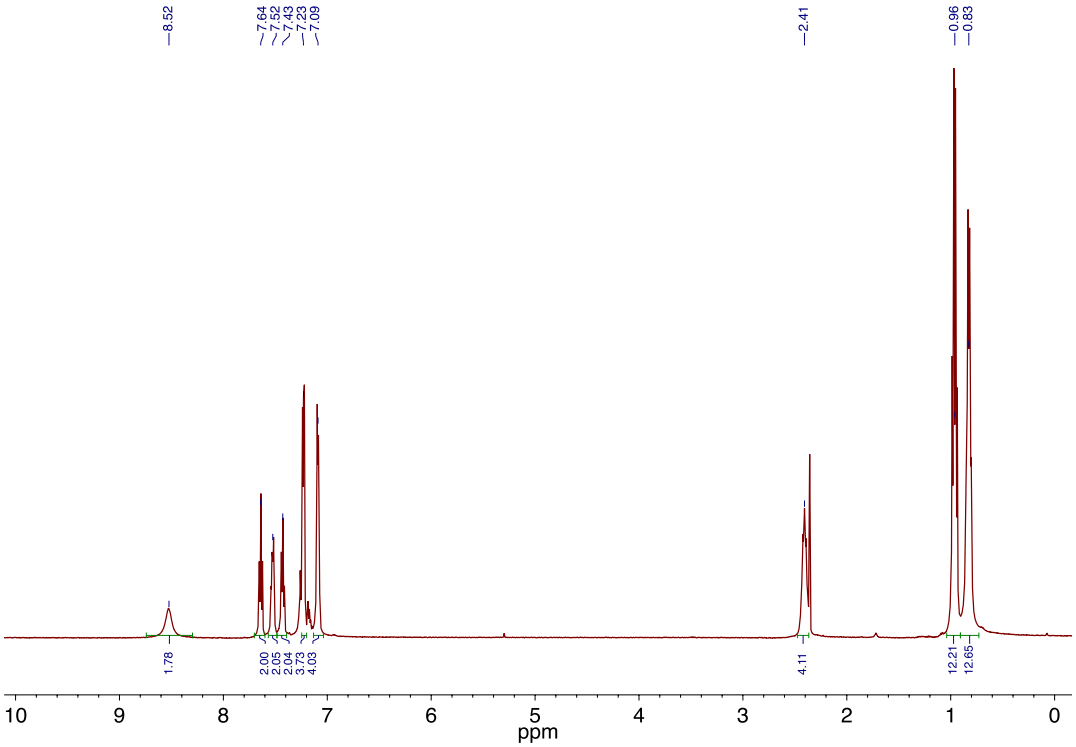

Figure 3.1.5.4. ^{1}H NMR spectrum of **Au(B_2P_2)Cl** recorded at 500 MHz in $CDCl_3$

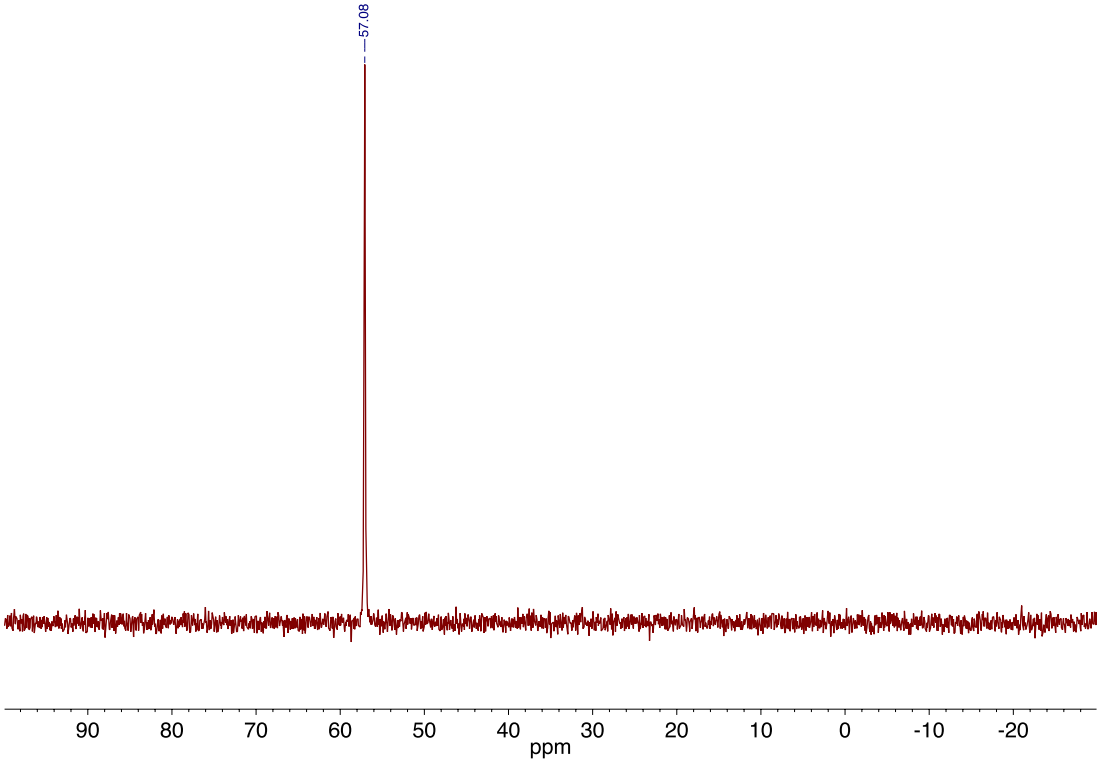

Figure 3.1.5.5. ^{31}P NMR spectrum of **Au(B_2P_2)Cl** recorded at 202 MHz in $CDCl_3$.

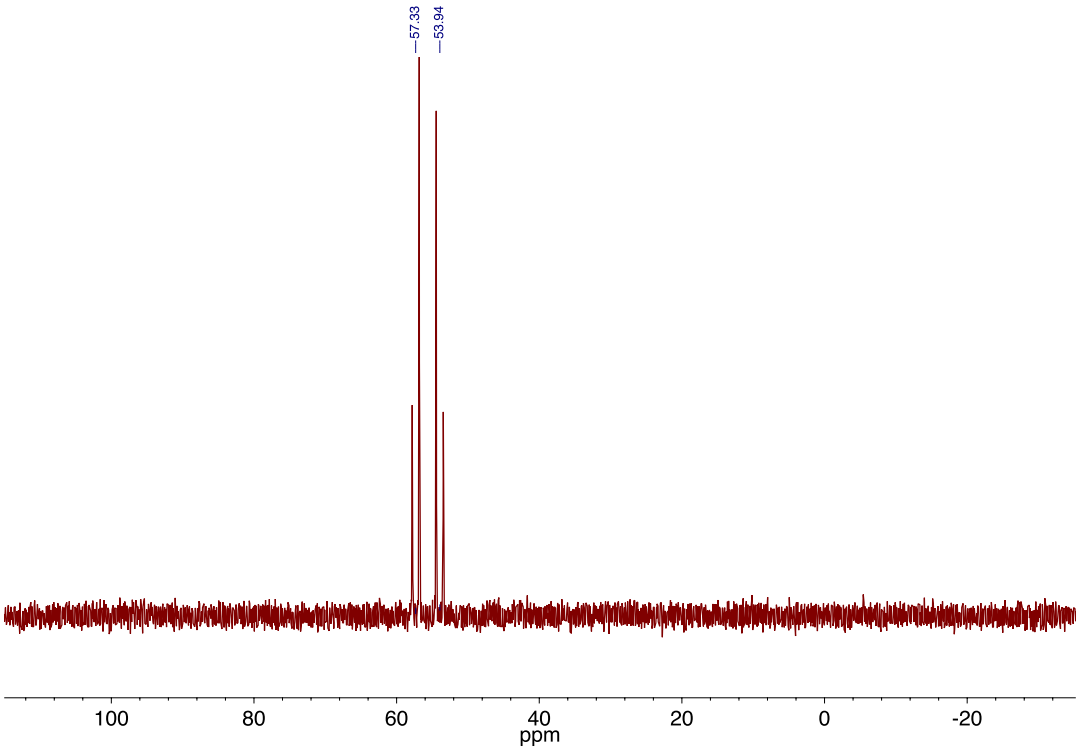

Figure 3.1.5.6. ^{31}P NMR spectrum of **Au(B_2P_2)Cl** recorded at 202 MHz in THF:Benzene (3:1).

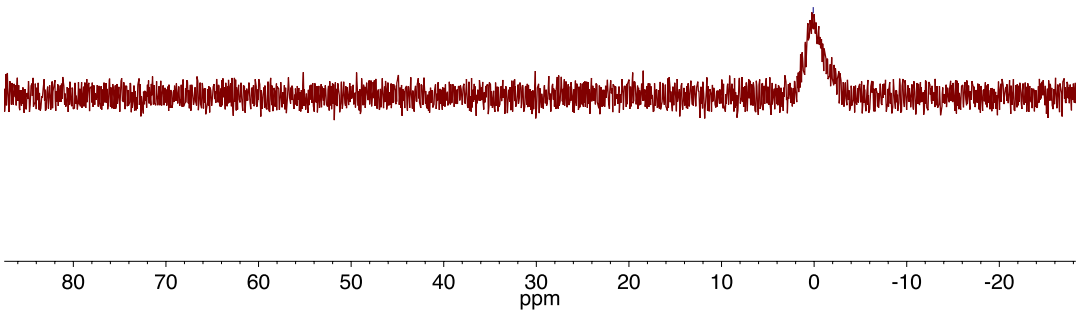

Figure 3.1.5.7. ^{11}B NMR spectrum of **Au(B_2P_2)Cl** recorded at 193 MHz in THF:Benzene (3:1).

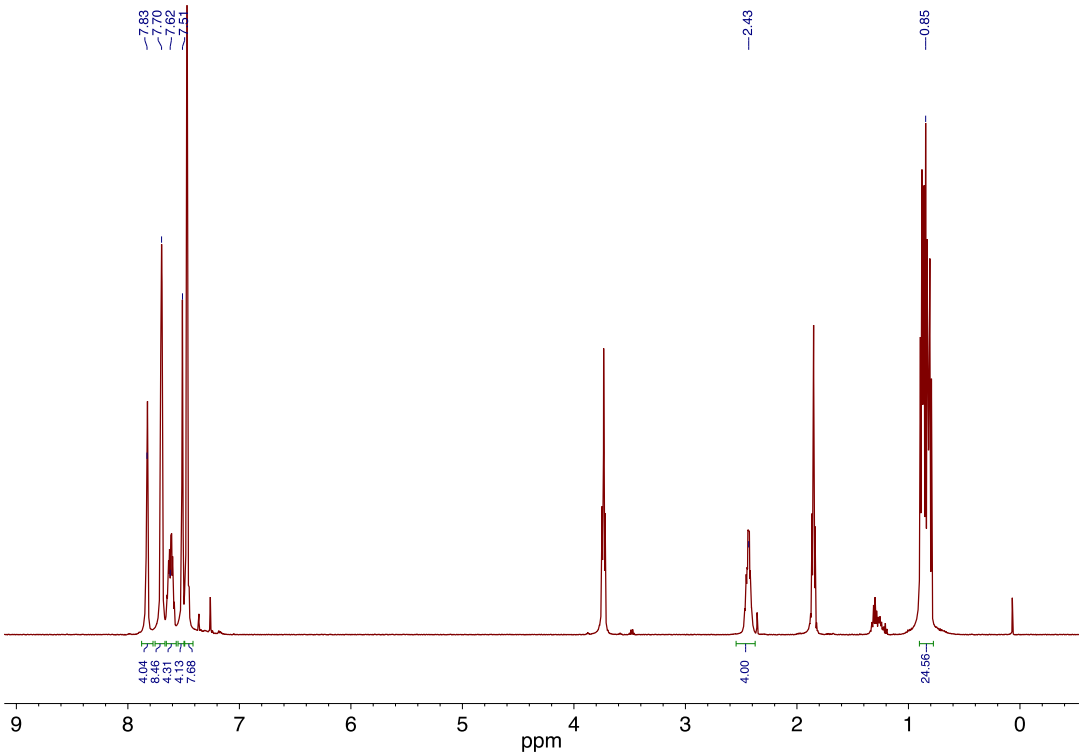

Figure 3.1.5.8. ^{1}H NMR spectrum of **[Au(B$_2$P$_2$)][BAr$^F_4$]** recorded at 600 MHz in CD_3CN.

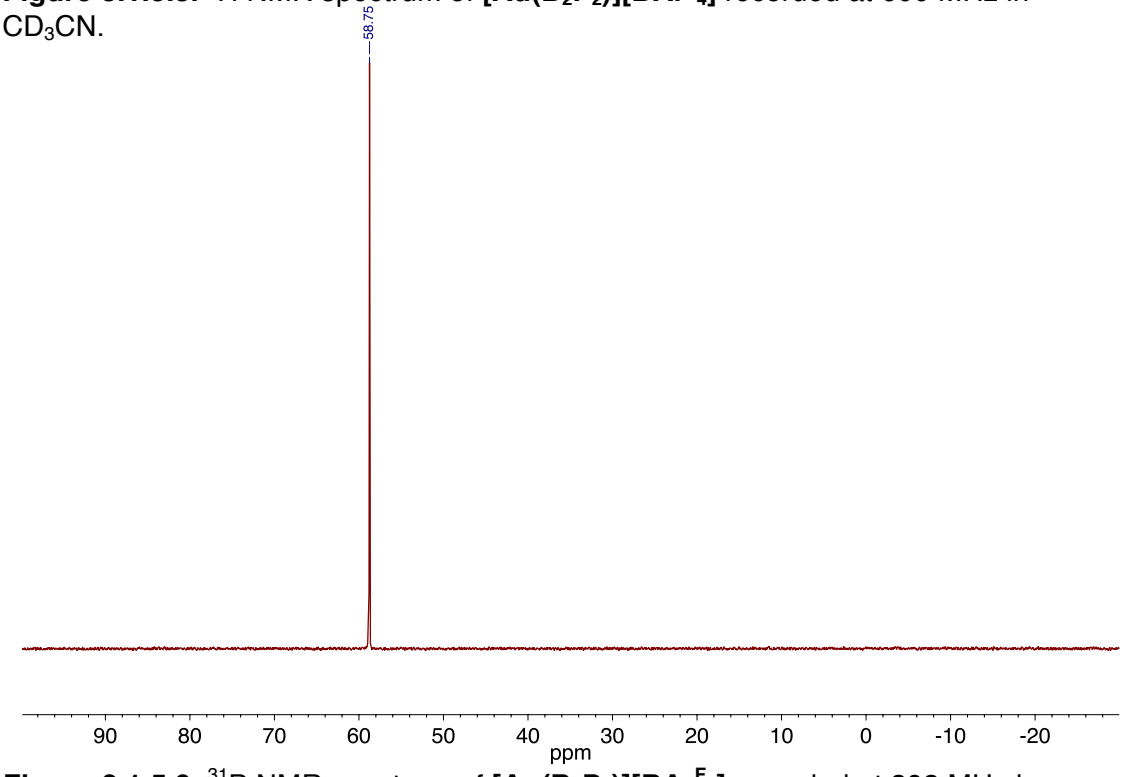

Figure 3.1.5.9. ^{31}P NMR spectrum of **[Au(B$_2$P$_2$)][BAr$^F_4$]** recorded at 202 MHz in CD_3CN.

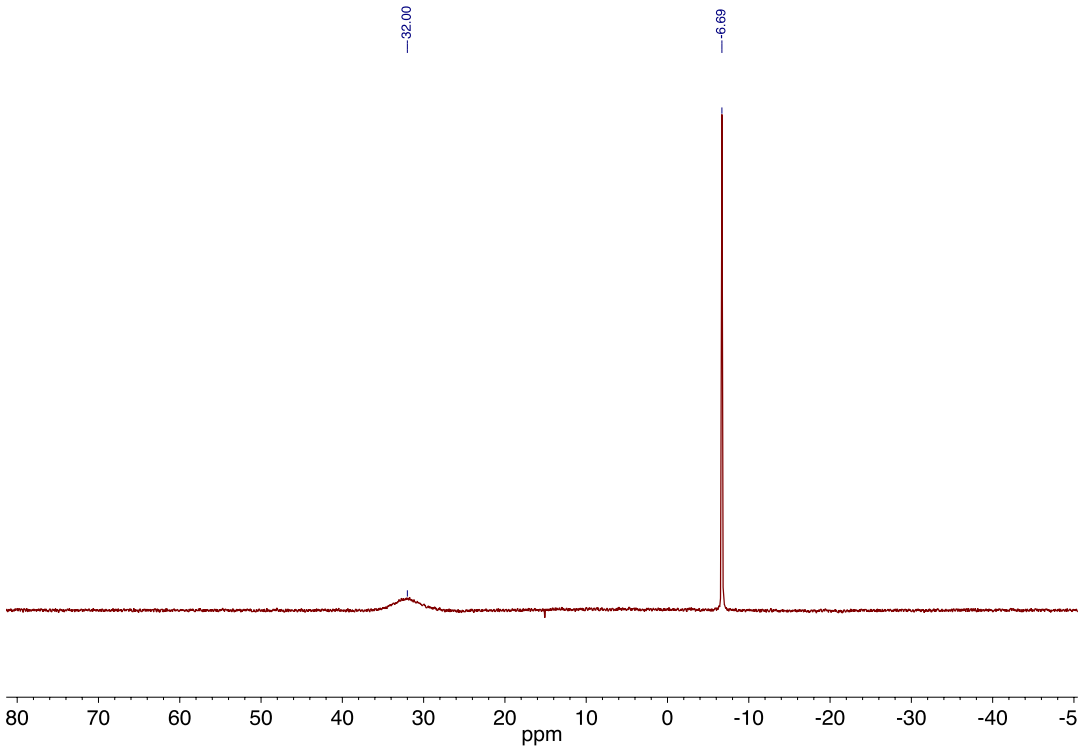

Figure 3.1.5.10. ^{11}B NMR spectrum of **[Au(B$_2$P$_2$)][BAr$^F_4$]** recorded at 193 MHz in CD_3CN.

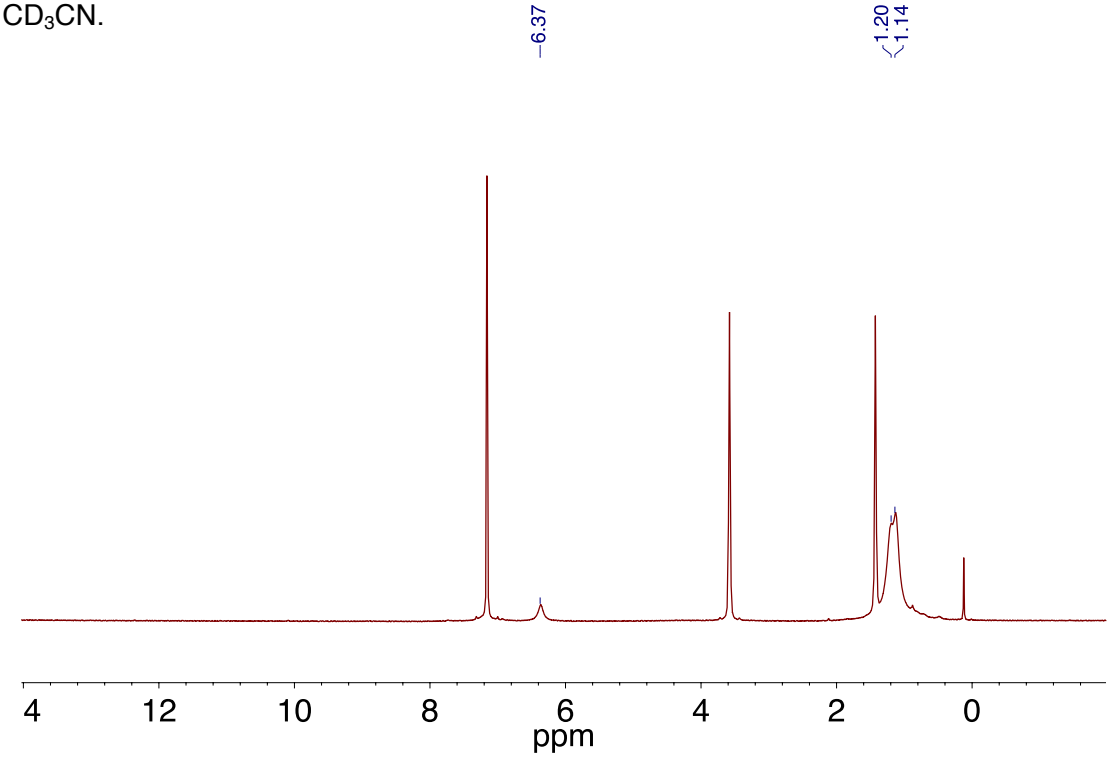

Figure 3.1.5.11. ^{1}H NMR spectrum of **Au(B$_2$P$_2$)** recorded at 500 MHz in C_6D_6.

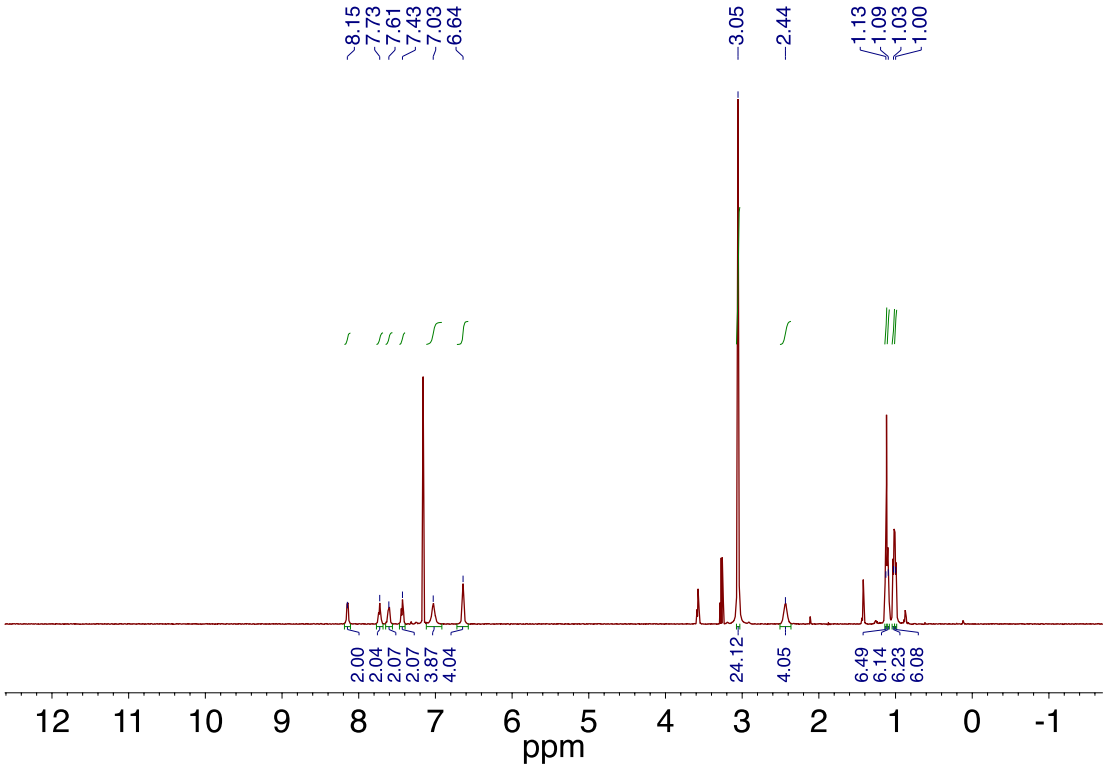

Figure 3.1.5.12. ^{1}H NMR spectrum of **[Au(B_2P_2)][K(18-c-6)]** recorded at 500 MHz in C_6D_6.

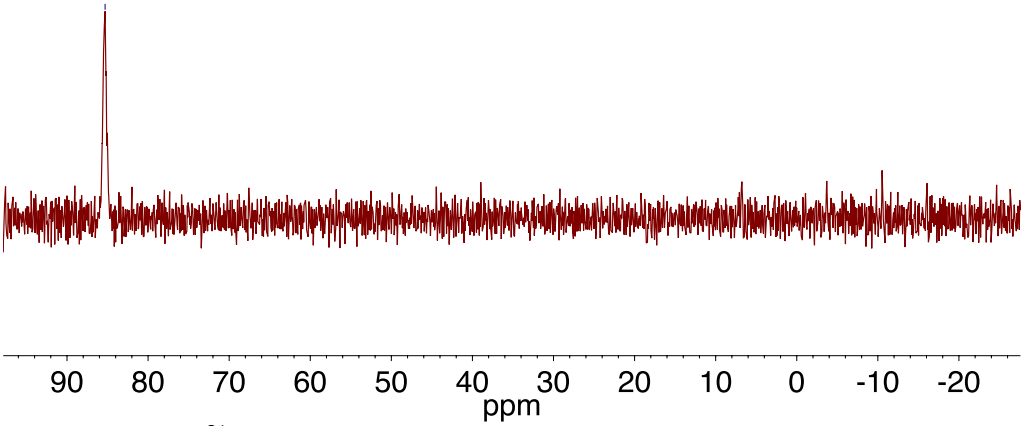

Figure 3.1.5.13. ^{31}P NMR spectrum of **[Au(B_2P_2)][K(18-c-6)]** recorded at 242 MHz in C_6D_6.

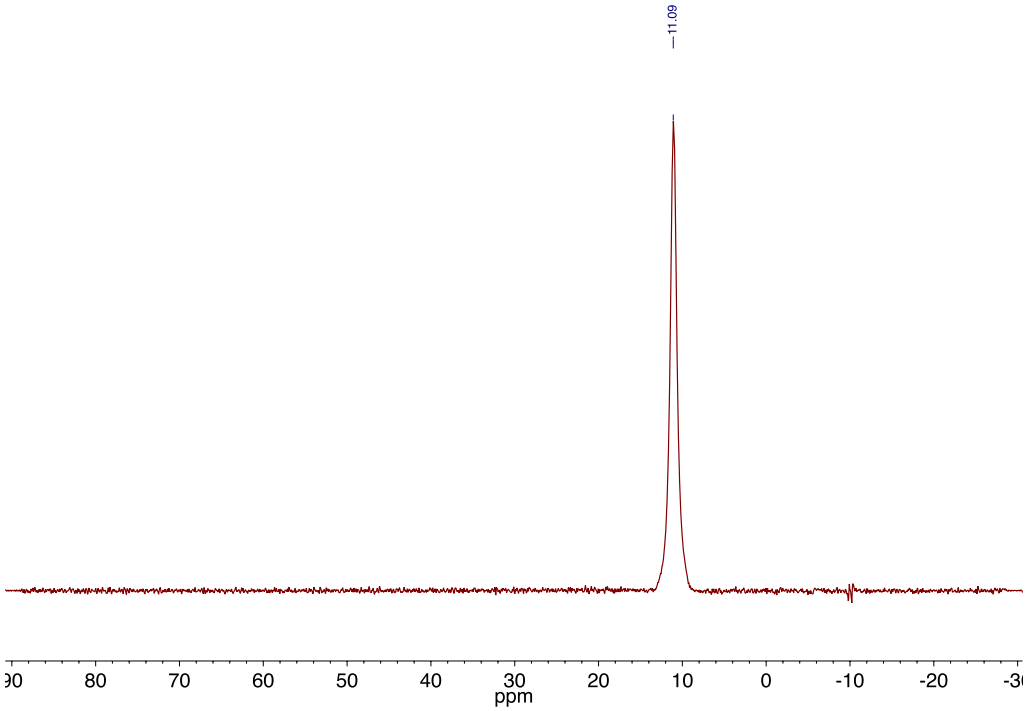

Figure 3.1.5.14. ^{11}B NMR spectrum of **[Au(B_2P_2)][K(18-c-6)]** recorded at 193 MHz in C_6D_6.

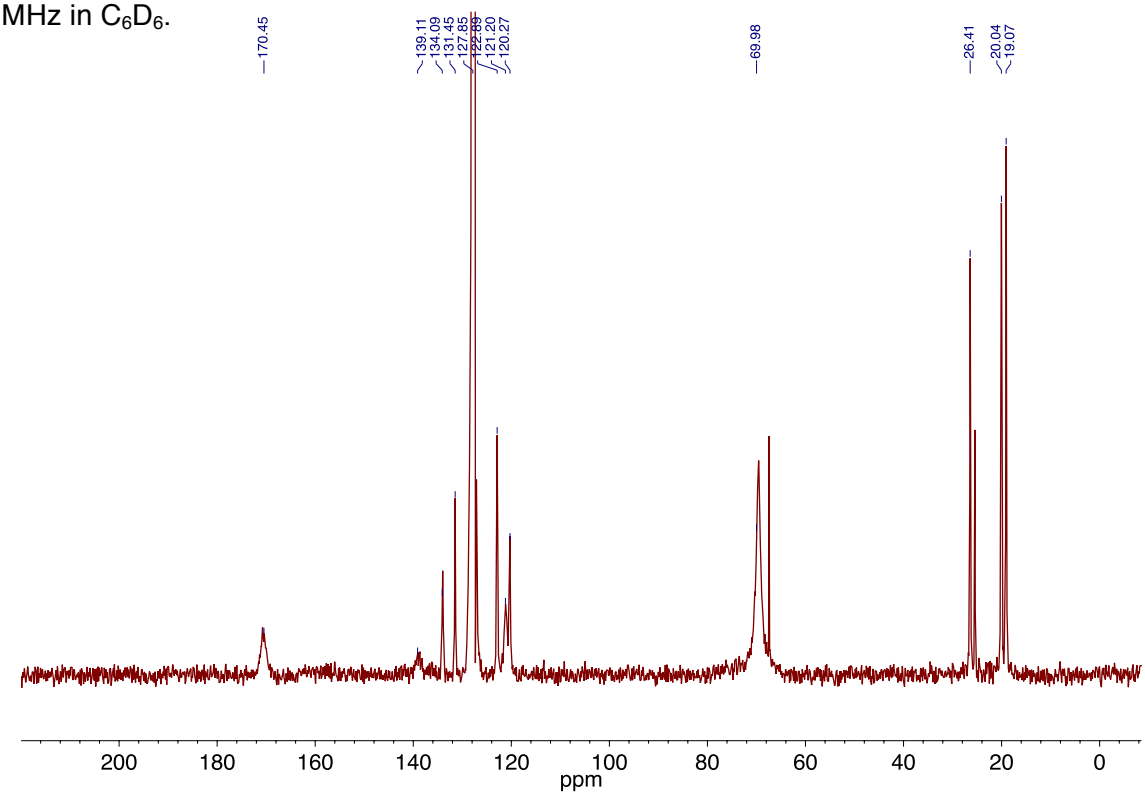

Figure 3.1.5.15. ^{13}C NMR spectrum of **[Au(B_2P_2)][K(18-c-6)]** recorded at 126 MHz in C_6D_6.

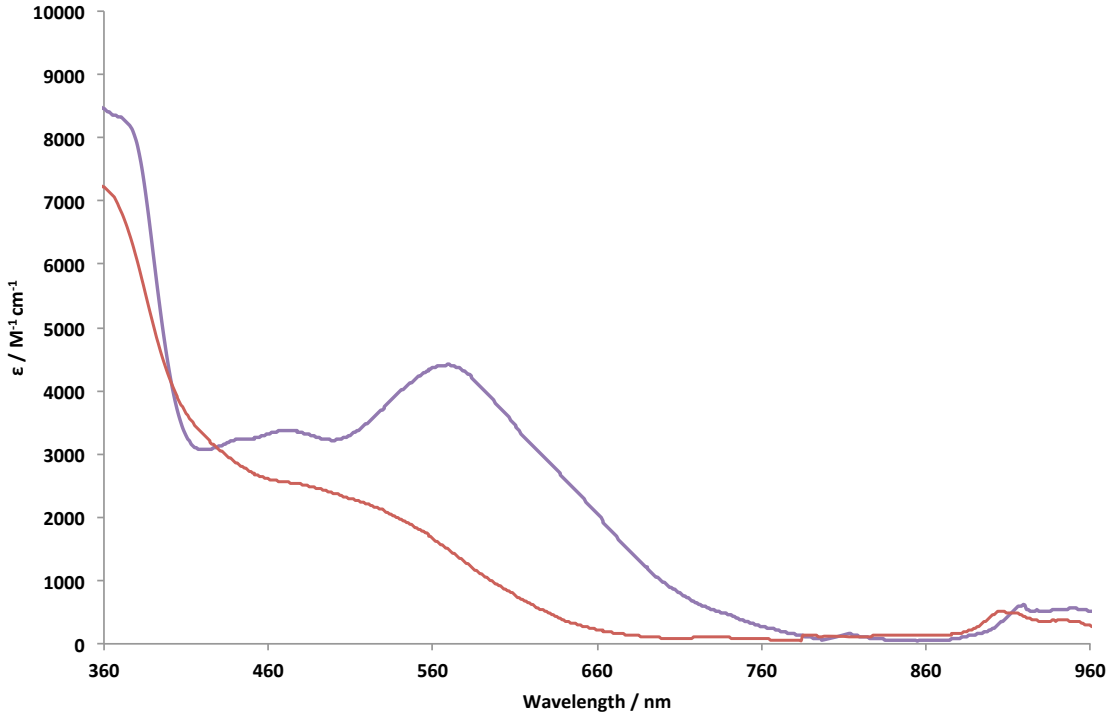

Figure 3.1.5.16. UV-vis spectrum of [Au(B_2P_2)][K(18-c-6)] (red trace) and Au(B_2P_2) (purple trace).

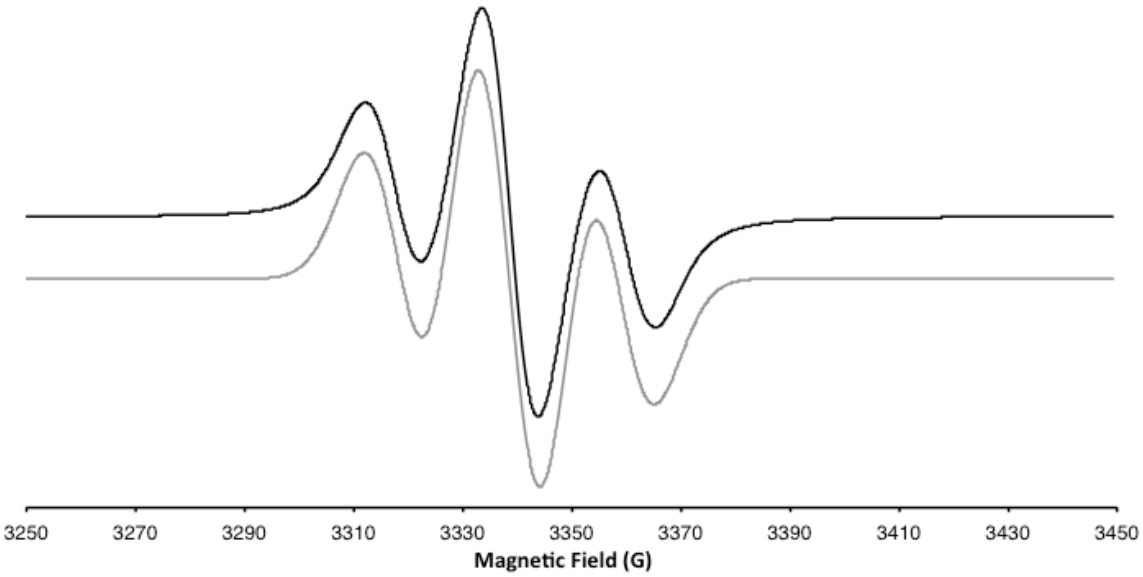

Figure 3.1.5.17. X-band EPR spectrum (9.310 GHz) of **Au(B_2P_2)** in 2-MeTHF at 298 K with a field modulation of 1.0 G (black) and its simulated spectrum (gray). Simulation parameters: g = 1.99216, A[31P] = 56 MHz, A[31P] = 56 MHz, lw = 1.54 mT.

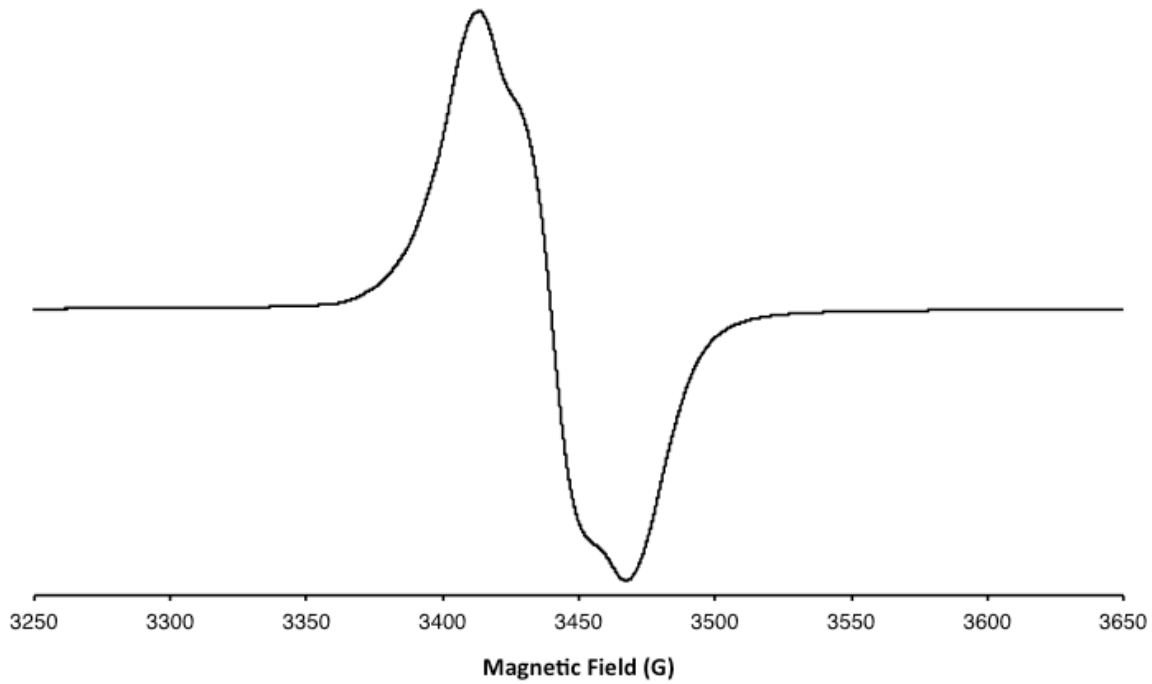

Figure 3.1.5.18. X-band EPR spectrum (9.602 GHz) of **Au(B_2P_2)** in 2-MeTHF at 108 K with a field modulation of 2.0 G

3.1.6) Cyclic Voltammetry Analysis

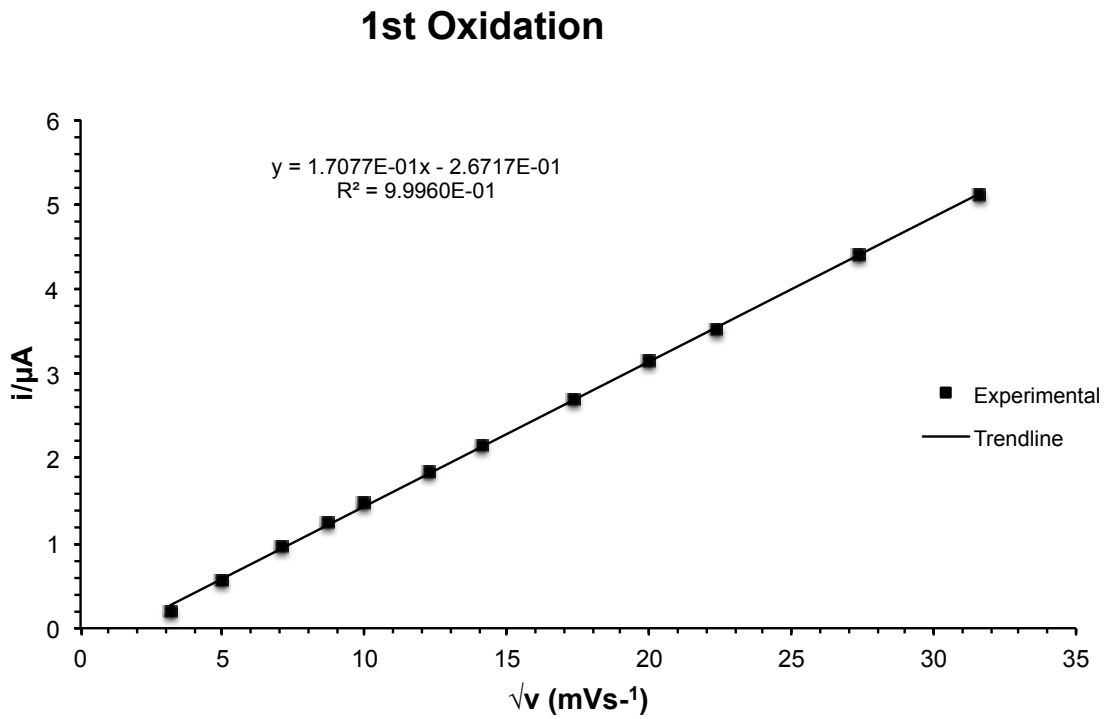

Figure 3.1.6.1. Plot of peak current vs. square root of the scan rate for the anodic peak corresponding to $[\mathbf{Au(B_2P_2)}]^{0/+1}$ oxidation at ca. −1.6 V.

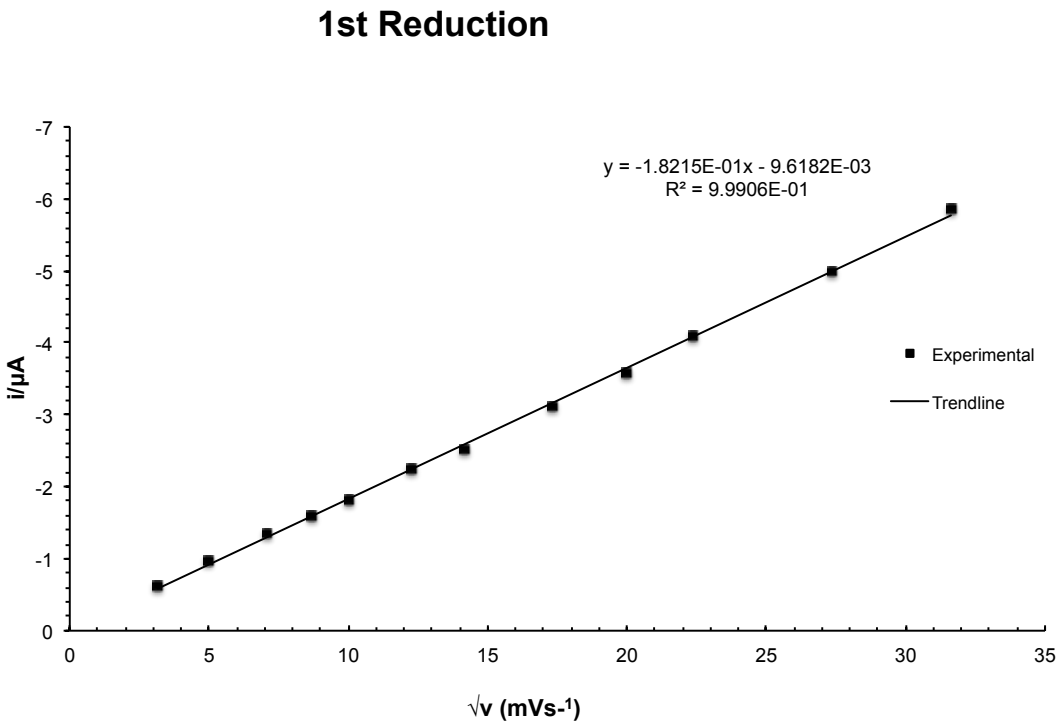

Figure 3.1.6.2. Plot of peak current vs. square root (scan rate) for the cathodic peak corresponding to $[\mathbf{Au(B_2P_2)}]^{+1/0}$ reduction at ca. −1.6 V.

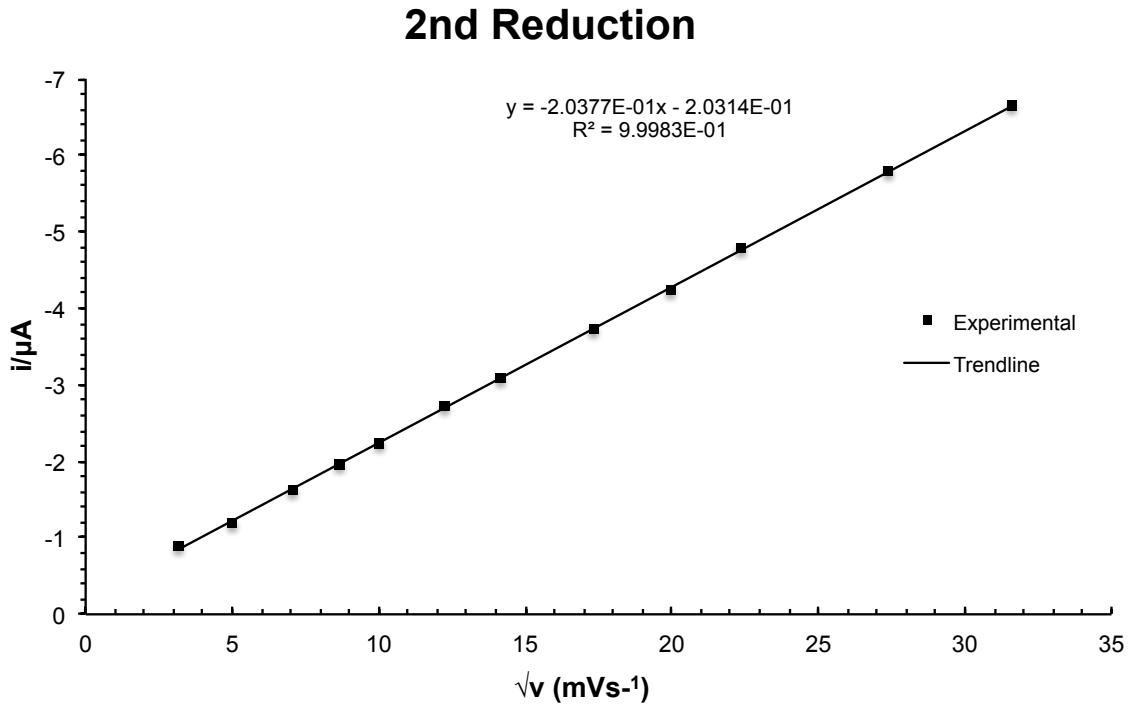

Figure 3.1.6.3. Plot of peak current vs. square root (scan rate) for the cathodic peak corresponding to [**Au(B$_2$P$_2$)**]$^{0/-1}$ reduction at ca. –2.0 V

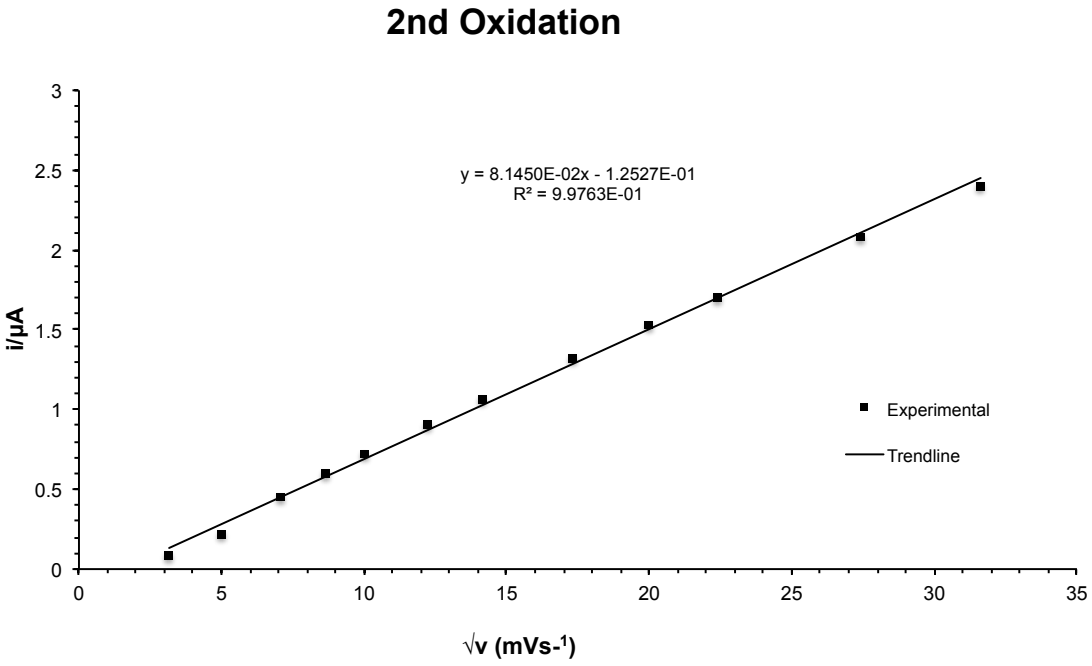

Figure 3.1.6.4. Plot of peak current vs. square root (scan rate) for the anodic peak corresponding to [**Au(B$_2$P$_2$)**]–1/0 oxidation at ca. –2.0 V.

3.1.7) X-Ray Crystallography

3.1.7.1.) General Considerations

Single crystals were coated with paratone oil and mounted on cryo-loop glass fibers. X-ray intensity data were collected at 100(2) K on a Bruker APEX2 [39] platform-CCD X-ray diffractometer system using fine-focus Mo K_α radiation (λ = 0.71073 Å, 50kV/30mA power). The CCD detector was placed at 5.0600 cm from the crystal. Frames were integrated using the Bruker SAINT software package [40] and using a narrow-frame integration algorithm. Absorption corrections were applied to the raw intensity data using the SADABS program.[41] The Bruker SHELXTL software package [42] was used for phase determination and structure refinement. Atomic coordinates, isotropic and anisotropic displacement parameters of all the non-hydrogen atoms were refined by means of a full matrix least-squares procedure on F^2. The H-atoms were included in the refinement in calculated positions riding on the atoms to which they were attached. Relevant details for individual data collections are reported below in Tables 3.1.7.1-3.1.7.4. For **[Au(B_2P_2)][BAr^F_4]**, there was one cation of $C_{36}H_{44}AuB_2P_2$ and one disordered anion of $B(C_8H_3F_6)_4$ present in the asymmetric unit of the unit cell. Two of the eight CF_3 groups of the anion were modeled with disorder (disordered site occupancy factor ratios were 92%/8% and 63%/33%/4%, see Figure 3.1.7.2).

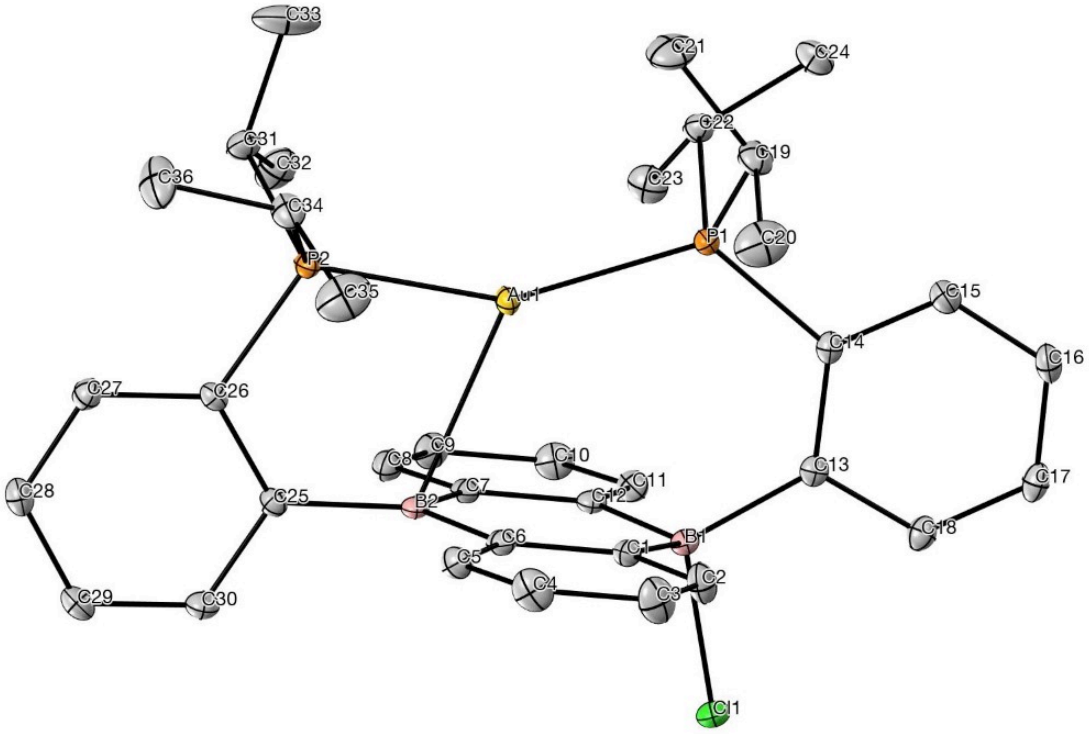

Figure 3.1.7.1. Labelled thermal ellipsoid plot (50%) for **Au(B_2P_2)Cl**.

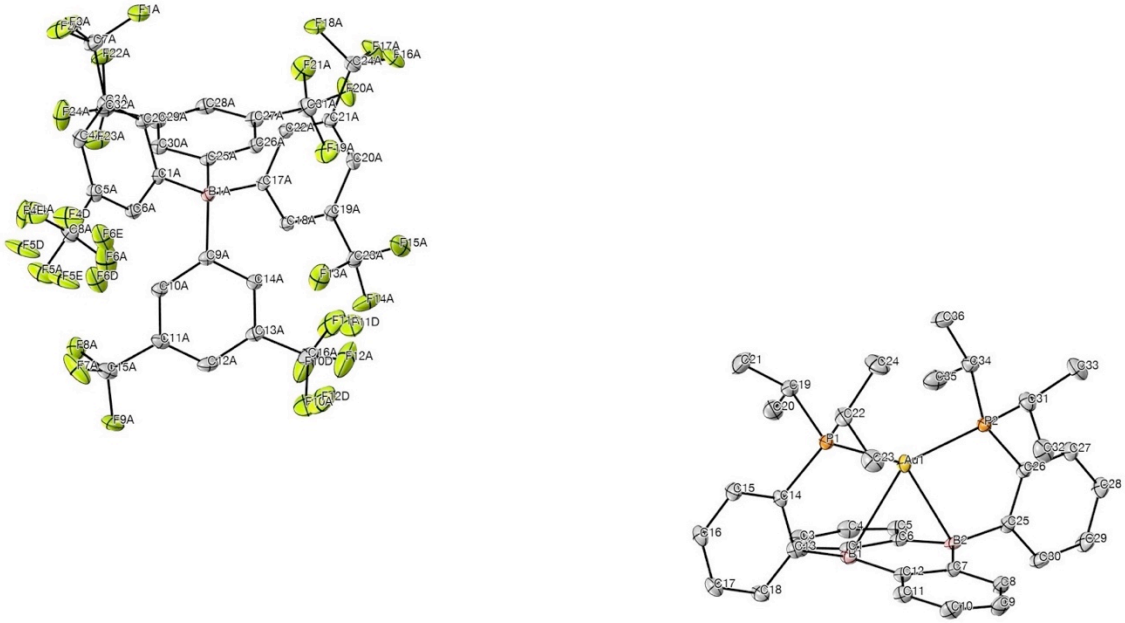

Figure 3.1.7.2. Labelled thermal ellipsoid plot (50%) for **[Au(B_2P_2)][BAr^F_4]**.

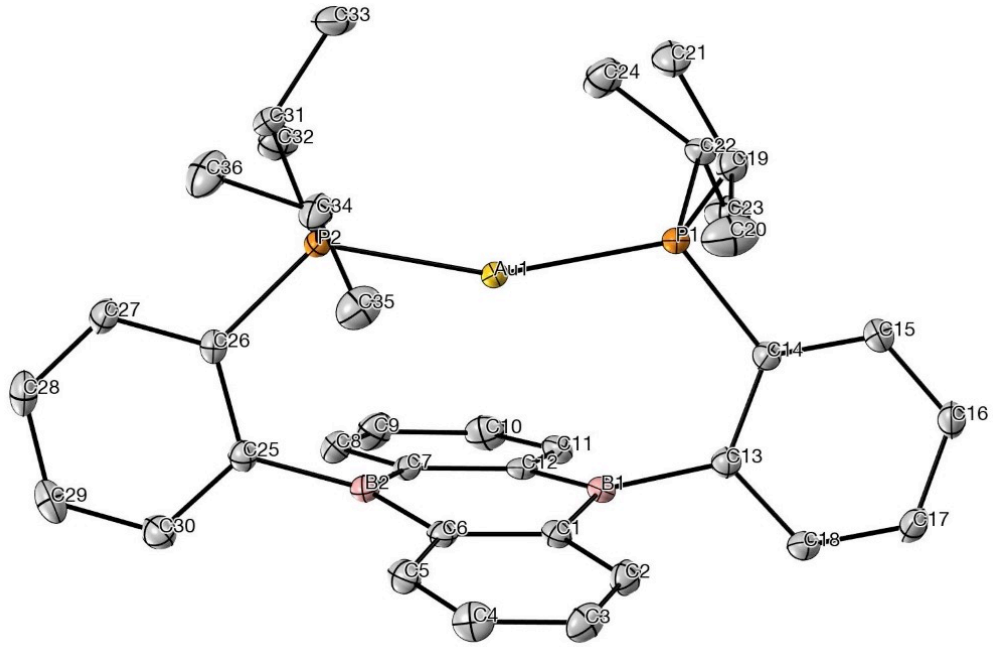

Figure 3.1.7.3. Labelled thermal ellipsoid plot (50%) for **Au(B_2P_2)**

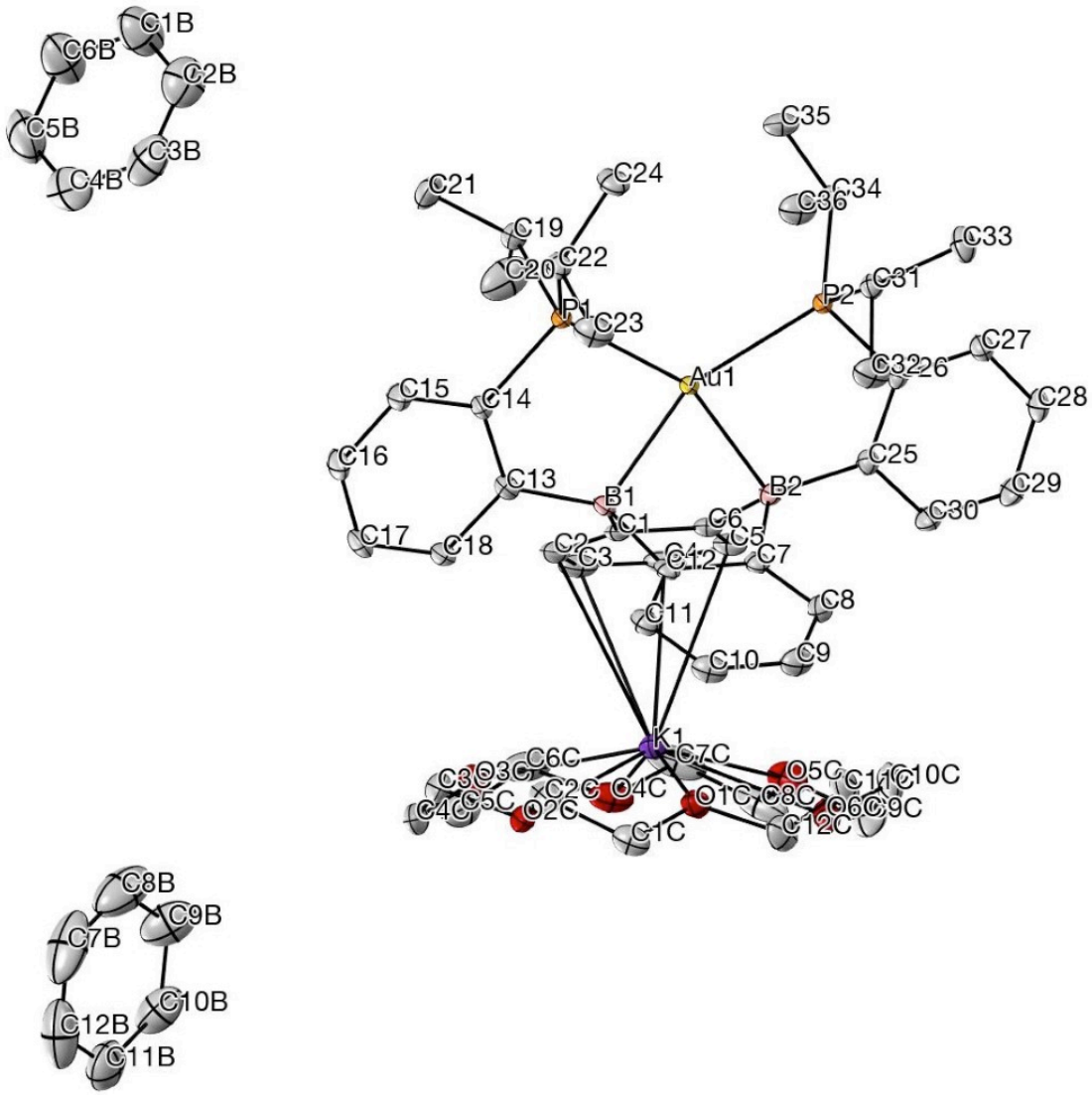

Figure 3.1.7.4. Labelled thermal ellipsoid plot (50%) for **[Au(B_2P_2)][K(18-c-6)]**.

Table 3.1.7.1. Crystal data and structure refinement for **Au(B_2P_2)Cl**.

Identification code	hh113JT57_0m	
Empirical formula	$C_{36}H_{44}AuB_2ClP_2$	
Formula weight	792.69 g/mol	
Temperature	100(2) K	
Wavelength	0.71073 Å	
Crystal system	Monoclinic	
Space group	$P2_1/n$ (#14)	
Unit cell dimensions	a = 9.6386(3) Å	α = 90°
	b = 21.2333(6) Å	β = 96.8338(5)°
	c = 16.4415(5) Å	γ = 90°
Volume	3341.00(17) Å^3	
Z	4	
Density (calculated)	1.576 mg/m^3	
Absorption coefficient	4.604 mm^{-1}	
F(000)	1584	
Crystal size	0.295 × 0.176 × 0.127 mm^3	
θ range for data collection	1.573 to 30.508°	
Index ranges	$-13 \le h \le 13$, $-30 \le k \le 30$, $-23 \le l \le 23$	
Reflections collected	97387	
Independent reflections	10212 [R_{int} = 0.0340]	
Completeness to θ = 25.242°	100.0 %	
Absorption correction	Semi-empirical from equivalents	
Refinement method	Full-matrix least-squares on F^2	
Data / restraints / parameters	10212 / 0 / 387	
Goodness-of-fit on F^2	1.051	
Final R indices [$I > 2\sigma_I$]	R_1 = 0.0164, wR_2 = 0.0363	
R indices (all data)	R_1 = 0.0201, wR_2 = 0.0376	
Largest diff. peak and hole	0.583 and –0.340 e/Å^3	

Table 3.1.7.2. Crystal data and structure refinement for **[Au(B_2P_2)][BAr^F_4]**.

Identification code	hh112JT56_0m	
Empirical formula	$C_{68}H_{56}AuB_3F_{24}P_2$	
Formula weight	1620.46 g/mol	
Temperature	100(2) K	
Wavelength	0.71073 Å	
Crystal system	Monoclinic	
Space group	$P2_1/c$ (#14)	
Unit cell dimensions	a = 17.6953(5) Å	α= 90°.
	b = 16.0112(5) Å	β= 90.3287(5)°.
	c = 23.6625(7) Å	γ = 90°.
Volume	6704.0(3) Å^3	
Z	4	
Density (calculated)	1.606 mg/m^3	
Absorption coefficient	2.350 mm^{-1}	
F(000)	3216	
Crystal size	0.435 x 0.211 x 0.127 mm^3	
θ range for data collection	1.715 to 30.034°.	
Index ranges	$-24 \le h \le 24$, $-22 \le k \le 22$, $-33 \le l \le 33$	
Reflections collected	189676	
Independent reflections	19617 [R_{int} = 0.0362]	
Completeness to θ = 25.242°	100.0 %	
Absorption correction	Semi-empirical from equivalents	
Refinement method	Full-matrix least-squares on F^2	
Data / restraints / parameters	19617 / 38 / 940	
Goodness-of-fit on F^2	1.034	
Final R indices [$I > 2\sigma_I$]	R_1 = 0.0222, wR_2 = 0.0525	
R indices (all data)	R_1 = 0.0283, wR_2 = 0.0549	
Largest diff. peak and hole	0.833 and -0.777 e/Å^3	

Table 3.1.7.3. Crystal data and structure refinement for **Au(B_2P_2).**

Identification code	hh96JT44_0m	
Empirical formula	$C_{36}H_{44}AuB_2P_2$	
Formula weight	757.24 g/mol	
Temperature	100(2) K	
Wavelength	0.71073 Å	
Crystal system	Monoclinic	
Space group	$P2_1/n$ (#14)	
Unit cell dimensions	a = 11.8407(4) Å	α= 90°.
	b = 15.9041(6) Å	β= 92.2581(6)°.
	c = 17.6890(6) Å	γ = 90°.
Volume	3328.5(2) Å^3	
Z	4	
Density (calculated)	1.511 mg/m^3	
Absorption coefficient	4.540 mm^{-1}	
F(000)	1516	
Crystal size	0.384 x 0.213 x 0.157 mm^3	
θ range for data collection	1.722 to 29.130°.	
Index ranges	$-16 \le h \le 16$, $-21 \le k \le 21$, $-24 \le l \le 24$	
Reflections collected	88422	
Independent reflections	8961 [R_{int} = 0.0426]	
Completeness to θ = 25.242°	100.0 %	
Absorption correction	Semi-empirical from equivalents	
Refinement method	Full-matrix least-squares on F^2	
Data / restraints / parameters	8961 / 0 / 378	
Goodness-of-fit on F^2	1.035	
Final R indices [$I > 2\sigma_I$]	R_1 = 0.0203, wR_2 = 0.0444	
R indices (all data)	R_1 = 0.0266, wR_2 = 0.0466	
Largest diff. peak and hole	1.961 and -0.728 e/Å^3	

Table 3.1.7.4. Crystal data and structure refinement for **[Au(B_2P_2)][K(18-c-6)]**.

Identification code	hh109JT53_0m
Empirical formula	$C_{60}H_{80}AuB_2KO_6P_2$
Formula weight	1216.86 g/mol
Temperature	100(2) K
Wavelength	0.71073 Å
Crystal system	Monoclinic
Space group	$P2_1/c$ (#14)
Unit cell dimensions	a = 13.6976(7) Å α = 90°.
	b = 36.5297(19) Å β = 118.6446(7)°.
	c = 13.4336(7) Å γ = 90°.
Volume	5899.1(5) Å^3
Z	4
Density (calculated)	1.370 mg/m^3
Absorption coefficient	2.666 mm^{-1}
F(000)	2504
Crystal size	0.585 x 0.182 x 0.029 mm^3
θ range for data collection	1.783 to 30.034°.
Index ranges	$-19 \le h \le 19$, $-51 \le k \le 51$, $-18 \le l \le 18$
Reflections collected	137019
Independent reflections	17234 [R_{int} = 0.0458]
Completeness to θ = 25.242°	99.9 %
Absorption correction	Semi-empirical from equivalents
Refinement method	Full-matrix least-squares on F^2
Data / restraints / parameters	17234 / 24 / 657
Goodness-of-fit on F^2	1.065
Final R indices [$I > 2\sigma_I$]	R_1 = 0.0247, wR_2 = 0.0465
R indices (all data)	R_1 = 0.0332, wR_2 = 0.0486
Largest diff. peak and hole	0.667 and -1.274 e/Å^3

3.1.8) Computational Procedures

3.1.8.1) General Considerations

All DFT calculations were performed using the Gaussian 09 software package.[43] Geometry optimizations were performed using the B3LYP (Becke, three-parameter, Lee-Yang-Parr) functional, the relativistic Stuttgart-Dresden (SDD) pseudopotential and basis set on Au, and the 6-31g(d,p) basis set on all other atoms. To avoid an extensive conformational search, the calculations were performed on a slightly truncated model in which isopropyl groups ($–CH(CH_3)_2$) are replaced by methyl group (CH_3). The structures were optimized without any symmetry restraints. Frequency analyses were performed on all calculations to verify that the obtained stationary points are in fact energy minima. Electronic density analyses (NBO and QTAIM) were performed on the density obtained from a single point calculation at the B3LYP/6-311+G(d,p); SDD (Au) level. NBO analyses up to the NLMO basis set were performed using the NBO6 program.[44] QTAIM[45] analysis was performed using the Multiwfn package[46] EPR parameters were evaluated on a single-point calculation using the SDD pseudopotential and basis sets on Au and the IGLO III basis set[47] on all other atoms. Details are reported in Figures 3.1.7.1–3.1.7.2 and Tables 3.1.7.1–3.1.7.2.

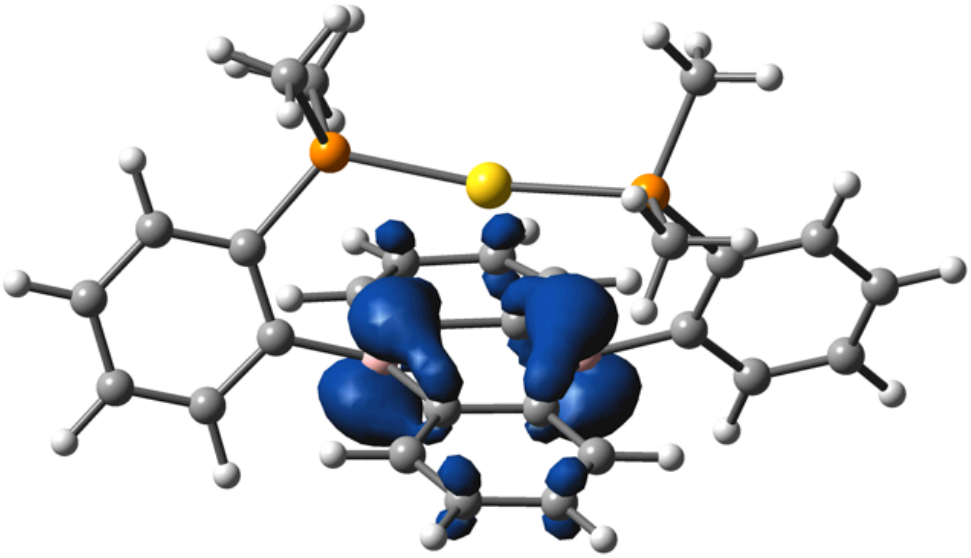

Figure 3.1.8.1. Spin density of compound **Au(B_2P_2)** calculated at the B3LYP/6-311+G(d,p);SDD(Au) level on a geometry optimized at the B3LYP/6-31G(d,p);SDD(Au) level.

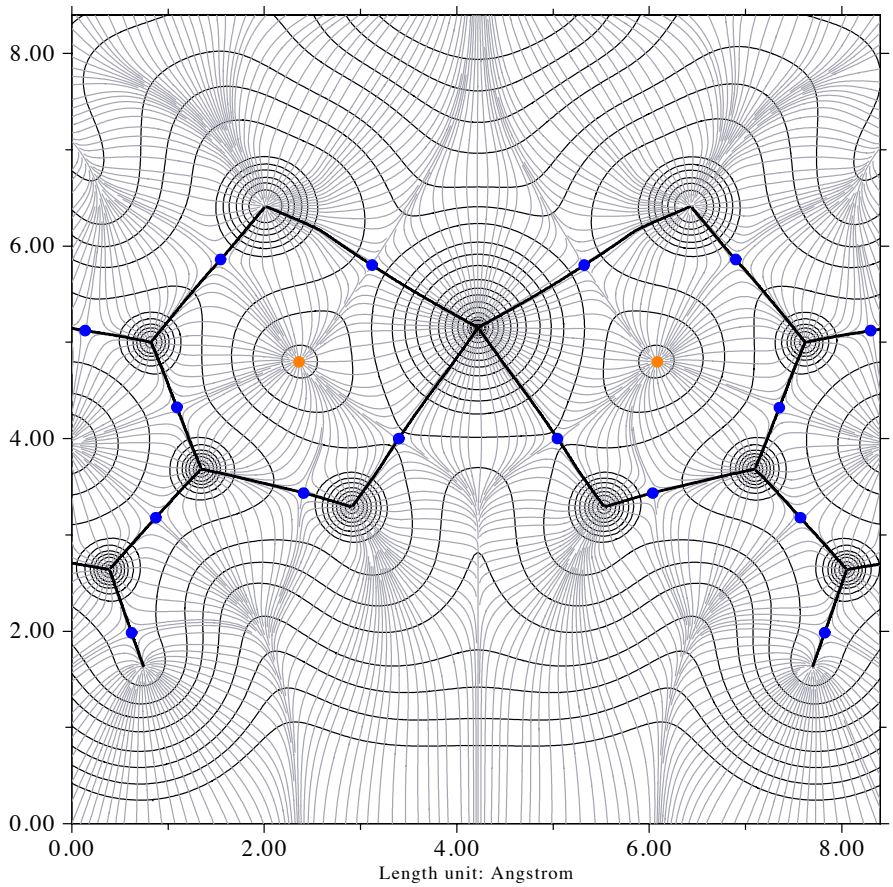

Figure 3.1.8.2. Contour map (black) and gradient lines (gray) of the electron density in the B–Au–B plane. Bond paths are depicted as black lines, bond (BCP) and ring (RCP) critical points as blue and orange circles, respectively

Table 3.1.8.1. Calculated Geometry of $[Au(B_2P_2^{Me})]^-$

Au	-0.00013091	-0.80937913	0.00230276
B	1.30961904	1.05289684	0.03608214
C	0.74930850	1.79589229	-1.29972300
C	1.45984160	2.38036399	-2.34735754
H	2.54991874	2.37865741	-2.33443524
C	0.79117034	2.95696157	-3.44635675

H	1.36317107	3.39524598	-4.26371349
C	-0.59733956	2.95288911	-3.48799711
H	-1.12190463	3.38711455	-4.33865047
C	-1.32755564	2.37382687	-2.43032020
H	-2.41622460	2.36552813	-2.48431657
C	-0.67831569	1.79379194	-1.34124320
B	-1.30901388	1.05358833	-0.03637121
C	-0.74845254	1.79530894	1.30004563
C	-1.45880640	2.37882870	2.34835875
H	-2.54888411	2.37748260	2.33542868
C	-0.78989572	2.95403075	3.44791022
H	-1.36169724	3.39163642	4.26576834
C	0.59864316	2.94938233	3.48952244
H	1.12334825	3.38248986	4.34065853
C	1.32866422	2.37112520	2.43130070
H	2.41732751	2.36230935	2.48527254
C	0.67920159	1.79256898	1.34154136
C	2.87475824	0.65730398	0.07092618
C	3.39746403	-0.65850489	0.03719853
C	4.78360114	-0.89534442	0.05594101
H	5.16697115	-1.91385004	0.02248101
C	5.68965652	0.15964855	0.11377886
H	6.75973584	-0.03466613	0.12940380
C	5.20113693	1.46932306	0.14978421
H	5.89451675	2.30725161	0.19372536
C	3.82792451	1.70181819	0.12716977
H	3.46592223	2.72685982	0.15202910
P	2.21167653	-2.07001405	-0.06345368
C	-2.87421332	0.65826729	-0.07094561
C	-3.39724492	-0.65734567	-0.03622177
C	-4.78341299	-0.89396933	-0.05585784
H	-5.16684593	-1.91248929	-0.02248165
C	-5.68926049	0.16110101	-0.11477577
H	-6.75936674	-0.03299693	-0.13096887
C	-5.20042611	1.47067990	-0.15102857
H	-5.89363170	2.30871917	-0.19559332
C	-3.82720034	1.70294480	-0.12802196
H	-3.46501747	2.72790655	-0.15327783
P	-2.21234669	-2.06951836	0.06538954
C	2.71346599	-2.91251471	-1.64698396
H	2.41684673	-2.27616861	-2.48483263
H	3.79346970	-3.08907003	-1.70154279

H	2.18719187	-3.86850276	-1.73501078
C	2.87039269	-3.27979036	1.19638920
H	3.93833933	-3.49385037	1.07518218
H	2.70565690	-2.86779503	2.19572344
H	2.31006800	-4.21659306	1.11412581
C	-2.72978728	-2.92493294	1.63712786
H	-2.44239578	-2.29506597	2.48308159
H	-3.81002526	-3.10347029	1.67976383
H	-2.20317336	-3.88093099	1.72281053
C	-2.85885489	-3.26833232	-1.21069322
H	-2.30168043	-4.20713000	-1.12971155
H	-3.92861221	-3.48018975	-1.10234963
H	-2.68243781	-2.84885738	-2.20488960

Total Energy: –1952.18114432

Table 3.1.8.2. Calculated Geometry of Au($B_2P_2^{Me}$)

Au	-0.00002613	-1.26243390	0.00104824
B	-1.47564568	1.56120977	-0.17279707
C	-0.86999379	1.71237105	1.23798384
C	-1.67915041	1.85683039	2.39633285
H	-2.76059491	1.89735948	2.27881322
C	-1.13670980	1.97075761	3.66746361
H	-1.78444503	2.10265958	4.53117100
C	0.26236965	1.91873449	3.83608147
H	0.69354237	2.00129966	4.83094398
C	1.08256566	1.77071382	2.72890981
H	2.15995771	1.73466371	2.87381017
C	0.56512230	1.68847557	1.40897065
B	1.47571516	1.56160643	0.17020642
C	0.87005341	1.71004751	-1.24086395
C	1.67920046	1.85247594	-2.39946523
H	2.76064271	1.89327849	-2.28202234
C	1.13675058	1.96409521	-3.67080223
H	1.78447947	2.09449335	-4.53474129
C	-0.26232393	1.91168959	-3.83932300
H	-0.69350451	1.99247587	-4.83432964
C	-1.08251222	1.76560656	-2.73188725
H	-2.15990183	1.72923902	-2.87671813
C	-0.56505765	1.68575659	-1.41180413

P	-2.32127376	-1.46154800	0.48321587
C	-3.00846782	1.16801391	-0.33769800
C	-3.47895156	-0.14455791	-0.07568013
C	-4.84073614	-0.46738899	-0.21443550
H	-5.19781672	-1.47231279	-0.00823302
C	-5.76133522	0.49619282	-0.61868879
H	-6.81074975	0.23552012	-0.72178473
C	-5.31959467	1.79199954	-0.89150391
H	-6.02763267	2.55251907	-1.21039785
C	-3.96975274	2.11139792	-0.75243618
H	-3.64233860	3.12583007	-0.96541061
P	2.32122835	-1.46232417	-0.48073509
C	3.00851398	1.16860174	0.33578522
C	3.47895471	-0.14439811	0.07583162
C	4.84073819	-0.46704037	0.21506395
H	5.19778046	-1.47230013	0.01043827
C	5.76137121	0.49714393	0.61778861
H	6.81078203	0.23660679	0.72126103
C	5.31966690	1.79338334	0.88861029
H	6.02772612	2.55437704	1.20632352
C	3.96983323	2.11259871	0.74906281
H	3.64244505	3.12736946	0.96045796
C	2.61234964	-1.65687821	-2.29165909
H	2.05290087	-2.52054879	-2.66187861
H	2.26087875	-0.75800799	-2.80325213
H	3.67901673	-1.79690014	-2.49194509
C	-2.97826509	-3.04182420	-0.21473524
H	-2.32172312	-3.85775557	0.09823818
H	-3.99357950	-3.25658520	0.12881150
H	-2.97178142	-2.98851009	-1.30598724
C	-2.61258345	-1.65285316	2.29445226
H	-3.67929346	-1.79235257	2.49486010
H	-2.05328295	-2.51590715	2.66632416
H	-2.26108665	-0.75309722	2.80446835
C	2.97835532	-3.04136185	0.21991160
H	2.32165407	-3.85784492	-0.09127763
H	3.99352030	-3.25677789	-0.12367280
H	2.97233807	-2.98601231	1.31106424

Total Energy: –1952.16316476

3.1.9) Reference

[1] McNaught, A. D.; Nic, M.; Jirat, J.; Wilkinson, A. *IUPAC. Compendium of Chemical Terminology, 2nd ed.* (the "Gold Book"). Blackwell Scientific Publications, Oxford **1997**.

[2] Cotton, F. A.; Wilkinson, G.; Murillo, C. A.; Bochmann, M. *Advanced Inorganic Chemistry, 6th Edition,* Wiley-Interscience, New York, New York, **1999**.

[3] Ellis, J. E. *Inorg. Chem.* **2006**, *45*, 3167-3186.

[4] Jansen, M. *Chem. Soc. Rev.* **2008**, *37*, 1826–1835.

[5] Dietzel, P. D. C.; Schmutzler, R. W.; Bard, A. J.; Jansen, M. *Chem. Commun.* **2001**, *621*, 2208–2209.

[6] Andersen, T.; Haugen, H. K.; Hotop, H. *J. Phys. Chem. Ref. Data* **1999**, *28*, 1511.

[7] Jansen, M. *Solid State Sci.* **2005**, *7*, 1464–1474.

[8] Nuss, N.; Jansen, M. *Angew. Chem. Int. Ed.* **2006**, *45*, 4369–4371.

[9] Thanh, N. T. K.; Maclean, N.; Mahiddine, S. *Chem. Rev.* **2014**, *114*, 7610–7630.

[10] Amgoune, A.; Bourissou, D. *Chem. Commun.* **2011**, *47*, 859–871.

[11] Buss, J. A.; Agapie, T. *Nature* **2016**, *529*, 72–75.

[12] Horak, K. T.; Agapie, T. *J. Am. Chem. Soc.* **2016**, *138*, 3343–3452.

[13] Supplementary X-ray crystallographic data for this paper are contained in CCDC entries 1504402–1504405 and can be obtained free of charge from The Cambridge Crystallographic Data Centre via www.ccdc.cam.ac.uk/data_request/cif.

[14] Bontemps, S.; Bouhadir, G.; Miqueu, K.; Bourissou, D. *J. Am. Chem. Soc.* **2006**, *128*, 12056–12057.

[15] Reus, C.; Weidlich, S.; Bolte, M.; Lerner, H.-W.; Wagner, M. *J. Am. Chem. Soc.* **2013**, *135*, 12892–12907.

[16] Hoffend, C.; Diefenbach, M.; Januszewski, E.; Bolte, M.; Lerner, H.-W.; Holthausen, M. C.; Wagner, M. *Dalton Trans.* **2013**, *42*, 13826–13837.

[17] a) Weinberger, D. S.; Melaimi, M.; Moore, C. E.; Rheingold, A. L.; Frenking, G.; Jerabek, P.; Bertrand, G. *Angew. Chem. Int. Ed.* **2013**, *52*, 8964–8967; b) Landis, C. R.; Hughes, R. P.; Weinhold, F. *Organometallics* **2015**, *34*, 3442–3449.

[18] Calculations were performed on model systems in which the isopropyl substituents on phosphorus were replaced with methyl groups. See Supplementary Materials for more information.

[19] Kutzelnigg, W.; Fleischer, U.; Schindler, M. *The IGLO-Method: Ab Initio Calculation and Interpretation of NMR Chemical Shifts and and Magnetic Susceptibilities*, Vol. 23 Springer-Verlag, Heidelberg, **1990**.

[20] Bolton, J. R.; Carrington, A.; McLachlan, A. D. *Molecular Physics* **1962**, *5*, 31–41.

[21] Allen, B. T.; Bond, A. *J. Phys. Chem.* **1964**.

[22] Ruiz, D. A.; Ung, G.; Melaimi, M.; Bertrand, G. *Angew. Chem. Int. Ed.* **2013**, *52*, 7590–7592.

[23] Kong, L.; Ganguly, R.; Li, Y.; Kinjo, R. *Chem. Sci.* **2015**, *6*, 2893–2902.

[24] Braunschweig, H.; Ewing, W. C.; Kramer, T.; Mattock, J. D.; Vargas, A.; Werner, C. *Chem. Eur. J.* **2015**, *21*, 12347–12356.

[25] Wynd, A. J.; McLennan, A. J.; Reed, D.; Welch, A. J. *J. Chem. Soc., Dalt. Trans.* **1987**, 2761–2768.

[26] a) Raubenheimer, H. G.; Schmidbaur, H. *Organometallics* **2012**, *31*, 2507–2522; b) Robilotto, T. J.; Bacsa, J.; Gray, T. G.; Sadighi, J. P. *Angew. Chem. Int. Ed.* **2012**, *51*, 12077–12080.

[27] Li, D.-Z.; Li, S.-D. *Int. J. Quantum Chem.* **2011**, *111*, 4418–4424.

[28] Bader, R. F. W. *Chem. Rev.* **1991**, *91*, 893–928.

[29] Weinhold, F.; Landis, C. R. *Valency and Bonding: A Natural Bond Orbital Donor-Acceptor Perspective*. Cambridge University Press, **2005**.

[30] Moret, M.-E.; Zhang, L.; Peters, J. C. *J. Am. Chem. Soc.* **2013**, *135*, 3792–3795.

[31] Kusevska, E. M.; Montero-Campillo, M.; Mó, O.; Yáñez, M. *Angew. Chem.* **2017**, *129*, 6892–6896.

[32] Bilodeau, R. C.; Scheer, M.; Haugen, H. K. *J. Phys. B* **1998**, *31*, 3885–3391.

[33] Bontemps, S.; Bouhadir, G.; Miqueu, K.; Bourissou, D. *J. Am. Chem. Soc.* **2006**, *128*, 12056–12057.

[34] Bieller, S.; Zhang, F.; Bolte, M.; Bats, J.W.; Lerner, H.–W.; Wagner, M. *Organometallics* **2004**, *23*, 2107–2113.

[35] Yakelis, N.; Bergman, R. *Organometallics* **2005**, *24*, 3579–3581.

[36] Scott, T.; Ooro, B.; Collins, D.; Shatruk, M.; Yakovenko, A.; Dunbar, K.; Zhou, H.–C. *Chem. Comm.* **2008**, 65-67.

[37] Led, J. J.; Gesmar, H. *Chem. Rev*. **1991**, *91*, 1413-1426.

[38] Stoll, S.; Schweiger, A. J. *Magn. Reson.* **2006**, *178*, 42-55.

[39] *APEX 2,* version 2014.1-1, Bruker (2014), Bruker AXS Inc., Madison, Wisconsin, USA.

[40] *SAINT,* version V8.34A, Bruker (2012), Bruker AXS Inc., Madison, Wisconsin, USA.

[41] *SADABS,* version 2012/1, Bruker (2012), Bruker AXS Inc., Madison, Wisconsin, USA.

[42] *SHELXTL,* version 2013/4, Bruker (2013), Bruker AXS Inc., Madison, Wisconsin, USA.

[43] Gaussian 09, Revision D.01, M. J. Frisch, G. W. Trucks, H. B. Schlegel, G. E. Scuseria, M. A. Robb, J. R. Cheeseman, G. Scalmani, V. Barone, B. Mennucci, G. A. Petersson, H. Nakatsuji, M. Caricato, X. Li, H. P. Hratchian, A. F. Izmaylov, J. Bloino, G. Zheng, J. L. Sonnenberg, M. Hada, M. Ehara, K. Toyota, R. Fukuda, J. Hasegawa, M. Ishida, T. Nakajima, Y. Honda, O. Kitao, H. Nakai, T. Vreven, J. A. Montgomery, Jr., J. E. Peralta, F. Ogliaro, M. Bearpark, J. J. Heyd, E. Brothers, K. N. Kudin, V. N. Staroverov, T. Keith, R. Kobayashi, J. Normand, K. Raghavachari, A. Rendell, J. C. Burant, S. S. Iyengar, J. Tomasi, M. Cossi, N. Rega, J. M. Millam, M. Klene, J. E. Knox, J. B. Cross, V. Bakken, C. Adamo, J. Jaramillo, R. Gomperts, R. E. Stratmann, O. Yazyev, A. J. Austin, R. Cammi, C. Pomelli, J. W. Ochterski, R. L. Martin, K. Morokuma, V. G. Zakrzewski, G. A. Voth, P. Salvador, J. J. Dannenberg, S. Dapprich, A. D. Daniels, O. Farkas, J. B. Foresman, J. V. Ortiz, J. Cioslowski, and D. J. Fox, Gaussian, Inc., Wallingford CT, **2013**.

[44] NBO 6.0. E. D. Glendening, J. K. Badenhoop, A. E. Reed, J. E. Carpenter, J. A. Bohmann, C. M. Morales, C. R. Landis, and F. Weinhold (Theoretical Chemistry Institute, University of Wisconsin, Madison, WI, 2013); http://nbo6.chem.wisc.edu/

[45] Bader, R. F. W. *Chem. Rev.* **1991**, *91*, 893–928.

[46] Lu, T.; Chen, F. *J. Comput. Chem.* **2012**, *33*, 580–592.

[47] Kutzelnigg, W.; Fleischer, U.; Schindler M. *The IGLO-Method: Ab Initio Calculation and Interpretation of NMR Chemical Shifts and Magnetic Susceptibilities, Vol. 23* Springer-Verlag, Heidelberg, **1990**.

3.2) CO_2 Reduction with Protons and Electrons with the Au(B_2P_2) Platform

3.2.1.) Introduction

Since their discovery by Schlesinger and Brown in the 1940s,[1] borohydrides have become ubiquitous reducing agents in the synthesis of fine and commodity chemicals.[2] More recently, borohydrides have attracted interest in energy storage applications,[3] both as a dense and readily handled source of H_2 and in the reduction of CO_2 to fuels such as formic acid and methanol. The first report of the reaction if $NaBH_4$ with CO_2 dates back to 1955 when Wartick and Pearson described the solution (dimethyl ether) and solid-state reactions with mass-balance and hydrolysis analysis.[4] Additionally, in 1967 these experiments were carried out in aqueous conditions to produce sodium formate from the reaction of $NaBH_4$ with CO_2.[5] The intrinsic role of the borohydride ion in CO_2 reduction was later investigated by Mizuta in 2014 who showed that, in the presence of a catalytic amount of $NaBH_4$, BH_3・THF effectively reduces CO_2 to trimethylboroxine.[6] A year later, Cummins et al. reported the direct reaction of $NaBH_4$ with CO_2 under high pressures yields the trisformatohydroborate $Na[(HB(OCHO)_3)]$ that could be hydrolyzed to yield formic acid.[7] Additional studies over the last decades have found that in the presence of a suitable catalyst, (HBpin) can reduce CO_2 to give HCO_2BPin,[8] CH_3OH,[9] HCOOH,[10] CO,[11] and/or CH_4.[12]

Despite their broad utility, one drawback to these reagents is the substantial energy required for their production owing to the use of alkali metal reductants. For example, millions of kg of $NaBH_4$ are produced each year by the NaH reduction of $B(OMe)_3$ in the Brown-Schlesinger process (Eq 1).[13]

$$B(OCH_3)_3 + 4\ NaH \rightarrow NaBH_4 + 3\ NaOCH_3 \text{ (Eq 1)}$$

NaH is prepared from the reaction of metallic Na with H_2 gas, and the reduction of NaCl to metallic Na is one of the most energy demanding electrochemical processes undertaken on a large scale. The process is carried out at high temperature (> 600 ºC), and although the thermodynamic potential of the reaction is already large at ca. 4 V, practical reaction rates require operating potentials of 8 V or more. As a result, the reduction of CO_2 with $NaBH_4$ (or reagents derived therefrom) produced in this way is wildly inefficient as a means of energy storage. Synthesis of B–H bonds from protons and electrons at modest potentials may be a way to alleviate these costs. Despite the significantly negative redox potentials required to access doubly reduced boranes ($\sim < -2.2$ V vs. Fc/Fc+),[14] there are several reports of protonation of a reduced boron center yielding a B-H bond. In 2006, Nozaki reported the isolation of the boryllithium compound $LiB(2,6\text{-}iPrC_6H_4)NCH_2)_2$, which reacts as a boryl anion equivalent, and showed that it could be protonated with H_2O to give the corresponding hydroborane.[15] Bertrand et al. have prepared the carbene-stabilized borylene $(CAAC)_2BH$ (CAAC = cyclic (alkyl)(amino)carbene) that could be protonated with trifluoromethanesulfonic

acid (TfOH) to yield the corresponding boronium salt.[16] A related bis(oxazol-2-ylidene)–phenylborylene system reported by Kinjo et al. produced a hydroborate via TfOH.[17] Furthermore, Wagner et. Al synthesized a diborylmethane anion that could be protonated with TfOH to yield the hydride bridged B-H-B species.[18] In none of these cases has the reactivity of the B–H bonds formed via protonation

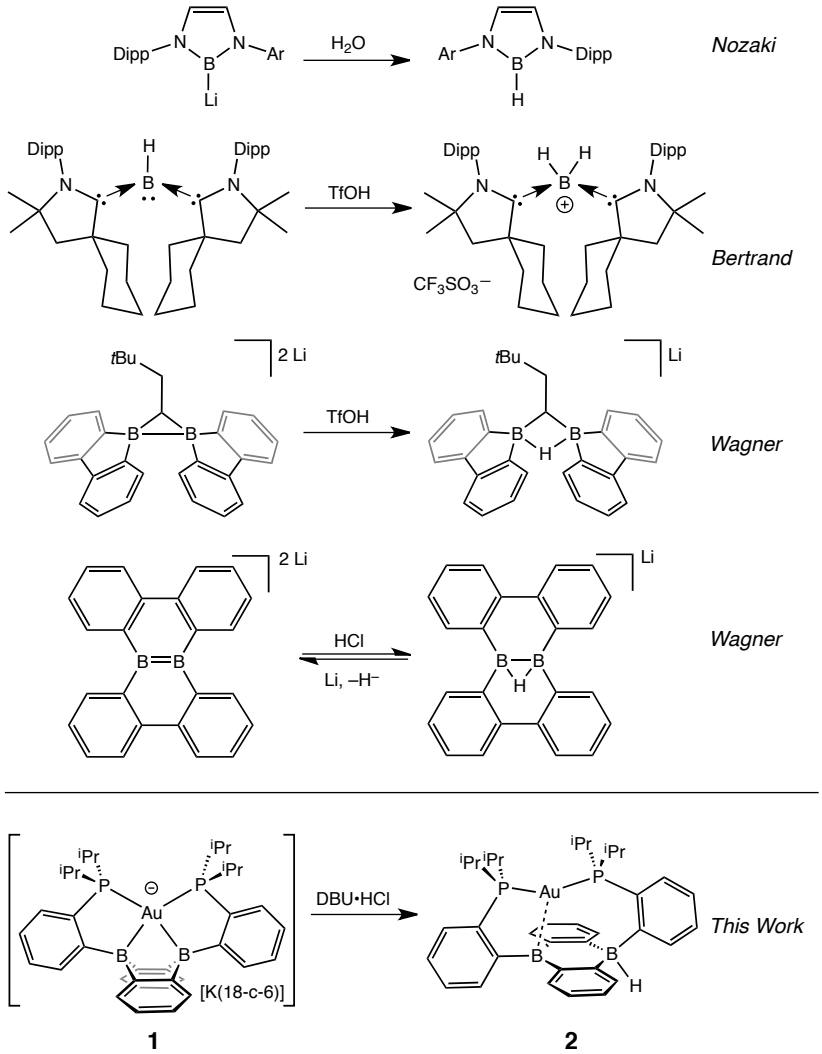

Figure 3.2.1. Previously reported examples of protonation yielding B-H bonds and this work.

been reported.

We recently reported the synthesis of the disphosphine tethered diboraanthracene ligand B_2P_2 (9,10-bis(2-(diisopropylphosphino)phenyl)-9,10-dihydroboranthrene) and its gold complexes. The anionic complex, [Au(B_2P_2)][K(18-c-6)] (**1**), which features an unprecedented boroauride moiety, could be accessed at remarkably mild potentials (–2.05 V vs. Fc/Fc^+, MeCN) owing to the formation of a strong 3-centered, 2-electron bond between Au and the two B atoms.[19] Considering that **1** can be thought of as a masked boron dianion, we wondered if protonation of this complex could provide direct access to a hydridic B–H unit, akin to the Mn/Cr-mediated reduction and protonation series of borazine presented by Szymczak et al.[20] We herein report the synthesis and characterization of this borohydride complex, [Au(B_2P_2)]H (**2**), which can be generated via direct hydride reduction of [Au(B_2P_2)]Cl (**3**), FLP-type dihydrogen activation, H-atom addition to the boron-centered radical complex Au(B_2P_2) (**4**) or, most notably, by protonation of **1** with mild organic acids. Borohydride **2** is sufficiently reactive to reduce CO_2 to formate, and cleavage of the resulting B–OCHO bond can be achieved either by addition of an electrophile (including H^+) or by one electron reduction. These results collectively represent a synthetic cycle for CO_2 reduction to formate with protons and electrons, with the key finding being the ability to generate a hydridic borohydride unit via protonation of a reduced borane accessed at reasonably mild potentials. This reaction sequence

establishes the chemical feasibility of electroreduction of CO_2, an area dominated by transition metal chemistry, via boron-centered reactivity. Further, given the recent application of boron-doped graphene to CO_2 electroreduction,[21] these molecules offer well-defined molecular models[22] of fundamental chemical processes that may underlie small molecule reactivity at doped graphitic carbon surfaces.

3.2.2.) Results and Discussions

Our initial synthetic approaches to a B–H containing derivative of [Au(B_2P_2)] targeted direct hydride for halide substitution. Addition of 1 equiv. K-selectride to **3** gave borohydride **2** in 89% yield. This complex could also be prepared in good yield by exposing **3** to a large excess (>10 eq.) of Et_3SiH. Additionally, **2** could be synthesized via FLP-type H_2 activation in the presence of DBU. Exposure of a THF solution of equimolar **3** and DBU to 1 atm H_2 resulted in the immediate formation of **2** as judged by ^{1}H, ^{11}B, and ^{31}P NMR spectroscopies. Single-crystal X-ray diffraction (XRD) studies of **2** show it to be a zwitterion in the solid state with an intact B–H bond on the DBA face opposite the Au center, analogous to the previously reported structure of zwitterion **3** (Figure 3.2.2). The H atom was located in the electron difference map and is bound to a quasi-tetrahedral B atom ($\Sigma\angle$CBC = 340.5°). On the opposite side of the DBA linker, the Au ion is bound by both P donors in a roughly linear fashion ($\angle$PAuP = 156.8°) with a single Au–B interaction (d_{AuB} = 2.644(1) Å) to one nearly-planar B

atom ($\Sigma\angle$CBC = 359.8°). The ^{1}H NMR spectrum of **2** features a signal at 5.09 ppm for a B–H proton resonance with the expected four-line pattern for coupling to a single ^{11}B atom (J_{BH} = 80 Hz). The ^{11}B NMR shows a corresponding doublet at –10.01 ppm (J_{BH} = 80 Hz) while the ^{31}P NMR spectrum features two doublets at 58.4 and 55.9 ppm (J_{PP} = 255.0 Hz), consistent with inequivalent phosphine ligands on the NMR timescale.

Given the precedent for H-atom transfer reactivity at boron,[23] we also targeted the synthesis of **2** from the neutral radical species **4** via H-atom addition. Reaction of Au(B_2P_2) with one equivalent of Bu_3SnH produces **2** and $Bu_3SnSnBu_3$ over 12 hours via apparent H-atom addition as judged by ^{1}H NMR

Scheme 3.2.1. Synthesis of **2** via reaction with H^-, $H^{\bullet}$ and H^+.

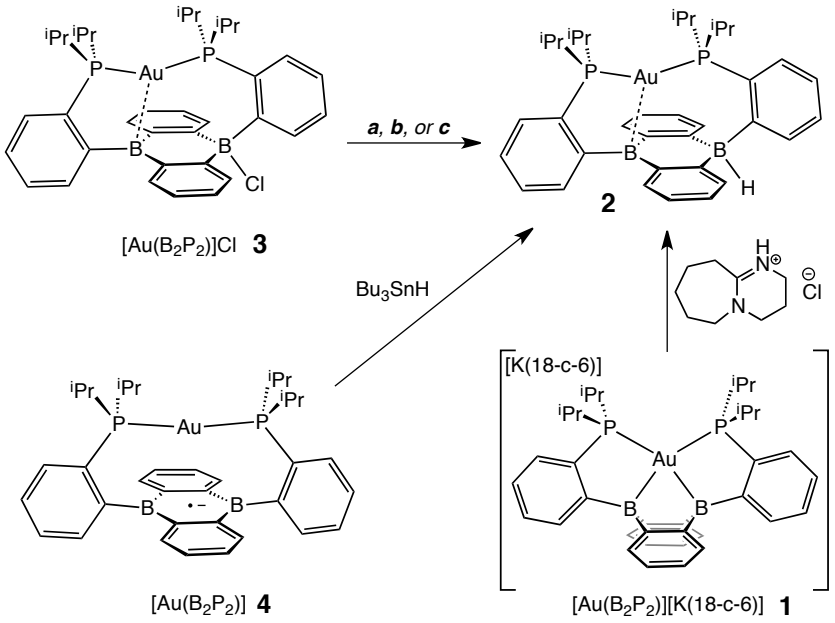

Reagent: ***a***) $HSiEt_3$ ***b***) K•Selectride ***c***) H_2/DBU

of reaction mixtures (see Experimental Section).

Addition of one equivalent of K-Selectride to $[Au(B_2P_2)]H$ in Et_2O gave the anionic diborohydride complex, $[Au(B_2P_2)H_2][K(Et_2O)]$ (**5**). Single-crystal XRD reveals **5** to be a dimer in the solid state, (Figure 3.2.2) with two $[Au(B_2P_2)H_2]^-$ units bridged by two $[K(Et_2O)]^+$ cations via contacts between the B–H and K atoms. The $[(Au(B_2P_2)H_2]^-$ component features a linear P–Au–P moiety (∠P-Au-P = 161.9°) that sits above the DBA core with no appreciable interaction between Au and B ($d_{AuB} > 3.25$ Å). The H atoms bound to both B atoms were located on the electron difference map and both B centers exhibit a pseudo-tetrahedral geometry (Σ∠ = 337.5°). ^1H and ^{11}B NMR spectra feature a 4-line pattern and doublet, respectively, for the B–H moieties in **5**, analogous to the monoborohydride **2** (see Experimental Section, Figure 3.2.5.14).

Scheme 3.2.2. Synthesis of **5** and **7**.

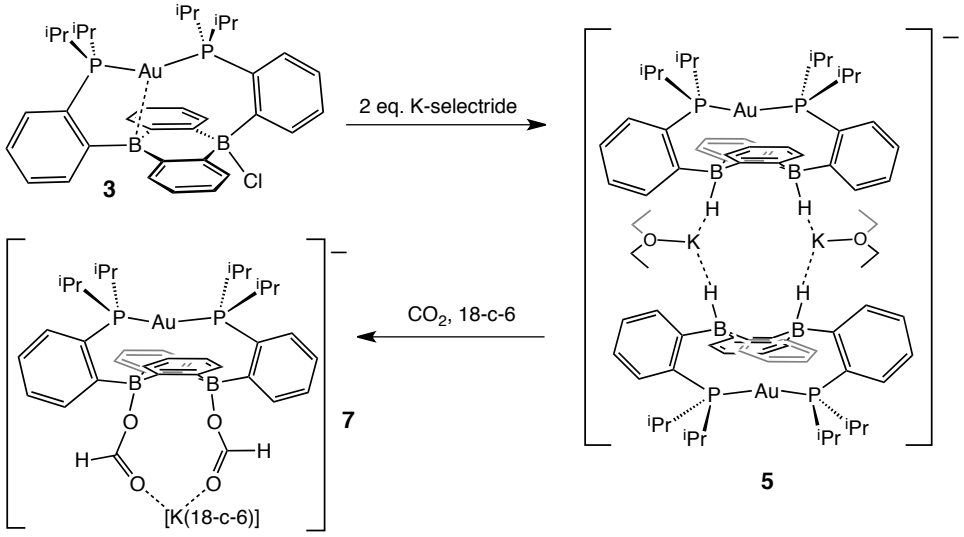

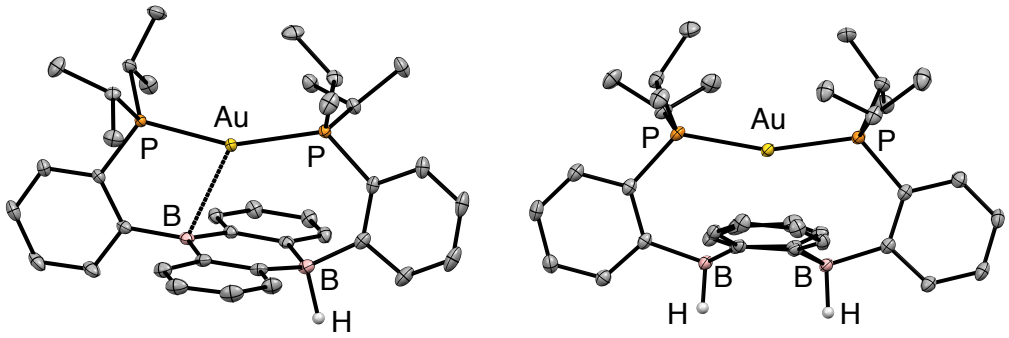

Figure 3.2.2. Thermal ellipsoid plots (50%) of [Au(B_2P_2)] H (**2**, left) and [Au(B_2P_2)H_2][K(Et_2O)] (**5**, right). Most hydrogen atoms and, in the case of **5**, counterions have been omitted for clarity.

To probe the accessing **2** via protonation of **1,** we exposed **1** to a series of organic acids. Addition of one equivalent of solid [Ph_2NH_2][Cl] or [2,6-Me_2py][Cl] to CD_3CN solutions of [(B_2P_2)Au][K(18-c-6)] resulted in immediate effervescence and formation of dark purple reaction mixtures. ^{1}H NMR analysis revealed formation of H_2, **3** and broad peaks for radical **4**, while ^{31}P and ^{11}B NMR spectra were consistent with the formation of **3** and **4**. Fortunately, addition of one equivalent of DBU•HCl (DBU = diazabicycloundecene) to a solution **1** in CD_3CN gave rise to a pale-yellow solution exhibiting ^{1}H, ^{11}B and ^{31}P NMR resonances that matched authentic samples of **2** (see Spectroscopic Data) with no H_2 being observed. Furthermore, **2** is stable to treatment with excess DBU•HCl.

With the borohydrides **2** and **5** in hand, we sought to examine their reactivity with CO_2. Exposure of a C_6D_6 solution of **2** to 1 atm CO_2 resulted in quantitative formation of the corresponding formato complex [Au(B_2P_2)]CO_2H (**6**) within seconds. The solid-state structure of **6** confirms the insertion of CO_2 into the B–H bond, with resulting formate ion bound through a single O to one boron atom.

The zwitterionic structure of **6** is analogous to **2** and **3**, with a tetrahedral boron center bound to the formate ($\Sigma\angle$CBC = 339.1°) and an intermediate length contact between Au and the non-formate bound B atom (d_{AuB} = 2.632 Å). ^{1}H NMR spectra of **6** in $CDCl_3$ is consistent with effective C_{2v} symmetry in solution, with a lone singlet in the ^{31}P NMR spectrum at 56.1 ppm and ^{11}B{^{1}H} NMR displaying a broad singlet at 26.9 ppm. Similar to **3**, the observed C_{2v} symmetry in solution along with ^{11}B chemical shift between that of bonafide three- and four-coordinate B centers in containing DBA molecules implies rapid exchange of the formate ion between each boron site of the DBA ring. The ^{13}C{^{1}H} NMR spectrum of **6** contains a resonance at 168.2 ppm for the formate carbon atom, and FT-IR spectroscopy revealed a strong band at 1672 cm^{-1} for the formate C=O stretch.

Scheme 3.2.3. Synthesis of **6** and its reaction with electrophiles and reductant to yield **3** and **4**, respectively.

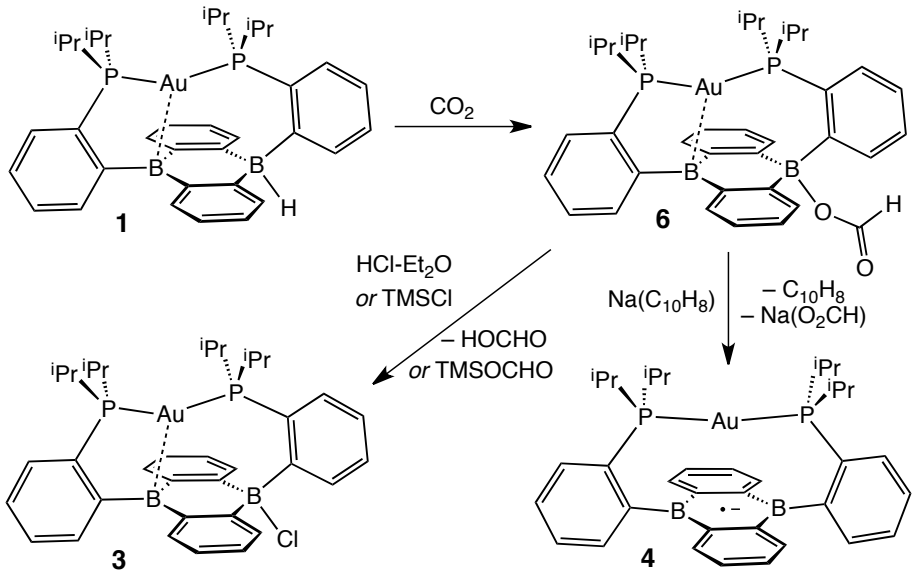

In a similar fashion, exposure of a solution of diborohydride **5** to 1 atm CO_2 cleanly gave the corresponding diformate complex, which was isolated as its 18-crown-6 adduct, $[Au(B_2P_2(CO_2H)_2)][K(18\text{-c-}6)]$ (**7**). Single-crystal XRD confirmed the insertion of CO_2 into both B–H bonds, with B atoms puckered out of planarity to accommodate each OCHO moiety. Additionally, the formate moieties in **7** were identified by ^1H NMR (8.34 ppm), $^{13}C\{^1H\}$ NMR (168.2 ppm) and FT-IR spectroscopy (C=O, 1672 cm^{-1}).

The facility of formate migration between the two B sites in **6** (*vide infra*) suggested that B–O bond cleavage and formate release might occur under reasonably mild conditions. First, we assessed the ability of electrophiles such as TMSCl and HCl to effect B–O bond scission. Treatment of **6** with excess TMSCl resulted in the immediate formation of **3** as judged by ^1H and ^{31}P NMR along with new resonances for $(CH_3)_3Si(OCHO)$ (see Experimental Section, Figure 3.2.5.13) that were identified by spectroscopic comparison to authentic samples. While silyl electrophiles have strong precedent to mediate E–O bond cleavage in main group systems,[24] we wondered if a suitable acid would be able to protonate the B–OCHO bond to yield formic acid. To this end, addition of $[Ph_2NH_2][Cl]$ or DBU•HCl to $CDCl_3$ solutions of **6** saw no observable reaction over the course of days at room temperature. However, addition of one equivalent of $HCl•Et_2O$ to $[Au(B_2P_2)]CO_2H$ resulted in the immediate formation of $[Au(B_2P_2)]Cl$ by ^1H and

^{31}P NMR spectroscopy with resonances for HCO_2H observed in the ^{1}H NMR spectrum.

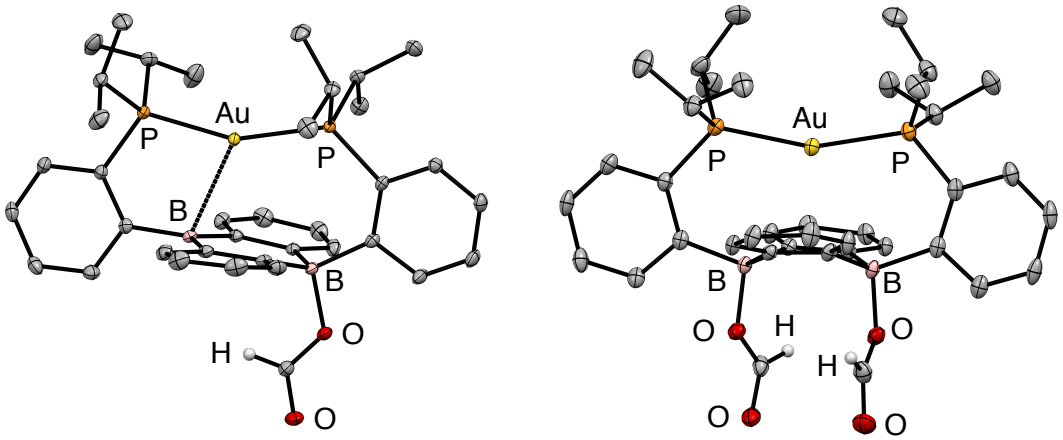

Figure 3.2.3. Thermal ellipsoid plots (50%) of $[Au(B_2P_2)]CO_2H$ (**6**, left) and $[Au(B_2P_2(CO_2H)_2)][K(18\text{-c-}6)]$ (**7**, right). Most hydrogen atoms and, in the case of **7**, counterions have been omitted for clarity.

Following successful electrophilic B–O bond cleavage in **6** to yield **3**, we wondered if, given the unique redox-activity of the DBA core, reductive cleavage of the B–OCHO unit would also be viable. In probing the feasibility of reductive cleavage of the formed B-OCHO moiety, cyclic voltammograms (CVs) of **6** (0.1 M $[N^nBu_4][PF_6]$ in CH_3CN, 100 mV/s scan rate) were collected and revealed a poorly reversible process at $E_{1/2} = -1.79$ V vs. Fc/Fc^+ which gave rise to a daughter wave at ~ –1.5 V (Experimental Section, Figure 3.2.6.39-43). This daughter process occurred at roughly the same potential as the oxidation of $[Au(B_2P_2)]^{0/+1}$; consistent with the hypothesis that one electron reduction of **6** forms **6**$^-$ which then undergoes formate dissociation on the CV timescale to afford neutral **4**.[19] To unambiguously confirm the liberation of formate ion, **6** was treated with 1

Scheme 3.2.4. Synthetic cycle for CO_2 reduction with the Au(B_2P_2) system.

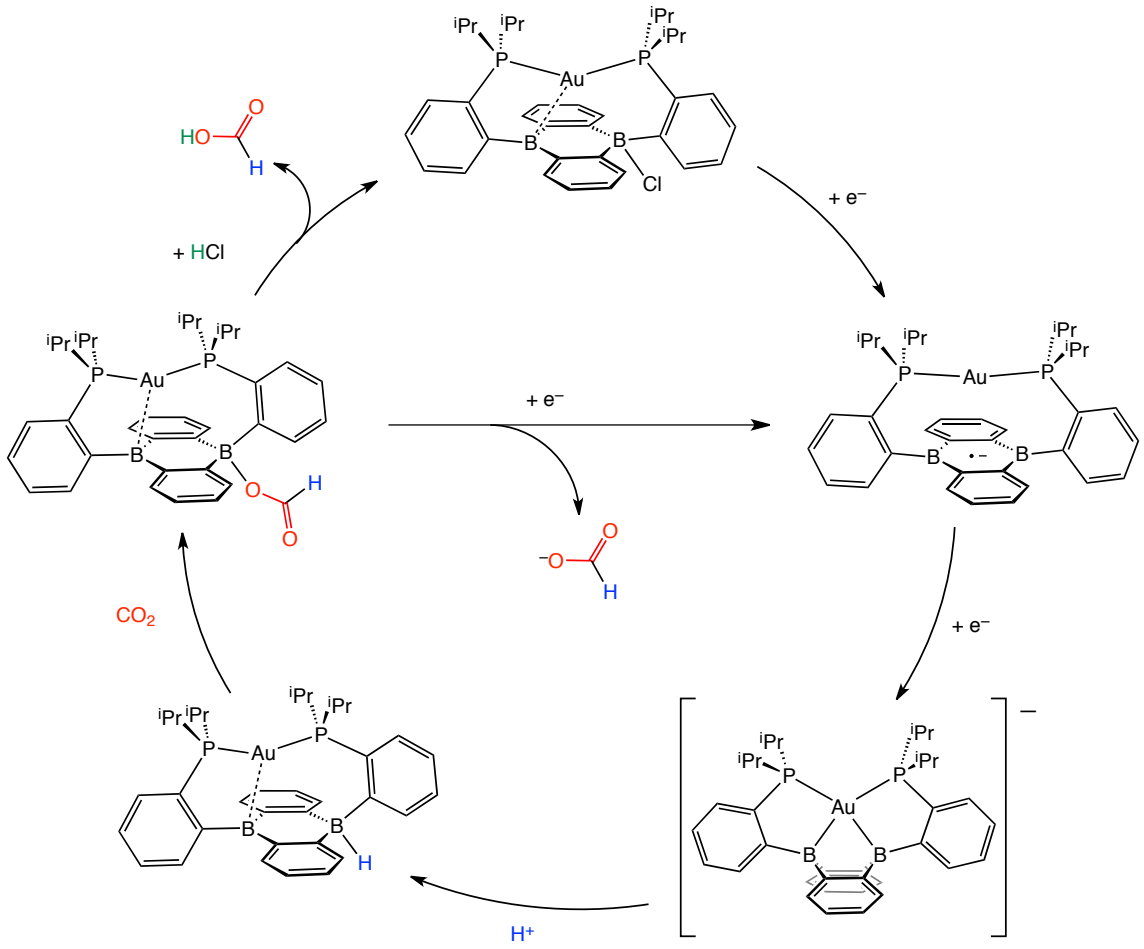

equivalent of Na($C_{10}H_8$)•0.5 in THF. A turbid, dark-purple solution immediately formed, indicating formation of **4**. The precipitated solids were collected by filtration and dissolved in D_2O with ^{1}H NMR analysis revealing formation of $NaCO_2H$ (see Experimental Section, Figure 3.2.5.12). To our knowledge, this is the only example of reductive cleavage of a B–OCHO bond to yield formate. This process is presumably driven by the accessible one-electron reduction chemistry of **6** (–1.74 V vs. Fc/Fc^+) enabled by the DBA core and speaks to the utility of frontier orbital modulation by incorporation of boron into polycyclic aromatic

hydrocarbon frameworks.[25] Collectively, these results outline a synthetic cycle for CO_2 reduction summarized in Scheme 3.2.4. As a proof of concept, we have carried out the synthetic sequence through multiple iterations to generate additional crops of $NaCO_2H$.

Scheme 3.2.5. Synthesis of **8** and **9**.

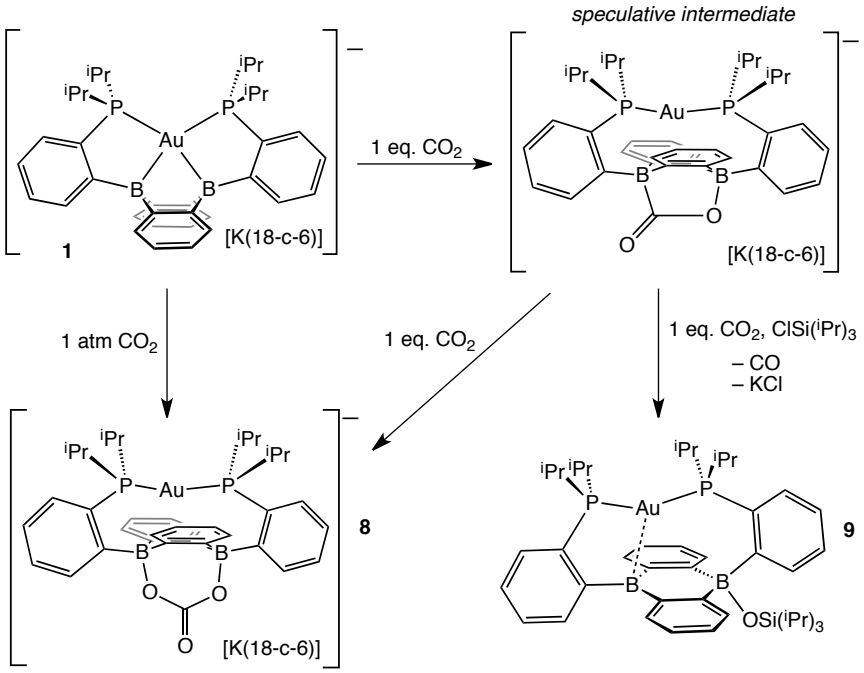

Having probed the $[Au(B_2P_2)]$ system for CO_2 reduction chemistry from its mono and di-hydrides, we additionally explored the direct reaction of CO_2 with **1**. Wagner et al. recently reported that 9,10-dilithio-9,10-diborataanthracene reacts with CO_2 to yield CO_3 and CO selectively.[21a] Reaction of **1** with 1 atm. of CO_2 in C_6D_6 resulted in the immediate formation of a colorless solution with no detectable precipitate. A single-crystal suitable for XRD studies was obtained from CO_2 saturated reaction mixtures and revealed the product to be the carbonate adduct, $[Au(B_2P_2)CO_3][K(18\text{-c-}6)]$ (**8**). The asymmetric unit of **8**

contains two crystallographically distinct molecules which are chemically equivalent in gross terms but exhibit minor variations in their geometries, most notably in their B–O distances, which range from 1.550(6) Å to 1.578(8) Å. This spread of B–O distances is consistent with a soft CO_3 binding potential, in agreement with Wagner's results. Solution spectroscopy of **8** is consistent with C_{2v} symmetry and the CO_3 unit was identified by $^{13}C\{^1H\}$ NMR (168.0 ppm) and FT-IR (1592 cm^{-1}) spectroscopies with $^{13}CO_2$ experiments confirming these assignments (see Spectroscopic Data).

In order to elucidate the mechanism of the formation of **8** from the reaction of **1** and CO_2, we explored the reaction by NMR spectroscopy at low temperature. Recent reports on reduced boron-containing heterocycles,[21] offer extensive precedent for the cycloaddition of CO_2 across the boron atoms, and we

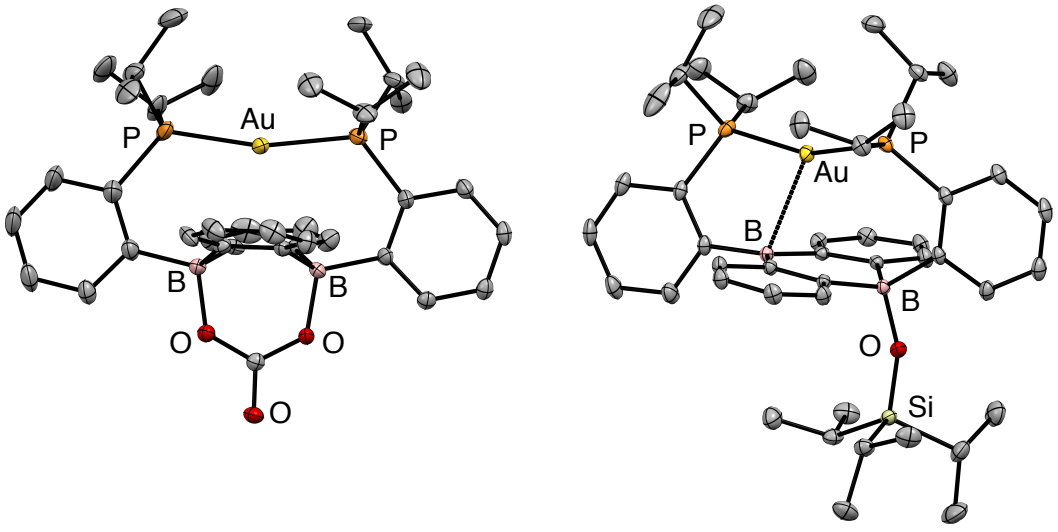

Figure 3.2.4. Thermal ellipsoid plots (50%) of $[Au(B_2P_2)CO_3][K(18\text{-c-}6)]$ (**8**, left) and $[Au(B_2P_2)]OSi(CHCH_3)_3$ (**9**, right). Hydrogen atoms and, in the case of **8**, counterions have been omitted for clarity.

sought to probe that possibility here. Attempts at trapping a cycloadduct via addition of a single equivalent of CO_2 to a frozen solution of the anion **1** in d_8-toluene followed by insertion into a precooled (–50 °C) NMR spectrometer and subsequent variable temperature NMR monitoring resulted in a 1:1 distribution of starting material **1** and the carbonate adduct **8**. When the same experiment was carried out with $^{13}CO_2$ enhanced intensity was observed corresponding to the Au(B_2P_2)-$^{13}CO_3$ resonance at 168.2 ppm along with free ^{13}CO at 184 ppm. We attempted to trap a cycloadduct intermediate during the formation of [Au(B_2P_2)CO_3][K(18-c-6)] with triisopropylsilyl chloride (TIPSiCl). Addition of 1 atm CO_2 to a thawing C_6D_6 solution of [Au(B_2P_2)][K(18-c-6)] and TIPSiCl resulted in the immediate formation of a pale yellow solution. ^1H NMR analysis revealed a product with C_s symmetry on the NMR timescale that featured new -Si($CHCH_3$) and -Si($CHCH_3$) resonances. ^{31}P NMR analysis features a set of doublets at 56.0 ($J_{P\text{-}P}$ = 240 Hz) and 52.5 ($J_{P\text{-}P}$ = 240 Hz) ppm while ^{11}B NMR featured a broad resonance at 51.5 and a sharper singlet at 2.99 ppm. Single-crystal XRD studies revealed the product to be the [Au(B_2P_2)]OSi($CHCH_3$)$_3$ zwitterion with a triisopropylsiloxide anion bound to one B atom in the solid state. Two crystallographically [Au(B_2P_2)]OSi($CHCH_3$)$_3$ distinct molecules are present in the asymmetric unit although their distances and angles are essentially identical (See Spectroscopic Data, Figure 3.2.5.49).

The formation of $[Au(B_2P_2)]OSi(CHCH_3)_3$ is concomitant with CO loss as judged by $^{13}CO_2$ labeling experiments however no intermediate was observed to explicate a cycloadduct intermediate. Monitoring of the reaction mixture by NMR spectroscopy under 1 atm. CO_2 present also did not lead to any further reaction, ruling out additional reaction of the -OSiTIP moiety with CO_2 as has been previously observed for metal-siloxide units.[26] The presence of ^{13}CO in both reaction spectra also support extrusion of CO from intake of the first equivalent of CO_2 by $[Au(B_2P_2)][K(18\text{-}c\text{-}6)]$..

3.2.3.) Concluding Remarks

In conclusion, we have synthesized a reactive borohydride, **2**, with the $Au(B_2P_2)$ system that was accessible via hydride exchange, radical H-atom addition, dihydrogen activation and protonation. Reaction of **2** with CO_2 resulted in rapid hydroboration of CO_2 to afford the formate zwitterion, **6**. CV studies on **6** showed an irreversible process at $E_{1/2} = -1.79$ V vs. Fc/Fc^+ which gave rise to a daughter wave at ~ –1.5 V that corresponds to the oxidation of $Au(B_2P_2)$. Stoichiometric reduction of **6** afforded the radical $[Au(B_2P_2)]$ and precipitated Na(OCHO) in a reductive B-O bond cleavage reaction. Additionally, electrophilic B-OCHO bond cleavage was displayed by reaction of **6** with either TMSCl or $HCl{\bullet}Et_2O$, providing TMS-OCHO and formic acid, respectively. Sequential reaction of $Au(B_2P_2)Cl$ with electrons, protons, CO_2 and electrons displays proof-of-principle catalysis with this system. Contrarily, direct reaction of

[Au(B_2P_2)][K(18-c-6)] with 1 atm. of CO_2 resulted in the formation of **8** that contained carbonate bound via both B atoms of the DBA ring. Trapping experiments suggested this process proceeded through a cycloaddition intermediate with concomitant CO loss as provided by $^{13}CO_2$ labeling studies however reaction of the anion **1** with 1 equivalent of CO_2 provided an equimolar mixture of **1** and carbonate containing **8**. Collectively these results provide access to three different CO_2 reductions products (NaOCHO, TMSOCHO, HOCHO) that can be selectively produced solely by choice of reagent (Na($C_{10}H_8$), TMSCl, HCl•Et_2O) or, in the case of the reaction of [Au(B_2P_2)][K(18-c-6)] with CO_2, choice of starting material. Generation of reactive borohydrides from protons and electrons under mild conditions has been displayed and provides a pathway to generate borohydride reducing equivalents catalytically. We are currently underway developing reaction conditions to make the MB_2P_2 systems amenable to electrocatalysis.

3.2.4.) Experimental Section

3.2.4.1) General Considerations

Unless otherwise noted, all manipulations were carried out using standard Schlenk or glovebox techniques under a N_2 atmosphere. Hexanes, benzene, toluene, and acetonitrile were dried and deoxygenated by argon sparge followed by passage through activated alumina in a solvent purification system from JC Meyer Solvent Systems followed by storage over 4 Å molecular sieves. THF and

Et_2O were distilled from sodium-benzophenone ketyl under N_2 followed by storage over 4 Å molecular sieves for at least 24 hours prior to use. Non-halogenated and non-nitrile containing solvents were tested with a standard purple solution of sodium benzophenone ketyl in THF to confirm effective oxygen and moisture removal prior to use. Hexamethyldisiloxane (HMDSO) was distilled from sodium metal and stored over 4 Å molecular sieves for 24 hours prior to use. All reagents were purchased from commercial suppliers and used without further purification unless otherwise noted. [Au(B_2P_2)]Cl (**3**), [Au(B_2P_2)] (**4**), [Au(B_2P_2)][K(18-c-6)] (**1**)[19] and DBU•HCl[27] were synthesized according to literature procedures. Na($C_{10}H_8$) was synthesized by modifying a literature procedure.[28] Elemental analyses were performed by Midwest Microlab, LLC, Indianapolis, IN. Deuterated solvents were purchased from Cambridge Isotope Laboratories Inc., degassed, and dried over activated 3Å molecular sieves for at least 24 h prior to use. NMR spectra were recorded on Varian Inova 500 MHz, Bruker Avance 600 MHz, and Bruker Avance 700 MHz spectrometers. ^{1}H and ^{13}C chemical shifts are reported in ppm relative to tetramethylsilane using residual solvent as an internal standard. Original ^{11}B NMR spectra were processed using MestReNova 10.0.2 with a backwards-linear prediction applied to eliminate background signal from the borosilicate NMR tube.[29] For ^{11}B NMR spectra with peaks overlapping the borosilicate signal, a manual baseline correction was applied. IR spectra were recorded using a Bruker Alpha FT-IR

with a universal sampling module collecting at 4 cm^{-1} resolution with 32 scans. X-ray diffraction studies were performed using a Bruker-AXS diffractometer. Cyclic Voltammetry (CV) experiments were performed using a Pine AFP1 potentiostat. The cell consisted of a glassy carbon working electrode, a Pt wire auxiliary electrode and a Pt wire pseudo-reference electrode. All potentials are referenced vs. the Fc/Fc^+ couple measured as an internal standard.

3.2.4.2) [Au(B_2P_2)]H (2).

*(**2**) Via K-Selectride*: **3** (0.050 g, 0.063 mmol) was suspended in Et_2O (4 mL) before adding K-Selectride (63 µL, 0.063 mmol, 1.0 M in THF) as an Et_2O solution (2 mL). The reaction was stirred 30 minutes during which time a colorless precipitate developed in a pale-yellow solution. The reaction was filtered through celite, concentrated *in vacuo* (ca. 2 mL) and added hexanes (4 mL) before further concentration *in vacuo* caused the product to precipitate. The product was rinsed with hexanes (2 x 1 mL) and dried *in vacuo*. Yield: 0.030 g, 64%.

*(**2**) Via $HSiEt_3$*: **3** (0.050 g, 0.063 mmol) was suspended in toluene (4 mL) before adding $HSiEt_3$ (0.029 g, 0.252 mmol) as a toluene solution (2 mL). The reaction was stirred 1 hour where it became homogenous. The reaction was concentrated *in vacuo* (ca. 2 mL) and added HMDSO (4 mL) before further concentration *in vacuo* caused the product to precipitate. The product was rinsed with hexanes (2 x 1 mL) and dried *in vacuo*. Additional crops could be obtained by further

concentration and HMDSO (ca.1 mL) addition to the mother liquor. Yield: 0.040 g, 84%.

*(**2**) Via H_2/DBU*: **3** (0.010 g, 0.019 mmol) was dissolved in THF (0.6 mL), added DBU (2.84 μL, 0.019 mmol) and subjected to three freeze-pump-thaw cycles before adding 1 atm. H_2. The reaction was sonicated 10 minutes before having its volatiles removed *in vacuo.* The pale-yellow foam was dissolved in toluene (2 x 1mL) and filtered through celite before removal of volatiles *in vacuo* furnished the product as a pale yellow solid. Yield: 0.009 g, 95%.

*(**2**) Via $HSnBu_3$*: **4** (0.050 g, 0.063 mmol) was dissolved in THF (2 mL) and added $HSnBu_3$ (0.020 g, 0.069 mmol) as a THF (1 mL) solution. The reaction was stirred 12 hours during which time a pale-yellow solution formed. The reaction was concentrated *in vacuo* (ca. 1 mL) before adding HMDSO (2 mL). Further concentration *in vacuo* caused the product to crystallize as a yellow solid that was collected, rinsed with hexanes (2 x 1 mL) and dried *in vacuo*. Yield: 0.042 g, 89%.

*(**2**) Via DBU•HCl*: 1 (0.015 g, 0.014 mmol) was dissolved in MeCN (2 mL) and added DBU•HCl (0.002 g, 0.014 mmol) as a MeCN (1 mL) solution. Immediately, the reaction became pale yellow before removing volatiles *in vacuo*. The pale-yellow residue was rinsed with hexanes (2 x 1 mL), dissolved in toluene (2 mL) and filtered through celite. Volatiles were removed *in vacuo* to yield the product as a pale yellow solid. Pre- and post-reaction ^{1}H, ^{31}P, ^{11}B NMR spectra are

shown in Figures 3.2.4.5-7. Yield: 0.011 g, 98%. X-ray quality crystals were grown by layering a concentrated toluene solution with HMDSO. ^{1}H NMR (500 MHz, C_6D_6) δ 8.95 (bs, 1H), 7.86 (d, *J* = 6.9 Hz, 2H), 7.61 (m, 1H), 7.50 (d, *J* = 7.4 Hz, 1H), 7.44 (d, *J* = 7.5 Hz, 2H), 7.31 (m, 2H), 7.27 (t, *J* = 7.3 Hz, 1H), 7.18 (m, 2H), 7.12 (t, *J* = 7.3 Hz, 1H), 7.03 (t, *J* = 7.2 Hz, 2H), 5.09 (m, J_{BH} = 80 Hz, 1H), 1.97 (m, 4H), 0.76 (d, *J* = 6.9 Hz, 6H), 0.73 (d, *J* = 7.1 Hz, 6H), 0.71 (d, *J* = 7.1 Hz, 3H), 0.68 (d, *J* = 6.9 Hz, 3H), 0.55 (d, *J* = 7.0 Hz, 3H), 0.52 (d, *J* = 6.9 Hz, 3H). ^{31}P{^{1}H} NMR (202 MHz, C_6D_6) δ 58.39 (d, *J* = 255.3 Hz), 55.91 (d, *J* = 255.0 Hz). ^{11}B NMR (193 MHz, THF:Benzene, 3:1) δ 52.45, –10.01 (d, *J* = 78.4 Hz). ^{13}C NMR (126 MHz, C_6D_6) δ 145.6 (d, *J* = 14.2 Hz), 142.1, 138.0, 135.7, 134.5 (d, *J* = 11.0 Hz), 134.2 (d, *J* = 10.5 Hz), 131.4 (d, *J* = 15.2 Hz), 130.7 (d, *J* = 13.7 Hz), 129.9, 126.3 (d, *J* = 6.0 Hz), 124.9 (d, *J* = 6.6 Hz), 122.7, 28.7 (d, *J* = 26.1 Hz), 27.4 (d, *J* = 25.7 Hz), 20.6 (d, *J* = 4.9 Hz), 20.1 (m), 19.7 (d, *J* = 3.7 Hz), 19.4. FTIR: ν_{max} (cm^{-1}) 2838, 2119 (B-H). Anal. Calcd for $C_{36}H_{45}AuB_2P_2$: C, 57.02 H, 5.98. Found: C, 56.89 H, 5.96.

3.2.4.3) [Au(B_2P_2)](H_2)]$_2$[μ-K_2(Et_2O)]$_2$ (5).

3 (0.034 g, 0.043 mmol) was suspended in Et_2O (4 mL). K-Selectride (89 μL, 2 mol. eq, 1.0 M in THF) was then added dropwise which caused the solution to become homogenous briefly before a colorless precipitate appeared. After stirring 40 minutes, the product was collected via filtration, dissolved in THF (2 x 2 mL) and layered with Et_2O (*ca.* 8 mL). The next day, colorless crystals had

appeared that were decanted from the mother liquor and dried *in vacuo*. Yield: 0.028 g, 75%. X-Ray quality crystals were grown by layering a concentrated THF solution with Et_2O. ^1H NMR (400 MHz, THF-d_8) δ 7.96 (d, J = 6.6 Hz, 4H), 7.57 (dt, J = 7.4, 3.8 Hz, 4H), 7.27 (t, J = 7.2 Hz, 4H), 7.23 – 7.14 (m, 4H), 6.67 – 6.60 (m, 8H), 6.54 (dd, J = 5.4, 3.3 Hz, 8H), 3.39 (q, J = 7.0 Hz, 4H), 3.27 (q, J = 68.4 Hz, 4H) 2.46 – 2.31 (m, 8H), 1.12 (t, J = 7.0 Hz, 6H), 1.11 (d, J = 7.0 Hz, 12H), 1.06 (d, J = 7.0 Hz, 12H), 0.74 (d, J = 7.0 Hz, 12H), 0.69 (d, J = 7.0 Hz, 12H). $^{31}P\{^1H\}$ NMR (202 MHz, THF-d_8) δ 50.3 (s).^{11}B NMR (160 MHz, THF-d_8) δ –8.66 (d, J = 71.8 Hz). ^{13}C NMR (151 MHz, THF-d_8) δ 174.4, 159.5, 143.8 (t, J = 7.3 Hz), 134.2 (t, J = 25.4 Hz), 133.2, 132.0, 128.9, 124.5, 123.1, 27.8 (t, J = 13.2 Hz), 22.6, 19.8. FTIR: ν_{max} (cm^{-1}) 2089, 1985 (BH). Anal. Calcd for $C_{80}H_{92}Au_2B_4K_2P_4$ (2 x $C_4H_{10}O$): C, 55.06 H, 6.47. Found: C, 55.16 H, 6.26.

3.2.4.4) [Au(B_2P_2)](CO_2H) (6).

A solution of **1** (0.020 g, 0.026 mmol) in benzene (3 mL) was subjected to three freeze-pump-thaw cycles prior to adding 1 atm. CO_2. The reaction was stirred 30 minutes before removing volatiles *in vacuo* to yield the product as a pale-yellow solid. Yield: 0.019 g, 90%. X-Ray quality crystals were grown by layering a concentrated THF solution with hexanes. A sample suitable for element analysis was prepared by layering a concentrated $CDCl_3$ solution with hexanes. ^1H NMR (500 MHz, $CDCl_3$) δ 8.40 (bs, 1H), 8.30 (d, J = 7.1 Hz, 2H), 7.69 (s, 1H), 7.64 (t, J = 7.3 Hz, 2H), 7.54-7.49 (m, 2H), 7.42 (t, J = 7.5 Hz, 2H), 7.18 (dd, J = 5.3, 3.4

Hz, 4H), 7.07 (dd, *J* = 5.5, 3.3 Hz, 2H), 7.03 (bs, 2H), 2.46-2.36 (m, 4H), 0.98 (d, *J* = 8.5 Hz, 6H), 0.95 (d, *J* = 8.3 Hz, 6H), 0.84 (d, *J* = 7.8 Hz, 6H), 0.81 (d, *J* = 7.8 Hz, 6H). $^{31}P\{^{1}H\}$ NMR (202 MHz, $CDCl_3$) δ 56.1 (s). $^{11}B\{^{1}H\}$ (193 MHz, $CDCl_3$) δ 26.9 (bs). ^{13}C NMR (126 MHz, $CDCl_3$) δ 168.2, 160.6, 153.1, 136.5, 136.1, 133.5 (t, *J* = 8.0 Hz), 131.6, 131.4, 131.3 (t, *J* = 26.4 Hz), 130.6, 130.2, 129.20, 128.5, 128.4, 126.0, 125.4, 28.4 (t, *J* = 14.2 Hz), 20.2, 19.7. FTIR: ν_{max} (cm^{-1}) 1672 (C=O). Anal. Calcd for $C_{37}H_{45}AuB_2O_2P_2$ (1 x $CDCl_3$): C, 49.52 H, 5.03. Found: C, 49.49 H, 5.51.

3.2.4.5) Reaction of $[Au(B_2P_2)](CO_2H)$ with $Na(C_{10}H_8)$.

6 (0.015 g, 0.019 mmol) was dissolved in THF (1 mL) and added a solution of $Na(C_{10}H_8)$ (0.004 g, 0.019 mmol) in THF (1 mL) at room temperature. Immediately a purple solution appeared, and a small amount of precipitate formed. The reaction was filtered through a celite-packed pipette and the filter was removed from the glovebox. The filter was dried with a stream of air and rinsed with D_2O into an NMR tube. ^{1}H NMR revealed a resonance at δ 8.28 for sodium formate that was in agreement with reported literature values.[30] See Figure 3.2.5.12 for the collected spectra.

3.2.4.6) Reaction of $[Au(B_2P_2)](CO_2H)$ with $HCl{\cdot}Et_2O$.

3 (0.012 g, 0.015 mmol) was dissolved in $CDCl_3$ (1 ml) before being added $HCl{\cdot}Et_2O$ (10 µl, 0.020 mmol, 2.0 M in Et_2O) at room temperature. The reaction was stirred 30 minutes before collecting ^{1}H and ^{31}P NMR data that matched the

reported spectra.[19] The sample used for NMR spectroscopy was then crystallized by layering with hexanes (1 mL) and subjected to single-crystal X-ray diffraction that confirmed the formation of [Au(B_2P_2)]Cl.

3.2.4.7) Reaction of [Au(B_2P_2)](CO_2H) with TMSCl.

3 (0.012 g, 0.015 mmol) was dissolved in $CDCl_3$ (0.7 mL) and transferred to an NMR tube before adding TMSCl (2 µL, 0.016 mmol). The tube was vigorously shaken for 5 minutes before collecting ^{1}H and ^{31}P NMR spectra. New resonances at δ 8.32 and 0.06 were observed for $(Me)_3SiOCHO$ in addition with peaks for [Au(B_2P_2)]Cl and excess TMSCl (δ 0.43). See Figure 3.2.5.13 for the ^{1}H NMR spectra.

3.2.4.8) [Au(B_2P_2)]($CO_2H)_2$][K(18-c-6)] (7).

A THF (3 mL) solution of **5** (0.020 g, 0.012 mmol) was added 18-crown-6 (0.003 g, 0.013 mmol) before being subjected to three freeze-pump-thaw cycles. 1 atm. CO_2 was added and the reaction was stirred 15 minutes before removing volatiles *in vacuo*. The product was rinsed with hexanes (1 mL) and Et_2O (1 mL) before being dried *in vacuo*. Yield: 0.012 g, 87%. X-ray quality crystals were grown by layering a concentrated benzene solution with hexanes. ^{1}H NMR (500 MHz, C_6D_6) δ 8.69 (d, *J* = 7.5 Hz, 2H), 8.34 (s, 2H), 7.58 (t, *J* = 7.4 Hz, 2H), 7.43 (s, 2H), 7.32 (t, *J* = 7.4 Hz, 2H), 7.26 – 7.19 (m, 4H), 7.07 – 6.99 (m, 4H), 3.27 (s, 24H), 2.23 (m, 4H), δ 0.94 (q, *J* = 7.4 Hz, 12H), 0.75 (q, *J* = 8.1 Hz, 12H).^{31}P{^{1}H} NMR (202 MHz, C_6D_6) δ 46.4 (s). ^{11}B{^{1}H} (160 MHz, C_6D_6) δ 1.83 (bs). ^{13}C NMR

(151 MHz, C_6D_6) δ 169.0, 168.7, 155.0, 136.0 (t, J = 6.1 Hz), 134.9 (t, J = 25.5 Hz), 134.4, 131.5, 129.2, 125.1, 124.5, 26.8 (t, J = 13.0 Hz), 22.4, 18.9. FTIR: ν_{max} (cm^{-1}) 1678 (C=O). Anal. Calcd for $C_{50}H_{70}AuB_2KO_{10}P_2$ (1x C_6H_{14}): C, 54.38 H, 6.85. Found: C, 53.92 H, 6.94.

3.2.4.9) [Au(B_2P_2)](CO_3)][K(18-c-6)] (8).

A solution of **1** (0.015 g, 0.014 mmol) in benzene (4 mL) was subjected to three freeze-pump-thaw cycles before adding 1 atm. CO_2. The reaction was stirred 15 minutes before removing volatiles *in vacuo* to yield a colorless solid. Yield: 0.14 g, 89%. X-ray quality crystals were grown over the course of two days by letting the reaction mixture stand in benzene under a CO_2 atmosphere. ^{1}H NMR (500 MHz, C_6D_6) δ 8.65 (d, J = 8.6 Hz, 2H), 7.66 (t, J = 7.2 Hz, 2H), 7.50 (dt, J = 7.7, 3.9 Hz, 2H), 7.39 (t, J = 7.3 Hz, 2H), 7.07 (dd, J = 5.2, 3.3 Hz, 4H), 7.01 (dd, J = 5.1, 3.4 Hz, 4H), 3.20 (s, 24H), 2.45 – 2.37 (m, 4H), 1.02 (d, J = 7.0 Hz, 6H), 0.99 (d, J = 7.0 Hz, 6H), 0.85 (d, J = 7.9 Hz, 6H), 0.82 (d, J = 7.8 Hz, 6H). ^{31}P NMR (202 MHz, C_6D_6) δ 43.59. ^{11}B{^{1}H} (242 MHz, C_6D_6) δ 0.83 (bs). ^{13}C NMR (126 MHz, C_6D_6) δ 168.0, 158.6, 155.3, 136.3 (t, J = 25.4 Hz), 133.3 (t, J = 5.8 Hz), 131.6, 130.5, 128.6, 124.9, 123.8, 70.3, 26.0 (t, J = 12.3 Hz), 23.2, 18.8. FT-IR: ν_{max} cm^{-1} 1592 (C=O). Despite numerous attempts, good elemental analysis of this compound was not obtained.

3.2.4.10) [Au(B_2P_2)]($^{13}CO_3$)][K(18-c-6)] (8-^{13}C).

The ^{13}C-labeled compound was synthesized similarly to **8** using $^{13}CO_2$. ^{1}H, ^{31}P and ^{11}B NMR were identical to **8**. The isotropically enriched carbon appears at 168.9 ppm in the ^{13}C NMR spectrum. ^{1}H NMR (600 MHz, C_6D_6) δ 8.65 (d, J = 7.1 Hz, 2H), 7.67 (t, J = 7.2 Hz, 2H), 7.50 (s, 2H), 7.40 (t, J = 7.5 Hz, 2H), 7.09 – 7.05 (m, 4H), 7.04 – 6.99 (m, 4H), 3.20 (s, 18H), 2.41 (s, 4H), 1.02 (d, J = 6.9 Hz, 6H), 1.00 (d, J = 7.0 Hz, 6H), 0.85 (d, J = 8.0 Hz, 6H), 0.82 (d, J = 8.3 Hz, 6H). ^{13}C NMR (151 MHz, C_6D_6) δ 168.9, 158.6, 158.2, 155.3, 136.3 (t, J = 25.0 Hz), 133.3, 131.6, 130.5, 129.0 – 128.5 (m), 124.8, 123.8, 70.2, 26.0 (t, J = 12.2 Hz), 23.2, 18.8. FT-IR: ν_{max} cm^{-1} 1549 (C=O).

3.2.4.11) [Au(B_2P_2)](O(Si(^{i}Pr)$_3$) (9).

1 (0.015 g, 0.014 mmol) was dissolved in benzene (5 mL) and frozen in a –196 °C bath prior to adding triisopropylsilyl chloride (0.003 g, 0.015 mmol) as a benzene (1 mL) solution. The mixture was briefly thawed and gently stirred to ensure homogeneity before being subject to three freeze-pump-thaw cycles prior to introducing 1 atm. CO_2. The reaction immediately began turning yellow and was stirred 15 minutes before removing volatiles *in vacuo*. The resulting yellow foam was washed with hexanes (3 x 1 mL), dissolved in toluene (2 x 1 mL), filtered through celite, layered with HMDSO (2 mL) and let stand overnight. The next day, the pale-yellow crystalline product was rinsed with hexanes (1 x1 mL) and dried *in vacuo*. Yield: 0.010 g, 73%. X-ray quality crystals were grown by

layering a concentrated toluene solution with HMDSO. ^{1}H NMR (500 MHz, C_6D_6) δ 9.61 (ddd, *J* = 7.5, 4.1, 1.2 Hz, 1H), 8.06 (d, *J* = 7.4 Hz, 1H), 7.84 (t, *J* = 7.4 Hz, 1H), 7.58 (d, *J* = 7.4 Hz, 2H), 7.41 (t, *J* = 8.5 Hz, 1H), 7.29 (t, *J* = 7.5 Hz, 1H), 7.27 (d, *J* = 7.1 Hz, 2H), 7.25 – 7.19 (m, 2H), 7.17-7.14 (m, 2H), 7.12 (t, *J* = 7.6 Hz, 1H), 6.94 (t, *J* = 7.3 Hz, 2H), 1.96 (tdd, *J* = 13.6, 7.7, 1.7 Hz, 4H), 1.20 (d, *J* = 7.4 Hz, 18H), 1.04 (dq, *J* = 15.1, 7.2 Hz, 3H), 0.75 (d, *J* = 6.9 Hz, 4H), 0.71 (d, *J* = 7.0 Hz, 4H), 0.68 (d, *J* = 6.9 Hz, 2H), 0.65 (d, *J* = 6.9 Hz, 2H), 0.49 (d, *J* = 7.0 Hz, 2H), 0.46 (d, *J* = 7.0 Hz, 2H). ^{31}P NMR (202 MHz, C_6D_6) δ 56.0 (d, *J* = 240.0 Hz), 52.5 (d, *J* = 239.9 Hz). ^{11}B NMR (160 MHz, C_6D_6) δ 51.5, –3.0. ^{13}C NMR (126 MHz, C_6D_6) δ 173.1, 170.7, 159.2 (d, *J* = 29.8 Hz), 140.7, 137.7 (d, *J* = 14.2 Hz), 137.4 (dd, *J* = 15.1, 9.0 Hz), 136.1 (d, *J* = 10.6 Hz), 135.2 (d, *J* = 9.4 Hz), 134.9 (d, *J* = 8.8 Hz), 132.3 (d, *J* = 13.6 Hz), 131.5 (t, *J* = 14.8 Hz), 131.1, 131.0, 129.8, 129.5 (d, *J* = 6.9 Hz), 129.1 (d, *J* = 6.8 Hz), 126.7, 124.3 (d, *J* = 8.7 Hz), 29.2, 29.0, 27.8, 27.6, 20.7, 20.2, 19.6, 14.3. MALDI MS: m/z 930.4087; Calcd. 930.4132.

3.2.5.) Spectroscopic Data

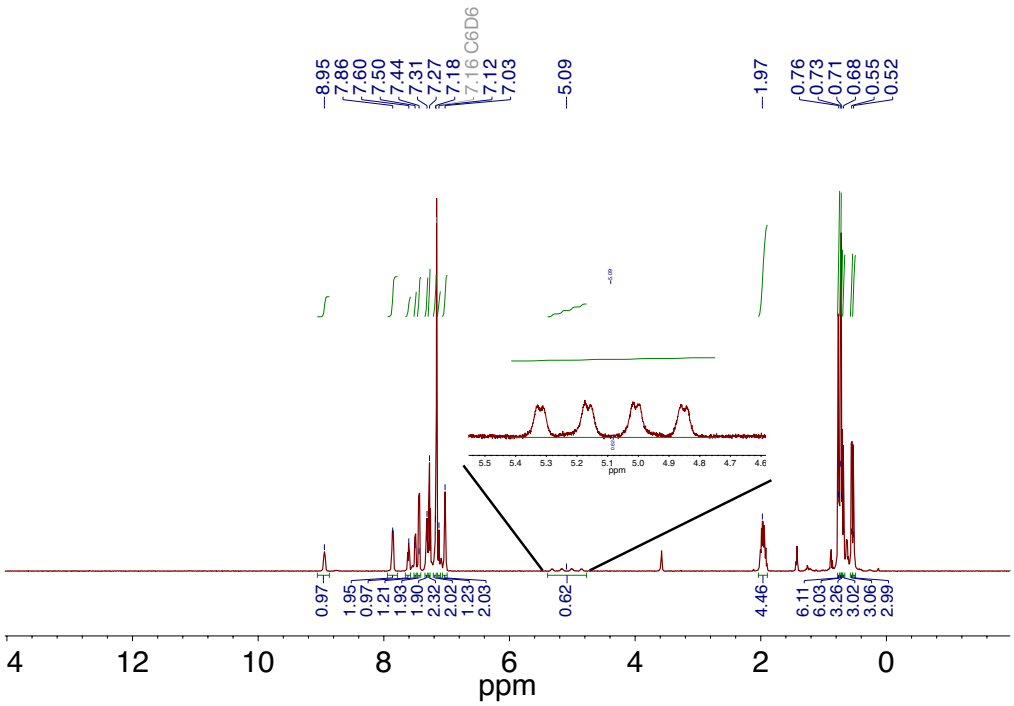

Figure 3.2.5.1. ^{1}H NMR spectrum of **[Au(B_2P_2)]H** recorded at 500 MHz in C_6D_6.

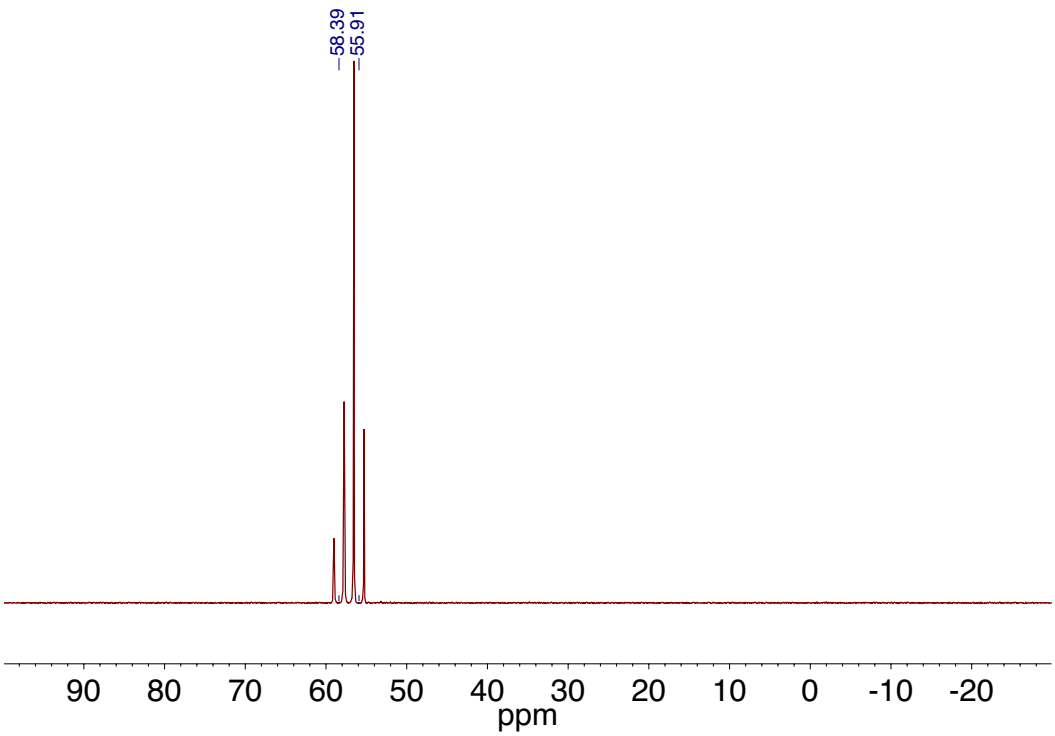

Figure 3.2.5.2. ^{31}P NMR spectrum of **[Au(B_2P_2)]H** recorded at 202 MHz in C_6D_6.

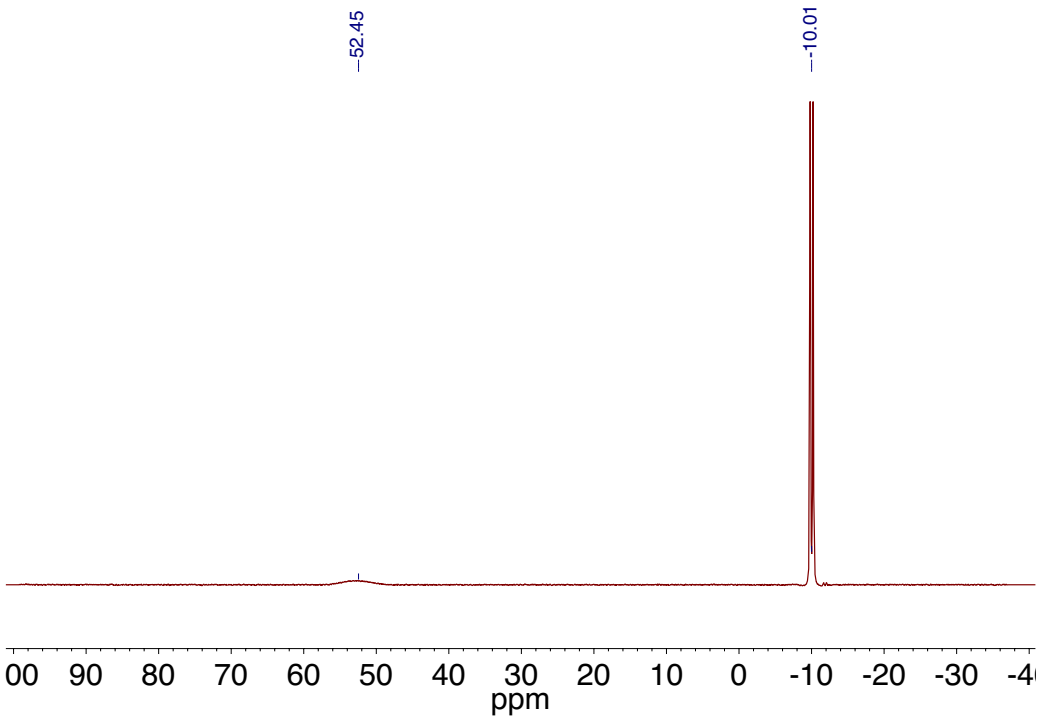

Figure 3.2.5.3. ^{11}B NMR spectrum of **[Au(B_2P_2)]H** recorded at 160 MHz in THF:C_6D_6 (1:1).

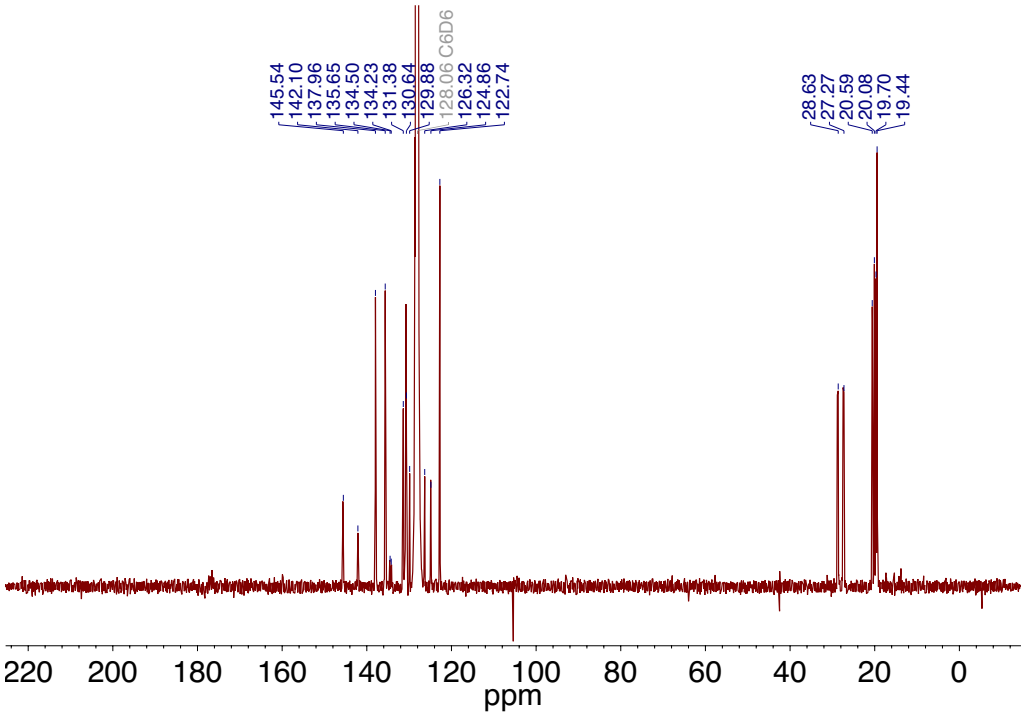

Figure 3.2.5.4. $^{13}C\{^1H\}$ NMR spectrum of **[Au(B_2P_2)]H** recorded at 126 MHz in C_6D_6.

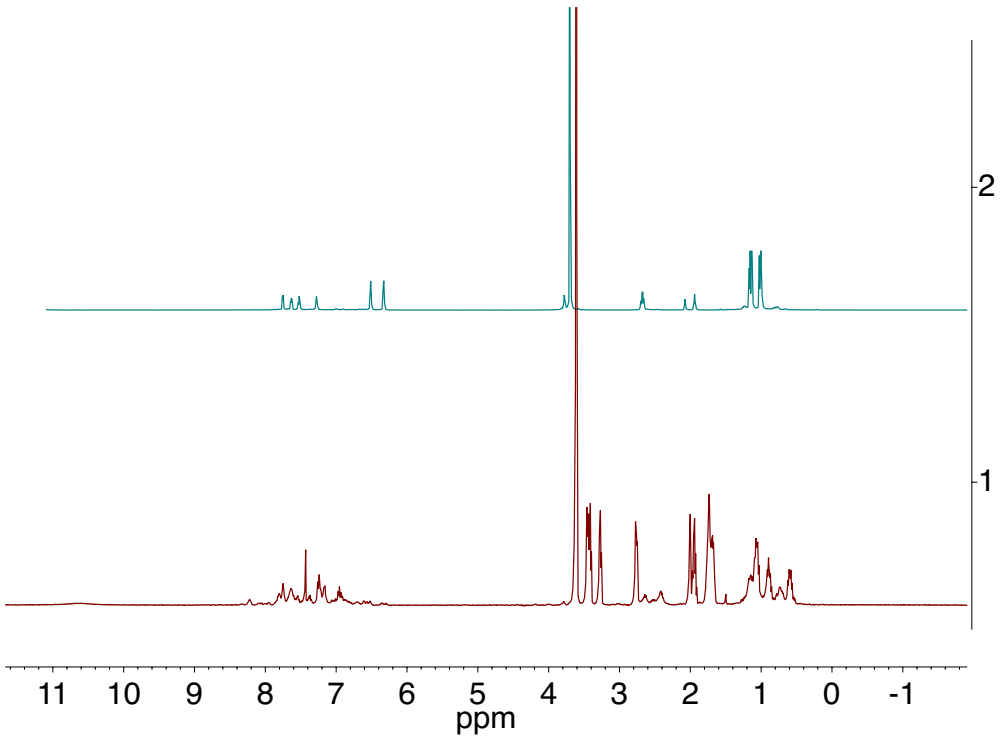

Figure 3.2.5.5. ^{1}H NMR spectra before (**cyan**) and after addition (**red**) of DBU•HCl to **[Au(B$_2$P$_2$)][K(18-c-6)]** recorded at 500 MHz in CD_3CN

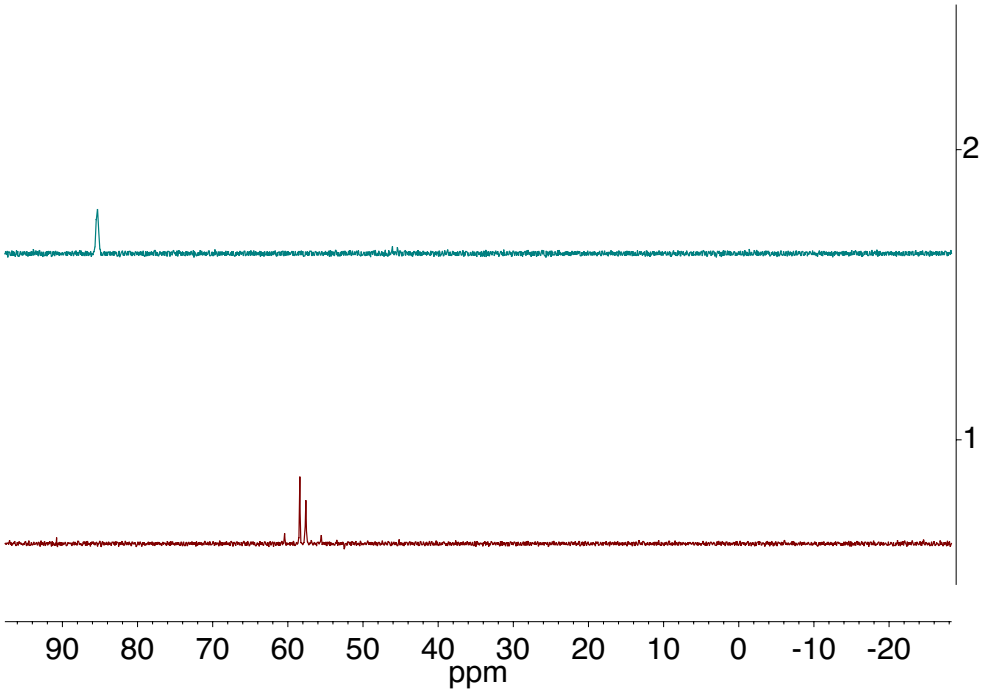

Figure 3.2.5.6. ^{31}P NMR spectra before (**cyan**) and after addition (**red**) of DBU•HCl to **[Au(B$_2$P$_2$)][K(18-c-6)]** recorded at 500 MHz in CD_3CN.

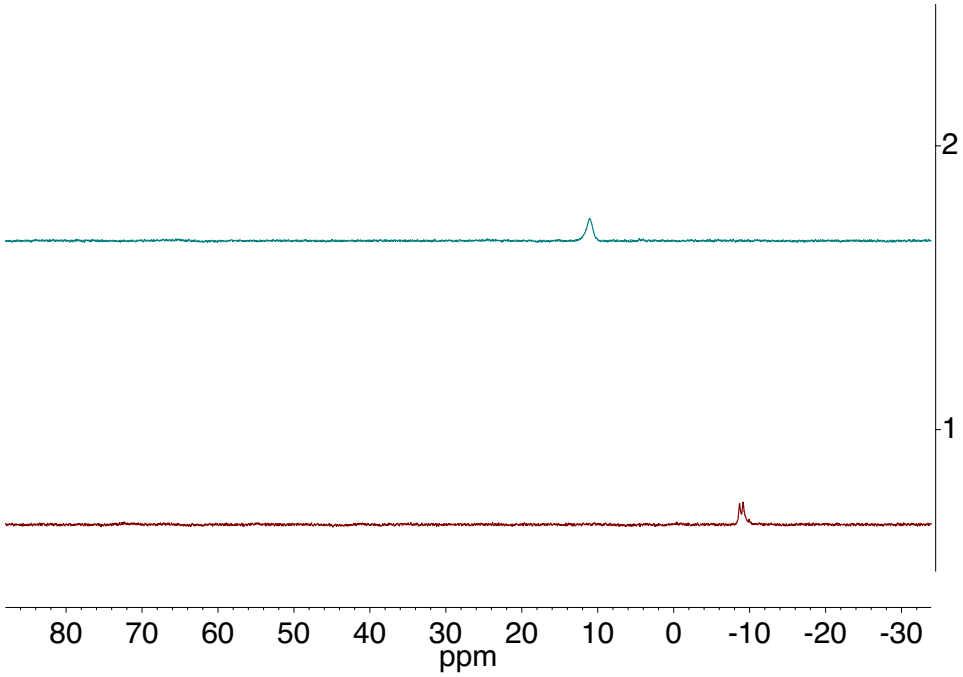

Figure 3.2.5.7. ^{11}B NMR spectra before (**cyan**) and after addition (**red**) of DBU•HCl to **[Au(B$_2$P$_2$)][K(18-c-6)]** recorded at 500 MHz in CD_3CN.

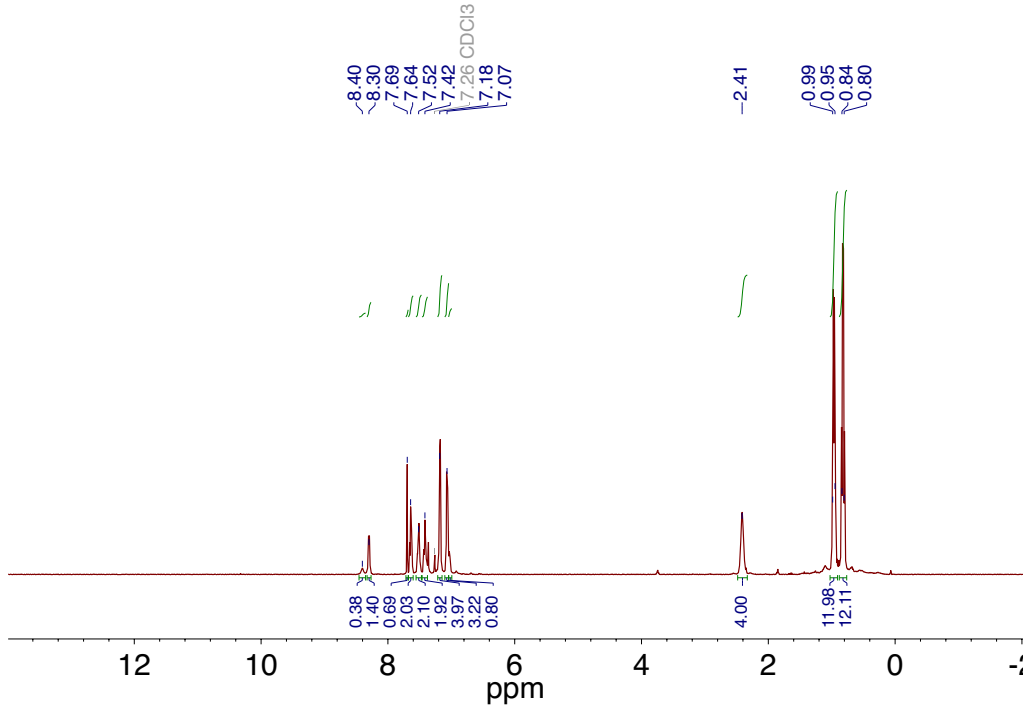

Figure 3.2.5.8. ^{1}H NMR spectrum of **[Au(B$_2$P$_2$)]CO$_2$H** recorded at 500 MHz in $CDCl_3$.

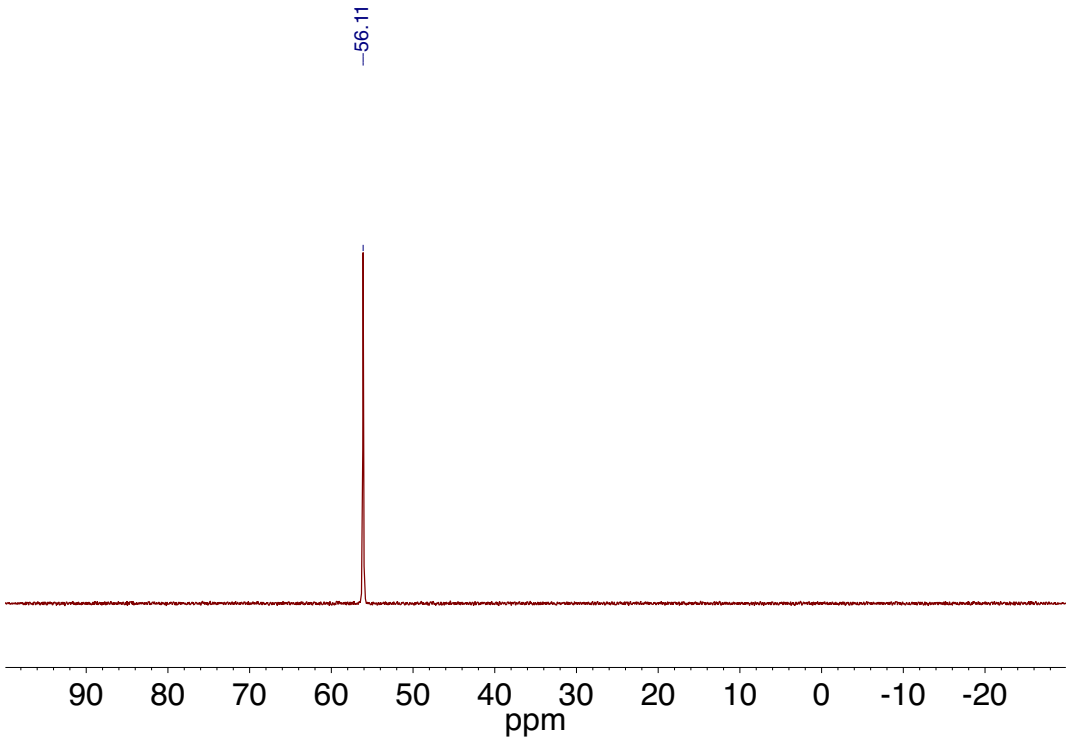

Figure 3.2.5.9. ^{31}P NMR spectrum of **[Au(B_2P_2)]CO_2H** recorded at 202 MHz in $CDCl_3$.

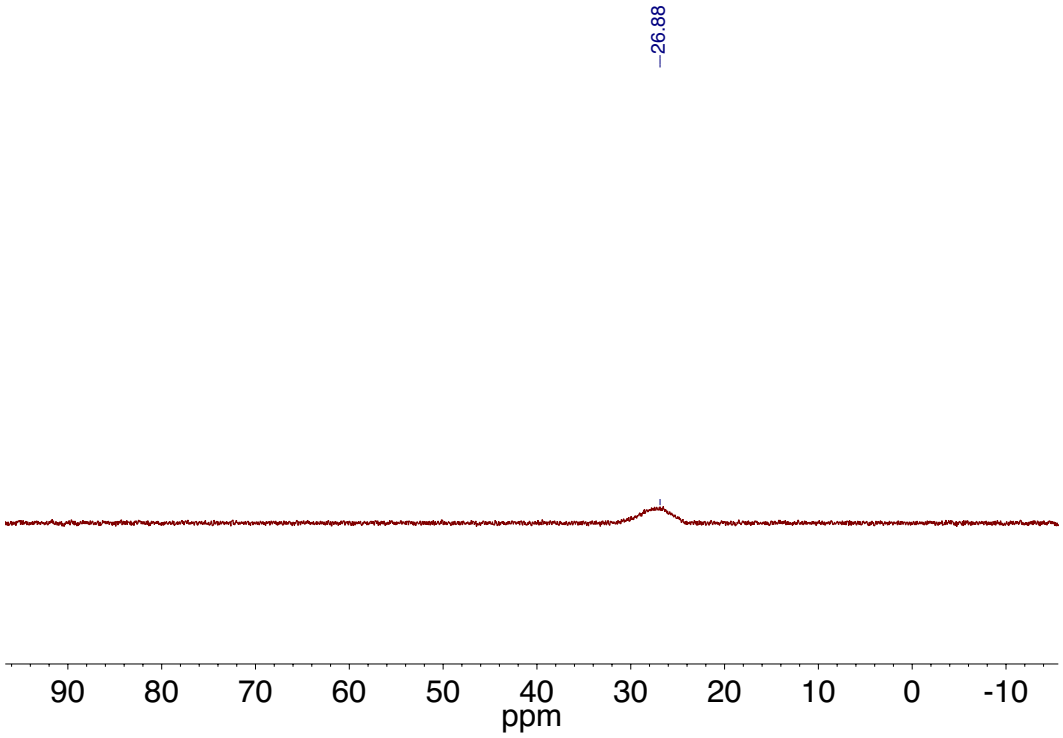

Figure 3.2.5.10. ^{11}B NMR spectrum of **[Au(B_2P_2)]CO_2H** recorded at 193 MHz in $CDCl_3$.

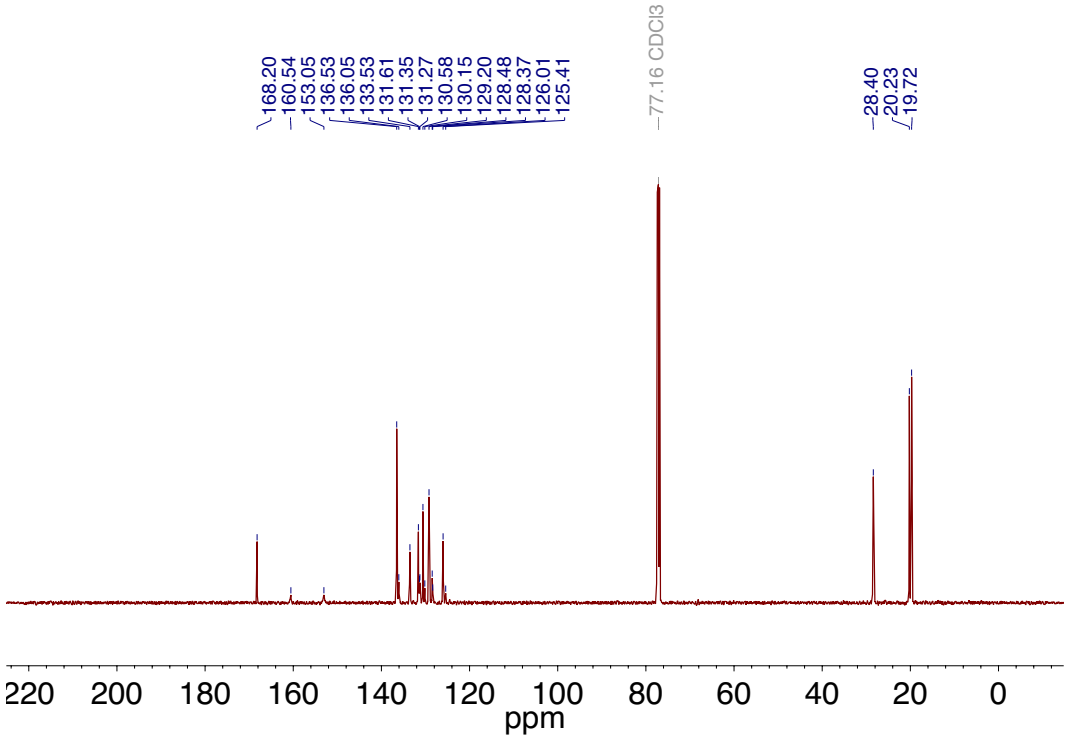

Figure 3.2.5.11. $^{13}C\{^{1}H\}$ NMR spectrum of **[Au(B_2P_2)]CO_2H** recorded at 126 MHz in $CDCl_3$.

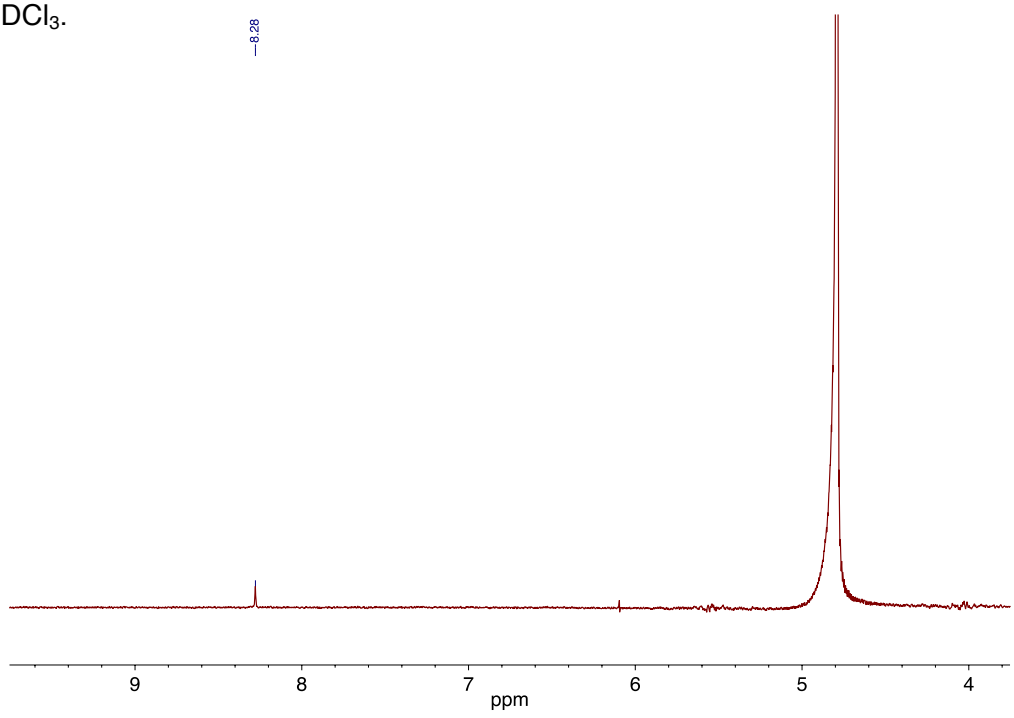

Figure 3.2.5.12. ^{1}H NMR spectrum of the filtered solid after the reaction of **[Au(B_2P_2)]CO_2H** with Na($C_{10}H_8$) recorded at 500 MHz in D_2O.

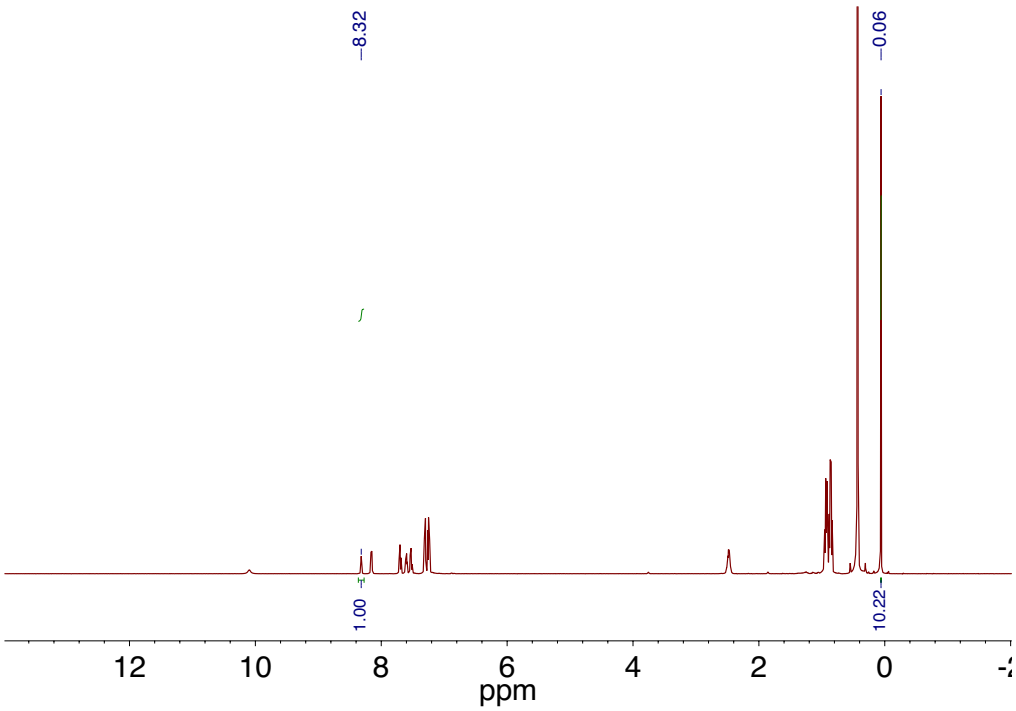

Figure 3.2.5.13. ^{1}H NMR spectrum after the reaction of **[Au(B_2P_2)]CO_2H** with TMSCl recorded at 500 MHz in $CDCl_3$. Selected peaks are for TMS-OCHO**.**

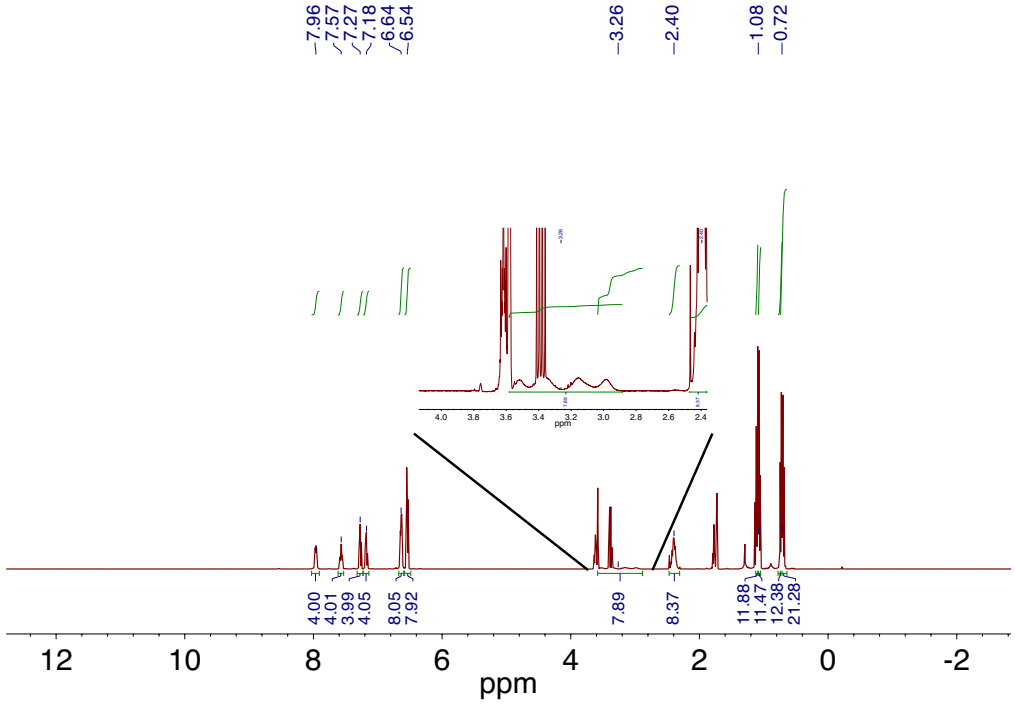

Figure 3.2.5.14. ^{1}H NMR spectrum of **[Au(B_2P_2)]$(H_2)]_2$[μ-$K_2(Et_2O)]_2$** recorded at 400 MHz in THF-d_8.

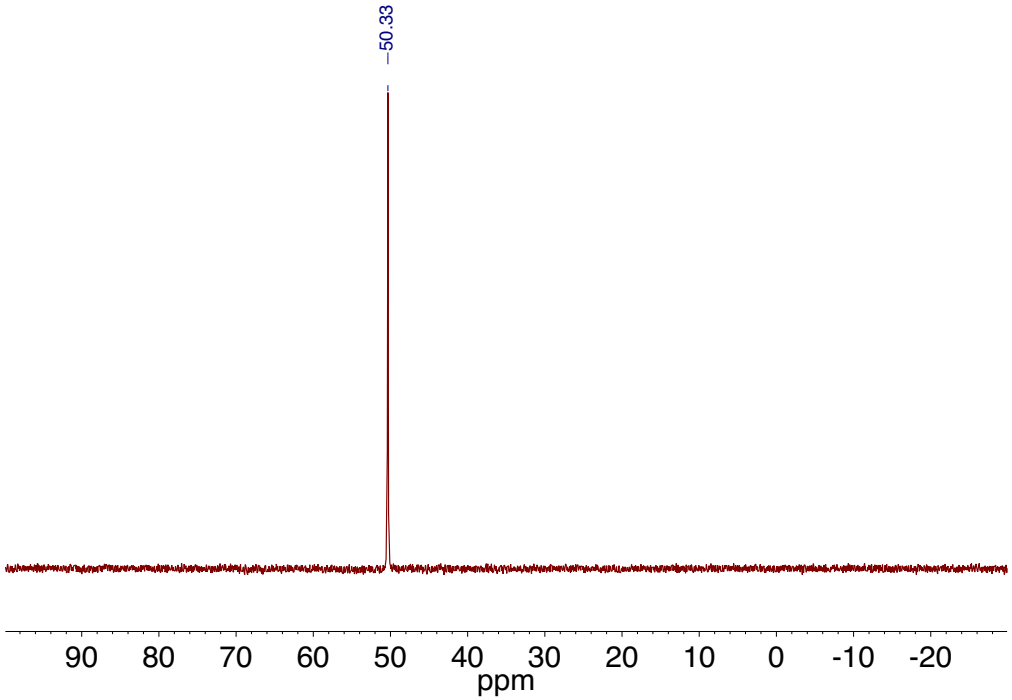

Figure 3.2.5.15. ^{31}P NMR spectrum of **[Au(B$_2$P$_2$)](H$_2$)]$_2$[μ-K$_2$(Et$_2$O)]$_2$** recorded at 162 MHz in THF-d_8.

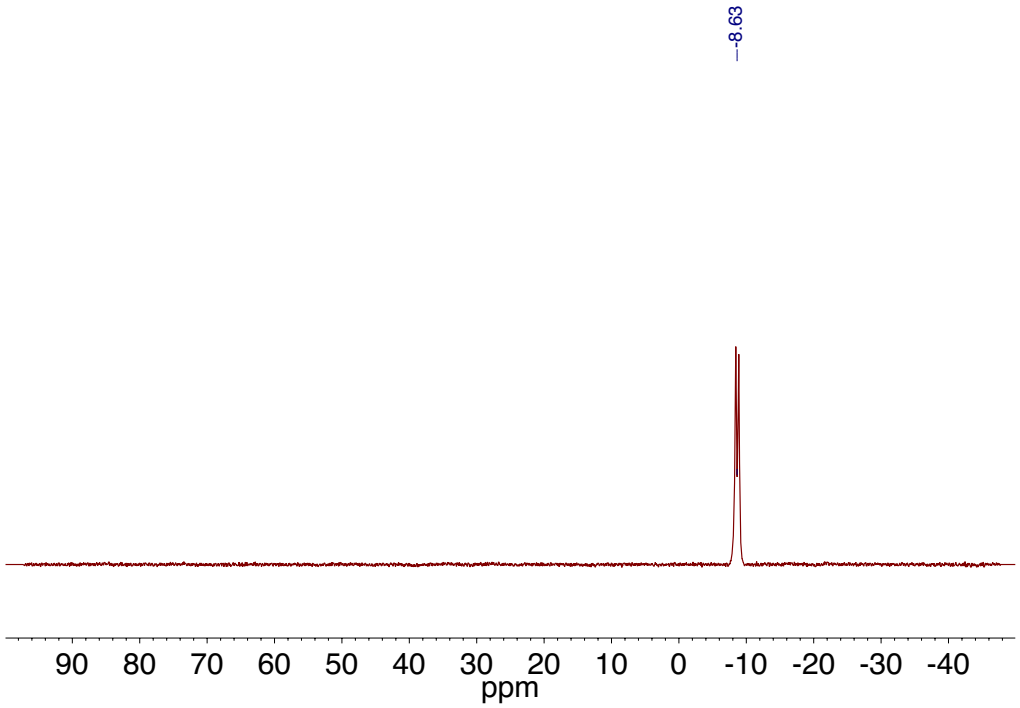

Figure 3.2.5.16. ^{11}B NMR spectrum of **[Au(B$_2$P$_2$)](H$_2$)]$_2$[μ-K$_2$(Et$_2$O)]$_2$** recorded at 128 MHz in THF-d_8.

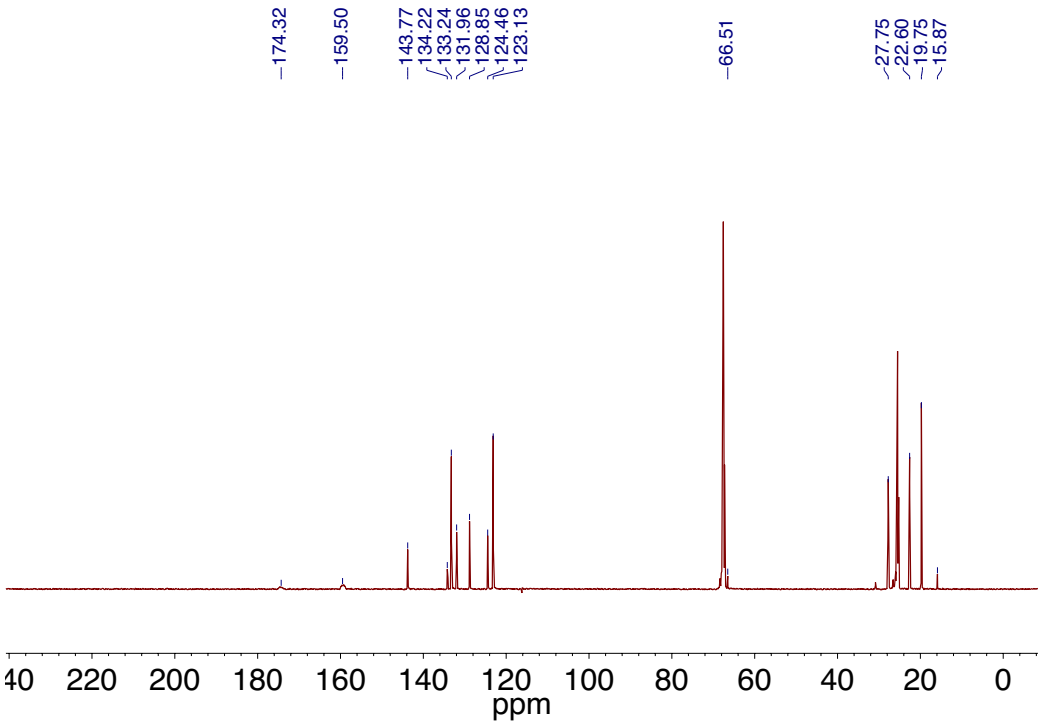

Figure 3.2.5.17. $^{13}C\{^{1}H\}$ NMR spectrum of **[Au(B$_2$P$_2$)](H$_2$)]$_2$[μ-K$_2$(Et$_2$O)]$_2$** recorded at 101 MHz in THF-d_8

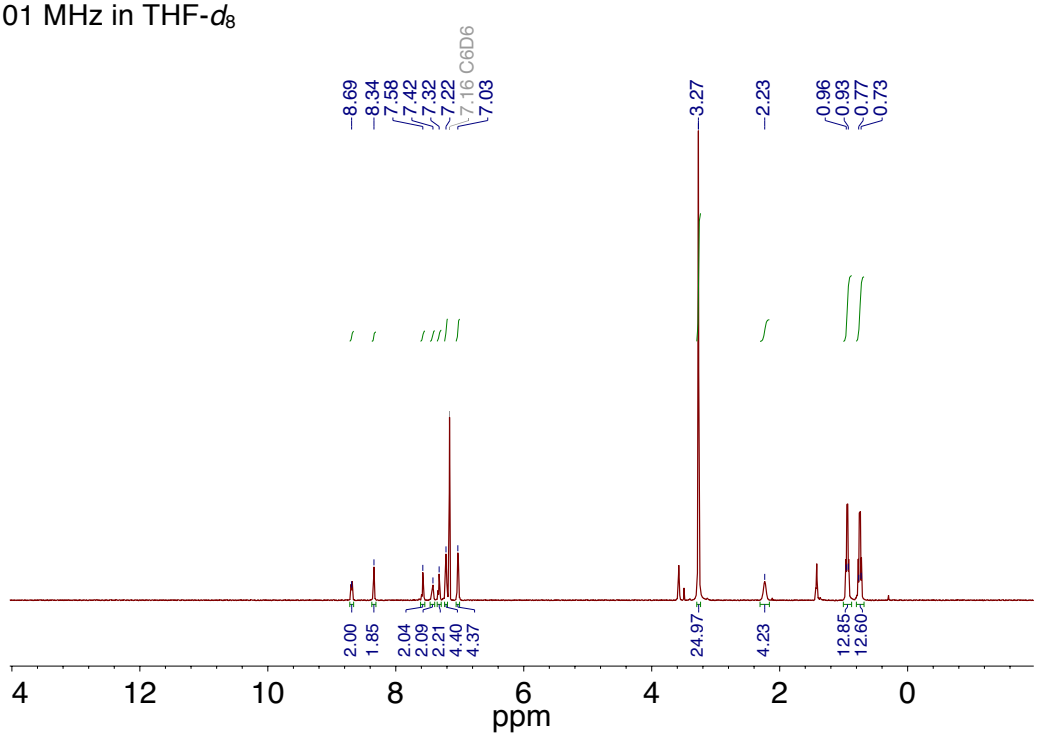

Figure 3.2.5.18. ^{1}H NMR spectrum of **[Au(B$_2$P$_2$)](CO$_2$H)$_2$][K(18-c-6)]** recorded at 500 MHz in C_6D_6.

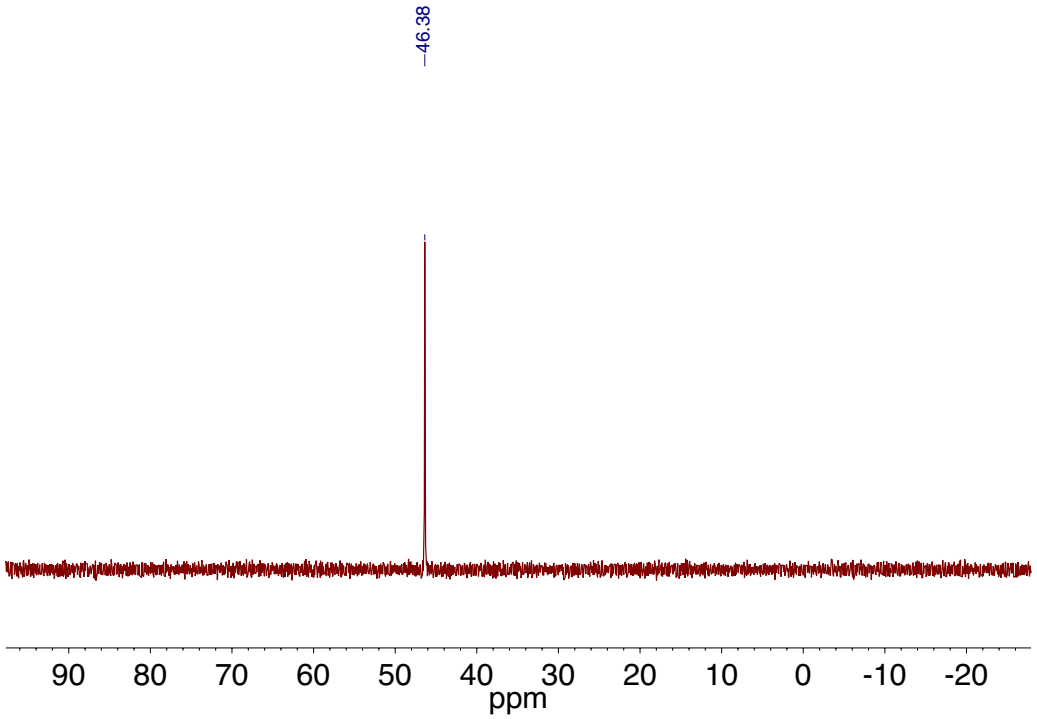

Figure 3.2.5.19. ^{31}P NMR spectrum of **[Au(B_2P_2)](CO_2H)$_2$][K(18-c-6)]** recorded at 162 MHz in C_6D_6.

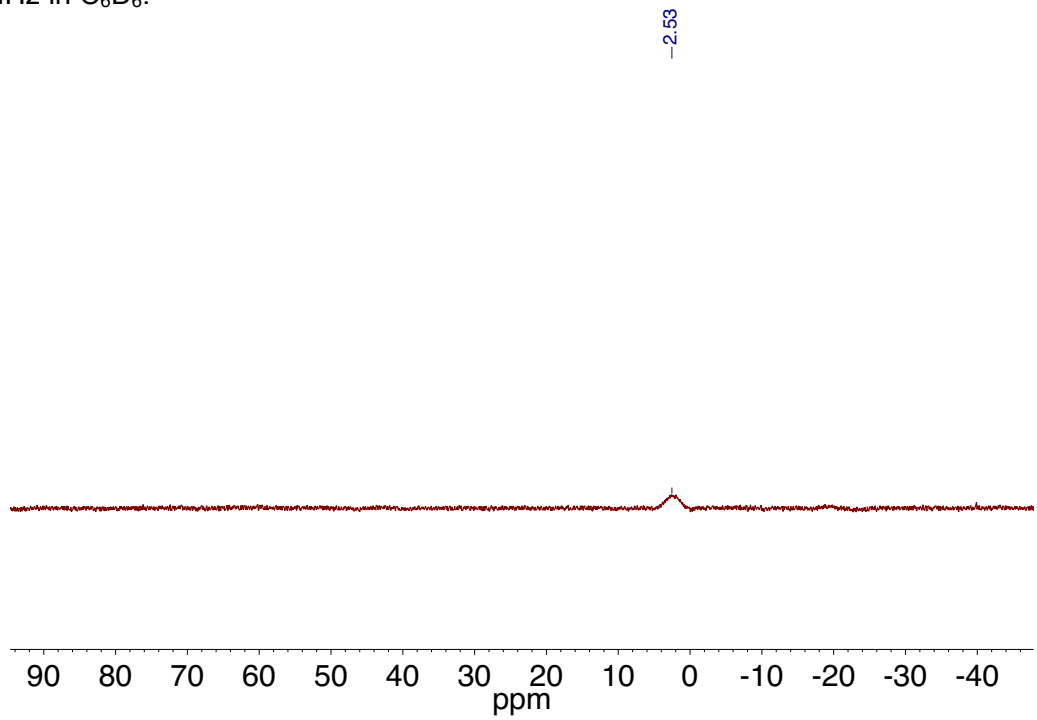

Figure 3.2.5.20. ^{11}B NMR spectrum of **[Au(B_2P_2)](CO_2H)$_2$][K(18-c-6)]** recorded at 128 MHz in C_6D_6.

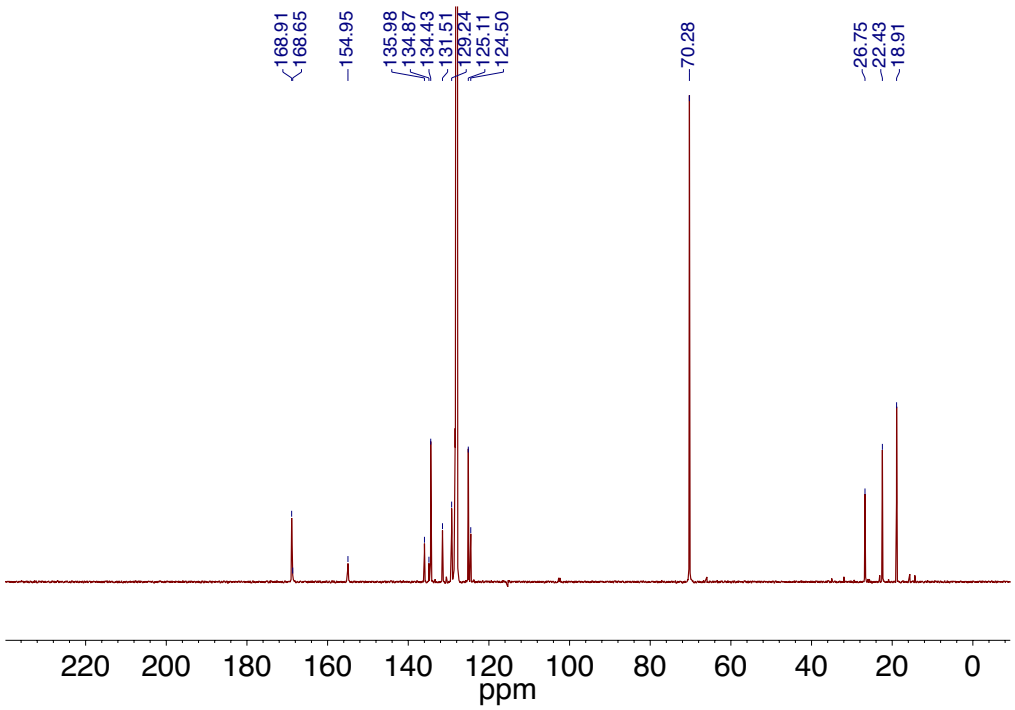

Figure 3.2.5.21. $^{13}C\{^{1}H\}$ NMR spectrum of **[Au(B_2P_2)](CO_2H)$_2$][K(18-c-6)]** recorded at 101 MHz in C_6D_6.

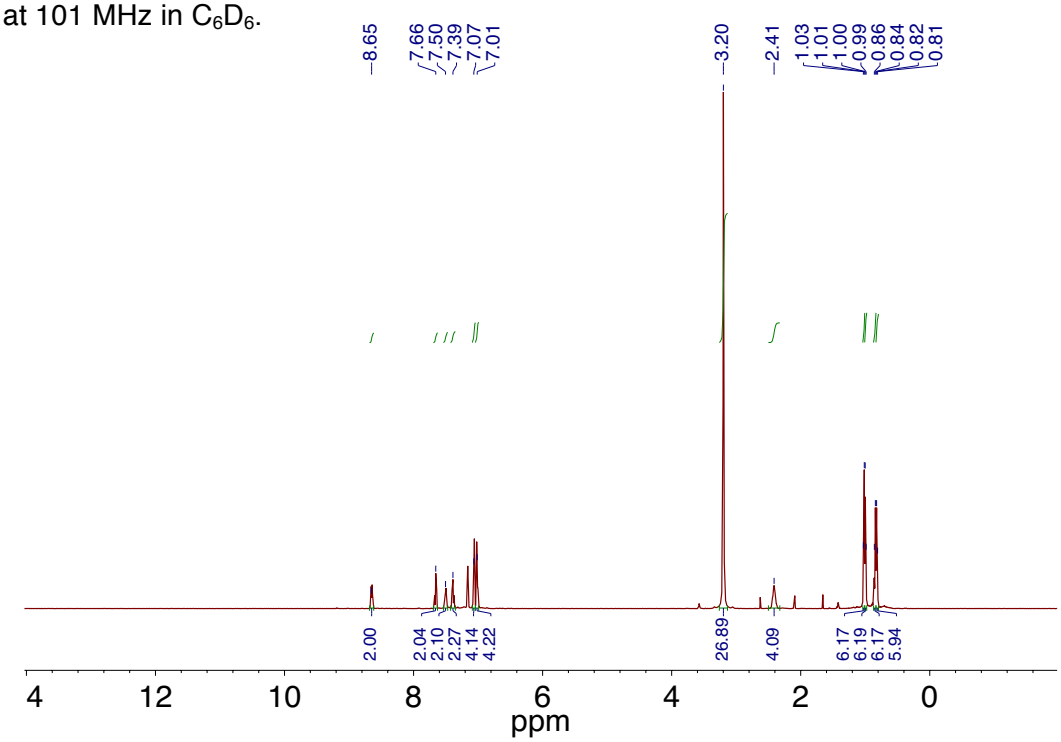

Figure 3.2.5.22. ^{1}H NMR spectrum of **[Au(B_2P_2)(CO_3)][K(18-c-6)]** recorded at 500 MHz in C_6D_6.

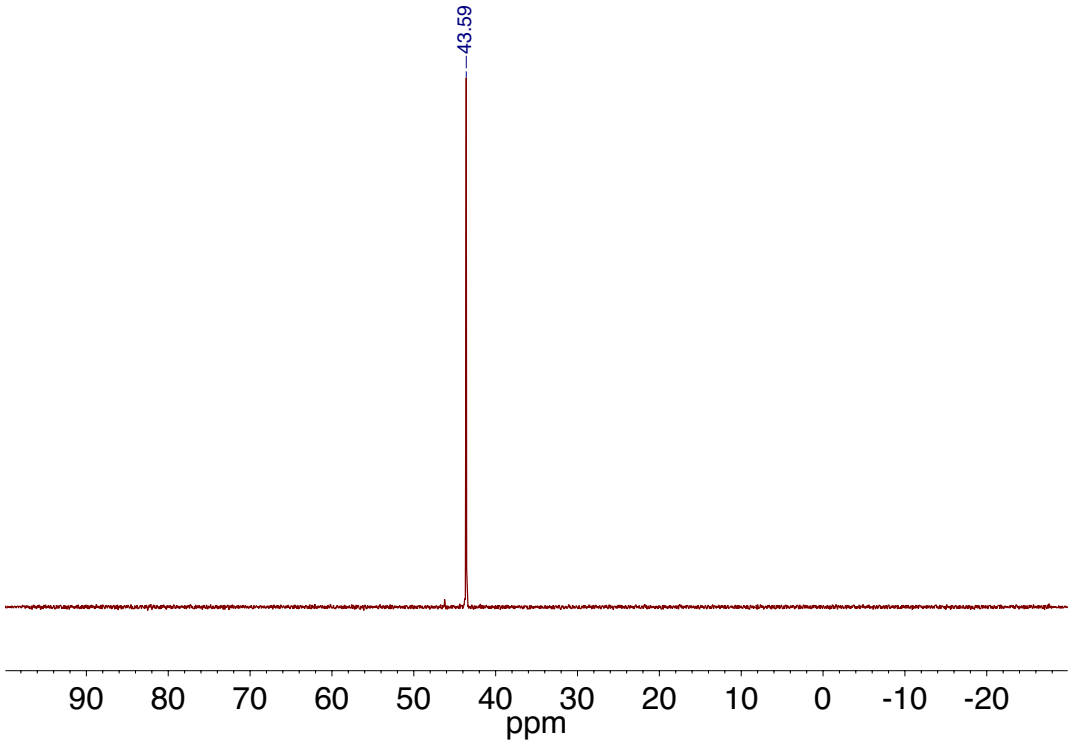

Figure 3.2.5.23. ^{31}P NMR spectrum of **[Au(B_2P_2)(CO_3)][K(18-c-6)]** recorded at 202 MHz in C_6D_6.

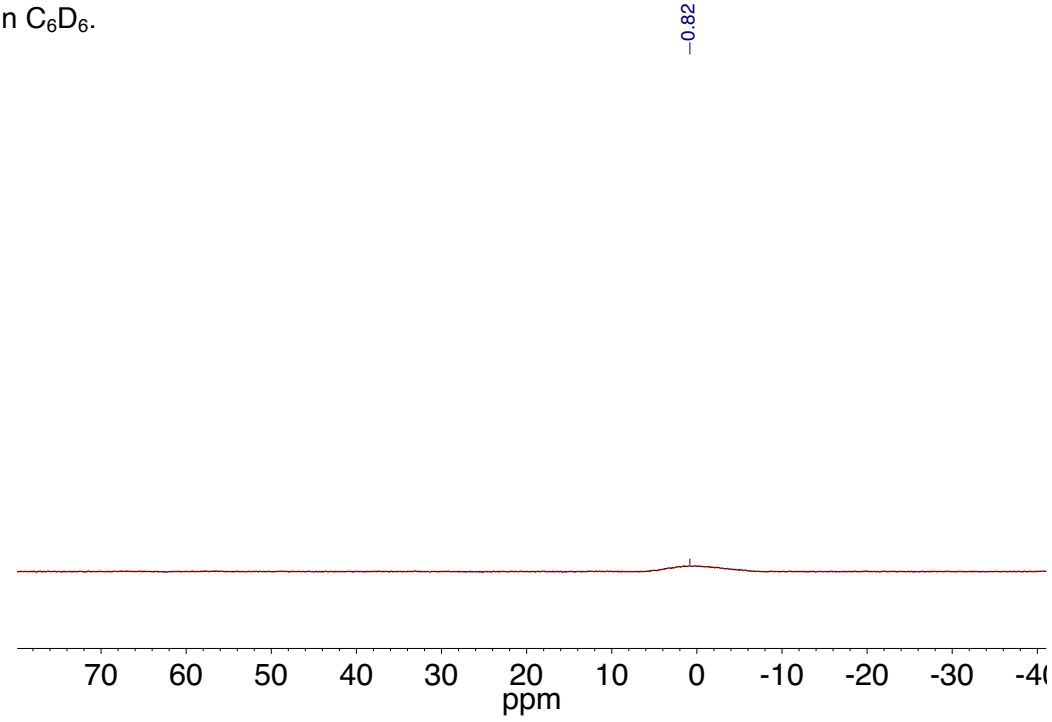

Figure 3.2.5.24. ^{11}B NMR spectrum of **[Au(B_2P_2)(CO_3)][K(18-c-6)]** recorded at 242 MHz in C_6D_6.

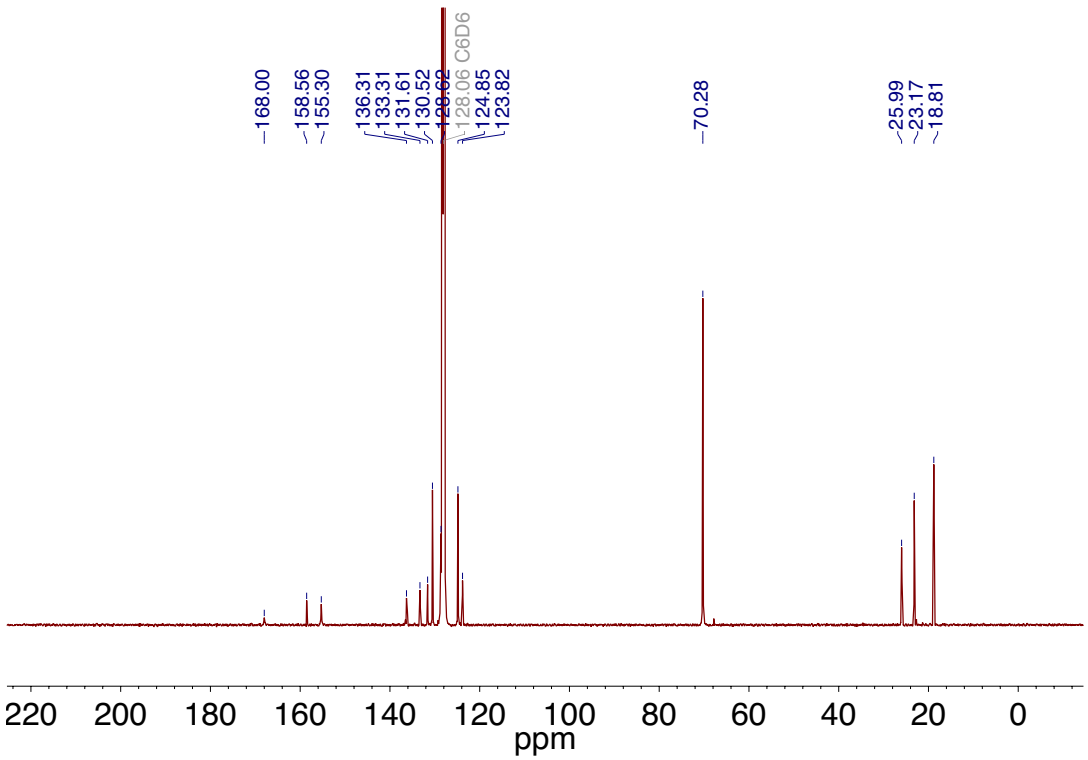

Figure 3.2.5.25. $^{13}C\{^{1}H\}$ NMR spectrum of **[Au(B_2P_2)(CO_3)][K(18-c-6)]** recorded at 126 MHz in C_6D_6.

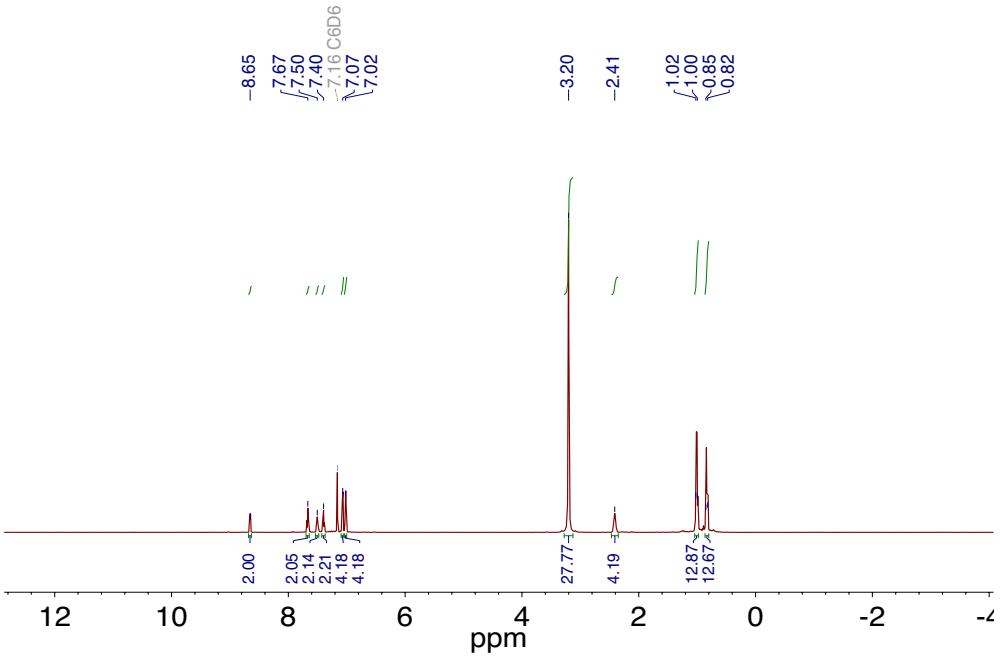

Figure 3.2.5.26. ^{1}H NMR spectrum of **[Au(B_2P_2)($^{13}CO_3$)][K(18-c-6)]**recorded at 500 MHz in C_6D_6.

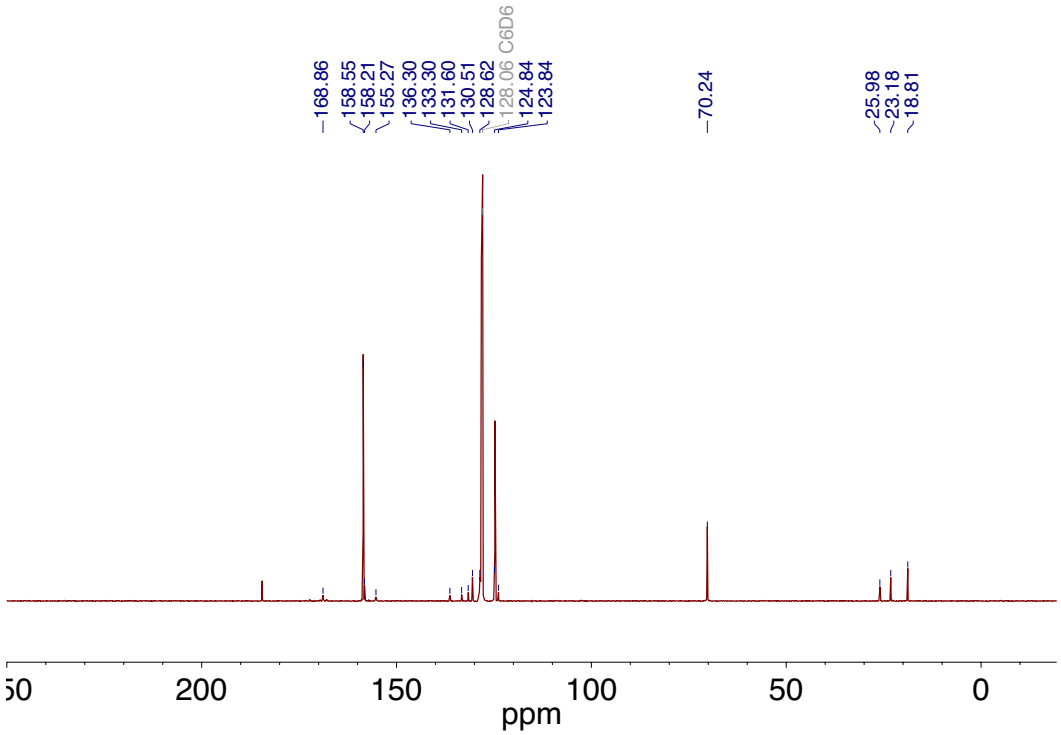

Figure 3.2.5.27. $^{13}C\{^{1}H\}$ NMR spectrum of **[Au(B_2P_2)($^{13}CO_3$)][K(18c6)]** recorded at 126 MHz in C_6D_6.

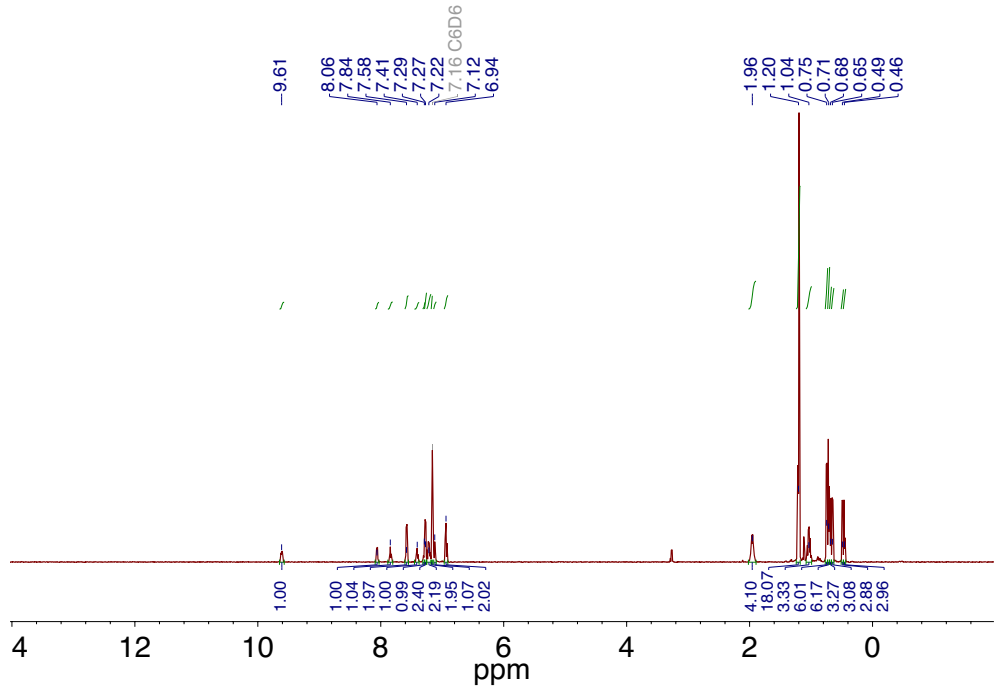

Figure 3.2.5.28. ^{1}H NMR spectrum of **[Au(B_2P_2)](O(Si(^{i}Pr)$_3$)** recorded at 500 MHz in C_6D_6.

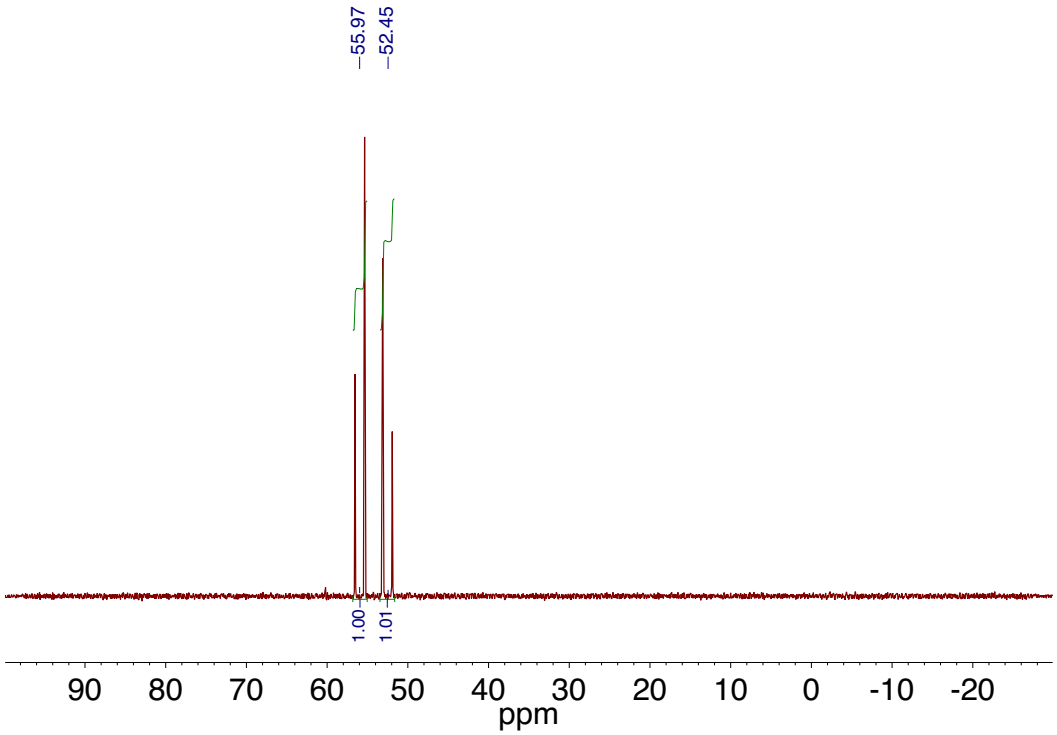

Figure 3.2.5.29. ^{31}P NMR spectrum of **[Au(B$_2$P$_2$)](O(Si(^{i}Pr)$_3$)** recorded at 202 MHz in C_6D_6.

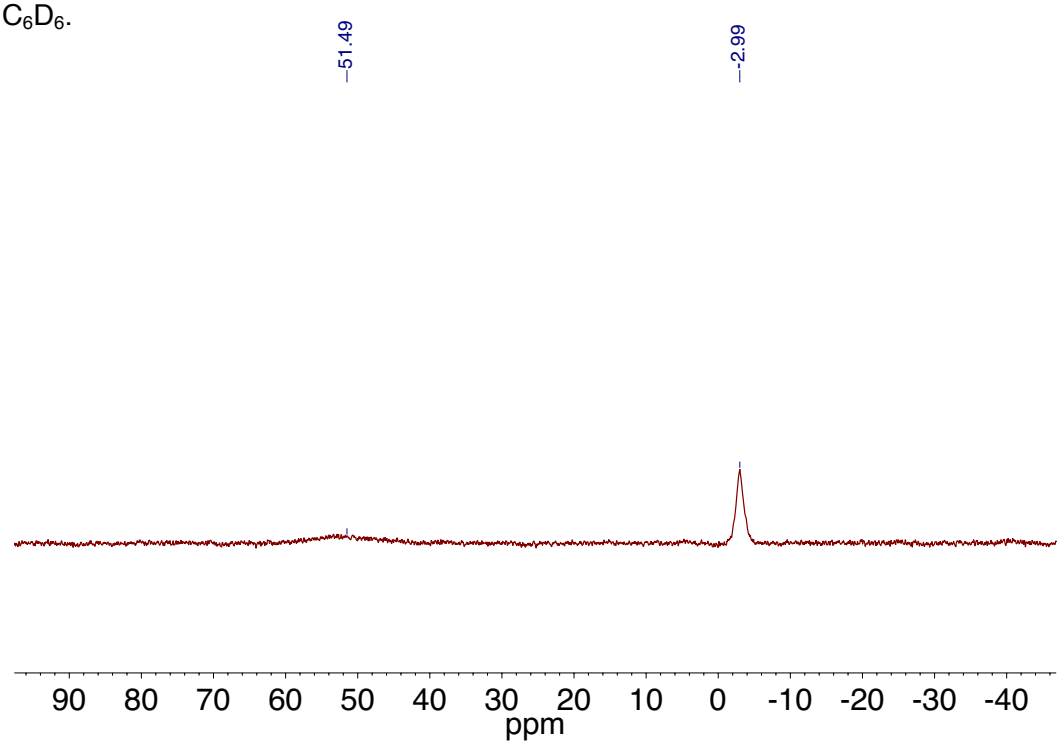

Figure 3.2.5.30. ^{11}B NMR spectrum of **[Au(B$_2$P$_2$)](O(Si(^{i}Pr)$_3$)** recorded at 160 MHz in C_6D_6.

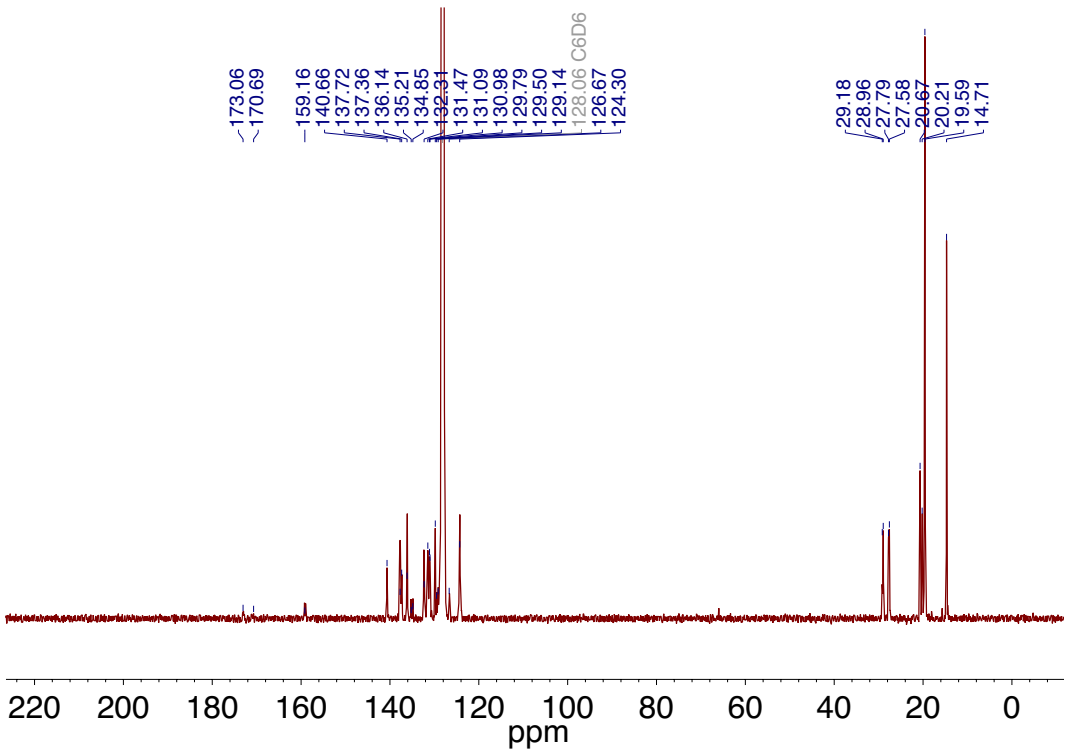

Figure 3.2.5.31. $^{13}C\{^{1}H\}$ NMR spectrum of **[Au(B_2P_2)](O(Si(^{i}Pr)$_3$)** recorded at 126 MHz in C_6D_6

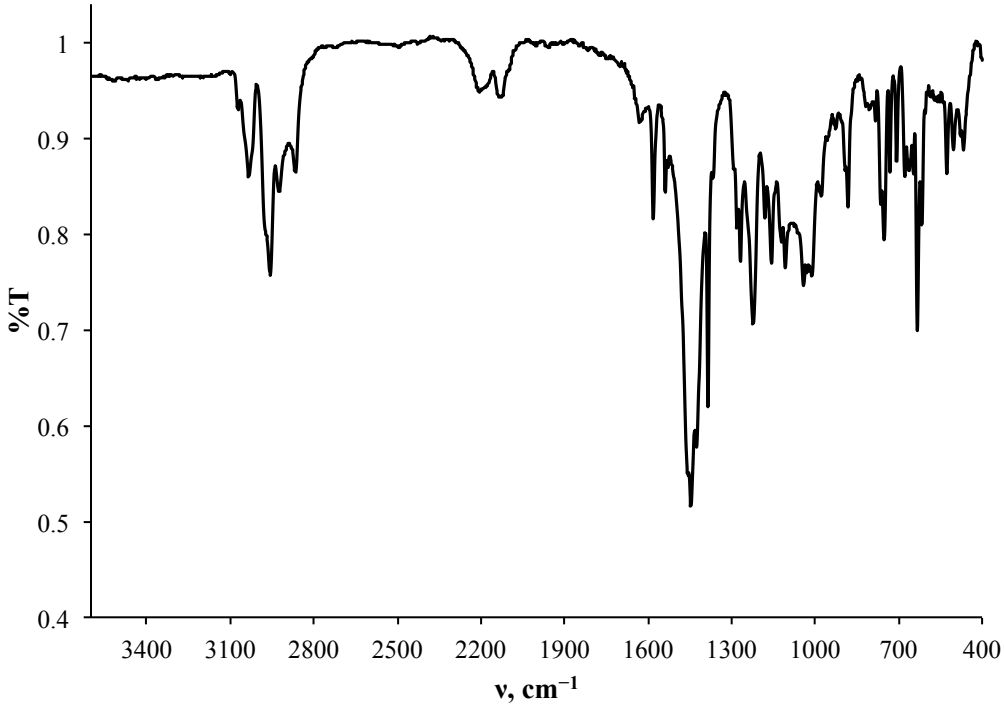

Figure 3.2.5.32. FT-IR spectrum of **[Au(B_2P_2)]H**.

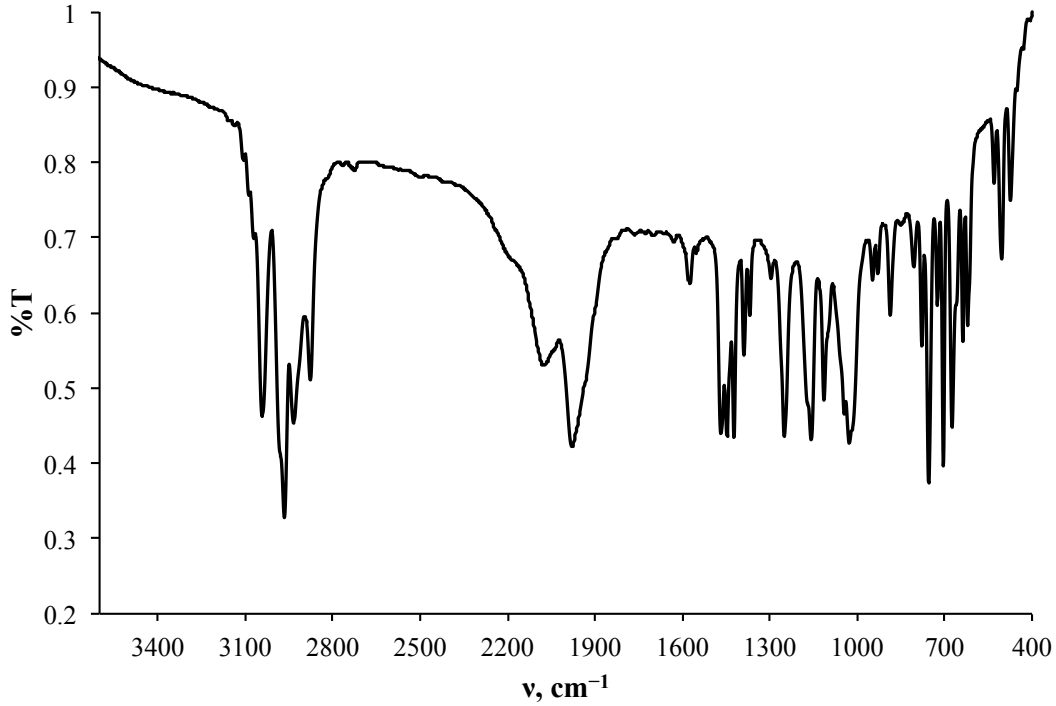

Figure 3.2.5.33. FT-IR spectrum of **[Au(B_2P_2)](H_2)]$_2$[μ-K_2(Et_2O)]$_2$**.

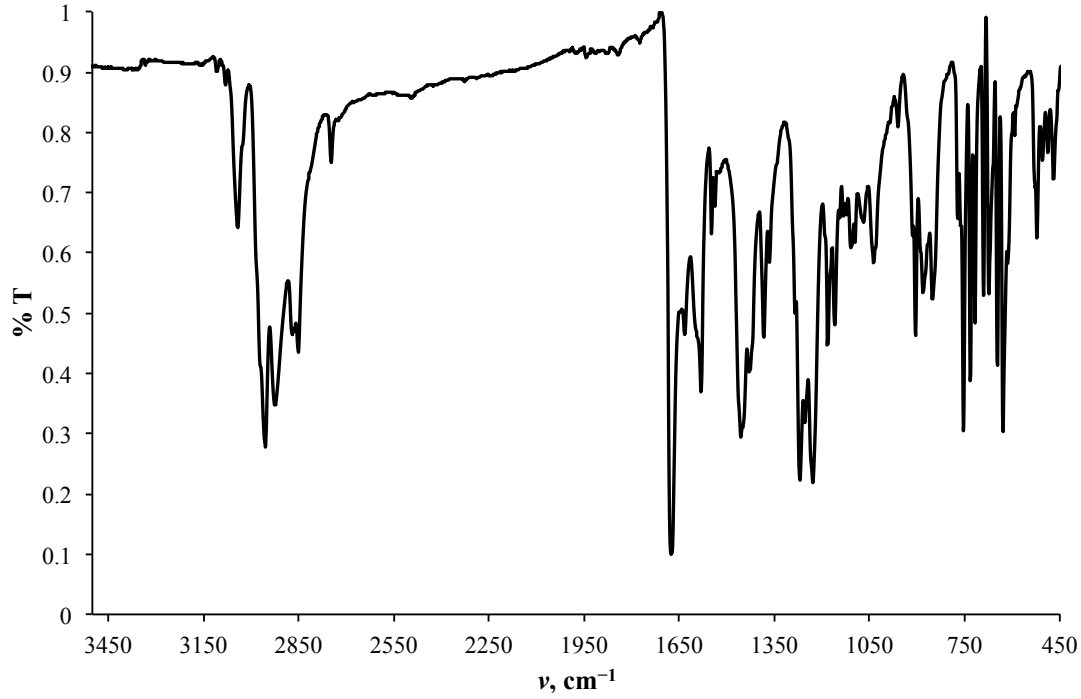

Figure 3.2.5.34. FT-IR spectrum of **[Au(B_2P_2)](CO_2H).**

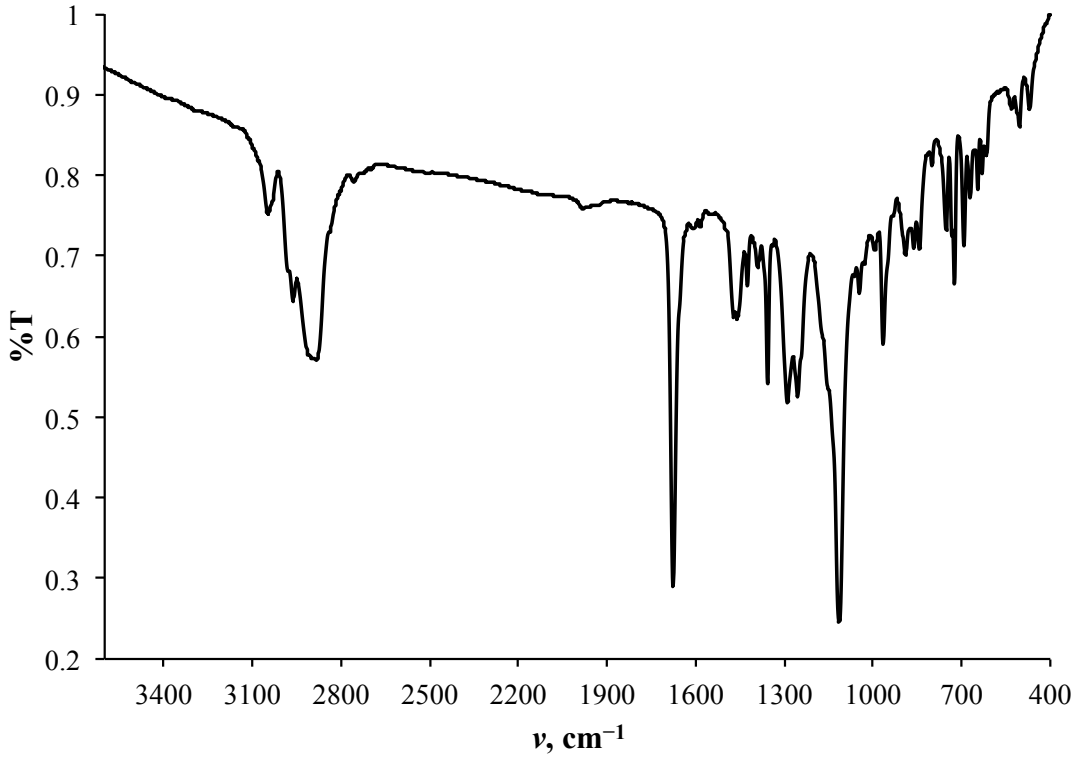

Figure 3.2.5.35. FT-IR spectrum of **[Au(B_2P_2)]($CO_2H)_2$][K(18-c-6)].**

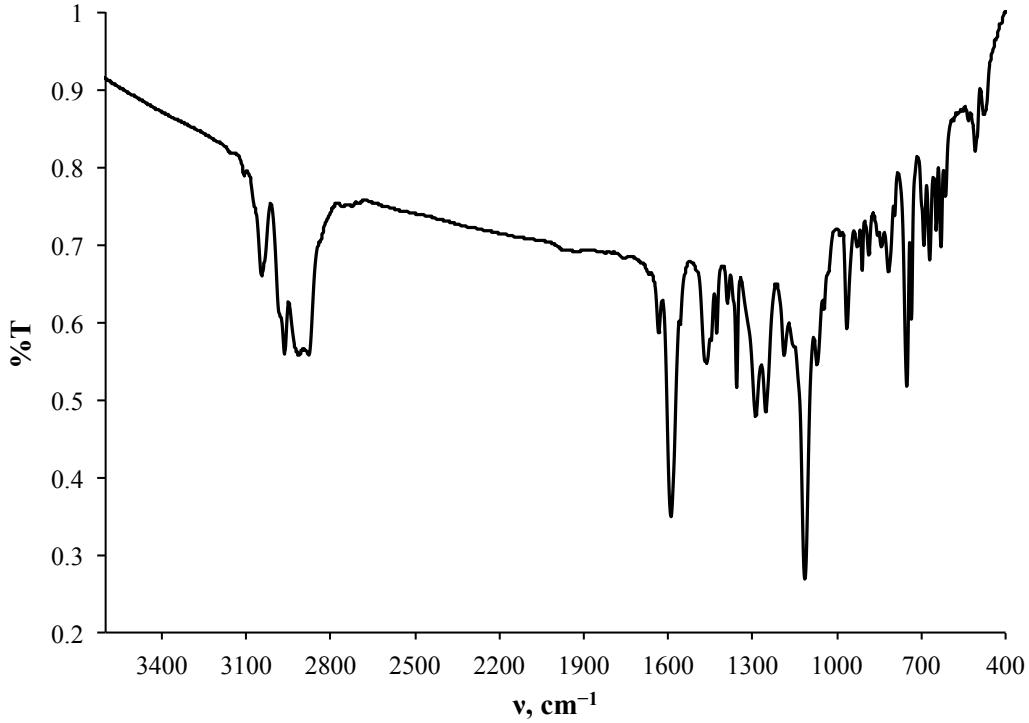

Figure 3.2.5.36. FT-IR spectrum of **[Au(B_2P_2)(CO_3)][K(18c6)].**

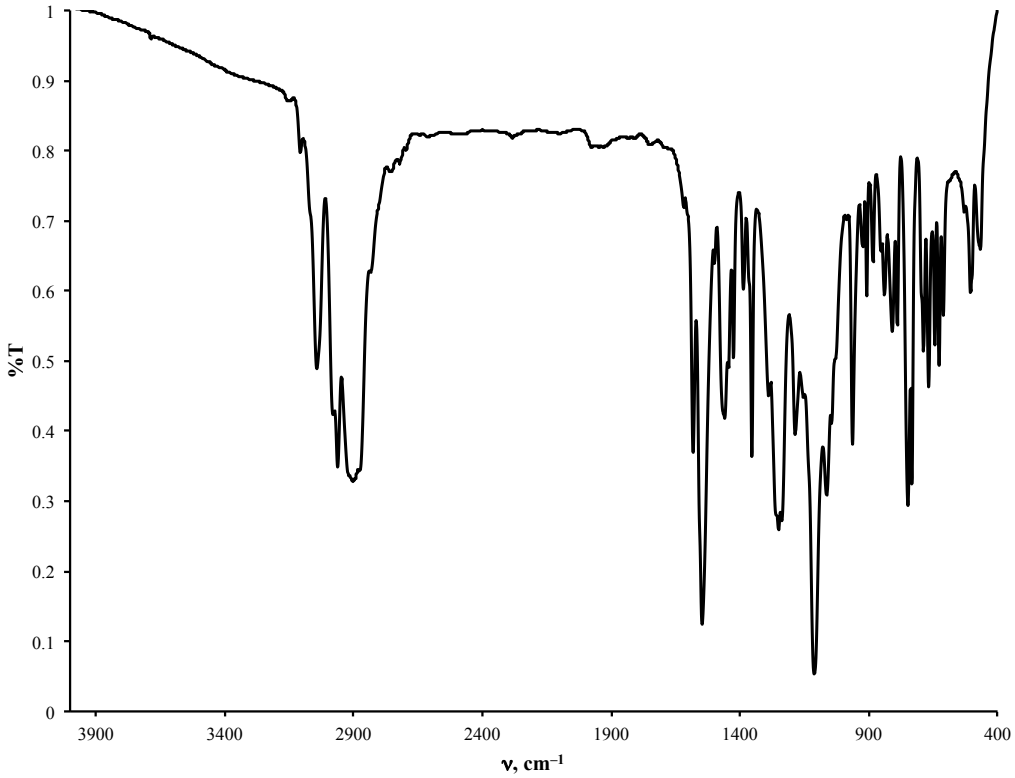

Figure 3.2.5.37. FT-IR spectrum of **[Au(B_2P_2)($^{13}CO_3$)][K(18c6)].**

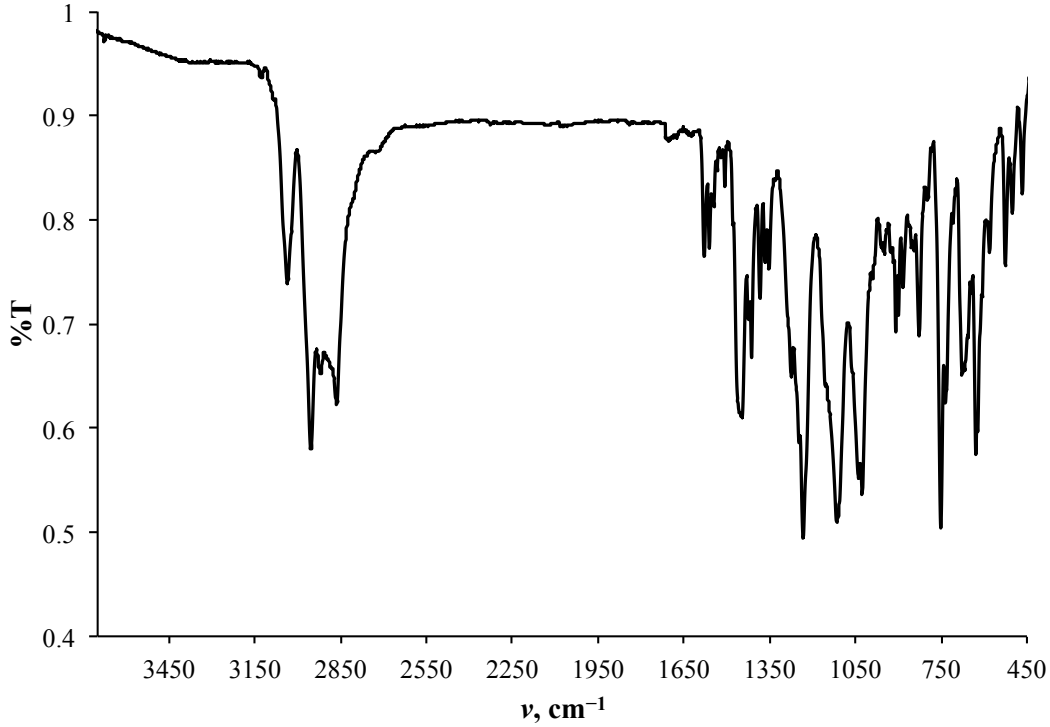

Figure 3.2.5.38. FT-IR spectrum of **[Au(B_2P_2)](O(Si(^{i}Pr)$_3$)).**

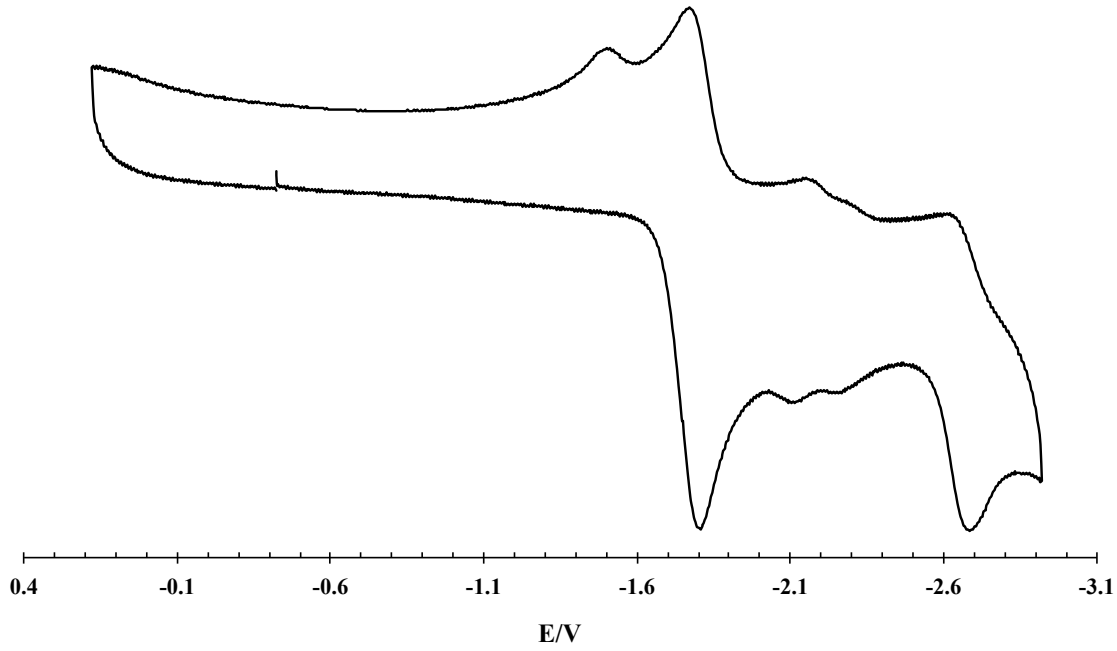

Figure 3.2.6.1. Cyclic voltammogram of **[Au(B_2P_2)](CO_2H)** in MeCN (0.1 M $n$$Bu_4NPF_6$ as electrolyte, scan rate 100 mV/s, potential vs. Fc^+/Fc) scanning cathodically to –2.8 V.

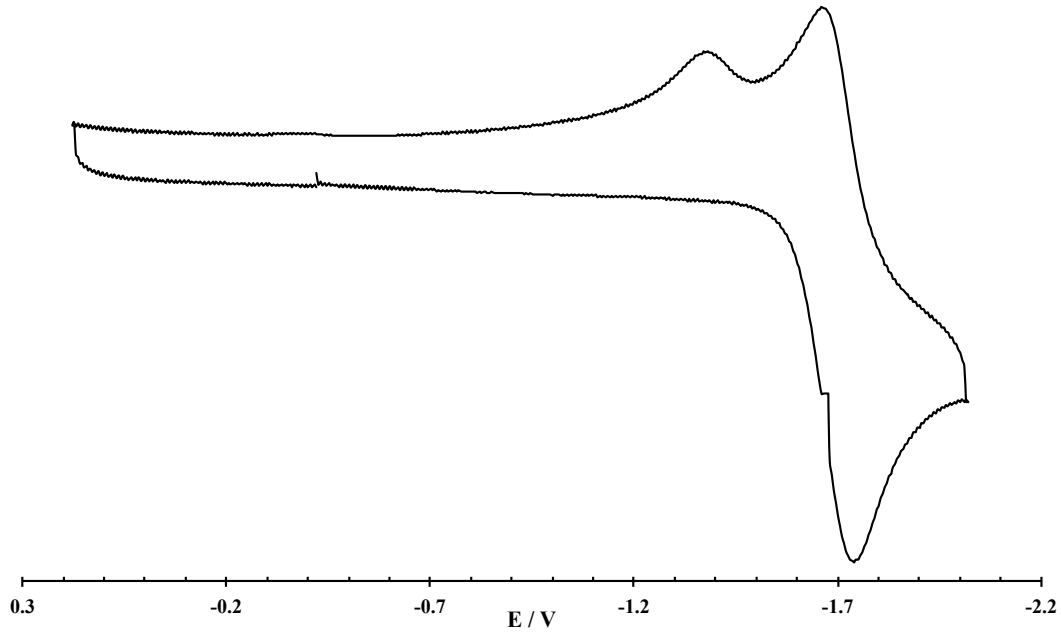

Figure 3.2.6.2. Cyclic voltammogram of **[Au(B_2P_2)](CO_2H)** in MeCN (0.1 M $n$$Bu_4NPF_6$ as electrolyte, scan rate 100 mV/s, potential vs. Fc^+/Fc) scanning cathodically to –2.0 V.

3.2.6) Cyclic Voltammetry

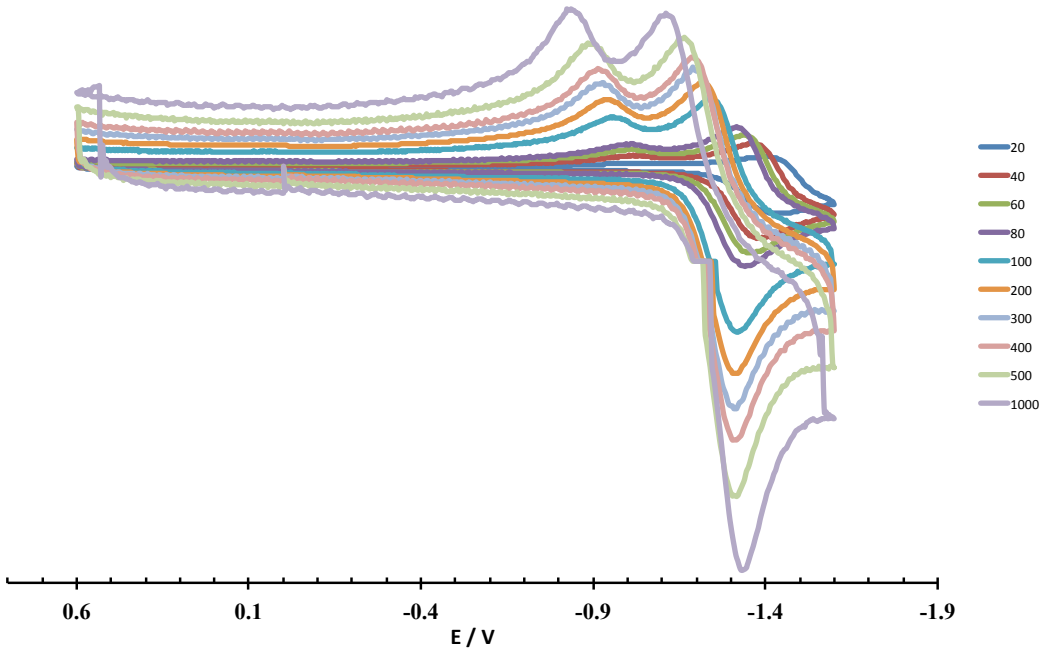

Figure 3.2.6.3. Cyclic voltammograms of **[Au(B_2P_2)](CO_2H)** in MeCN collected at variable scan rates (labeled in key, units of mV/s, 0.1 M *n*Bu_4NPF_6 as electrolyte).

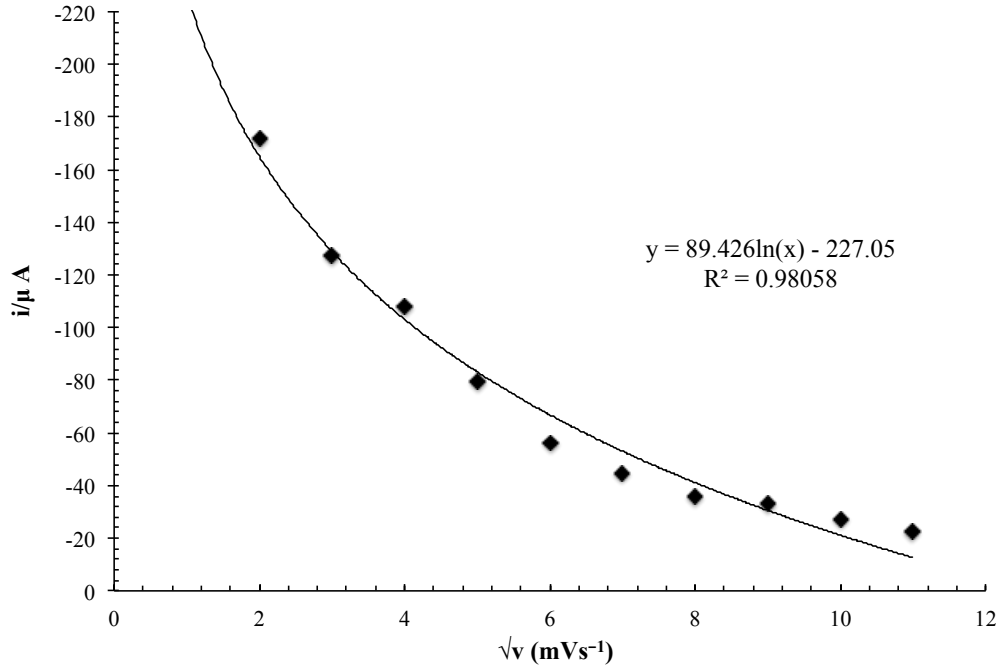

Figure 3.2.6.4. Plot of peak current vs. square root of scan rate for the cathodic peak corresponding to **[Au(B_2P_2)](CO_2H)^0/[Au(B_2P_2)](CO_2H)$^{-1}$** at ca. −1.79 V.

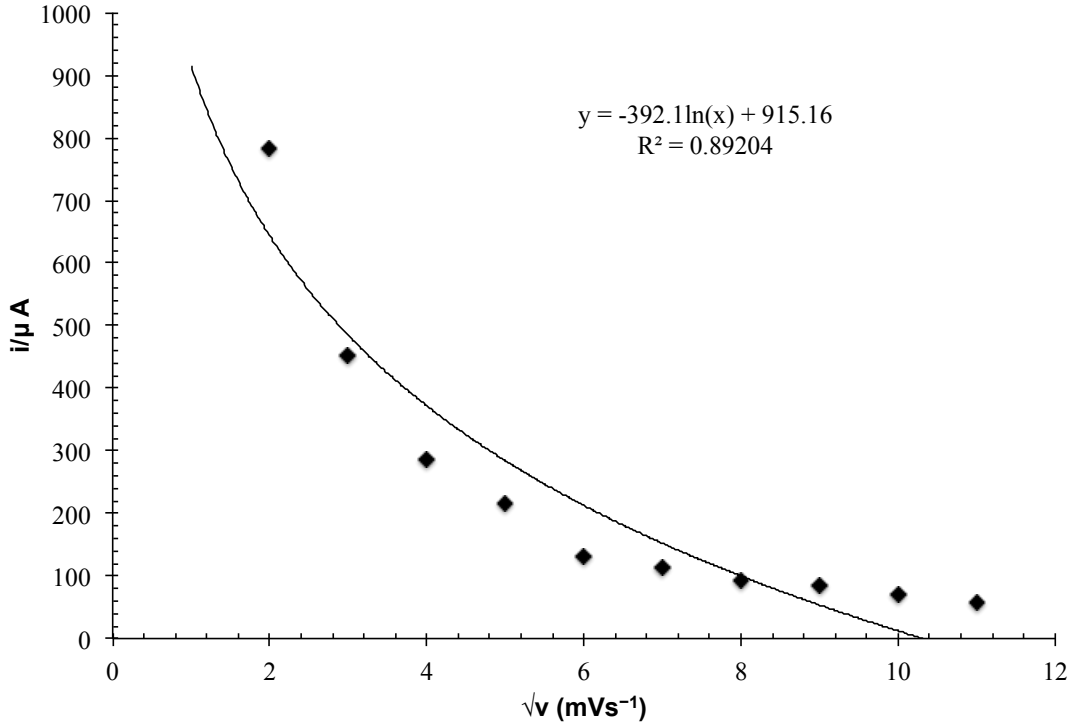

Figure 3.2.6.5. Plot of peak current vs. square root of scan rate for the anodic peak corresponding to $\mathbf{[Au(B_2P_2)](CO_2H)^{-1}/[Au(B_2P_2)](CO_2H)^0}$ at ca. –1.79 V.

3.2.7) X-Ray Crystallography

3.2.7.1.) General Considerations

Single crystals were coated with paratone oil and mounted on cryo-loop glass fibers. X-ray intensity data were collected at 100(2) K on a Bruker APEX2[31] platform-CCD X-ray diffractometer system using fine-focus Mo K_α radiation (λ = 0.71073 Å, 50kV/30mA power). The CCD detector was placed at 5.0600 cm from the crystal. Frames were integrated using the Bruker SAINT software package[32] and using a narrow-frame integration algorithm. Absorption corrections were applied to the raw intensity data using the SADABS program.[33] The Bruker

SHELXTL software package[34] was used for phase determination and structure refinement. Atomic coordinates, isotropic and anisotropic displacement parameters of all the non-hydrogen atoms were refined by means of a full matrix least-squares procedure on F^2. The H-atoms were included in the refinement in calculated positions riding on the atoms to which they were attached. Relevant details for individual data collections are reported in Tables 3.2.7.1–3.2.7.6.

Figure 3.2.7.1. Labelled thermal ellipsoid plot (50%) for **[Au(B_2P_2)]H**

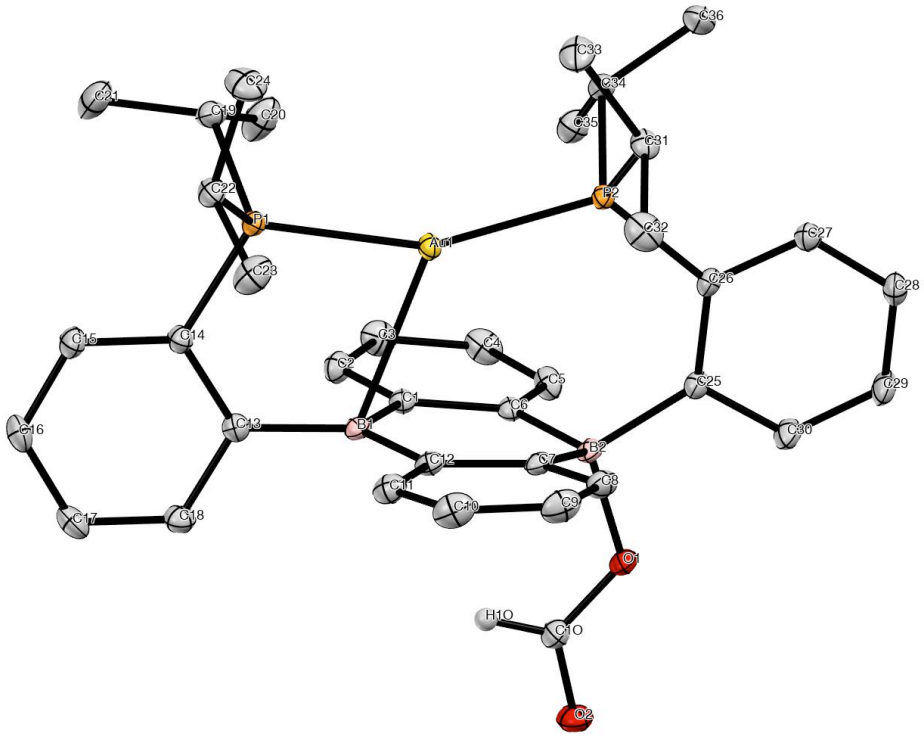

Figure 3.2.7.2. Labelled thermal ellipsoid plot (50%) for **[Au(B_2P_2)](CO_2H)**.

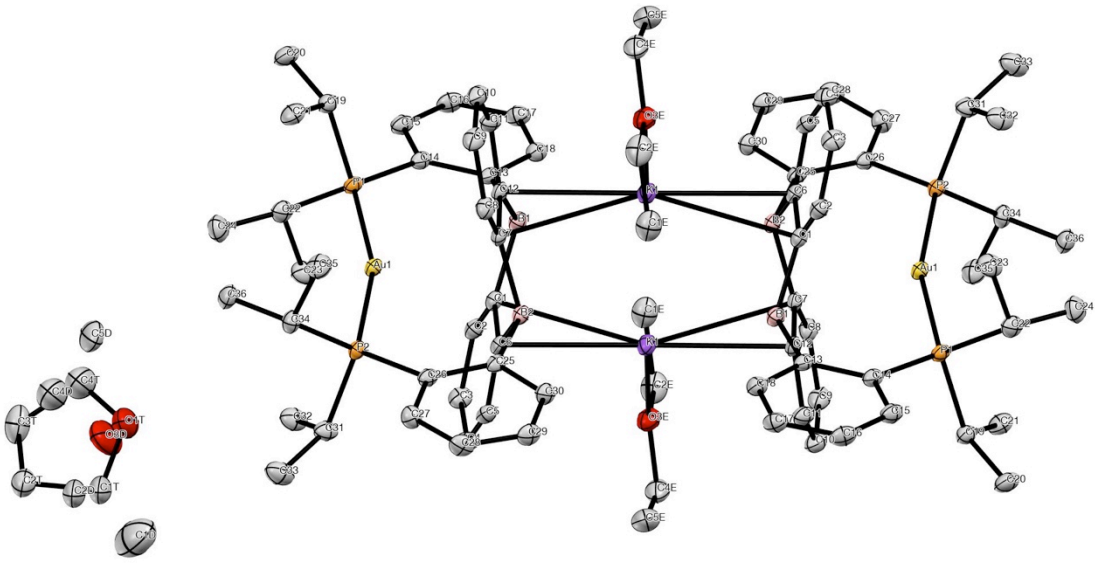

Figure 3.2.7.3. Labelled thermal ellipsoid plot (50%) for **[Au(B_2P_2)](H_2)]$_2$[μ-K_2(Et_2O)]$_2$**.

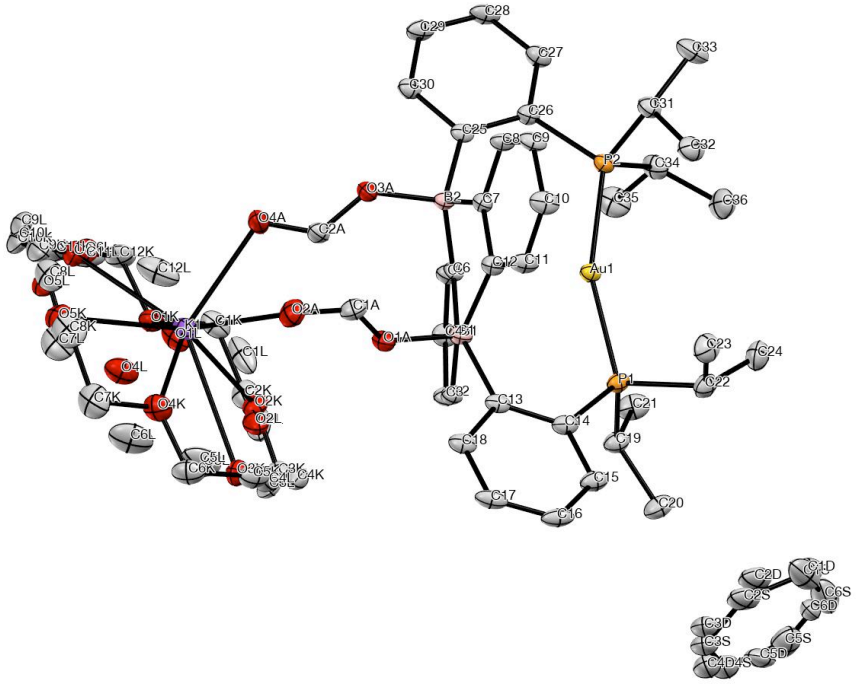

Figure 3.2.7.4. Labelled thermal ellipsoid plot (50%) for **[Au(B_2P_2)](CO_2H)$_2$][K(18-c-6)]**.

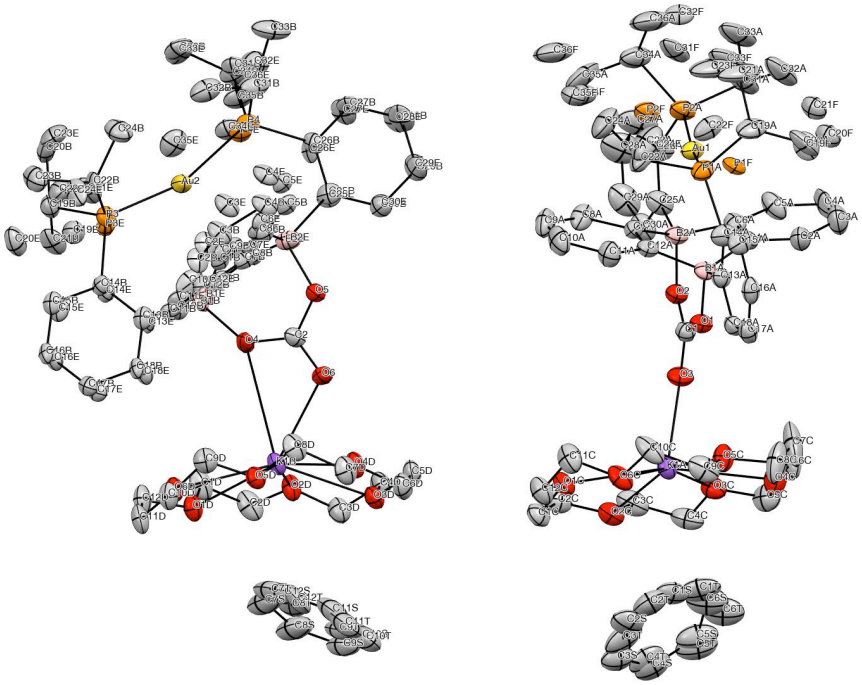

Figure 3.2.7.5. Labelled thermal ellipsoid plot (50%) for **[Au(B_2P_2)(CO_3)][K(18-c-6)]**.

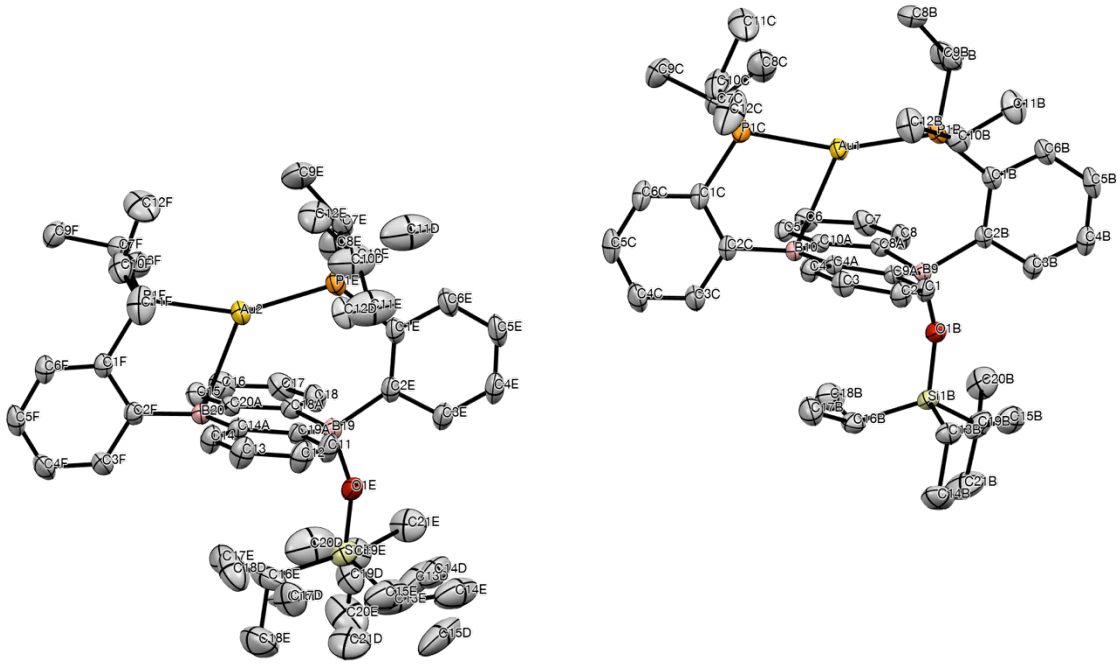

Figure 3.2.7.6. Labelled thermal ellipsoid plot (50%) for **[Au(B_2P_2)](O(Si(^{i}Pr)$_3$)**.

Table 3.2.7.1. Crystal data and structure refinement for **[Au(B_2P_2)]H**.

Identification code	hh94JT43_0m	
Empirical formula	$C_{42}H_{51}AuB_2P_2$	
Formula weight	836.35 g/mol	
Temperature	100(2) K	
Wavelength	0.71073 Å	
Crystal system	Monoclinic	
Space group	P 21/c	
Unit cell dimensions	a = 13.6605(2) Å	α = 90°.
	b = 18.5231(3) Å	β = 97.9128(5)°.
	c = 14.7583(2) Å	γ = 90°.
Volume	3698.81(10) Å^3	
Z	4	
Density (calculated)	1.502 mg/m^3	
Absorption coefficient	4.093 mm^{-1}	
F(000)	1688	
Crystal size	0.508 x 0.221 x 0.162 mm^3	
θ range for data collection	1.775 to 34.336°.	
Index ranges	$-21 \le h \le 21$, $-29 \le k \le 29$, $-23 \le l \le 23$	
Reflections collected	236591	
Independent reflections	15490 [R_{int} = 0.0303]	
Completeness to θ = 25.242°	100.0 %	
Absorption correction	Semi-empirical from equivalents	
Refinement method	Full-matrix least-squares on F^2	
Data / restraints / parameters	15490 / 0 / 435	
Goodness-of-fit on F^2	1.035	
Final R indices [$I > 2\sigma_I$]	R_1 = 0.0161, wR_2 = 0.0373	
R indices (all data)	R_1 = 0.0203, wR_2 = 0.0386	
Largest diff. peak and hole	1.230 and –0.708 e/Å^3	

Table 3.2.7.2. Crystal data and structure refinement for **[Au(B_2P_2)](CO_2H)**.

Identification code	hh108JT52_0m	
Empirical formula	$C_{37}H_{45}AuB_2O_2P_2$	
Formula weight	802.25 g/mol	
Temperature	100(2) K	
Wavelength	0.71073 Å	
Crystal system	Monoclinic	
Space group	P 21/c	
Unit cell dimensions	a = 10.7350(4) Å	α = 90°.
	b = 19.4697(6) Å	β = 107.5607(5)°.
	c = 16.9388(6) Å	γ = 90°.
Volume	3375.3(2) Å^3	
Z	4	
Density (calculated)	1.579 mg/m^3	
Absorption coefficient	4.486 mm^{-1}	
F(000)	1608	
Crystal size	0.361 x 0.283 x 0.202 mm^3	
θ range for data collection	1.638 to 30.034°.	
Index ranges	$-15 \le h \le 15$, $-27 \le k \le 27$, $-23 \le l \le 23$	
Reflections collected	95114	
Independent reflections	9868 [R_{int} = 0.0260]	
Completeness to θ = 25.242°	100.0 %	
Absorption correction	Semi-empirical from equivalents	
Refinement method	Full-matrix least-squares on F^2	
Data / restraints / parameters	9868 / 0 / 405	
Goodness-of-fit on F^2	1.049	
Final R indices [$I > 2\sigma_I$]	R_1 = 0.0149, wR_2 = 0.0353	
R indices (all data)	R_1 = 0.0176, wR_2 = 0.0362	
Largest diff. peak and hole	0.924 and –0.291 e/Å^3	

Table 3.2.7.3. Crystal data and structure refinement for **[Au(B_2P_2)](H_2)]$_2$[μ-K_2(Et_2O)]$_2$**.

Identification code	hh190JT93r_0m	
Empirical formula	$C_{88}H_{128.50}Au_2B_4K_2O_4P_4$	
Formula weight	1889.65 g/mol	
Temperature	100(2) K	
Wavelength	0.71073 Å	
Crystal system	Monoclinic	
Space group	P 21/n	
Unit cell dimensions	a = 17.3226(5) Å	α = 90°.
	b = 14.0750(4) Å	β = 108.2727(5)°.
	c = 18.5251(5) Å	γ = 90°.
Volume	4289.0(2) Å^3	
Z	2	
Density (calculated)	1.463 mg/m^3	
Absorption coefficient	3.637 mm^{-1}	
F(000)	1929	
Crystal size	0.321 x 0.193 x 0.102 mm^3	
θ range for data collection	1.853 to 30.508°.	
Index ranges	$-24 \le h \le 24$, $-20 \le k \le 20$, $-26 \le l \le 26$	
Reflections collected	101496	
Independent reflections	13085 [R_{int} = 0.0375]	
Completeness to θ = 25.242°	100.0 %	
Absorption correction	Semi-empirical from equivalents	
Refinement method	Full-matrix least-squares on F^2	
Data / restraints / parameters	13085 / 38 / 521	
Goodness-of-fit on F^2	1.060	
Final R indices [$I > 2\sigma_I$]	R_1 = 0.0211, wR_2 = 0.0398	
R indices (all data)	R_1 = 0.0326, wR_2 = 0.0429	
Largest diff. peak and hole	1.030 and –0.977 e/Å^3	

Table 3.2.7.4. Crystal data and structure refinement for **[Au(B_2P_2)](CO_2H)$_2$][K(18-c-6)]**.

Identification code	hh218JT106_0m	
Empirical formula	$C_{56}H_{76}AuB_2KO_{10}P_2$	
Formula weight	1228.79 g/mol	
Temperature	100(2) K	
Wavelength	0.71073 Å	
Crystal system	Triclinic	
Space group	P –1	
Unit cell dimensions	a = 9.4884(3) Å	α = 82.1272(5)°.
	b = 16.6011(5) Å	β = 83.3368(5)°.
	c = 18.4187(5) Å	γ = 81.8270(5)°.
Volume	2830.91(15) Å^3	
Z	2	
Density (calculated)	1.442 mg/m^3	
Absorption coefficient	2.784 mm^{-1}	
F(000)	1260	
Crystal size	0.332 x 0.153 x 0.083 mm^3	
θ range for data collection	1.573 to 28.282°.	
Index ranges	$-12 \le h \le 12$, $-22 \le k \le 22$, $-24 \le l \le 24$	
Reflections collected	79048	
Independent reflections	14037 [R_{int} = 0.0329]	
Completeness to θ = 25.242°	100.0 %	
Absorption correction	Semi-empirical from equivalents	
Refinement method	Full-matrix least-squares on F^2	
Data / restraints / parameters	14037 / 96 / 821	
Goodness-of-fit on F^2	1.036	
Final R indices [$I > 2\sigma_I$]	R_1 = 0.0191, wR_2 = 0.0427	
R indices (all data)	R_1 = 0.0221, wR_2 = 0.0439	
Largest diff. peak and hole	0.800 and –0.511 e/Å^3	

Table 3.2.7.5. Crystal data and structure refinement for **[Au(B_2P_2)(CO_3)][K(18-c-6)]**.

Identification code	hh233JT117_0m	
Empirical formula	$C_{55}H_{74}AuB_2KO_9P_2$	
Formula weight	1198.76 g/mol	
Temperature	100(2) K	
Wavelength	0.71073 Å	
Crystal system	Triclinic	
Space group	P –1	
Unit cell dimensions	a = 17.085(3) Å	α = 91.133(2)°.
	b = 17.761(3) Å	β = 91.253(2)°.
	c = 18.264(3) Å	γ = 90.383(2)°.
Volume	5539.7(15) $Å^3$	
Z	4	
Density (calculated)	1.437 mg/m^3	
Absorption coefficient	2.842 mm^{-1}	
F(000)	2456	
Crystal size	0.564 x 0.122 x 0.040 mm^3	
θ range for data collection	1.584 to 25.681°.	
Index ranges	$-20 \le h \le 20$, $-21 \le k \le 21$, $-22 \le l \le 22$	
Reflections collected	65770	
Independent reflections	20977 [R_{int} = 0.0623]	
Completeness to θ = 25.242°	99.8 %	
Absorption correction	Semi-empirical from equivalents	
Refinement method	Full-matrix least-squares on F^2	
Data / restraints / parameters	20977 / 18 / 1501	
Goodness-of-fit on F^2	1.036	
Final R indices [$I > 2\sigma_I$]	R_1 = 0.0464, wR_2 = 0.0972	
R indices (all data)	R_1 = 0.0677, wR_2 = 0.1063	
Largest diff. peak and hole	2.966 and –1.520 e/$Å^3$	

Table 3.2.7.6. Crystal data and structure refinement for **[Au(B_2P_2)](O(Si(^{i}Pr)$_3$)**.

Identification code	hh241JT120_0m	
Empirical formula	$C_{45}H_{65}AuB_2OP_2Si$	
Formula weight	930.58 g/mol	
Temperature	180(2) K	
Wavelength	0.71073 Å	
Crystal system	Monoclinic	
Space group	$P2_1/c$	
Unit cell dimensions	a = 20.6988(5) Å	α = 90°.
	b = 22.0547(5) Å	β = 92.3184(5)°.
	c = 19.2806(5) Å	γ = 90°.
Volume	8794.5(4) Å^3	
Z	8	
Density (calculated)	1.406 mg/m^3	
Absorption coefficient	3.478 mm^{-1}	
F(000)	3808	
Crystal color	light yellow	
Crystal size	0.406 x 0.278 x 0.182 mm^3	
θ range for data collection	1.690 to 29.575°	
Index ranges	$-28 \le h \le 28$, $-30 \le k \le 30$, $-26 \le l \le 26$	
Reflections collected	198681	
Independent reflections	24666 [R_{int} = 0.0280]	
Completeness to θ = 25.242°	100.0 %	
Absorption correction	Semi-empirical from equivalents	
Refinement method	Full-matrix least-squares on F^2	
Data / restraints / parameters	24666 / 381 / 1065	
Goodness-of-fit on F^2	1.023	
Final R indices [$I > 2\sigma_I$]	R_1 = 0.0222, wR_2 = 0.0498	
R indices (all data, 0.72 Å)	R_1 = 0.0286, wR_2 = 0.0519	
Largest diff. peak and hole	1.201 and –1.023 e/Å^3	

3.2.8) References

[1] Schlesinger, H. I.; Brown, H. C. *J. Am. Chem. Soc.* **1940**, *62* (12), 3429.

[2] (a) Brown, H. C.; Krishnamurthy, S. *Tetrahedron* **1979**, *35* (5), 567. (b) Brown, H. C.; Mead, E. J.; Subba Rao, B. C. *J. Am. Chem. Soc.* **1955**, *77* (23), 6209.

[3] (a) Ma, J.; Choudhury, N. A.; Sahai, Y. *Renew. Sust. Energ. Rev.* **2010**, *14* (1), 183. (b) Paskevicius, M.; Jepsen, L. H.; Schouwink, P.; Cerny, R.; Ravnsbaek, D.; Filinchuk, Y.; Dornheim, M.; Besenbacher, F.; Jensen, T. R. *Chem. Soc. Rev.* **2017**, *46* (5), 1565.

[4] (a) Wartik, T.; Pearson, R. K. *J. Am. Chem. Soc.* **1955**, *77*, 1075. (b) Wartik, T.; Pearson, R. K. *J. Inorg. Nucl. Chem.* **1958**, *7* (4), 404.

[5] Eisenberg, F., Jr.; Bolden, A. H. Formate Contamination in Borohydride Reductions. *Carbohydr. Res.* **1967**, *5*, 349– 350

[6] Fujiwara, K.; Yasuda, S.; Mizuta, T. *Organometallics* **2014**, *33* (22), 6692.

[7] Knopf, I.; Christopher, C. *Organometallics* **2015**, *34* (9), 1601.

[8] (a) Bontemps, S.; Vendler, L.; Sabo-Etienne, S. *Angew. Chem. Int. Ed.* **2012**, *124* (7), 1703. (b) Legare, M.-A.; Courtemanche, M.-A.; Fontaine, F.-G. *Chem. Comm.* **2014**, *50* (77), 11362.

[9] (a) Chakraborty, S.; Zhang, J.; Krause, J.; Guan, H. *J. Am. Chem. Soc.* **2010**, *132* (26), 8872. (b) Sgro, M. J.; Stephan, D. W. *Angew. Chem. Int. Ed.* **2012**, *51* (45), 11343. (c) Courtemanche, M.-A.; Legare, M.-A.; Maron, L.; Fontaine, F.-G. *J. Am. Chem. Soc.* **2014**, *136* (30), 10708. (d) Das Neves Gomes, C.; Biondiaux, E.; Thuery, P.; Cantat, T. *Chem. Eur. J.* **2014**, *20* (23), 7098. (e) Wang, T.; Stephan, D. W. *Chem. Comm.* **2014**, *50* (53), 7007. (f) Wang, T.; Stephan, D. W. *Chem. Eur. J.* **2014**, *20* (11), 3036.

[10] (a) Shintani, R.; Nozaki, K. *Organometallics* **2013**, *32* (8), 2459.

[11] (a) Laitar, D. S.; Muller, P.; Sadighi, J. P. *J. Am. Chem. Soc.* **2005**, *127* (49), 17196. (b) Zhao, H.; Lin, Z.; Marder, T. B. *J. Am. Chem. Soc.* **2006**, *128* (49), 15637.

[12] Berkefeld, A.; Piers, W. E.; Masood, P*J. Am. Chem. Soc.* **2010**, *132* (31), 10660.

[13] Rittmeyer, P.; Wietelmann, U. *Ullmann's Encyclopedia of Industrial Chemistry*; 2000.

[14] (a) Asakawa, H.; Lee, K.-H.; Furukawa, K.; Lin, Z.; Yamashita, M. *Chem. Eur. J.* **2015**, *21* (11), 4267. (b) Chiu, C.-W.; Gabbai, F. P. *Organometallics.* **2008**, *27* (7), 1657. (c) Chiu, C.-W.; Kim, Y.; Gabbai, F. P *J. Am. Chem. Soc.* **2009**, *131* (1), 60. (d) Edwin, J.; Bochmann, M.; Boehm, M. C.; Brennan, D. E.; Geiger, W. E.; Krueger, C.; Pebler, J.; Pritzkow, H.; Siebert, W. *J. Am. Chem. Soc.* **1983**, *105* (9), 2582. (e) Herberich, G. E.; Buller, B.; Hessner, B.; Oschmann, W. *J. Organomet. Chem.* **1980**, *195* (3), 253. (f) Januszewski, E.; Bolte, M.; Lerner, H.-W.; Holthausen, M.; Wagner, M. *Dalton Transactions* **2013**, *42* (38), 13826. (g) Kwaan, R. J.; Harlan, J. C.; Norton, J. R. *Organometallics* **2001**, *20* (17), 3818. (h) Lorbach, A.; Hubner, A.; Wagner, M. *Dalton Transactions* **2012**, *41* (20), 6048. (i) Muller, P.; Gangnus, B.; Pritzkow, H.; Schulz, H.; Stephan, M.; Siebert, W. *J. Organomet. Chem.* **1995**, *487* (1–2), 235.

[15] Segawa, Y.; Yamashita, M.; Nozaki, K. *Science* **2006**, *314* (5796), 113.

[16] Kinjo, R.; Donnadieu, B.; Celik, M. A.; Frenking, G.; Bertrand, G. *Science* **2011**, *333* (6042), 610.

[17] Kong L.,Li Y., Ganguly R., Vidovic D. Kinjo R. *Angew. Chem. Int. Ed.*, **2014**, 53, 9280–9283.

[18] (a) Hübner, A.; Kaese, T.; Diefenbach, M.; Endeward, B.; Bolte, M.; Lerner, H.-W.; Holthausen, M. C.; Wagner, M. A *J. Am. Chem. Soc.* **2015**, *137* (10), 3705. (b) Kaese, T.; Budy, H.; Bolte, M.; Lerner, H.-W.; Wagner, M. *Angew. Chem. Int. Ed.* **2017**, *56* (26), 7546.

[19] Taylor, J. W.; McSkimming, A.; Moret, M.-E.; Harman, W. H. *Angew. Chem. Int. Ed.* **2017**, *56* (35), 10413.

[20] (a) Carter, T. J.; Kampf, J. W.; Szymczak, N. K. *Angew. Chem. Int. Ed.* **2012**, *51* (52), 13168. (b) Carter, T. J.; Wang, J. Y.; Szymczak, N. K. *Organometallics* **2014**, *33* (7), 1540. (c) Carter, T. J.; Heiden, Z. M.; Szymczak, N. K. *Chem. Sci.* **2015**, *6* (12), 7258.

[21] (a) Sreekanth, N.; Nazrulla, M. A.; Vineesh, T. V.; Sailaja, K.; Phani, K. L. *Chem. Commun.* **2015**, *51* (89), 16061. (b) Tai, T. B.; Nguyen, M. T. **2013**, *19* (9), 2942.

[22] (a) Grotthuss, von, E.; Prey, S. E.; Bolte, M.; Lerner, H.-W.; Wagner, M. *Angew. Chem. Int. Ed.* **2018**. (b) Taylor, J. W.; McSkimming, A.; Guzman, C. F.; Harman, W. H. *J. Am. Chem. Soc.* **2017**, *139* (32), 11032. (c) Wu, D.; Kong, L.; Li, Y.; Ganguly, R.; Kinjo, R. *Nat. Commun.* **2015**, *6*, 7340.

[23] (a) Su, Y.; Kinjo, R. *Coord. Chem. Rev.* **2017**, *352*, 346. (b) Feng, P.-Y.; Liu, Y.-H.; Lin, T.-S.; Peng, S.-M.; Chiu, C.-W. *Angew. Chem. Int. Ed.* **2014**, *53* (24), 6237. (c) Su, Y.; Li, Y.; Ganguly, R.; Kinjo, R. *Chem. Sci.* **2017**, *8* (11), 7419. (d) Wang, B.; Li, Y.; Ganguly, R.; Webster, R. D.; Kinjo, R. *Angew. Chem. Int. Ed.* **2018**, *57* (26), 7826.

[24] Schnurr, A.; Vitze, H.; Bolte, M.; Lerner, H.-W.; Wagner, M. Rigid, *Organometallics* **2010**, *29* (22), 6012.

[25] (a) Jaska, C. A.; Emslie, D. J. H.; Bosdet, M. J. D.; Piers, W. E.; Sorensen, T. S.; Parvez, M. *J. Am. Chem. Soc.* **2006**, *128* (33), 10885. (b) Zhang, Z.; Penev, E. S.; Yakobson, B. I. *Chem. Soc. Rev.* **2017**, *46*, 6746. (c) Hertz, V. M.; Bolte, M.; Lerner, H.-W.; Wagner, M. *Angew. Chem. Int. Ed.* **2015**, *54* (30), 8800. (d) Su, B.; Kinjo, R. *Synthesis* **2017**, *49* (14), 2985.

[26] (a) Sattler, W.; Parkin, G. *J. Am. Chem. Soc.* **2011**, *133* (25), 9708. (b) Kornev, A. N.; Chesnokova, T. A.; Zhezlova, E. V.; Zakharov, L. N.; Fukin, G. K.; Kursky, Y. A.; Domrachev, G. A.; Lickiss, P. D. *J. Organomet. Chem.* **1999**, *587*, 113–121.

[27] Yang, Z. Z.; He, L. N.; Miao, C. X.; Chanfreau, S. *Adv. Synth. Catal.* **2010**, *352* (13), 2233.

[28] Scott, T. A.; Ooro, B. A.; Collins, D. J.; Shatruk, M.; Yakovenko, A.; Dunbar, K. R.; Zhou, H.-C. *Chem. Commun.* **2009**, *1*, 65.

[29] Led, J. J.; Gesmar, H. *Chem. Rev.*, **1991**, *91*, 1413.

[30] Gottlieb, H. E.; Kotlyar, V.; Nudelman, *J. Org. Chem.* **1997**, *62*, 7512.

[31] APEX 2, version 2014.1-1, Bruker (2014), Bruker AXS Inc., Madison, Wisconsin, USA.

[32] SAINT, version V8.34A, Bruker (2012), Bruker AXS Inc., Madison, Wisconsin, USA.

[33] SADABS, version 2012/1, Bruker (2012), Bruker AXS Inc., Madison, Wisconsin, USA.

[34] SHELXTL, version 2013/4, Bruker (2013), Bruker AXS Inc., Madison, Wisconsin, USA.

3.3) Water Reactivity of the Au(B_2P_2) Redox Series: Hydroxide Exchange, Water Stability and Water Splitting

3.3.1) Introduction

The electrolysis of water to oxygen and hydrogen is considered an important transformation for renewable fuel technologies.[1] Current production of H_2 proceeds via the energy intensive steam-reformation process and the combustion byproducts produced thereof have helped to peak research efforts in realizing alternative methods of H_2 production from water.[2] Transition metals have been targeted for this reaction[3] however catalytic H_2 evolution from H_2O with molecular systems remains rare.[4] Alternatively, transition-metal free systems for H_2O activation and H_2 evolution that utilized doped graphene materials have garnered much interest.[5] Boron doping in particular has emerged as an effective approach with examples including utilize boron-doped graphene,[6] boron nanoparticles[7] and other boron-doped materials.[8] These systems are prone to difficulties in determining reaction mechanism, especially operation under basic conditions, and molecular analogs provide one way to inform these systems.[9] Opportunely, main-group oxidative addition and reductive elimination have undergone a significant research effort over the last two decades.[10] In this vein, numerous examples of H_2O addition to yield main-group-hydride/hydroxides have been reported from reaction of H_2O with low-valent main-group centers.[11] In particular, aromatic boron heterocycles have shown the ability to perform

oxidative addition type reactions, adding E-H bonds in a 1,4-fashion across the heterocycle.[12] Notably, the ability to cycle these main-group systems back to a reactive molecule following H_2O activation has not been reported and offers a unique challenge. The incorporation of reactive main-group centers within redox-

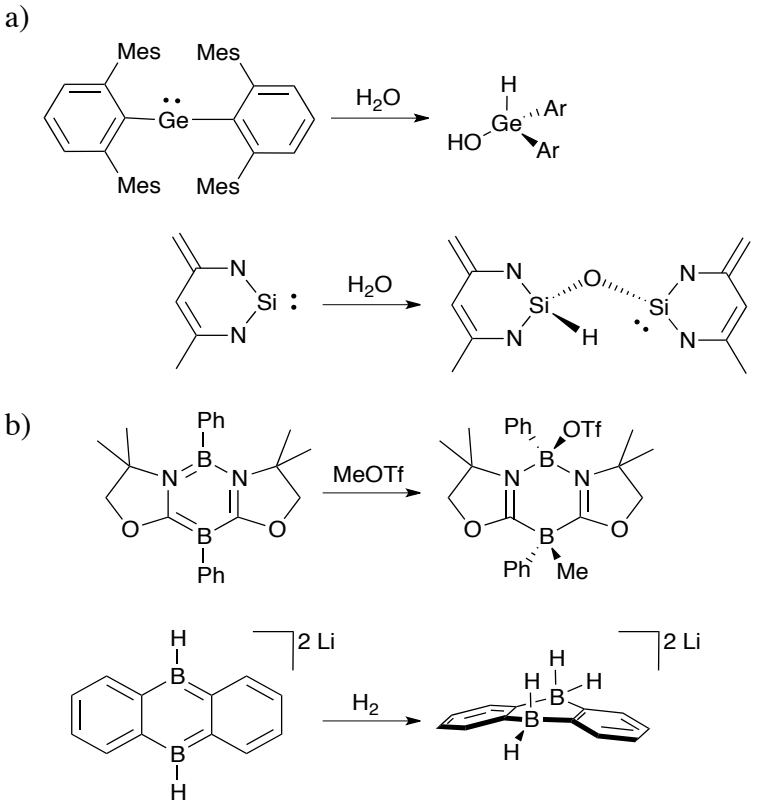

Figure 3.3.1. a) Examples of oxidative addition of H_2O at select low-valent main-group centers. b) E-H bond addition across 1,4-disposed diboron heterocycles.

active frameworks has recently emerged as a viable means to cleave strong bonds, such as the B-O bond, in order to regenerate reactive species for further reaction.[13]

The 9,10-dihydro-9,10-diboraanthracene (DBA) molecule has resurfaced as a rare example of a redox-active main group system that can also perform

multiple-electron bond activations with CO_2, O_2, C_2H_4 and H_2.[14] Furthermore, thermodynamically more accessible redox couples to produce reduced boron compounds have been realized via the incorporation of cationic appendages to distal sites,[15] stabilization with NHCs,[16] expansion of the boron-incorporated pi-conjugated system,[17] and transition-metal coordination.[18] Recently we developed a diboranthracene based disphosphine ligand (B_2P_2) and reported its Cu, Ag[19] and Au complexes.[20] The Au complex displayed multiple reversible redox couples, with the most reduced species being generated at mild potentials (–2.05 V vs. Fc/Fc+). This potential is on the cathodic side of the reduction of $H_2O \rightarrow$ ½ $O_2 + H_2$ and we were interested in the prospect of reducing H_2O to H_2 with $[Au(B_2P_2)]^{-1}$. This challenge is also dependent on the stability of $[Au(B_2P_2)]Cl$ towards H_2O. Previously we reported solution spectroscopy of $[Au(B_2P_2)]Cl$ that suggested facile exchange between the proximal boron centers at room temperature, as judged by NMR spectroscopies revealing a compound possessing C_2 symmetry. Effective boron p-orbital shielding is a known method of stabilizing DBA molecules against H_2O attack at boron[21] and we were intrigued as to whether anion shuttling would serve a similar purpose in $[Au(B_2P_2)]X$ (X = Cl, OH) systems. Herein we report the water stability of the $[Au(B_2P_2)]Cl$ complex, its reaction with hydroxide, as well as the reaction of $[Au(B_2P_2)]^{-1}$ with H_2O.

3.3.2) Results and Discussions

Synthesis of the hydroxide substituted compound, [Au(B_2P_2)]OH (**1**), was first carried out by exposing [Au(B_2P_2)]Cl to an excess of H_2O to test the water stability of [Au(B_2P_2)]Cl. Remarkably, no reaction occurred over the course of weeks in a CD_3CN:D_2O (2:1) solution as judged by NMR spectroscopies. Addition of excess triethylamine to a suspension of [Au(B_2P_2)]Cl in toluene:H_2O (10:1) however led to the formation [Au(B_2P_2)]OH in 89% yield as a pale-yellow solid. Solution NMR spectroscopy revealed a singlet at 48.52 ppm in the ^{31}P NMR along with a ^{1}H NMR spectra with averaged C_2 symmetry. The single-crystal XRD structure of **1** showed a hydroxide ion bound to one pseudo tetrahedral B atom ($\Sigma_{CBC\angle}$ = 336.9 °) with a distance of 1.529(2) Å. A Au-B contact of 2.615(1) Å occupies the other B atom on the opposite face of the DBA ring and is slightly longer than the analogous distance in [Au(B_2P_2)]Cl ($d_{Au\text{-}B}$=2.575 (2)Å). The discrepancy between solid-state and solution symmetry for **1** implied the potential rapid exchange of hydroxide ion between B atoms of the DBA ring. To investigate this, **1** was subjected to variable-temperature NMR

Scheme 3.3.1. Synthesis of **1**.

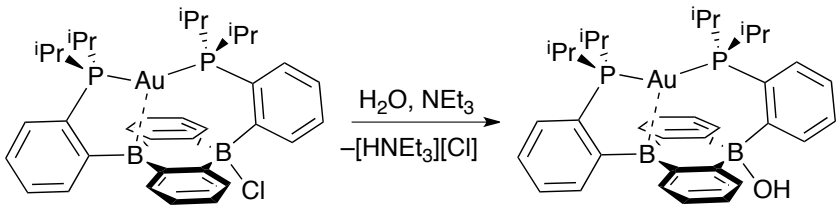

spectroscopies. A solution of **1** in toluene-d_8 was incrementally cooled to –45 °C during which time the singlet at 48.59 ppm broadened and re-coalesced to a set of doublets at 48.59 ppm (J_{PP} = 242 Hz) (Figure 3.3.3). Additionally, the ^{1}H NMR at –45°C of **1** was consistent with C_s symmetry (see Spectroscopic Data, Figure 3.3.5.5) while the ^{11}B{^{1}H} NMR had two signals (see Spectroscopic Data, Figure 3.3.5.7); a broad peak at 36.36 ppm and a sharp signal at –5.57 ppm corresponding to distinct three- and four-coordinate B atoms, respectively. From the VT-^{31}P NMR data, an Eyring plot was constructed (see Computational Analysis, Figure 3.3.6.10.) and thermal parameters were extracted. A coalescence temperature of –18 °C was determined, corresponding to an

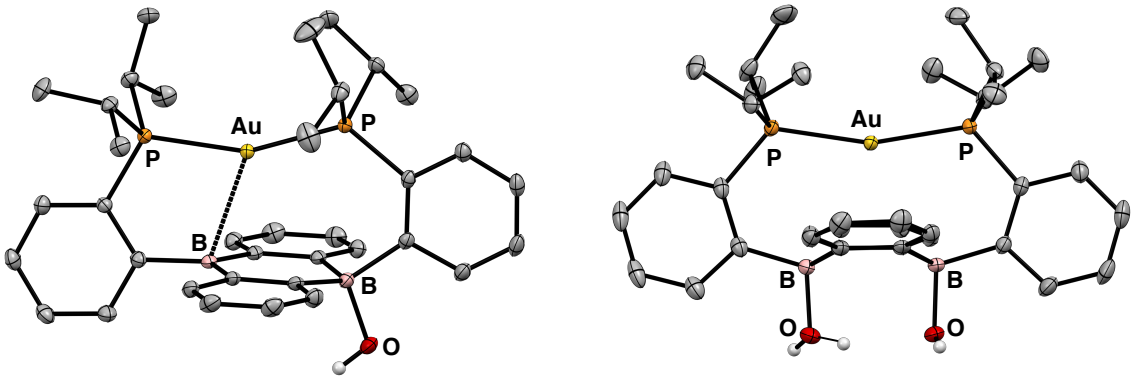

Figure 3.3.2. Thermal ellipsoid plots (50%) of [Au(B_2P_2)]OH (**1**, left) and the H_2O adduct [Au(B_2P_2)](OH)(H_2O) (**2-H_2O**, right).

enthalpy of activation of ΔH = 51 kJ/mol and an entropy of activation of ΔS = 0 kJ/mol. The calculated entropy of zero suggests an intramolecular process consistent with hydroxide shuttling between boron sites.[22]

Further experimental evidence to support the exchange of hydroxide (and chloride) anions between boron sites was sought by measuring the relative Lewis acidity of **1** by the Gutmann-Becket method,[23] along with $[Au(B_2P_2)]Cl$ and the free cation, $[Au(B_2P_2)][BAr^F{}_4]$. Acceptor numbers (ANs) of 0, 0, and 69 were determined in THF (AN = 45.25) for the series $[Au(B_2P_2)]OH$, $[Au(B_2P_2)]Cl$ and $[Au(B_2P_2)][BAr^F{}_4]$, respectively. These results reinforce the observed H_2O stability of **1** and $[Au(B_2P_2)]Cl$. However, when allowing a benzene solution of **1** to stand in the presence of excess water colorless crystals formed. Single-crystal XRD

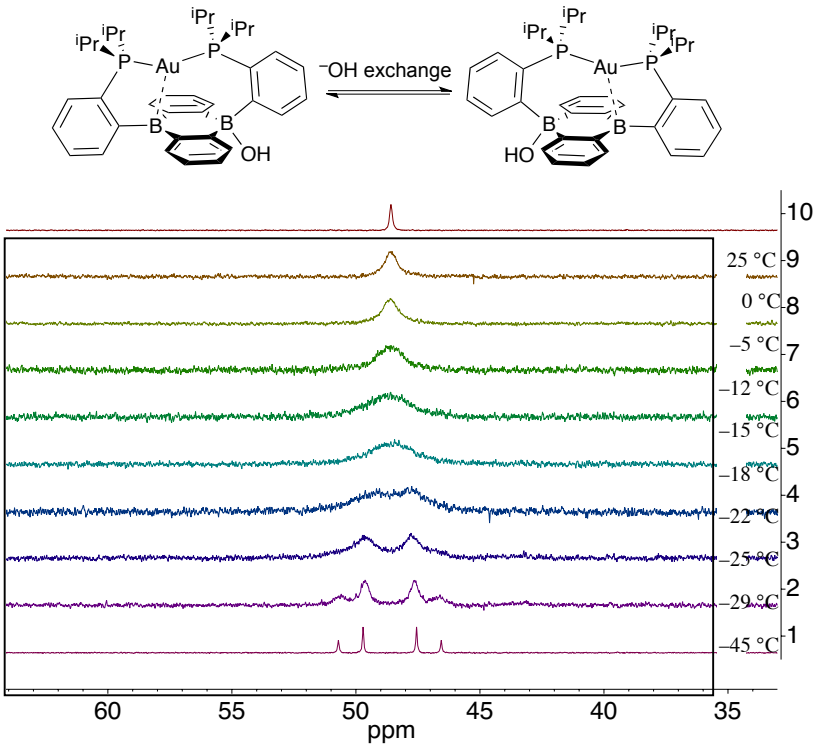

Figure 3.3.3. Variable Temperature ^{31}P NMR of **1**

revealed a water addition product where the other B atom in **1** binds an equivalent of H_2O, affording $[Au(B_2P_2)](OH)(H_2O)$ (**1-H_2O**). Each B atom is

puckered from the DBA ring to adopt a pseudo-tetrahedral geometry ($\Sigma_{CBC\angle}$ = 338.4 and 339.7°) with B-O bond lengths of 1.596(2) and 1.587(2) Å. The opposite face of the DBA ring retains a slightly bent P-Au-P unit (∠PAuP = 161.9°). Additionally, disordered H atoms located in the electron difference map between the two O atoms suggests some degree of H-bonding between each B-OH unit in the solid-state. The occurrence of **1-H_2O** and the recently reported reaction of H_2 with the [Au(B_2P_2)]Cl/DBU system suggests that in the presence of

Scheme 3.3.2. Synthesis of **2** and **3**.

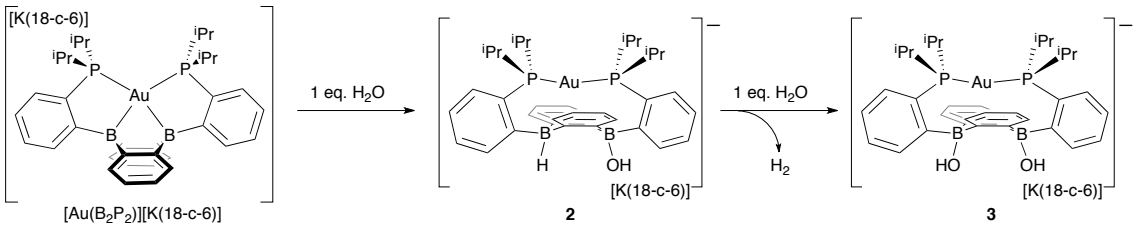

a suitable base, the DBA unit can still effectively act as a Lewis acid.

Having gauged the stability of the cationic Au(B_2P_2)]X (X = Cl, OH) complexes to H_2O, we sought to investigate the reaction of the reduced species, Au(B_2P_2)][K(18-c-6)], towards H_2O. Addition of 1 equivalent of H_2O to a solution of Au(B_2P_2)][K(18-c-6)] at 0° C rapidly led to a nearly colorless solution. ^{1}H NMR revealed a four-line signal for B-H coupling at 4.19 ppm ($J_{B\text{-}H}$ = 84 Hz) with ^{11}B NMR displaying a doublet at –9.73 ppm ($J_{B\text{-}H}$ = 75.4 Hz) and a broader singlet at –0.89 ppm. ^{31}P NMR revealed a mixture, with a set of doublets at 48.27 (J_{PP} = 276.9 Hz) and a singlet at 45.46 ppm. The relative ratio of the two products was ~ 4:1 with the doublet containing product being predominant. Nonetheless, a

single-crystal suitable for XRD was obtained from the mixture and revealed the major product to be the formal 1,4-addition product of H-OH across the DBA unit, [Au(B_2P_2)(H)(OH)][K(18-c-6)] (**2**). Each B-atom was pseudo-tetrahedral (chronic whole molecule disorder prohibited measurement of angles and distances) with the B-bound H atom being located in the electron difference map. In the solid-state, **2** had co-crystallized with an additional molecule of the dihydroxide complex, [Au(B_2P_2)($OH)_2$][K(18-c-6)] (**3**). The presence of **3** in the solid-state was attributed to the singlet containing species in the ^{31}P NMR of reaction mixture of **2** and its direct isolation was pursued. Addition of **2** equivalents of H_2O to [Au(B_2P_2)][K(18-c-6)] resulted in immediate loss of color accompanied by effervescence. ^{1}H NMR experiments confirmed the loss of H_2 with ^{31}P NMR revealing a singlet at 45.46 ppm and ^{11}B{^{1}H} NMR showing a broad singlet at –1.10 ppm. Single-crystal XRD studies on **3** showed analogously puckered B-atoms from the DBA ring with pseudo-tetrahedral geometries ($\Sigma_{CBC\angle}$ = 333.8 and

Scheme 3.3.3. Regeneration of [Au(B_2P_2)]Cl from **3** by HCl•Et_2O.

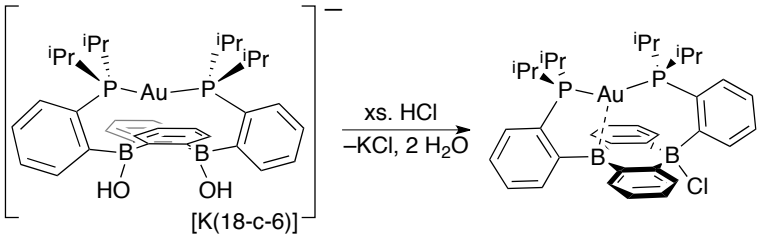

336.0 °) enforced by B-O bonds of 1.530(3) and 1.509(3) Å. The facile 1,4-addition of H_2O to the DBA core of [Au(B_2P_2)][K(18-c-6)] is reminiscent of reactions reported for symmetric[24] and asymmetric[12,25] 1,4-diboron heterocycles

with small molecules. However, turnover of these systems following bond activations steps is limited and we sought to investigate reaction conditions to revert **3** to [Au(B_2P_2)]Cl.[26] Following an acid screening, HCl•Et_2O was identified as competent for the transformation of **3** to [Au(B_2P_2)]Cl with no observed decomposition by ^{1}H and ^{31}P NMR. This reaction highlights the unique stability of the [Au(B_2P_2)] system and these results begin to elucidate a synthetic scheme for H_2 evolution with the [Au(B_2P_2)] system.

3.3.3) Concluding Remarks

In conclusion, the stability of the [Au(B_2P_2)]Cl system to H_2O was demonstrated. [Au(B_2P_2)]Cl and **1** are found to be poor Lewis acids by the Gutmann-Becket method with **1** displaying facile hydroxide exchange between B atoms of the DBA ring as evidenced by ^{31}P VT-NMR and low temperature ^{1}H and ^{11}B NMR. To the best of our knowledge, this is the first example of facile hydroxide exchange between B centers. Additionally, the reaction of the reduced complex Au(B_2P_2)][K(18-c-6)] with 1 equivalent of H_2O produces the 1,4-addition product **2** that, upon addition of a second equivalent of H_2O, **2** rapidly evolves H_2 to yield the dihydroxide compound **3**. [Au(B_2P_2)]Cl can be regenerated from **3** via HCl•Et_2O and provides a synthetic cycle for H_2 evolution from H_2O. Modifications of the Au(B_2P_2) system in order to perform electrocatalytic H_2O reduction is currently being explored.

3.3.4) Experimental Section

3.3.4.1) General Considerations

Unless otherwise noted, all manipulations were carried out using standard Schlenk or glovebox techniques under a N_2 atmosphere. Hexanes, benzene, toluene, and acetonitrile were dried and deoxygenated by argon sparge followed by passage through activated alumina in a solvent purification system from JC Meyer Solvent Systems followed by storage over 4 Å molecular sieves. THF and Et_2O were distilled from sodium-benzophenone ketyl under N_2 followed by storage over 4Å molecular sieves for at least 24 hours prior to use. Non-halogenated and non-nitrile containing solvents were tested with a standard purple solution of sodium benzophenone ketyl in THF to confirm effective oxygen and moisture removal prior to use. Hexamethyldisiloxane (HMDSO) was distilled from sodium metal and stored over 4Å molecular sieves for 24 hours prior to use. All reagents were purchased from commercial suppliers and used without further purification unless otherwise noted. 9,10-bis(2-(diisopropylphosphino)phenyl)-9,10-dihydroboranthrene (B_2P_2), [Au(B_2P_2)]Cl, and [Au(B_2P_2)][K(18-c-6)] were synthesized according to literature procedures.[20] Distilled H_2O used for the synthesis of **1**, **1-H_2O**, **2** and **3** was degassed by sparging with argon 15 minutes prior to use. Triethylamine (NEt_3) was distilled from CaH_2 and stored over 3 Å sieves for 24 hours in the dark prior to use. Elemental analyses were performed by Midwest Microlab, LLC, Indianapolis, IN.

Deuterated solvents were purchased from Cambridge Isotope Laboratories Inc., degassed, and dried over activated 3Å molecular sieves for at least 24 h prior to use. NMR spectra were recorded on Varian Inova 500 MHz, Bruker Avance 600 MHz, and Bruker NEO 400 MHz spectrometers. Variable Temperature NMR spectra were collected on a Bruker Avance 600 MHz spectrometer that had been pre-referenced with an internal thermometer for accurate temperature readings. ^{1}H and ^{13}C chemical shifts are reported in ppm relative to tetramethylsilane using residual solvent as an internal standard. ^{11}B chemical shifts are reported in ppm relative to $BF_3 \cdot Et_2O$. Original ^{11}B NMR spectra were processed using MestReNova 10.0.2 with a backwards-linear prediction applied to eliminate background signal from the borosilicate NMR tube. For ^{11}B NMR spectra with peaks overlapping the borosilicate signal, a manual baseline correction was applied. IR spectra were recorded using a Bruker Alpha FT-IR with a universal sampling module collecting at 4 cm^{-1} resolution with 32 scans.

3.3.4.2) [Au(B_2P_2)]OH (1).

[Au(B_2P_2)]Cl (0.028 g, 0.035 mmol) was suspended in toluene (4 mL) before adding H_2O (1.9 µL, 0.11 mmol) followed by NEt_3 (17 µL, 0.12 mmol) which resulted in the precipitation of a colorless solid over 30 minutes. The reaction was filtered through celite, concentrated *in vacuo* (ca. 1 mL) and added hexanes (3 mL) to precipitate the product. The product was rinsed with hexanes (2 x 1 mL) and dried *in vacuo*. Yield: 0.024 g, 89%. X-ray quality crystals were grown by

layering a concentrated toluene solution with hexanes. ^{1}H NMR (500 MHz, C_6D_6) δ 8.71 (d, *J* = 5.7 Hz, 2H), 7.80 (t, *J* = 6.9 Hz, 2H), 7.34 (t, *J* = 7.5 Hz, 2H), 7.30 (m, 2H), 7.08 (m, 4H), 6.88 (m, 4H), 2.05 (m, 4H), 0.82 (d, *J* = 7.2 Hz, 6H), 0.79 (d, *J* = 7.2 Hz, 6H), 0.64 (d, *J* = 7.9 Hz, 6H), 0.61 (d, *J* = 8.0 Hz, 6H). ^{31}P{^{1}H} NMR (242 MHz, C_6D_6, 25 °C) δ 48.52 (s). ^{31}P NMR (243 MHz, toluene-d_8, –45 °C) δ 47.47 (d, *J* = 242.3 Hz), 44.32 (d, *J* = 241.7 Hz). ^{11}B{^{1}H} NMR (193 MHz, toluene-d_8, –45 °C) δ 36.4, –5.6. ^{13}C{^{1}H} NMR (126 MHz, C_6D_6) δ 168.0, 156.9, 135.3, 134.0, 133.4, 131.2, 129.9, 126.7, 124.8, 27.3 (t, *J* = 12.9 Hz), 21.4, 19.3. FT-IR: ν_{max} cm^{-1} 3662 (OH). MALDI MS: *m/z* 774.2784; Calcd. For 774.2797.

3.3.4.3) [Au(B_2P_2)](OH)(H_2O) (1-H_2O).

A solution of **1** (0.010 g, 0.013 mmol) in C_6D_6 (0.6 mL) was added H_2O (0.46 µl, 0.023 mmol). The mixture was sonicated 5 minutes prior to collecting NMR spectra. Removal of volatiles *in vacuo* and dissolution of the residue in C_6D_6 (0.6 mL) showed spectroscopically pure **1**. X-Ray quality crystals of **1-H_2O** were grown by letting a saturated solution as prepared above stand for one week. ^{1}H NMR (600 MHz, C_6D_6) δ 8.89 (s, 2H), 7.96 – 7.86 (m, 2H), 7.51 – 7.44 (m, 2H), 7.42 (s, 2H), 7.18 (s, 4H), 6.95 (s, 4H), 2.15 (s, 4H), 0.97 – 0.85 (m, 12H), 0.69 (d, *J* = 7.7 Hz, 12H). ^{31}P NMR (162 MHz, C_6D_6) δ 48.03 (s). ^{11}B{^{1}H} NMR (128 MHz, C_6D_6) δ 6.57.

3.3.4.4) [Au(B_2P_2)(H)(OH)][K(18-c-6)] (2).

[Au(B_2P_2)][K(18-c-6)] (0.020 g, 0.019 mmol) was dissolved in THF (1 mL) before adding a solution of water (0.34 μL, 0.019 mmol) in THF (2 mL) dropwise over 5 minutes at 0 °C. The reaction was stirred 30 minutes where it became colorless. The reaction was concentrated *in vacuo* (ca. 0.3 mL) and added pentane (2 mL) before being placed at –35 °C overnight. The next day, colorless crystals had formed that were decanted from the mother liquor, rinsed with hexanes (ca. 1 mL) and dried *in vacuo* to yield the product in ~80 purity (as judged by ^{31}P NMR) with the sole byproduct being **3**. X-ray quality crystals were grown by layering a concentrated benzene solution with hexanes. ^{1}H NMR (400 MHz, C_6D_6) δ 9.24 (dd, *J* = 7.3, 3.3 Hz, 1H), 8.58 (s, 1H), 7.83 (t, *J* = 7.1 Hz, 1H), 7.70 (t, *J* = 7.2 Hz, 1H), 7.62 (t, *J* = 7.5 Hz, 1H), 7.55 (t, *J* = 7.5 Hz, 2H), 7.46 (t, *J* = 7.3 Hz, 2H), 7.31 (d, *J* = 6.9 Hz, 2H), 7.23 (d, *J* = 6.7 Hz, 2H), 7.11 (t, *J* = 6.6 Hz, 2H), 7.06 (t, *J* = 6.5 Hz, 2H), 4.57 – 3.81 (m, 1H), 3.13 (s, 24H), 2.39 (tq, *J* = 14.2, 7.0 Hz, 4H), 1.05 (dt, *J* = 13.2, 6.4 Hz, 12H), 0.92 (d, *J* = 3.4 Hz, 3H), 0.91 (d, *J* = 3.4 Hz, 3H), 0.88 (d, *J* = 3.7 Hz, 3H), 0.86 (d, *J* = 3.7 Hz, 3H). ^{31}P NMR (162 MHz, C_6D_6) δ 48.27 (d, *J* = 276.9 Hz). ^{11}B NMR (128 MHz, C_6D_6) δ –0.89, –9.73 (d, *J* = 75.4 Hz). ^{13}C NMR (151 MHz, C_6D_6) δ 175.5, 161.6, 159.8, 143.3 (d, *J* = 14.9 Hz), 136.3, 136.2, 135.5, 135.3, 134.1, 133.8, 133.2, 132.6, 132.2, 131.3 (d, *J* = 29.3 Hz), 124.6, 124.0, 123.5 (d, *J* = 6.3 Hz), 123.0, 70.0, 27.0 (d, *J* = 7.3 Hz), 26.8 (d,

J = 6.9 Hz), 22.5 (d, J = 7.7 Hz), 22.4 (d, J = 7.7 Hz), 19.2, 19.1. FT-IR: ν_{max} cm^{-1} 3668, 3596 (O-H), 1741 (B-H).

3.3.4.5) $[Au(B_2P_2)(OH)_2][K(18\text{-}c\text{-}6)]$ (2).

$[Au(B_2P_2)][K(18\text{-}c\text{-}6)]$ (0.020 g, 0.019 mmol) was dissolved in toluene (4 mL) before adding H_2O (0.72 μL, 0.040 mmol). The reaction was stirred 30 minutes where it became colorless. Volatiles were removed *in vacuo* to yield the product as a colorless solid. Yield: 0.19 g, 92%. X-ray quality crystals and samples suitable for elemental analysis were acquired by layering a concentrated benzene solution with HMDSO. ^{1}H NMR (400 MHz, C_6D_6) δ 9.22 (dd, J = 7.6, 1.7 Hz, 2H), 7.84 (t, J = 7.7 Hz, 2H), 7.54 (dt, J = 8.5, 4.3 Hz, 2H), 7.45 (t, J = 8.0 Hz, 2H), 7.25 (dd, J = 5.3, 3.4 Hz, 4H), 7.07 (dd, J = 5.3, 3.3 Hz, 4H), 3.19 (s, 24H), 2.49 – 2.29 (m, 4H), 1.06 (d, J = 7.0 Hz, 6H), 1.02 (d, J = 7.0 Hz, 6H), 0.89 (d, J = 7.4 Hz, 6H), 0.85 (d, J = 7.2 Hz, 6H). $^{31}P\{^{1}H\}$ NMR (202 MHz, C_6D_6) δ 45.46 (s).$^{11}B\{^{1}H\}$ NMR (128 MHz, C_6D_6) δ –1.10 (s). ^{13}C NMR (151 MHz, C_6D_6) δ 174.00, 160.75, 136.32, 135.12, 134.96, 132.63, 131.03, 124.63, 123.72, 69.99, 26.76 (t, J = 12.8 Hz), 22.58, 19.00. FT-IR: ν_{max} cm^{-1} 3043 (O-H). Anal. Calcd for $C_{48}H_{70}AuB_2KO_8P_2$: C, 52.66 H, 6.45. Found: C, 53.15 H, 6.25.

3.3.5) Spectroscopic Data

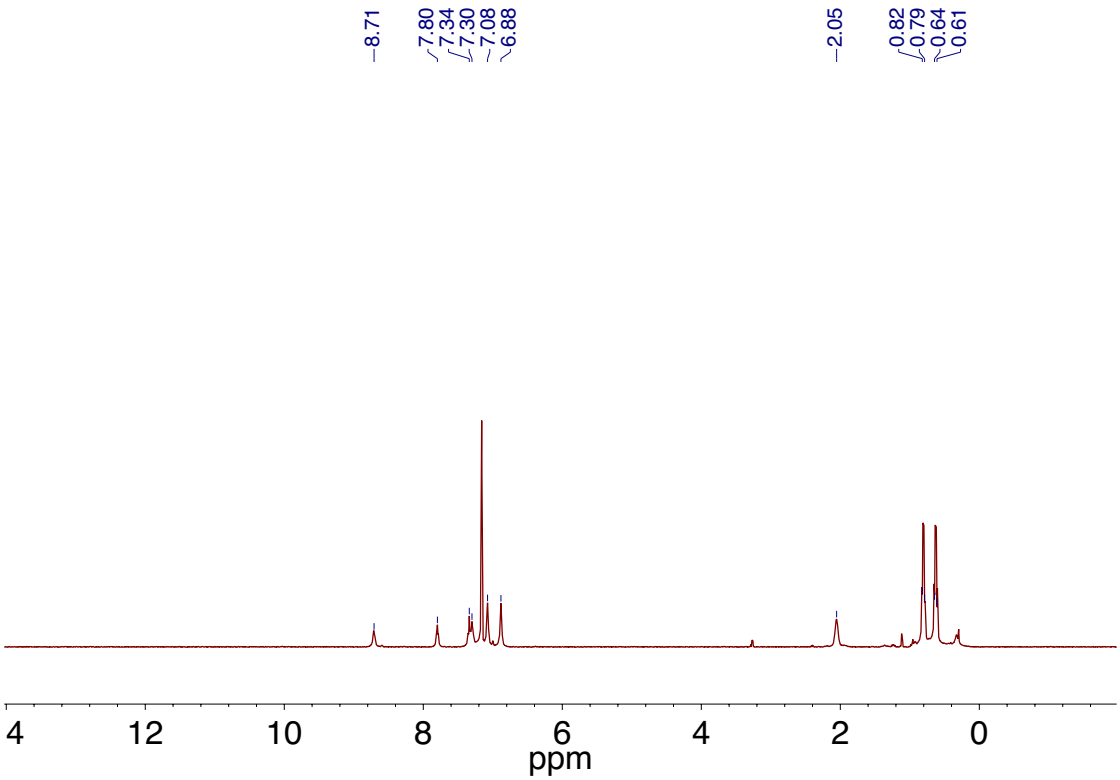

Figure 3.3.5.1. ^{1}H NMR spectrum of **[Au(B_2P_2)]OH** recorded at 500 MHz in C_6D_6.

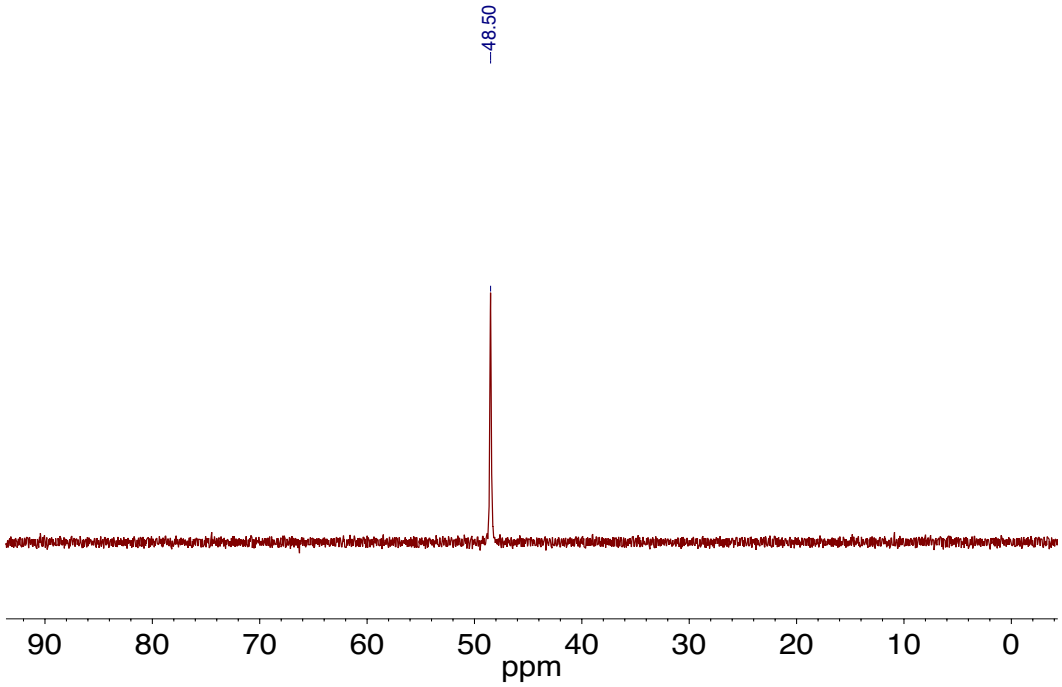

Figure 3.3.5.2. ^{31}P NMR spectrum of **[Au(B_2P_2)]OH** recorded at 242 MHz in C_6D_6.

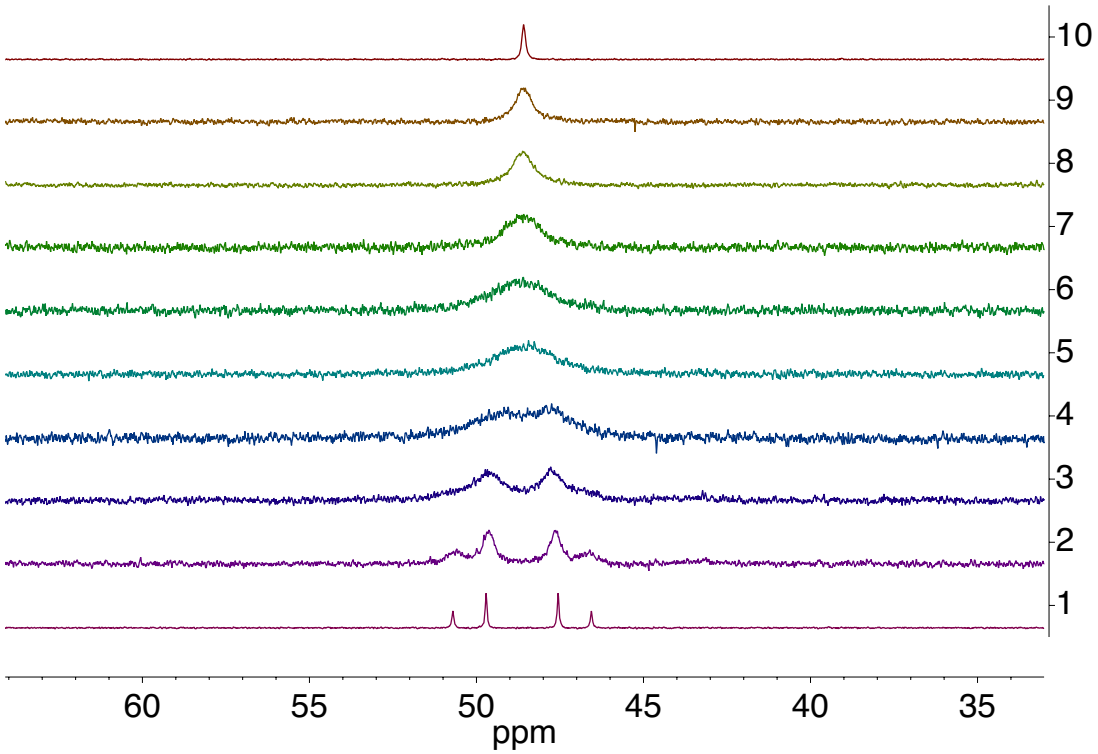

Figure 3.3.5.3. ^{31}P VT-NMR spectra of **[Au(B_2P_2)]OH** recorded at 242 MHz in toluene-d_8. Spectra 10-1 were collected at 25, 0, –5, –12, –15, –18, –22, –25, –29 and –45 °C, respectively.

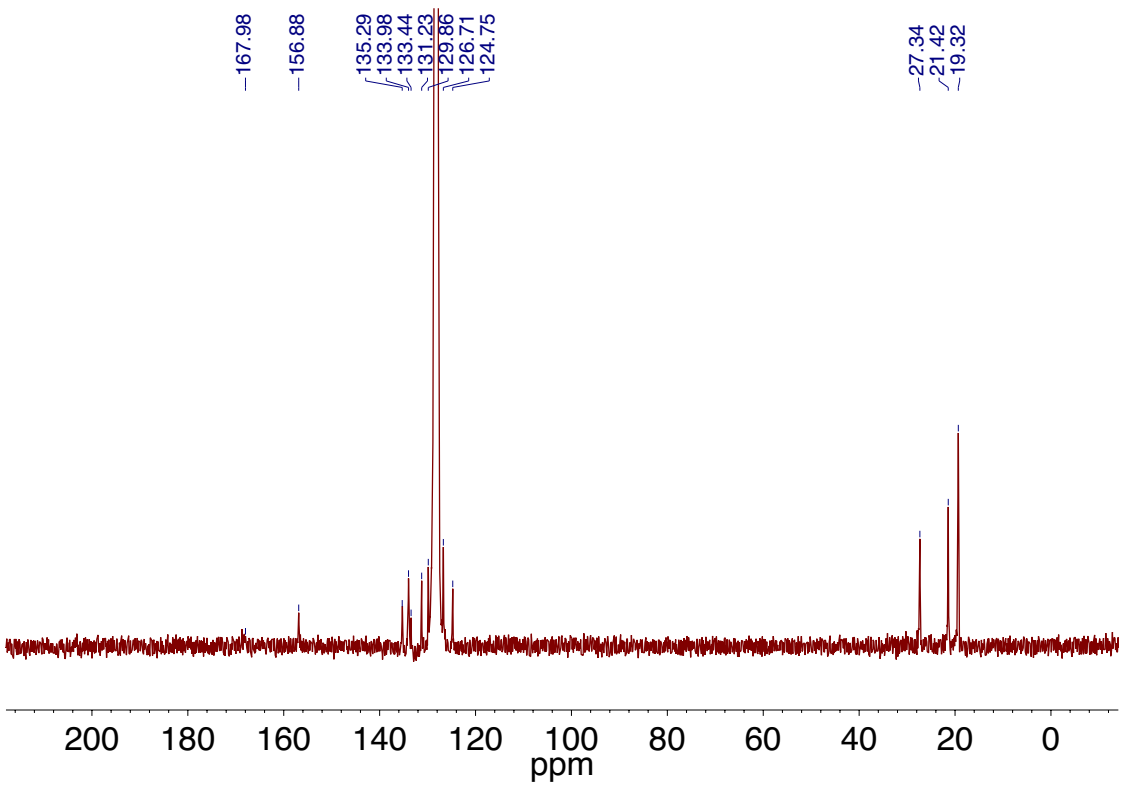

Figure 3.3.5.4. ^{13}C NMR spectrum of **[Au(B_2P_2)]OH** recorded at 126 MHz in C_6D_6

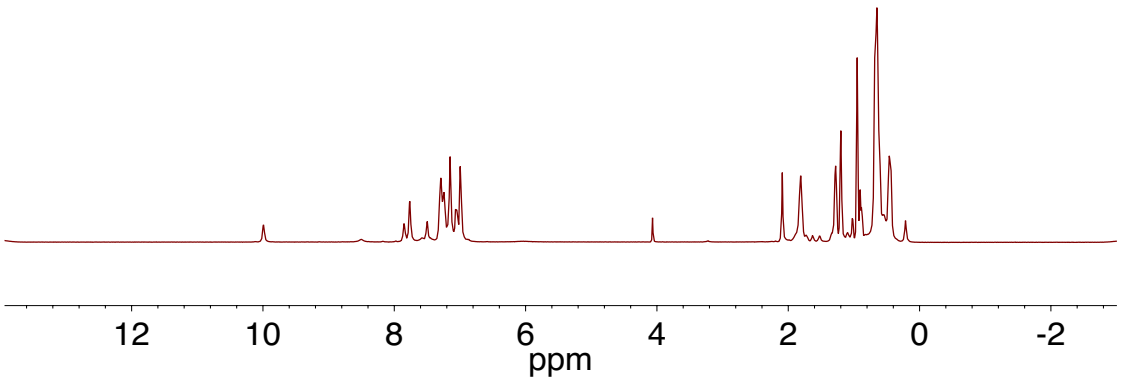

Figure 3.3.5.5. ^{1}H NMR spectrum of **[Au(B_2P_2)]OH** recorded at 600 MHz in toluene-d_8 at –45 °C.

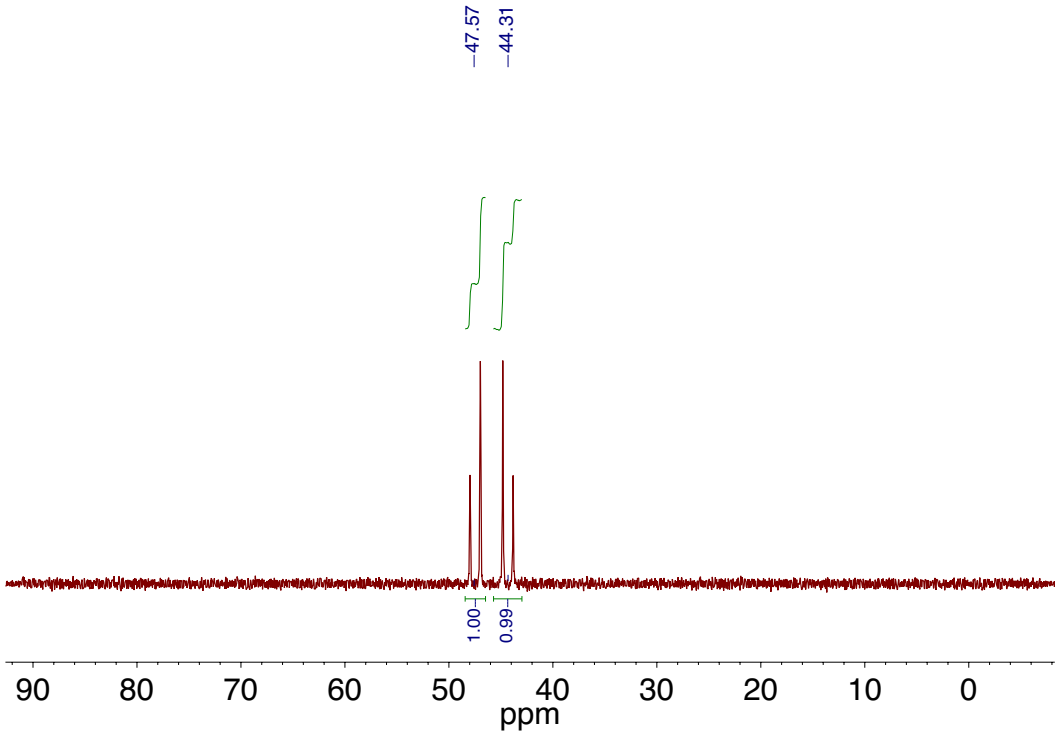

Figure 3.3.5.6. ^{31}P NMR spectrum of **[Au(B_2P_2)]OH** recorded at 242 MHz in toluene-d_8 at –45 °C.

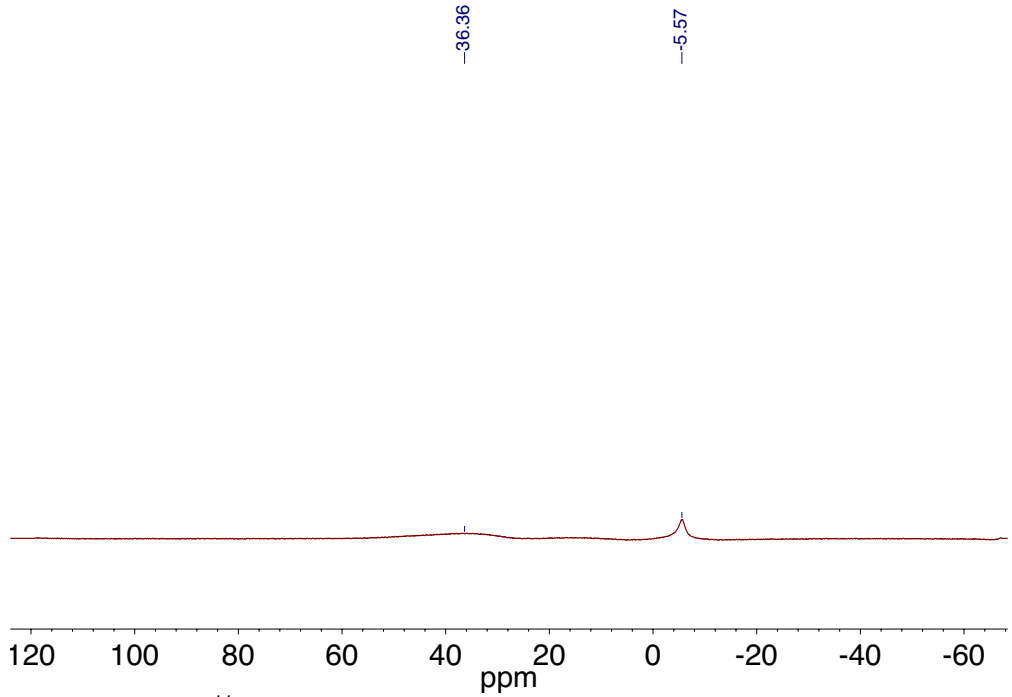

Figure 3.3.5.7. ^{11}B NMR spectrum of **[Au(B_2P_2)]OH** recorded at 242 MHz in toluene-d_8 at –45° C.

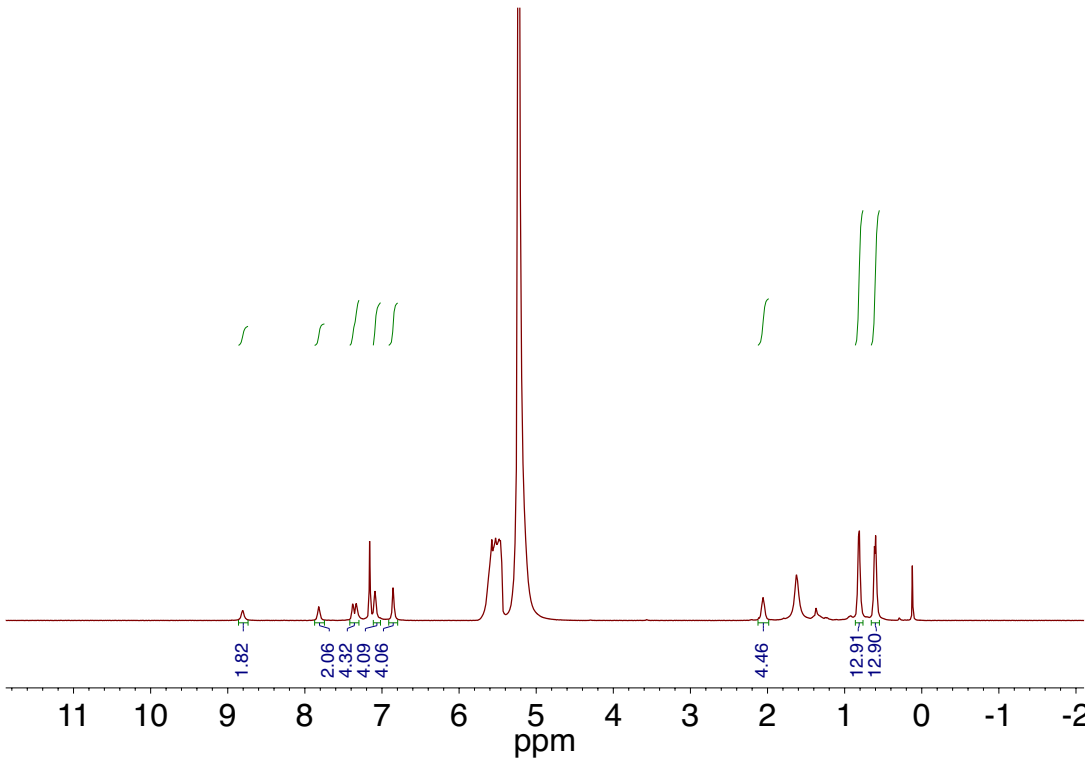

Figure 3.3.5.8. ^{1}H NMR spectrum of **[Au(B$_2$P$_2$)](OH)(H$_2$O)** recorded at 500 MHz in C_6D_6

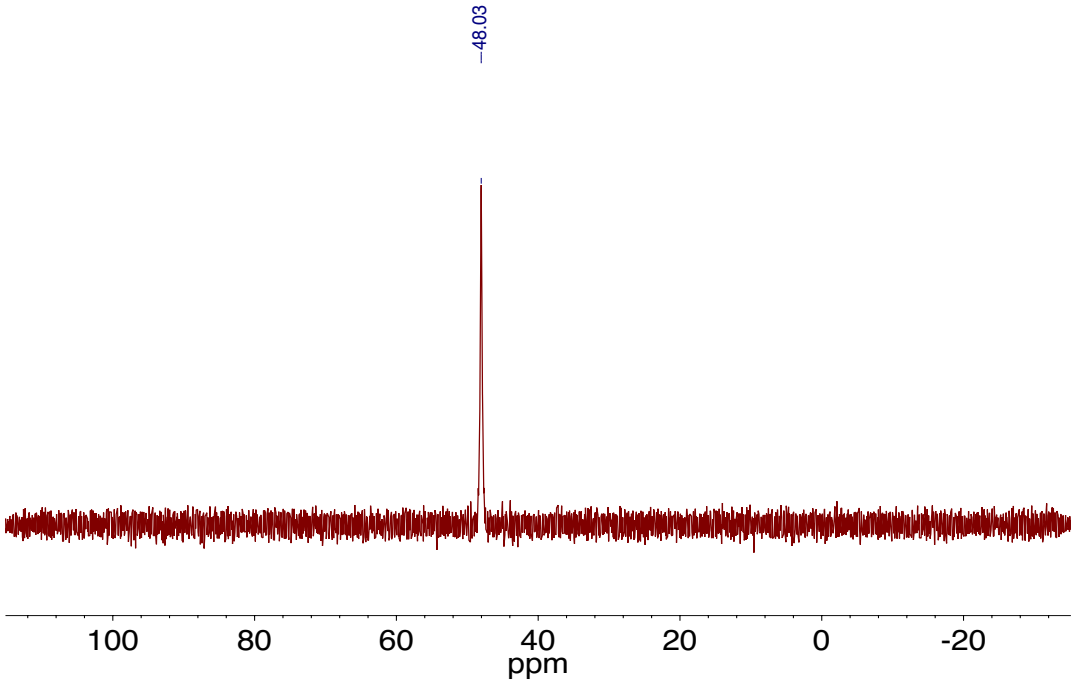

Figure 3.3.5.9. ^{31}P NMR spectrum of **[Au(B$_2$P$_2$)](OH)(H$_2$O)** recorded at 162 MHz in C_6D_6.

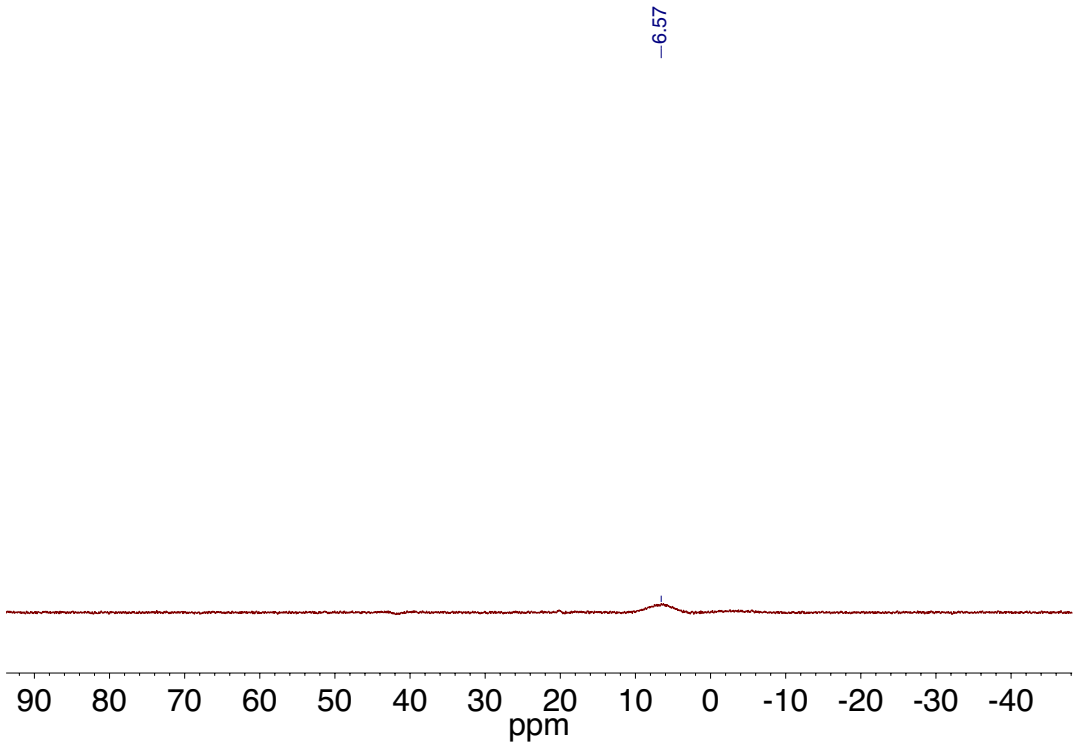

Figure 3.3.5.10. ^{11}B NMR spectrum of **[Au(B$_2$P$_2$)](OH)(H$_2$O)** recorded at 128 MHz in C_6D_6.

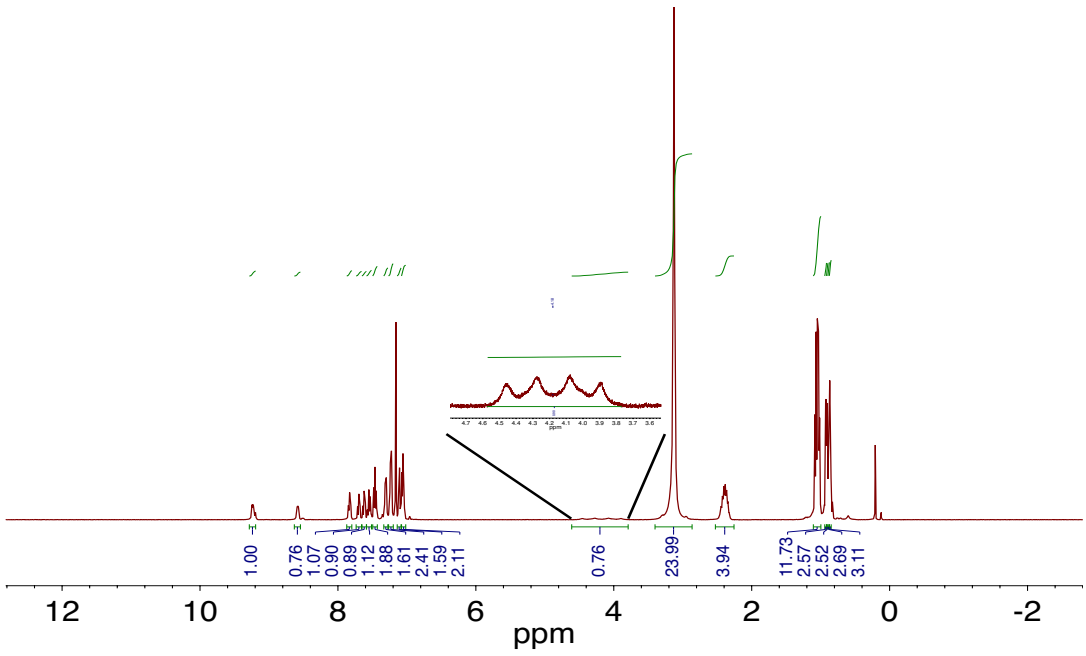

Figure 3.3.5.11. ^{1}H NMR spectrum of **[Au(B$_2$P$_2$)(H)(OH)][K(18-c-6)]** recorded at 400 MHz in C_6D_6.

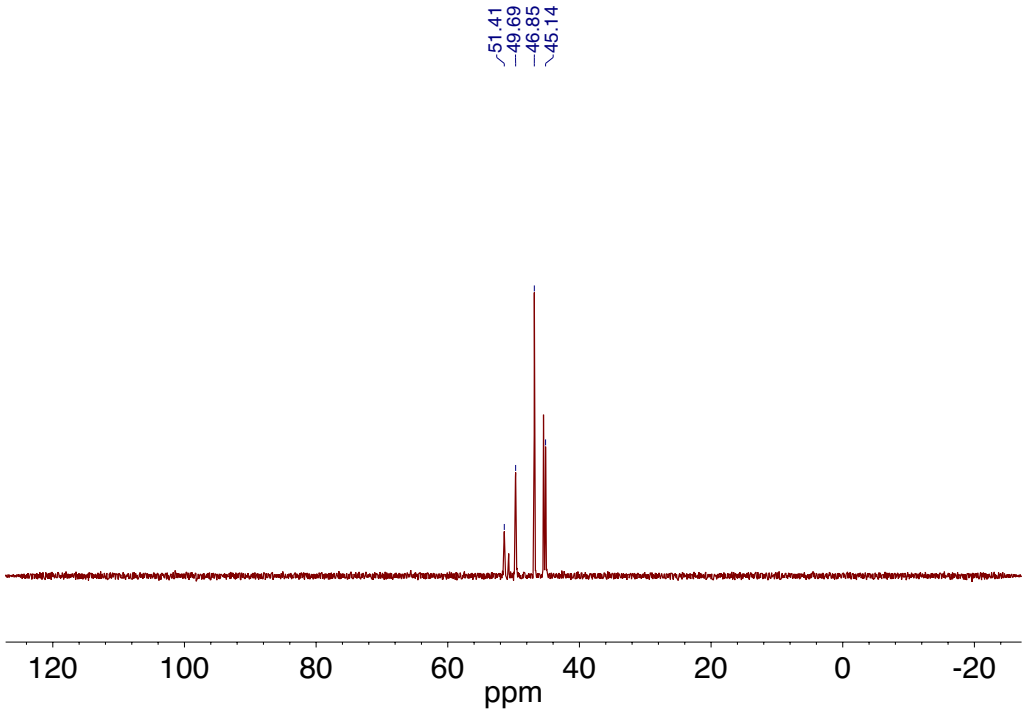

Figure 3.3.5.12. ^{31}P NMR spectrum of **[Au(B_2P_2)(H)(OH)][K(18-c-6)]** recorded at 162 MHz in C_6D_6.

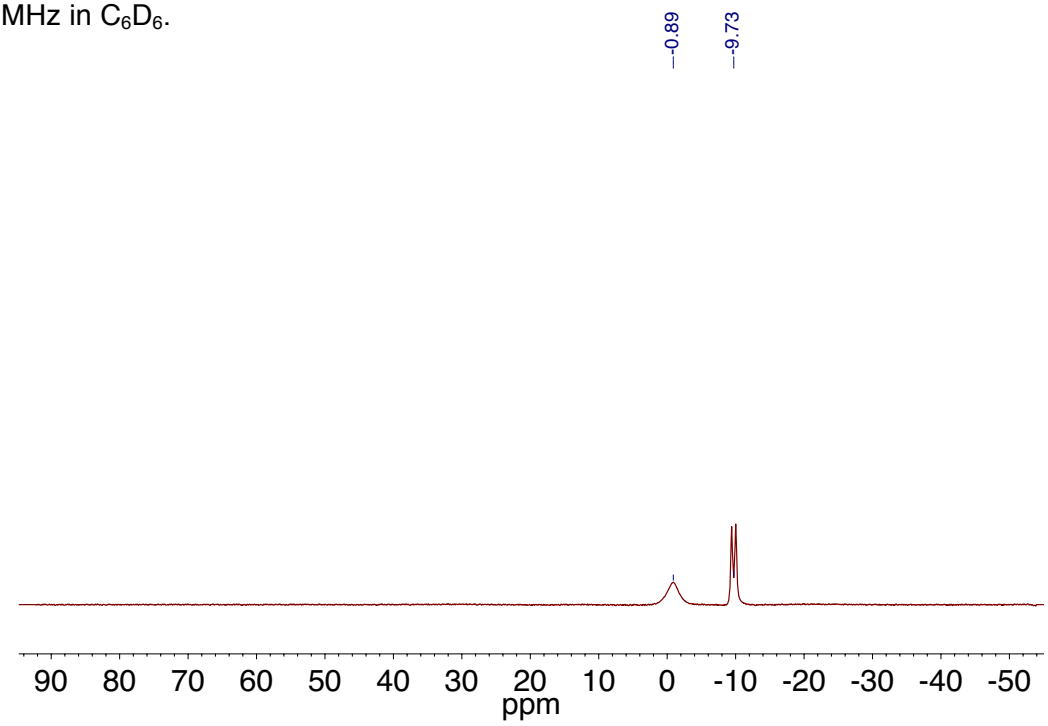

Figure 3.3.5.13. ^{11}B NMR spectrum of **[Au(B_2P_2)(H)(OH)][K(18-c-6)]** recorded at 128 MHz in C_6D_6.

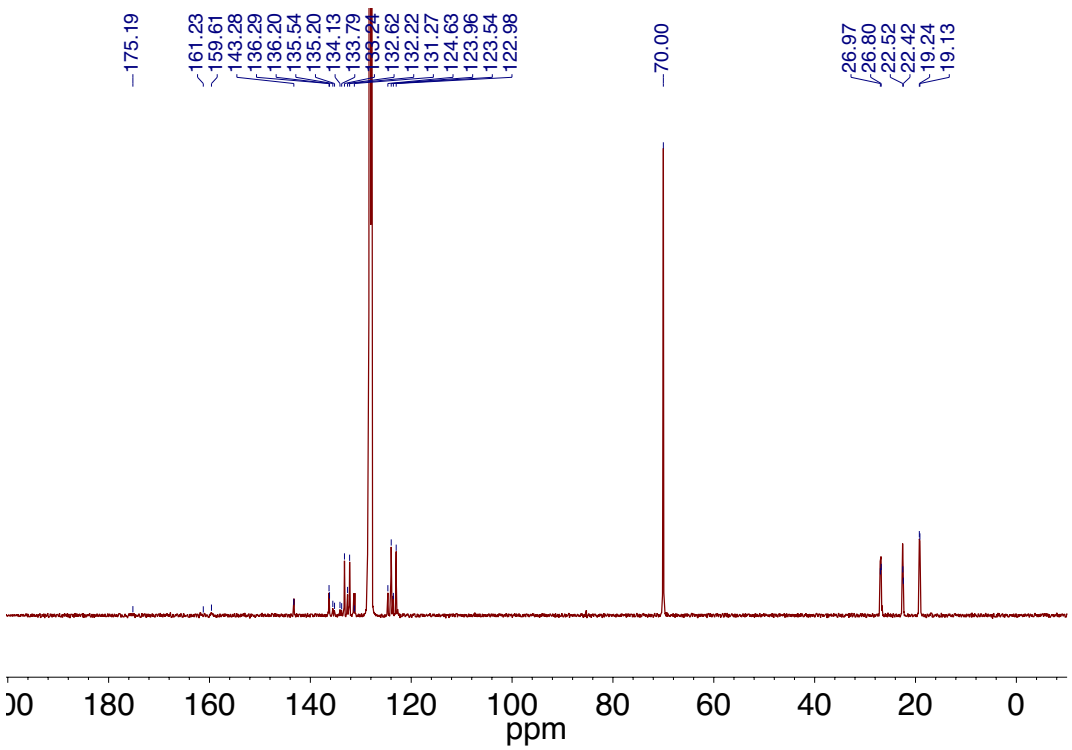

Figure 3.3.5.14. ^{13}C NMR spectrum of **[Au(B_2P_2)(H)(OH)][K(18-c-6)]** recorded at 151 MHz in C_6D_6.

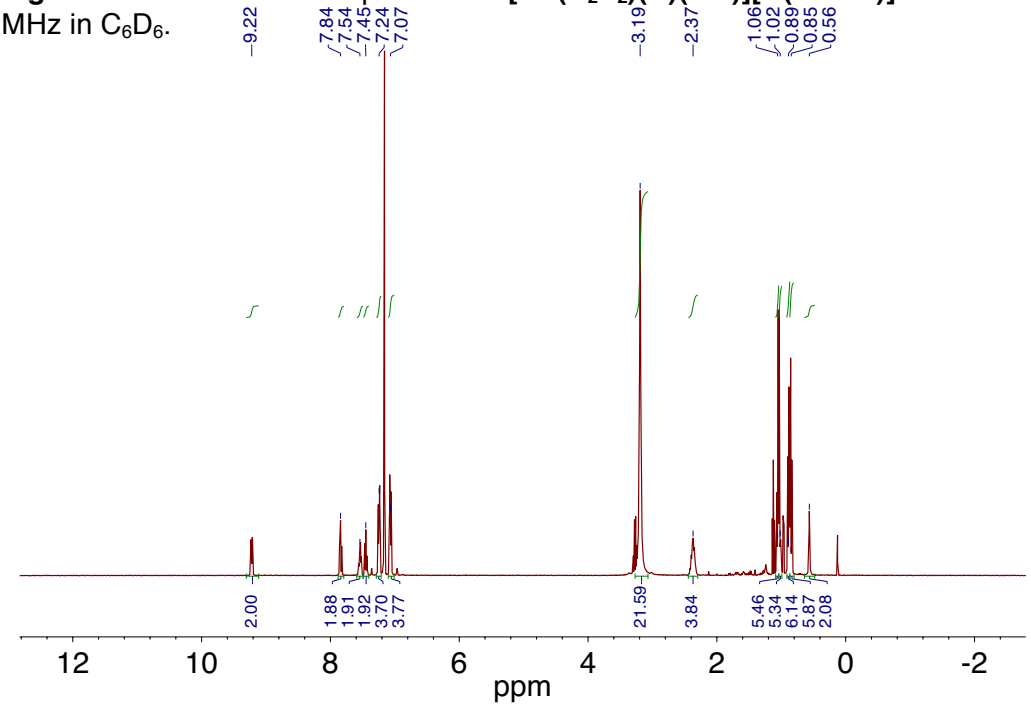

Figure 3.3.5.15. ^{1}H NMR spectrum of **[Au(B_2P_2)$(OH)_2$][K(18-c-6)]** recorded at 126 MHz in C_6D_6.

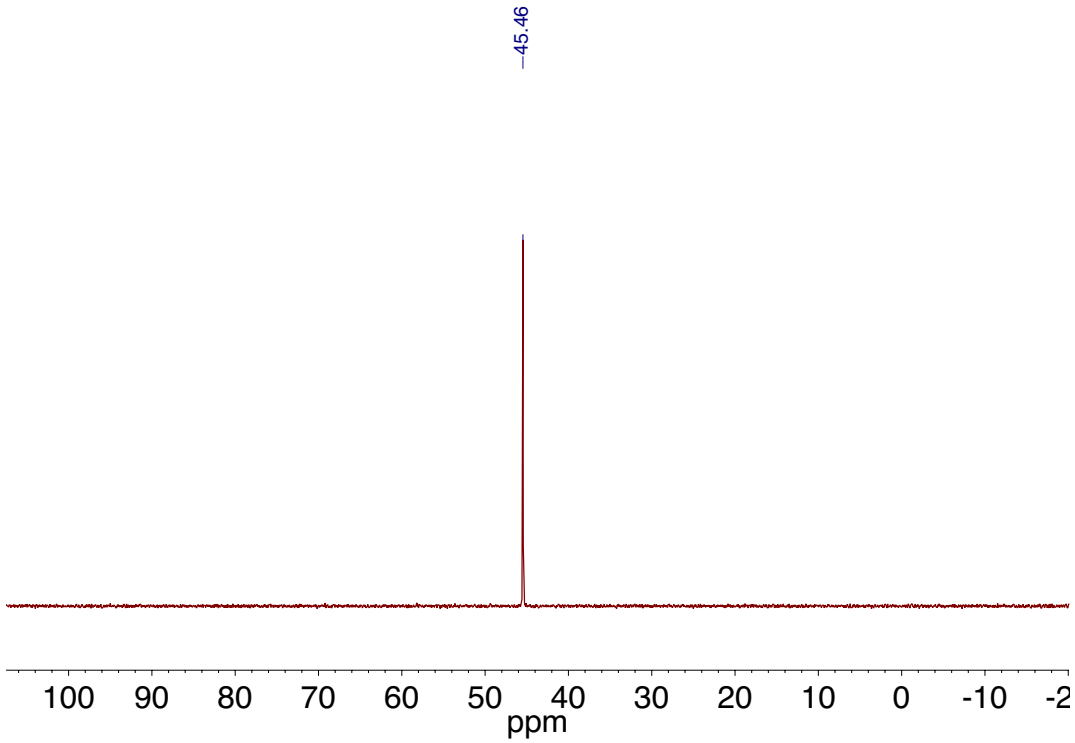

Figure 3.3.5.16. ^{31}P NMR spectrum of **[Au(B$_2$P$_2$)(OH)$_2$][K(18-c-6)]** recorded at 202 MHz in C_6D_6.

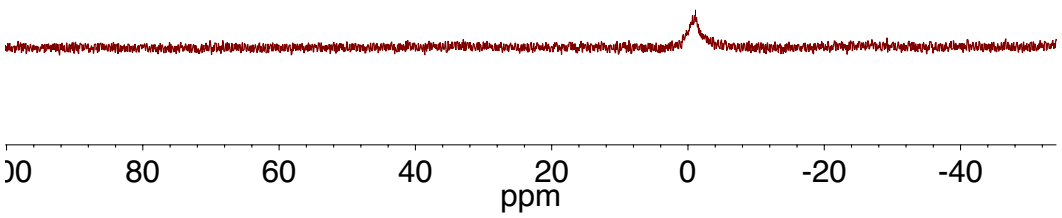

Figure 3.3.5.17. ^{11}B NMR spectrum of **[Au(B$_2$P$_2$)(OH)$_2$][K(18-c-6)]** recorded at 128 MHz in C_6D_6.

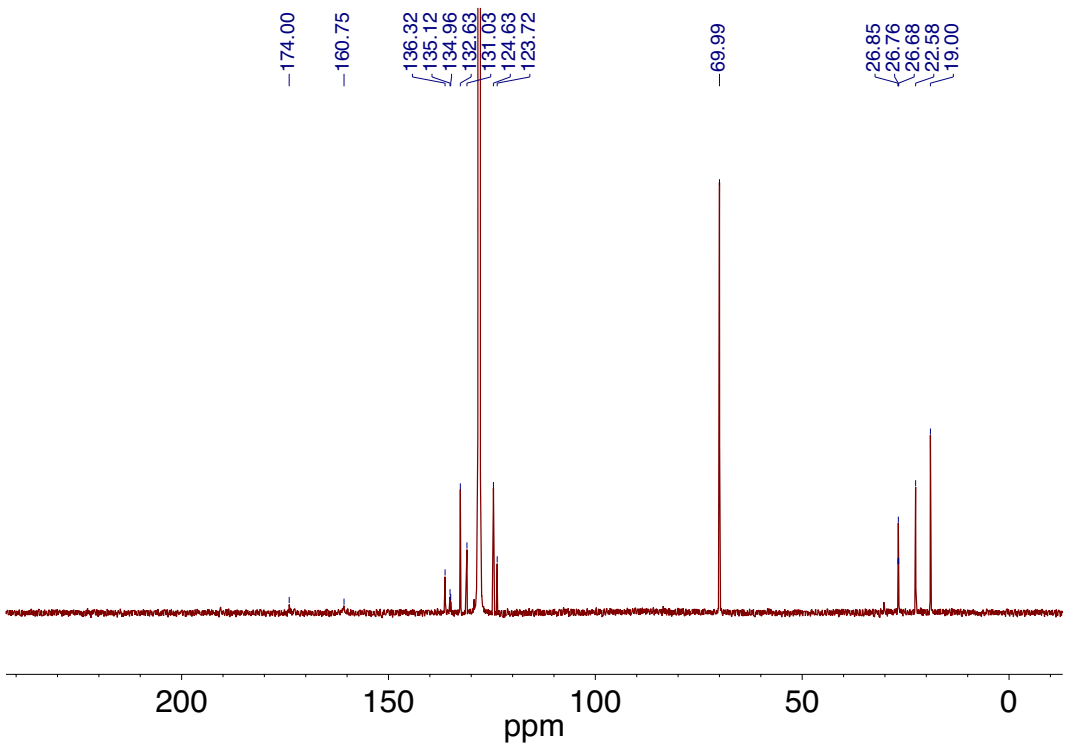

Figure 3.3.5.18. ^{13}C NMR spectrum of **[Au(B_2P_2)$(OH)_2$][K(18-c-6)]** recorded at 151 MHz in C_6D_6

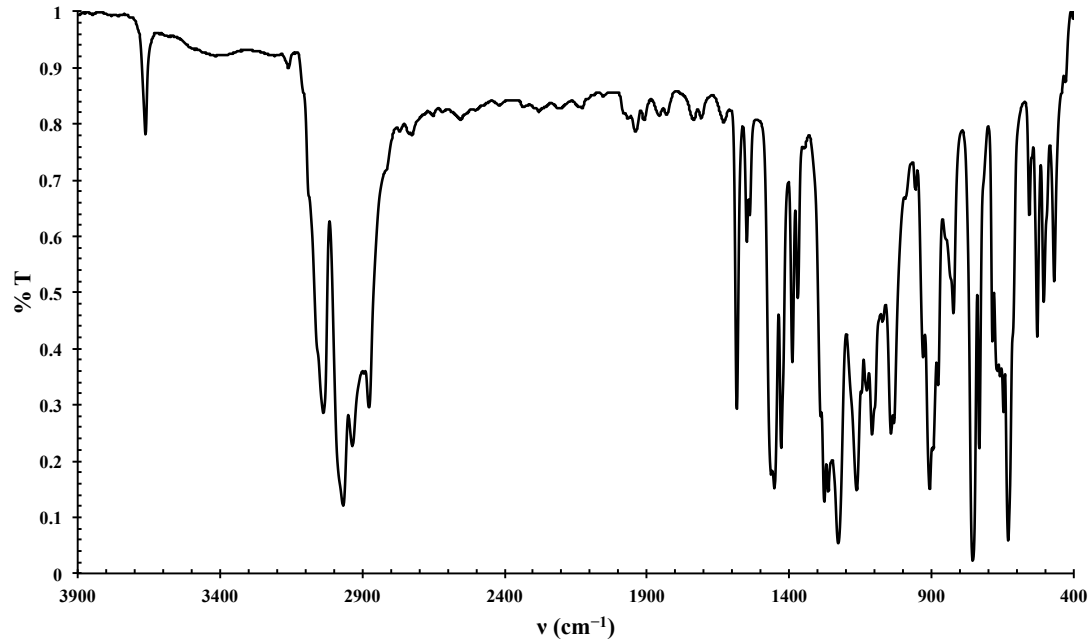

Figure 3.3.5.19. FT-IR spectrum of **[Au(B_2P_2)]OH**.

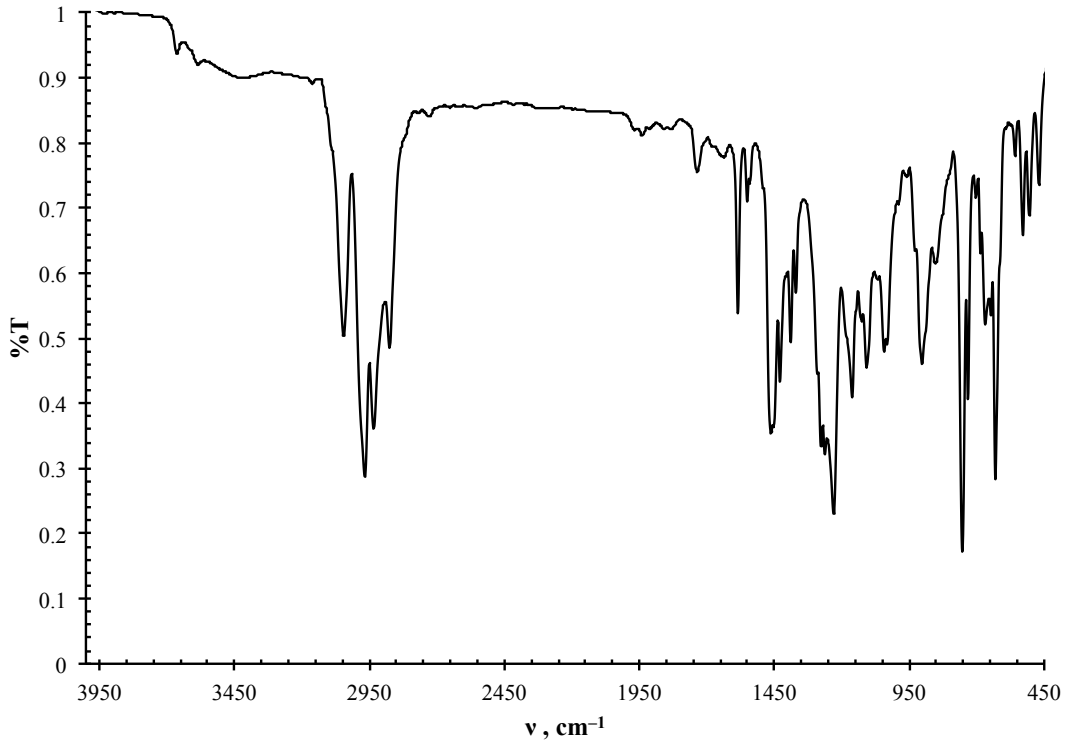

Figure 3.3.5.20. FT-IR spectrum of **[Au(B_2P_2)(H)(OH)][K(18-c-6)].**

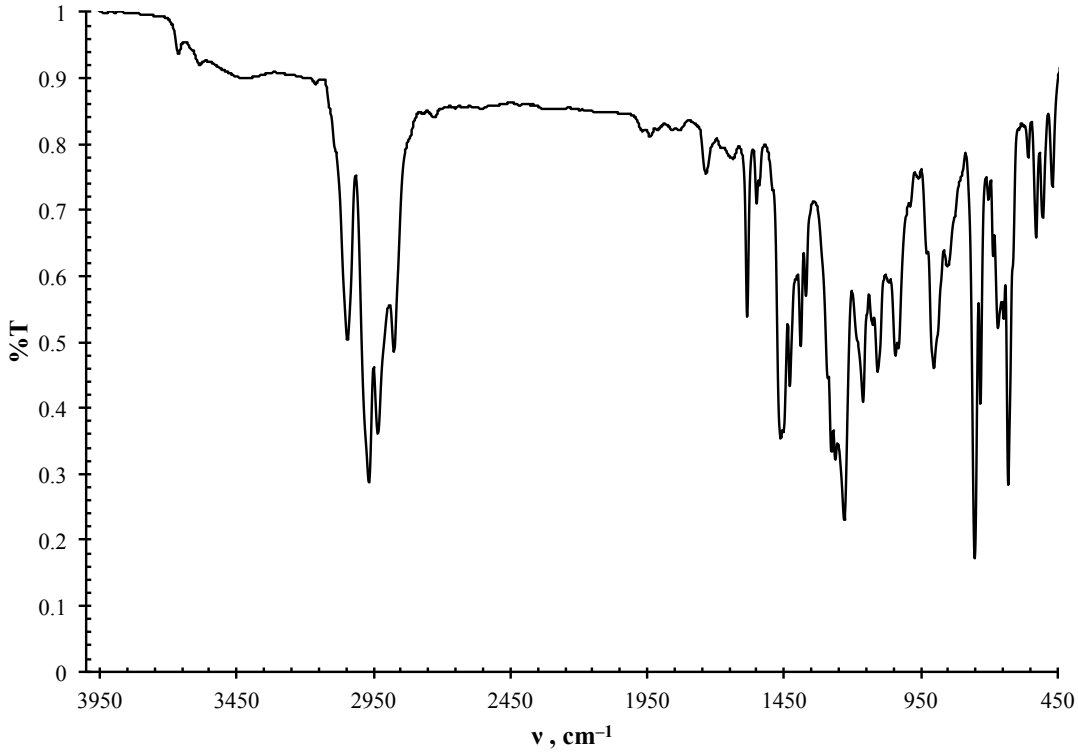

Figure 3.3.5.21. FT-IR spectrum of **[Au(B_2P_2)$(OH)_2$][K(18-c-6)].**

3.3.6.) Computational Analysis

3.3.6.1) General Considerations

Variable temperature dynamic exchange constants were simulated using Spinworks (V4.2.0, Copyright © 2015, Kirk Marat, University of Manitoba) with the DNMR3 simulation module.[27] Exchange rates were computationally fit to the data prior to compiling in the Eyring plot.

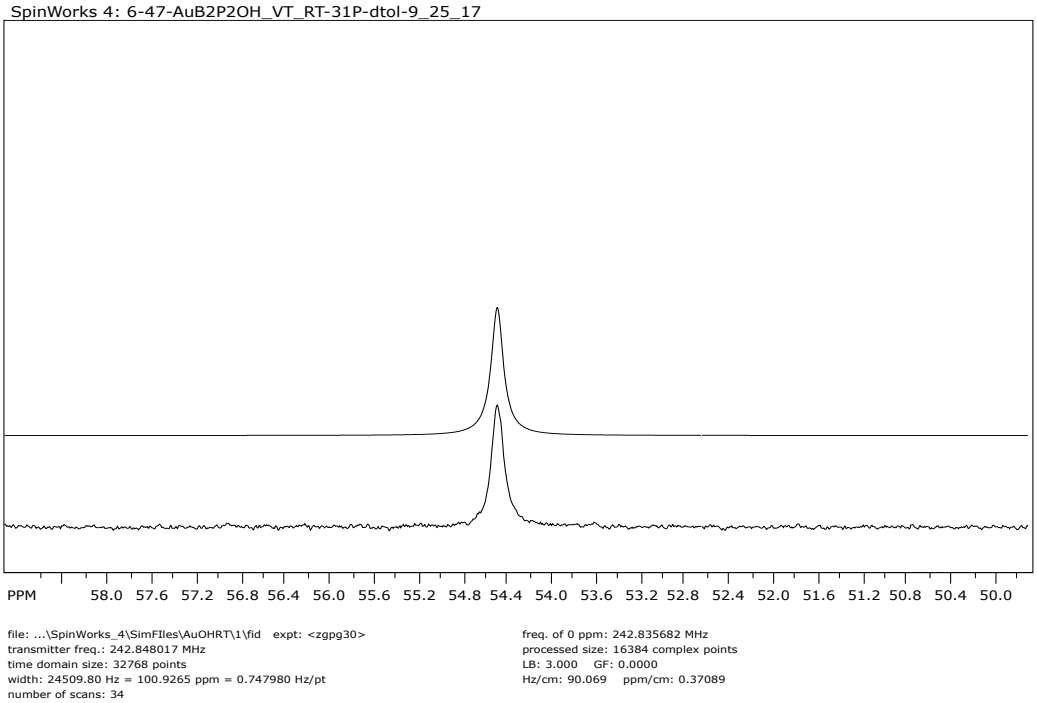

Figure 3.3.6.1. VT-^{31}P NMR spectrum of **[Au(B_2P_2)]OH** (bottom) recorded at 242 MHz in toluene-d_8 at 25 °C and its simulation (top).

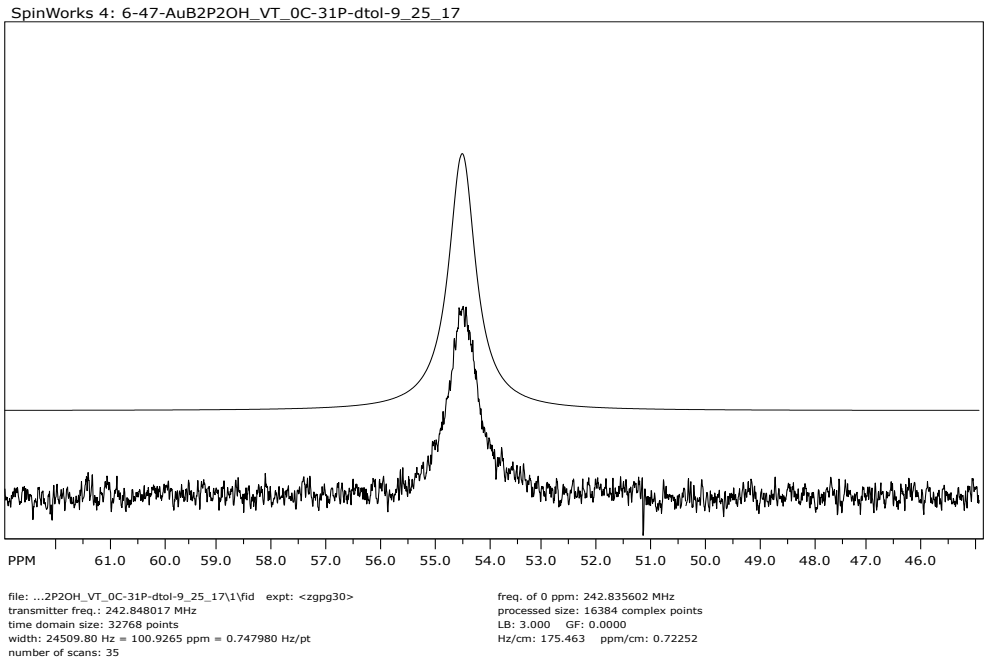

Figure 3.3.6.2. VT-^{31}P NMR spectrum of **[Au(B$_2$P$_2$)]OH** (bottom) recorded at 242 MHz in toluene-d_8 at 0 °C and its simulation (top).

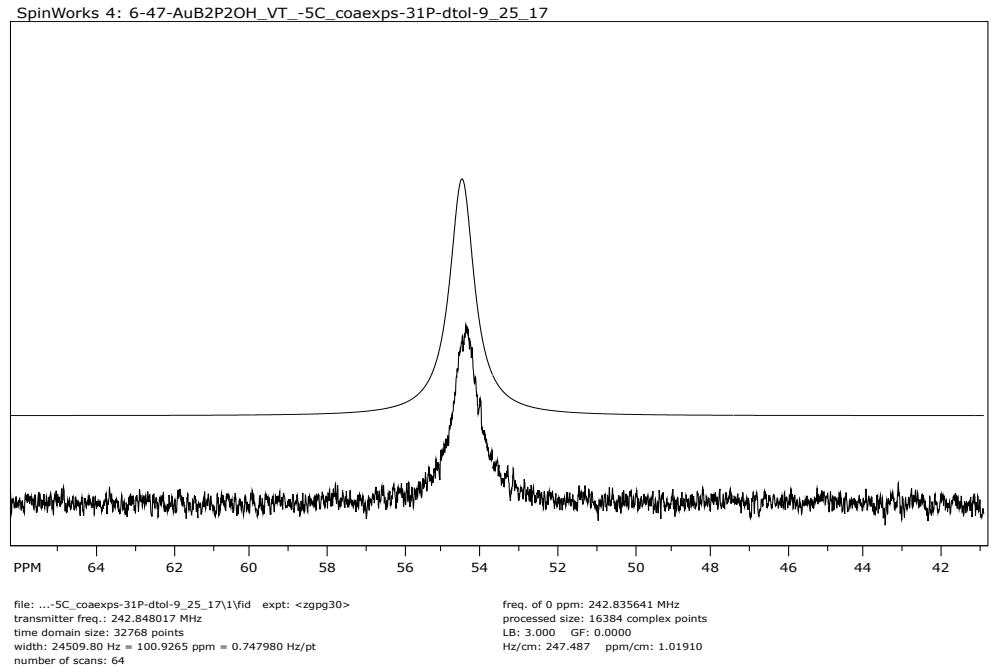

Figure 3.3.6.3. VT-^{31}P NMR spectrum of **[Au(B$_2$P$_2$)]OH** (bottom) recorded at 242 MHz in toluene-d_8 at –5 °C and its simulation (top).

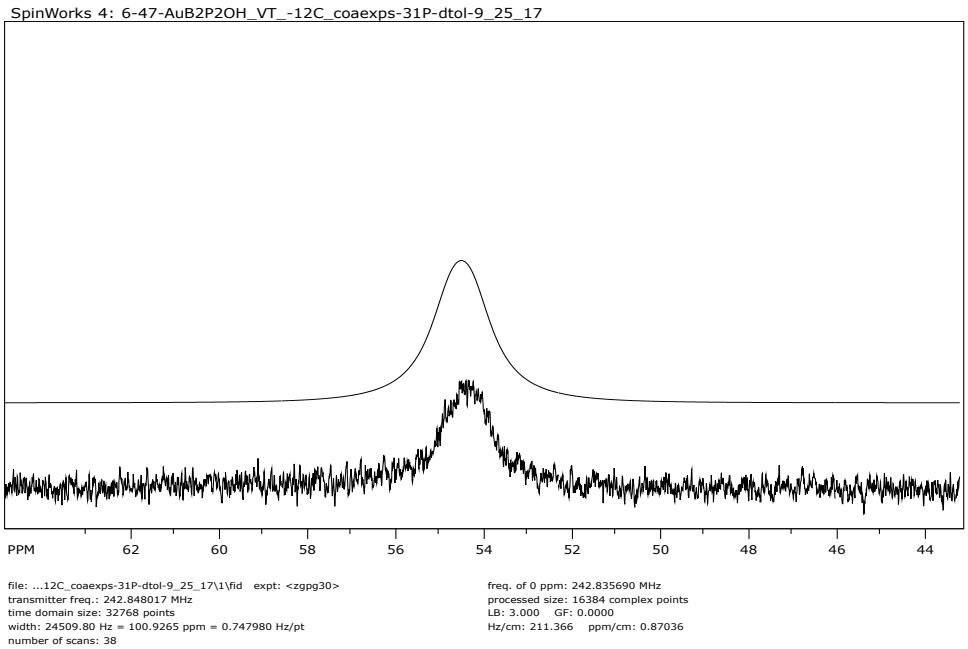

Figure 3.3.6.4. VT-^{31}P NMR spectrum of **[Au(B$_2$P$_2$)]OH** (bottom) recorded at 242 MHz in toluene-d_8 at –12 °C and its simulation (top).

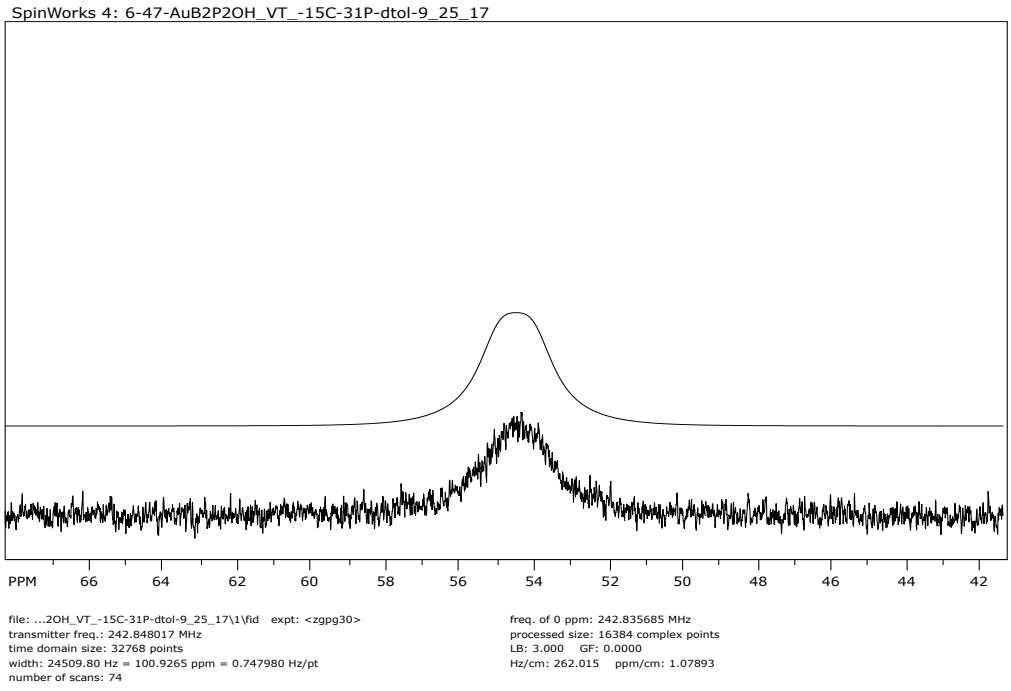

Figure 3.3.6.5. VT-^{31}P NMR spectrum of **[Au(B$_2$P$_2$)]OH** (bottom) recorded at 242 MHz in toluene-d_8 at –15 °C and its simulation (top).

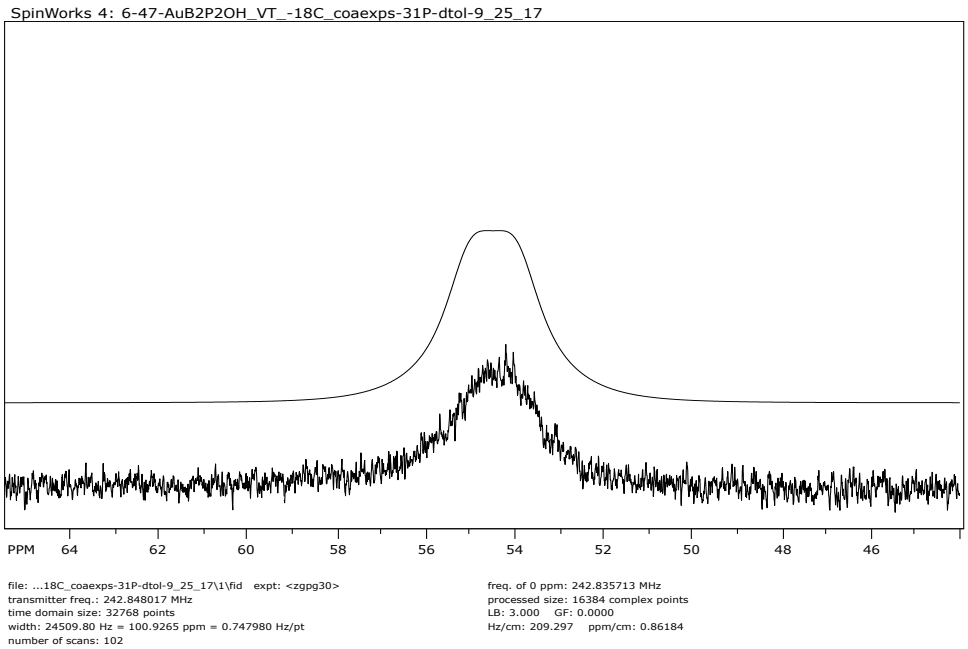

Figure 3.3.6.6. VT-^{31}P NMR spectrum of **[Au(B$_2$P$_2$)]OH** (bottom) recorded at 242 MHz in toluene-d_8 at –18 °C and its simulation (top).

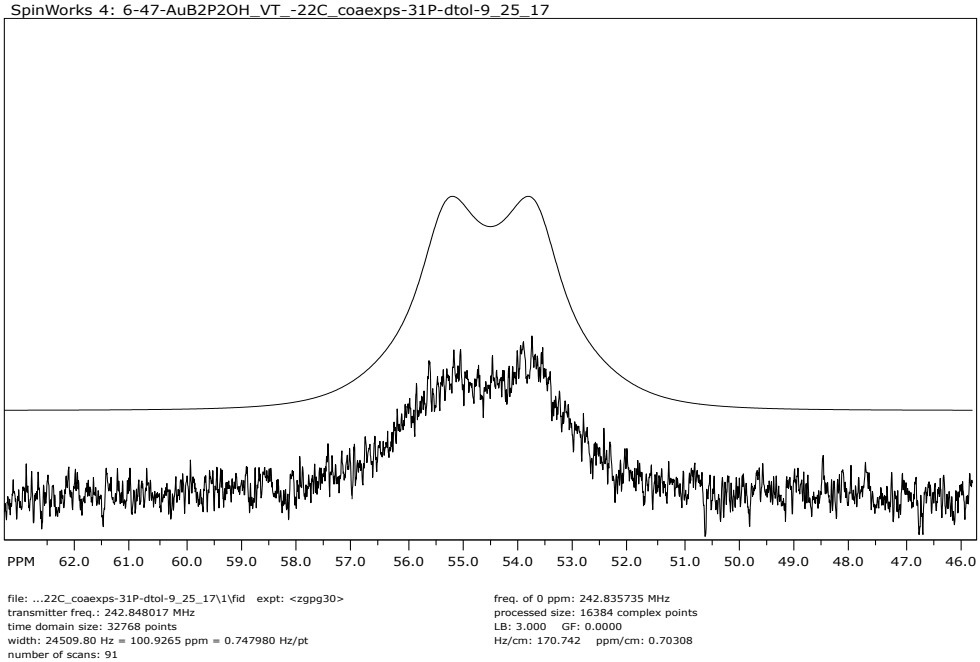

Figure 3.3.6.7. VT-^{31}P NMR spectrum of **[Au(B$_2$P$_2$)]OH** (bottom) recorded at 242 MHz in toluene-d_8 at –22 °C and its simulation (top).

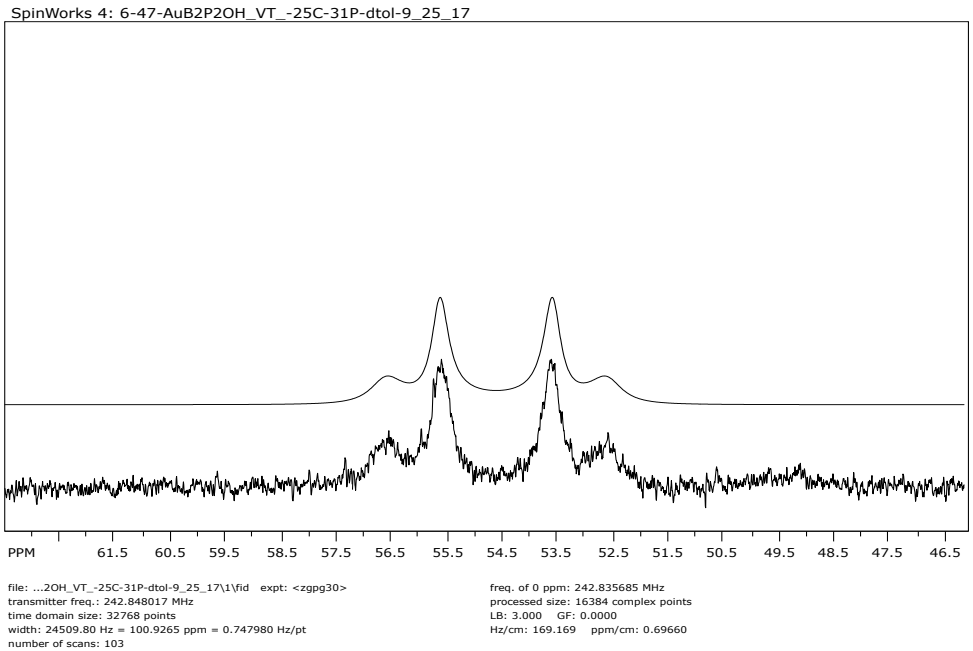

Figure 3.3.6.8. VT-^{31}P NMR spectrum of **[Au(B_2P_2)]OH** (bottom) recorded at 242 MHz in toluene-d_8 at –25 °C and its simulation (top)

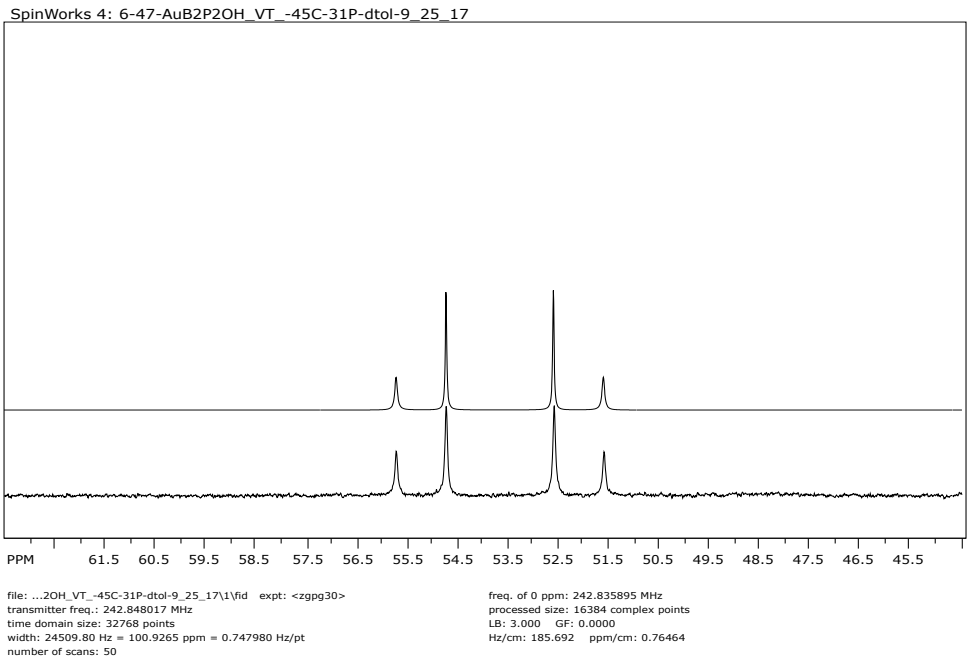

Figure 3.3.6.9. VT-^{31}P NMR spectrum of **[Au(B_2P_2)]OH** (bottom) recorded at 242 MHz in toluene-d_8 at –45 °C and its simulation (top).

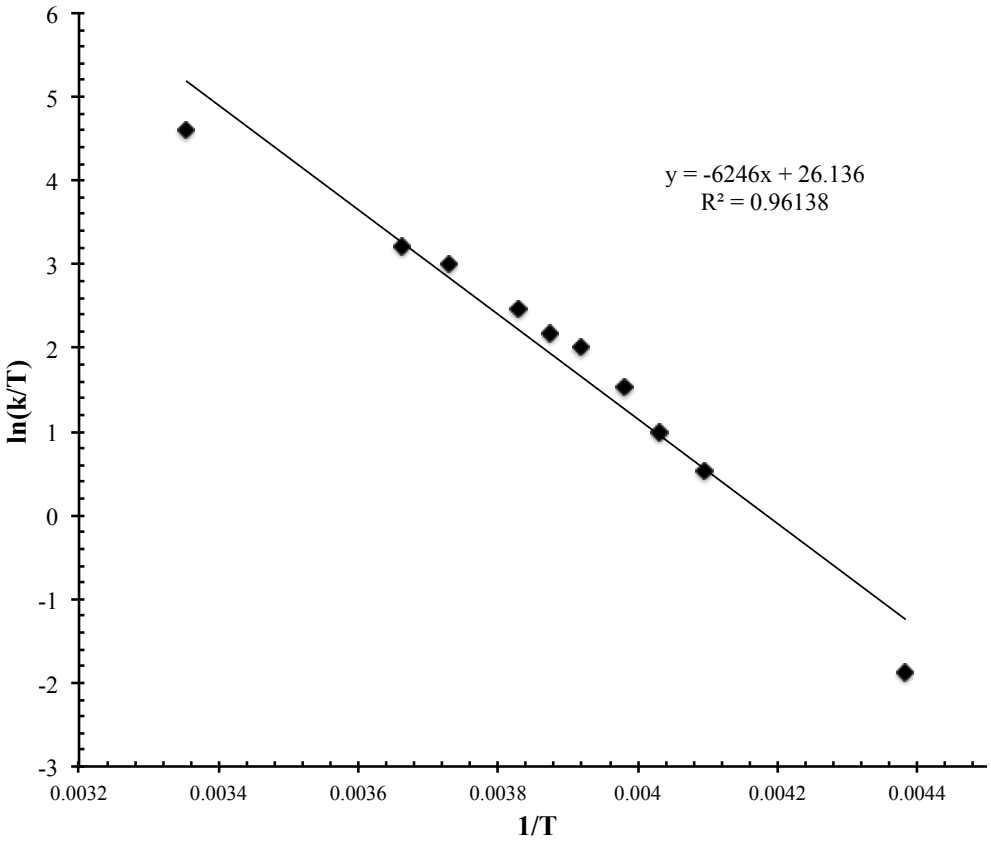

Figure 3.3.6.10. Eyring plot constructed from the simulated rates calculated from VT-^{31}P NMR measurements of **1** in toluene-d_8. The slope, intercept and R^2 value are inlayed and were used to extract thermal parameters of activation.

3.3.7) X-Ray Crystallography

3.3.7.1) General Considerations

Single crystals were coated with paratone oil and mounted on cryo-loop glass fibers. X-ray intensity data were collected at 100(2) K on a Bruker APEX2[28] platform-CCD X-ray diffractometer system using fine-focus Mo K_α radiation (λ = 0.71073 Å, 50kV/30mA power). The CCD detector was placed at 5.0600 cm from the crystal. Frames were integrated using the Bruker SAINT software package[29] and using a narrow-frame integration algorithm. Absorption corrections were

applied to the raw intensity data using the SADABS program.[30] The Bruker SHELXTL software package[31] was used for phase determination and structure refinement. Atomic coordinates, isotropic and anisotropic displacement parameters of all the non-hydrogen atoms were refined by means of a full matrix least-squares procedure on F^2. The H-atoms were included in the refinement in calculated positions riding on the atoms to which they were attached. Relevant details for individual data collections are reported in Tables 3.3.7.1–3.3.7.4.

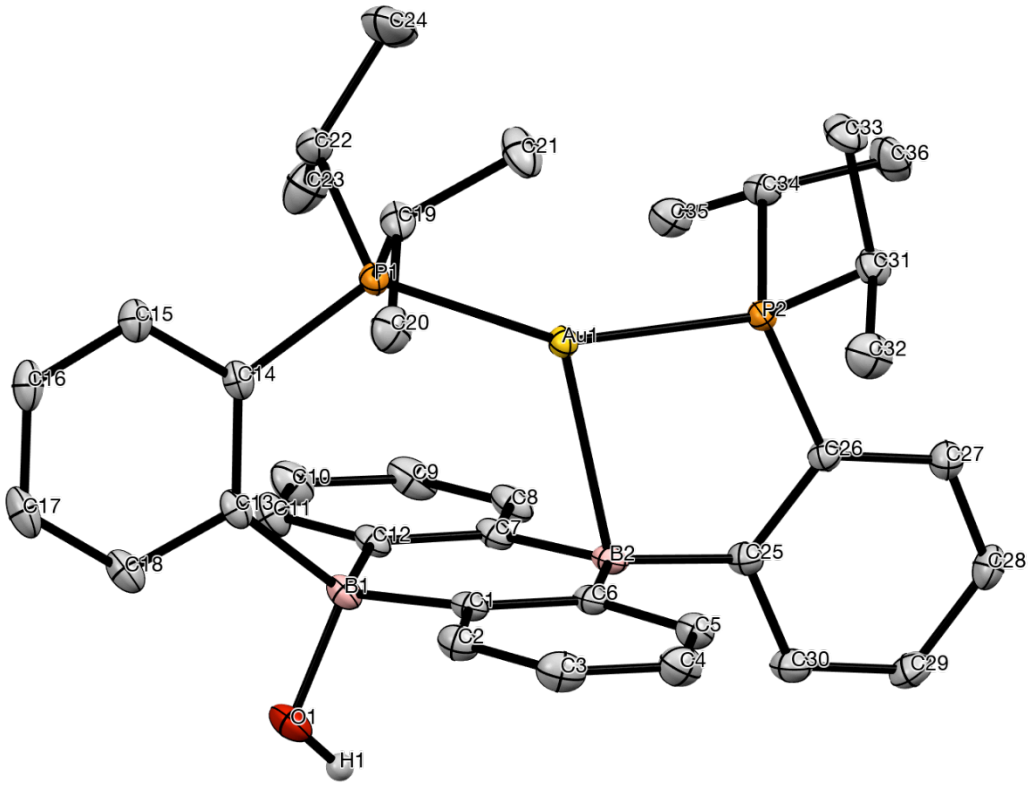

Figure 3.3.7.1. Labelled thermal ellipsoid plot (50%) for **[Au(B_2P_2)]OH**.

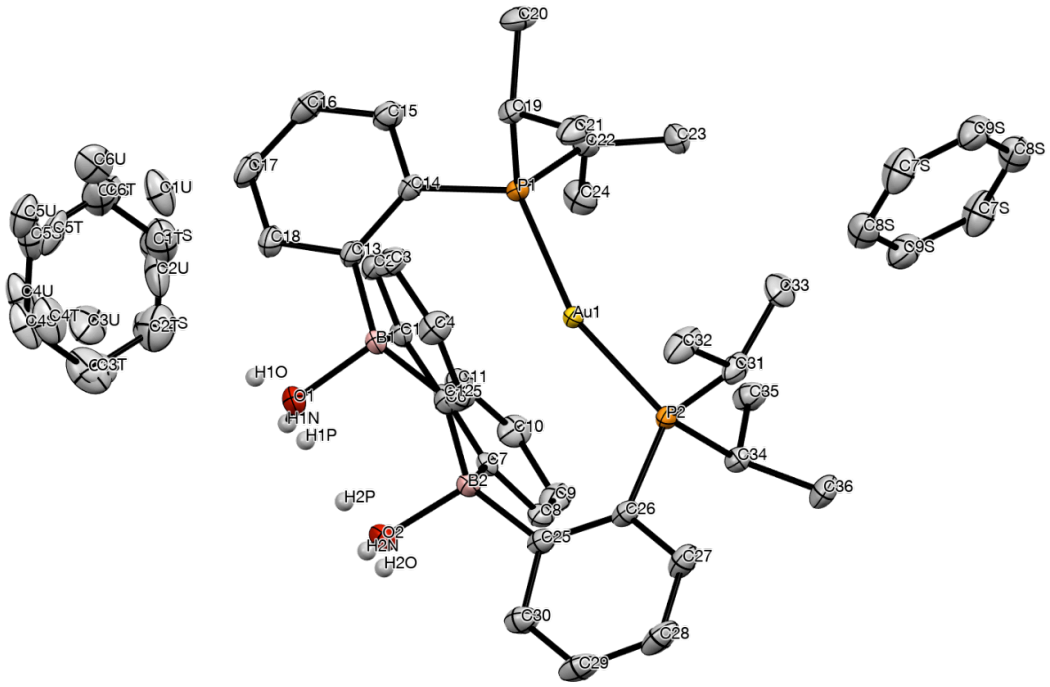

Figure 3.3.7.2. Labelled thermal ellipsoid plot (50%) for **[Au(B_2P_2)](OH)(H_2O)**.

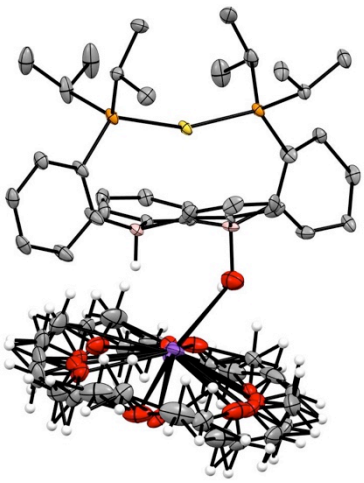

Figure 3.3.7.3. Labelled thermal ellipsoid plot (30%) for **[Au(B_2P_2)(H)(OH)][K(18-c-6)]**.

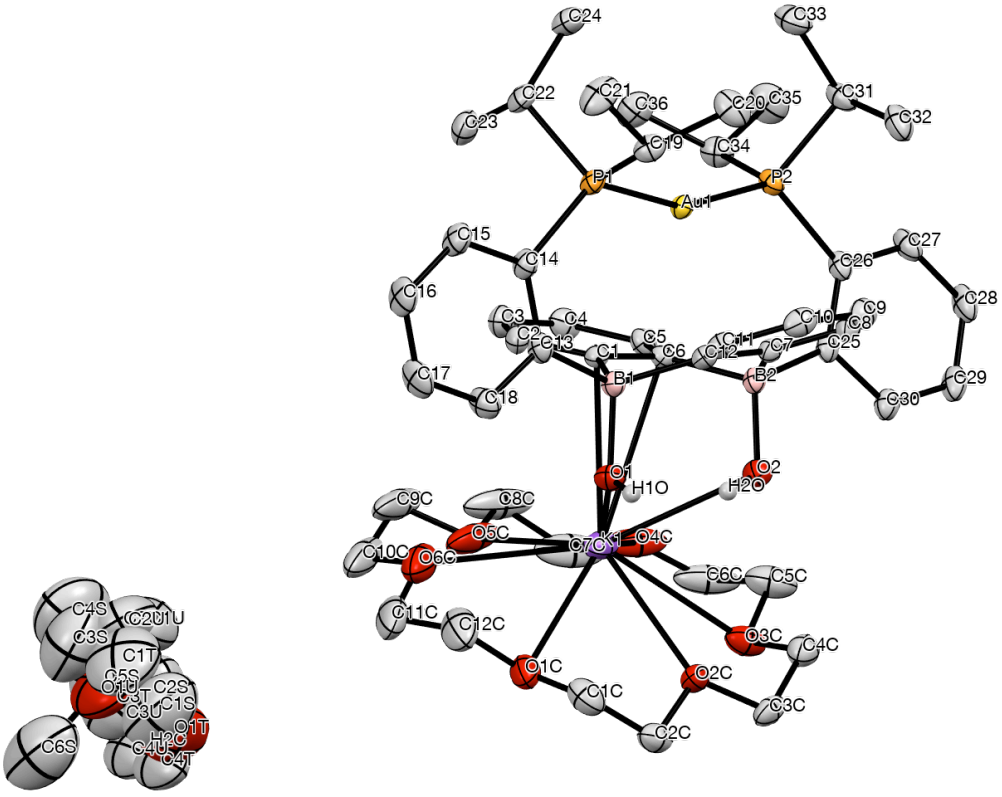

Figure 3.3.7.4. Labelled thermal ellipsoid plot (50%) for **[Au(B_2P_2)$(OH)_2$][K(18-c-6)]**.

Table 3.3.7.1. Crystal data and structure refinement for **[Au(B_2P_2)]OH** (**1**).

Identification code	hh246JT122r_0m	
Empirical formula	$C_{36}H_{45}AuB_2OP_2$	
Formula weight	774.24 g/mol	
Temperature	100(2) K	
Wavelength	0.71073 Å	
Crystal system	Orthorhombic	
Space group	P b c a	
Unit cell dimensions	a = 19.5549(3) Å	α = 90°.
	b = 17.1275(3) Å	β = 90°.
	c = 19.6848(3) Å	γ = 90°.
Volume	6592.96(18) $Å^3$	
Z	8	
Density (calculated)	1.560 mg/m^3	
Absorption coefficient	4.588 mm^{-1}	
F(000)	3104	
Crystal size	0.368 x 0.302 x 0.198 mm^3	
θ range for data collection	1.889 to 30.506°.	
Index ranges	$-27 \le h \le 27$, $-24 \le k \le 24$, $-28 \le l \le 28$	
Reflections collected	236655	
Independent reflections	10069 [R_{int} = 0.0290]	
Completeness to θ = 25.242°	100.0 %	
Absorption correction	Semi-empirical from equivalents	
Refinement method	Full-matrix least-squares on F^2	
Data / restraints / parameters	10069 / 0 / 388	
Goodness-of-fit on F^2	1.053	
Final R indices [$I > 2\sigma_I$]	R_1 = 0.0148, wR_2 = 0.0344	
R indices (all data)	R_1 = 0.0203, wR_2 = 0.0369	
Largest diff. peak and hole	0.733 and –0.305 e/$Å^3$	

Table 3.3.7.2. Crystal data and structure refinement for [**Au(B_2P_2)](OH)(H_2O)** (**1-H_2O**).

Identification code	hh207JT102_0m	
Empirical formula	$C_{53}H_{81}AuB_2KO_{8.50}P_2$	
Formula weight	1173.80 g/mol	
Temperature	100(2) K	
Wavelength	0.71073 Å	
Crystal system	Monoclinic	
Space group	P 21/n	
Unit cell dimensions	a = 12.4601(4) Å	α = 90°.
	b = 27.1704(10) Å	β = 94.0898(6)°.
	c = 16.4408(6) Å	γ = 90°.
Volume	5551.8(3) Å^3	
Z	4	
Density (calculated)	1.404 mg/m^3	
Absorption coefficient	2.833 mm^{-1}	
F(000)	2420	
Crystal size	0.425 x 0.339 x 0.115 mm^3	
θ range for data collection	1.499 to 29.130°.	
Index ranges	$-17 \le h \le 17$, $-37 \le k \le 37$, $-22 \le l \le 22$	
Reflections collected	121598	
Independent reflections	14933 [R_{int} = 0.0320]	
Completeness to θ = 25.242°	100.0 %	
Absorption correction	Semi-empirical from equivalents	
Refinement method	Full-matrix least-squares on F^2	
Data / restraints / parameters	14933 / 472 / 700	
Goodness-of-fit on F^2	1.055	
Final R indices [$I > 2\sigma_I$]	R_1 = 0.0213, wR_2 = 0.0479	
R indices (all data)	R_1 = 0.0264, wR_2 = 0.0498	
Largest diff. peak and hole	0.815 and –1.115 e/Å^3	

Table 3.3.7.3. Crystal data and structure refinement for **[Au(B_2P_2)(H)(OH)][K(18-c-6)]** (**2**).

Identification code	hh264JT130	
Empirical formula	$C_{48}H_{69.47}AuB_2KO_{7.53}P_2$	
Formula weight	1086.53 g/mol	
Temperature	100(2) K	
Wavelength	0.71073 Å	
Crystal system	Triclinic	
Space group	P–1	
Unit cell dimensions	a = 11.5721(3) Å	α = 77.4593(5)°.
	b = 13.3494(4) Å	β = 77.1738(5)°.
	c = 17.4347(5) Å	γ = 68.9764(5)°.
Volume	2423.17(12) $Å^3$	
Z	2	
Density (calculated)	1.489 mg/m^3	
Absorption coefficient	3.237 mm^{-1}	
F(000)	1111	
Crystal size	0.442 x 0.355 x 0.336 mm^3	
θ range for data collection	1.653 to 28.282°	
Index ranges	$-15 \le h \le 15$, $-17 \le k \le 17$, $-23 \le l \le 23$	
Reflections collected	84102	
Independent reflections	12016 [R_{int} = 0.0197]	
Completeness to θ = 25.242°	99.9 %	
Absorption correction	Semi-empirical from equivalents	
Refinement method	Full-matrix least-squares on F^2	
Data / restraints / parameters	12016 / 1216 / 923	
Goodness-of-fit on F^2	1.076	
Final R indices [$I > 2\sigma_I$]	R_1 = 0.0141, wR_2 = 0.0355	
R indices (all data, 0.75 Å)	R_1 = 0.0148, wR_2 = 0.0357	
Largest diff. peak and hole	0.607 and –0.558 $e/Å^3$	

Table 3.3.7.4. Crystal data and structure refinement for **[Au(B_2P_2)$(OH)_2$][K(18-c-6)]** (**3**).

Identification code	hh207JT102_0m	
Empirical formula	$C_{53}H_{81}AuB_2KO_{8.50}P_2$	
Formula weight	1173.80 g/mol	
Temperature	100(2) K	
Wavelength	0.71073 Å	
Crystal system	Monoclinic	
Space group	P 21/n	
Unit cell dimensions	a = 12.4601(4) Å	α = 90°.
	b = 27.1704(10) Å	β = 94.0898(6)°.
	c = 16.4408(6) Å	γ = 90°.
Volume	5551.8(3) Å^3	
Z	4	
Density (calculated)	1.404 mg/m^3	
Absorption coefficient	2.833 mm^{-1}	
F(000)	2420	
Crystal size	0.425 x 0.339 x 0.115 mm^3	
θ range for data collection	1.499 to 29.130°.	
Index ranges	$-17 \le h \le 17$, $-37 \le k \le 37$, $-22 \le l \le 22$	
Reflections collected	121598	
Independent reflections	14933 [R_{int} = 0.0320]	
Completeness to θ = 25.242°	100.0 %	
Absorption correction	Semi-empirical from equivalents	
Refinement method	Full-matrix least-squares on F^2	
Data / restraints / parameters	14933 / 472 / 700	
Goodness-of-fit on F^2	1.055	
Final R indices [$I > 2\sigma_I$]	R_1 = 0.0213, wR_2 = 0.0479	
R indices (all data)	R_1 = 0.0264, wR_2 = 0.0498	
Largest diff. peak and hole	0.815 and –1.115 e/Å^3	

3.3.8) References

[1] A) Turner, J. A. *Science*, **2004**, *305*, 972–974. b) Muradov, N.; Veziroglu T. *Int. J. Hydrogen Energy*, **2008**, *33*, 6804–6839.

[2] a) Lewis, N. S.; Nocera, D. G. *Proc. Natl. Acad. Sci.* **2006**, *103* (43), 15729. b) Gray, H. B. *Nature* **2009**, *1* (1), 7.

[3] a) Ozerov, O. V. *Chem. Soc. Rev.* **2009**, *38* (1), 83. b) Piers, W. E. *Organometallics* **2011**, *30* (1), 13. c) Klahn, M.; Beweries, T. *Rev. Inorg. Chem.* **2014**, *34* (3), 177. d) O. Blum and D. Milstein, *J. Am. Chem. Soc.*, 2002, **124**, 11456–11467.

[4] a) Karunadasa, H. I.; Chang, C. J.; Long, J. R. *Nature* **2010**, *464* (7293), 1329. b) Gross, M. A.; Reynal, A.; Durrant, J. R.; Reisner, E. *J. Am. Chem. Soc.* **2014**, *136* (1), 356.

[5] a) Xia Z. *Nat. Energy*, **2016**, *1*, 7520. b) Zheng, Y.; Jiao, Y.; Li, L. H.; Xing, T.; Chen, Y.; Jaroniec, M.; Qiao, S. Z. *ACS Nano* **2014**, *8* (5), 5290.

[6] Chen, Y.; Yu, G.; Chen, W.; Liu, Y.; Li, G.-D.; Zhu, P.; Tao, Q.; Li, Q.; Liu, J.; Shen, X.; Li, H.; Huang, X.; Wang, D.; Asefa, T.; Zou, X. *J. Am. Chem. Soc.* **2017**, *139* (36), 12370.

[7] Rohani, P.; Kim, S.; Swihart, M. T. *Adv. Energy Mater.* **2016**, *6* (12).
[8] a) Xu, W.; Chen, C.; Tang, C.; Li, Y.; Xu, L. *Sci. Rep.* **2018**, *8* (1). b) Rao, C. N. R.; Chhetri, M. *Adv. Mater. Weinheim* **2018**, *54*, e1803668. c) Grotthuss, von, E.; John, A.; Kaese, T.; Wagner, M. *A. J. Org. Chem.* **2017**, *7* (1), 37.

[9] a) Zou, X.; Zhang, Y. *Chem. Soc. Rev.* **2015**, *44* (15), 5148. b) Hisatomi, T.; Kubota, J.; Domen, K. *Chem. Soc. Rev.* **2014**, *43* (22), 7520.

[10] a) Chu, T.; Nikonov, G. I. *Chem. Rev.* **2018**, *118* (7), 3608. b) Power, P. P. *Nature* **2010**, *463* (7278), 171.

[11] a) Frey, G. D.; Lavallo, V.; Donnadieu, B.; Schoeller, W. W.; Bertrand, G. *Science* **2007**, *316* (5823), 439. b) Meltzer, A.; Inoue, S.; Präsang, C.; Driess, M. *J. Am. Chem. Soc.* **2010**, *132* (9), 3038. c) Robinson, T. P.; De Rosa, D. M.; Aldridge, S.; Goicoechea, J. M. *Angew. Chem. Int. Ed.* **2015**, *54* (46), 13758. d) Wang, W.; Inoue, S.; Yao, S.; Driess, M. *Organometallics* **2011**, *30* (23), 6490. e) Tay, M. Q. Y.; Lu, Y.; Ganguly, R.; Vidovic, D. *Chem. Eur. J.* **2014**, *20* (22), 6628.

f) Erickson, J. D.; Vasko, P.; Riparetti, R. D.; Fettinger, J. C.; Tuononen, H. M.; Power, P. P. *Organometallics* **2015**, *34* (24), 5785.

[12] a) Wang, B.; Li, Y.; Ganguly, R.; Hirao, H.; Kinjo, R. *Nat Commun* **2016**, *7*. b) Wu, D.; Kong, L.; Li, Y.; Ganguly, R.; Kinjo, R. *Nat Commun* **2015**, *6*, 7340. c) Geri, J. B.; Szymczak, N. K. *J. Am. Chem. Soc.* **2017**, *139* (29), 9811. d) Wu, D.; Li, Y.; Ganguly, R.; Kinjo, R. *Chem. Commun.* **2017**, *53* (95), 12734. e) Lorbach, A.; Bolte, M.; Lerner, H.-W.; Wagner, M. *Organometallics* **2010**, *29* (22), 5762. f) Grotthuss, von, E.; Diefenbach, M.; Bolte, M.; Lerner, H.-W.; Holthausen, M. C.; Wagner, M. *Angew. Chem. Int. Ed.* **2016**, *55* (45), 14067.

[13] a) J. W. Taylor, W. H. Harman. *Unpublished*. b) Januszewski, E.; Lorbach, A.; Grewal, R.; Bolte, M.; Bats, J. W.; Lerner, H.-W.; Wagner, M. *Chem. Eur. J.* **2011**, *17* (45), 12696.

[14] Taylor, J. W.; McSkimming, A.; Guzman, C. F.; Harman, W. H. *J. Am. Chem. Soc.*, **2017**, *139* (32), pp 11032–11035

[15] Chiu, C.-W.; Kim, Y.; Gabbaï, F. P. *J. Am. Chem. Soc.* **2009**, *131* (1), 60.

[16] a) Matsumoto, T.; Gabbaï, F. P. *Organometallics* **2009**, *28* (15), 4252. b) Wood, T. K.; Piers, W. E.; Keay, B. A.; Parvez, M. *Angew. Chem. Int. Ed.* **2009**, *48* (22), 4009. c) Braunschweig, H.; Chiu, C.-W.; Radacki, K.; Kupfer, T. *Angew. Chem. Int. Ed.* **2010**, *49* (11), 2041.

[17] a) Hoffend, C.; Diefenbach, M.; Januszewski, E.; Bolte, M.; Lerner, H.-W.; Holthausen, M. C.; Wagner, M. *Dalton Trans.* **2013**, *42* (38), 13826. b) Reus, C.; Weidlich, S.; Bolte, M.; Lerner, H.-W.; Wagner, M. *J. Am. Chem. Soc.* **2013**, *135* (34), 12892. c) Januszewski, E.; Lorbach, A.; Grewal, R.; Bolte, M.; Bats, J. W.; Lerner, H.-W.; Wagner, M. *Chem. Eur. J.* **2011**, *17* (45), 12696. d) Dou, C.; Saito, S.; Matsuo, K.; Hisaki, I.; Yamaguchi, S. *Angew. Chem. Int. Ed.* **2012**, *51* (49), 12206.

[18] a) Schulz, H.; Pritzkow, H.; Siebert, W. *Chem. Ber.* **1991**, *124* (10), 2203. b) Müller, P.; Gangnus, B.; Pritzkow, H.; Schulz, H.; Stephan, M.; Siebert, W. *J. Organomet. Chem.* **1995**, *487* (1-2), 235. c) Böhnke, J.; Braunschweig, H.; Jimenez-Halla, J. O. C.; Krummenacher, I.; Stennett, T. E. *J. Am. Chem. Soc.* **2018**, *140* (2), 848.

[19] Taylor, J. W.; McSkimming, A.; Moret, M.-E.; Harman, W. H. *Inorg. Chem.* **2018**, *57* (24), 15406.

[20] Taylor, J. W.; McSkimming, A.; Moret, M.-E.; Harman, W. H. *Angew. Chem. Int. Ed.* **2017**, *56* (35), 10413.

[21] a) Muller, P.; Huck, S.; Köppel, H.; Pritzkow, H.; Siebert, W. *Z. Naturforsch. B.* **1995**, *50* (10), 1476. b) Dou, C.; Saito, S.; Yamaguchi, S. *J. Am. Chem. Soc.* **2013**, *135* (25), 9346.

[22] a) Eyring, H. *Chem. Rev.* **1935**, *17* (1), 65. b) Atheaux, I.; Delpech, F.; Donnadieu, B.; Sabo-Etienne, S.; Chaudret, B.; Hussein, K.; Barthelat, J. C.; Braun, T.; Duckett, S. B.; Perutz, R. N. *Organometallics* **2002**, *21* (24), 5347.

[23] Beckett, M. A.; Strickland, G. C.; Holland, J. R.; Sukumar Varma, K. *Polymer* **1996**, *37* (20), 4629.

[24] a) Grotthuss, von, E.; Prey, S. E.; Bolte, M.; Lerner, H.-W.; Wagner, M. *Angew. Chem. Int. Ed.* **2018**. b) Grotthuss, von, E.; Nawa, F.; Bolte, M.; Lerner, H.-W.; Wagner, M. *Tetrahedron* **2019**, *75* (1), 26.

[25] Di Wu; Ganguly, R.; Li, Y.; Hoo, S. N.; Hirao, H.; Kinjo, R. *Chem. Sci.* **2015**, *6* (12), 7150.

[26] a) Schnurr, A.; Vitze, H.; Bolte, M.; Lerner, H.-W.; Wagner, M. *Organometallics* **2010**, *29* (22), 6012. b) Das, A.; Hübner, A.; Weber, M.; Bolte, M.; Lerner, H.-W.; Wagner, M. *Chem. Commun.* **2011**, *47* (40), 11339.

[27] Stephenson, D. S.; Binsch, G. *J. Magn. Reson.* **1978**, *30*, 625.
[28] *APEX 2,* version 2014.1-1, Bruker (2014), Bruker AXS Inc., Madison, Wisconsin, USA.

[29] *SAINT,* version V8.34A, Bruker (2012), Bruker AXS Inc., Madison, Wisconsin, USA

[30] *SADABS,* version 2012/1, Bruker (2012), Bruker AXS Inc., Madison, Wisconsin, USA

[31] *SHELXTL,* version 2013/4, Bruker (2013), Bruker AXS Inc., Madison, Wisconsin, USA.

3.4) Reductive Transformations of Carbonyl-Containing Compounds by a Multi-Functional Diboraanthracene Platform

3.4.1) Introduction

The activation of element-element bonds with main-group centers is a rapidly growing research domain.[1] Frustrated Lewis pairs (FLPs),[2] main-group multiple bonds[3] and low-valent main-group centers[4] have emerged as leading approaches to enact “transition-metal like” transformations of small molecules. Driven by current issues facing society[5] and industrial demand,[6] a vast majority of the reactions performed by these systems are done on saturated substrates containing C=O and C=C bonds. The hydrogenation of C=C bonds, generally via hydroboration or hydrosilylation, is by far the most common example of the reduction of carbonyl compounds by main-group systems.[7] Surprisingly, the first *catalytic* hydrogenation of C=O moieties by FLP systems was reported as recently as 2014.[8] Common issues with these systems are irreversible degradation of the borane following C=O bond activation[9] and subsequent lack of turnover following formation of strong B-O bonds.[10] Alternative products from C=O activation including pinacol couplings,[11] McMurry couplings,[12] Tischenko dimerizations,[13] carbonyl olefination[14] and many others,[15] have been limited or nonexistent and presents an avenue of inquiry for main-group systems.

Aromatic and reduced boron containing heterocycles have been targeted as enticing reaction platforms given their ability to accept two-electrons at

increasingly mild potentials and to perform cooperative bond activation steps at proximal boron centers.[16] The 9,10-dihydro-9,10-diboraanthrecene (DBA) molecule has recently begun being explored as a platform for small molecule activation by Wagner and ourselves. DBA is capable of undergoing two redox events that, upon second reduction, yields a reactive core that has been shown to split H_2,[17] CO_2,[18] dichalogenides[19] and cycloadd ketones.[20] As a ligand for transition-metals, DBA has shown the ability to stabilize low-valent transition-metasLigands containing hemilabile pi-systems shown the ability to stabilize multiple redox states during bond activation steps. We recently reported the B_2P_2 ligand and its Cu, Ag,[21] Au[22] and Ni[23] complexes. In the case of Au, the anion, [Au(B_2P_2)][K(18-c-6)], could be accessed at mild potentials (–2.05 V vs. Fc/Fc^+) and was identified as a donor-acceptor complex of anionic Au (auride).[24] We have reported that this complex undergoes protonation at the B atoms with weak acids to yield a borohydride that can then reduce CO_2 to formate.[25] Furthermore, direct reaction with CO_2 yields a CO_3 complex that was postulated to proceed through a cycloaddition intermediate. In another report, we presented the 1,4-addtion of H_2O to [Au(B_2P_2)][K(18-c-6)] that yielded a mixed hydride/hydroxide complex that, upon addition of a second equivalent of H_2O, rapidly releases H_2. Importantly, the DBA-bound reduction products can be released with strong acids or reductants, making these systems in principle catalytic. The reactivity of the [Au(B_2P_2)]^n (n = +1, 0, –1) redox series with “traditional” substrates prompted us

to examine its reactivity with carbonyl containing compounds to provide further mechanistic insight and reactivity trends. Herein we disclose the diverse reactions of [Au(B_2P_2)][K(18-c-6)] with formaldehyde, acetone and benzaldehyde.

3.4.2) Results and Discussions

Investigation of the reaction of [Au(B_2P_2)][K(18-c-6)] with carbonyl compounds was initiated with formaldehyde. Monomeric formaldehyde was generated via exposure of paraformaldehyde to acidic Amberlite resin (126^+) in Et_2O suspensions. Following distillation of an Et_2O solution of CH_2O into a flask containing [Au(B_2P_2)][K(18-c-6)], a colorless solution rapidly forms that was identified as the formal head-to-tail coupling of two CH_2O units, [Au(B_2P_2)(OCH_2OCH_2)][K(18-c-6)] (**1**). A single-crystal of **1** suitable for XRD was obtained and revealed a -B-O-CH_2-O-CH_2-O-B- six-membered heterocycle

Scheme 3.4.1. Synthesis of **1**.

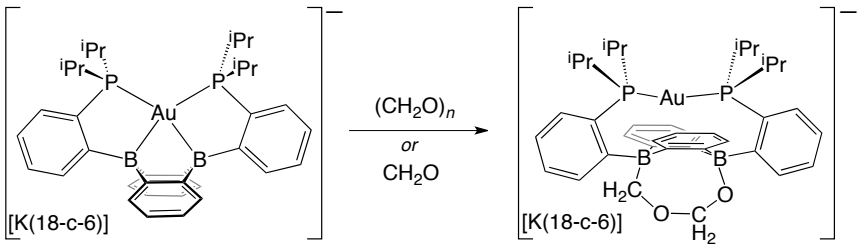

1

across the DBA face with a roughly linear P-Au-P (∠PAuP = 158.2 °) moiety on the opposite face. The methylformato unit has O-C bond lengths on the order of O-C single bonds with distances of 1.371 (2), 1.427(2), and 1.485(2) Å. Each B

atom of the DBA heterocycle is puckered out of planarity ($\Sigma_{CB(0)C\angle}$ = 336.0°, $\Sigma_{CB(C)C\angle}$ = 333.9°) with their pseudo-tetrahedral geometry completed by B-O and

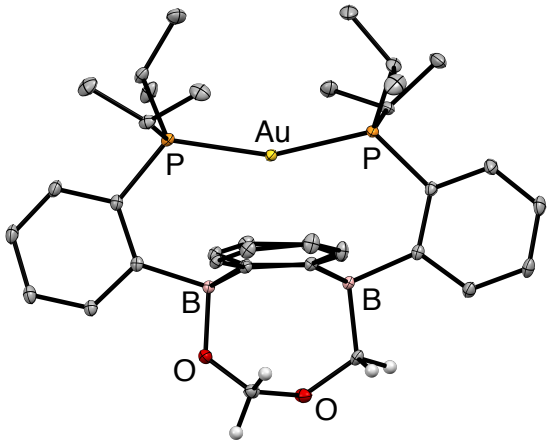

Figure 3.4.1. Labelled thermal ellipsoid plot (50%) of [Au(B_2P_2)(OCH_2OCH_2)][K(18-c-6)] (**1**).

B-C linkages of 1.528(2) and 1.651(2) Å, respectively. Additionally, the FT-IR spectrum of **1** contained no C=O moieties (see Spectroscopic Data, Figure 3.5.5.32) consistent with the assignment of single-bonds throughout the -OCH_2OCH_2- moiety. Solution NMR spectroscopy is consistent with the observed solid-state C_s symmetry. The methylene resonances of the -OCH_2OCH_2- moiety were detected as singlets at 4.80 and 4.21 ppm in the ^{1}H NMR spectrum. ^{11}B{^{1}H} NMR provided two resonances at –0.13 and –12.28 ppm for the B-O and B-C bound B atoms, respectively while the ^{31}P NMR spectra featured a set of doublets at 48.72 (J_{PP} = 266.7 Hz) and 45.43 (J_{PP} = 270.9 Hz) ppm.

Interestingly, the reaction of [Au(B_2P_2)][K(18-c-6)] with paraformaldehyde in THF was complete in 15 minutes and provided exclusively **1** in 94% yield. The selective addition of both monomeric formaldehyde and polymeric

paraformaldehyde to produce **1** is formally a head-to-tail dimerization of formaldehyde to an ester (methylformate dianion), a process reminiscent of the Tishchenko reaction. The Tishchenko dimerization is traditionally carried out by aluminum alkoxides[13a] however boric acid[26] have been found to perform this reaction through Lewis acid coordination of formaldehyde units prior to attack of a second equivalent of formaldehyde to the polarized C atom of the coordinated unit. However, recent reports of [4+2] cycloaddition reactions of carbonyl compounds with boron heterocycles necessitates inclusion in mechanistic considerations for the dimerization of formaldehyde by $[Au(B_2P_2)][K(18\text{-}c\text{-}6)]$. Metal-catalyzed Tishchenko reactions that rely on coupling of π-complexed carbonyl moieties have been reported[27] and a related cycloaddition cascade may be operative in the case of $[Au(B_2P_2)][K(18\text{-}c\text{-}6)]$.

The reaction of $[Au(B_2P_2)][K(18\text{-}c\text{-}6)]$ with acetone was explored in the hopes that mechanistic insights for the reaction of $[Au(B_2P_2)][K(18\text{-}c\text{-}6)]$ with C=O units may be obtained. Contrary to the reaction with formaldehyde, addition of acetone to $[Au(B_2P_2)][K(18\text{-}c\text{-}6)]$ did not result in an immediate reaction. Heating

Scheme 3.4.2. Synthesis of **2**.

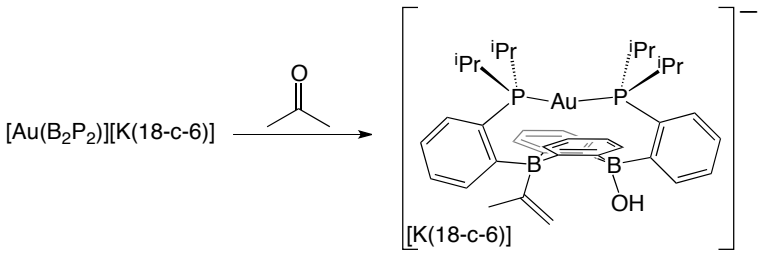

2

of a solution of [Au(B_2P_2)][K(18-c-6)] and one equivalent of acetone at 60 °C in C_6D_6 for 48 hours led to the formation of a colorless solution with ^{31}P NMR showing predominantly a set of doublets at 48.62 (J_{PP} = 268.5 Hz) and 44.96 (J_{PP} = 271.4 Hz) along with a singlet at 45.46 ppm in roughly a 4:1 ratio. The resonance at 45.46 ppm was identified as the previously reported dihydroxide product, [Au(B_2P_2)($OH)_2$][K(18-c-6)], and is likely the result of small amount of residual H_2O from the acetone drying process[28] as well as self-condensation competing at elevated reaction temperatures in the presence of Lewis acids. Notably, by running the reaction with three equivalents of acetone, reaction times of 10 hours at 60 °C were obtained in comparable product distributions. Following workup, single-crystal XRD studies revealed the product as the reductive deoxygenation product with distinct hydroxide and propene units on each B atom of the DBA heterocycle, [Au(B_2P_2)(C_3H_5)(OH)][K(18-c-6)] (**2**). Bond metrics of the B-bound $CH_3C{=}CH_2$ unit gave a distinct single bond C-C distance of 1.479(2) Å and double bond C=C distance of 1.358(2) Å with a B-C bond of 1.661(2) Å. Each B-atom of the DBA is pseudo-tetrahedral ($\Sigma_{CB(0)C\angle}$ = 334.6°, $\Sigma_{CB(C)C\angle}$ = 332.4°) to accommodate the hydroxide and propene units with a pseudo-linear P-Au-P unit (∠P-Au-P = 158.4 °) on the opposite face of the DBA heterocycle. ^{1}H NMR spectroscopy of **2** in C_6D_6 shows the two diasterotopic propene C-Hs at 5.34 and 4.79 ppm with the former appearing as a broad singlet while the resonance at 4.79 ppm is resolved as a doublet (J = 6.6 Hz) and consistent with

geminal C-H coupling. The propene CH_3 unit is detected as a singlet at 2.37 ppm. A ^{1}H-^{13}C HSQC experiment conducted in THF-d_8 (owing to the inability to get saturated solutions of **2** in C_6D_6) located the C atoms of the propene unit at 177.8 (B-*C*), 115.8 (CH_3C=*C*H_2) and 26.3 (*C*H_3C=CH_2) ppm (See Spectroscopic Data, Figure 3.4.5.19). $^{11}B\{^{1}H\}$ NMR spectroscopy of **2** in C_6D_6 displays two distinct B atoms, with signals at –0.77 and –7.93 ppm. Additionally, the O-*H* resonance was detected in the ^{1}H NMR spectrum as a singlet at 1.16 ppm and FT-IR spectroscopy produced a sharp band at 3572 cm^{-1}.

The formation of **2** was unexpected as there are very limited examples of acetone deoxygenation to propene and hydroxide by a molecular system.[29]

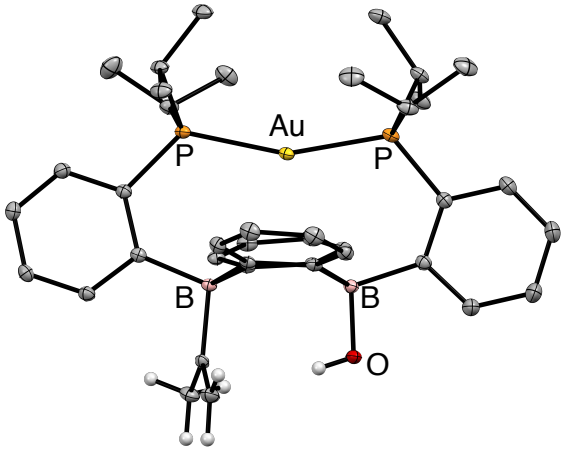

Figure 3.4.2. Labelled thermal ellipsoid plot (50%) of [Au(B_2P_2)(C_3H_5)(OH)][K(18-c-6)] (**2**).

Monitoring of the reaction of [Au(B_2P_2)][K(18-c-6)] with 1 equivalent of acetone at 60 °C showed the formation of various intermediates during the formation of **2** over the course of 2 days that could not be identified. Notably, no H_2 or

dehydrogenation products (B-H, ^{11}B NMR) were observed during the formation of **2** as judged by NMR spectroscopies, suggesting a dehydrogenation step likely not being operative. The formation of **2** suggests the possibility for α-H atom migration and to test this, the reaction was carried out in the presence of catalytic DBU (10% mol.). The reaction was monitored by ^{1}H, ^{31}P and ^{11}B spectroscopy and was shown to be complete within ~36 hours, whereas DBU free experiments took ~48 hours. These experiments suggest a role for a base in α-H atom transfer however the role of the [K(18-c-6-)] unit in cooperative reactivity can't be ruled out.[30] Alternatively, it was found that by adding 0.33 equivalents of NaI•3(C_3H_6O) complex[31] to [Au(B_2P_2)][K(18-c-6)] in THF a colorless solution appeared within 1 hour at room temperature. Analysis of the reaction mixture by NMR spectroscopies confirmed the formation of **2** with less than 10% relative formation of [Au(B_2P_2)($OH)_2$][K(18-c-6)] to **2**. The exact role of NaI•3(C_3H_6O) in aiding the formation of **2** isn't entirely clear, however the increase in rate may be attributed to the NaI•3(C_3H_6O) salt featuring pre-activated acetone units for reaction with [Au(B_2P_2)][K(18-c-6)] or alternatively pre-coordinated base (NaI) may assist in α-H atom migration to an O atom of the acetone unit involved in reaction.

The reactions of [Au(B_2P_2)][K(18-c-6)] with formaldehyde and acetone prompted us to explore the reaction with benzaldehyde. Initial reaction of [Au(B_2P_2)][K(18-c-6)] with excess benzaldehyde (~10 eq) in toluene rapidly

produces a colorless solution prior to the slow precipitation (30 mins) of a colorless crystalline solid, identified as $[Au(B_2P_2)(C_{14}H_{12}O_2)][K(18\text{-c-}6)]$ (**4**). Single-crystal XRD data of **4** revealed a DBA bound 1,2-diphenyl-1,2-ethanediolate moiety, the result of formal pinacol-coupling of two benzaldehyde units. Each B atom is pseudo-tetrahedral ($\Sigma_{CBC}\angle$ = 337.2, 335.2°) with B-O distances of 1.511(8) and 1.519(8) Å enabled by a nearly linear P-Au-P (∠P-Au-P = 157.9 °) on the opposite face of the DBA. Each O-C bond (1.400(6), 1.406(7)

Scheme 3.4.3. Synthesis of **3** and **4**.

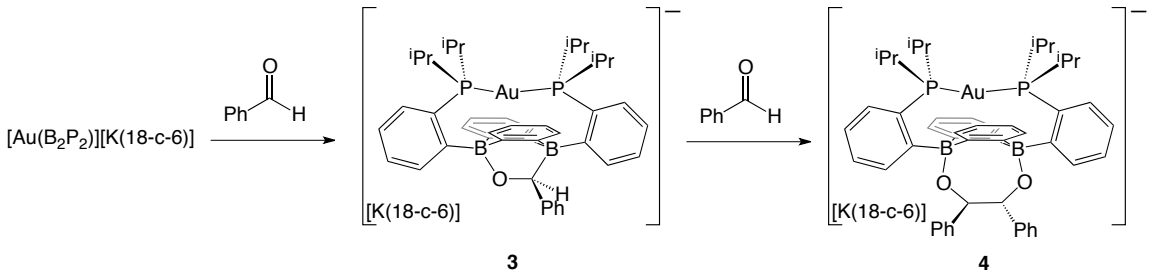

Å) and newly formed C-C bond (1.576(7)Å) are consistent with single bond distances with FT-IR spectroscopy showing no carbonyl stretches > 1600 cm^{-1} (See Spectroscopic Data, Figure 3.4.5.34). Solution NMR spectroscopy was consistent with the observed C_2 solid-state symmetry of **4** with the C-H resonances of the 1,2-diphenyl-1,2-ethanediolate moiety being located at 4.06 ppm in the ^1H NMR and 85.7 ppm in the ^{13}C NMR, as determined by ^1H-^{13}C HSQC experiments.

The presence of two equivalents of benzaldehyde in **4** prompted us to investigate the addition of 1 equivalent of benzaldehyde to $[Au(B_2P_2)][K(18\text{-c-}6)]$.

Slow addition of 1 equivalent of benzaldehyde in toluene to a solution of $[Au(B_2P_2)][K(18\text{-c-}6)]$ in the same solvent rapidly produced a nearly colorless solution with no observed precipitate that was identified as $[Au(B_2P_2)(C_7H_6O)][K(18\text{-c-}6)]$ **(3)**. ^{31}P NMR analysis of **3** showed a set of doublets at 49.57 (J_{PP} = 259.5 Hz) and 44.11 (J_{PP} = 259.0 Hz) ppm while $^{11}B\{^1H\}$ NMR showed two signals at 0.03 and –7.96 ppm, both consistent with a molecule

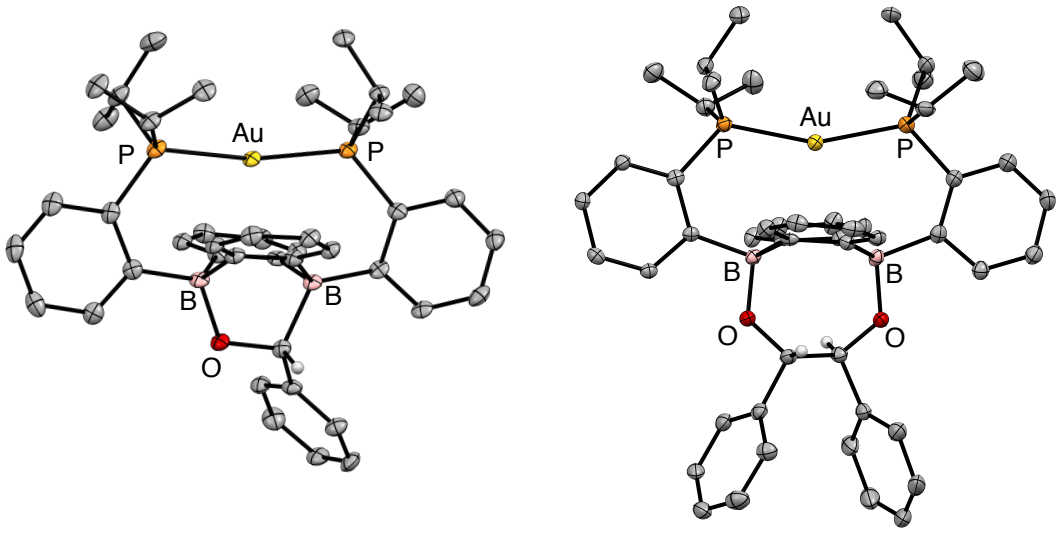

Figure 3.4.3. Labelled thermal ellipsoid plots (30%) of $[Au(B_2P_2)(C_7H_6O)][K(18\text{-c-}6)]$ (**3**) (left) and $[Au(B_2P_2)(C_{14}H_{12}O_2)][K(18\text{-c-}6)]$ (**4**) (right).

possessing C_s symmetry. On letting a solution of **3** stand for 1 week, a red solution formed concomitant with a colorless precipitate. Analysis of the supernatant revealed NMR spectra consistent with $[Au(B_2P_2)][K(18\text{-c-}6)]$ while the precipitate was identified as **4** by NMR spectroscopy. Despite the eventual disproportionation of **3** into $[Au(B_2P_2)][K(18\text{-c-}6)]$ and **4**, a single-crystal of **3** suitable for XRD was obtained and revealed it to be the formal cycloaddition of a

single equivalent of benzaldehyde to the DBA heterocycle. The B atoms of the DBA heterocycle are puckered out of planarity ($\Sigma_{CB(0)C}\angle$ = 334.8°, $\Sigma_{CB(C)C}\angle$ = 333.7°) with B-O and B-C distances of 1.549(7) and 1.727(9) Å, respectively. The benzaldehyde unit has an O-C bond of 1.471(7) Å, on the order of O-C single bonds, with FT-IR measurements of **3** confirming loss of the C=O band (see Spectroscopic Data, Figure 3.4.5.33) and ^{1}H NMR spectroscopy locating the C-H moiety of the aldehyde at 3.88 ppm. The other side of the DBA ring has a significantly bent P-Au-P unit ($\angle$PAuP = 168.9 °) that is the least linear of the series **1-4**. The conversion of **3** to **4** was confirmed by addition of 1 equivalent of benzaldehyde to **3** providing **4** in quantitative yields. To the best of our knowledge, this is the first example of a pinacol coupling that proceeds through a cycloaddition intermediate.

3.4.3) Concluding Remarks

In closing, the [Au(B_2P_2)][K(18-c-6)] has been shown to be a remarkably versatile reaction platform for reductive transformations of C=O containing small molecules. While [4+2] cycloadditions have become well known for 1,4-disposed diboron heterocycles, [Au(B_2P_2)][K(18-c-6)] represents a unique case as bonding of the DBA B atoms with Au breaks the planarity of the DBA ring and provides an intruguing question as to *how* it performs these reactions. The reaction chemistry of the Au(B_2P_2) system can be described as formal oxidative addition of Au^{-1} to Au^{+1} mediated by the two B atoms of the DBA heterocycle. The reversal of roles

for transition-metal and ligand in the Au(B_2P_2) system are in some ways related to other reaction-noninnocent ligands such as β-diketiminato (NacNac) and PNP pincer ligand systems.[32] Leveraging transition metal redox chemistry to enable multi-electron reactivity at main-group centers represents an intriguing design principle for redox-active ligand design and small molecule activation with these systems. Efforts to expand this approach are ongoing in our lab.

3.4.4) Experimental Section

3.4.4.1) General Considerations

Unless otherwise noted, all manipulations were carried out using standard Schlenk or glovebox techniques under a N_2 atmosphere. Hexanes, benzene, toluene, and acetonitrile were dried and deoxygenated by argon sparge followed by passage through activated alumina in a solvent purification system from JC Meyer Solvent Systems followed by storage over 4 Å molecular sieves. THF and Et_2O were distilled from sodium-benzophenone ketyl under N_2 followed by storage over 4Å molecular sieves for at least 24 hours prior to use. Non-halogenated and non-nitrile containing solvents were tested with a standard purple solution of sodium benzophenone ketyl in THF to confirm effective oxygen and moisture removal prior to use. Hexamethyldisiloxane (HMDSO) was distilled from sodium metal and stored over 4Å molecular sieves for 24 hours prior to use. Monomeric formaldehyde, anhydrous acetone and NaI•3(C_6H_7O) were obtained by literature procedures.[31,33-34] All other reagents were purchased from

commercial suppliers and purified according to literature procedures. $[Au(B_2P_2)][K(18\text{-c-}6)]$ was synthesized according to a literature procedure.[22] Elemental analyses were performed by Midwest Microlab, LLC, Indianapolis, IN. Deuterated solvents were purchased from Cambridge Isotope Laboratories Inc., degassed, and dried over activated 3 Å molecular sieves for at least 24 h prior to use. NMR spectra were recorded on Bruker NEO 400 MHz and Bruker Avance 600 MHz spectrometers. ^{1}H and ^{13}C chemical shifts are reported in ppm relative to tetramethylsilane using residual solvent as an internal standard. ^{11}B chemical shifts are reported in ppm relative to $BF_3 \cdot Et_2O$. Original ^{11}B NMR spectra were processed using MestReNova 10.0.2 with a backwards-linear prediction applied to eliminate background signal from the borosilicate NMR tube.[35] For ^{11}B NMR spectra with peaks overlapping the borosilicate signal, a manual baseline correction was applied. IR spectra were recorded using a Bruker Alpha FT-IR with a universal sampling module collecting at 4 cm^{-1} resolution with 32 scans.

3.4.4.2) $[Au(B_2P_2)(OCH_2OCH_2)][K(18\text{-c-}6)]$ (1).

(**1**) *Via paraformaldehyde:* A solution of $[Au(B_2P_2)][K(18\text{-c-}6)]$ (0.032 g, 0.030 mmol) in THF (2 mL) was added paraformaldehyde (0.010 g) at once. The reaction was stirred 1 hour before diluting with hexanes (4 mL) and filtering through celite. The filtrate was placed at –35 °C for 12 hours during which time the product precipitated as a colorless, crystalline solid. The solid was washed with hexanes (2 x 1mL) and dried *in vacuo*. Yield: 0.031 g, 94%.

(**1**) *Via gaseous formaldehyde from a modified literature procedure:* A Schlenk flask was charged with paraformaldehyde, (1.0 g, 30 mmol) Amberlite 126^{+} Resin (0.030 g) and diethyl ether (10 mL). The mixture was stirred 30 minutes prior to slow distillation at 40 °C into a Schlenk flask containing a stirring solution of [Au(B_2P_2)][K(18-c-6)] (0.032 g, 0.030 mmol) in THF (2 mL). As distillation commenced, a colorless solution began developing. Once distillation was finished, the flask containing the product had it volatiles removed *in vacuo*. The residue was washed with pentane (2 x 2 mL), dissolved in THF (1 mL), diluted with pentane (5 mL) and stored at –35 °C for 12 hours during which time the product precipitated at a colorless, crystalline solid. The solid was washed with hexanes (2 x 1mL) and dried *in vacuo*. Yield: 0.023 g, 70%. A single-crystal suitable for XRD analysis was obtained by layering a concentrated benzene solution with HMDSO. ^{1}H NMR (400 MHz, C_6D_6) δ 9.30 (dd, *J* = 7.7, 3.6 Hz, 1H), 8.35 (d, *J* = 4.6 Hz, 1H), 7.74 (t, *J* = 7.3 Hz, 2H), 7.60 (dt, *J* = 15.6, 7.6 Hz, 4H), 7.48 (t, *J* = 7.3 Hz, 2H), 7.35 (d, *J* = 7.3 Hz, 2H), 7.29 (d, *J* = 7.1 Hz, 2H), 7.12 (t, *J* = 6.9 Hz, 2H), 7.07 (d, *J* = 6.4 Hz, 2H), 4.80 (s, 2H), 4.21 (s, 2H), 3.14 (s, 24H), 2.41 (dh, *J* = 23.5, 7.4 Hz, 4H), 1.06 (ddd, *J* = 12.6, 6.8, 3.3 Hz, 12H), 0.94 (d, *J* = 7.1 Hz, 3H), 0.89 (td, *J* = 6.8 Hz, 6H), 0.85 (d, *J* = 7.3 Hz, 3H). ^{31}P NMR (162 MHz, C_6D_6) δ 48.72 (d, *J* = 266.7 Hz), 45.54 (d, *J* = 270.9 Hz). ^{11}B NMR (128 MHz, C_6D_6) δ –0.13, –12.28. FT-IR: ν_{max} cm^{-1} 1116 (C-O). ^{13}C{^{1}H} NMR (126 MHz, C_6D_6) δ 137.88, 137.77, 135.95, 135.83, 135.35, 134.94, 134.44, 134.10,

132.24, 131.83, 131.56, 130.79, 124.59, 123.78, 123.73, 123.50, 123.45, 123.31, 91.64, 69.77, 27.12, 26.92, 26.77, 26.57, 22.71, 22.66, 19.23, 18.93. Anal. Calcd for $C_{50}H_{72}AuB_2KO_8P_2$(1x C_4H_8O): C, 54.37 H, 6.76. Found: C, 53.92 H, 6.94.

3.4.4.3) [Au(B_2P_2)(C_3H_5)(OH)][K(18-c-6)] (2).

*(**2**) Via acetone:* A solution of [Au(B_2P_2)][K(18-c-6)] (0.036 g, 0.034 mmol) and acetone (7.5 *μ*L, 0.102 mmol) in benzene (5 mL) was heated at 60 °C for 10 hours. The pale yellow solution was diluted with pentane (5 mL), filtered through celite and stored at –15 °C where a pale yellow solid appeared. The mother liquor was decanted and the solid washed with pentane (2 x 1 mL). The residue was dissolved in THF/benzene (1:1, 1 mL), diluted with pentane (6 mL) and stored at –15 °C overnight. The next day, colorless crystals had formed that were separated by filtration, washed with pentane (2 x 1 mL) and dried *in vacuo*. Yield: 0.027 g, 71 %.

*(**2**) Via [NaI•3(C_3H_6O)]:* A solution of [Au(B_2P_2)][K(18-c-6)] (0.030 g, 0.028 mmol) in THF (2 mL) was added NaI•3(C_3H_6O) (0.003 g, 0.030 mmol) as a THF solution (2 mL). The reaction was stirred 1 hour during which time a colorless solution appeared. The reaction had its volatiles removed *in vacuo* before washing the residue with pentane (1 x 1mL). The colorless solid was then dissolved in benzene/pentane (1:3, 6 mL) and placed at –15 °C overnight where pale yellow solid appeared. The residue was dissolved in THF/benzene (1:1, 1 mL), diluted with pentane (6 mL) and stored at –15 °C overnight. The next day, colorless

crystals had formed that were separated by filtration, washed with pentane (2 x 1 mL) and dried *in vacuo*. Yield: 0.020 g, 63 %. A single-crystal suitable for XRD analysis was obtained by layering a benzene solution with HMDSO. ^{1}H NMR (400 MHz, C_6D_6) δ 8.93 (ddd, J = 7.5, 3.4, 1.3 Hz, 1H), 8.70 (s, 1H), 7.67 (t, J = 7.4 Hz, 1H), 7.60 (q, J = 8.0 Hz, 2H), 7.56 – 7.50 (m, 2H), 7.45 (t, J = 7.3 Hz, 1H), 7.36 (s, 3H), 7.20 (s, 2H), 7.09 (s, 3H), 5.34 (s, 1H), 4.79 (d, J = 6.6 Hz, 1H), 3.03 (s, 24H), 2.62 – 2.48 (m, 1H), 2.37 (s, 3H), 1.19 – 0.75 (m, 24H). ^{31}P NMR (162 MHz, C_6D_6)) δ 48.62 (d, J = 268.5 Hz), 44.96 (d, J = 271.4 Hz). ^{11}B{^{1}H} NMR (128 MHz, C_6D_6) δ –0.77, –7.93. ^{1}H NMR (600 MHz, THF-d_8) δ 8.60 (ddd, J = 7.4, 3.7, 1.3 Hz, 1H), 7.85 (dd, J = 6.5, 4.0 Hz, 1H), 7.54 (t, J = 7.7 Hz, 1H), 7.51 (t, J = 7.6 Hz, 1H), 7.32 (t, J = 7.8 Hz, 1H), 7.20 (t, J = 7.4 Hz, 1H), 7.12 (t, J = 7.4 Hz, 1H), 7.08 (t, J = 7.4 Hz, 1H), 6.82 (d, J = 6.9 Hz, 1H), 6.65 – 6.62 (m, 1H), 6.61 – 6.51 (m, 6H), 4.78 (s, 1H), 4.05 – 3.98 (m, 1H), 2.46 (dddd, J = 24.0, 21.7, 10.7, 6.0 Hz, 2H), 2.40 – 2.27 (m, 2H), 1.50 (s, 3H), 1.17 (dd, J = 12.8, 7.0 Hz, 3H), 1.14 – 1.11 (m, 3H), 1.11 – 1.07 (m, 3H), 1.03 (dd, J = 14.3, 6.9 Hz, 3H), 0.77 – 0.74 (m, 3H), 0.73 (dd, J = 7.2, 5.0 Hz, 3H), 0.68 (dd, J = 17.4, 7.3 Hz, 3H), 0.57 (dd, J = 16.7, 7.1 Hz, 3H). ^{31}P NMR (243 MHz, THF-d_8) δ 46.31 (d, J = 269.6 Hz), 42.84 (d, J = 271.2 Hz). ^{11}B NMR (192 MHz, THF-d_8) δ –3.33, –10.56. ^{13}C NMR (151 MHz, THF-d_8) δ 177.83 (m), 174.57 (m), 162.65 (m), 160.72 (m), 140.33 (d, J = 14.3 Hz), 137.01 (d, J = 14.8 Hz), 135.92 (d, J = 8.0 Hz), 135.64 (d, J = 7.7 Hz), 135.46 (d, J = 7.1 Hz), 135.17 (d, J = 7.2 Hz), 134.65 (d, J = 7.2

Hz), 132.60 (d, J = 8.0 Hz), 131.74, 131.28, 129.20, 128.83, 128.68, 128.51, 128.37, 123.49, 123.36 (d, J = 6.5 Hz), 123.26, 123.12, 122.98, 115.8, 70.93, 29.36, 28.10 (d, J = 24.9 Hz), 27.83 – 27.42 (m), 27.34, 26.98 (d, J = 24.8 Hz), 26.56, 25.89 (d, J = 20.3 Hz), 24.11 (d, J = 8.4 Hz), 23.73 (d, J = 8.2 Hz), 22.24 (d, J = 7.0 Hz), 22.08 (d, J = 7.5 Hz), 20.04 (d, J = 4.1 Hz), 18.96 (d, J = 14.7 Hz). FT-IR: ν_{max} cm^{-1} 3572 (O-H). Anal. Calcd for $C_{51}H_{74}AuB_2KO_7P_2$: C, 54.75 H, 6.67. Found: C, 54.07 H, 6.38.

3.4.4.4) [Au(B_2P_2)(C_7H_6O)][K(18-c-6)] (3).

A solution of [Au(B_2P_2)][K(18-c-6)] (0.032 g, 0.030 mmol) in toluene (4 mL) was added benzaldehyde (3.07 μL, 0.030 mmol)) as a toluene solution (2 mL) dropwise. The reaction was stirred 15 minutes during which time a colorless solution appeared. The reaction had its volatiles removed *in vacuo* before washing the residue with pentane (3 x 1mL). The colorless solid was then dissolved in benzene/pentane (1:3, 6 mL) and placed at –15 °C overnight. The next day, colorless crystals had appeared that were collected on a filter, washed with pentane (2 x 1mL) and dried *in vacuo*. Yield: 0.029 g, 83 %. A single-crystal suitable for XRD analysis was obtained by layering a saturated benzene solution with pentane ^{1}H NMR (500 MHz, C_6D_6) δ 8.66 (ddd, J = 5.8, 4.2, 0.9 Hz, 1H), 8.26 (ddt, J = 6.1, 4.0, 1.8 Hz, 1H), 7.68 (q, J = 6.1 Hz, 2H), 7.63 (t, J = 7.8 Hz, 1H), 7.48 (dt, J = 20.4, 7.3 Hz, 2H), 7.34 (t, J = 8.4 Hz, 1H), 7.25 (t, J = 7.1 Hz, 1H), 7.05 (ddd, J = 12.3, 8.0, 5.3 Hz, 6H), 7.00 (d, J = 6.9 Hz, 2H), 6.97 (t, J = 7.9

Hz, 2H), 6.89 (t, *J* = 7.2 Hz, 1H), 6.76 (d, *J* = 7.3 Hz, 2H), 6.71 (d, *J* = 6.7 Hz, 1H), 3.88 (s, 1H), 2.90 (s, 25H), 2.79 (dd, *J* = 16.2, 8.7 Hz, 2H), 2.62 – 2.47 (m, 2H), 2.41 (ddd, *J* = 14.0, 7.0, 3.5 Hz, 1H), 1.19 (d, *J* = 7.0 Hz, 3H), 1.17 (d, *J* = 7.1 Hz, 3H), 1.10 – 0.98 (m, 18H), 0.96 (d, *J* = 7.0 Hz, 3H), 0.93 (d, *J* = 7.1 Hz, 3H), 0.88 (t, *J* = 7.1 Hz, 3H), 0.80 (d, *J* = 7.4 Hz, 3H), 0.76 (d, *J* = 7.4 Hz, 3H). ^{31}P NMR (202 MHz, C_6D_6) δ 49.57 (d, *J* = 259.5 Hz), 44.11 (d, *J* = 259.0 Hz). ^{11}B{^{1}H} NMR (160 MHz, C_6D_6) δ 0.03, –7.96. ^{13}C{^{1}H} NMR (151 MHz, C_6D_6) δ 171.23, 162.74, 156.24, 155.56, 154.42, 137.7 (d, *J* = 7.2 Hz), 137.5 (d, *J* = 6.0 Hz), 137.4 (d, *J* = 7.1 Hz), 137.23 (d, *J* = 5.8 Hz), 134.90 (d, *J* = 11.2 Hz), 132.95 (d, *J* = 11.4 Hz), 132.19, 131.84, 131.34, 129.58, 129.38, 128.59, 127.14, 126.49, 125.79, 124.23, 123.53, 123.24, 122.82 (t, *J* = 6.3 Hz), 122.45, 121.86, 76.79, 69.67, 26.88 (d, *J* = 23.2 Hz), 26.54 (d, *J* = 23.9 Hz), 25.58 (d, *J* = 22.9 Hz), 25.36, 24.97 (d, *J* = 2.1 Hz), 24.91 (d, *J* = 2.1 Hz), 22.24 (d, *J* = 6.7 Hz), 22.13 (d, *J* = 7.5 Hz), 20.51 (d, *J* = 8.8 Hz), 20.35 (d, *J* = 8.1 Hz), 17.94, 17.82.

3.4.4.5) Au(B_2P_2)($C_{14}H_{12}O_2$)][K(18-c-6)$(THF)_2$] (4).

A solution of [Au(B_2P_2)][K(18-c-6)] (0.031 g, 0.029 mmol) in toluene (4 mL) was added benzaldehyde (0.007g, 0.061 mmol) as a toluene solution (2 mL) dropwise. The reaction was stirred 1 hour during which time a colorless crystalline solid precipitated. The reaction was concentrated *in vacuo* (*ca.* 2 mL) before collecting the colorless crystalline solid on a filter. The solid was dissolved in THF and layered with pentane (4 mL) and allowed to stand overnight. The next

day, colorless crystals had formed that were filtered, washed with pentane (2 x 1 mL) and dried *in vacuo*. An additional crop was obtained by layering the filtrate with pentane (*ca.* 3 mL). Yield: 0.036 g, 88 %. A single-crystal suitable for XRD analysis was obtained by vapor diffusion of pentane into a saturated THF solution. ^{1}H NMR (400 MHz, THF-d_8) δ 8.93 – 8.85 (m, 2H), 7.47 (dt, J = 7.5, 4.1 Hz, 2H), 7.25 (t, J = 7.2 Hz, 2H), 7.07 (t, J = 7.3 Hz, 2H), 6.86 (d, J = 7.1 Hz, 4H), 6.77 (d, J = 6.9 Hz, 2H), 6.64 – 6.57 (m, 6H), 6.56 – 6.47 (m, 6H), 4.06 (s, 2H), 3.47 (s, 24H), 2.47 (ddd, J = 11.8, 7.9, 4.6 Hz, 2H), 2.38 (ddd, J = 11.8, 7.9, 4.6 Hz, 2H), 1.14 (d, J = 7.8 Hz, 6H), 1.11 (d, J = 7.0 Hz, 6H), 0.72 (td, J = 16.6, 7.5 Hz, 12H). ^{31}P NMR (162 MHz, THF-d_8) δ 44.43 (s). ^{11}B NMR (128 MHz, THF-d_8) δ –0.74. ^{13}C{^{1}H} NMR (101 MHz, THF-d_8) δ 152.27, 138.00 (t, J = 7.3 Hz), 133.35, 132.56, 130.40, 128.92, 128.10, 126.13, 124.14, 123.72, 123.39, 123.18, 85.73, 71.31, 30.82, 27.43 (d, J = 12.4 Hz), 27.18 (d, J = 11.7 Hz), 26.94 (d, J = 12.6 Hz), 23.48 (t, J = 4.1 Hz), 22.97, 19.65, 19.21. Anal. Calcd for $C_{62}H_{80}AuB_2KO_8P_2$: C, 58.50 H, 6.33. Found: C, 58.75 H, 6.38.

3.4.5) Spectroscopic Data

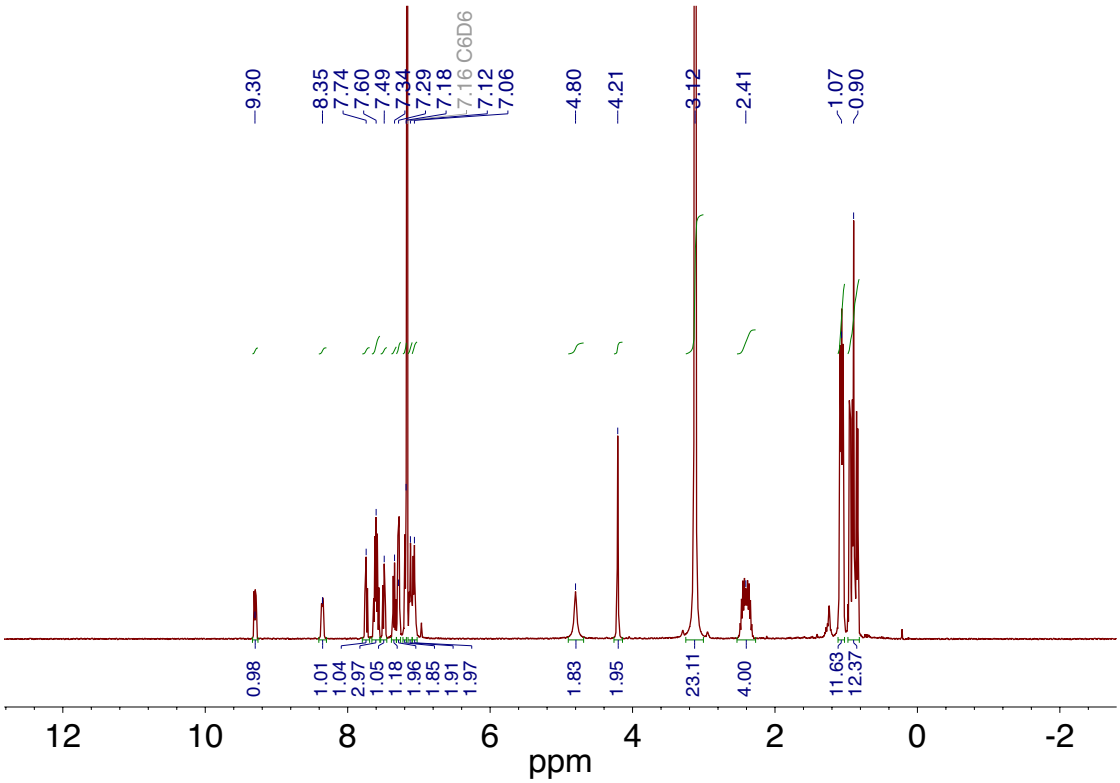

Figure 3.4.5.1. ^{1}H NMR spectrum of **[Au(B_2P_2)(OCH_2OCH_2)][K(18-c-6)]** recorded at 400 MHz in C_6D_6.

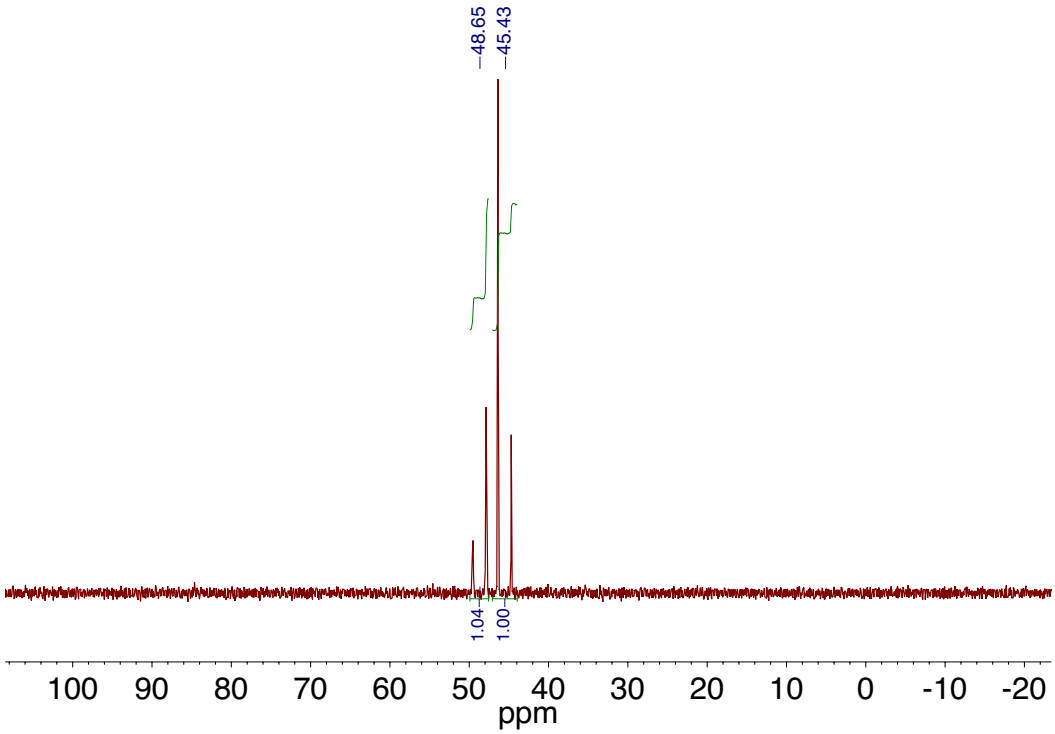

Figure 3.4.5.2. ^{31}P NMR spectrum of **[Au(B_2P_2)(OCH_2OCH_2)][K(18-c-6)]** recorded at 162 MHz in C_6D_6

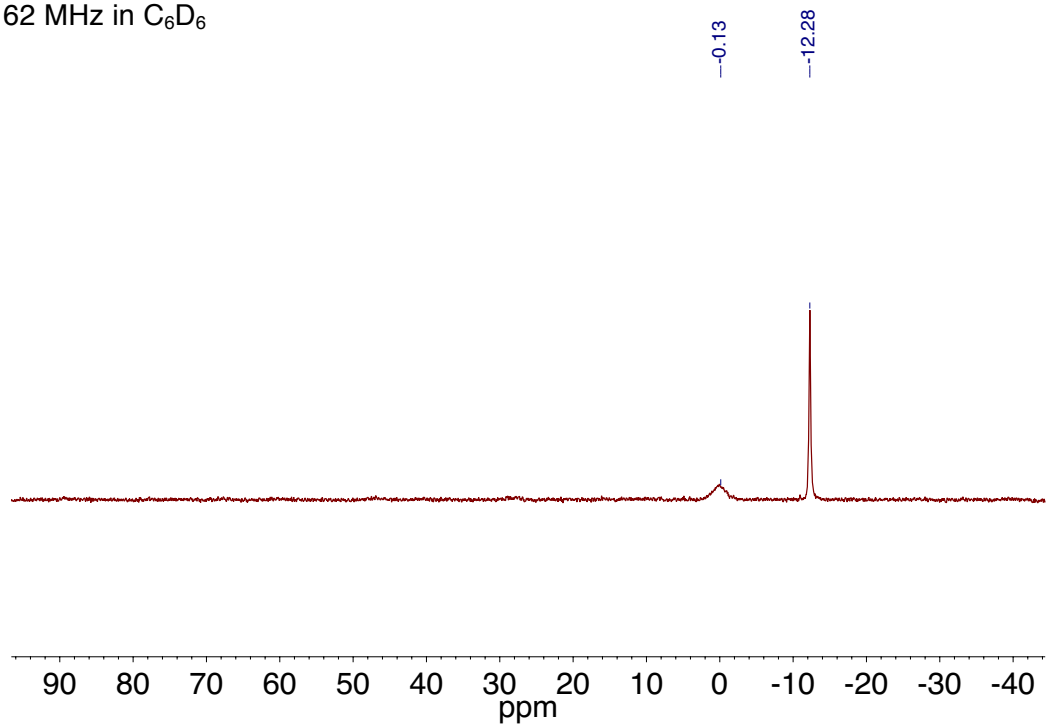

Figure 3.4.5.3. ^{11}B{^{1}H} NMR spectrum of **[Au(B_2P_2)(OCH_2OCH_2)][K(18-c-6)]** recorded at 128 MHz in C_6D_6.

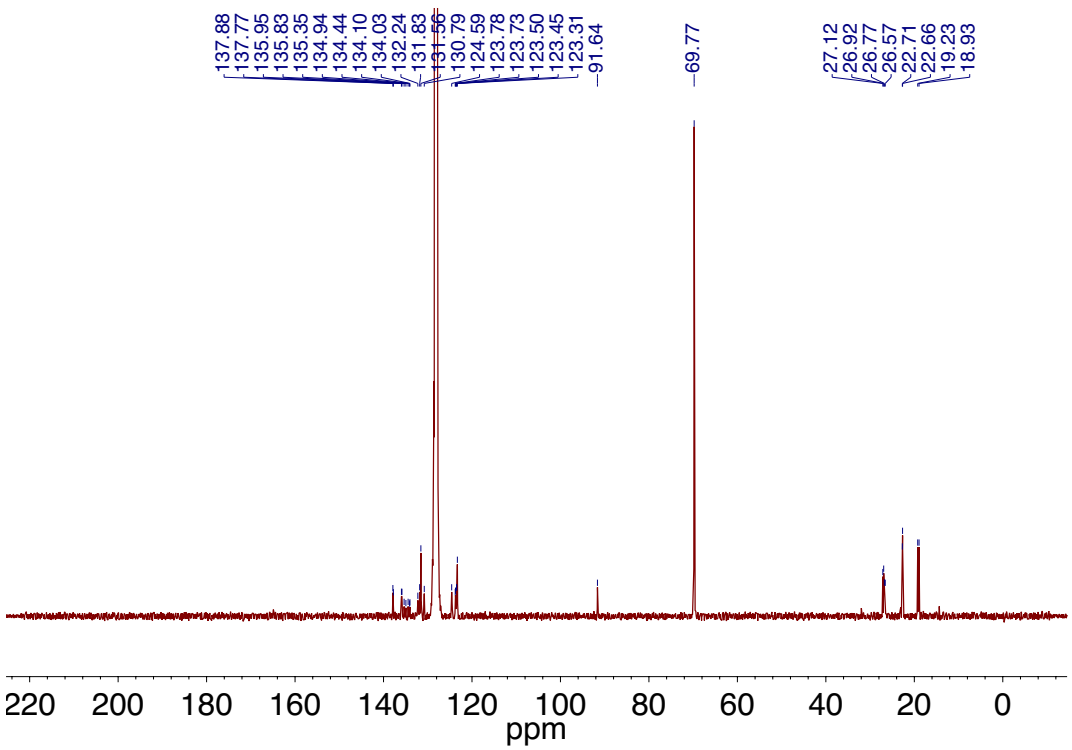

Figure 3.4.5.4. $^{13}C\{^{1}H\}$ NMR spectrum of **[Au(B_2P_2)(OCH_2OCH_2)][K(18-c-6)]** recorded at 126 MHz in C_6D_6.

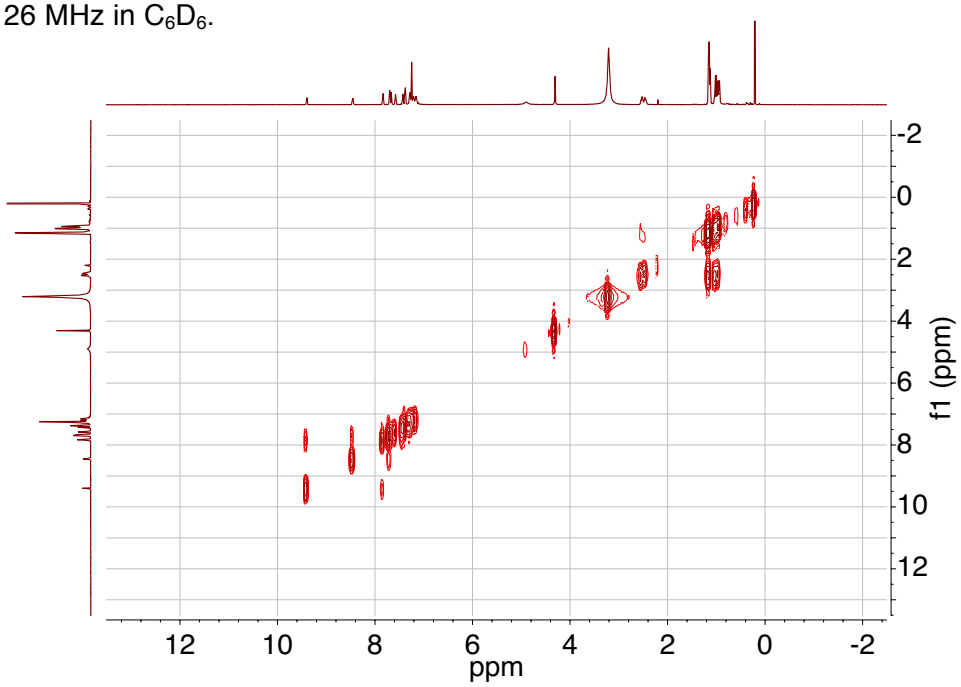

Figure 3.4.5.5. ^{1}H-^{1}H COSY NMR spectrum of **[Au(B_2P_2)(OCH_2OCH_2)][K(18-c-6)]** recorded at 400 MHz in C_6D_6.

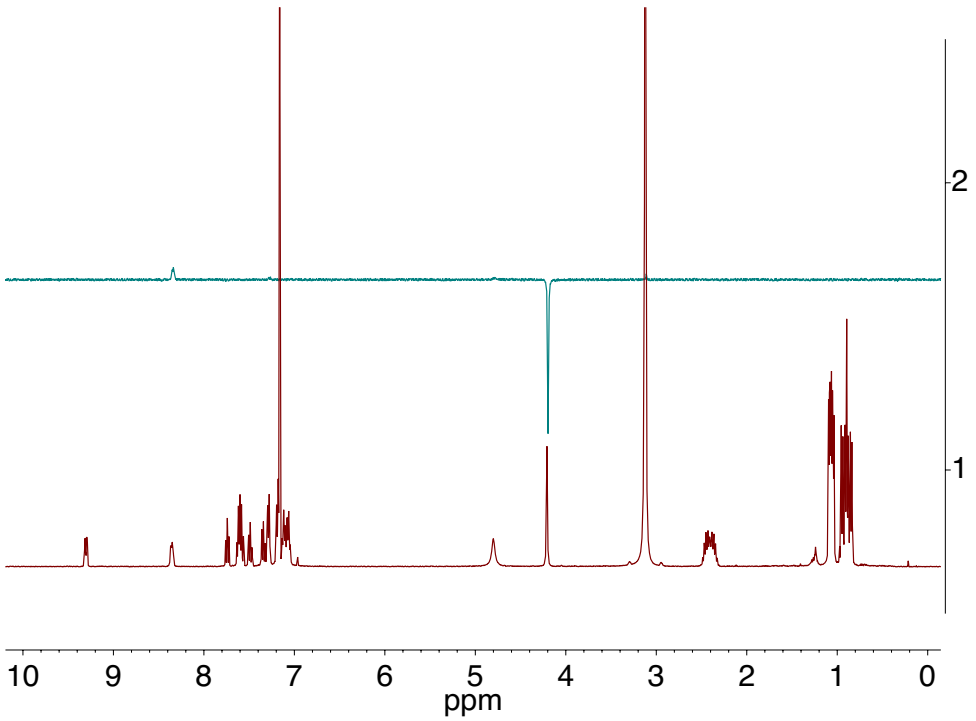

Figure 3.4.5.6. ^{1}H-1D NOE NMR spectrum of **[Au(B_2P_2)(OCH_2OCH_2)][K(18-c-6)]** recorded at 400 MHz in C_6D_6.

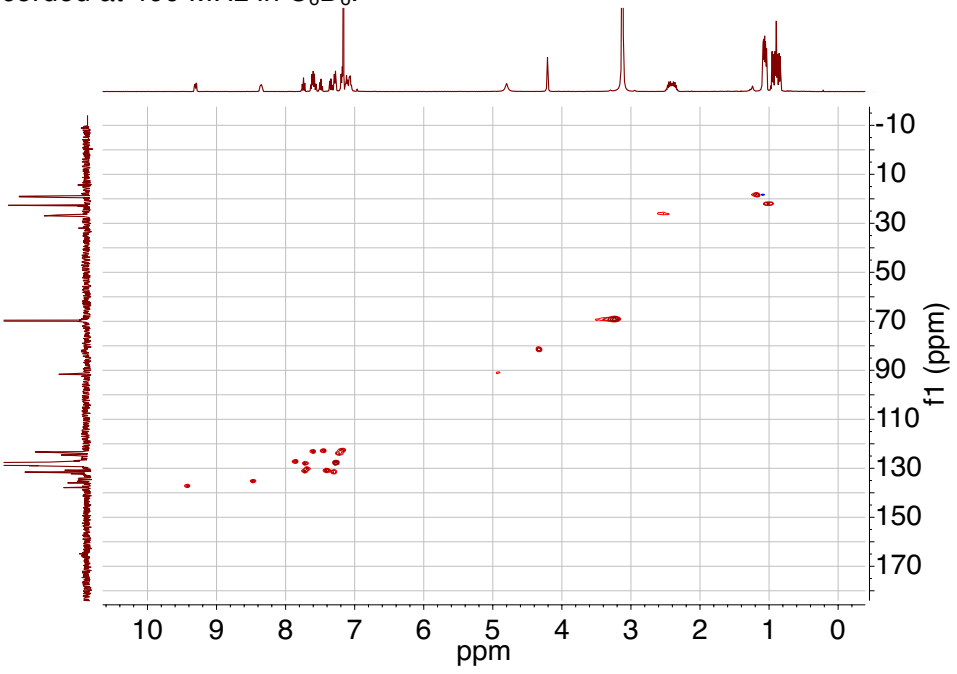

Figure 3.4.5.7. ^{1}H-^{13}C HSQC NMR spectrum of **[Au(B_2P_2)(OCH_2OCH_2)][K(18-c-6)]** recorded at 400 (^{1}H) MHz in C_6D_6.

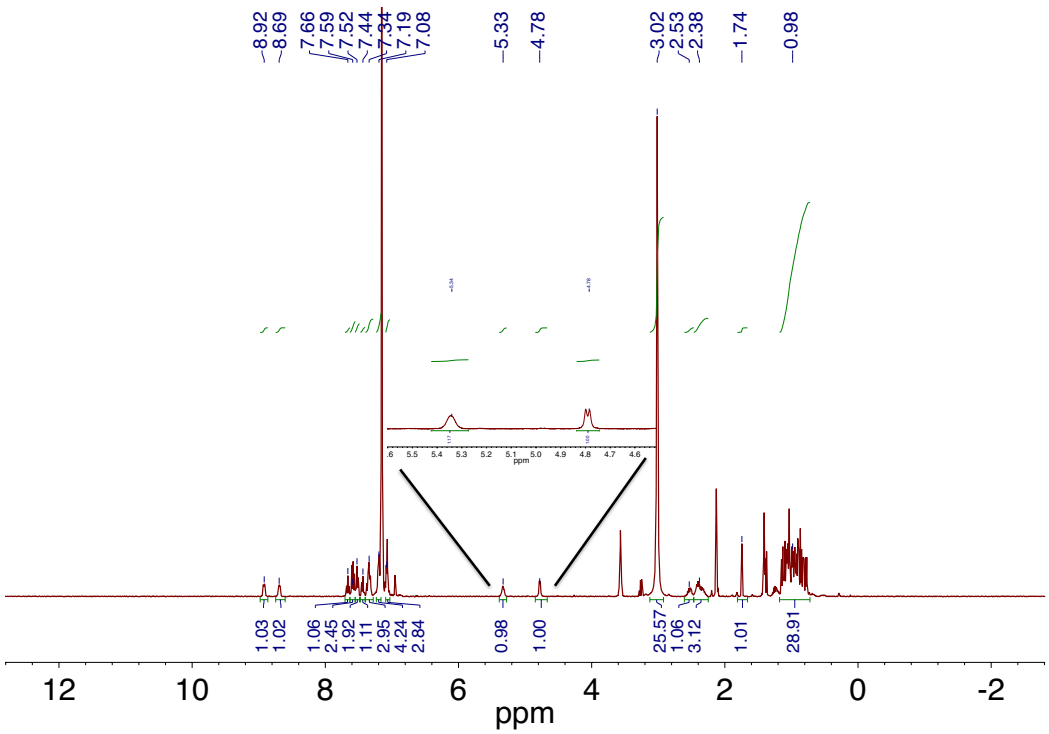

Figure 3.4.5.8. ^{1}H NMR spectrum of **[Au(B_2P_2)(C_3H_5)(OH)][K(18-c-6)]** recorded at 400 MHz in C_6D_6.

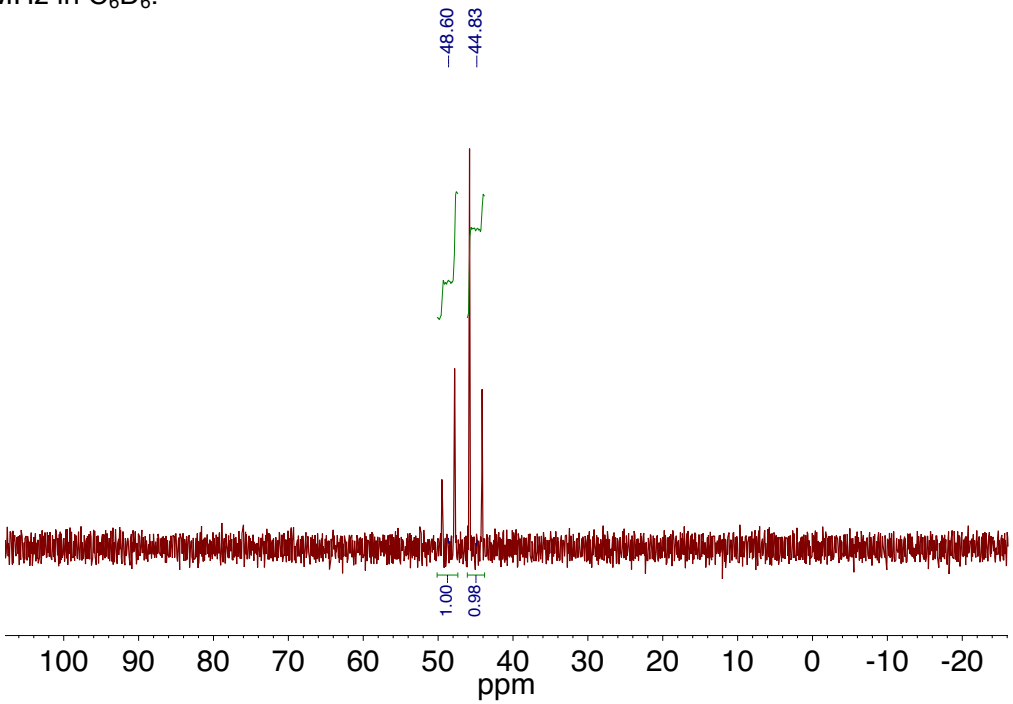

Figure 3.4.5.9. ^{31}P NMR spectrum of **[Au(B_2P_2)(C_3H_5)(OH)][K(18-c-6)]** recorded at 162 MHz in C_6D_6.

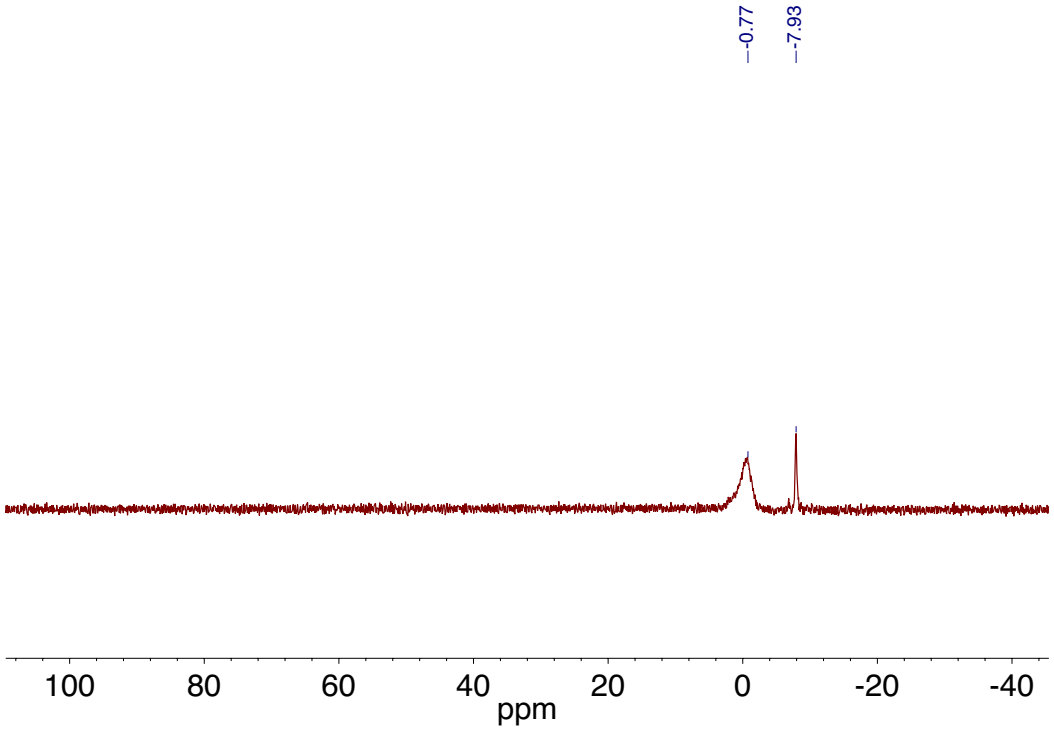

Figure 3.4.5.10. $^{11}B\{^{1}H\}$ NMR spectrum of **[Au(B_2P_2)(C_3H_5)(OH)][K(18-c-6)]** recorded at 128 MHz in C_6D_6.

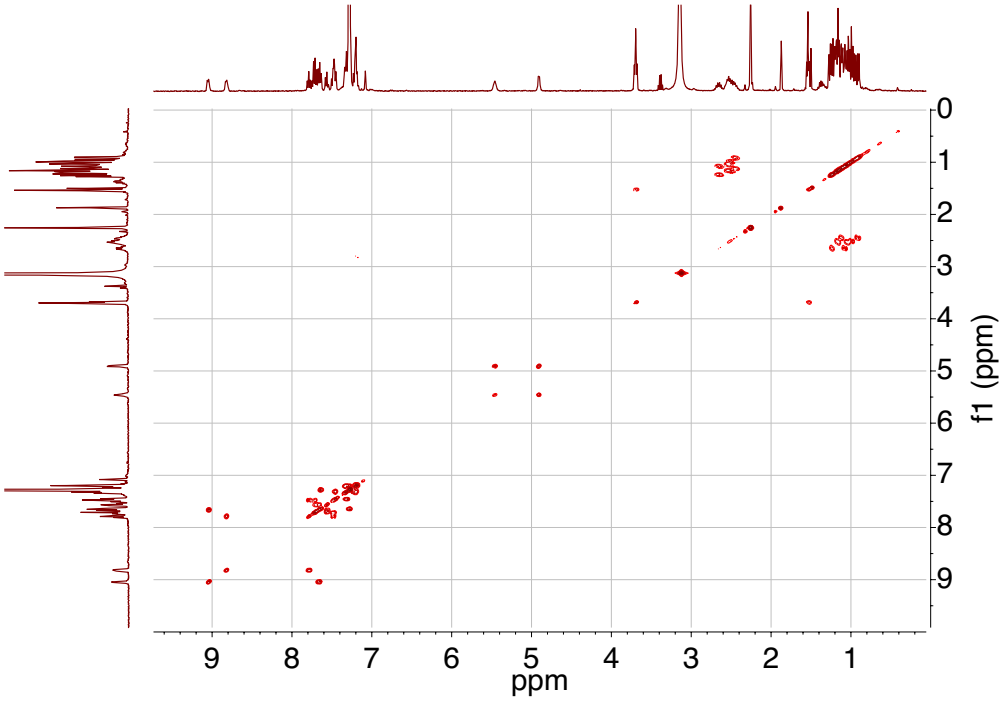

Figure 3.4.5.11. ^{1}H-^{1}H COSY NMR spectrum of **[Au(B_2P_2)(C_3H_5)(OH)][K(18-c-6)]** recorded at 500 MHz in C_6D_6.

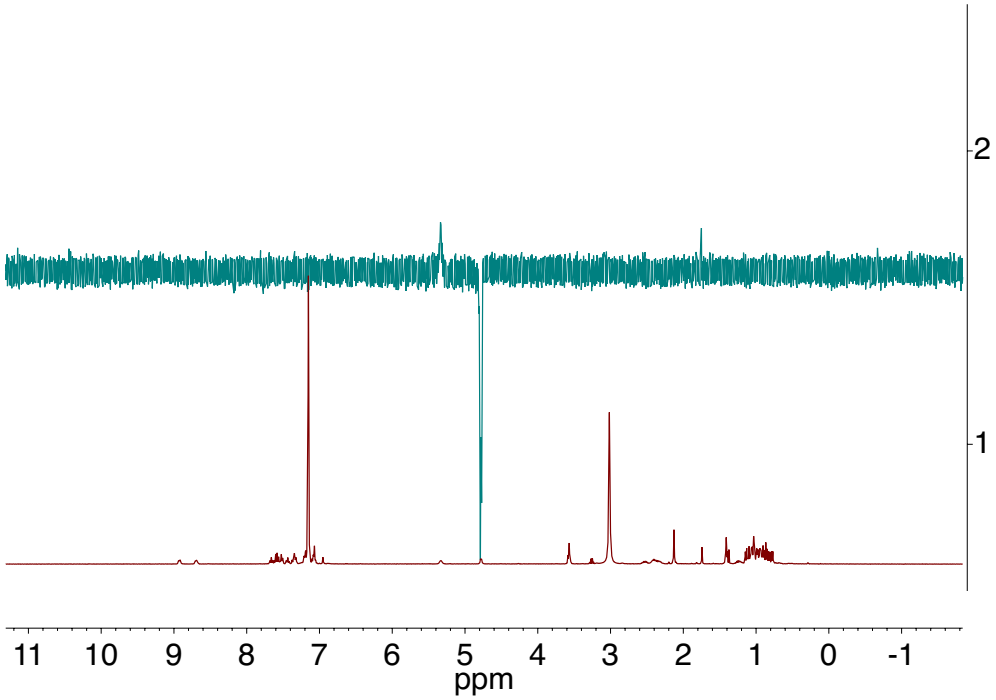

Figure 3.4.5.12. 1H-1D NOE NMR spectrum of **[Au(B_2P_2)(C_3H_5)(OH)][K(18-c-6)]** recorded at 400 MHz in C_6D_6.

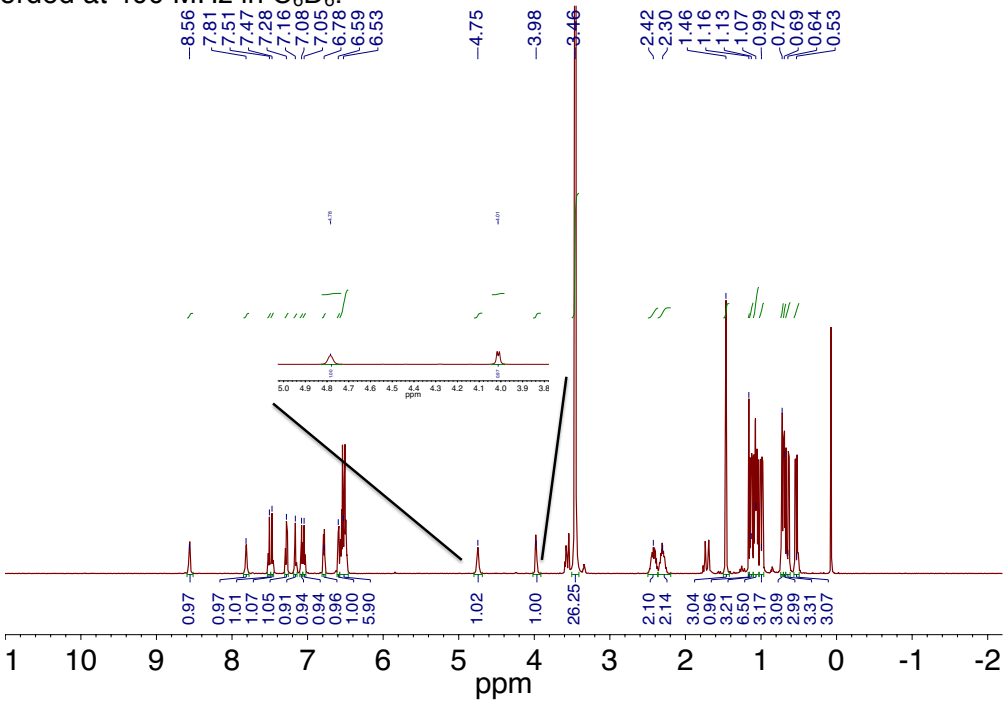

Figure 3.4.5.13. ^{1}H NMR spectrum of **[Au(B_2P_2)(C_3H_5)(OH)][K(18-c-6)]** recorded at 600 MHz in THF-d_8.

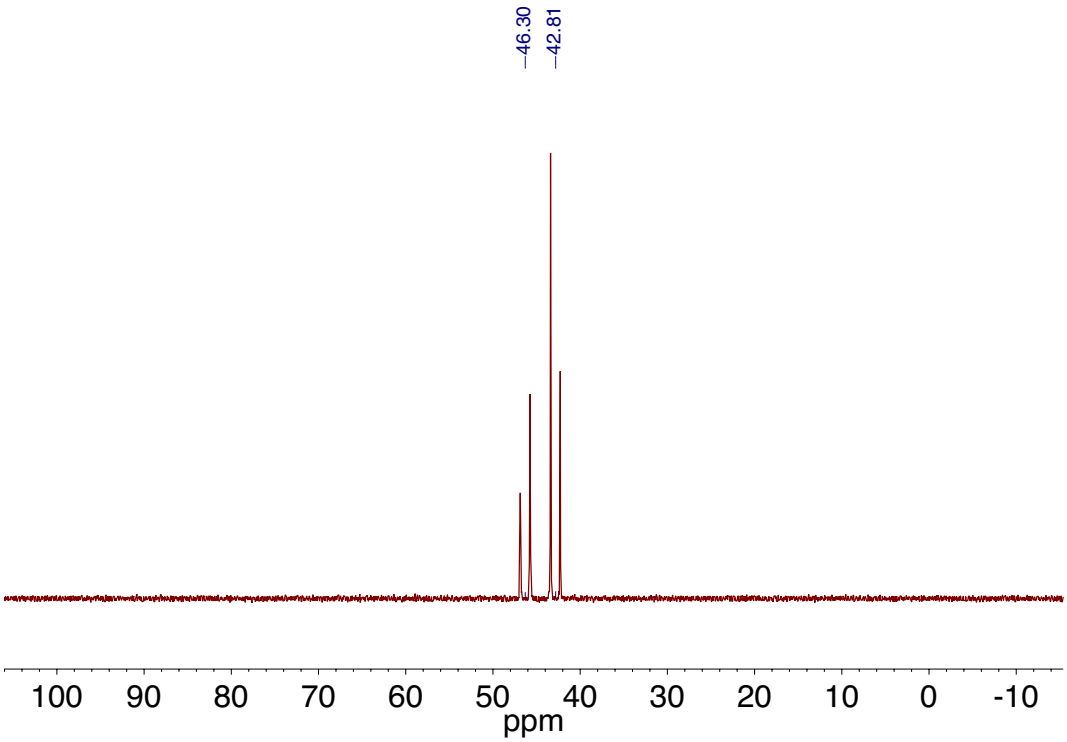

Figure 3.4.5.14. ^{31}P NMR spectrum of **[Au(B_2P_2)(C_3H_5)(OH)][K(18-c-6)]** recorded at 243 MHz in THF-d_8.

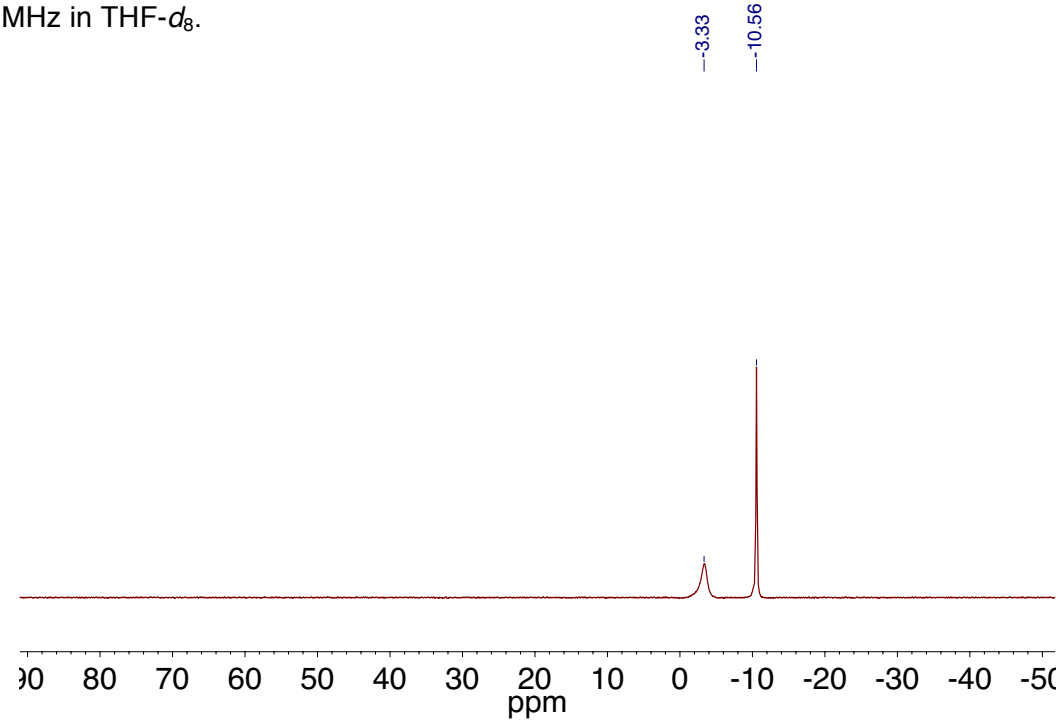

Figure 3.4.5.15. ^{11}B{^{1}H} NMR spectrum of **[Au(B_2P_2)(C_3H_5)(OH)][K(18-c-6)]** recorded at 192 MHz in THF-d_8.

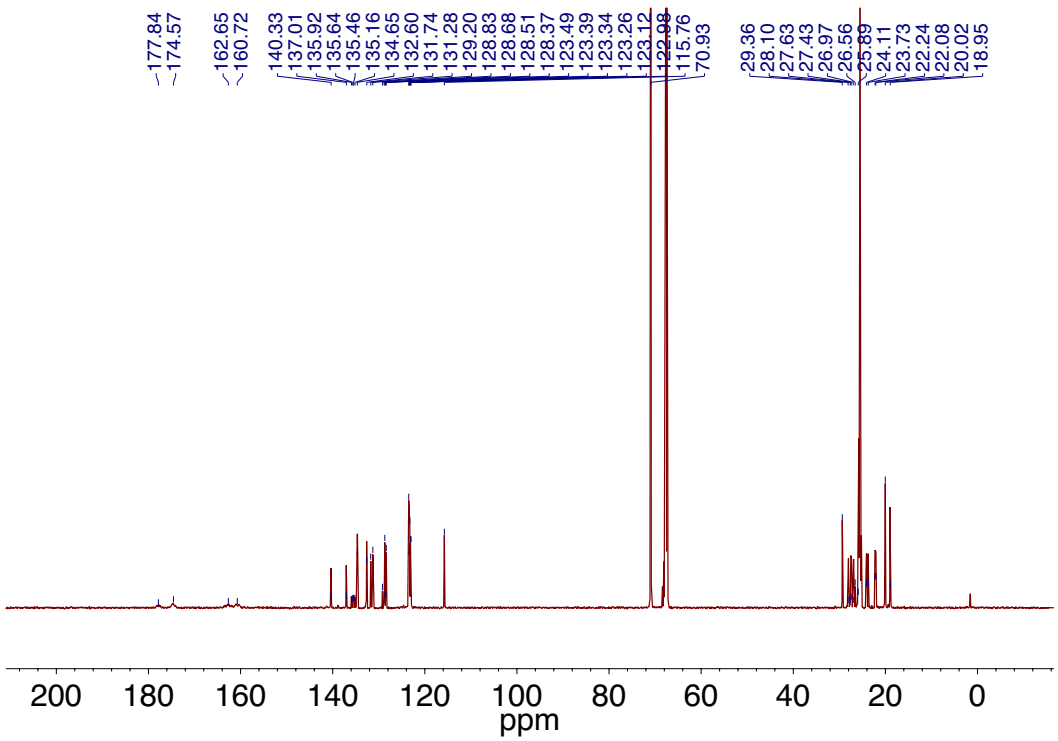

Figure 3.4.5.16. $^{13}C\{^{1}H\}$ NMR spectrum of **[Au(B_2P_2)(C_3H_5)(OH)][K(18-c-6)]** recorded at 151 MHz in THF-d_8.

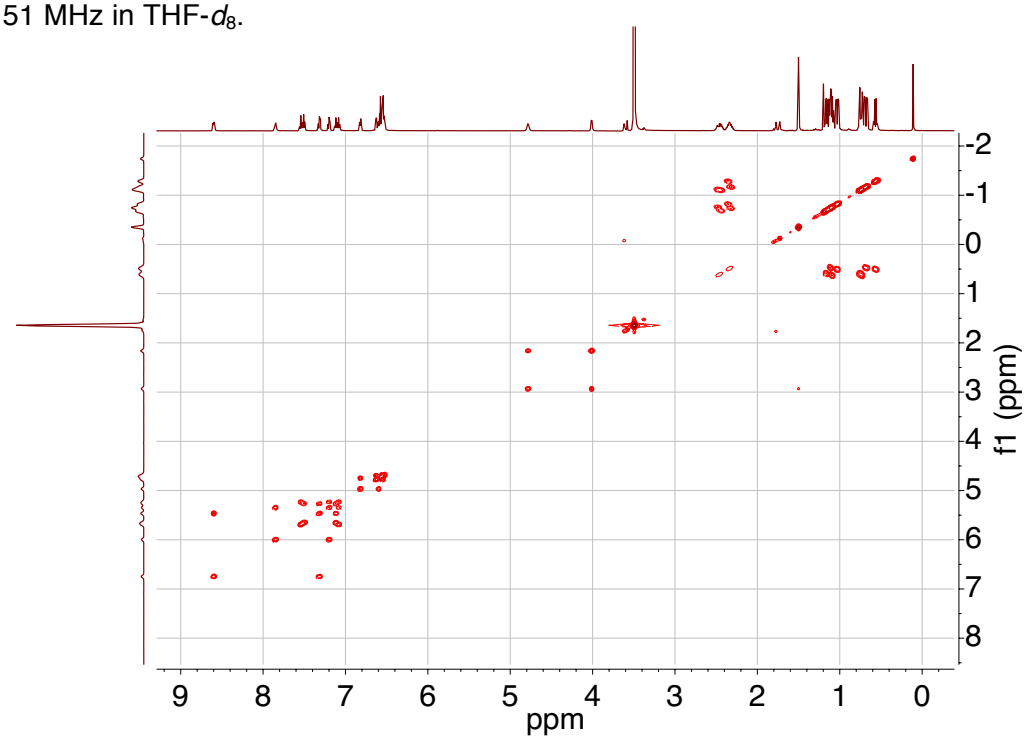

Figure 3.4.5.17. ^{1}H-^{1}H COSY NMR spectrum of **[Au(B_2P_2)(C_3H_5)(OH)][K(18-c-6)]** recorded at 600 MHz in THF-d_8.

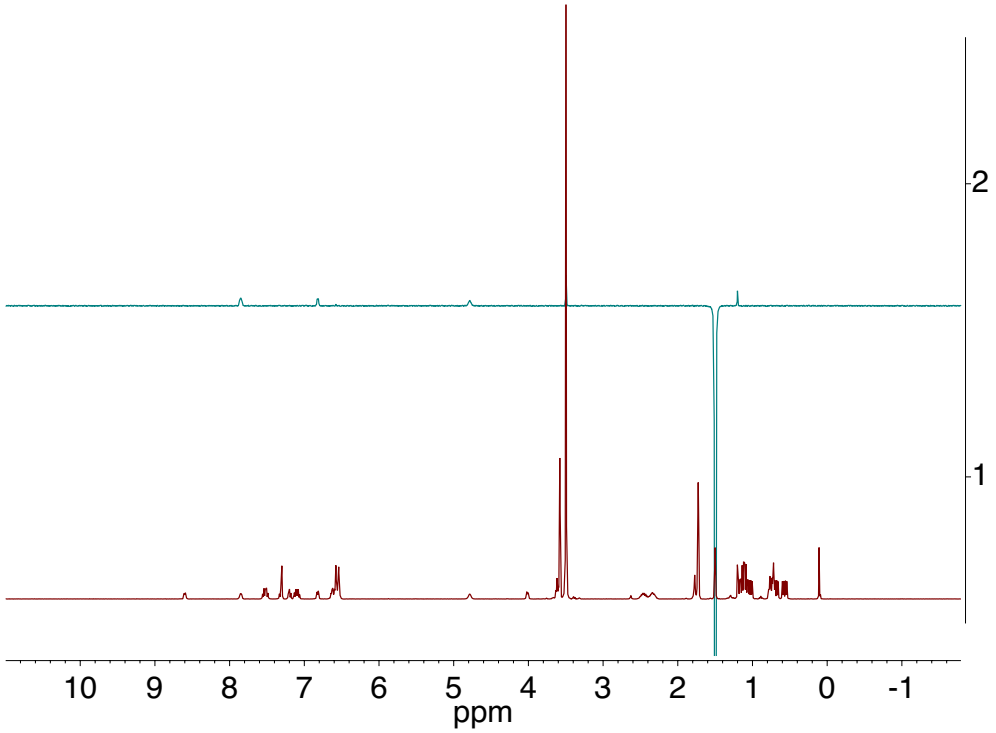

Figure 3.4.5.18. ^{1}H-1D NOE NMR spectrum of **[Au(B_2P_2)(C_3H_5)(OH)][K(18-c-6)]** recorded at 400 MHz in THF-d_8.

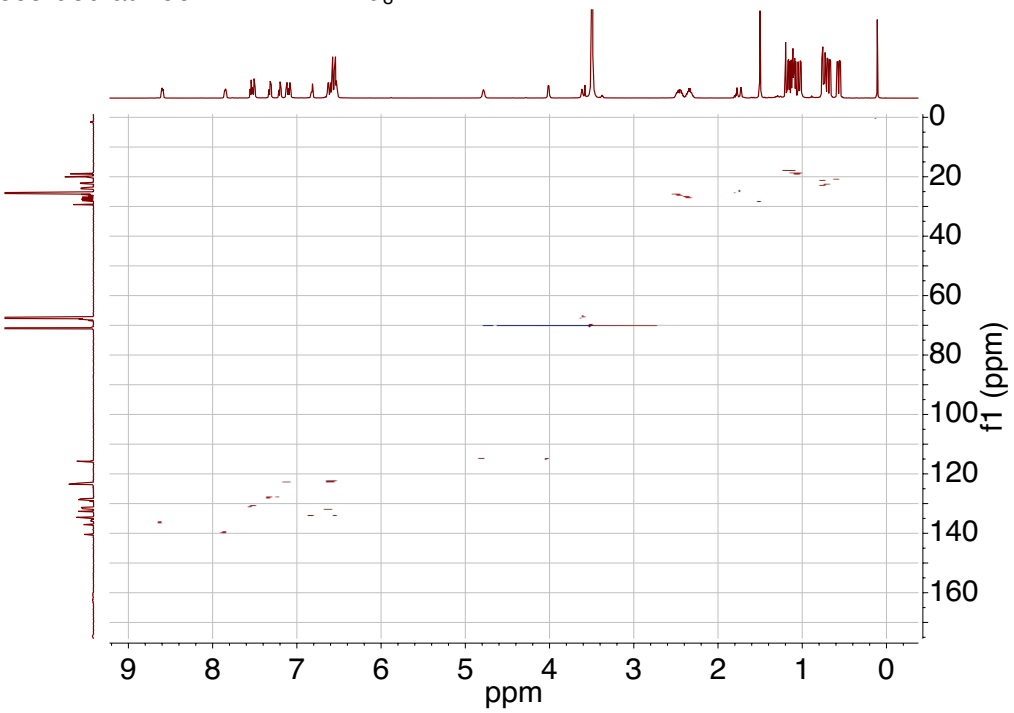

Figure 3.4.5.19. ^{1}H-^{13}C HSQC NMR spectrum of **[Au(B_2P_2)(C_3H_5)(OH)][K(18-c-6)]** recorded at 600 (^{1}H) MHz in THF-d_8.

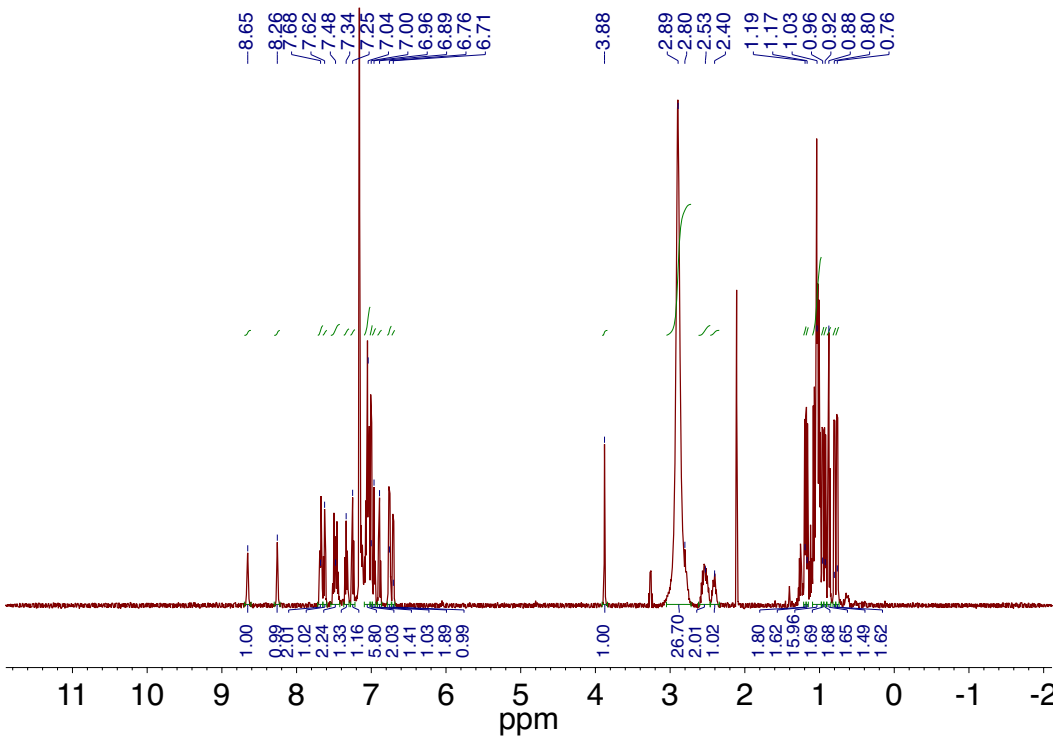

Figure 3.4.5.20. ^{1}H NMR spectrum of **[Au(B_2P_2)(C_7H_6O)][K(18-c-6)]** recorded at 400 MHz in C_6D_6.

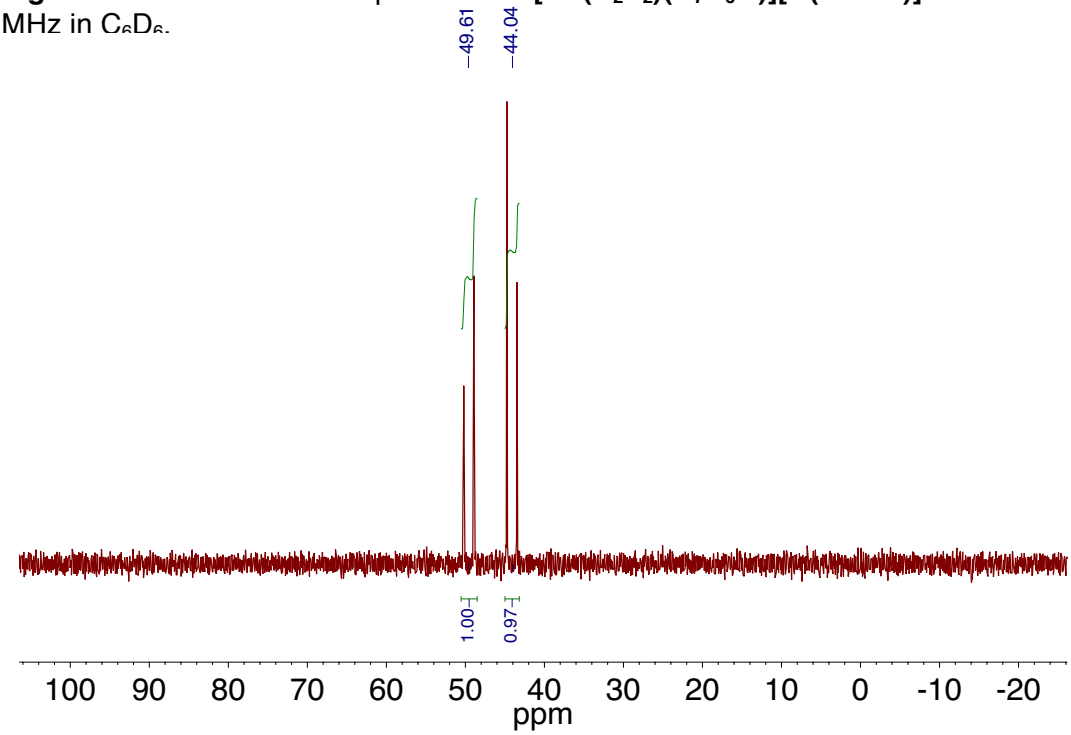

Figure 3.4.5.21. ^{31}P NMR spectrum of **[Au(B_2P_2)(C_7H_6O)][K(18-c-6)]** recorded at 202 MHz in C_6D_6.

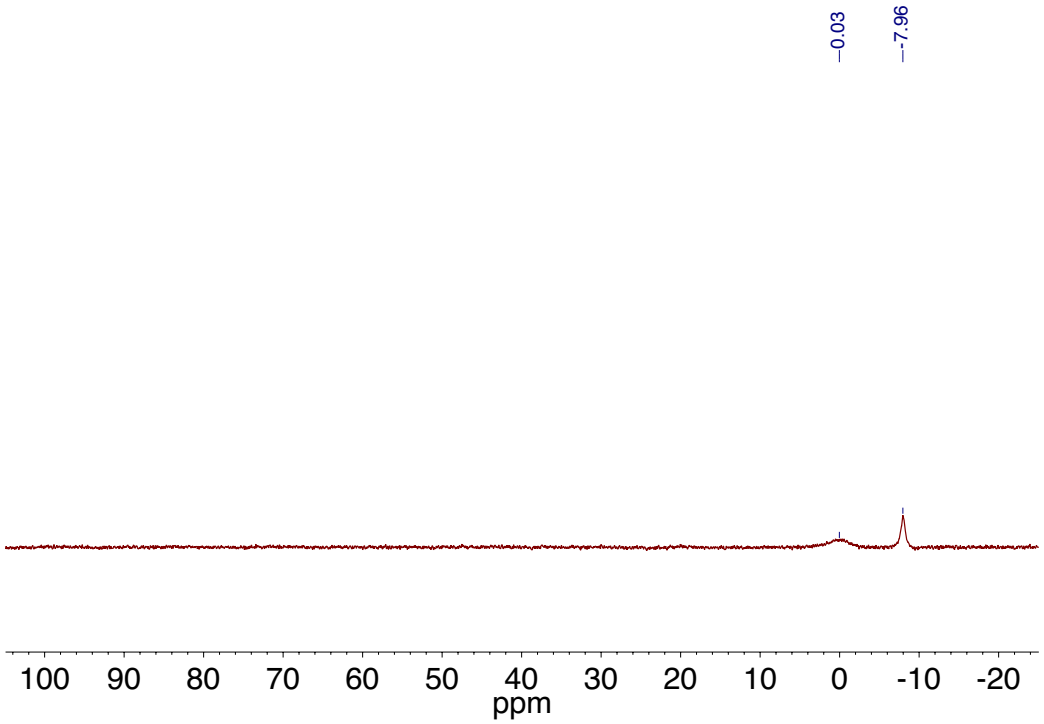

Figure 3.4.5.22. $^{11}B\{^{1}H\}$ NMR spectrum of **[Au(B_2P_2)(C_7H_6O)][K(18-c-6)]** recorded at 160 MHz in C_6D_6.

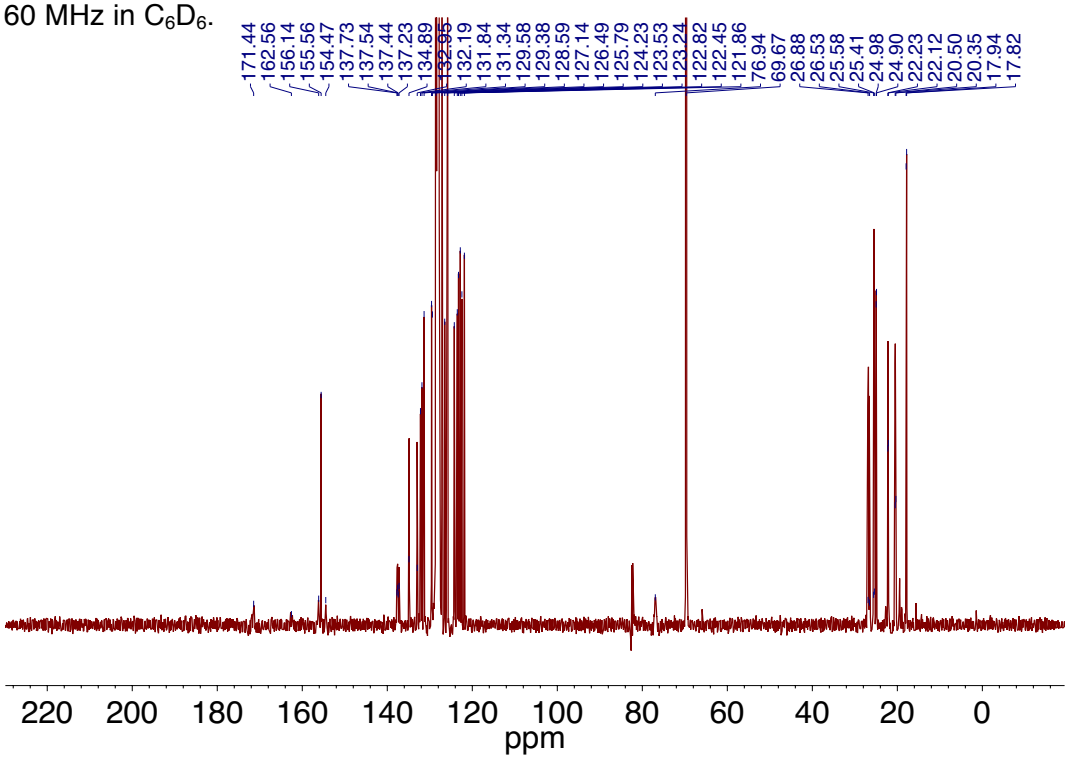

Figure 3.4.5.23. $^{13}C\{^{1}H\}$ NMR spectrum of **[Au(B_2P_2)(C_7H_6O)][K(18-c-6)]** recorded at 151 MHz in C_6D_6.

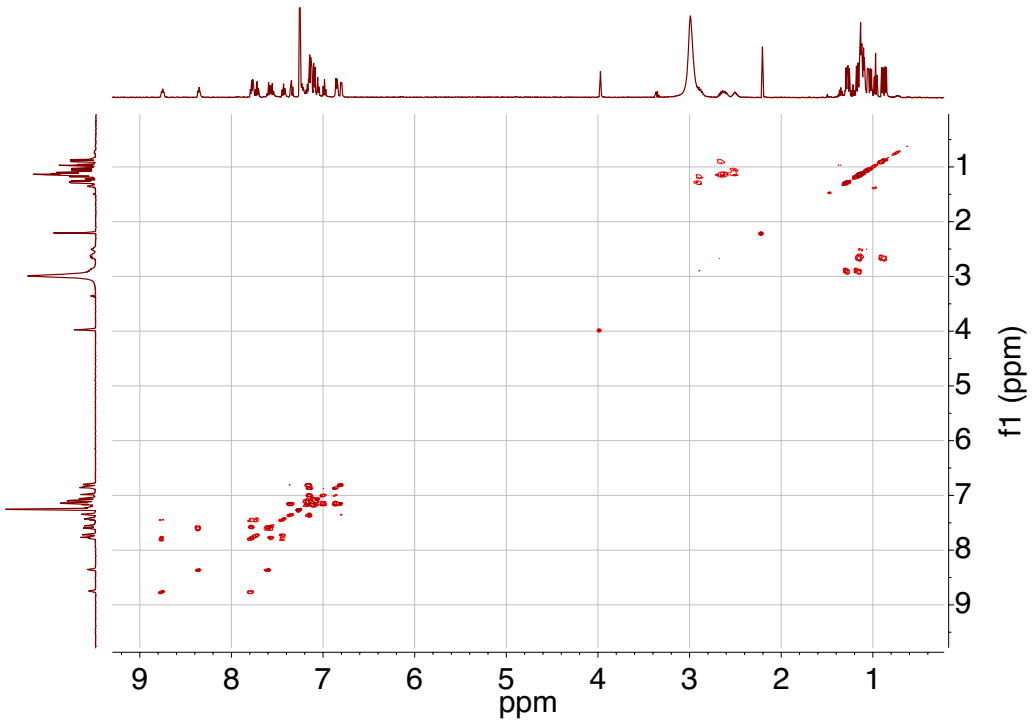

Figure 3.4.5.24. ^{1}H-^{1}H COSY NMR spectrum of **[Au(B_2P_2)(C_7H_6O)][K(18-c-6)]** recorded at 500 MHz in C_6D_6.

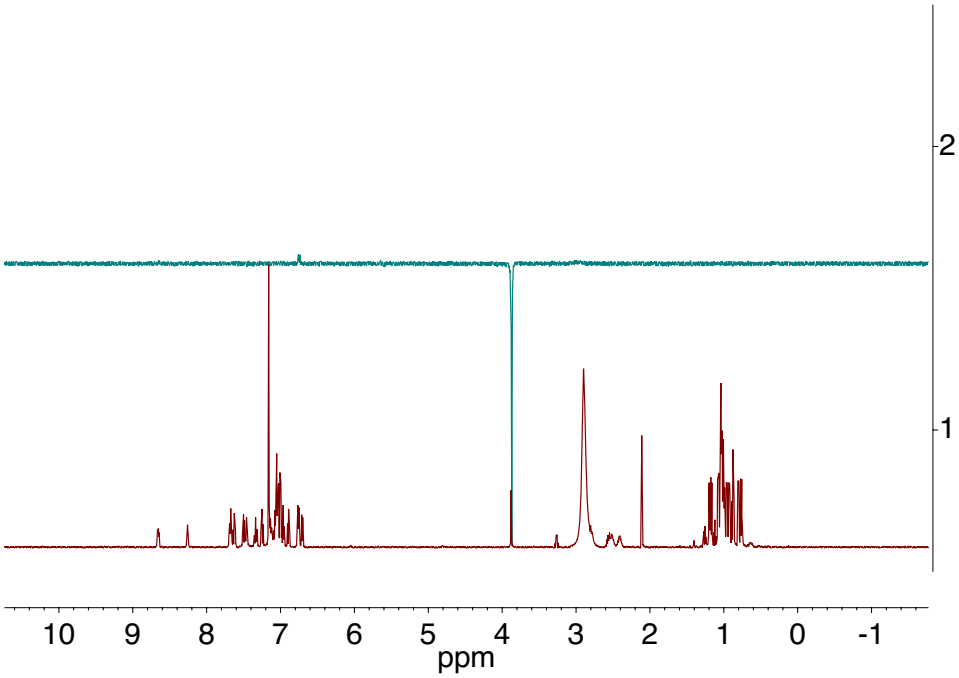

Figure 3.4.5.25. ^{1}H-1D NOE spectrum of **[Au(B_2P_2)(C_7H_6O)][K(18-c-6)]** recorded at 400 MHz in C_6D_6.

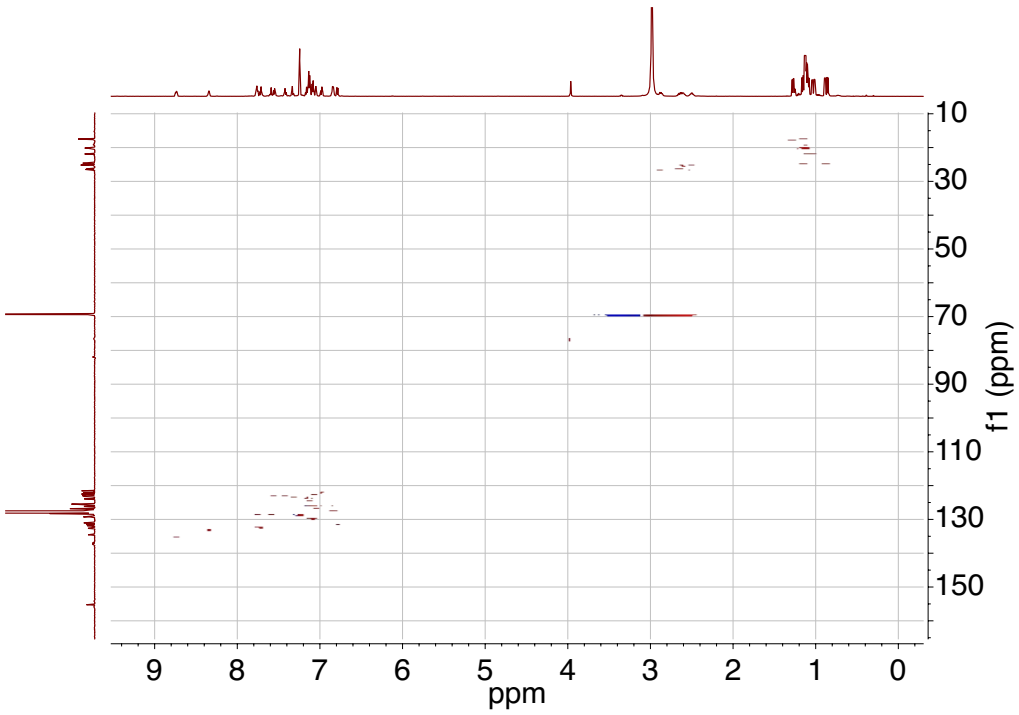

Figure 3.4.5.26. ^{1}H-^{13}C HSQC spectrum of **[Au(B_2P_2)(C_7H_6O)][K(18-c-6)]** recorded on a 600 MHz spectrometer in C_6D_6.

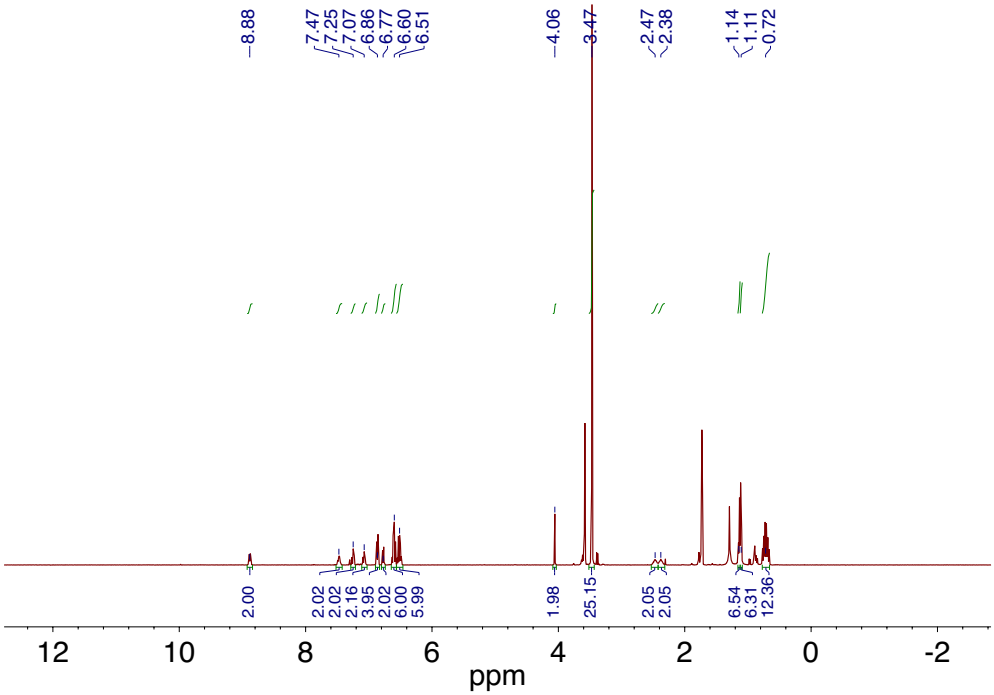

Figure 3.4.5.27. ^{1}H NMR spectrum of **[Au(B_2P_2)($C_{14}H_{12}O_2$)][K(18-c-6)($THF)_2$]** recorded at 500 MHz in THF-d_8.

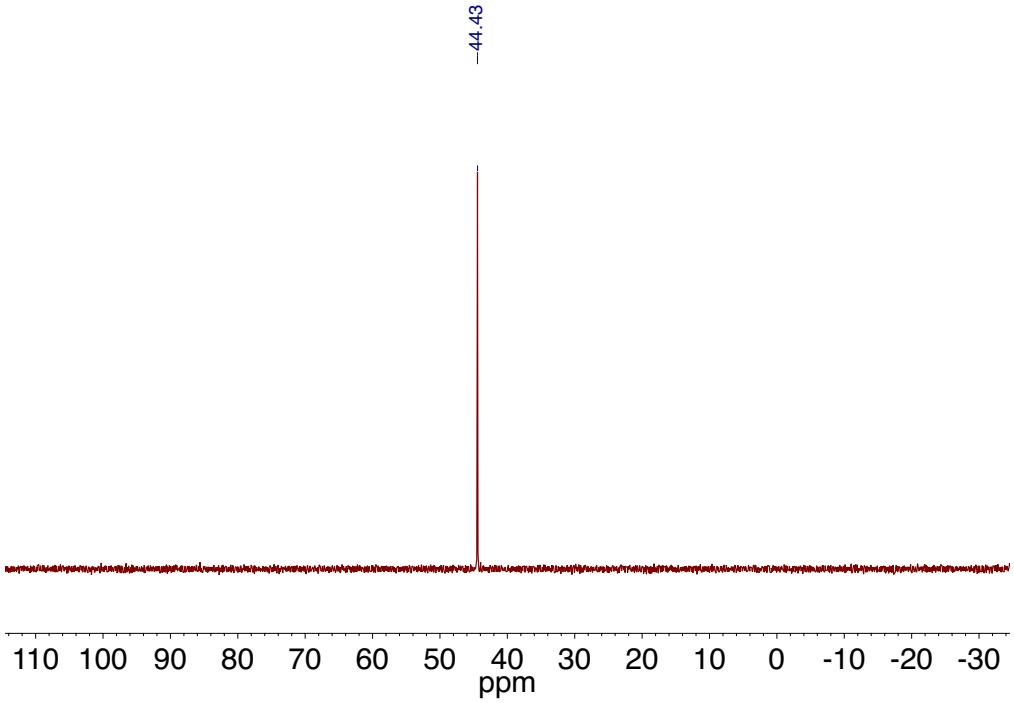

Figure 3.4.5.28. ^{31}P NMR spectrum of **[Au(B_2P_2)($C_{14}H_{12}O_2$)][K(18-c-6)(THF)$_2$]** recorded at 162 MHz in THF-d_8.

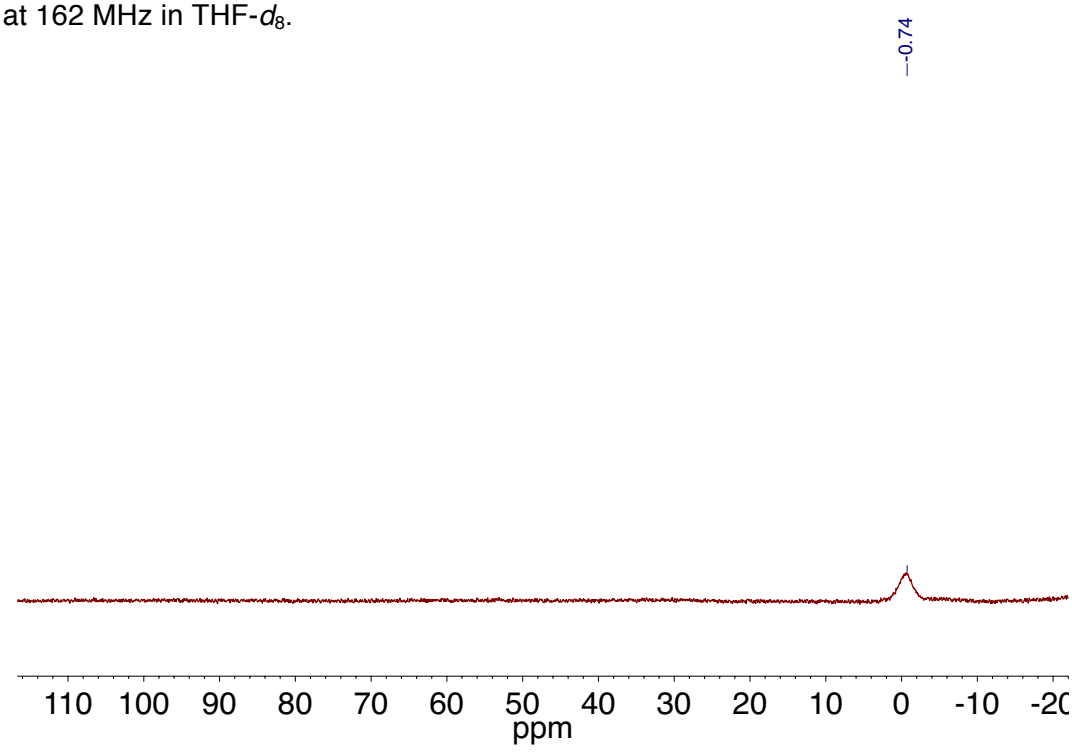

Figure 3.4.5.29. ^{11}B{^{1}H} NMR spectrum of **[Au(B_2P_2)($C_{14}H_{12}O_2$)][K(18-c-6)(THF)$_2$]** recorded at 128 MHz in THF-d_8.

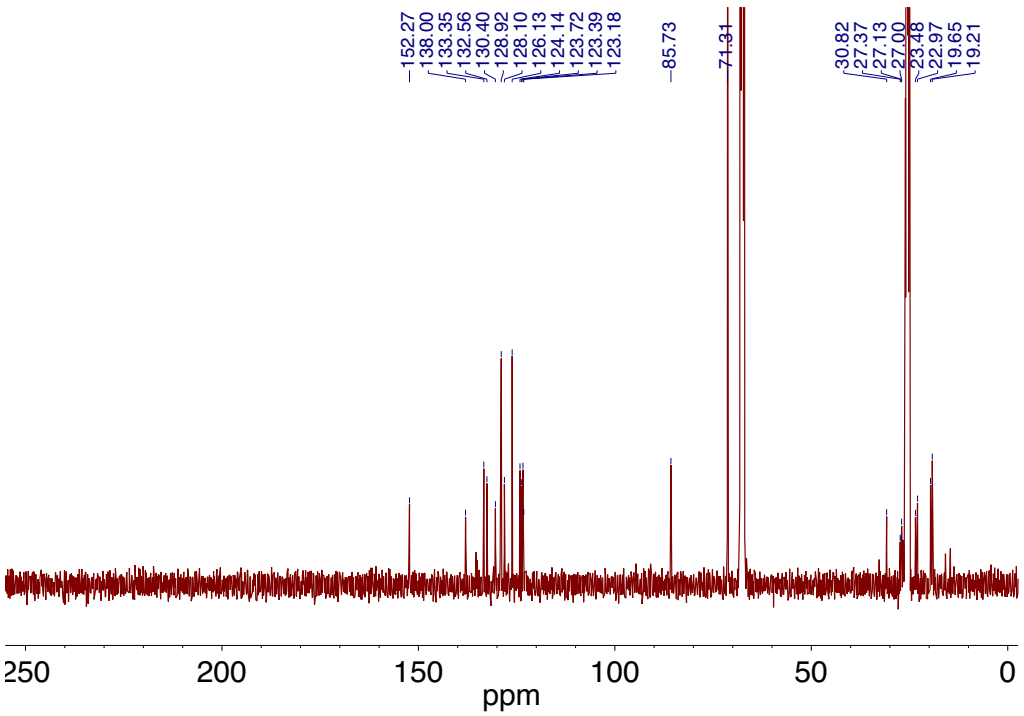

Figure 3.4.5.30. $^{13}C\{^{1}H\}$ NMR spectrum of **[Au(B_2P_2)($C_{14}H_{12}O_2$)][K(18-c-6)(THF)$_2$]** recorded at 101 MHz in THF-d_8.

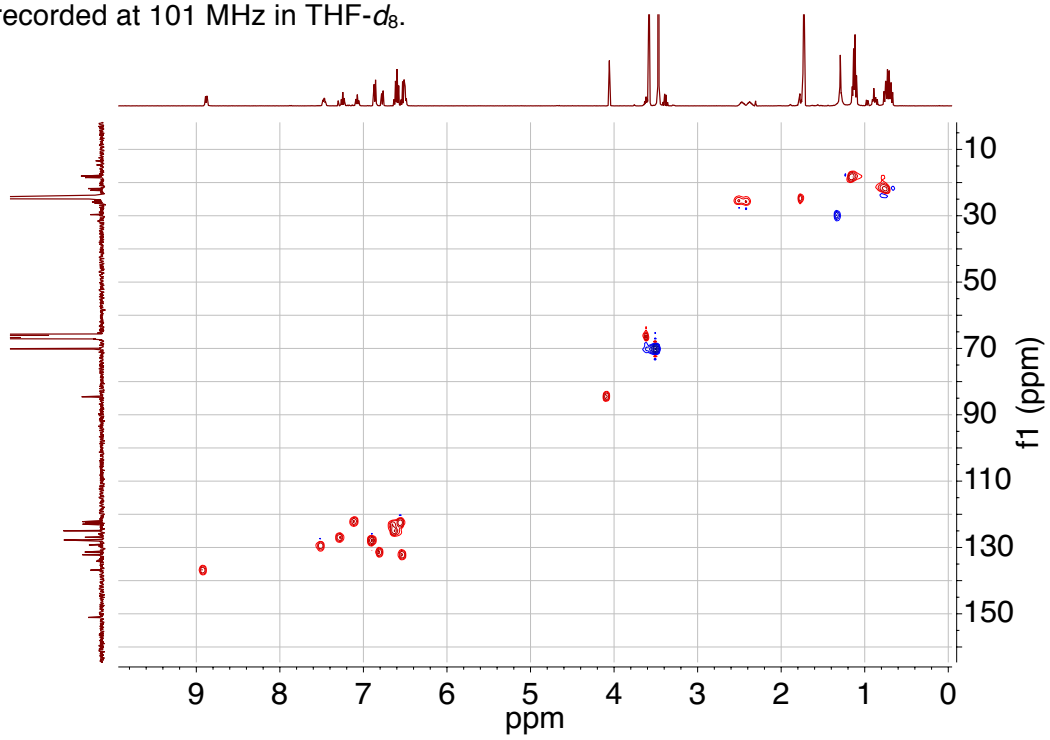

Figure 3.4.5.31. ^{1}H-^{13}C HSQC NMR spectrum of **[Au(B_2P_2)($C_{14}H_{12}O_2$)][K(18-c-6)(THF)$_2$]** recorded at 400 (^{1}H) MHz in C_6D_6.

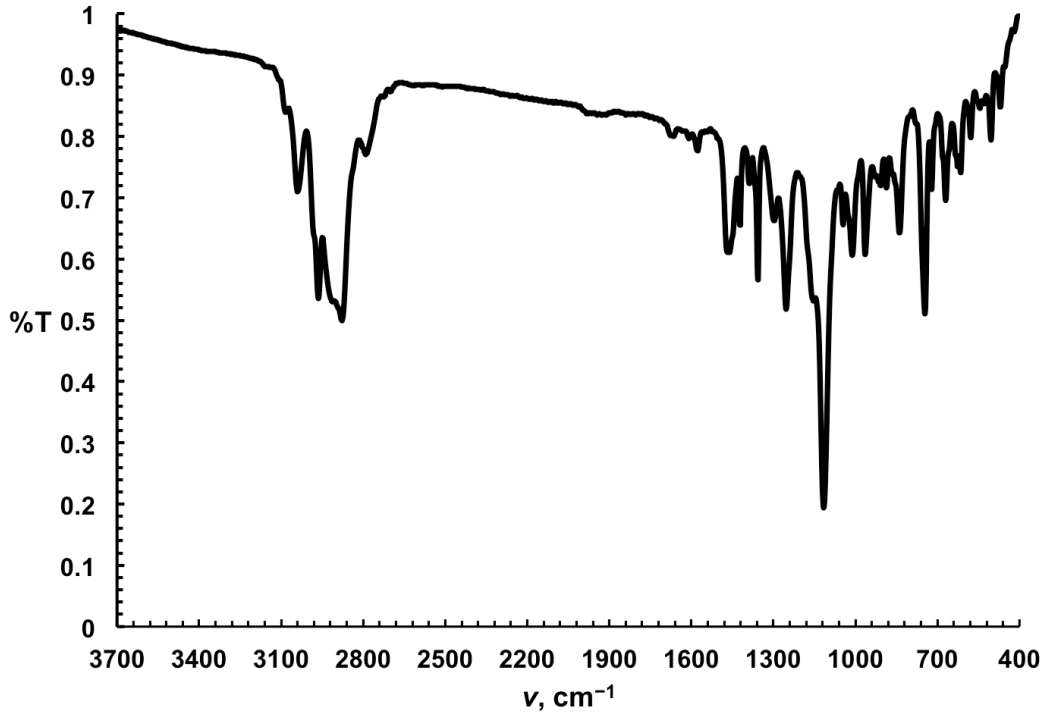

Figure 3.4.5.32. FT-IR spectrum of **[Au(B_2P_2)(OCH_2OCH_2)][K(18-c-6)]**.

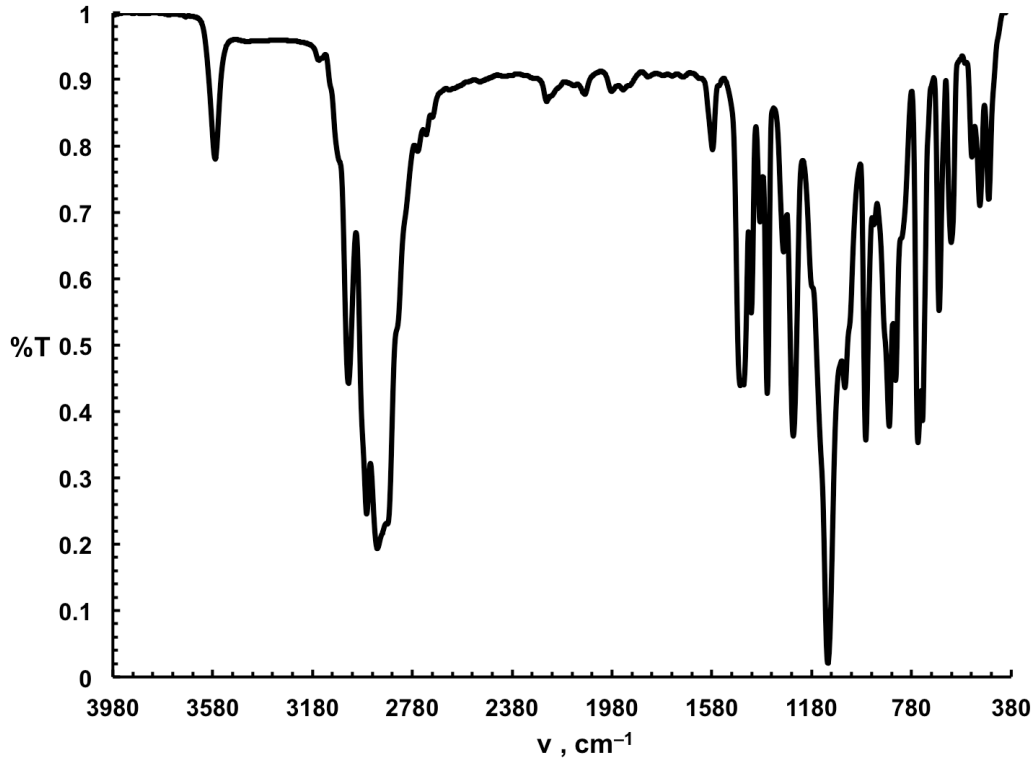

Figure 3.4.5.33. FT-IR spectrum of **[Au(B_2P_2)(C_3H_5)(OH)][K(18-c-6)].**

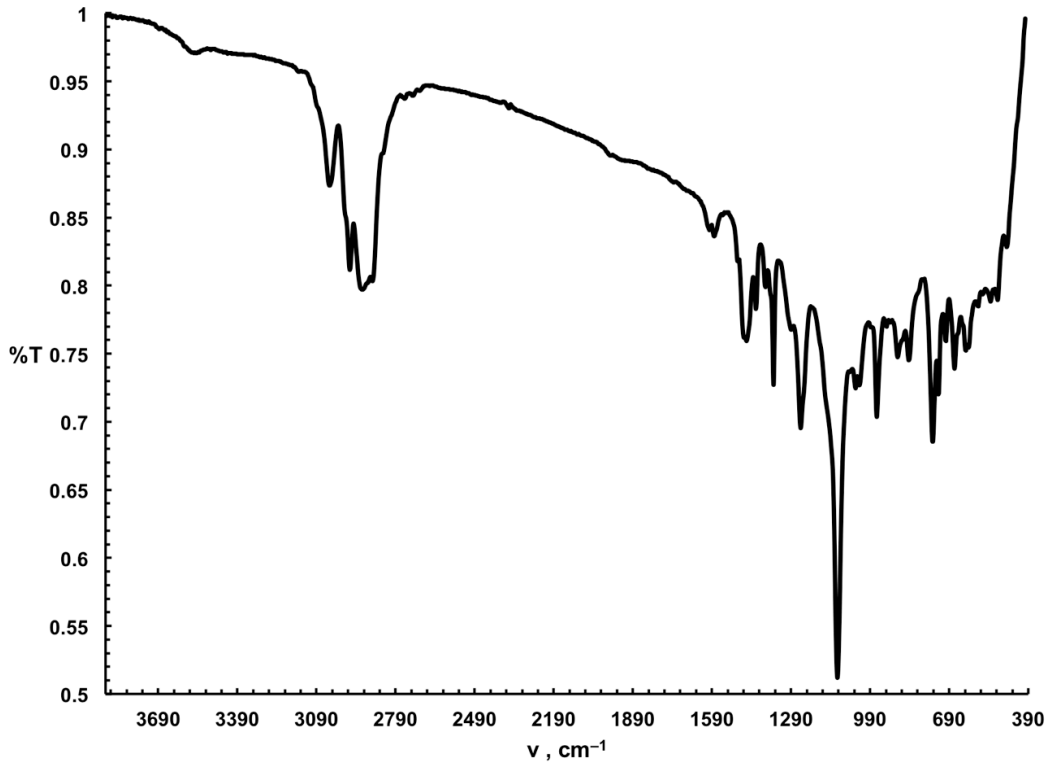

Figure 3.4.5.34. FT-IR spectrum of **[Au(B_2P_2)(C_7H_6O)][K(18-c-6)]**.

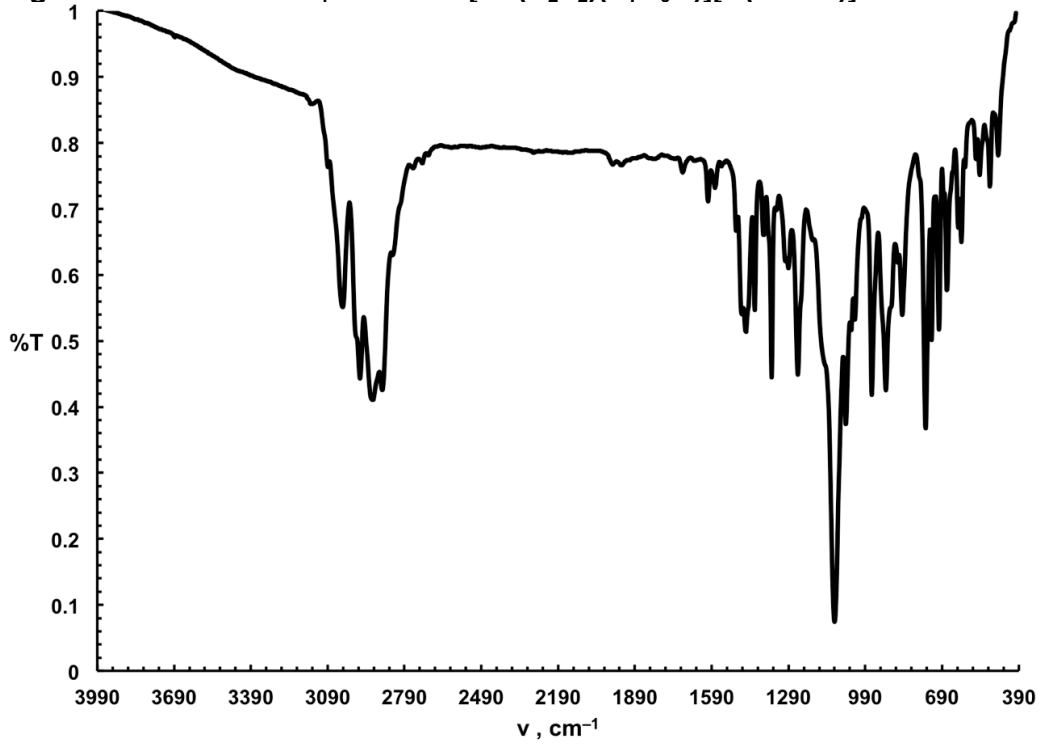

Figure 3.4.5.35. FT-IR spectrum of **[Au(B_2P_2)($C_{14}H_{12}O_2$)][K(18-c-6)($THF)_2$].**

3.4.6) X-Ray Crystallography

3.4.6.1.) General Considerations

Single crystals were coated with paratone oil and mounted on cryo-loop glass fibers. X-ray intensity data were collected at 100(2) K on a Bruker APEX2[36] platform-CCD X-ray diffractometer system using fine-focus Mo K_α radiation (λ = 0.71073 Å, 50kV/30mA power). The CCD detector was placed at 5.0600 cm from the crystal. Frames were integrated using the Bruker SAINT software package[37] and using a narrow-frame integration algorithm. Absorption corrections were applied to the raw intensity data using the SADABS program.[38] The Bruker SHELXTL software package[39] was used for phase determination and structure refinement. Atomic coordinates, isotropic and anisotropic displacement parameters of all the non-hydrogen atoms were refined by means of a full matrix least-squares procedure on F^2. The H-atoms were included in the refinement in calculated positions riding on the atoms to which they were attached. Relevant details for individual data collections are reported in Tables 3.4.6.1–3.4.6.4.

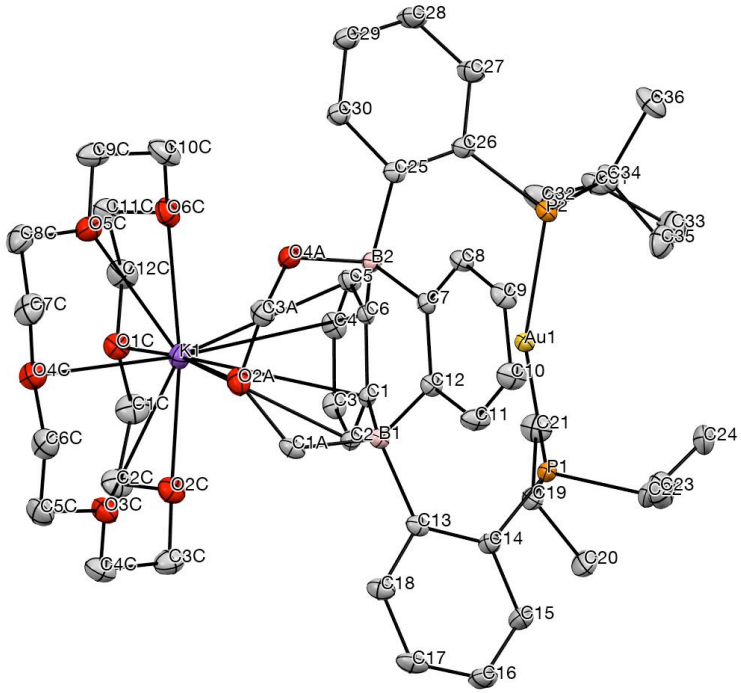

Figure 3.4.6.1. Labeled thermal ellipsoid plot (50%) **for [Au(B_2P_2)(OCH_2OCH_2)][K(18-c-6)]**.

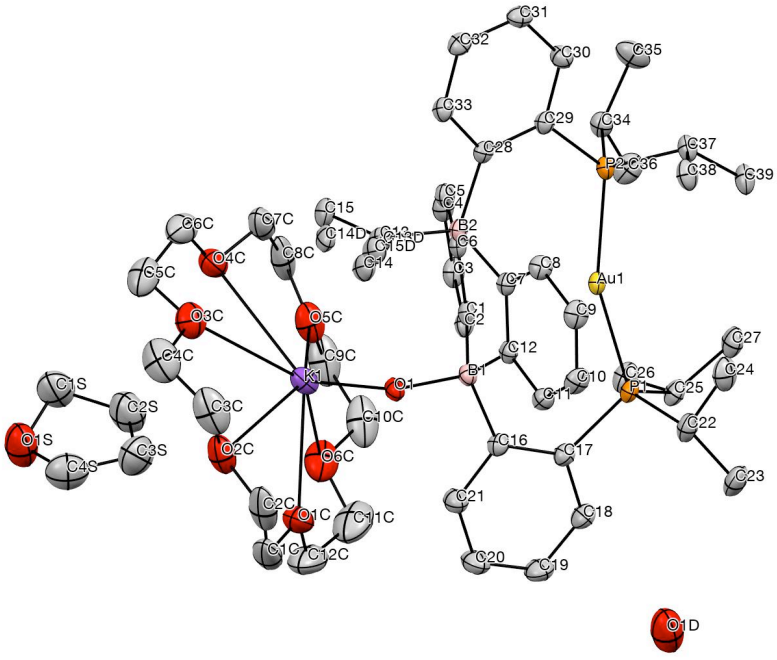

Figure 3.4.6.2. Labeled thermal ellipsoid plot (50%) for **[Au(B_2P_2)(C_3H_5)(OH)][K(18-c-6)].**

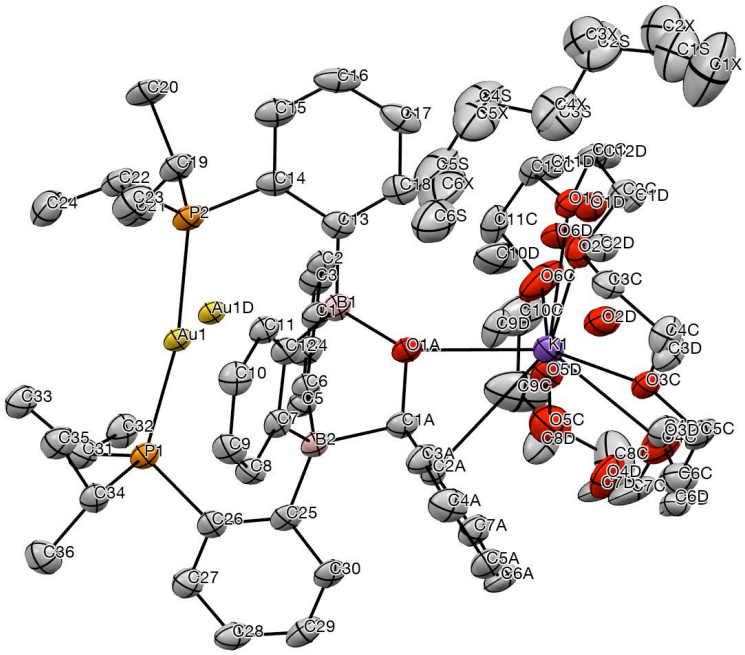

Figure 3.4.6.3. Labeled thermal ellipsoid plot (50%) for **[Au(B_2P_2)(C_7H_6O)][K(18-c-6)]**.

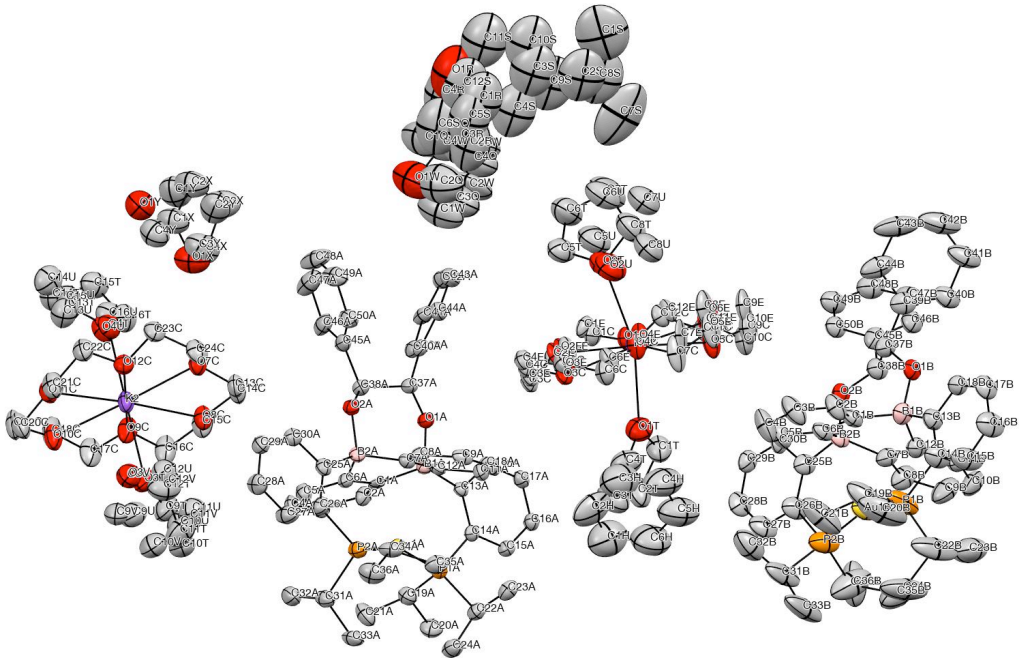

Figure 3.4.6.4. Labeled thermal ellipsoid plot (50%) for **[Au(B_2P_2)($C_{14}H_{12}O_2$)][K(18-c-6)(THF)$_2$].**

Table 3.4.6.1. Crystal data and structure refinement **for [Au(B_2P_2)(OCH_2OCH_2)][K(18-c-6)]**.

Identification code	hh248JT123_0m	
Empirical formula	$C_{50}H_{72}AuB_2KO_8P_2$	
Formula weight	1120.70 g/mol	
Temperature	100(2) K	
Wavelength	0.71073 Å	
Crystal system	Triclinic	
Space group	P –1	
Unit cell dimensions	a = 10.0837(2) Å	α = 81.7553(5)°.
	b = 14.1067(2) Å	β = 84.4017(5)°.
	c = 18.4824(3) Å	γ = 73.8383(5)°.
Volume	2494.48(7) $Å^3$	
Z	2	
Density (calculated)	1.492 mg/m^3	
Absorption coefficient	3.148 mm^{-1}	
F(000)	1148	
Crystal size	0.584 x 0.571 x 0.514 mm^3	
θ range for data collection	1.768 to 28.700°.	
Index ranges	$-13 \le h \le 13$, $-19 \le k \le 19$, $-24 \le l \le 24$	
Reflections collected	98727	
Independent reflections	12884 [R_{int} = 0.0199]	
Completeness to θ = 25.242°	100.0 %	
Absorption correction	Semi-empirical from equivalents	
Refinement method	Full-matrix least-squares on F^2	
Data / restraints / parameters	12884 / 0 / 585	
Goodness-of-fit on F^2	1.078	
Final R indices [$I > 2\sigma_I$]	R_1 = 0.0149, wR_2 = 0.0370	
R indices (all data)	R_1 = 0.0154, wR_2 = 0.0372	
Largest diff. peak and hole	1.277 and –0.446 e/$Å^3$	

Table 3.4.6.2. Crystal data and structure refinement for **[Au(B_2P_2)(C_3H_5)(OH)][K(18-c-6)].**

Identification code	hh191JT94r_0m	
Empirical formula	$C_{55}H_{82}AuB_2KO_8P_2$	
Formula weight	1190.83 g/mol	
Temperature	100(2) K	
Wavelength	0.71073 Å	
Crystal system	Monoclinic	
Space group	P 21/c	
Unit cell dimensions	a = 19.9307(6)Å	α = 90°.
	b = 14.7178(4)Å	β= 110.8122(5)°.
	c = 20.3785(6)Å	γ = 90°.
Volume	5587.7(3) Å^3	
Z	4	
Density (calculated)	1.416 mg/m^3	
Absorption coefficient	2.815 mm^{-1}	
F(000)	2456	
Crystal size	0.384 x 0.284 x 0.167 mm^3	
θ range for data collection	1.749 to 29.130°.	
Index ranges	$-27 \le h \le 27$, $-20 \le k \le 20$, $-27 \le l \le 27$	
Reflections collected	121534	
Independent reflections	15037 [R_{int} = 0.0221]	
Completeness to θ = 25.242°	100.0 %	
Absorption correction	Semi-empirical from equivalents	
Refinement method	Full-matrix least-squares on F^2	
Data / restraints / parameters	15037 / 18 / 667	
Goodness-of-fit on F^2	1.039	
Final R indices [$I > 2\sigma_I$]	R_1 = 0.0186, wR_2 = 0.0446	
R indices (all data)	R_1 = 0.0212, wR_2 = 0.0457	
Largest diff. peak and hole	0.941 and –0.581 e/Å^3	

Table 3.4.6.3. Crystal data and structure refinement for **[Au(B_2P_2)(C_7H_6O)][K(18-c-6)]**.

Identification code	hh257JT128_0m
Empirical formula	$C_{61}H_{88}AuB_2KO_7P_2$
Formula weight	1252.94 g/mol
Temperature	100(2) K
Wavelength	0.71073 Å
Crystal system	Triclinic
Space group	P –1
Unit cell dimensions	a = 11.3469(11) Å α = 103.9421(14)°. b = 13.0442(13) Å β = 95.7811(14)°. c = 21.464(2) Å γ = 101.0043(15)°.
Volume	2990.5(5) $Å^3$
Z	2
Density (calculated)	1.391 mg/m^3
Absorption coefficient	2.633 mm^{-1}
F(000)	1296
Crystal size	0.324 x 0.108 x 0.051 mm^3
θ range for data collection	1.650 to 26.371°.
Index ranges	$-14 \le h \le 14$, $-16 \le k \le 16$, $-26 \le l \le 26$
Reflections collected	53298
Independent reflections	12231 [R_{int} = 0.0692]
Completeness to θ = 25.242°	100.0 %
Absorption correction	Semi-empirical from equivalents
Refinement method	Full-matrix least-squares on F^2
Data / restraints / parameters	12231 / 1064 / 895
Goodness-of-fit on F^2	1.058
Final R indices [$I > 2\sigma_I$]	R_1 = 0.0509, wR_2 = 0.1149
R indices (all data)	R_1 = 0.0715, wR_2 = 0.1245
Largest diff. peak and hole	2.593 and –2.471 e/$Å^3$

Table 3.4.6.4. Crystal data and structure refinement for **[Au(B_2P_2)($C_{14}H_{12}O_2$)][K(18-c-6)$(THF)_2$].**

Identification code	hh256JT127_0m	
Empirical formula	$C_{79.12}H_{112.34}AuB_2KO_{11.15}P_2$	
Formula weight	1561.53 g/mol	
Temperature	100(2) K	
Wavelength	0.71073 Å	
Crystal system	Monoclinic	
Space group	P 21/c	
Unit cell dimensions	a = 14.6392(19) Å	α = 90°.
	b = 45.535(6) Å	β= 96.0286(16)°.
	c = 23.842(3) Å	γ = 90°.
Volume	15805(3) Å^3	
Z	8	
Density (calculated)	1.312 mg/m^3	
Absorption coefficient	2.011 mm^{-1}	
F(000)	6514	
Crystal size	0.469 x 0.392 x 0.046 mm^3	
θ range for data collection	1.593 to 25.350°.	
Index ranges	$-17 \le h \le 17$, $-54 \le k \le 54$, $-28 \le l \le 28$	
Reflections collected	211642	
Independent reflections	28913 [R_{int} = 0.0852]	
Completeness to θ = 25.242°	99.8 %	
Absorption correction	Semi-empirical from equivalents	
Refinement method	Full-matrix least-squares on F^2	
Data / restraints / parameters	28913 / 1966 / 2252	
Goodness-of-fit on F^2	1.041	
Final R indices [$I > 2\sigma_I$]	R_1 = 0.0609, wR_2 = 0.1362	
R indices (all data)	R_1 = 0.0837, wR_2 = 0.1472	
Largest diff. peak and hole	3.450 and –2.397 e/Å^3	

3.4.7) References

[1] a) Erker, G., *Dalton Trans.* **2005**, *2*, 1883–1890.; b) Power, P. P. *Nature* **2010**, *463* (7278), 171.; c) Wilkins, L. C.; Melen, R. L., *Coord. Chem. Rev.* **2016**, *324*, 123–139.; d) Chu, T.; Nikonov, G. I. *Chem. Rev.* **2018**, *118* (7), 3608.

[2] a) Cabrera, L.; Welch, G. C.; Masuda, J. D.; Wei, P.; Stephan, D. W. *Inorg. Chim. Acta* **2006**, *359* (9), 3066. b) Stephan, D. W. *Org. Biomol. Chem.* **2008**, *6* (9), 1535. c) Stephan, D. W.; Erker, G. *Angew. Chem. Int. Ed.* **2015**, *54* (22), 6400. d) Stephan, D. W. *J. Am. Chem. Soc.* **2015**, *137* (32), 10018.

[3] a) Power, P. P. *Nature* **2010**, *463* (7278), 171. b) Power, P.P. *J. Chem. Soc., Dalton Trans.* **1998**, (18), 2939. c) Cowley, A. H. *Polyhedron* **1984**, *3* (4), 389.d) Wang, Y.; Robinson, G. H. *Chem. Commun.* **2009**, *32* (35), 5201. e) Franz, D.; Inoue, S. *Dalton Trans.* **2016**, *45* (23), 9385. f) Braunschweig, H.; Dewhurst, R. D.; Hammond, K.; Mies, J.; Radacki, K.; Vargas, A. *Science* **2012**, *336* (6087), 1420. g) Sekiguchi, A.; Kinjo, R.; Ichinohe, M. *Science* **2004**, *305* (5691), 1755.

[4] a) Frey, G. D.; Lavallo, V.; Donnadieu, B.; Schoeller, W. W.; Bertrand, G. *Science* **2007**, *316* (5823), 439. b) Yao, S.; Xiong, Y.; Driess, M. *Acc. Chem. Res.* **2017**, *50* (8), 2026. c) Wilson, D. J. D.; Dutton, J. L. *Chem. Eur. J.* **2013**, *19* (41), 13626. d) Zhao, L.; Hermann, M.; Holzmann, N.; Frenking, G. *Coord. Chem. Rev.* **2017**, *344*, 163. e) Braunschweig, H.; Krummenacher, I.; Légaré, M.-A.; Matler, A.; Radacki, K.; Ye, Q. *J. Am. Chem. Soc.* **2017**, *139* (5), 1802.

[5] a) Lewis, N. S.; Nocera, D. G. *Proc. Natl. Acad. Sci.* **2006**, *103* (43), 15729. b) Gray, H. B. *Nature* **2009**, *1* (1), 7.

[6] Bartholomew, C. H.; Farrauto, R. J. *Fundamentals of Industrial Catalytic Processes,* 2nd ed.; Wiley-AlChE, 2005.

[7] a) Ménard, G.; Stephan, D. W. *Angew. Chem. Int. Ed.* **2011**, *123* (36), 8546. b) Zhao, X.; Stephan, D. W. *Chem. Commun.* **2011**, *47* (6), 1833. c) Marek, A.; Pedersen, M. H. F. *Tetrahedron* **2015**, *71* (6), 917. d) Chase, P. A.; Welch, G. C.; Jurca T.; Stephan D. W. *Angew. Chem., Int. Ed.*, **2007**, *49*, 8050.

[8] Scott, D. J.; Fuchter, M. J.; Ashley, A. E. *J. Am. Chem. Soc.* **2014**, *136* (45), 15813.

[9] a) Lindqvist, M.; Sarnela, N.; Sumerin, V.; Chernichenko, K.; Leskela, M.; Repo, T. *Dalton Trans*. **2012**, *41*, 4310. b) Longobardi, L. E.; Tang, C.; Stephan, D. W. *Dalton Trans.* **2014**, *43* (42), 15723.
[10] Stephan, D. W.; Greenberg, S.; Graham, T. W.; Chase, P.; Hastie, J. J.; Geier, S. J.; Farrell, J. M.; Brown, C. C.; Heiden, Z. M.; Welch, G. C.; Ullrich, M. *Inorg. Chem.* **2011**, *50* (24), 12338.

[11] A) Nakajima, M.; Fava, E.; Loescher, S.; Jiang, Z.; Rueping, M. *Angew. Chem. Int. Ed.* **2015**, *54* (30), 8828. B) Wirth, T. *Angew. Chem. Int. Ed.* **1996**, *35* (1), 61.

[12] McMurry, J. E. *Chem. Rev.* **1989**, *89* (7), 1513.

[13] a) Tischenko W. *Chem. Zentralbl.* **1906**, *77*, 1309. b) Crimmin, M. R.; Barrett, A. G. M.; Hill, M. S.; Procopiou, P. A. *Org. Lett.* **2007**, *9* (2), 331.

[14] a) Odom, A. L. *Dalton Trans.* **2011**, *40* (12), 2689. b) Niyomchon, S.; Oppedisano, A.; Aillard, P.; Maulide, N. *Nat Commun* **2017**, *8* (1), 1091.

[15] a) Otera, J. *Modern Carbonyl Chemistry*; Wiley-VCH, 2007. b) S. L. Marquard, M. W. Bezpalko, B. M. Foxman, C. M. Thomas, *J. Am. Chem. Soc.* **2013**, *135*, 6018–6021.

[16] A) Wu, D.; Kong, L.; Li, Y.; Ganguly, R.; Kinjo, R. *Nat Commun.* **2015**, *6*, 7340. B) Wang, B.; Li, Y.; Ganguly, R.; Hirao, H.; Kinjo, R. *Nat Commun.* **2016**, *7*. C) Di Wu; Ganguly, R.; Li, Y.; Hoo, S. N.; Hirao, H.; Kinjo, R. *Chem. Sci.* **2015**, *6* (12), 7150. D) Taylor, J. W.; McSkimming, A.; Guzman, C. F.; Harman, W. H. *J. Am. Chem. Soc.* **2017**, *139* (32), 11032.

[17] Grotthuss, von, E.; Diefenbach, M.; Bolte, M.; Lerner, H.-W.; Holthausen, M. C.; Wagner, M. *Angew. Chem. Int. Ed.* **2016**, *55* (45), 14067.

[18] Grotthuss, von, E.; Prey, S. E.; Bolte, M.; Lerner, H.-W.; Wagner, M. *Angew. Chem. Int. Ed.* **2018**.

[19] Grotthuss, von, E.; Nawa, F.; Bolte, M.; Lerner, H.-W.; Wagner, M. *Tetrahedron* **2019**, *75* (1), 26.

[20] Lorbach, A.; Bolte, M.; Lerner, H.-W.; Wagner, M. *Organometallics* **2010**, *29* (22), 5762.
[21] Taylor, J. W.; McSkimming, A.; Moret, M.-E.; Harman, W. H. *Inorg. Chem.* **2018**, *57* (24), 15406.

[22] Taylor, J. W.; McSkimming, A.; Moret, M.-E.; Harman, W. H. *Angew. Chem. Int. Ed.* **2017**, *56* (35), 10413.

[23] Essex, L.A.; Taylor, J.W.; Harman, W.H. *Tetrahedron* **2018**, *75*, 2255.

[24] a) Jansen, M. *Chem. Soc. Rev.* **2008**, *37* (9), 1826. b) Nuss, H.; Jansen, M. *Angew. Chem. Int. Ed.* **2006**, *45* (26), 4369. c) Jansen, M. *Solid State Sci.* **2005**, *7* (12), 1464.

[25] Taylor, J. W.; McSkimming, A.; Harman, W. H. *Unpublished*.

[26] Stapp, P. R. *J. Org. Chem.* **1973**, *38* (7), 1433.

[27] Hoshimoto, Y.; Ohashi, M.; Ogoshi, S. *J. Am. Chem. Soc.* **2011**, *133* (13), 4668.

[28] Burfield, D. R.; Smithers, R. H. *J. Org. Chem.* **1978**, *43* (20), 3966.

[29] J. C. Flores, M. Mena, P. Royo, R. Serrano, *J. Am. Chem. Soc., Chem.Commun.* **1989**, 617–618.

[30] a) Park, J.; Morimoto, Y.; Lee, Y.-M.; Nam, W.; Fukuzumi, S. *J. Am. Chem. Soc.* **2011**, *133*, 5236. b) Park, Y. J.; Ziller, J. W.; Borovik, A. S. *J. Am. Chem. Soc.* **2011**, *133*, 9258. c) Kundu, S.; Miceli, E.; Farquhar, E.; Pfaff, F. F.; Kuhlmann, U.; Hildebrandt, P.; Braun, B.; Greco, C.; Ray, K. *J. Am. Chem. Soc.* **2012,** *134*, 14710. d) Lacy, D. C.; Park, Y. J.; Ziller, J. W.; Yano, J.; Borovik, A. S. *J. Am. Chem. Soc.* **2012**, *134*, 17526. e) Chen, J.; Lee, Y.-M.; Davis, K. M.; Wu, X.; Seo, M. S.; Cho, K.-B.; Yoon, H.; Park, Y. J.; Fukuzumi, S.; Pushkar, Y. N.; Nam, W. *J. Am. Chem. Soc.* **2013**, *135*, 6388. f) Herbert, D. E.; Lionetti, D.; Rittle, J.; Agapie, T. *J. Am. Chem. Soc.* **2013**, *135*, 19075. g) Grubel, K.; Brennessel, W. W.; Mercado, B. Q.; Holland, P. L. *J. Am. Chem. Soc.* **2014**, *136* (48), 16807.

[31] Shipsey, K.; Werner, E. A. *J. Chem. Soc., Trans.* **1913**, *103*, 1255.

[32] a) Abdalla, J. A. B.; Riddlestone, I. M.; Tirfoin, R.; Aldridge, S. *Angew. Chem. Int. Ed.* **2015**, *54* (17), 5098. b) Khusnutdinova, J. R.; Milstein, D. *Angew. Chem. Int. Ed.* **2015**, *54* (42), 12236.

[33] Schlosser, M.; Jenny, T.; Guggisberg, Y. *Synlett* **1990**, *11*, 704.

[34] Burfield, D. R.; Smithers, R. H. *J. Org. Chem.*, **1978**, *43*, 3966–3968.

[35] Led, J. J.; Gesmar, H., *Chem. Rev*. **1991**, *91*, 1413-1426.

[36] *APEX 2,* version 2014.1-1, Bruker (2014), Bruker AXS Inc., Madison, Wisconsin, USA.

[37] *SAINT,* version V8.34A, Bruker (2012), Bruker AXS Inc., Madison, Wisconsin, USA.

[38] *SADABS,* version 2012/1, Bruker (2012), Bruker AXS Inc., Madison, Wisconsin, USA.

[39] *SHELXTL,* version 2013/4, Bruker (2013), Bruker AXS Inc., Madison, Wisconsin, USA.

Chapter 4) Copper and Silver Complexes of a Redox-Active Diphosphine-Diboraanthracene Ligand

4.1) Introduction

Ligand design is a powerful tool for controlling redox processes at transition metal centers.[1] Beyond modification of the ligand types in the first coordination sphere, the use of redox-active supporting ligands can directly augment the orbital manifold available to a transition metal center or enable redox events at a remote site within the complex.[2] Such ligands can enable challenging multi-electron reactivity[3] and/or provide for the modulation of reactivity as a result of electron transfer events.[4] In a related sense, chelating scaffolds featuring acceptor or Z-type ligands can play a similar role,[5] in that they contain empty orbitals that are capable of mediating redox events on their own or can bind reversibly to the transition metal to stabilize metal-centered reduction events,[6] a process that can be considered a formal oxidation of the metal center in some cases.[7]

In our efforts to develop new platforms for the redox activation of small molecules, we have developed an interest in ligands containing the 9,10-dihydro-9,10-diboraathracene (DBA) unit,[8] as it combines intrinsic redox activity and the ability to serve as a Z-type ligand to transition metals. DBA-based molecules have garnered interest as components in organic optoelectronics[9] and have thus been the subject of extensive studies on their synthesis and physical properties,

including their redox chemistry.[10] Furthermore, DBA derivatives are known to bind to zerovalent transition metal fragments from groups 8–10 to give electronically saturated complexes with hexahapto coordination of the central B_2C_4 ring.[11] In some cases, multimetallic complexes are formed in which additional metal fragments bind to the flanking phenylene moieties or to the opposite face of the central ring in an "inverse sandwich" topology.[12] Although some of these complexes feature reversible reduction events, electrochemical oxidation is typically irreversible,[11] highlighting the need for electron-rich metal fragments to coordinate strongly to the electron deficient DBA core. In order to prevent irreversible dissociation of the DBA ligand upon oxidation and preserve its ability to function as an electron reservoir even when not coordinated directly to a metal, we have employed a buttressing strategy similar to that found in many transition metal–borane complexes.[13] Our first-generation DBA-based ligand, B_2P_2, features two *o*-diisopropylphosphinophenyl substituents at the B atoms of the DBA ring system. These phosphine donors situate a transition metal over the face of the central C_4B_2 ring and are structurally similar to the *p*-terphenyldiphosphine ligands employed by Agapie to support a range of arene and heteroarene complexes of mono- and bimetallic transition metal complexes.[14] Both the redox-activity and acceptor ligand functionality of B_2P_2 were instrumental in our recent preparation of the first example of a molecular auride complex via sequential two-electron reduction of a Au(I) starting

material.[15] Given the unique Au chemistry enabled by B_2P_2, we were interested in its complexes with the other coinage metals. Herein, we report the synthesis and characterization of Cu(I) and Ag(I) complexes of B_2P_2 and their reduction to give neutral zwitterionic complexes in which the additional electron resides primarily on the DBA core.

4.2) Results and Discussion

Our initial attempts to prepare Cu complexes of B_2P_2 began with the Cu(I) halides. The reaction of equimolar amounts of B_2P_2 and CuCl in THF gave a dark red solution which was revealed by ^{31}P NMR to contain a 1:1 mixture of unreacted B_2P_2 and a new species with a single ^{31}P resonance at 27.5 ppm. Addition of a second equivalent of CuCl led to consumption of the remaining B_2P_2 and complete conversion to the new product after several hours. Following workup, this species was isolated in 93% yield and shown by single-crystal X-ray

Scheme 4.1. Synthesis of Bimetallic Copper Halide Complexes of B_2P_2

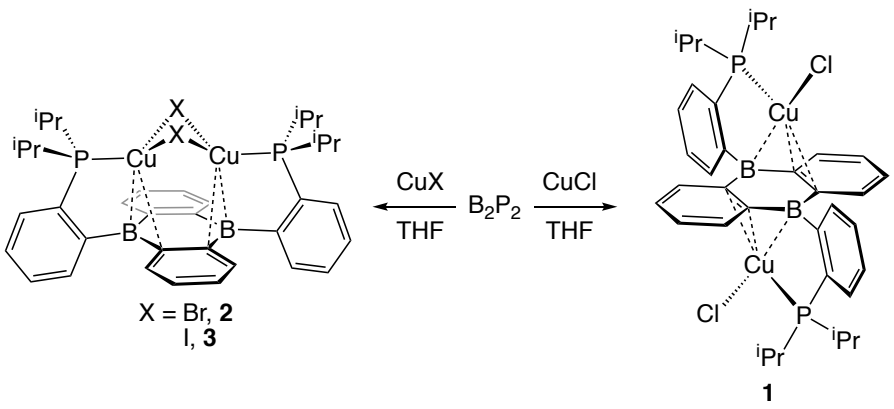

diffraction (XRD) to be the bimetallic complex $(CuCl)_2(B_2P_2)$ (**1**) in which the crystallographically equivalent Cu centers reside on opposite faces of the DBA core and are each ligated by a single phosphine (Figure 4.1, left). The Cu centers feature short contacts to a C=C unit (d_{Cu-C} = 2.208(1) and 2.364(1) Å) and one B atom (d_{Cu-B} = 2.283(1) Å). The second Cu–B contact is significantly longer at 2.778(1) Å. Similar η^3(*B,C,C*) coordination of arylborane ligands to CuCl fragments has been observed by Bourissou[16] and Hoefelmeyer,[17] although the Cu–B distances in **1** are appreciably shorter. The ^{11}B NMR signal for **1** at 39.7 ppm is modestly downfield of that for B_2P_2 (34.1 ppm), although the free ligand ^{11}B resonance likely reflects transient P–B interaction in solution at room temperature.[18] For comparison, 9,10-Mes_2DBA, which has bona fide three-coordinate boron centers, exhibits a ^{11}B resonance at 73.2 ppm.[19]

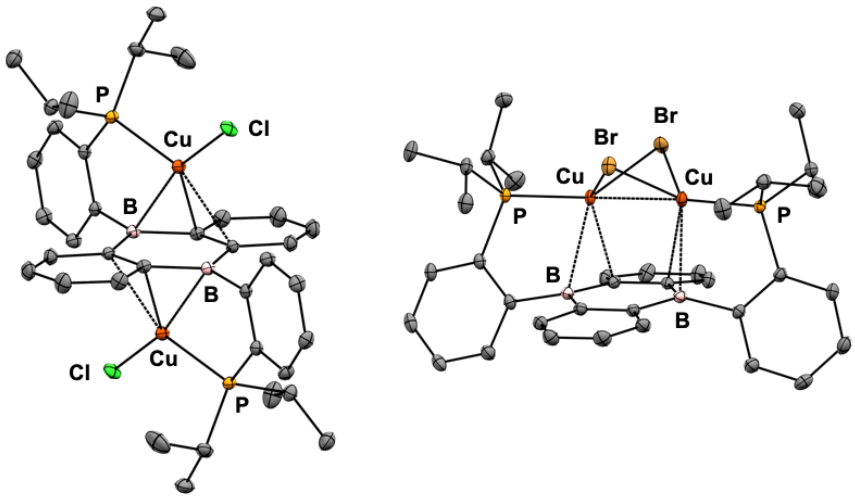

Figure 4.1. Thermal ellipsoid representations (50%) of $(CuCl)_2(B_2P_2)$ (**1**, left) and $Cu_2(\mu\text{-}Br)_2(B_2P_2)$ (**2**, right). Unlabeled ellipsoids correspond to carbon, and hydrogen atoms and solvent molecules have been omitted for clarity.

Reaction of B_2P_2 with two equivalents of CuBr resulted in a dark green solution shown by ^{31}P NMR to contain a mixture of two new products with resonances at 28.1 and 22.3 ppm in a ~9:1 ratio. Column chromatography on silica gel under anaerobic conditions separated the minor orange-red product (<5% isolated yield) from a dark-green species. Single-crystal XRD of the dark-green compound revealed the major species to be $Cu_2(\mu\text{-}Br_2)(B_2P_2)$ (**2**), in which a butterfly-shaped Cu_2Br_2 unit is ligated by both phosphine donors on the same face of the DBA core. Each Cu center engages the central ring in an $\eta^2(B,C)$ bonding mode with distances typical of Cu(I) phenylborane complexes (d_{Cu-B} =

Scheme 4.2. Synthesis of Cationic Copper(I) Complexes of B_2P_2

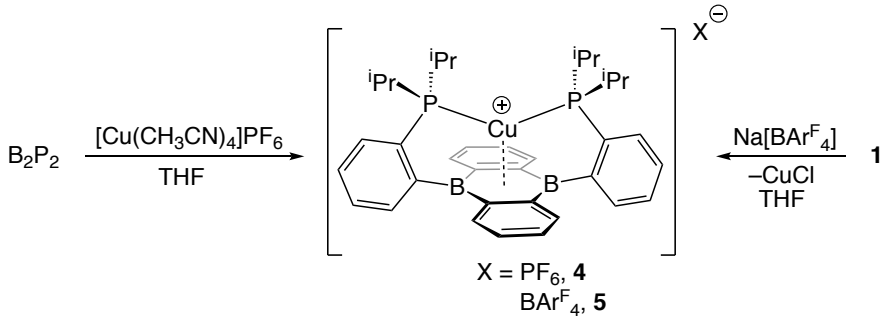

2.546(2), 2.530(2) Å; d_{Cu-C} = 2.293(2), 2.372(2) Å).[16] The ^{11}B NMR spectrum of **2** contains a single resonance at 56.6 ppm, consistent with the longer Cu–B distances in **2** relative to **1**. The orange-red minor product was identified by a preliminary single-crystal XRD structure to be a constitutional isomer of **2** (**2'**)

structurally analogous to **1** with mononuclear Cu sites on opposite faces of the DBA core (Figure 4.7.3, X-Ray Crystallography). The ratio of **2** to **2'** does not change upon heating and heating a solution of pure **2** in C_6D_6 at 80 ºC for 3 days resulted in no observable formation of **2'** by ^{1}H or ^{31}P NMR. The iodide complex $Cu_2(\mu\text{-}I_2)(B_2P_2)$ (**3**), structurally analogous to **2**, formed quantitatively by addition of two equivalents of CuI to B_2P_2.[20]

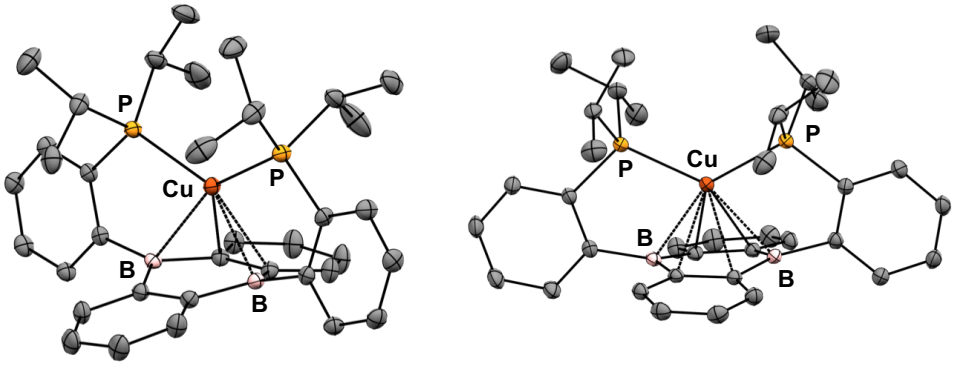

Figure 4.2. Thermal ellipsoid representations (50%) of the two crystallographically distinct cations in $[Cu(B_2P_2)][PF_6]$ (**4**). Unlabeled ellipsoids correspond to carbon, and hydrogen atoms, solvent molecules and the minor component of a single disordered *iso*-propyl substituent have been omitted for clarity.

The mononuclear Cu cation $[Cu(B_2P_2)]^+$ was synthesized via two routes. Addition of $[Cu(CH_3CN)_4][PF_6]$ to B_2P_2 gave $[Cu(B_2P_2)][PF_6]$ (**4**), whereas treatment of **1** with $Na[BAr^F{}_4]$ resulted in anion metathesis and expulsion of CuCl to give $[Cu(B_2P_2)][BAr^F{}_4]$ (**5**). Both **4** and **5** were examined by single-crystal XRD. The asymmetric unit of compound **4** contains two crystallographically inequivalent $[Cu(B_2P_2)]^+$ cations with distinct bonding arrangements between Cu and the DBA core, both of which are depicted in Figure 4.2. In one of these

Scheme 4.3. Synthesis of Silver Complexes of B_2P_2

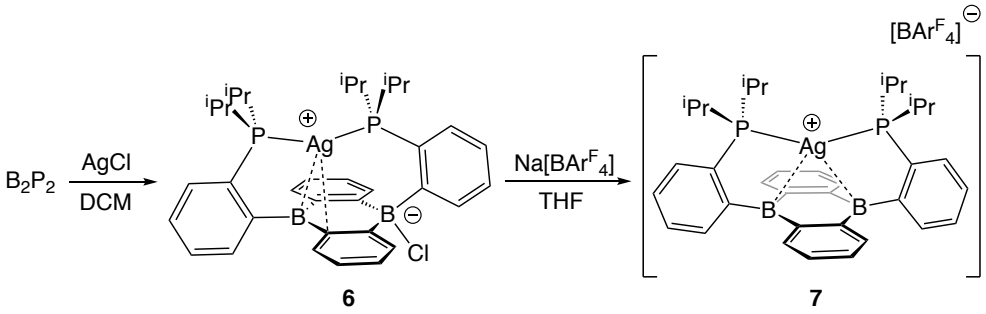

cations, the Cu center binds the central C_4B_2 ring in a η^6 fashion with Cu–B distances of 2.328(2) and 2.359(2) Å and Cu–C contacts ranging from 2.442(2) to 2.560(2) Å. The other cation features η^4(*B,C,C,B*) binding of the Cu center to the DBA core with Cu–B distances of 2.383(2) and 2.406(2) Å and Cu–C distances of 2.295(1) and 2.372(1) Å. The remaining two Cu–C distances in the central ring are >2.75 Å. The solid-state structure of the cation in **5** is qualitatively similar to the η^6 variant described above with minor differences in bond lengths (see X-Ray Crystallography). Similar structural variability was observed by Bourissou in chelating diphosphine borane complexes of Cu(I).[16] These structural data highlight the soft potential energy surface experienced by Cu(I) bound to arylboranes and caution against over-interpretation of the bond metrics in a single-crystal structure for complexes of this type. Solution NMR spectra of **4** are consistent with a single species of C_{2v} symmetry.

In contrast to **1**, metalation of B_2P_2 with AgCl readily affords the monometallic species Ag(B_2P_2)Cl (**6**), which is shown by single-crystal XRD to be a zwitterion in the solid state, with an intact B–Cl bond, analogous to the

previously reported Au analogue.[15] The Ag center engages the other B center in $\eta^2(B,C)$ bonding on the opposite face of the DBA linker (d_{Ag-B} = 2.508(1) Å, d_{Ag-C} = 2.581(1) Å). In $CDCl_3$ solution, the ^{31}P NMR spectrum of **6** contains a four-line pattern consistent with a single phosphorus environment coupled to ^{107}Ag (J = 440 Hz) and ^{109}Ag (J = 503 Hz). Taken together with the significantly upfield ^{11}B NMR resonance at 0.45 ppm, these data are suggestive of rapid chloride exchange between the two B centers on the NMR time scale. In a mixture of 3:1

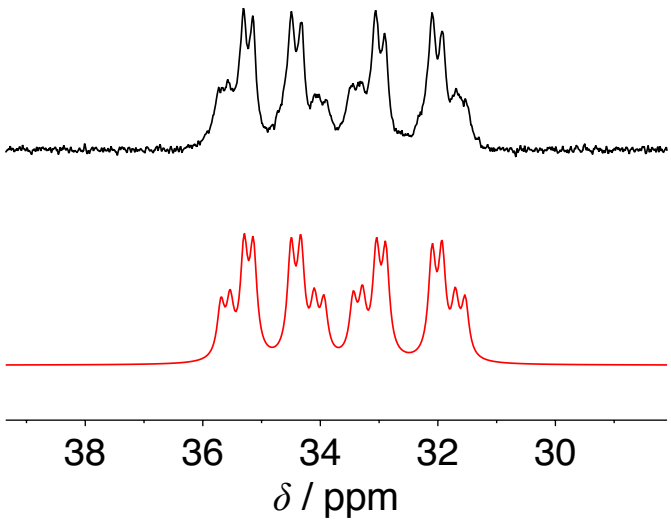

Figure 4.3. ^{31}P NMR spectrum of $Ag(B_2P_2)Cl$ (**6**) in 3:1 THF-d^8:C_6D_6 (top) and its simulation (bottom) with the following parameters: $\delta(^{31}P_a)$ = 33.05 ppm, $\delta(^{31}P_b)$ = 34.26 ppm, $^2J(P_a,P_b)$ = 80 Hz, $^1J(^{107}Ag,^{31}P_a)$ = 453 Hz, $^1J(^{107}Ag,^{31}P_b)$ = 423 Hz, $^1J(^{109}Ag,^{31}P_a)$ = 521 Hz, $^1J(^{109}Ag,^{31}P_b)$ = 486.5 Hz, linewidth = 30 Hz. See Supporting Information for detailed assignment.

THF-d^8:C_6D_6, this fluxionality is slow enough to allow the observation of a 16-line pattern due to two Ag isotopomers (^{107}Ag and ^{109}Ag) with inequivalent coupled ^{31}P nuclei (Figures 4.3 and 4.5.22). Anion metathesis of **6** with $Na[BAr^F{}_4]$

provided the molecular salt $[Ag(B_2P_2)][BAr^F{}_4]$ (**7**), the cation of which features a ^{11}B resonance at 29.2 ppm, consistent with equivalent, approximately planar

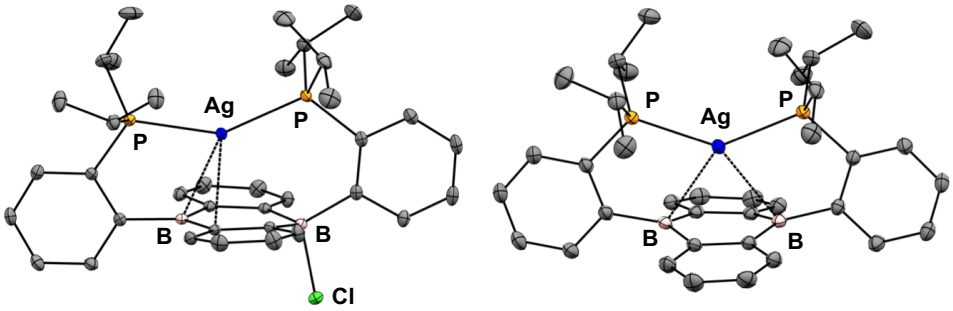

Figure 4.4. Thermal ellipsoid representations (50%) of $Ag(B_2P_2)Cl$ (**6**, left) and the cation in $[Ag(B_2P_2)][BAr^F{}_4]$ (**7**, right). Unlabeled ellipsoids correspond to carbon, and hydrogen atoms and solvent molecules have been omitted for clarity.

boron centers. This structure is maintained in the solid state, with Ag–B distances of 2.539(1) and 2.595(1) Å. Only one Ag–C distance in **7** is shorter than 2.7 Å at 2.671(1) Å. Compounds **6** and **7** are rare examples of Ag borane complexes, the only other structurally characterized example being the metallaboratrane reported by Maron, Ozerov, and Bourissou which features a Ag–B distance of 2.540(2) Å.[21]

The redox chemistry of the $[M(B_2P_2)]^+$ cations (M = Cu, Ag) was explored by cyclic voltammetry (CV). Cyclic voltammograms of **4** performed in 0.1 M $[Bu_4N][PF_6]$ in CH_3CN revealed a multitude of irreversible reduction processes when scanned to potentials near the reductive limit of the solvent (See Cyclic Voltammetry, Figure 4.6.2). However, when the first reduction event is isolated, a

quasireversible feature is observed at $E_{½}$ = –1.66 V vs. Fc/Fc^{+} (100 mV/s scan rate, Figure 5, top). CVs of **7** display a reversible process at $E_{½}$ = –1.56 V *vs.* Fc/Fc^{+} (Figure 4.5, bottom) with scans to more negative potentials revealing a single, irreversible process at –2.21 V (See Cyclic Voltammetry, Figure 4.6.4). For comparison, the neutral, metal-free analogue 9,10-Mes_2-DBA features reversible redox events at $E_{½}$ = –1.62 and –2.48 V.[15] Gabbaï has shown that arylborane redox potentials can be tuned by the sequential addition of remote cationic groups resulting in anodic shifts of ~250 mV per unit of charge.[22] The

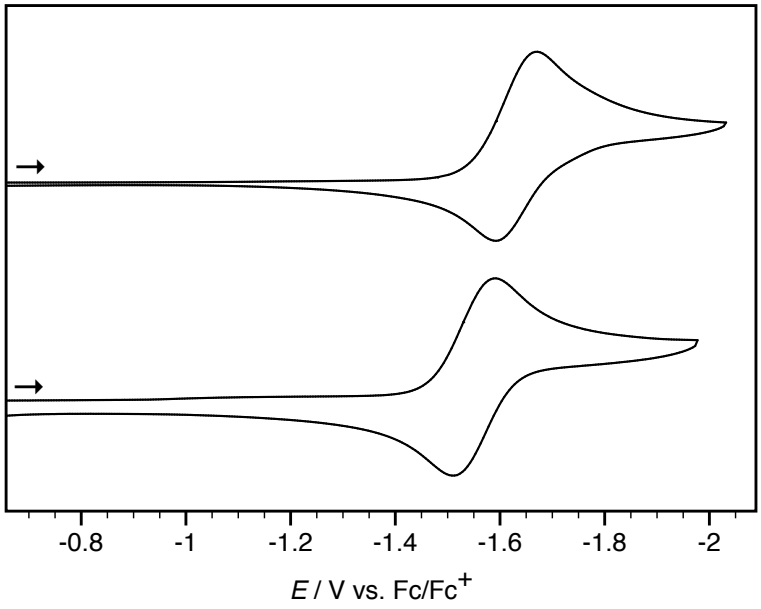

Figure 4.5. Cyclic voltammograms of $[(B_2P_2)Cu][PF_6]$ (**4**, top) and $[(B_2P_2)Ag][BAr^F{}_4]$ (**7**, bottom) measured in 0.1 M [*n*-Bu_4N][PF_6] in CH_3CN at a scan rate of 100 mV/s.

absence of this phenomenon in cationic complexes of B_2P_2 may be due to the fact that the disruption of the M□B interaction upon reduction (*vide infra*) results in a qualitatively similar shift of the redox potential in the opposite direction. The absence of a reversible second reduction event in either **4** or **7** contrasts with the electrochemical behavior of $[Au(B_2P_2)]^+$ which exhibits fully reversible redox processes at $E_{½}$ = –1.60 and –2.05 V *vs.* Fc/Fc^+ corresponding to the $[Au(B_2P_2)]^{+1/0}$ and $[Au(B_2P_2)]^{0/-1}$ redox couples, respectively.[15] These results highlight the unique electrochemical behavior of $[Au(B_2P_2)]^n$ resulting from the availability of the relatively low-lying Au 6s orbital to participate in redox processes.[23]

As the CV measurements on **4** and **7** suggested that the neutral $M(B_2P_2)$ (M = Cu, Ag) species might be at least transiently stable, we attempted to synthesize them (Scheme 4.4). Attempts to isolate $Cu(B_2P_2)$ via reduction of various Cu(I) precursors inevitably led to the precipitation of elemental Cu and the isolation of free B_2P_2, consistent with the limited reversibility of the redox

Scheme 4.4. Synthesis of Neutral Copper and Silver B_2P_2 Complexes

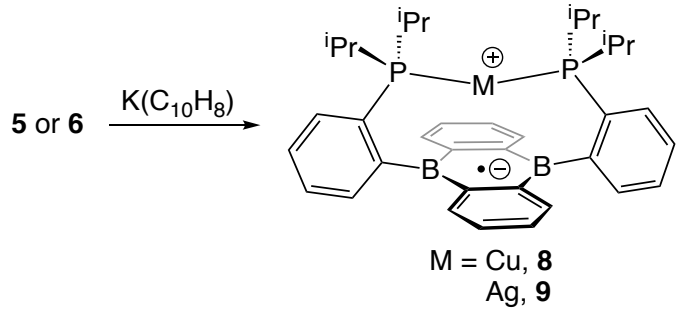

M = Cu, **8**
Ag, **9**

process observed by CV at 100 mV/s at ambient temperature. However, reduction of **5** with $K(C_{10}H_8)$ in thawing 2-methyltetrahydrofuran (2-MeTHF) allowed for the characterization of deep magenta $Cu(B_2P_2)$ (**8**) by X-band EPR spectroscopy at 228 K (Figure 4.6, top). The isotropic signal centered at $g = 2.02$ is a triplet that is well simulated by a hyperfine interaction of 36 MHz with two equivalent ^{31}P nuclei. In contrast to **8**, reduction of **6** with $K(C_{10}H_8)$ in toluene

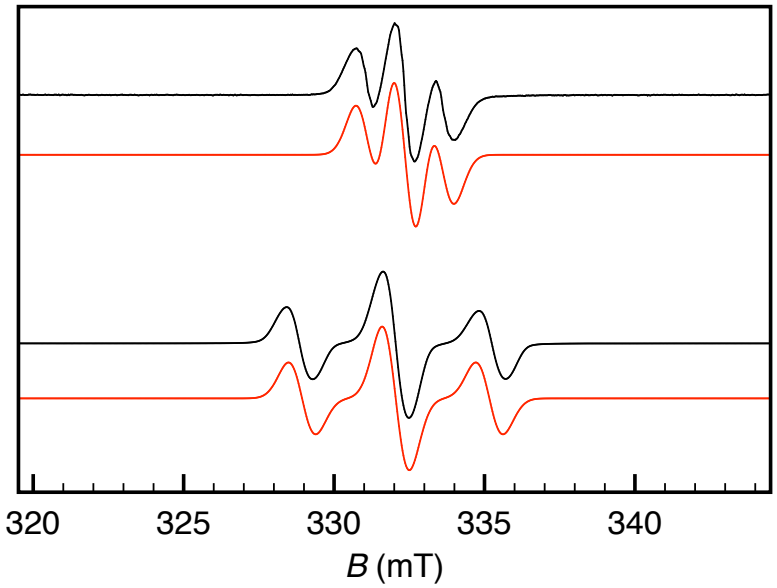

Figure 4.6. X-band electron paramagnetic resonance spectra (black) and simulation (red) of the neutral radicals $Cu(B_2P_2)$ (**8**, top) and $Ag(B_2P_2)$ (**9**, bottom).

gave dark purple $Ag(B_2P_2)$ (**9**), which was sufficiently stable at room temperature to be isolated. The X-band EPR spectrum of **9** at 228 K (Figure 4.6, bottom) is also a triplet due to ^{31}P coupling with a larger value of $A_{iso}[^{31}P] = 90$ MHz. The previously reported Au complex $Au(B_2P_2)$ has a similar X-band EPR spectrum with $A_{iso}[^{31}P] = 56.5$ MHz.[15] Although **9** is thermally and photochemically

sensitive, it was crystallized from toluene/HMDSO at –35 ºC and characterized by single-crystal XRD (Figure 4.7). The solid-state structure of **9** features only two Ag–C distances of less than 3 Å (2.718(2) and 2.767(2) Å), and long Ag–B distances at 2.890(2) and 2.893(2) Å, significantly longer than those found in either **6** or **7**. Similar to the analogous gold complex, the lengthened Ag–B distances in **9** is consistent with the disruption of a weak Ag□B dative interaction by the population of the boron-based acceptor orbital upon reduction. Compound **9** is thus best described as a zwitterion featuring a negatively charged DBA core

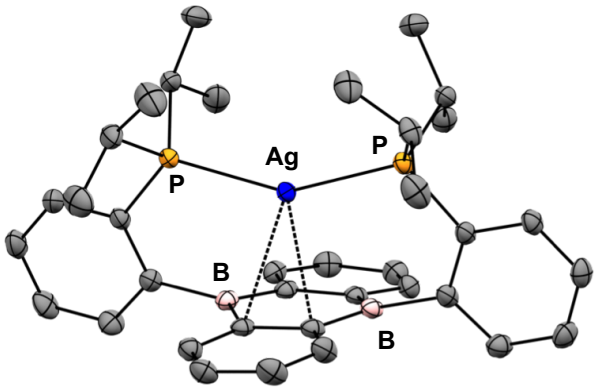

Figure 4.7. Thermal ellipsoid representation (50%) of $Ag(B_2P_2)$ (**9**). Unlabeled ellipsoids correspond to carbon, and hydrogen atoms and solvent molecules have been omitted for clarity.

tethered to a diphosphine-supported Ag(I) cation. Density functional theory (DFT) calculations carried out on the geometry of a truncated model of **9** in which the isopropyl groups were replaced by methyls optimized at the B3LYP/6-31G(d,p);SDD(Ag) level confirm this description of the electronic structure, with the spin density born primarily by the two B atoms (Figure 4.8). The EPR

hyperfine parameters were also calculated from the density obtained at the B3LYP/IGLOIII;SDD(Ag) level for the optimized model complex of **9**, yielding a computed value for $A_{iso}[^{31}P]$ of 64 MHz, in rough agreement with the experimental value of 90 MHz. The large observed ^{31}P hyperfine interaction is interesting given that the unpaired electron resides primarily on the B centers. However, EPR parameters computed for a model of **9** in which the Ag had been removed while keeping the geometry of the ligand identical (Figure 4.8.1) revealed qualitatively similar hyperfine constants ($A_{iso}[^{31}P]$ = 52 MHz), suggesting

a limited role for the metal in the observed coupling. We instead hypothesize that this hyperfine interaction is the result of hyperconjugation mediated by the phenylene linker.[24]

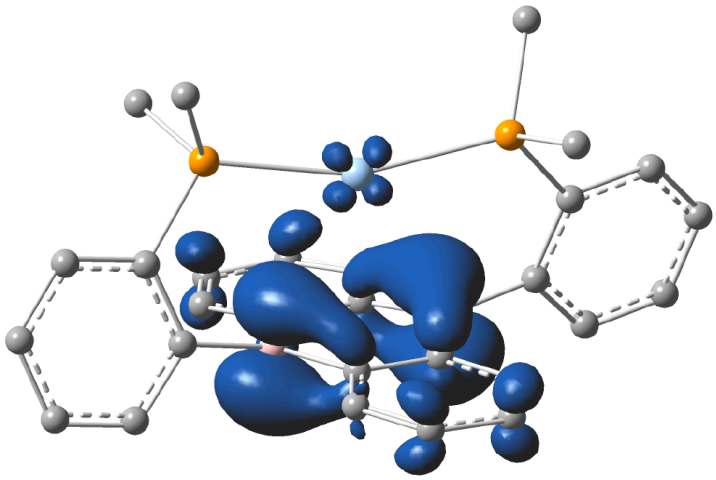

Figure 4.8. Spin density of a truncated model of $Ag(B_2P_2)$ (**9**) calculated at the B3LYP/IGLOIII;SDD(Ag) level on a geometry optimized at the B3LYP/6-31G(d,p);SDD(Ag) level.

4.3) Concluding Remarks

In conclusion, we have synthesized a series of Cu and Ag complexes of the diboraanthracene-diphosphine ligand B_2P_2. In the case of the bimetallic Cu halide complexes **1**–**3**, the binding motif is halide dependent such that CuCl complex **1** features a CuCl unit bound by a single phosphine on both faces of the DBA core whereas CuBr and CuI complexes **2** and **3** contain Cu_2X_2 butterfly cores bound by both phosphine donors on a single face of the DBA core. The monometallic cation $[Cu(B_2P_2)]^+$ can be synthesized either from these bimetallic species by anion metathesis with $NaBAr^F{}_4$ or via direct metalation with $[Cu(CH_3CN)_3][PF_6]$. In contrast, AgCl forms a neutral monometallic complex **6** with B_2P_2 in which the Cl atom is bound to B on the opposite face of the phosphine ligated Ag cation. Subsequent anion metathesis with $NaBAr^F{}_4$ affords the molecular salt **7**. Compounds **1**–**7** feature relatively short M–B distances consistent with a Z-type designation for DBA in these compounds. The monometallic Cu(I) and Ag(I) complexes of B_2P_2 feature reductions at ca. –1.6 V versus Fc/Fc^+. The reversibility of this process in the Cu complex is limited at room temperature, but fully reversible in the case of the Ag complex. One electron reduction of **6** affords the isolable zwitterionic radical $Ag(B_2P_2)$ in which the unpaired spin is born primarily by the B atoms, disrupting the Ag□B interaction in the precursor. These results highlight the ability of DBA to serve as

both a Z-type ligand and redox reservoir. The development of small molecule activation processes that harness this behavior are currently underway.

4.4) Experimental Section

4.4.1) General Considerations

Unless otherwise noted, all manipulations were carried out using standard Schlenk or glovebox techniques under an atmosphere of purified dinitrogen. Tetrahydrofuran (THF), dichloromethane (DCM), diethyl ether (Et_2O), toluene, benzene, and n-hexane were dried and deoxygenated by sparging with argon and passage through activated alumina in a solvent purification system from JC Meyer Solvent Systems. 2-Methyltetrahydrofuran (2-MeTHF) was distilled from purple sodium benzophenone ketyl and stored over 4 Å molecular sieves for at least 24 hr prior to use. Non-halogenated solvents were tested with a standard purple solution of sodium benzophenone ketyl in THF to confirm effective oxygen and moisture removal. All reagents were purchased from commercial suppliers and used without further purification unless otherwise noted. 9,10-bis(2-(diisopropylphosphino)phenyl)-9,10-dihydroboranthrene (B_2P_2),[15] sodium tetrakis[3,5-bis(trifluoromethyl)phenyl]borate ($Na[BAr^F_4]$),[25] and $K(C_{10}H_8)(THF)_{0.5}$[26] were synthesized according to literature procedures. Elemental analyses for **6** and **7** were performed by Midwest Microlab, LLC, Indianapolis, IN. Elemental analyses for all other compounds were performed by Desert Analytics Tucson, AZ. Deuterated solvents were purchased from

Cambridge Isotope Laboratories Inc., degassed, and dried over activated 4 Å molecular sieves for at least 24 h prior to use. NMR spectra were recorded on Varian Inova 400 and 500 MHz and Bruker Avance 600 MHz spectrometers. ^{1}H chemical shifts are reported in ppm relative to tetramethylsilane using residual protiated solvent an internal standard. ^{31}P and ^{11}B chemical shifts are reported in ppm relative to 85% aqueous H_3PO_4 and $BF_3{\cdot}Et_2O$, respectively. A backwards linear prediction was applied to ^{11}B NMR spectra using MestReNova 10.0.2 to eliminate background signals from the borosilicate NMR tube.[27] The ^{31}P NMR spectrum of compound **6** was simulated using the MestReNova 9.0.1 software suite. EPR X-band spectra were obtained on a Bruker EMX spectrometer controlled by Bruker Win-EPR software suite version 3.0 and simulated using the Easyspin software suite.[28] UV-Vis spectra were recorded using a Cary Bio 500 spectrometer using a 1 cm path length quartz cuvette with a solvent background subtraction applied. Mass spectrometry data was recorded using a Waters GCT high-resolution mass spectrometer operating in liquid injected field desorption ionization (LIFDI) mode. X-ray diffraction studies were performed using a Bruker-AXS diffractometer. Cyclic Voltammetry (CV) experiments were performed using a Pine AFP1 potentiostat. The cell consisted of a glassy carbon working electrode, a Pt wire auxiliary electrode and a Pt wire pseudo-reference electrode. All potentials are referenced versus the ferrocene/ferrocenium couple measured as an internal standard.

4.4.2) $(CuCl)_2(B_2P_2)$ (1).

To a 20 mL scintillation vial containing CuCl (0.0372 g, 0.376 mmol) was added a solution of B_2P_2 (0.100 g, 0.179 mmol) in THF (3 mL). The reaction was stirred for 12 hours before having its solvent removed *in vacuo*. The red/brown foam was dissolved in benzene (4 mL) and filtered through celite before having its solvent removed *in vacuo* to yield the product as a red-brown solid. Yield (0.126 g, 93%). Red-orange crystals suitable for single-crystal XRD were grown by slow evaporation of a benzene solution. ^{1}H NMR (500 MHz, $CDCl_3$) δ 8.71 (d, J = 7.4 Hz, 2H), 7.75 (t, J = 7.2 Hz, 2H), 7.52 (m, J = 5.6, 3.2 Hz, 8H), 7.44 (dd, J = 5.8, 3.2 Hz, 4H), 7.36 (s, 2H), 2.23 (m, 4H), 0.96 (d, J = 7.1 Hz, 6H), 0.93 (d, J = 7.1 Hz, 6H), 0.87 (d, J = 7.1 Hz, 6H), 0.84 (d, J = 7.2 Hz, 6H). $^{31}P\{^{1}H\}$ NMR (202 MHz, $CDCl_3$) 27.47 (s). $^{11}B\{^{1}H\}$ (160 MHz, $CDCl_3$) δ 39.69. $^{13}C\{^{1}H\}$ (126 MHz, $CDCl_3$) δ 152.9 (m), 136.8, 134.4 (d, J = 41.1 Hz), 133.1, 132.7 (d, J = 21.0 Hz), 132.6 (d, J = 21.0 Hz), 131.2 (d, J = 14.1 Hz), 128.5, 127.8, 25.8 (d, J = 19.7 Hz), 19.7, 19.0. UV-Vis (THF): λ_{max} nm (ε_{max} M^{-1} cm^{-1}) 398 (1.2×10^4), 611 (2.4×10^3). LIFDI MS: *m/z* 758.1061; Calcd. for 758.1073. Anal. Calcd for $C_{36}H_{44}B_2Cu_2Cl_2P_2$ (0.5 x C_6H_6): C, 58.75 H, 5.94. Found: C, 59.39 H, 5.94.

4.4.3) $Cu_2(\mu\text{-}Br)_2(B_2P_2)$ (2).

To a 20 mL scintillation vial containing CuBr (0.0539 g, 0.376 mmol) was added a solution of B_2P_2 (0.100 g, 0.179 mmol) in THF (3 mL). The reaction was stirred for 6 hours before having its volatiles removed *in vacuo*. The green/black foam

was added Et_2O (5 mL) before again removing volatiles *in vacuo*. The green/black residue was then dissolved in minimum toluene (1 mL) and passed through a silica column with hexanes:THF (1:8) as eluent (R_f = 0.47). The combined fractions were combined and had solvent removed *in vacuo* to yield the product as a black/green powder. Yield (0.135 g, 89%). Black-green crystals suitable for single-crystal XRD were grown by slow evaporation of a concentrated benzene solution. ^{1}H NMR (400 MHz, C_6D_6) δ 7.61 (bs, 4H), 7.39 (d, J = 7.1 Hz, 2H), 7.24 (m, 6H), 7.15 (m, 4H), 2.19 (dq, J = 14.0, 7.0 Hz, 4H), 1.18 (d, J = 6.9 Hz, 6H), 1.13 (d, J = 6.9 Hz, 6H), 1.05 (d, J = 6.8 Hz, 6H), 1.01 (d, J = 6.9 Hz, 6H). ^{31}P{^{1}H} NMR (202 MHz, C_6D_6) 28.1 (s). ^{11}B{^{1}H} (160 MHz, C_6D_6) δ 56.55. ^{13}C{^{1}H} (101 MHz, C_6D_6) δ 156.3 (m), 143.7, 141.3, 134.6 (d, J = 35.8 Hz), 133.1 (d, J = 20.0 Hz), 132.7, 131.4, 130.0, 127.5, 25.6 (d, J = 18.9 Hz), 19.2, 18.3. UV-Vis (THF): λ_{max} nm (ε_{max} M^{-1} cm^{-1}) 414 (4.3 × 10^3), 623 (1.6 x 10^3). LIFDI MS: *m/z* 846.0023; Calcd. for 846.0043 Anal. Calcd. for $C_{36}H_{44}B_2Br_2Cu_2P_2$ (1 x $C_4H_{10}O$): C, 52.15 H, 5.91. Found: C, 51.79, H, 6.23. A small amount of red-orange **$(CuBr)_2(B_2P_2)$ (2')** was separated via column chromatography (R_f = 0.92). A preliminary single-crystal XRD structure sufficient to obtain connectivity was obtained on a red-orange crystal grown via slow evaporation of a benzene solution. ^{31}P{^{1}H} NMR (202 MHz, C_6D_6) 22.3 (s).

4.4.4) $Cu_2(\mu\text{-}I)_2(B_2P_2)$ (3).

To a 20 mL scintillation vial containing CuI (0.0716 g, 0.376 mmol) was added a solution of B_2P_2 (0.100 g, 0.179 mmol) in THF (4 mL). The reaction was stirred 3 hours before having its volatiles removed *in vacuo*. The black/green residue was redissolved in toluene (3 x 1 mL) and filtered through celite before removing volatiles *in vacuo* to yield the product as a black/green powder. Yield (0.152 g, 90%). Black-green crystals suitable to confirm the connectivity of **3** by preliminary single-crystal XRD were grown by slow evaporation of a toluene solution. ^{1}H NMR (500 MHz, C_6D_6) δ 7.57 (dd, J = 5.3, 3.4 Hz, 4H), 7.38 (d, J = 6.9 Hz, 2H), 7.25 (m, 4H), 7.21 (t, J = 7.5 Hz, 4H), 7.14 (dd, J = 5.4, 3.3 Hz, 4H), 2.32 (dq, J = 14.5, 7.1 Hz, 4H), 1.22 (d, J = 6.9 Hz, 6H), 1.18 (d, J = 6.9 Hz, 6H), 1.08 (d, J = 6.9 Hz, 6H), 1.05 (d, J = 6.9 Hz, 6H). $^{31}P\{^{1}H\}$ NMR (202 MHz, C_6D_6) 23.64 (s). $^{11}B\{^{1}H\}$ (160 MHz, C_6D_6) δ 56.08. $^{13}C\{^{1}H\}$ (126 MHz, C_6D_6) δ 155.3 (m), 142.3, 141.1, 133.9 (d, J = 34.3 Hz), 132.7, 132.6, 132.6, 130.8, 129.5, 25.3 (d, J = 18.6 Hz), 18.9 (d, J = 5.1 Hz), 17.6. UV-Vis (THF): λ_{max} nm (ε_{max} $M^{-1}cm^{-1}$) 495 (3.8×10^3), 624 (2.3×10^3). LIFDI MS*: m/z* 939.9810; Calcd. for 939.9786. Anal. Calcd for $C_{36}H_{44}B_2Cu_2I_2P_2$ (1 x $C_4H_{10}O$): C, 47.32 H, 5.36. Found: C, 46.96, H, 5.45.

4.4.5) $[Cu(B_2P_2)][PF_6]$ (4).

To a 20 mL scintillation vial containing $[Cu(CH_3CN)_4][PF_6]$ (0.065 g, 0.177 mmol) was added a solution of B_2P_2 (0.100 g, 0.179 mmol) in THF (3 mL). The reaction was stirred for 12 hours at which point a light yellow precipitate had formed. Et_2O

(5 mL) was added to induce further precipitation of the product before decanting the mother liquor, washing the solid with Et_2O (2 x 3 mL) and drying the pale-yellow solid *in vacuo*. Yield (0.127 g, 94 %). Yellow crystals suitable for single-crystal XRD were grown by vapor diffusion of pentane into a concentrated THF solution. ^{1}H NMR (500 MHz, CD_3CN) δ 8.01 (d, *J* = 7.3 Hz, 2H), δ 7.76 (m, 4H), δ 7.57 (t, *J* = 7.9 Hz, 2H), δ 7.36 (s, 8H), δ 2.34 (m, 4H), 0.82 (dd, *J* = 14.2, 7.0 Hz, 12H), 0.70 (dd, *J* = 14.2, 7.0 Hz, 12H). $^{31}P\{^{1}H\}$ NMR (202 MHz, CD_3CN) 21.6 (s). $^{11}B\{^{1}H\}$ (160 MHz, CD_3CN) δ 27.1. ^{13}C NMR (126 MHz, CD_3CN) δ 156.3, 144.2, 138.3, 134.0, 133.3 (t, *J* = 8.6 Hz), 132.6 (t, *J* = 21.7 Hz), 131.60, 127.9, 26.8 (t, *J* = 10.2 Hz), 20.3, 19.3. LIFDI MS*: m/z* 623.2391; Calcd. for 623.2400. Anal. Calcd for $C_{36}H_{44}B_2CuF_6P_3$: C, 56.24, H, 5.77. Found: C, 56.24, H, 6.11.

4.4.6) [Cu(B_2P_2)][BAr^F_4] (5).

To a solution of **1** (0.133 g, 0.176 mmol) in THF (1 mL) was added Na[BAr^F_4] (0.156 g, 0.176 mmol) as an Et_2O (4 mL) solution. The reaction was stirred 30 minutes during which time ample colorless precipitate had appeared. The mixture was filtered through celite, diluted with toluene (8 mL), and concentrated *in vacuo* resulting in crystallization of the product. The solid was washed with toluene (2 mL) and hexane (1 mL) and dried *in vacuo*. Yield (0.204 g, 78%). Pale yellow crystals suitable for single-crystal XRD were grown by layering a concentrated THF solution with hexane. ^{1}H NMR (500 MHz, $CDCl_3$) δ 7.86 (m, 4H), 7.69 (bs, 8H (BAr^F_4)), 7.65 (m, 4H), 7.62 (m, 4H), 7.58 (dd, *J* = 5.5, 3.4 Hz, 4H), 7.50 (s,

4H), 2.35 (dq, *J* = 14.1, 7.1 Hz, 4H), 0.88 (d, *J* = 7.0 Hz, 6H), 0.85 (d, *J* = 6.9 Hz, 6H), 0.69 (d, *J* = 7.1 Hz, 6H), 0.65 (d, *J* = 7.1 Hz, 6H). $^{31}P\{^{1}H\}$ NMR (202 MHz, $CDCl_3$) 28.84 (s). $^{11}B\{^{1}H\}$ (160 MHz, $CDCl_3$) δ 47.21, –9.20 (BAr^{F}_{4}). The reaction proceeds similarly when **2** or **3** are used as starting materials.

4.4.7) Ag(B_2P_2)Cl (6).

A solution of B_2P_2 (0.100 g, 0.179 mmol) in DCM (5 mL) was added to a stirring suspension of AgCl (0.033g, 0.232 mmol, 1.3 mol.eq.) in DCM (5 mL). The mixture was stirred in the dark for 6 hrs before being filtered, layered with 8 mL toluene and concentrated *in vacuo* to crystallize the product. The golden yellow solid was washed with benzene (2 mL) and Et_2O (3 mL). The product is light-sensitive and should be stored/crystallized in the dark. Yield (0.089 g, 71%). Pale yellow crystals suitable for single-crystal XRD were grown by layering a concentrated THF solution with toluene. ^{1}H NMR (600 MHz, $CDCl_3$) δ 8.47 (s, 2H), 7.63 (t, *J* = 7.8 Hz, 2H), 7.56 (m, 2H), 7.43 (t, *J* = 7.3 Hz, 2H), 7.30 (m, 4H), 7.15 (s, 4H), 2.23 (s, 4H), 0.96 (d, *J* = 7.6 Hz, 6H), 0.93 (d, *J* = 7.6 Hz, 6H), 0.76 (s, 12H). $^{31}P\{^{1}H\}$ NMR (242 MHz, $CDCl_3$) 31.41 (overlapping doublets) (*J* (^{107}Ag, ^{31}P) = 440 Hz, (*J* (^{109}Ag,^{31}P) = 503 Hz). $^{11}B\{^{1}H\}$ (160 MHz, THF:benzene, 1:1) δ 0.45. ^{13}C NMR (126 MHz, $CDCl_3$) δ 158.5, 139.8, 137.0, 134.8, 132.5, 131.5, 129.9, 129.4, 126.2, 26.6 (m), 20.8, 20.5. Anal. Calcd for $C_{36}H_{44}AgB_2ClP_2$: C, 54.72 H, 6.07. Found: C, 55.03 H, 6.44.

4.4.8) [Ag(B_2P_2)][BAr^F_4] (7).

A solution of **6** (0.033 g, 0.048 mmol) in THF (4 mL) was added to a stirring solution of Na[BAr^F_4] (0.042 g, 0.0472 mmol, 1 mol.eq.) in Et_2O (2 mL). The mixture was stirred 2 hours before precipitated NaCl was removed via filtration. The filtrate was added hexanes (ca. 5 mL) before concentration *in vacuo* caused the product to crystallize. The pale yellow solid was collected and washed with hexanes (2 mL) and Et_2O (1mL). The product is light-sensitive and should be stored/crystallized in the dark. Yield (0.069 g, 96%). Pale yellow crystals suitable for single-crystal XRD were grown by layering a concentrated THF solution with hexane. ^{1}H NMR (500 MHz, CD_3CN) δ 8.13 (d, J = 7.3 Hz, 2H), 7.91 (dt, J = 7.2, 3.4 Hz, 2H), 7.87 (t, J = 1.9 Hz, 2H), 7.84 (s, 8H), 7.81 (s, 4H), 7.72 (t, J = 7.5 Hz, 2H), 7.49 (s, 8H), 2.50 (dhept, J = 14.0, 6.7 Hz, 4H), 1.06 (d, J = 7.0 Hz, 6H), 1.03 (d, J = 7.0 Hz, 6H), 0.89 (d, J = 7.1 Hz, 6H), 0.85 (d, J = 7.1 Hz, 6H). ^{31}P{^{1}H} NMR (242 MHz, CD_3CN) δ 34.57 (overlapping doublets) (J(^{107}Ag, ^{31}P) = 440 Hz, J(^{109}Ag, ^{31}P = 508 Hz). ^{11}B{^{1}H} (160 MHz, CD_3CN) δ 29.20, -6.66 (BAr^F_4). ^{13}C NMR (126 MHz, CD_3CN) δ 162.6 (q, J_{B-C} = 49.9 Hz, BAr^F_4), 155.8, 148.5, 138.2, 135.7 (BAr^F_4), 134.1, 133.6 (t, J_{P-C} = 19.3 Hz), 133.2 (t, J_{P-C} = 8.1 Hz), 132.0, 131.3, 130.0 (q, J_{C-F} = 32.8 Hz, BAr^F_4), 128.2, 125.5 (q, J_{C-F} = 271.6 Hz, BAr^F_4), 118.7 (BAr^F_4), 27.3, 20.9, 20.7. LIFDI MS: 667.2150; Calcd. for 667.2155. Anal. Calcd for $C_{68}H_{56}AgB_3F_{24}P_2$ (1 x $(C_2H_5)_2O$: C, 53.86 H, 4.14. Found: C, 54.13 H, 4.15.

4.4.9) Low-Temperature Preparation of $Cu(B_2P_2)$ (8).

To a frozen solution of **5** (2 mg, 1.34 μmol) in 2-MeTHF (1 mL) was added $K(C_{10}H_8)(THF)_{0.5}$ (0.0003 mg, 1.61 μmol). The slurry was manually stirred 5 minutes whereupon a dark magenta color developed. The slurry was then filtered through a fiberglass filter that had been precooled with a thawing 2-MeTHF rinse into a precooled EPR tube. The tube was sealed and immediately placed into a liquid N_2 bath until it was inserted into a precooled X-Band Bruker EMX EPR spectrometer.

4.4.10) $Ag(B_2P_2)$ (9).

To a 20 mL scintillation vial was added **6** (0.237 g, 0.336 mmol) and toluene (5 mL) before adding $K(C_{10}H_8)(THF)_{0.5}$ (0.068 g, 0.336 mmol) as a solid at once. The reaction was stirred 30 minutes at room temperature before being rapidly filtered through celite and removing volatiles *in vacuo*. The deep purple residue was washed with hexanes (2 x 2 mL), extracted into minimal THF (1 mL) and layered with hexanes (2 mL) and placed at –35 °C to crystallize. The next day, the mother liquor was decanted and the black/purple crystalline solid dried *in vacuo*. Yield (0.135 g, 60%). Purple-black crystals suitable for single-crystal XRD were grown by layering a concentrated toluene solution with HMDSO and letting stand at –35 °C. As a result of its light and thermal sensitivity, satisfactory elemental analysis of this compound could not be obtained.

4.5) Spectroscopic Data

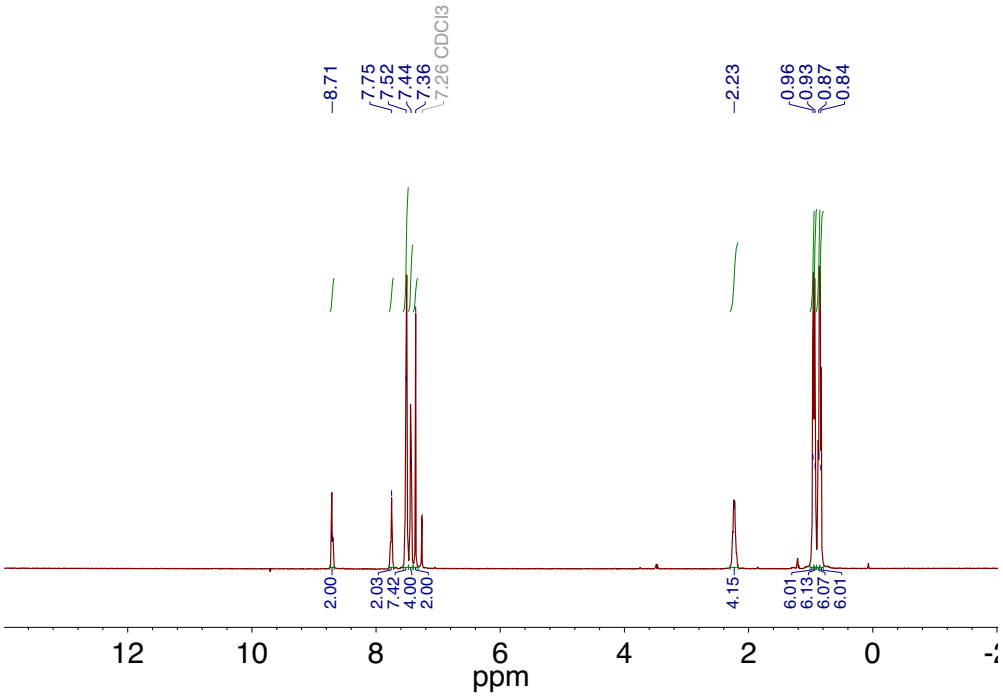

Figure 4.5.1. ^{1}H NMR spectrum of **$(CuCl)_2(B_2P_2)$** recorded at 500 MHz in $CDCl_3$.

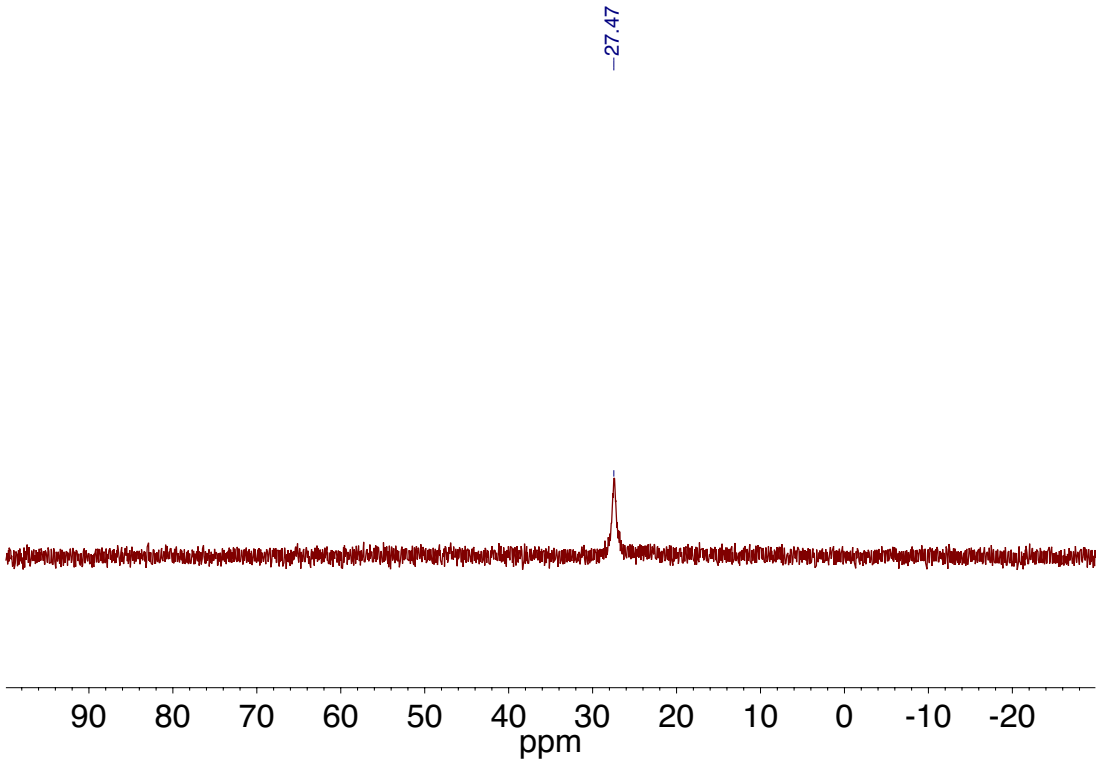

Figure 4.5.2. ^{31}P NMR spectrum of **$(CuCl)_2(B_2P_2)$** recorded at 202 MHz in $CDCl_3$.

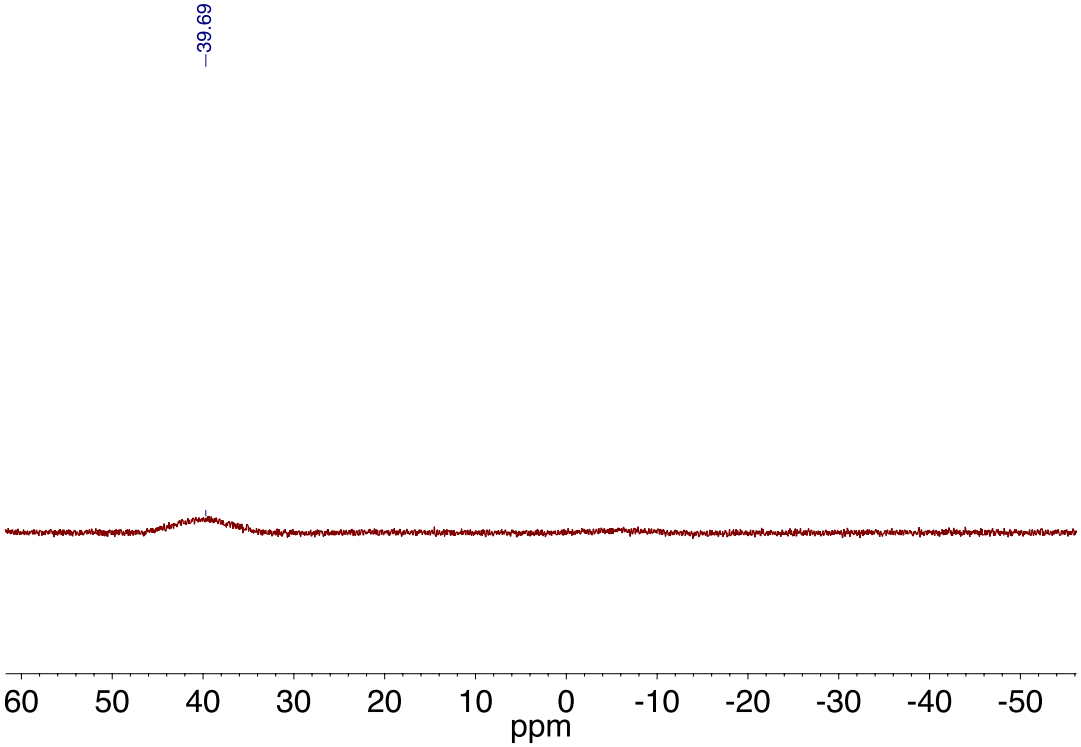

Figure 4.5.3. ^{11}B NMR spectrum of **$(CuCl)_2(B_2P_2)$** recorded at 160 MHz in $CDCl_3$.

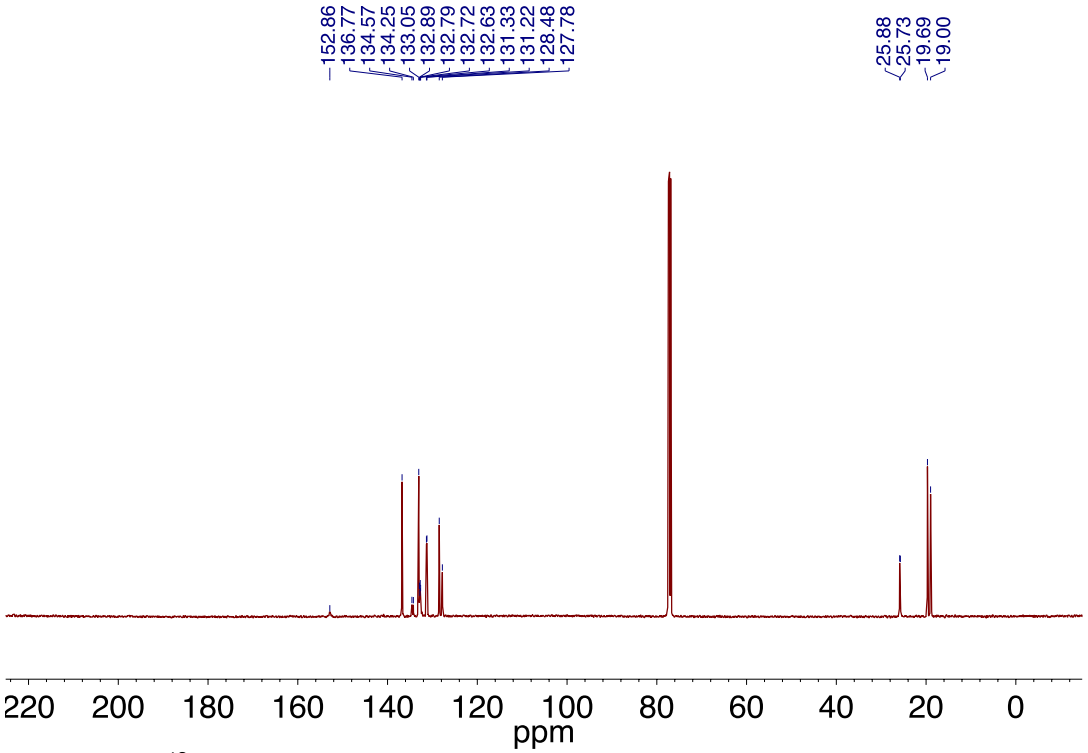

Figure 4.5.4. ^{13}C NMR spectrum of **$(CuCl)_2(B_2P_2)$** recorded at 126 MHz in $CDCl_3$.

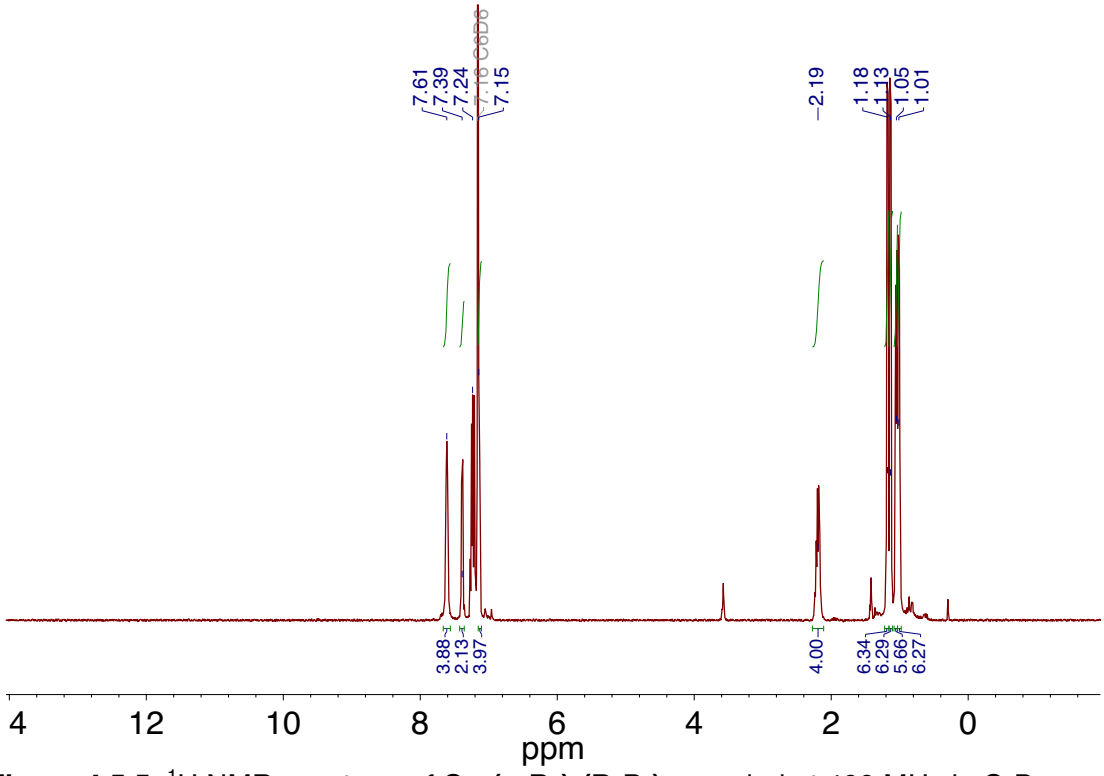

Figure 4.5.5. ^{1}H NMR spectrum of **$Cu_2(\mu\text{-}Br)_2(B_2P_2)$** recorded at 400 MHz in C_6D_6.

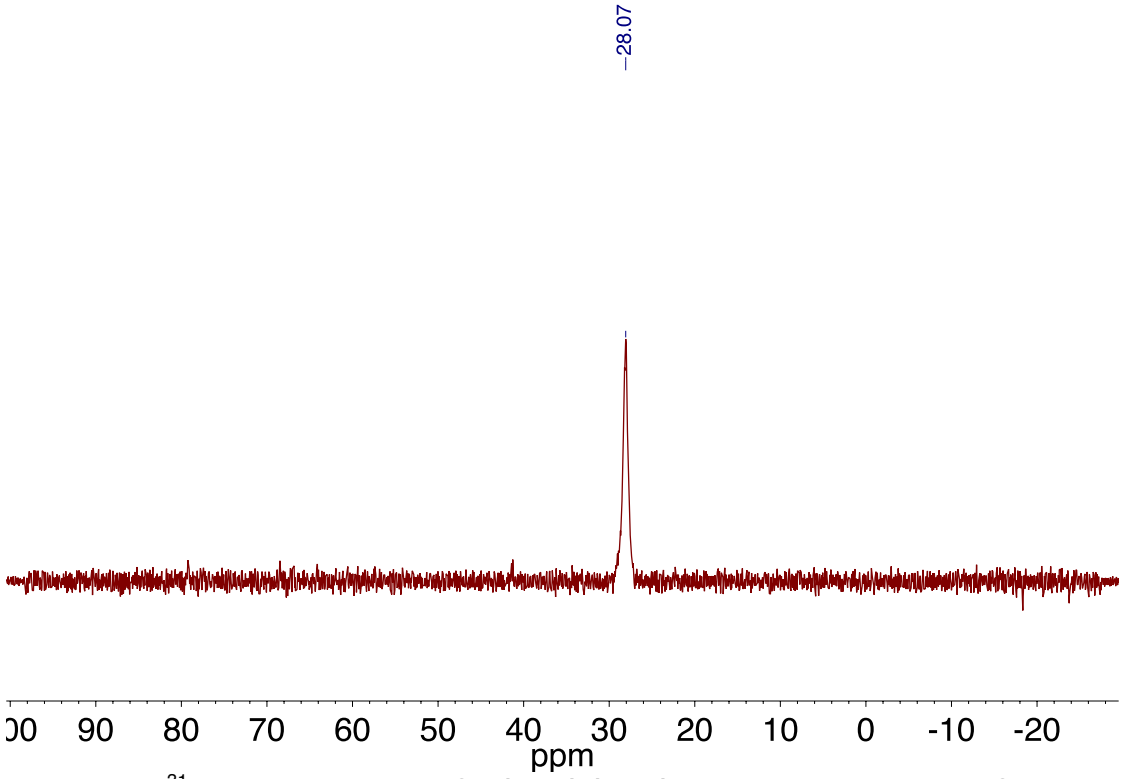

Figure 4.5.6. ^{31}P NMR spectrum of **$Cu_2(\mu\text{-}Br)_2(B_2P_2)$** recorded at 202 MHz in C_6D_6.

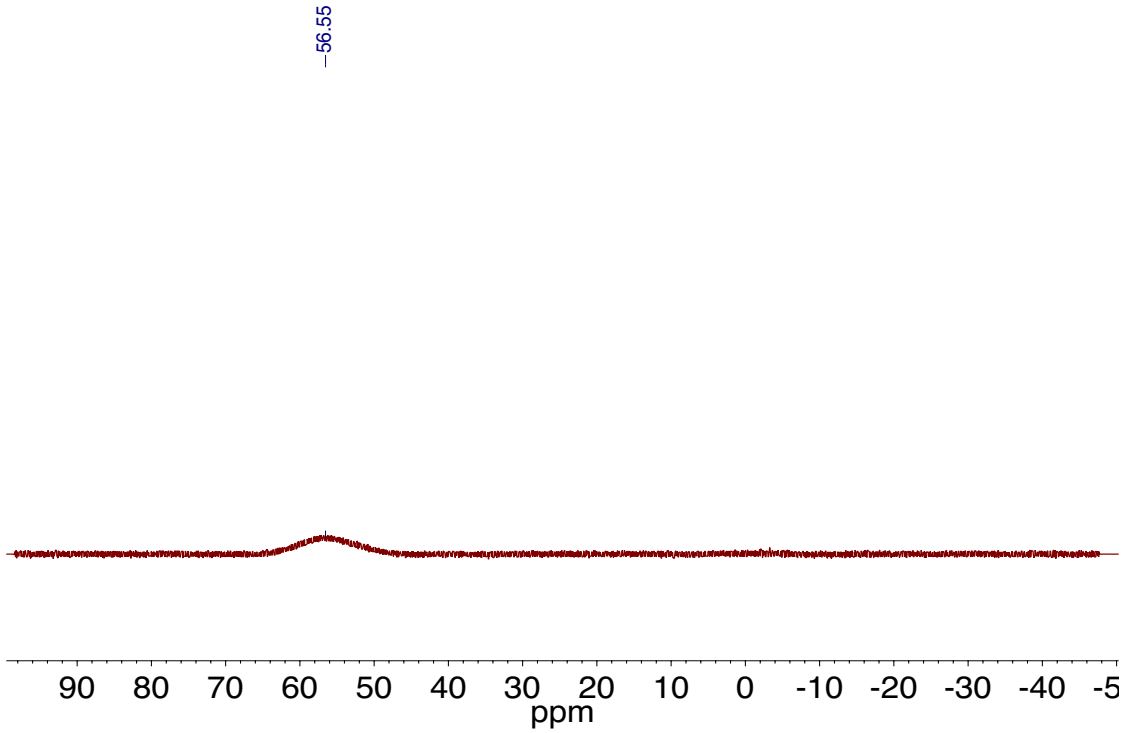

Figure 4.5.7. ^{11}B NMR spectrum of **$Cu_2(\mu\text{-}Br)_2(B_2P_2)$** recorded at 160 MHz in C_6D_6.

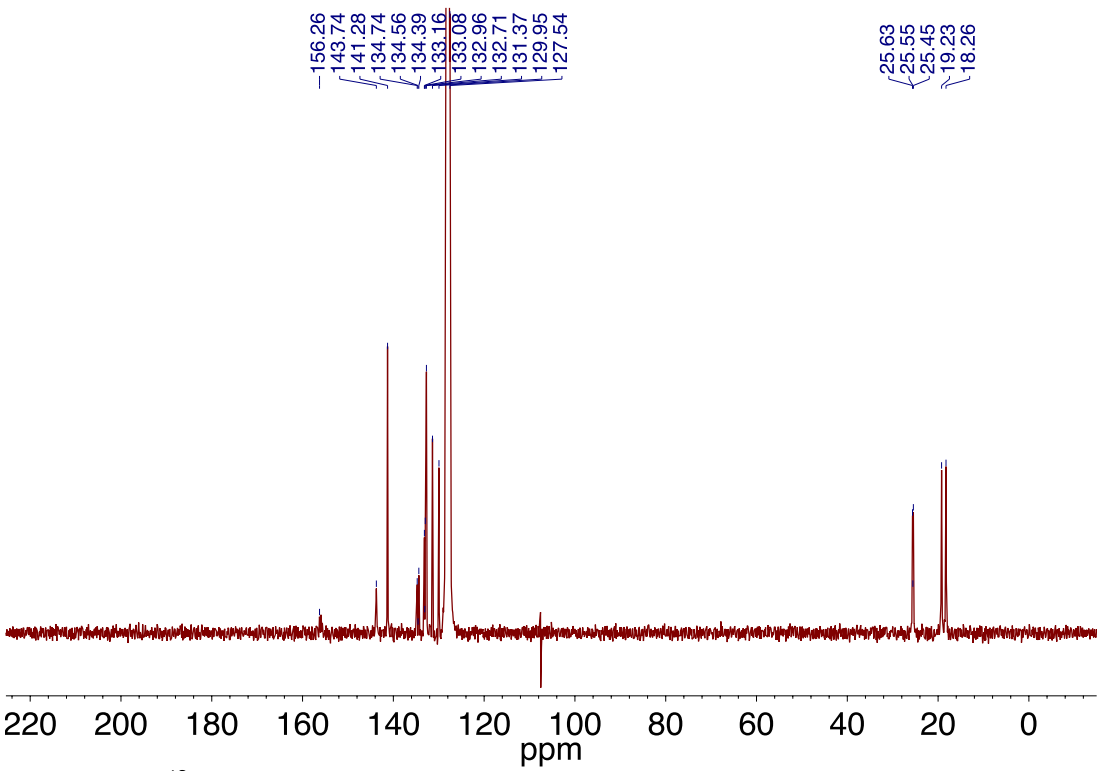

Figure 4.5.8. ^{13}C NMR spectrum of **$Cu_2(\mu\text{-}Br)_2(B_2P_2)$** recorded at 101 MHz in C_6D_6.

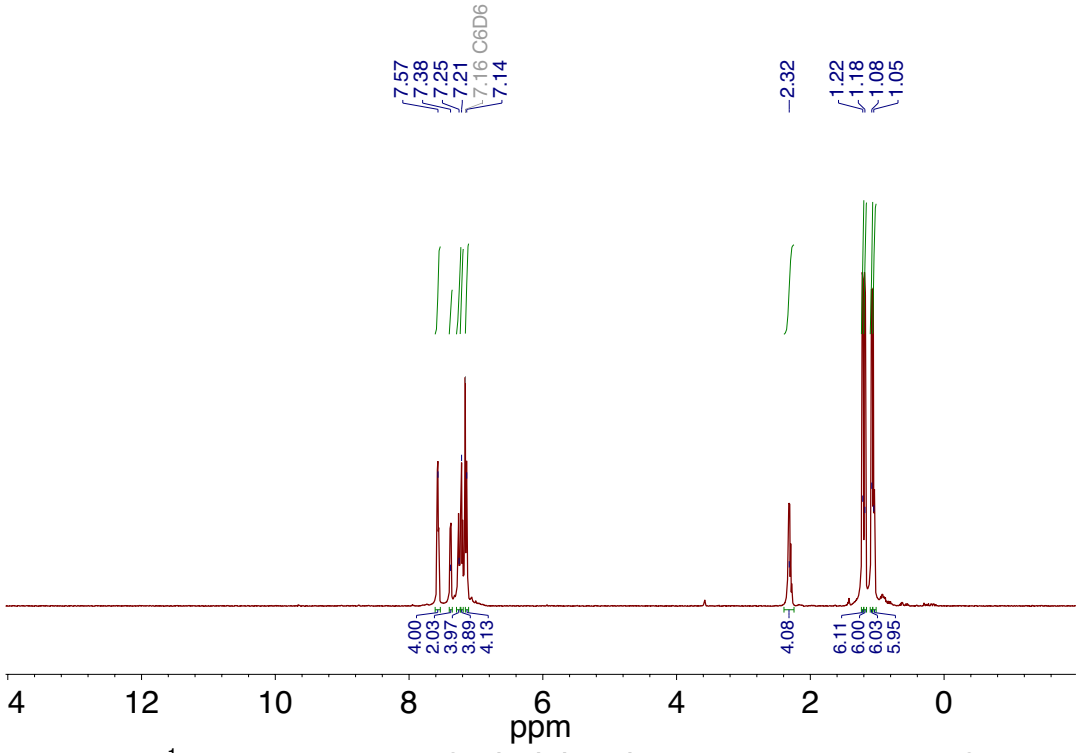

Figure 4.5.9. ^{1}H NMR spectrum of **$Cu_2(\mu\text{-}I)_2(B_2P_2)$** recorded at 500 MHz in C_6D_6.

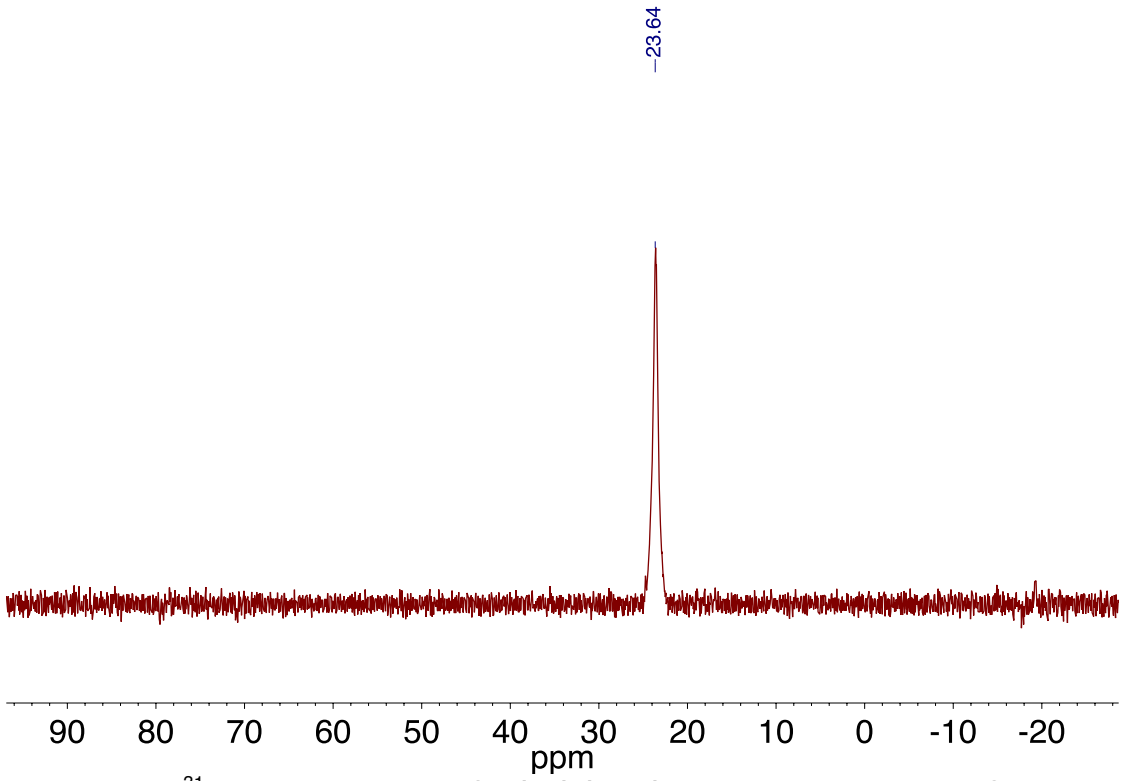

Figure 4.5.10. ^{31}P NMR spectrum of **$Cu_2(\mu\text{-}I)_2(B_2P_2)$** recorded at 202 MHz in C_6D_6.

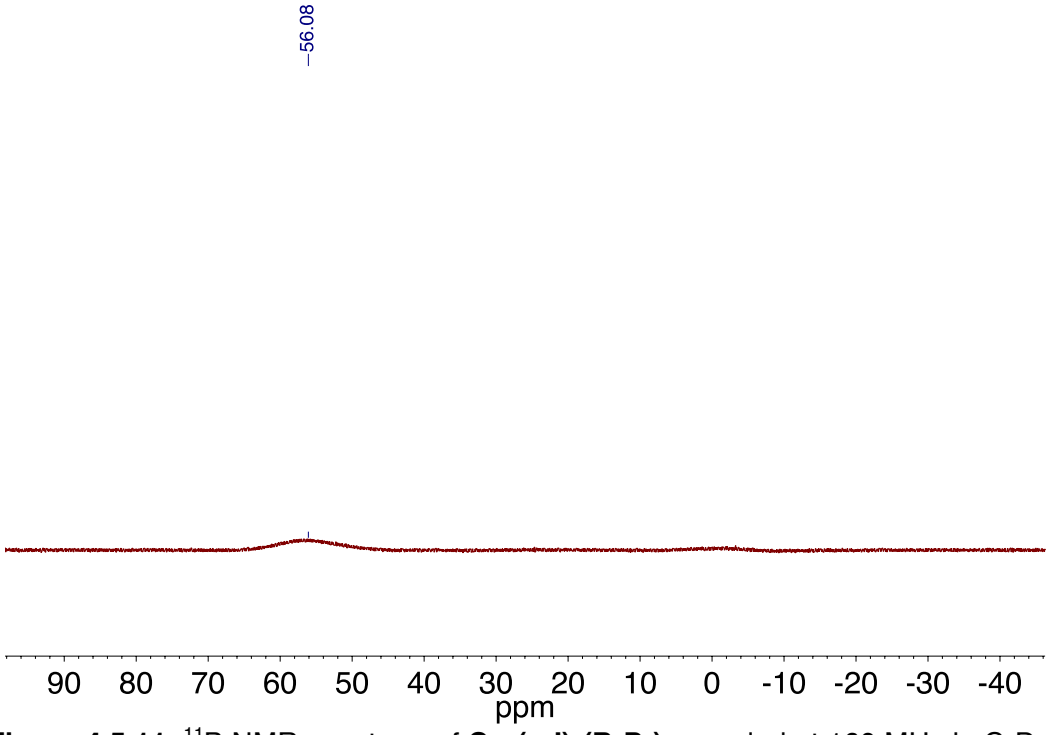

Figure 4.5.11. ^{11}B NMR spectrum of **$Cu_2(\mu\text{-}I)_2(B_2P_2)$** recorded at 160 MHz in C_6D_6.

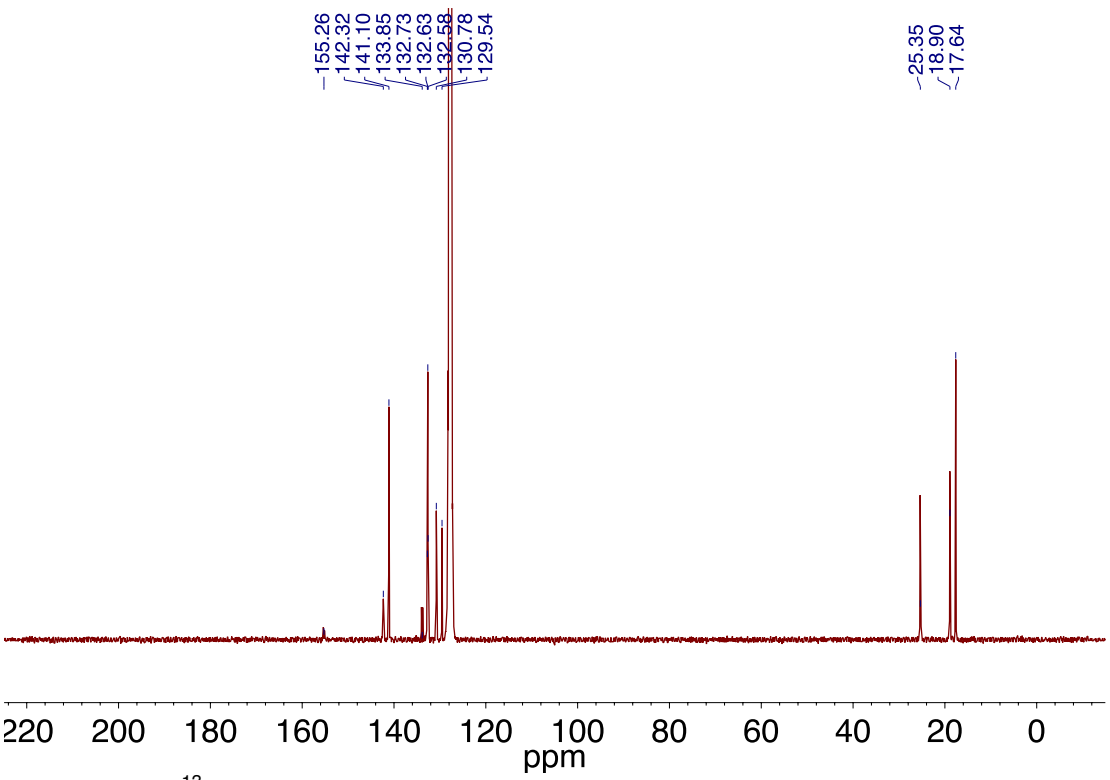

Figure 4.5.12. ^{13}C NMR spectrum of **$Cu_2(\mu\text{-}I)_2(B_2P_2)$** recorded at 126 MHz in C_6D_6.

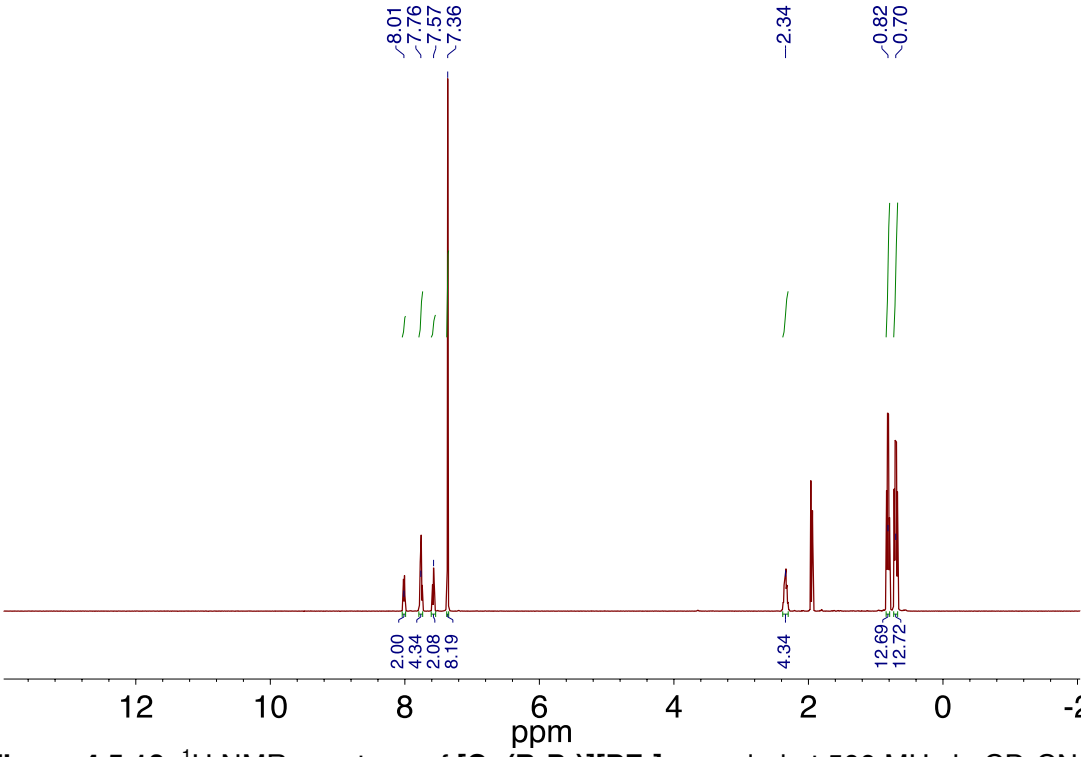

Figure 4.5.13. ^{1}H NMR spectrum of **$[Cu(B_2P_2)][PF_6]$** recorded at 500 MHz in CD_3CN.

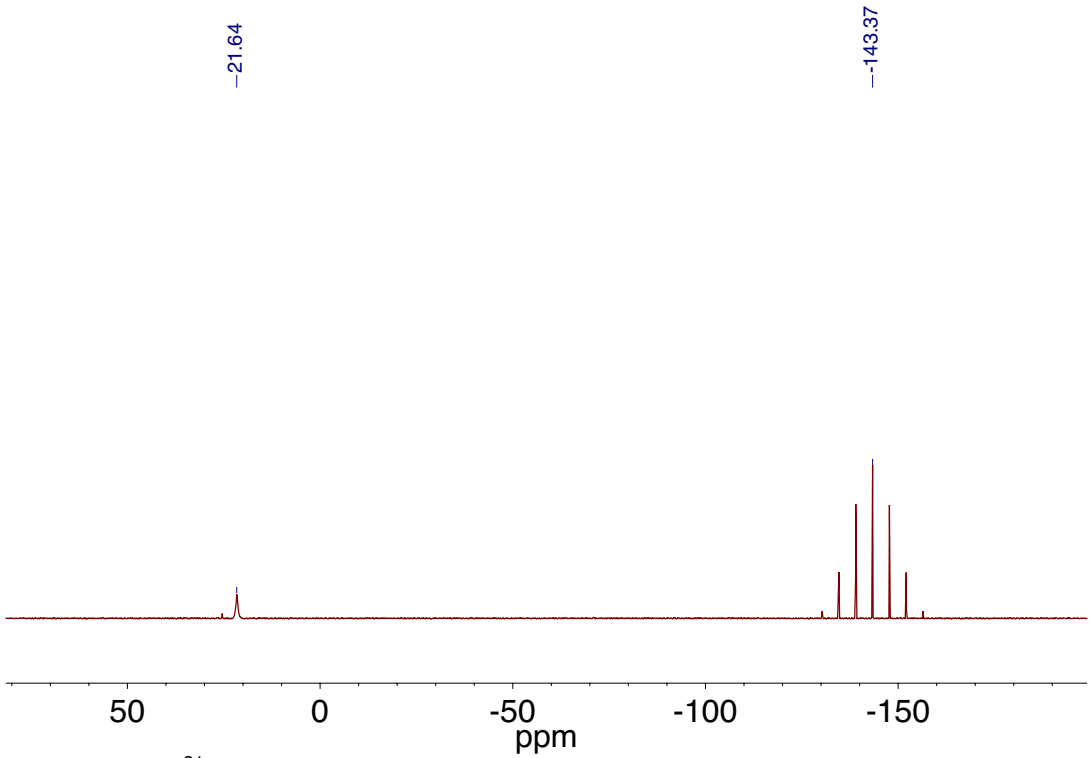

Figure 4.5.14. ^{31}P NMR spectrum of **[Cu(B_2P_2)][PF_6]** recorded at 202 MHz in CD_3CN.

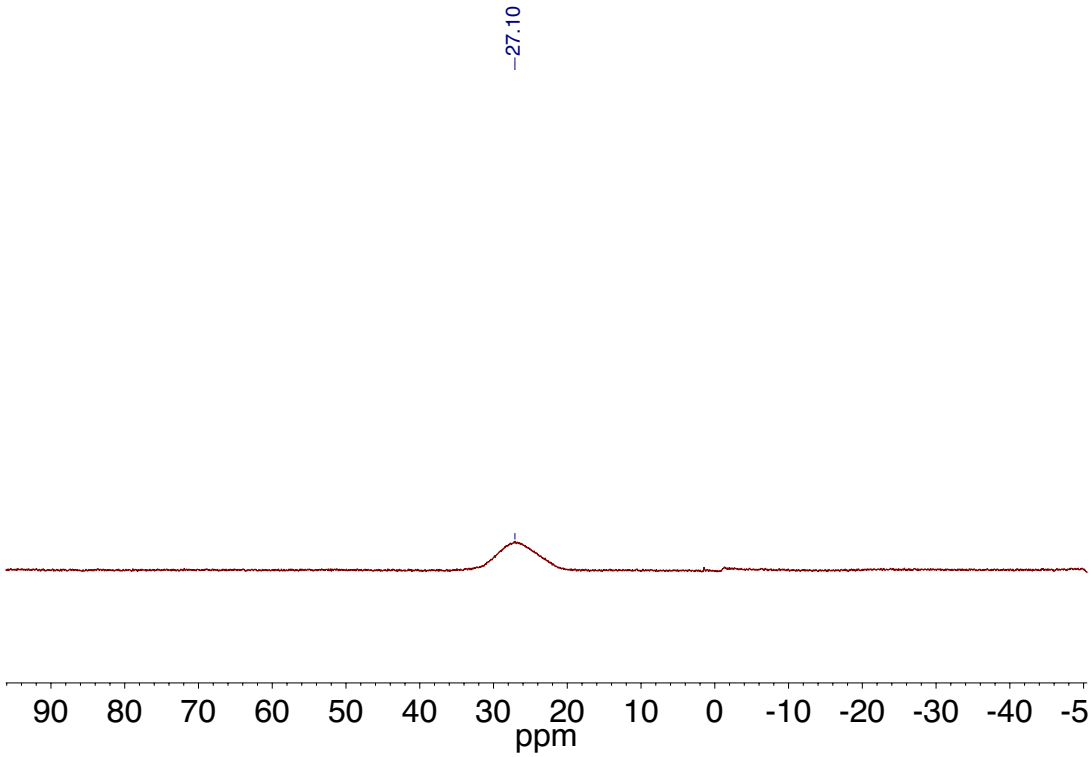

Figure 4.5.15. ^{11}B NMR spectrum of **[Cu(B_2P_2)][PF_6]** recorded at 160 MHz in CD_3CN.

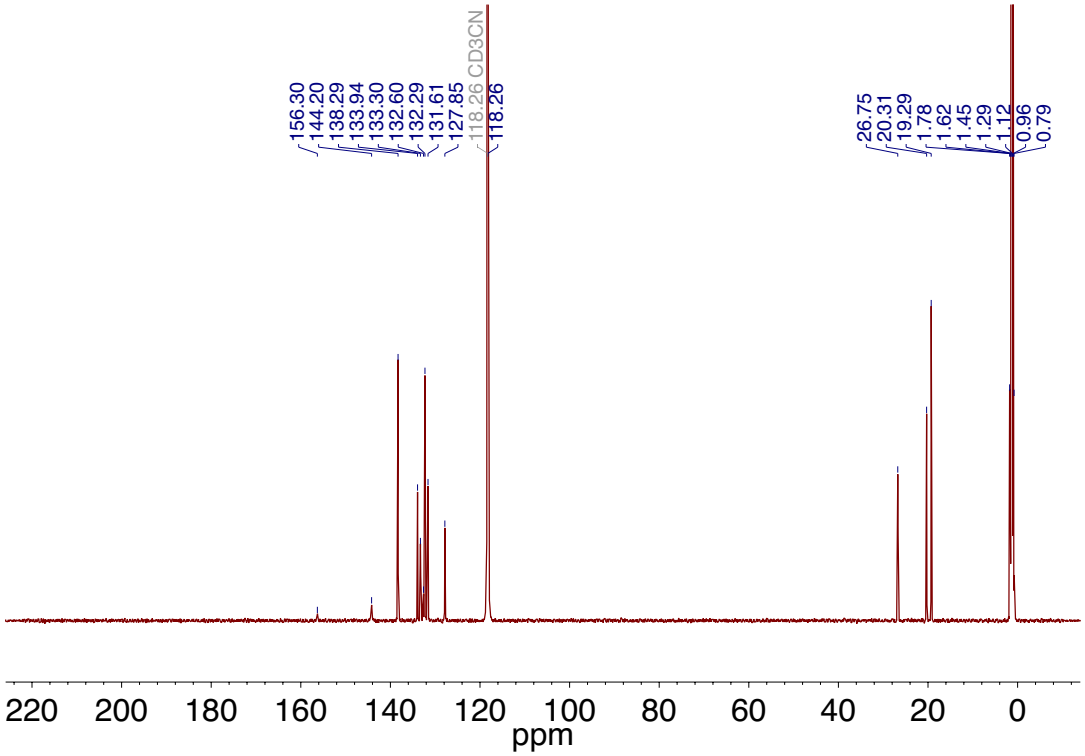

Figure 4.5.16. ^{13}C NMR spectrum of **[Cu(B_2P_2)][PF_6]** recorded at 126 MHz in CD_3CN.

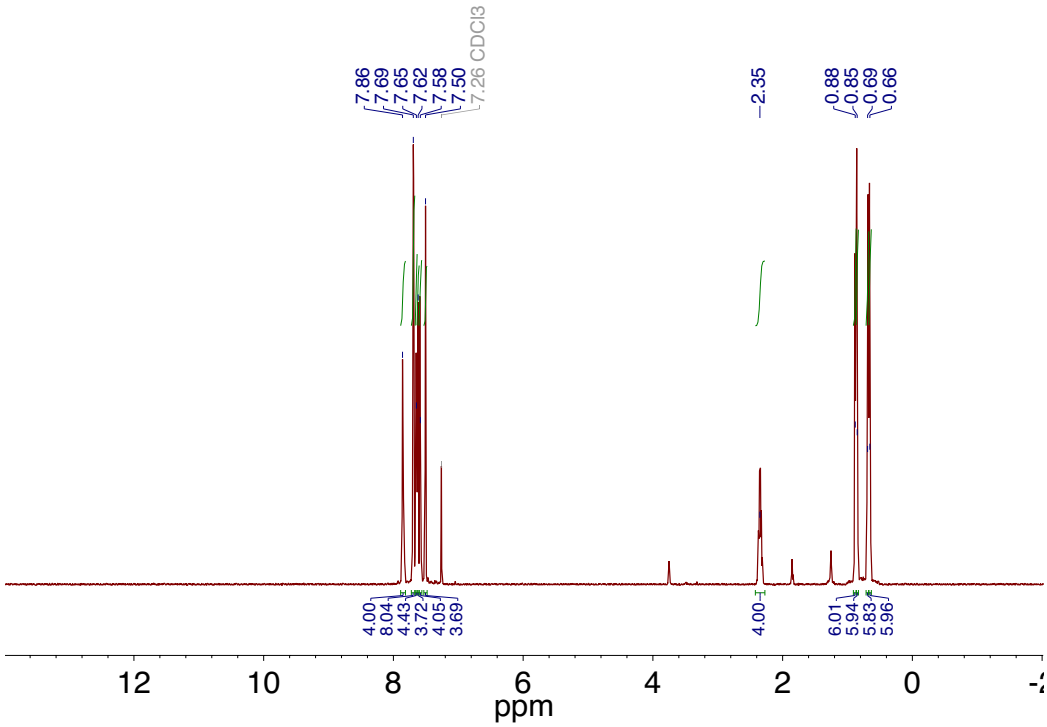

Figure 4.5.17. ^{1}H NMR spectrum of **[Cu(B_2P_2)][BAr^F_4]** recorded at 500 MHz in CD_3CN.

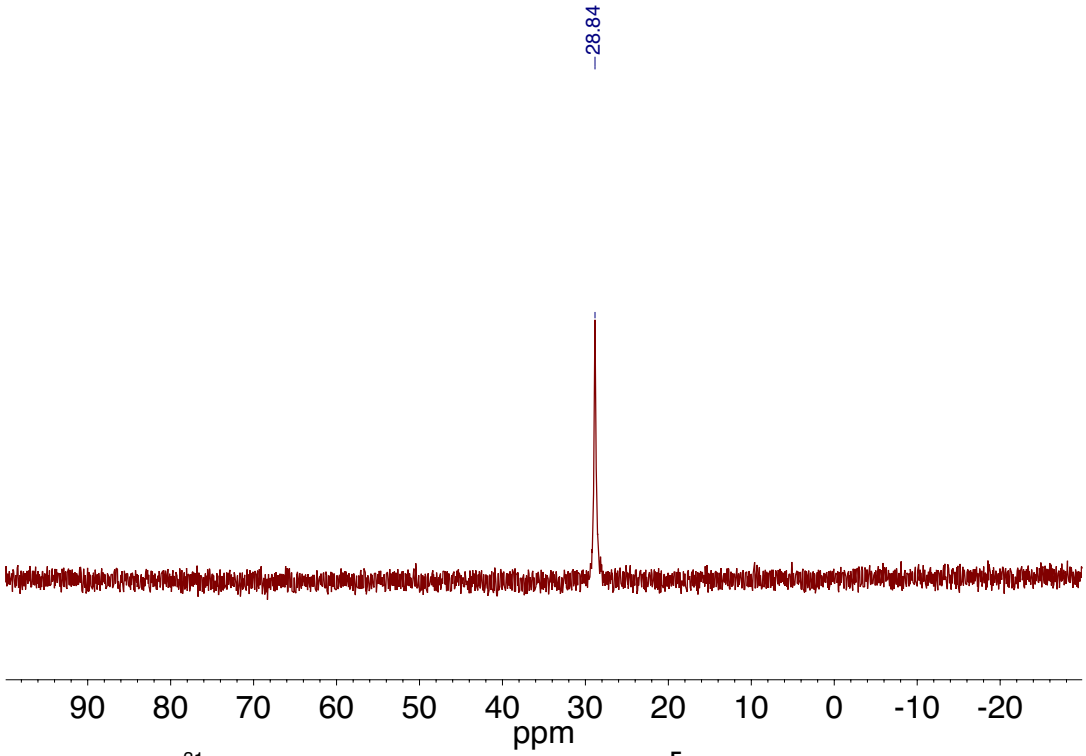

Figure 4.5.18. ^{31}P NMR spectrum of **[Cu(B_2P_2)][BAr^F_4]** recorded at 202 MHz in CD_3CN.

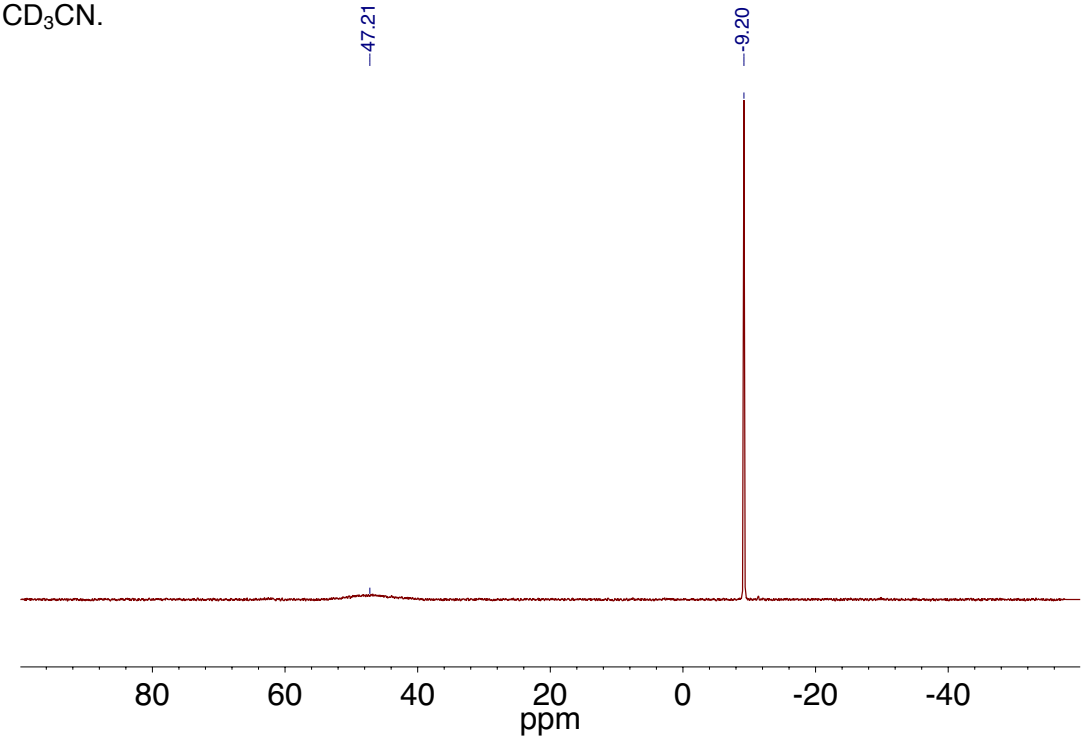

Figure 4.5.19. ^{11}B NMR spectrum of **[Cu(B_2P_2)][BAr^F_4]** recorded at 160 MHz in CD_3CN.

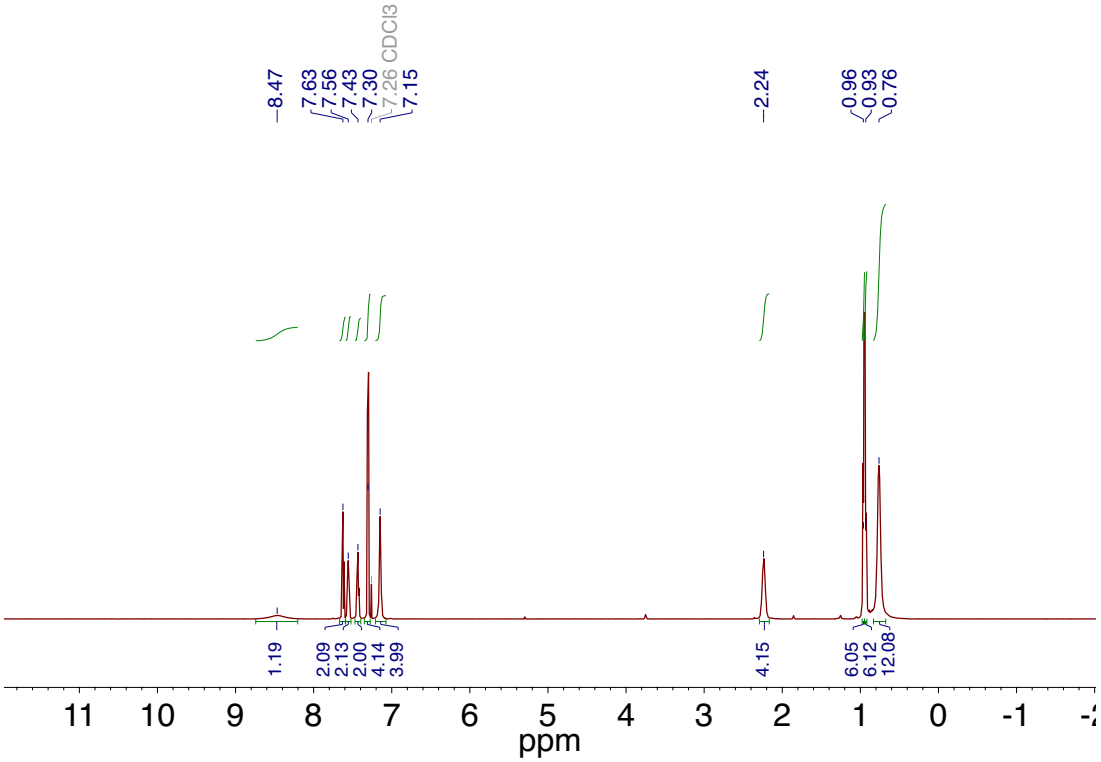

Figure 4.5.20. ^{1}H NMR spectrum of **Ag(B_2P_2)Cl** recorded at 600 MHz in $CDCl_3$.

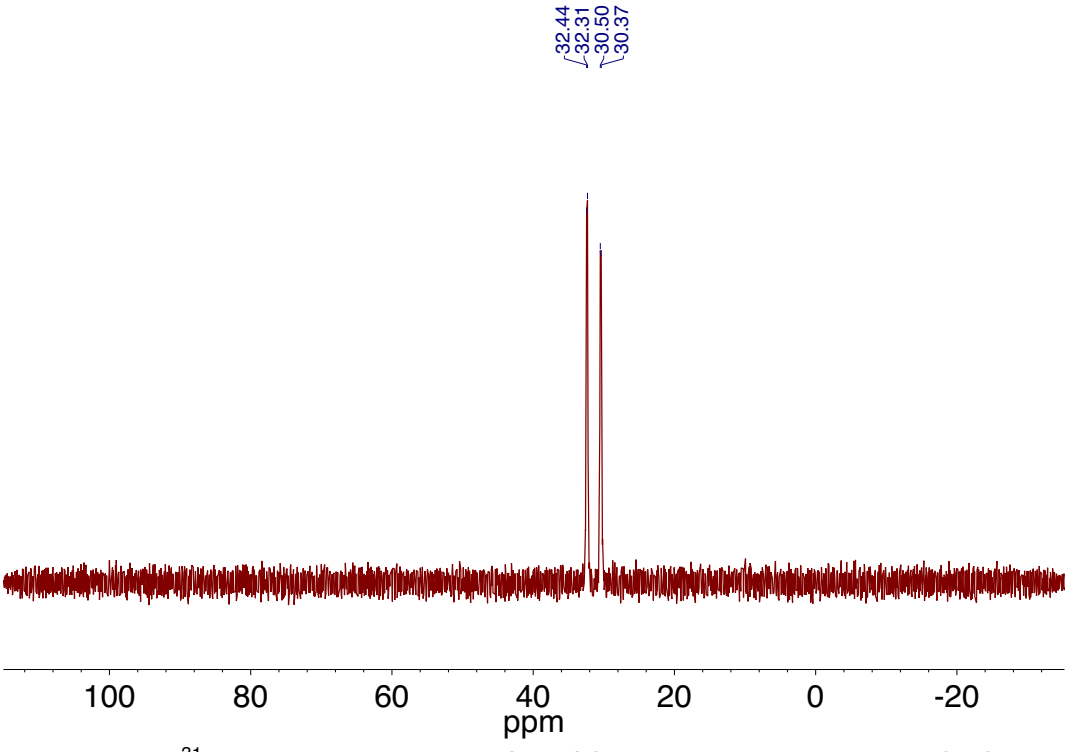

Figure 4.5.21. ^{31}P NMR spectrum of **Ag(B_2P_2)Cl** recorded at 242 MHz in $CDCl_3$.

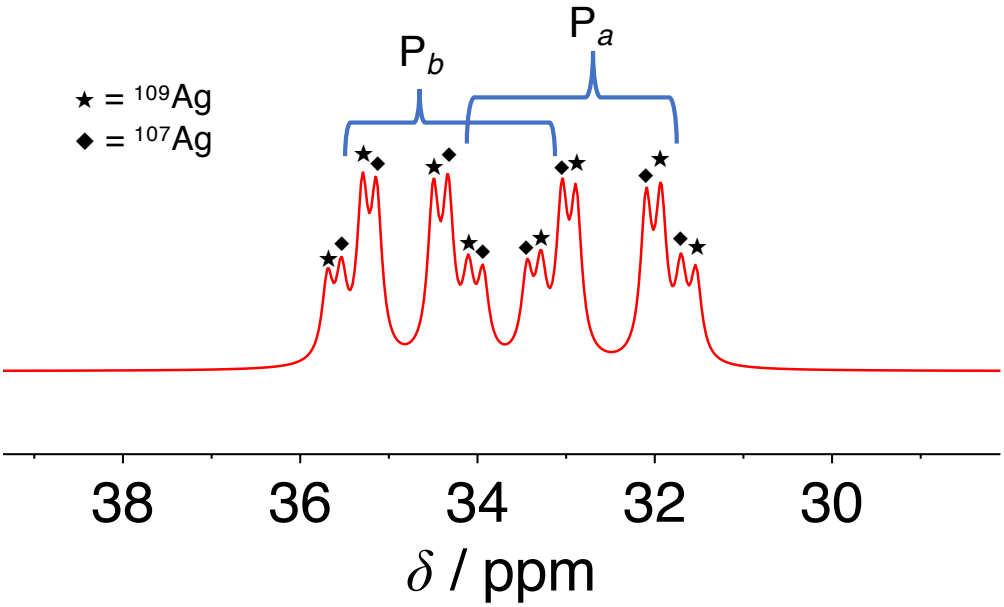

Figure 4.5.22. Simulated ^{31}P NMR spectrum of **Ag(B_2P_2)Cl** in 3:1 THF-d^8:C_6D_6 with peak assignments for the ^{107}Ag and ^{109}Ag isotopomers.

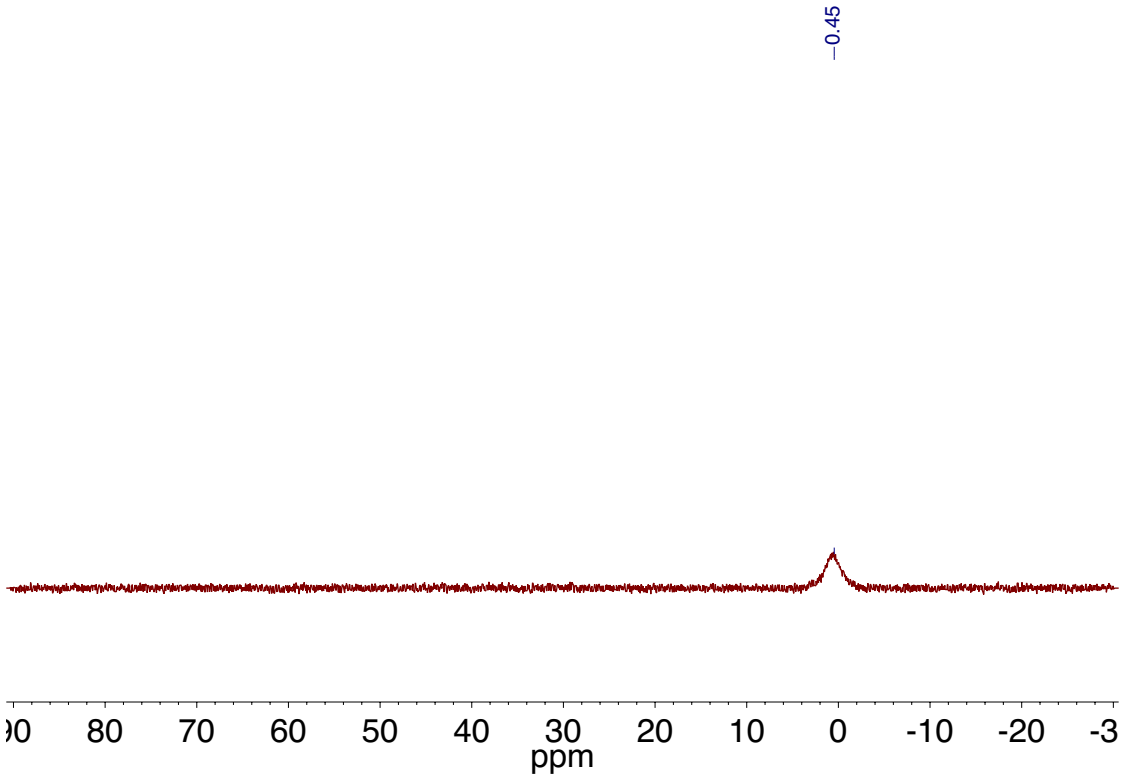

Figure 4.5.23. ^{11}B NMR spectrum of **Ag(B_2P_2)Cl** recorded at 160 MHz in THF:benzene (1:1).

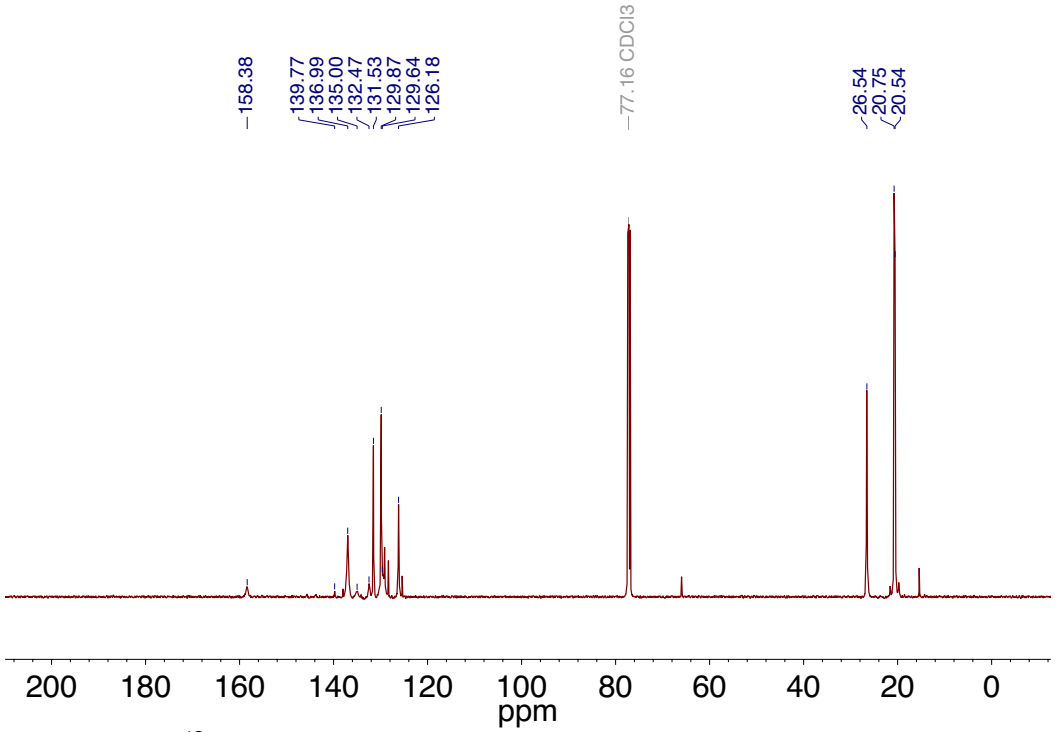

Figure 4.5.24. ^{13}C NMR spectrum of **Ag(B_2P_2)Cl** recorded at 126 MHz in $CDCl_3$.

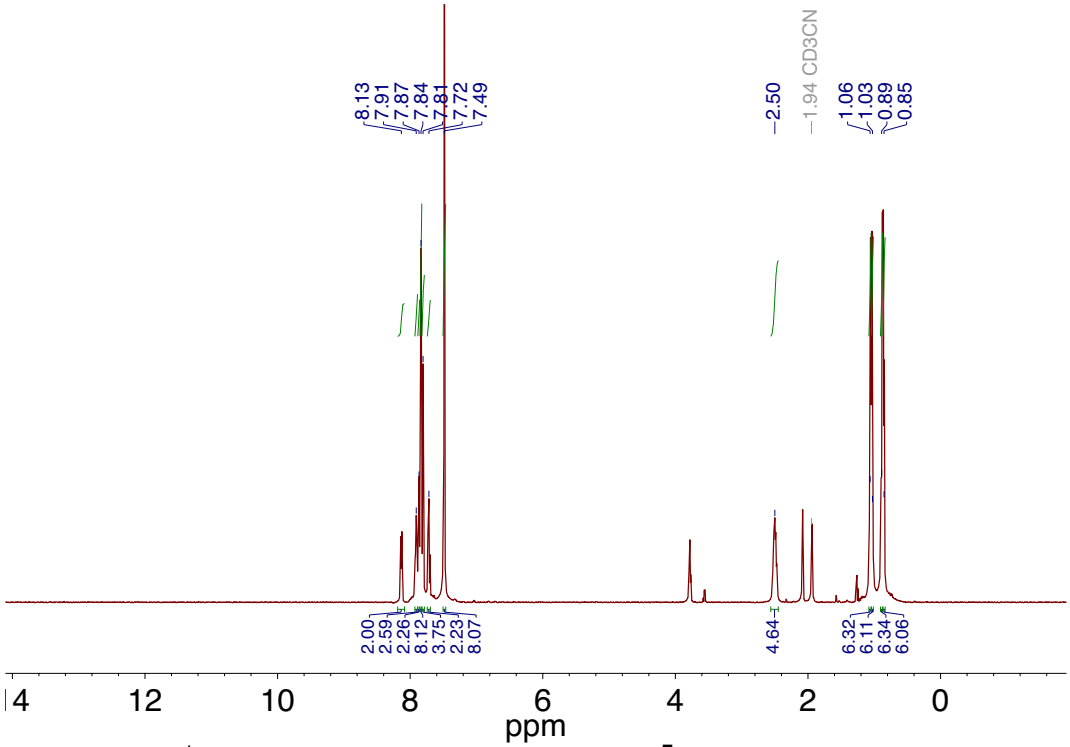

Figure 4.5.25. ^{1}H NMR spectrum of **[Ag(B_2P_2)][BAr^F_4]** recorded at 500 MHz in CD_3CN.

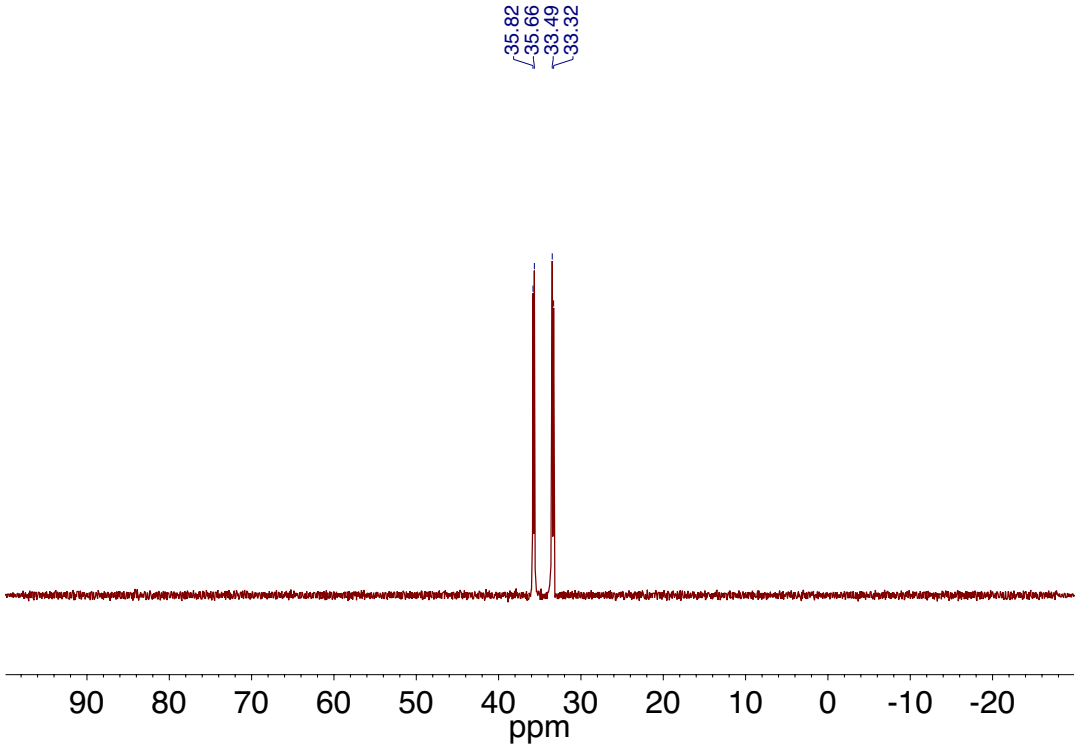

Figure 4.5.26. ^{31}P NMR spectrum of **[Ag(B_2P_2)][BAr^F_4]** recorded at 242 MHz in CD_3CN.

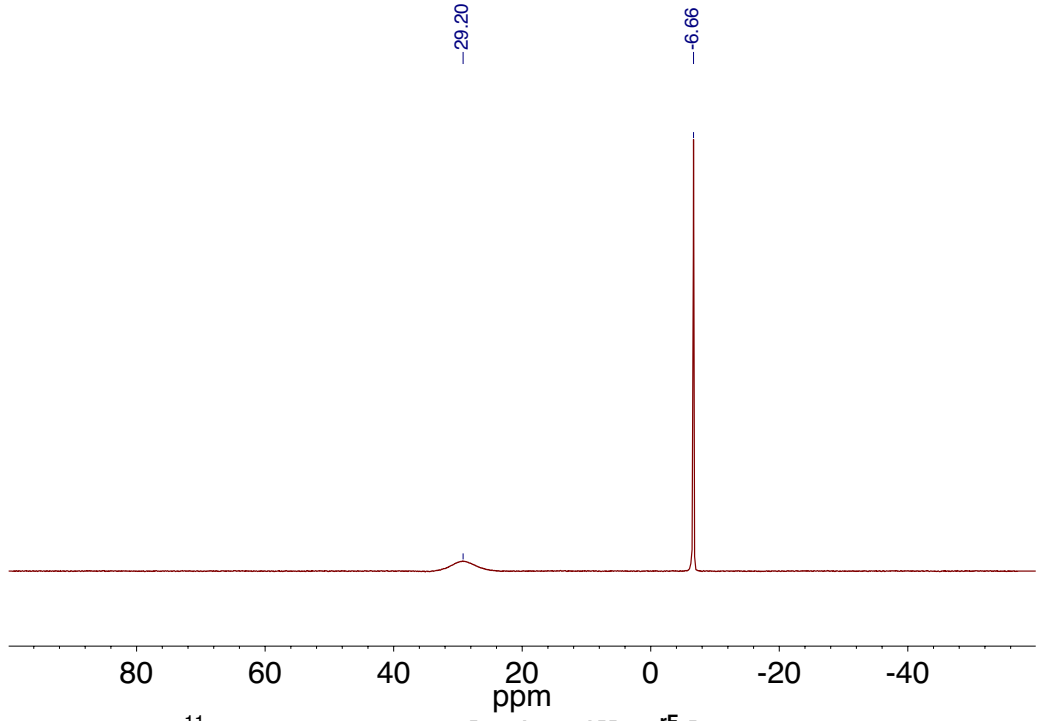

Figure 4.5.27. ^{11}B NMR spectrum of **[Ag(B_2P_2)][BA^{rF}_4]** recorded at 193 MHz in CD_3CN.

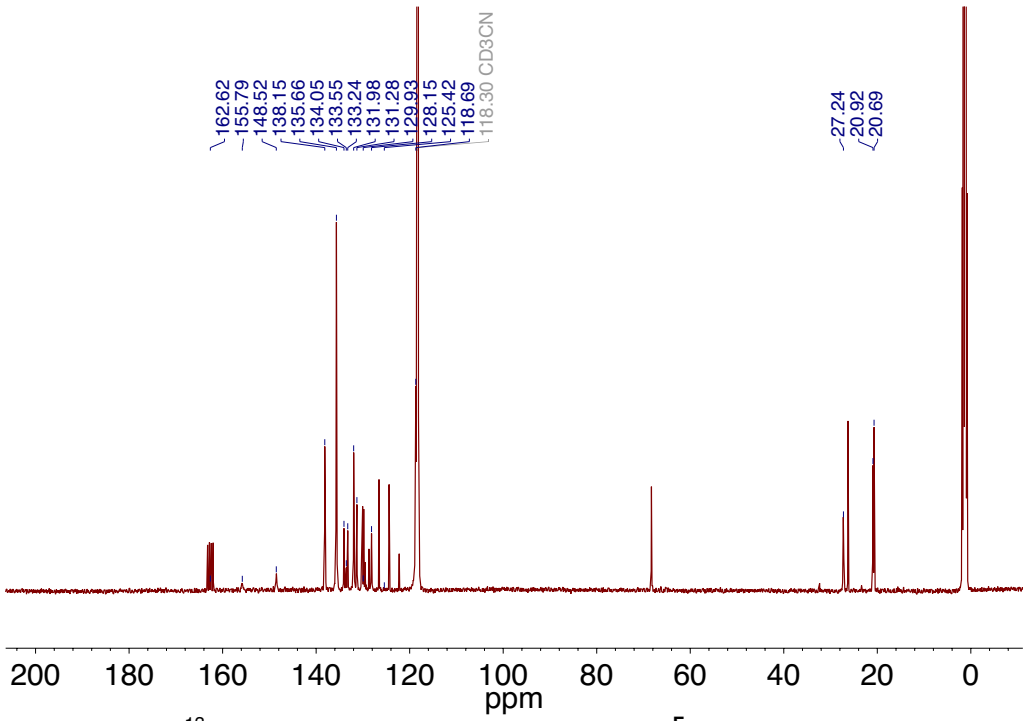

Figure 4.5.28. ^{13}C NMR spectrum of **[Ag(B_2P_2)][BAr^F_4]** recorded at 126 MHz in CD_3CN.

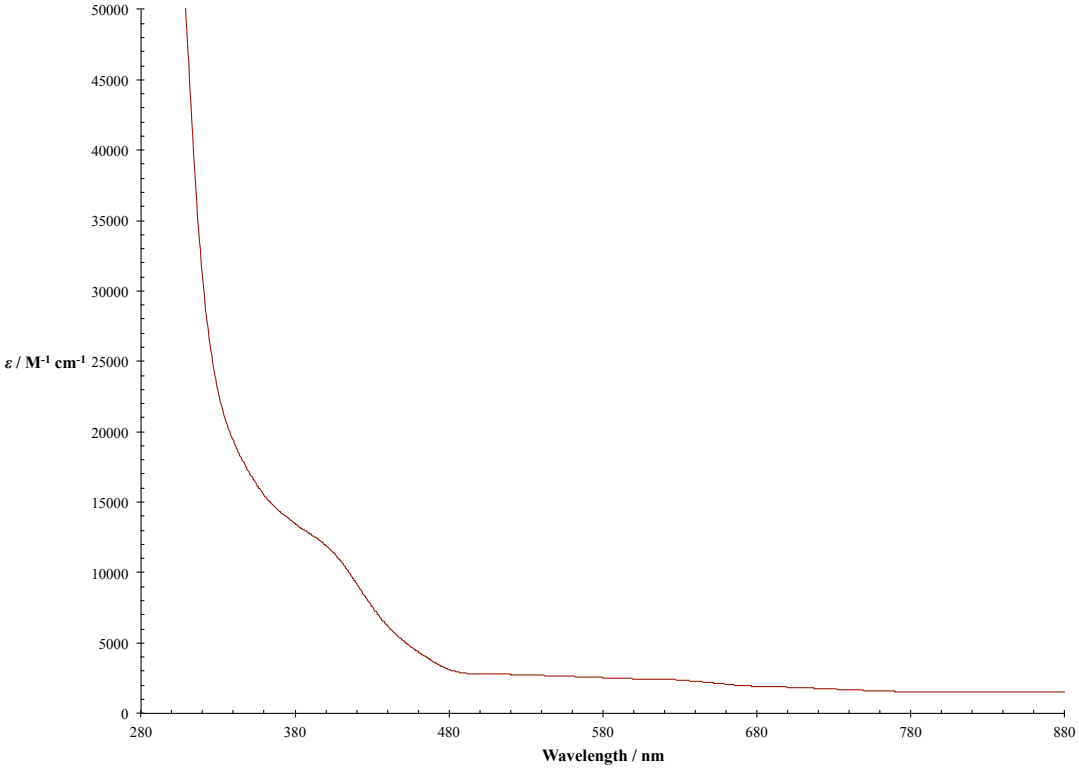

Figure 4.5.29. UV-Vis spectrum of 4.45 x 10^{-4} M **$(CuCl)_2(B_2P_2)$** in THF.

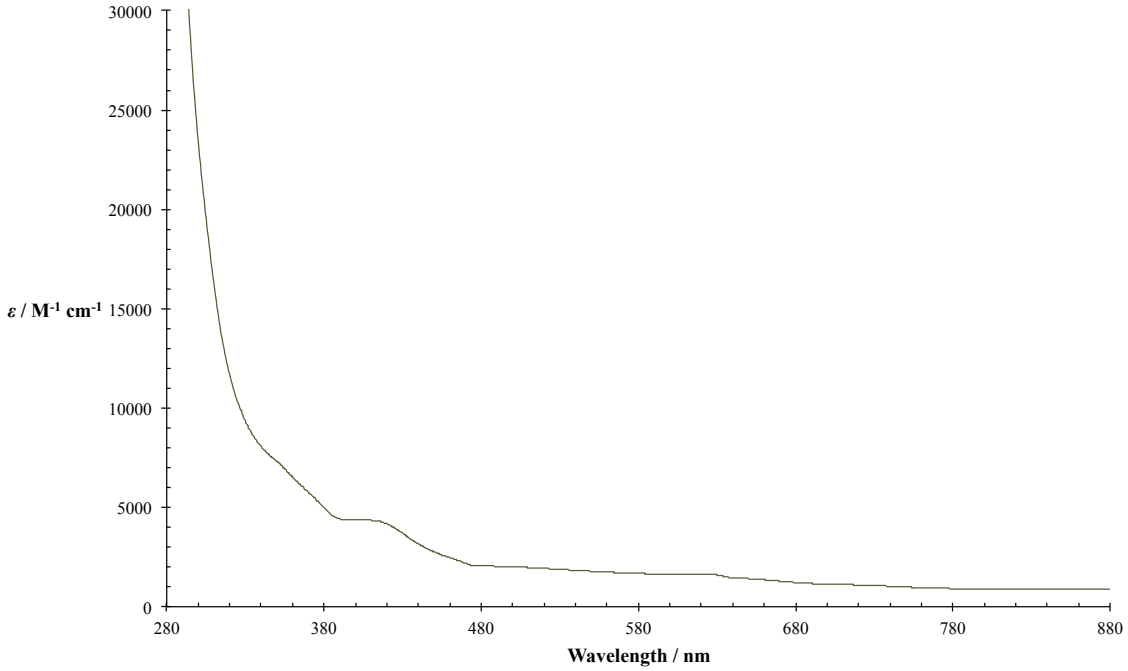

Figure 4.5.30. UV-Vis spectrum of 7.55 x 10^{-5} M **$Cu_2(\mu\text{-}Br)_2(B_2P_2)$** in THF.

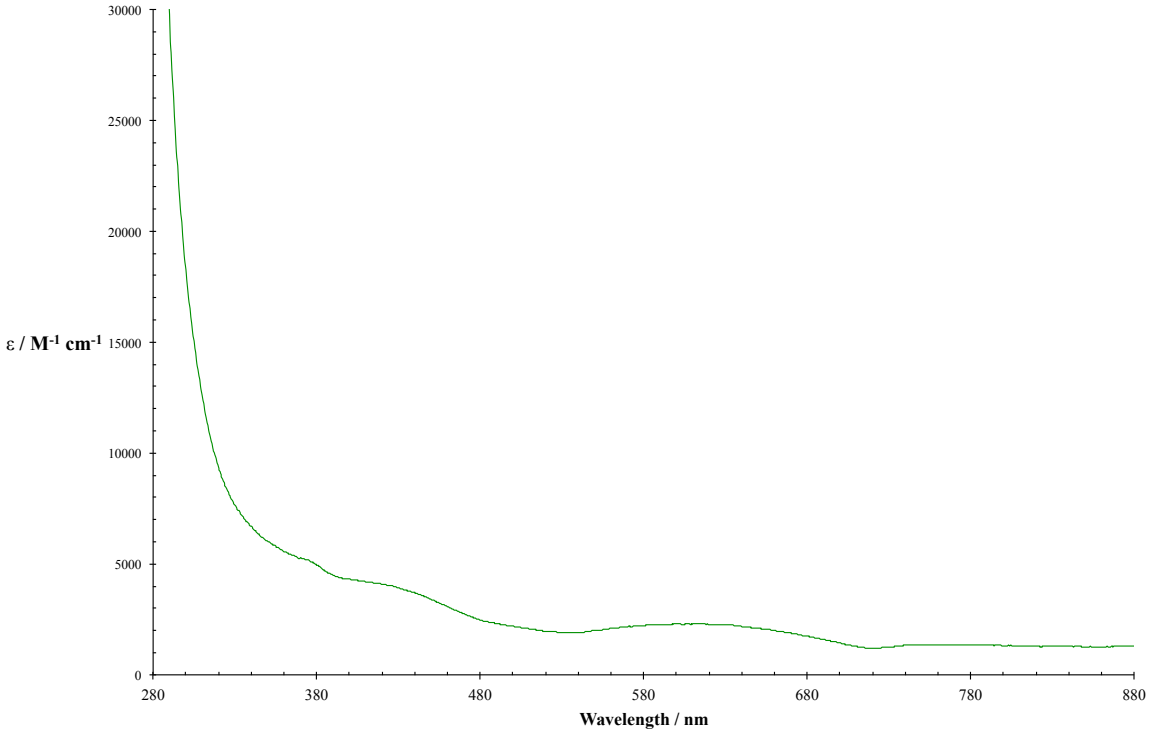

Figure 4.5.31. UV-Vis spectrum of 6.78 x 10^{-5} M **$Cu_2(\mu\text{-}I)_2(B_2P_2)$** in THF.

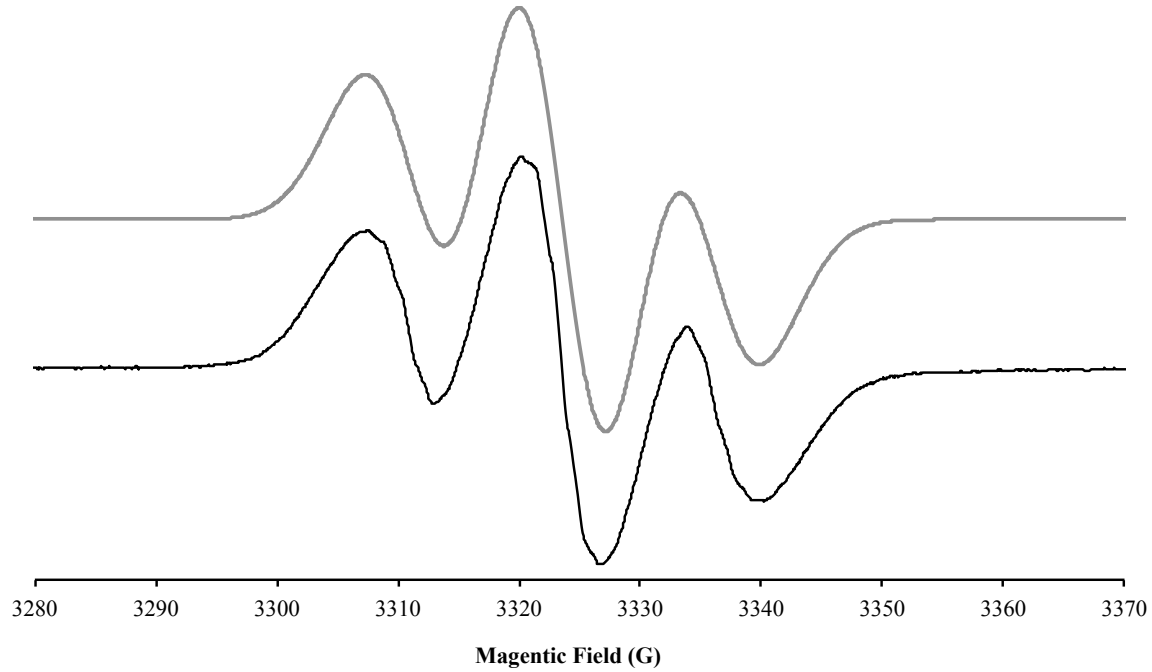

Figure 4.5.32. X-band EPR spectrum (9.318 GHz) of **Cu(B_2P_2)** in 2-MeTHF at 228 K (**black**) and its simulated spectrum (gray). Simulation parameters: g = 2.01504; $A_{iso}[^{31}P_a]$ = 36 MHz, $A_{iso}[^{31}P_b]$ = 36 MHz; lw = 1.06.

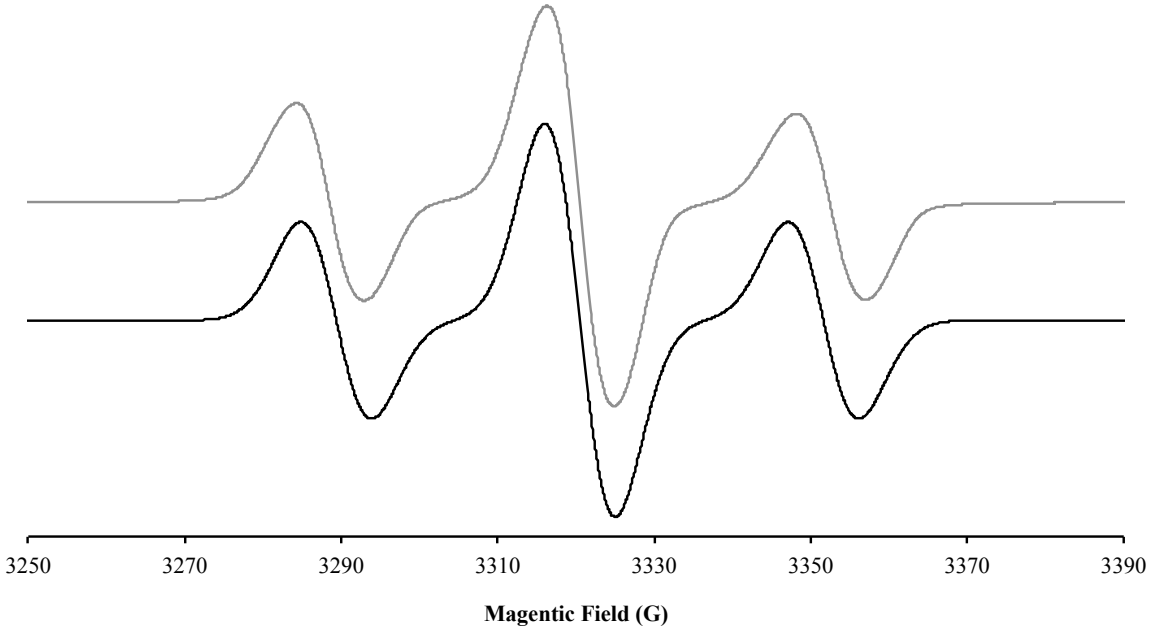

Figure 4.5.33. X-band EPR spectrum (9.315 GHz) of **Ag(B_2P_2)** in toluene at 228 K (**black**) and its simulated spectrum (gray). Simulation parameters: g = 2.017; $A_{iso}[^{31}P_a]$ = 90 MHz, A_{iso} $[^{31}P_b]$ = 90 MHz; lw = 1.03.

4.6) Cyclic Voltammetry

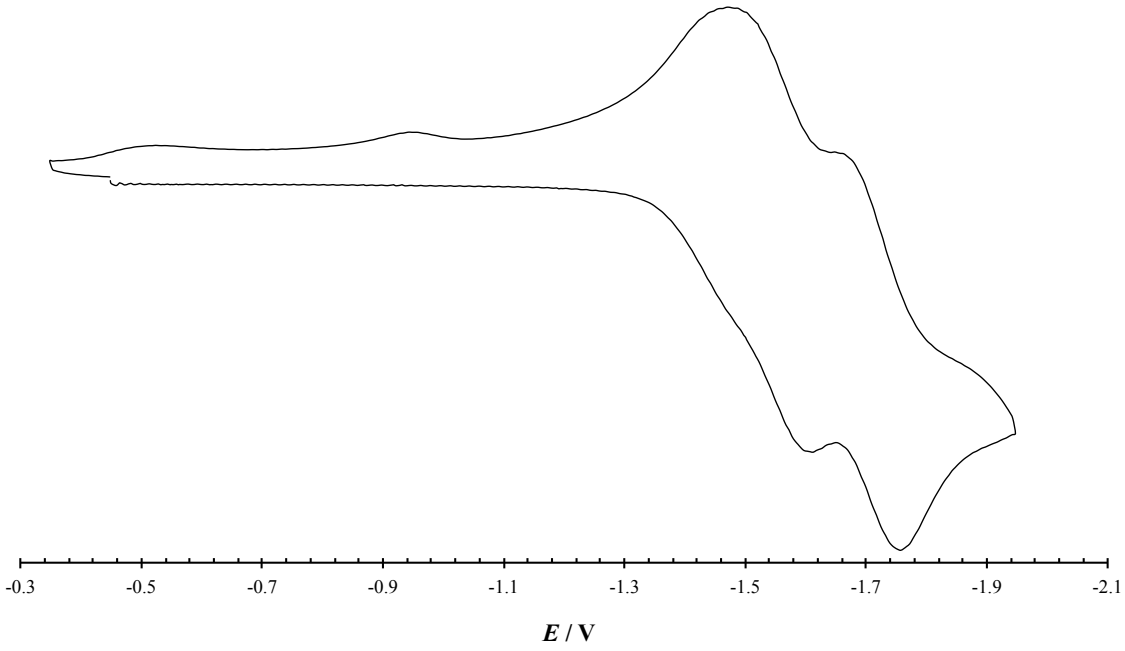

Figure 4.6.1. Cyclic voltammogram of **$Cu_2(\mu\text{-}Br)_2(B_2P_2)$** in THF. (0.1 M nBu$_4NPF_6$ as electrolyte, scan rate 100 mV/s, potential vs. Fc^+/Fc).

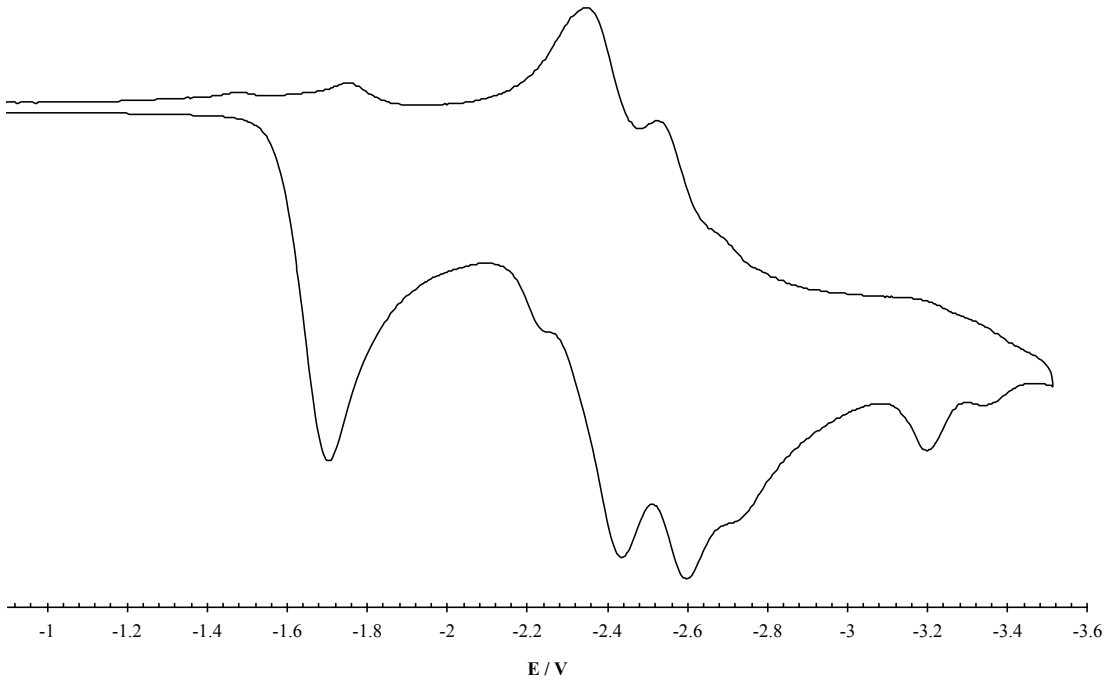

Figure 4.6.2. Cyclic voltammogram of **[Cu(B_2P_2)][PF_6]** in acetonitrile. (0.1 M $n$$Bu_4NPF_6$ as electrolyte, scan rate 100 mV/s, potential vs. Fc^+/Fc).

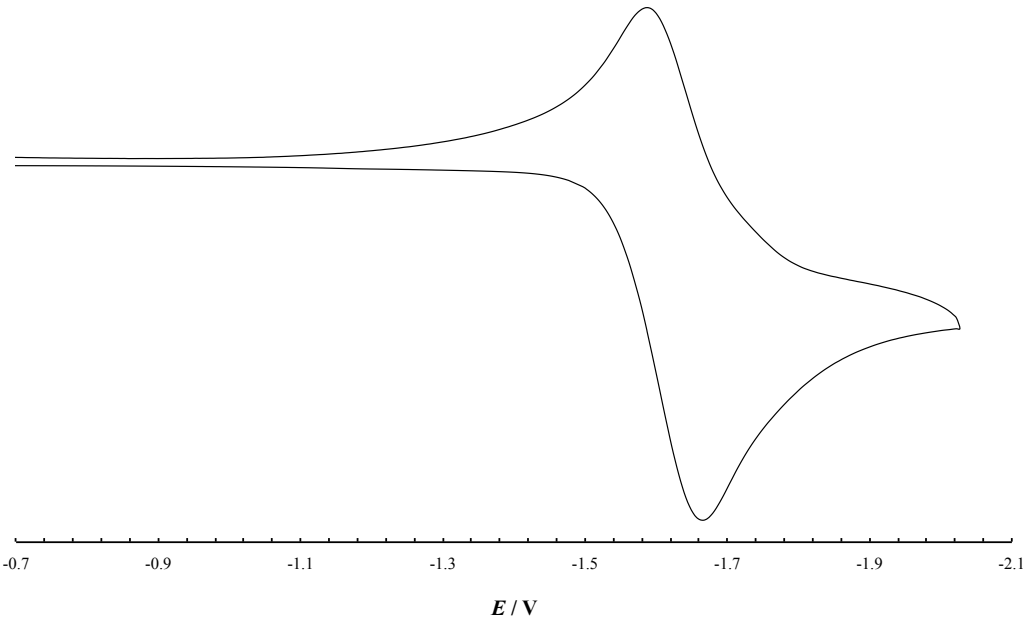

Figure 4.6.3. Cyclic voltammogram of the first redox couple for **[Cu(B_2P_2)][PF_6]** in acetonitrile. (0.1 M $n$$Bu_4NPF_6$ as electrolyte, scan rate 100 mV/s, potential vs. Fc^+/Fc).

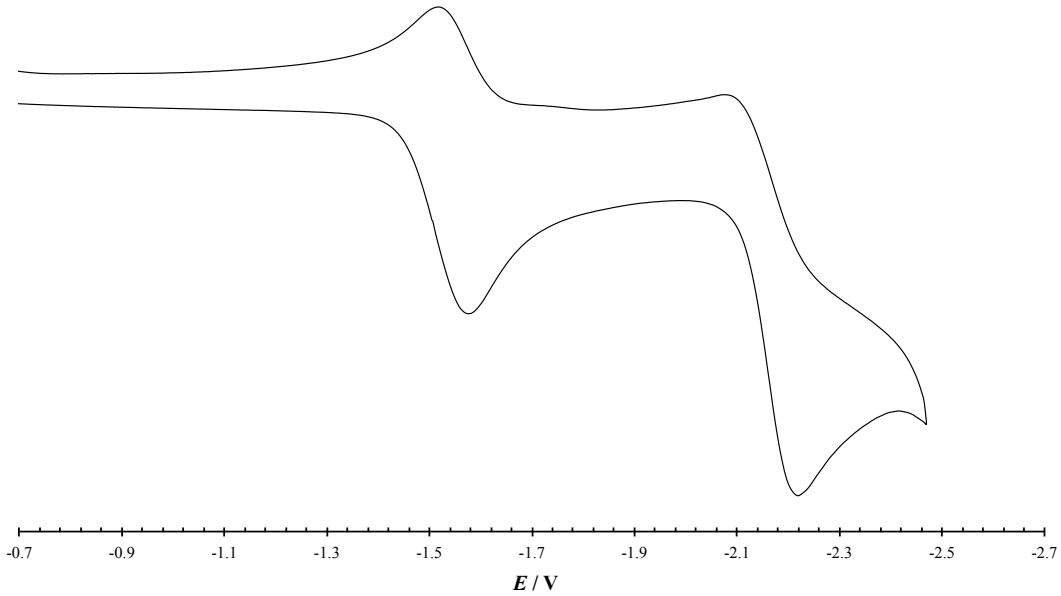

Figure 4.6.4. Cyclic voltammogram of **[Ag(B_2P_2)][BAr^F_4]** in acetonitrile. (0.1 M $n$$Bu_4NPF_6$ as electrolyte, scan rate 100 mV/s, potential vs. Fc^+/Fc).

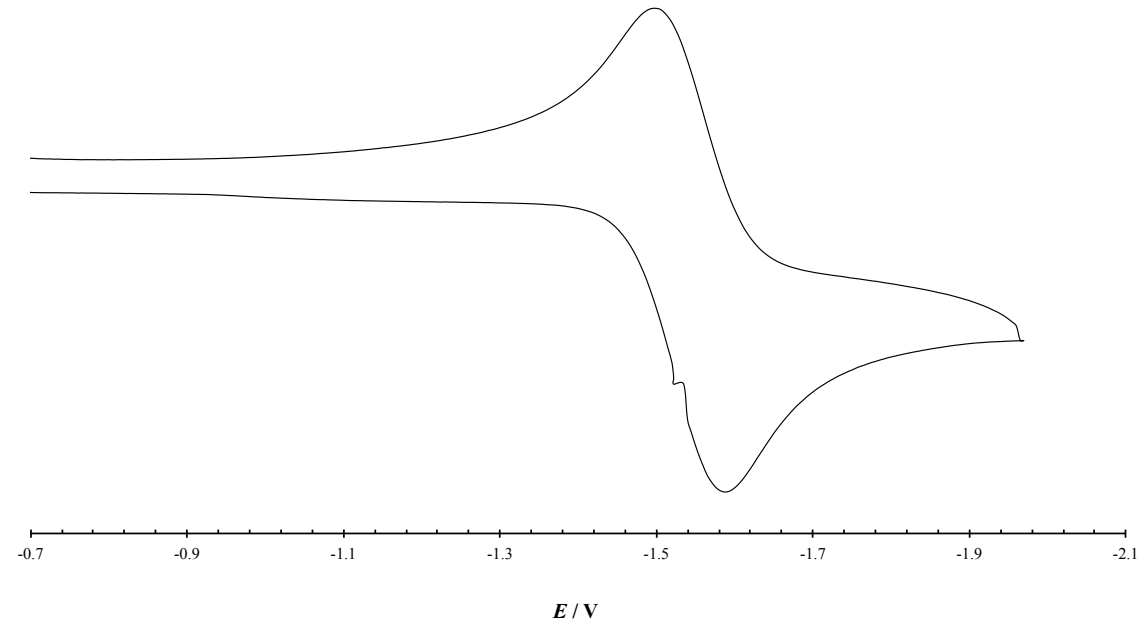

Figure 4.6.5. Cyclic voltammogram of the first redox couple for **[Ag(B_2P_2)][BAr^F_4]** in acetonitrile. (0.1 M $n$$Bu_4NPF_6$ as electrolyte, scan rate 100 mV/s, potential vs. Fc^+/Fc).

4.7) X-Ray Crystallography

4.7.1) General Considerations

Single crystals were coated with paratone oil and mounted on cryo-loop glass fibers. X-ray intensity data were collected at 100(2) K on a Bruker APEX2[29] platform-CCD X-ray diffractometer system using fine-focus Mo K_α radiation (λ = 0.71073 Å, 50kV/30mA power). The CCD detector was placed at 5.0600 cm from the crystal. Frames were integrated using the Bruker SAINT software package[30] and using a narrow-frame integration algorithm. Absorption corrections were applied to the raw intensity data using the SADABS program.[31] The Bruker SHELXTL software package[32] was used for phase determination and structure refinement. Atomic coordinates, isotropic and anisotropic displacement parameters of all the non-hydrogen atoms were refined by means of a full matrix least-squares procedure on F^2. The H-atoms were included in the refinement in calculated positions riding on the atoms to which they were attached. Relevant details for individual data collections are reported in Tables 4.7.1-4.7.9.

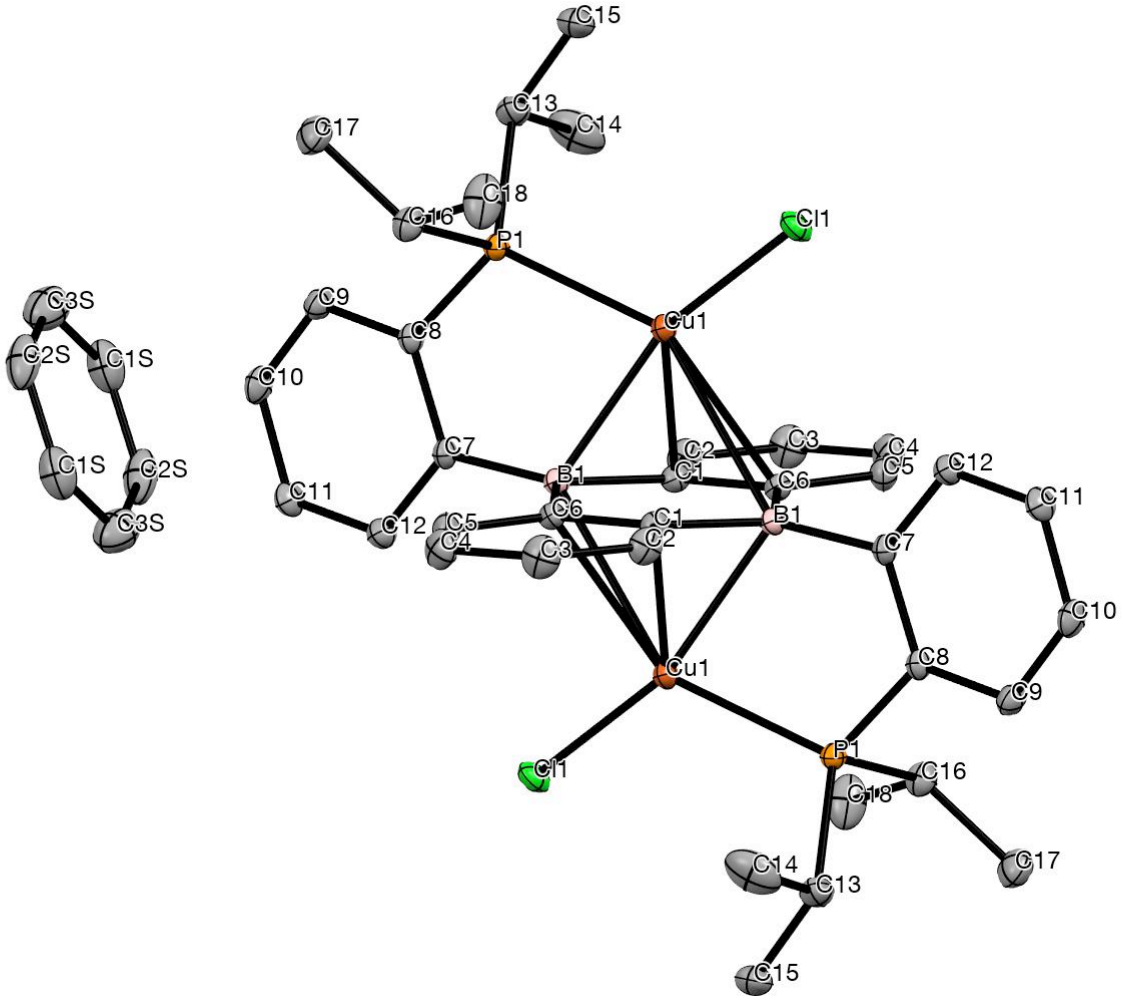

Figure 4.7.1. Labelled thermal ellipsoid plot (50%) for **$(CuCl)_2(B_2P_2)$**.

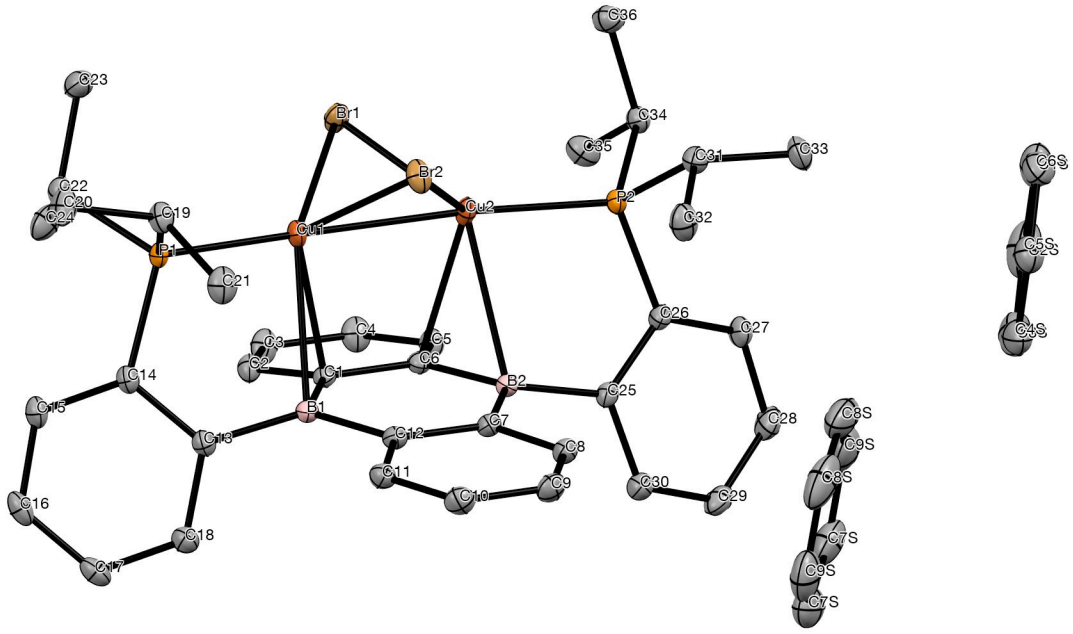

Figure 4.7.2. Labelled thermal ellipsoid plot (50%) for **$Cu_2(\mu\text{-}Br)_2(B_2P_2)$.**

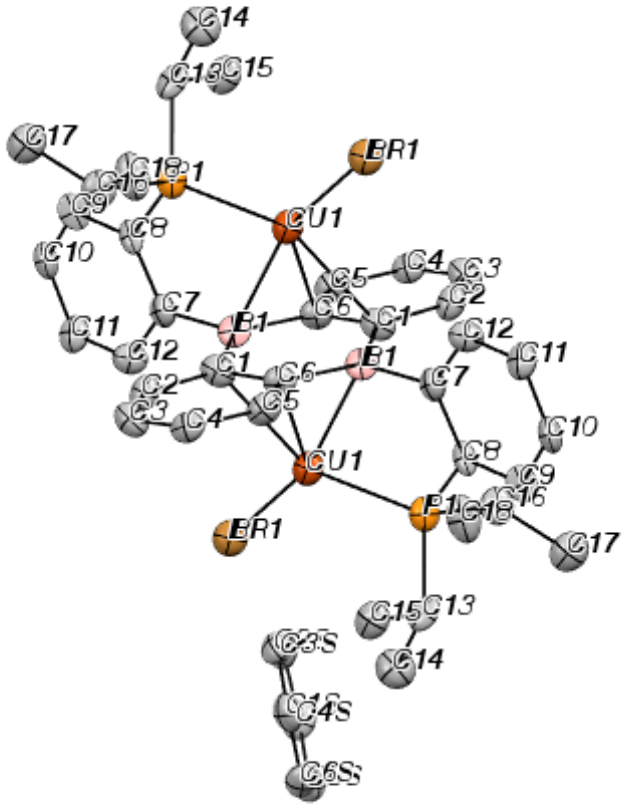

Figure 4.7.3. Labelled thermal ellipsoid plot (50%) generated from a preliminary data set for **$(CuBr)_2(B_2P_2)$**.

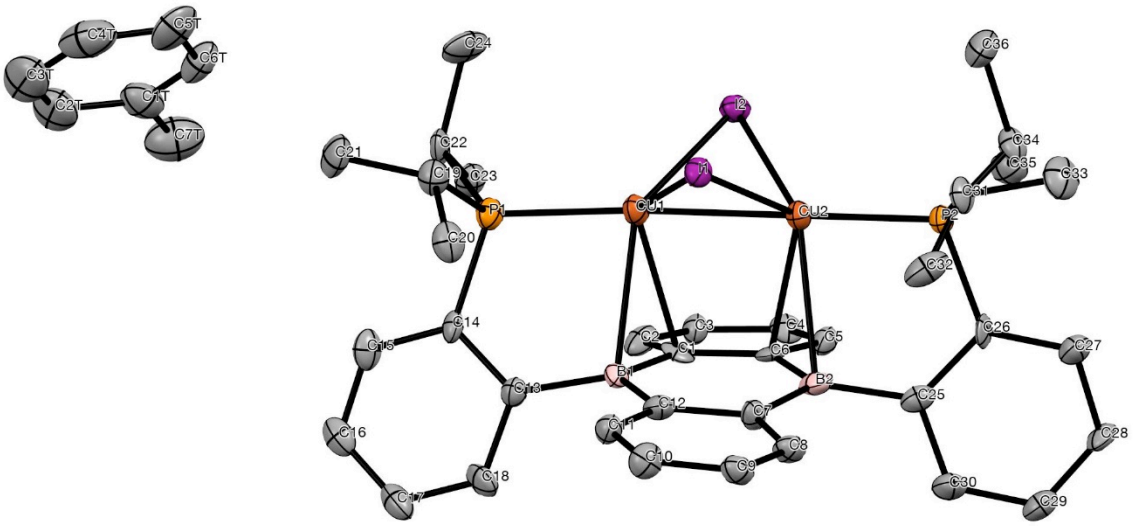

Figure 4.7.4. Labelled thermal ellipsoid plot generated from a preliminary data set for **$Cu_2(\mu\text{-}I)_2(B_2P_2)$**.

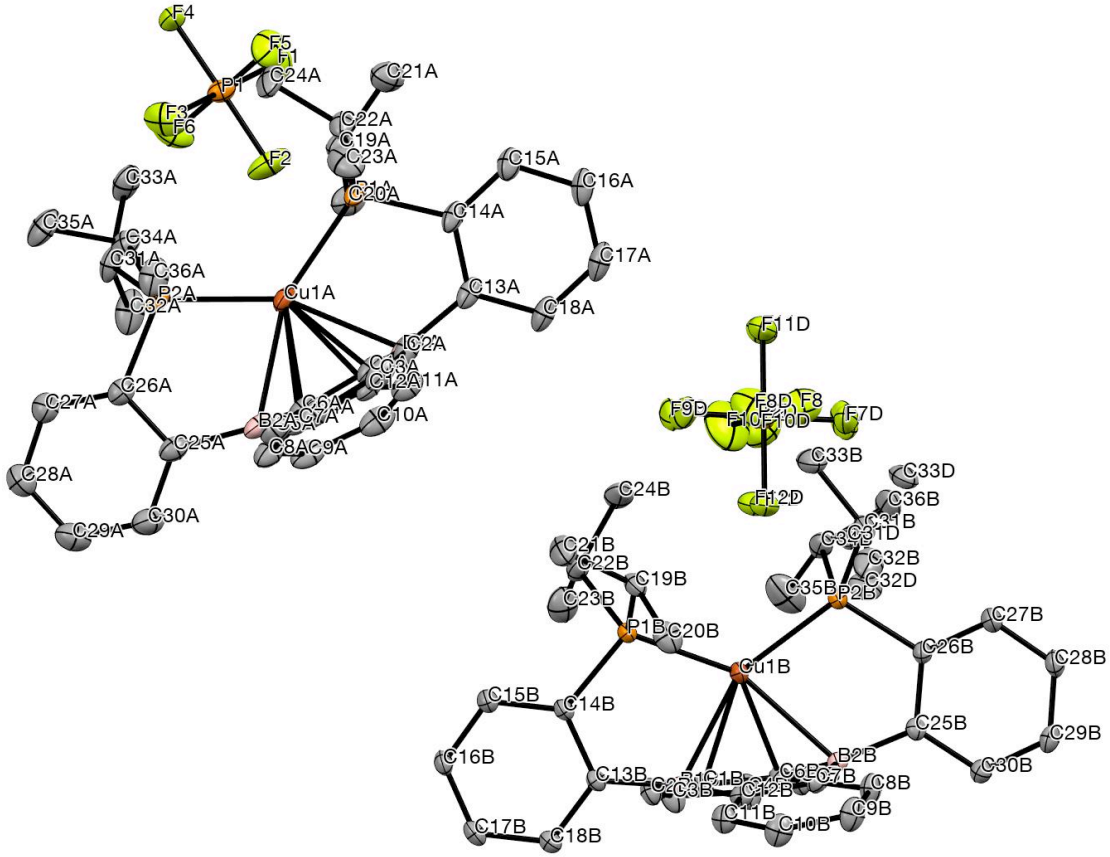

Figure 4.7.5. Labelled thermal ellipsoid plot (50%) for **$[Cu(B_2P_2)][PF_6]$**.

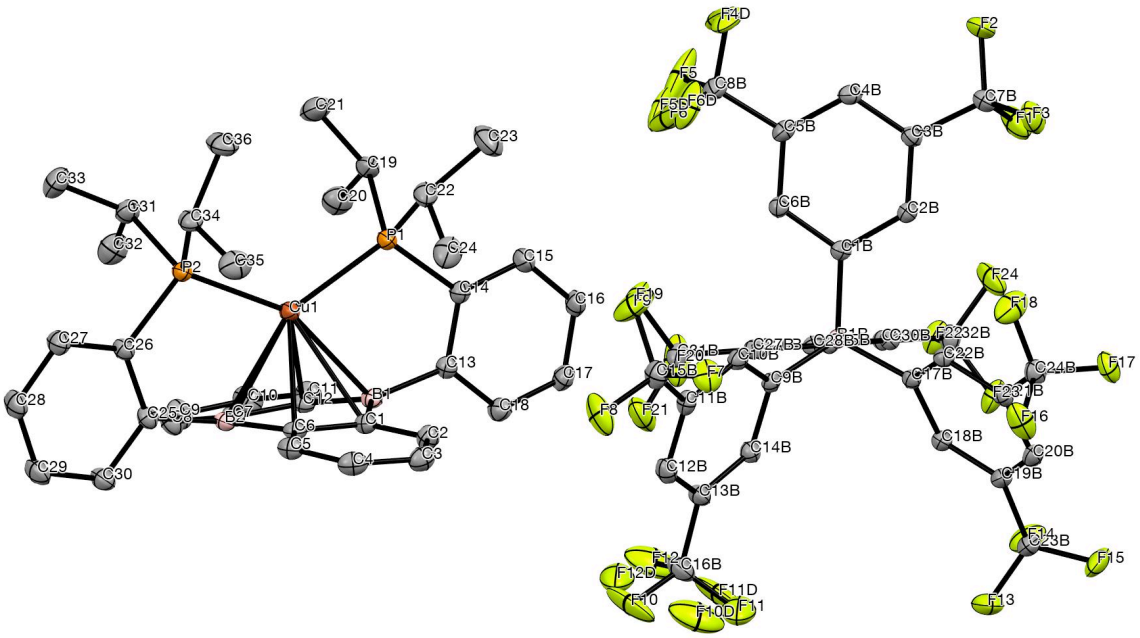

Figure 4.7.6. Labelled thermal ellipsoid plot (50%) for **[Cu(B_2P_2)][BAr^F_4]**.

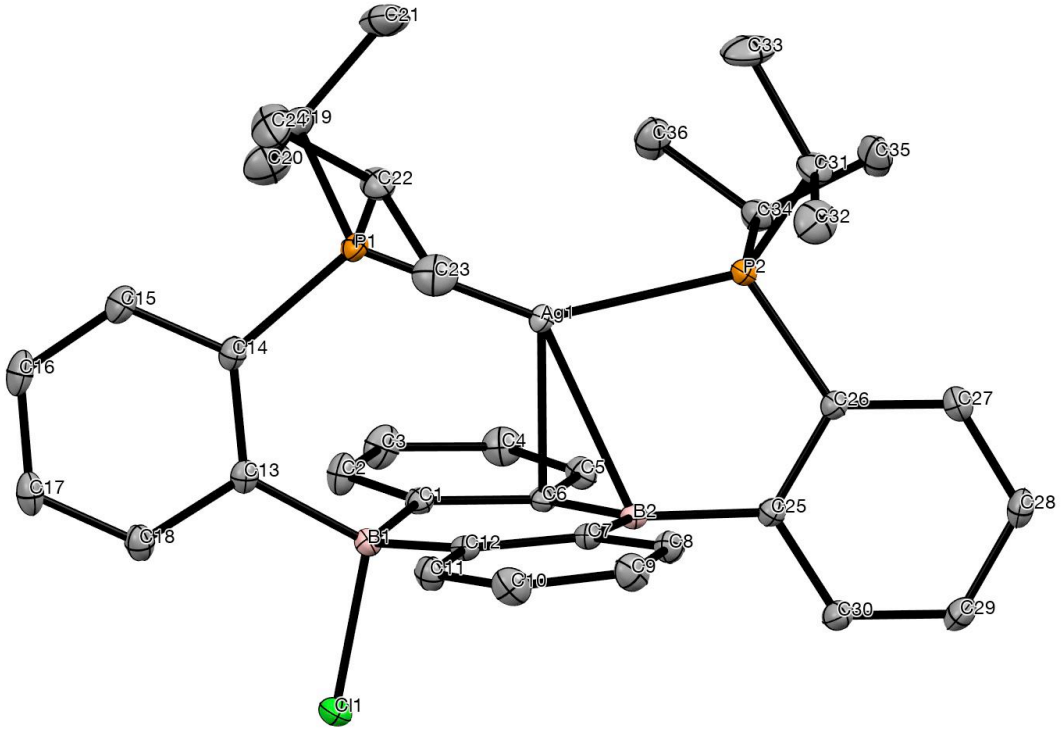

Figure 4.7.7. Labelled thermal ellipsoid plot (50%) for **Ag(B_2P_2)Cl**.

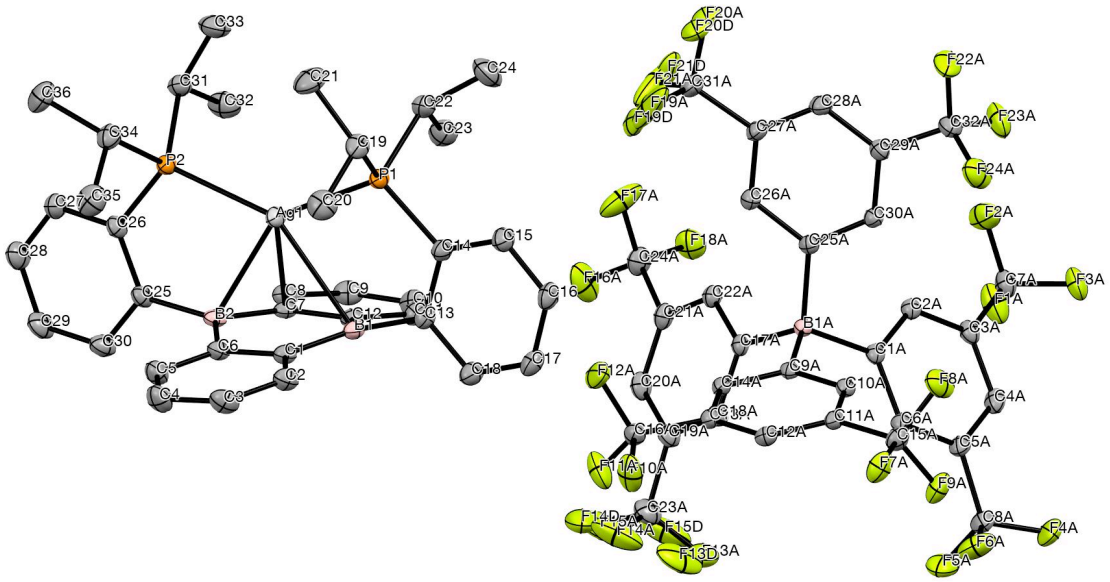

Figure 4.7.8. Labelled thermal ellipsoid plot (50%) for **[Ag(B$_2$P$_2$)][BAr$^F_4$]**.

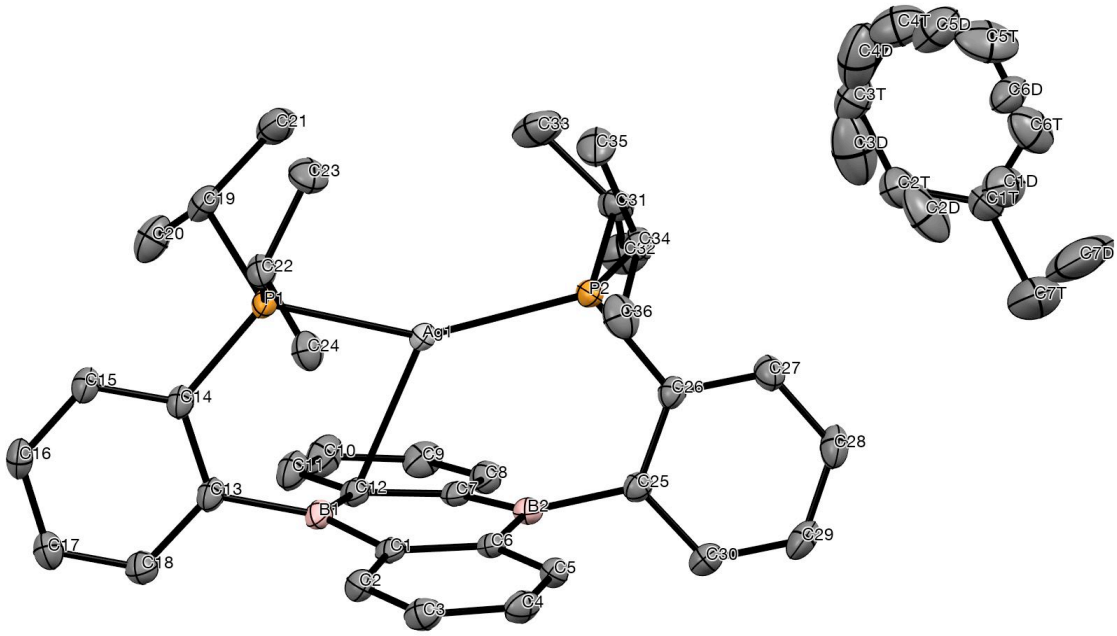

Figure 4.7.9. Labelled thermal ellipsoid plot (50%) for **Ag(B$_2$P$_2$)**.

Table 4.7.1. Crystal data and structure refinement for **$(CuCl)_2(B_2P_2)$** .

Identification code	hh47JT27_0m	
Empirical formula	$C_{42}H_{50}B_2Cl_2Cu_2P_2$	
Formula weight	836.36 g/mol	
Temperature	100(2) K	
Wavelength	0.71073 Å	
Crystal system	Monoclinic	
Space group	P 21/n	
Unit cell dimensions	a = 8.2399(2) Å	α = 90°.
	b = 18.0179(5) Å	β= 104.3189(5)°.
	c = 14.1233(4) Å	γ = 90°.
Volume	2031.69(9) Å^3	
Z	2	
Density (calculated)	1.367 mg/m^3	
Absorption coefficient	1.286 mm^{-1}	
F(000)	868	
Crystal size	0.322 x 0.188 x 0.142 mm^3	
θ range for data collection	1.869 to 30.508°.	
Index ranges	$-11 \le h \le 11$, $-25 \le k \le 25$, $-20 \le l \le 20$	
Reflections collected	59095	
Independent reflections	6207 [R_{int} = 0.0364]	
Completeness to θ = 25.242°	100.0 %	
Absorption correction	Semi-empirical from equivalents	
Refinement method	Full-matrix least-squares on F^2	
Data / restraints / parameters	6207 / 0 / 230	
Goodness-of-fit on F^2	1.045	
Final R indices [$I > 2\sigma_I$]	R_1 = 0.0244, wR_2 = 0.0600	
R indices (all data)	R_1 = 0.0305, wR_2 = 0.0631	
Largest diff. peak and hole	0.486 and –0.321 e/Å^3	

Table 4.7.2. Crystal data and structure refinement for **$Cu_2(\mu\text{-}Br)_2(B_2P_2)$**.

Identification code	hh19JT10_0m	
Empirical formula	$C_{45}H_{53}B_2Br_2Cu_2P_2$	
Formula weight	964.33 g/mol	
Temperature	100(2) K	
Wavelength	0.71073 Å	
Crystal system	Tetragonal	
Space group	I –4	
Unit cell dimensions	a = 17.8955(8) Å	α = 90°.
	b = 17.8955(8) Å	β = 90°.
	c = 26.7049(12) Å	γ = 90°.
Volume	8552.2(9) Å^3	
Z	8	
Density (calculated)	1.498 mg/m^3	
Absorption coefficient	2.969 mm^{-1}	
F(000)	3928	
Crystal size	0.467 x 0.324 x 0.305 mm^3	
θ range for data collection	1.525 to 30.996°.	
Index ranges	$-25 \le h \le 25$, $-25 \le k \le 25$, $-38 \le l \le 38$	
Reflections collected	125283	
Independent reflections	13623 [R_{int} = 0.0340]	
Completeness to θ = 25.242°	99.9 %	
Absorption correction	Semi-empirical from equivalents	
Refinement method	Full-matrix least-squares on F^2	
Data / restraints / parameters	13623 / 0 / 486	
Goodness-of-fit on F^2	1.047	
Final R indices [$I > 2\sigma_I$]	R_1 = 0.0183, wR_2 = 0.0440	
R indices (all data)	R_1 = 0.0200, wR_2 = 0.0445	
Absolute structure parameter	–0.0055(16)	
Largest diff. peak and hole	0.669 and –0.227 e/Å^3	

Table 4.7.3. Crystal data and structure refinement for **[Cu(B_2P_2)][PF_6]**.

Identification code	hh31JT19_0m	
Empirical formula	$C_{36}H_{44}B_2CuF_6P_3$	
Formula weight	768.78 g/mol	
Temperature	100(2) K	
Wavelength	0.71073 Å	
Crystal system	Orthorhombic	
Space group	P b c a	
Unit cell dimensions	a = 27.1673(6) Å	α = 90°.
	b = 18.1154(4) Å	β = 90°.
	c = 29.2280(7) Å	γ = 90°.
Volume	14384.5(6) Å^3	
Z	16	
Density (calculated)	1.420 mg/m^3	
Absorption coefficient	0.798 mm^{-1}	
F(000)	6368	
Crystal size	0.496 x 0.417 x 0.366 mm^3	
θ range for data collection	1.520 to 30.999°.	
Index ranges	$-39 \le h \le 39$, $-26 \le k \le 26$, $-42 \le l \le 42$	
Reflections collected	343803	
Independent reflections	22919 [R_{int} = 0.0433]	
Completeness to θ = 25.242°	100.0 %	
Absorption correction	Semi-empirical from equivalents	
Refinement method	Full-matrix least-squares on F^2	
Data / restraints / parameters	22919 / 318 / 975	
Goodness-of-fit on F^2	1.055	
Final R indices [$I > 2\sigma_I$]	R_1 = 0.0342, wR_2 = 0.0810	
R indices (all data)	R_1 = 0.0459, wR_2 = 0.0869	
Largest diff. peak and hole	0.696 and –0.527 e/Å^3	

Table 4.7.4. Crystal data and structure refinement for **[Cu(B_2P_2)][BAr^F_4]**.

Identification code	hh21JT12_0m	
Empirical formula	$C_{68}H_{56}B_3CuF_{24}P_2$	
Formula weight	1487.03 g/mol	
Temperature	100(2) K	
Wavelength	0.71073 Å	
Crystal system	Monoclinic	
Space group	P 21/*c*	
Unit cell dimensions	*a* = 17.6424(7) Å	*α* = 90°.
	b = 15.9184(6) Å	*β* = 90.654(1)°.
	c = 23.6757(9) Å	*γ* = 90°.
Volume	6648.6(4) $Å^3$	
Z	4	
Density (calculated)	1.486 mg/m^3	
Absorption coefficient	0.486 mm^{-1}	
F(000)	3016	
Crystal size	0.549 x 0.163 x 0.057 mm^3	
θ range for data collection	1.542 to 30.508°.	
Index ranges	$-25 \le h \le 25$, $-22 \le k \le 22$, $-33 \le l \le 33$	
Reflections collected	155469	
Independent reflections	20287 [R_{int} = 0.0470]	
Completeness to *θ* = 25.242°	100.0 %	
Absorption correction	Semi-empirical from equivalents	
Refinement method	Full-matrix least-squares on F^2	
Data / restraints / parameters	20287 / 114 / 929	
Goodness-of-fit on F^2	1.011	
Final *R* indices [$I > 2\sigma_I$]	R_1 = 0.0379, wR_2 = 0.0868	
R indices (all data)	R_1 = 0.0569, wR_2 = 0.0967	
Largest diff. peak and hole	0.625 and –0.629 e/$Å^3$	

Note: Level B alerts in the CIF for this compound are related to disordered fluorine atoms associated with the CF_3 groups on the BAr^F_4 anion.

Table 4.7.5. Crystal data and structure refinement for **$Ag(B_2P_2)Cl$**.

Identification code	hh123JT62_0m	
Empirical formula	$C_{36}H_{44}AgB_2ClP_2$	
Formula weight	703.59 g/mol	
Temperature	100(2) K	
Wavelength	0.71073 Å	
Crystal system	Monoclinic	
Space group	P 21/n	
Unit cell dimensions	a = 9.6621(5) Å	α = 90°.
	b = 21.0105(11) Å	β = 97.7173(8)°.
	c = 16.5894(9) Å	γ = 90°.
Volume	3337.2(3) Å^3	
Z	4	
Density (calculated)	1.400 mg/m^3	
Absorption coefficient	0.805 mm^{-1}	
F(000)	1456	
Crystal size	0.455 x 0.239 x 0.228 mm^3	
θ range for data collection	1.573 to 30.506°.	
Index ranges	$-13 \le h \le 13$, $-30 \le k \le 30$, $-23 \le l \le 23$	
Reflections collected	97134	
Independent reflections	10177 [R_{int} = 0.0290]	
Completeness to θ = 25.242°	100.0 %	
Absorption correction	Semi-empirical from equivalents	
Refinement method	Full-matrix least-squares on F^2	
Data / restraints / parameters	10177 / 0 / 387	
Goodness-of-fit on F^2	1.046	
Final R indices [$I > 2\sigma_I$]	R_1 = 0.0205, wR_2 = 0.0503	
R indices (all data)	R_1 = 0.0244, wR_2 = 0.0522	
Largest diff. peak and hole	0.463 and –0.246 e/Å^3	

Table 4.7.6. Crystal data and structure refinement for **[Ag(B_2P_2)][BAr^F_4]**.

Identification code	hh120JT60_0m	
Empirical formula	$C_{68}H_{56}AgB_3F_{24}P_2$	
Formula weight	1531.36 g/mol	
Temperature	100(2) K	
Wavelength	0.71073 Å	
Crystal system	Monoclinic	
Space group	P 21/c	
Unit cell dimensions	a = 17.6946(4) Å	α = 90°.
	b = 16.0719(4) Å	β = 90.3111(5)°.
	c = 23.6304(6) Å	γ = 90°.
Volume	6720.1(3) Å^3	
Z	4	
Density (calculated)	1.514 mg/m^3	
Absorption coefficient	0.456 mm^{-1}	
F(000)	3088	
Crystal size	0.458 x 0.221 x 0.204 mm^3	
θ range for data collection	1.532 to 30.034°.	
Index ranges	$-24 \le h \le 24$, $-22 \le k \le 22$, $-33 \le l \le 33$	
Reflections collected	222811	
Independent reflections	19669 [R_{int} = 0.0351]	
Completeness to θ = 25.242°	100.0 %	
Absorption correction	Semi-empirical from equivalents	
Refinement method	Full-matrix least-squares on F^2	
Data / restraints / parameters	19669 / 30 / 923	
Goodness-of-fit on F^2	1.035	
Final R indices [$I > 2\sigma_I$]	R_1 = 0.0296, wR_2 = 0.0739	
R indices (all data)	R_1 = 0.0358, wR_2 = 0.0777	
Largest diff. peak and hole	0.737 and –0.509 e/Å^3	

Table 4.7.7. Crystal data and structure refinement for **$Ag(B_2P_2)$**.

Identification code	hh230JT115_0m	
Empirical formula	$C_{43}H_{52}AgB_2P_2$	
Formula weight	760.27 g/mol	
Temperature	100(2) K	
Wavelength	0.71073 Å	
Crystal system	Orthorhombic	
Space group	P b c a	
Unit cell dimensions	a = 15.2862(6) Å	α = 90°.
	b = 16.6849(7) Å	β = 90°.
	c = 29.9695(12) Å	γ = 90°.
Volume	7643.7(5) Å^3	
Z	8	
Density (calculated)	1.321 mg/m^3	
Absorption coefficient	0.641 mm^{-1}	
F(000)	3176	
Crystal size	0.512 x 0.127 x 0.119 mm^3	
θ range for data collection	1.903 to 30.508°.	
Index ranges	$-21 \le h \le 21$, $-23 \le k \le 23$, $-42 \le l \le 42$	
Reflections collected	116540	
Independent reflections	11666 [R_{int} = 0.0474]	
Completeness to θ = 25.242°	100.0 %	
Absorption correction	Semi-empirical from equivalents	
Refinement method	Full-matrix least-squares on F^2	
Data / restraints / parameters	11666 / 258 / 483	
Goodness-of-fit on F^2	1.140	
Final R indices [$I > 2\sigma_I$]	R_1 = 0.0338, wR_2 = 0.0720	
R indices (all data)	R_1 = 0.0484, wR_2 = 0.0764	
Largest diff. peak and hole	0.504 and –0.757 e/Å^3	

Table 4.7.8. Unit cell parameters for **$(CuBr)_2(B_2P_2)$**.

Identification code	hh20JT11_0m	
Empirical formula	$C_{42}H_{50}Cu_2Br_2B_2P_2$	
Formula weight	925.33 g/mol	
Temperature	100(2) K	
Wavelength	0.71073 Å	
Crystal system	Monoclinic	
Space group	P $2_1/n$	
Unit cell dimensions	a = 8.241(5) Å	α = 90°.
	b = 14.302(8) Å	β = 91.638(14)°.
	c = 19.129(11) Å	γ = 90°.
Volume	4375.2(5) $Å^3$	
Z	4	
Crystal size	0.495 x 0.119 x 0.089 mm^3	

Table 4.7.9 Unit cell parameters for **$Cu_2(\mu\text{-}I)_2(B_2P_2)$**.

Identification code	hh72JT37_0m	
Empirical formula	$C_{43}H_{52}Cu_2I_2B_2P_2$	
Formula weight	1033.36 g/mol	
Temperature	100(2) K	
Wavelength	0.71073 Å	
Crystal system	Orthorhombic	
Space group	P 2_1 2_1 2_1	
Unit cell dimensions	a = 11.408(2) Å	α = 90°.
	b = 17.958(3) Å	β = 90°.
	c = 21.356(4) Å	γ = 90°.
Volume	4375.2(5) $Å^3$	
Z	4	
Crystal size	0.386 x 0.127 x 0.035 mm^3	

4.8) Computational Procedures

4.8.1) General Considerations

All DFT calculations were performed using the Gaussian 09 software package.[33] Geometry optimizations were performed using the B3LYP (Becke, three-parameter, Lee-Yang-Parr) functional, the relativistic Stuttgart-Dresden (SDD) pseudopotential and basis set on Ag, and the 6-31g(d,p) basis set on all other atoms. To avoid an extensive conformational search, the calculations were performed on a slightly truncated model in which isopropyl groups ($–CH(CH_3)_2$) are replaced by methyl group (CH_3). The structures were optimized without any symmetry restraints. Frequency analyses were performed on all calculations to verify that the obtained stationary points are in fact energy minima. EPR parameters were evaluated on a single-point calculation using the SDD pseudopotential and basis sets on Ag and the IGLO III basis set[34] on all other atoms.

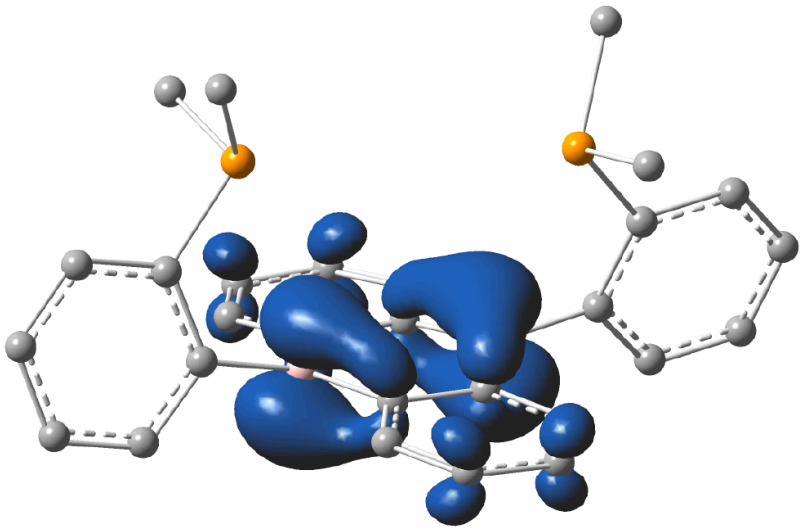

Figure 4.8.1. Spin density of a truncated model of **Ag(B_2P_2)** calculated at the B3LYP/IGLOIII;SDD(Ag) level on a geometry optimized at the B3LYP/6-31G(d,p);SDD(Ag) level, but with the Ag atom removed. Hydrogen atoms are omitted for clarity.

4.9) References

[1] Stradiotto, M.; Lundgren, R. J., Eds. *Ligand Design in Metal Chemistry: Reactivity and Catalysis*; John Wiley and Sons: Chichester, UK, Hoboken, NJ, 2016.

[2] Lyaskovskyy, V.; de Bruin, B. *ACS Catal.* **2012**, *2* (2), 270–279.

[3] (a) Praneeth, V. K. K.; Ringenberg, M. R.; Ward, T. R.. *Angew. Chem. Int. Ed.* **2012**, *51* (41), 10228. (b) Luca, O. R.; Crabtree, R. H. *Chem. Soc. Rev.* **2013**, *42* (4), 1440. (c) Chirik, P. J.; Wieghardt, K. *Science* **2010**, *327* (5967), 794. (d) Chirik, P. J *Acc. Chem. Res.* **2015**, *48* (6), 1687. (e) Stanciu, C.; Jones, M. E.; Fanwick, P. E.; Abu-Omar, M. M. *J. Am. Chem. Soc.* **2007**, *129* (41), 12400. (e) Blackmore, K. J.; Lal, N.; Ziller, J. W.; Heyduk, A. F. *J. Am. Chem. Soc.* **2008**, *130* (9), 2728. (f) Myers, T.; Berben, L. *J. Am. Chem. Soc.* **2013**, *135* (27), 9988.

[4] (a) Lorkovic, I. M.; Duff, R. R.; Wrighton, M. S. *J. Am. Chem. Soc.* **1995**, *117* (12), 3617–3618. (b) Ringenberg, M. R.; Kokatam, S. L.; Heiden, Z. M.; Rauchfuss, T. B. *J. Am. Chem. Soc.* **2008**, *130* (3), 788. (c) Wang, X.; Thevenon, A.; Brosmer, J. L.; Yu, I.; Khan, S. I.; Mehrkhodavandi, P.; Diaconescu, P. L. *J. Am. Chem. Soc.* **2014**, *136* (32), 11264–11267. (d) Wang, K., Stiefel, E. I.

Science **2001**, *291* (5501), 106. (e) Slone, C. S.; Mirkin, C. A.; Yap, G. P. A.; Guzei, I. A.; Rheingold, A. L. *J. Am. Chem. Soc.* **1997**, *119* (44), 10743.

[5] (a) Amgoune, A.; Bourissou, D. *Chem. Commun.* **2011**, *47* (3), 859. (b) Braunschweig, H.; Dewhurst, R. D. *Dalton Trans.* **2011**, *40* (3), 549.

[6] (a) Jones, J. S.; Wade, C. R.; Gabbaï, F. P. *Angew. Chem. Int. Ed.* **2014**, *53* (34), 8876. (b) Moret, M.-E.; Zhang, L.; Peters, J. C. *J. Am. Chem. Soc.* **2013**, *135* (10), 3792–3795. (c) Moret, M.-E.; Peters, J. C. *Angew. Chem. Int. Ed.* **2011**, *50* (9), 2063–2067. (d) Moret, M.-E.; Peters, J. C. *J. Am. Chem. Soc.* **2011**, *133* (45), 18118–18121. (e) Suess, D. L. M.; Peters, J. C. *J. Am. Chem. Soc.* **2013**, *135* (34), 12580–12583.

[7] (a) Hill, A. F. *Organometallics* **2006**, *25* (20), 4741–4743. (b) Parkin, G. *Organometallics* **2006**, *25* (20), 4744–4747.

[8] (a) Muller, P.; Huck, S.; Köppel, H.; Pritzkow, H.; Siebert, W. *Zeitschrift für Naturforschung B.* **1995**, *50* (10), 1476. (b) Agou, T.; Sekine, M.; Kawashima, T. *Tetrahedron Lett.* **2010**, *51* (38), 5013.

[9] (a) Lorbach, A.; Hübner, A.; Wagner, M. *Dalton Trans.* **2012**, *41* (20), 6048. (b) Hoffend, C.; Schödel, F.; Bolte, M.; Lerner, H.-W.; Wagner, M. *Chem. Eur. J.* **2012**, *18* (48), 15394. (c) Lorbach, A.; Bolte, M.; Li, H.; Lerner, H.-W.; Holthausen, M. C.; Jäkle, F.; Wagner, M. *Angew. Chem. Int. Ed.* **2009**, *48* (25), 4584.

[10] Hoffend, C.; Diefenbach, M.; Januszewski, E.; Bolte, M.; Lerner, H.-W.; Holthausen, M. C.; Wagner, M. *Dalton Trans.* **2013**, *42* (38), 13826.

[11] Müller, P.; Gangnus, B.; Pritzkow, H.; Schulz, H.; Stephan, M.; Siebert, W. *J. Organomet. Chem.* **1995**, *487* (1-2), 235.

[12] Schulz, H.; Pritzkow, H.; Siebert, W. *Chemische Berichte* **1991**, *124* (10), 2203.

[13] (a) Hill, A.; Owen, G.; White, A.; Williams, D. *Angew. Chem. Int. Ed.* **1999**, *38* (18), 2759–2761. (b) Bontemps, S.; Bouhadir, G.; Miqueu, K.; Bourissou, D. *J. Am. Chem. Soc.* **2006**, *128* (37), 12056–12057.

[14] (a) Lin, S.; Day, M. W.; Agapie, T. *J. Am. Chem. Soc.* **2011**, *133* (11), 3828. (b) Horak, K. T.; Velian, A.; Day, M. W.; Agapie, T. *Chem. Commun.* **2014**, *50* (34), 4427. (c) Buss, J. A.; Edouard, G. A.; Cheng, C.; Shi, J.; Agapie, T. *J. Am. Chem.*

Soc. **2014**, 136 (32), 11272-11275. (d) Buss, J. A.; Agapie, T. *Nature* **2016**, *529* (7584), 72–75.

[15] Taylor, J. W.; McSkimming, A.; Moret, M.-E.; Harman, W. H. *Angew. Chem. Int. Ed.* **2017**, *56* (35), 10413–10417.

[16] Sircoglou, M.; Bontemps, S.; Mercy, M.; Miqueu, K.; Ladeira, S.; Saffon, N.; Maron, L.; Bouhadir, G.; Bourissou, D. *Inorg. Chem.* **2010**, *49* (9), 3983.

[17] Son, J.-H.; Pudenz, M. A.; Hoefelmeyer, J. D. *Dalton Trans.* **2010**, *39* (45), 11081.

[18] Bontemps, S.; Bouhadir, G.; Dyer, P. W.; Miqueu, K.; Bourissou, D. *Inorg. Chem.* **2007**, *46* (13), 5149–5151.

[19] Reus, C.; Weidlich, S.; Bolte, M.; Lerner, H.-W.; Wagner, M. C-Functionalized, *J. Am. Chem. Soc.* **2013**, *135* (34), 12892.

[20] The spectroscopic data for **3** is similar to that of **2**, and its qualitative structure was confirmed by a preliminary X-ray diffraction study (see SI).

[21] Sircoglou, M.; Bontemps, S.; Bouhadir, G.; Saffon, N.; Miqueu, K.; Gu, W.; Mercy, M.; Chen, C.-H.; Foxman, B. M.; Maron, L.; Ozerov, O. V.; Bourissou, D. *J. Am. Chem. Soc.* **2008**, *130* (49), 16729–16738.

[22] Chiu, C.-W.; Kim, Y.; Gabbaï, F. P. *J. Am. Chem. Soc.* **2009**, *131* (1), 60–61.

[23] Jansen, M. *Chem. Soc. Rev.* **2008**, *37* (9), 1826–11.

[24] (a) McConnell, H. M. *J. Chem. Phys.* **1956**, *24* (4), 764–766. (b) Bolton, J. R.; Carrington, A.; McLachlan, A. D. *Molecular Physics* **1962**, *5* (1), 31–41. (c) Allen, B. T.; Bond, A. *J. Phys. Chem.* **1964**. (d) Valenzuela, J. A.; Bard, A. J. *J. Phys. Chem.* **1969**, *73* (4), 779–788.

[25] Yakelis, N. A.; Bergman, R. G. *Organometallics* **2005**, *24* (14), 3579–3581.

[26] Scott, T. A.; Ooro, B. A.; Collins, D. J.; Shatruk, M.; Yakovenko, A.; Dunbar, K. R.; Zhou, H.-C. *Chem. Commun.* **2009**, *47* (1), 65–67.

[27] Led, J. J.; Gesmar, H. *Chem. Rev.* **1991**, *91* (7), 1413–1426.

[28] Stoll, S.; Schweiger, A. *J. Magn. Reson.* **2006**, *178* (1), 42–55.

[29] APEX 2, version 2014.1-1, Bruker (2014), Bruker AXS Inc., Madison, Wisconsin, USA.

[30] SAINT, version V8.34A, Bruker (2012), Bruker AXS Inc., Madison, Wisconsin, USA.

[31] SADABS, version 2012/1, Bruker (2012), Bruker AXS Inc., Madison, Wisconsin, USA.

[32] SHELXTL, version 2013/4, Bruker (2013), Bruker AXS Inc., Madison, Wisconsin, USA.

[33] Gaussian 09, Revision D.01, M. J. Frisch, G. W. Trucks, H. B. Schlegel, G. E. Scuseria, M. A. Robb, J. R. Cheeseman, G. Scalmani, V. Barone, B. Mennucci, G. A. Petersson, H. Nakatsuji, M. Caricato, X. Li, H. P. Hratchian, A. F. Izmaylov, J. Bloino, G. Zheng, J. L. Sonnenberg, M. Hada, M. Ehara, K. Toyota, R. Fukuda, J. Hasegawa, M. Ishida, T. Nakajima, Y. Honda, O. Kitao, H. Nakai, T. Vreven, J. A. Montgomery, Jr., J. E. Peralta, F. Ogliaro, M. Bearpark, J. J. Heyd, E. Brothers, K. N. Kudin, V. N. Staroverov, T. Keith, R. Kobayashi, J. Normand, K. Raghavachari, A. Rendell, J. C. Burant, S. S. Iyengar, J. Tomasi, M. Cossi, N. Rega, J. M. Millam, M. Klene, J. E. Knox, J. B. Cross, V. Bakken, C. Adamo, J. Jaramillo, R. Gomperts, R. E. Stratmann, O. Yazyev, A. J. Austin, R. Cammi, C. Pomelli, J. W. Ochterski, R. L. Martin, K. Morokuma, V. G. Zakrzewski, G. A. Voth, P. Salvador, J. J. Dannenberg, S. Dapprich, A. D. Daniels, O. Farkas, J. B. Foresman, J. V. Ortiz, J. Cioslowski, and D. J. Fox, Gaussian, Inc., Wallingford CT, **2013**.

[34] W. Kutzelnigg, U. Fleischer, M. Schindler *The IGLO-Method: Ab Initio Calculation and Interpretation of NMR Chemical Shifts and Magnetic Susceptibilities, Vol. 23* Springer-Verlag, Heidelberg, **1990**

Chapter 5) Iron Complexes of a Redox-Active Diphosphine-Diboraanthracene Ligand

5.1) Introduction

The increasing interest in base metals for catalysis[1] has spurred the development of redox-active and non-innocent ligands that assist in providing additional electron equivalents to transition metals with the aim of performing multielectron bond-making and -breaking processes.[2] An important design principle for these systems is hemilability, the ability of the electron donor or acceptor moiety within the coordination sphere of a transition metal to allow for adaptable steric and electronic profiles throughout the course of a reaction mechanism.[3] Additionally, redox-active ligands possessing low-lying empty orbitals or high lying filled orbitals at energies comparable to d orbitals can mediate electron transfer events.[4] Tethered pi-systems within the coordination sphere of the metal have shown great promise in this regard,[5] with Agapie's *p*-terphenyl system exemplifying ligand hemilability.[6] Concurrently, borane-containing ligands have shown particular promise as they are easily incorporated into planar conjugated frameworks,[7] display redox activity[8] and stabilize low-valent transition metal ions.[9] Furthermore, the flexibility of metal-borane interactions during redox and reaction events has been instrumental for advances in N_2 reduction,[10] H_2 activation,[11] and CO reduction.[12]

We have been exploring the 9,10-dihydro-9,10-diboraanthracene (DBA) incorporating diphosphine ligand, B_2P_2, as a redox reservoir and hemilabile ligand for transition metals.[13] Additionally, reduced forms of DBA can function as a platform for small molecule activation including H_2 cleavage,[14] CO_2 disproportionation,[15] chalcogenide cleavage[16] and [4+2] cycloadditions of O_2, CO_2 and ethylene.[17] As the free ligand, B_2P_2 features two reversible redox couples at –2.18 and –2.71 V (vs. Fc/Fc^+, THF, 0.1 M $[nBu_4N][PF_6]$, 100 mV/s) while previously reported $M(B_2P_2)$ (M = Ni, Cu, Ag, Au) complexes possess unique redox chemistry different from that of the free ligand. In our studies on Ni, we noticed a cathodic shift of the $Ni(B_2P_2)$ reduction potentials compared to those of B_2P_2, while the coinage metals, isolated as formal +1 salts, featured the most positive 1st reduction potentials. The results were formulated to be the result of increased back-bonding between a d^{10} Ni center with B-based DBA orbitals whereas the coinage series has limited backbonding interactons with the C_4B_2 core. Eager to extend the coordination chemistry of B_2P_2 with late transition metals, iron was targeted as it readily forms complexes with chelating phosphine ligands and features rich redox chemistry. Herein we report the synthesis and characterization of the three-membered redox series of $Fe(B_2P_2)$ (+1, 0, –1). EPR and NMR spectroscopy are used to ascertain spin states with electron counting formalisms providing satisfying qualitative support of the experimental data. Additionally, reaction chemistry with CO is reported and its singly and doubly

reduced redox members are isolated with cyclic voltammetry providing insight into the redox potentials.

5.2) Results and Discussions

A reductive metalation procedure whereby B_2P_2 and $FeBr_2$ were initially complexed in THF followed by reduction with Rieke Mg in toluene afforded $Fe(B_2P_2)$ (**1**) in 63% yield as a rust orange solid. Isolation of the coordination product "$FeBr_2(B_2P_2)$" was unsuccessful and further *in situ* reduction was required. ^{1}H NMR spectroscopy of **1** provided a spectrum consistent with paramagnetism while Evan's method measurements in C_6D_6 afforded a value of

Scheme 5.1. Synthesis of **1**, $\mathbf{1}^+$ and $\mathbf{1}^-$.

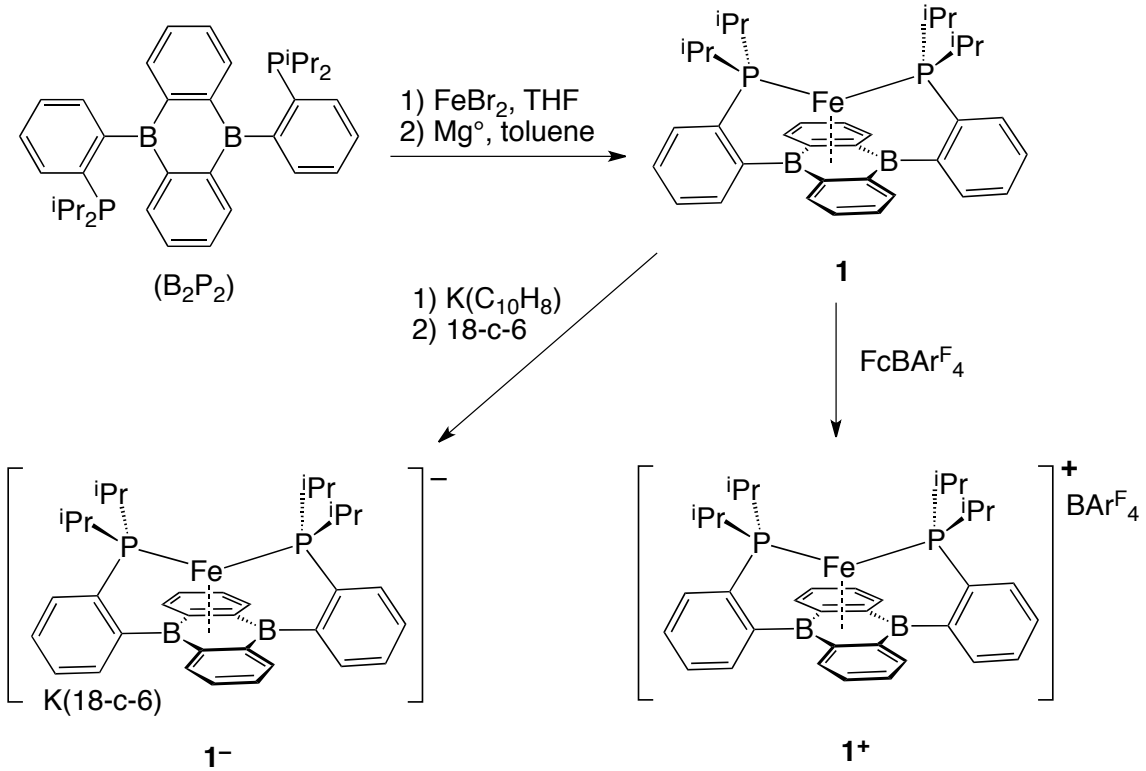

μ_{eff} = 2.8 ± 0.2. EPR spectra collected of **1** were silent, supporting the Evan's method predicted S = 1 spin state. Single-crystal XRD studies of **1** showed a Fe center bound η^6 to the DBA heterocycle with both P atoms completing its coordination sphere. The Fe-B distances were 2.224(1) and 2.218(2) Å while the Fe-C contacts were 2.300(1), 2.348(1) and 2.303(1) and 2.354(1) Å. To assess the extent of the redox-chemistry possessed by **1**, cyclic voltammetry was collected in THF (0.1 M [^{n}BuN$_4$][PF$_6$], 100 mV/s, vs. Fc/Fc$^+$) and revealed three redox processes. Reductive scans revealed a reversible redox couple at $E_{1/2}$ = –2.16 V with a second, irreversible event at the edge of the reductive window for THF at $E_{1/2}$ = –3.56 V. Oxidative scans revealed a quasi-reversible redox couple at $E_{1/2}$ = –0.46 V. Isolation of the redox members was investigated.

Oxidation of **1** was carried out by addition of 1 equivalent of [Fc][BAr$^F{}_4$] in THF. Following workup, **1$^+$** was isolated as a thermally sensitive yellow/green solid. Single-crystal XRD studies of **1$^+$** showed the expected complex salt with Fe bound in an n^6 fashion to the DBA core. The Fe-B distances were longer than in **1** ($d_{Fe\text{-}B}$ = 2.314(3), 2.350(3) Å) with Fe-C distances also lengthening ($d_{Fe\text{-}C}$Avg. = , 2.429 Å). ^{1}H NMR spectra collected of **1$^+$** were consistent with paramagnetism with Evan's method data (μ_{eff} = 3.8 ± 0.2) suggesting a high-spin, S = 3/2 electronic configuration. EPR spectra of **1$^+$** collected as a powder at 108 K showed an axial signal with g = 3.69 and 1.90 with no discernable hyperfine interactions. Notably, B_2P_2 lacks a corresponding oxidation feature in its CV and

taken together with EPR spectroscopy and Evan's method measurements, the formation of $\mathbf{1}^{+}$ was consistent with a Fe centered oxidation event.

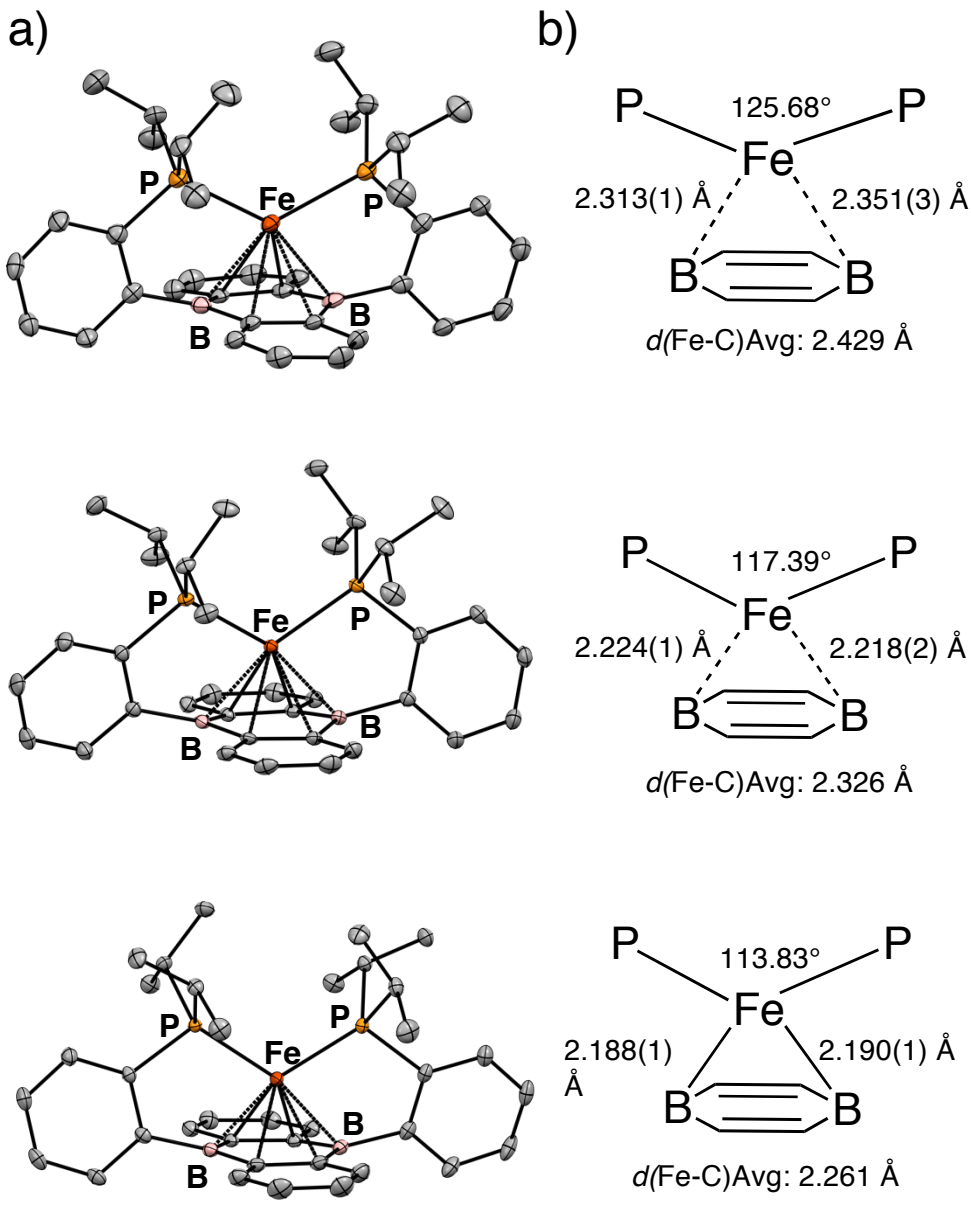

Figure 5.1. (a) Labelled thermal ellipsoid plots of $\mathbf{1}^{+}$ (top), **1** (middle) and $\mathbf{1}^{-}$ (bottom). Hydrogen atoms and, in the case of $\mathbf{1}^{+}$ and $\mathbf{1}^{-}$, counterions are omitted for clarity. (b) Line drawings of the P-Fe-DBA cores with relevant distances and angles inlayed.

Single electron reduction of **1** was carried out in toluene by addition of 2 equivalents of KC_8 to produce a deep red solution that, following encapsulation of the K^+ counterion by 18-crown-6 (18-c-6), gave $[Fe(B_2P_2)][K(18\text{-c-}6)]$ ($\mathbf{1}^-$). A

Scheme 5.2. Synthesis of **2**.

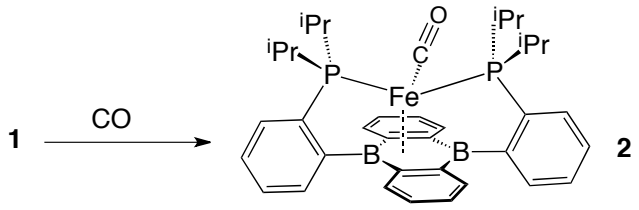

single-crystal of $\mathbf{1}^-$ suitable for XRD analysis was obtained and revealed the Fe center coordinated η^6 to the DBA core. The Fe-B and Fe-C distances in $\mathbf{1}^-$ are contracted compared to **1** ($d_{Fe\text{-}B}$ = 2.190(1), 2.188(1); $d_{Fe\text{-}C}$ = [2.285(1), 2.304(1); 2.219(1), 2.235(1)]) while the bonds within the B_2C_4 heterocycle are nearly identical to **1**. The DBA heterocycle also remains flat about the 9,10-DBA junction ($\Sigma_{CBC\angle}$ = 360.0°, 359.9°) with an unremarkable K(18-c-6) unit on the opposite face of the P-Fe-P unit. Solution spectroscopy is consistent with paramagnetism with Evan's method giving a value of μ_{eff} = 1.5 ± 0.2. EPR spectroscopy collected at 111 K in 2-MeTHF reveals an axial signal with g = 2.05, 1.99, 1.99. These data suggest an Fe centered reduction as bona fide ligand-based $M(B_2P_2)$ radicals have been characterized and feature drastically lengthened M-DBA bonds and ^{31}P hyperfine coupling in their EPR spectra. Furthermore, analysis of the CV of **1** places the potential to generate $\mathbf{1}^-$ at –2.16V vs. Fc/Fc+. This

potential is significantly (~600 mV) more negative than single electron reduction of other M(B_2P_2) complexes as well as the B_2P_2 ligand alone. Additionally, the significant amount of structurally characterized complexes with Fe in a formal –1 oxidation state provides further support for this formulation.[18] Computational inquiries are underway to complete the electronic picture for **1**$^-$.

The formulated 16 e$^-$ complex **1** was added CO to test the effect additional π-accepting ligands have on the Fe(B_2P_2) redox chemistry. Addition of 1 atm CO to a toluene solution of **1** resulted in the immediate darkening of solution to brown/black. Following workup, Fe(CO)(B_2P_2) (**2**) was isolated as a crystalline brown solid in 97% yield. Single-crystal XRD studies of **2** revealed a single CO ligand bound to the Fe center with additional coordination to the DBA heterocycle and P ligands. Despite multiple attempts at adjusting the crystal system **2** grows in, chronic whole molecule disorder was prevalent, and a detailed discussion of bond lengths and angles is omitted. Solution NMR spectroscopy of **2** gave spectra consistent with diamagnetism with a single, slightly broadened ^{31}P NMR signal at 64.94 ppm and an ^{11}B{^{1}H} NMR resonance at 28.82 ppm. The Fe-bound CO was detected in the ^{13}C NMR at 222.8 ppm as a triplet ($J_{P\text{-}C}$ = 33.9 Hz) while FT-IR spectra of **2** show a strong band at 1901 cm^{-1}. CVs of **2** (THF, 0.1 M [^{n}BuN$_4$][PF_6], 100 mV/s, vs. Fc/Fc$^+$) revealed two reversible redox processes at $E_{1/2}$ = –1.76, –2.32 V and a third, irreversible redox process at $E_{1/2}$ = 0.02 V. The broadening of the oxidation associated with the **2**$^{2-/1-}$ couple is

the result of geometry changes of the DBA fragment upon forming $\mathbf{2}^{2-}$, based on single-crystal XRD studies of the redox series $\mathbf{2}^{-}$ and $\mathbf{2}^{2-}$. The irreversibility of the process at $E_{1/2} = 0.02$ V is due to loss of a CO ligand upon oxidation. Notably the redox couples for **2** are significantly anodically shifted and are separated by ~600 mV while those for **1** are more negative and separated by ~1.4 V.

Synthetic access to [Fe(CO)(B_2P_2)][K(18-c-6)] ($\mathbf{2}^{-}$) was achieved by the addition of 1 equivalent of KNapth to a solution of **2** in toluene and was isolated

Scheme 5.3. Synthesis of $\mathbf{2}^{-}$ and $\mathbf{2}^{2-}$

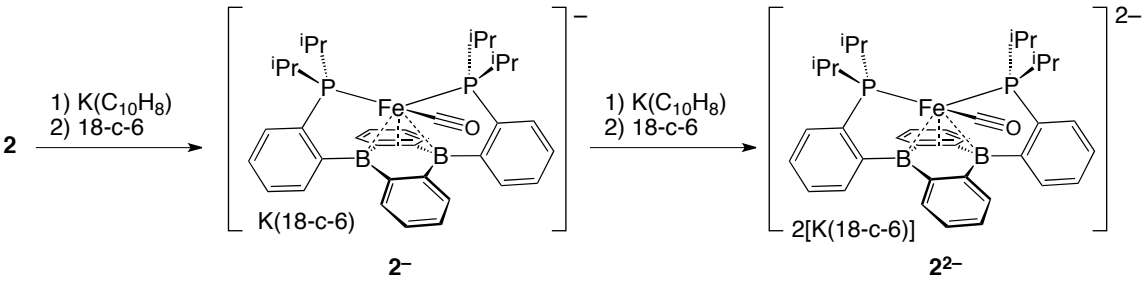

as a red/black crystalline solid. Single-crystal XRD studies of ($\mathbf{2}^{-}$) show a bent DBA fragment ($\Sigma_{CBC\angle} = 356.5°, 356.6°$) that is coordinated η^4 to the Fe center with Fe-C contacts of 2.126(1) and 2.125(1) Å and Fe-B contacts of 2.326(1) and 2.352(2) Å. The Fe-CO unit remains intact with Fe-CO and FeC-O distances of 1.761(1) and 1.170(2) Å, respectively. The K(18-c-6) unit remains associated with the DBA-phenylene unit on the opposite face of the P-Fe-P unit. Solution spectroscopy is consistent with paramagnetism, with Evan's method measurements of $\mu_{eff} = 1.5 \pm 0.2$ and X-band EPR measurements in 2-MeTHF at 104 K displaying a rhombic signal ($g = 2.01, 2.01, 1.99$). FT-IR spectra showed a mildly activated Fe-CO unit with a strong band at 1892 cm^{-1}.

Further reduction of $\mathbf{2}^{-}$ with excess KC_8 in THF afforded the deep green dianion [Fe(CO)(B_2P_2)][2(K(18-c-6))] ($\mathbf{2}^{2-}$). Solution NMR spectroscopy of $\mathbf{2}^{2-}$ in THF-d_8 confirmed its diamagnetism at room temperature, although its NMR resonances were broadened (see SI, Figures S9-11). ^{31}P NMR analysis showed a broad signal at 82.03 ppm and ^{11}B NMR showed a single resonance at 3.89 ppm, drastically up field from neutral **2**. Single-crystal XRD studies on $\mathbf{2}^{2-}$ showed

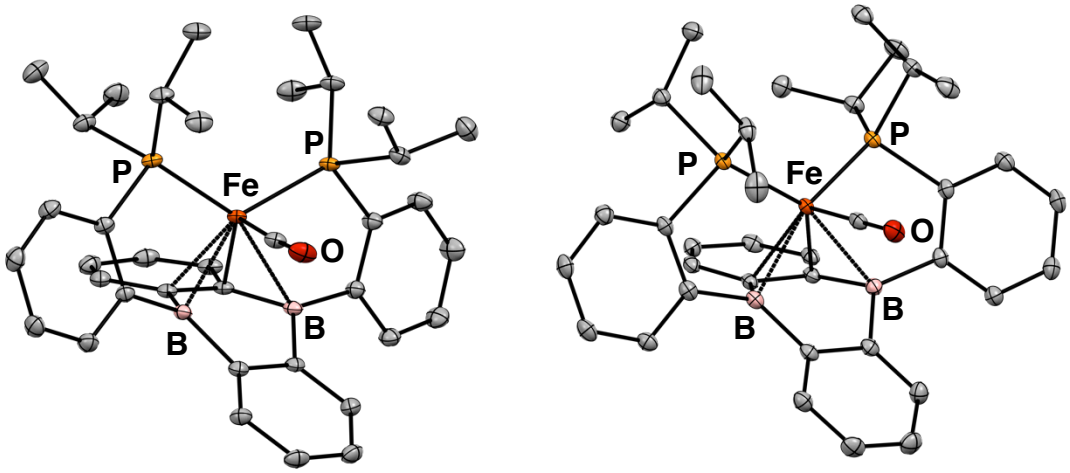

Figure 5.2. Labelled thermal ellipsoid plots of $\mathbf{2}^{-}$ and $\mathbf{2}^{2-}$. Hydrogen atoms and counterions are omitted for clarity.

qualitatively identical connections as $\mathbf{2}^{-}$ however notable bond distance changes were observed. At Fe, the Fe-B distances shortened to 2.261(1) and 2.272(2) Å while the Fe-C contacts lengthened to 2.130(1) and 2.141(1) Å. The Fe-bound CO unit had a lengthened C-O distance of 1.194(2) Å while the Fe-CO distance shortened to 1.707(1) Å, consistent with an increased back-bonding interaction on reduction. Additionally, the second K(18-c-6) was contacted to the CO unit with FT-IR spectroscopy showing a band at 1753 cm^{-1}, signaling a weakened C-

O bond however attempts at functionalizing the Fe-bound CO unit were unsuccessful.

5.3) Concluding Remarks

In summary, a redox series of Fe complexes with the B_2P_2 ligand were synthesized and characterized. CVs of the neutral Fe complex **1** showed three redox events with two, the oxidative event (**1**$^+$) and 1st reductive event (**1**$^-$), being isolable and characterized with the third being too sensitive for manipulation. Addition of CO to the 16 e$^-$ complex **1** afforded the diamagnetic CO-adduct **2**. CVs of **2** showed two reversible couples with latent oxidative events attributed to geometric changes at DBA upon reduction. Both **2**$^-$ and **2**$^{2-}$ feature η^4 coordination of Fe to the DBA heterocycle with increased C-O and decreased Fe-CO distances upon reduction. The flexibility of the DBA unit in B_2P_2 was displayed, transitioning between η^6 and η^4 binding to Fe during redox events. The tethering of diphosphine ligands to DBA enables oxidation of **1** to **1**$^+$, whereas multimetallic DBA complexes often suffer from irreversible chemical oxidation.[19] These results highlight the ability to stabilize multiple redox states within the hemilabile B_2P_2 ligand framework. Further small-molecule activation and catalysis with the Fe(B_2P_2) complexes is being explored.

5.4) Experimental Section

5.4.1) General Considerations

Unless otherwise noted, all manipulations were carried out using standard Schlenk or glovebox techniques under a dinitrogen atmosphere. Solvents were dried and deoxygenated by sparging with argon and passage through activated alumina in a solvent purification system from SG Waters USA, LLC. Hexamethyldisiloxane (HMDSO) was distilled from sodium metal and stored over 4 Å molecular sieves for 24 hours prior to use. Non-halogenated solvents were tested with a standard purple solution of sodium benzophenone ketyl in tetrahydrofuran in order to confirm effective oxygen and moisture removal. 9,10-Bis(2-(diisopropylphosphino)phenyl)-9,10-dihydroboranthrene (B_2P_2), ferrocenium tetrakis[3,5-bis(trifluoromethyl)phenyl]borate ([Fc][BAr^F_4]),[20] and potassium napthalenide ($K(C_{10}H_8)(THF)_{0.5}$)[21] were synthesized according to literature procedures. Elemental analyses were performed by Midwest Microlab, LLC, Indianapolis, IN. Deuterated solvents were purchased from Cambridge Isotope Laboratories Inc., degassed, and dried over activated 4 Å molecular sieves for at least 24 hr prior to use. NMR spectra were recorded on Bruker Avance 600 MHz and Bruker NEO 400 MHz spectrometers. ^{1}H chemical shifts are reported in ppm relative to tetramethylsilane using residual solvent as internal standards. ^{31}P and ^{11}B chemical shifts are reported in ppm relative to 85% aqueous H_3PO_4 and $BF_3{\cdot}Et_2O$, respectively. ^{11}B NMR spectra were manipulated

with MestReNova 10.0.2. and had a backwards LP applied to eliminate background signal from the borosilicate NMR tube.[22] EPR X-band spectra were obtained on a Bruker EMX spectrometer controlled by Bruker Win-EPR software suite version 3.0. Simulations were performed using the Easyspin software suite.[23] X-ray diffraction studies were performed using a Bruker-AXS diffractometer. IR spectra were recorded using a Bruker Alpha FT-IR with a universal sampling module collecting at 4 cm–1 resolution with 32 scans. Cyclic Voltammetry (CV) experiments were performed using a Pine AFP1 potentiostat. The cell consisted of a glassy carbon working electrode, a Pt wire auxiliary electrode and a Pt wire pseudo-reference electrode. All potentials are referenced vs. the Fc/Fc^+ couple measured as an internal standard.

5.4.2) Fe(B_2P_2) (1).

B_2P_2 (0.556 g, 0.993 mmol) was dissolved in THF (10 mL), added $FeBr_2(THF)_2$ (0.357 g, 1 mol. Eq.) and heated to 50 °C for 10 hours. Following heating, volatiles were removed *in vacuo* and the red foam was suspended in Et_2O (5 mL) prior to having volatiles removed *in vacuo*. The residue was suspended in toluene (8 mL) prior to adding Rieke Mg (0.030 g, 1.16 mmol) and stirring for 5 hours. The dark orange/red mixture was filtered through celite and had its volatiles removed *in vacuo*. The residue was dissolved in THF (2 mL) and passed through a 1” silica plug with THF:pentane (1:4) as eluent. The resulting red/orange filtrate had its volatiles removed *in vacuo* to yield **1** as a red/orange

powder. Yield 0.383 g, 63%. A single-crystal suitable for XRD was obtained by slow evaporation of a saturated pentane solution. ^{1}H NMR (400 MHz, C_6D_6) δ 21.79, 11.10, 3.31, 2.42, -0.02, -1.46, -1.80, -2.22, -13.74. Evans Method (C_6D_6): μ_B 2.8 ± 0.2. UV-Vis (THF): λ_{max} nm (ε_{max} M^{-1} cm^{-1}) 375 (3.5 × 10^3), 480 (7.0 x 10^2), 795 (3.3 x 10^2), 930 (5.6 x 10^2). MALDI MS*: m/z* 617.2805; Calcd. for 617.2532.

5.4.3) [Fe(B_2P_2)][BAr^F_4] (1^+).

A solution of **1** (0.011 g, 0.017 mmol) in THF (2 mL) was added [Fc][BAr^F_4] (0.019 g, 1 mol. eq.) at –15 °C and stirred for 30 minutes at that temperature. Volatiles were removed *in vacuo* before washing the yellow/green residue with cold toluene (2 x 3 mL, –15 °C chilled). The residue was dissolved in minimal THF (ca. 0.2 mL) and layered with a solution of toluene:pentane (1:1) before being let stand overnight at –15 °C. The next day, yellow/green crystals formed that had the mother liquor decanted prior to washing with hexanes (2 x 1 mL) and drying *in vacuo*. Yield 0.019 g, 75%. **1^+** is thermally sensitive and should be stored in the fridge. ^{1}H NMR (500 MHz, THF-d_8) δ 36.75, 31.85, 30.71, 21.72, 10.55, 7.85, 7.63, –2.11, –9.00, –10.05, –14.71. Evans Method (THF-d_8): μ_B 3.8 ± 0.2. UV-Vis (THF): λ_{max} nm (ε_{max} M^{-1} cm^{-1}) 365 (4.1 × 103), 445 (2.04 x 103), 510 (3.2 x 102), 650 (2.2 x 102), 835 (5.0 x 102). Due to its sensitivity, and despite multiple attempts, accurate elemental analysis was not obtained for **1^+**.

5.4.4) [Fe(B_2P_2)][K(18-c-6)] (1^-).

To a solution of **1** (0.087 g, 0.141 mmol) in toluene (5 mL) was added KC_8 (0.023 g, 1.2 mol. Eq.) as a single portion. The reaction was stirred 1 hour before being filtered through celite and having its volatiles removed *in vacuo*. The residue was rinsed with pentane (3 x 2 mL) prior to dissolving in THF (1 mL), adding 18-crown-6 (0.023 g, 0.141 mmol), layering with pentane (4 mL), and placing at –15 °C for 10 hours. Black/red crystals formed that were filtered, rinsed with pentane (3 x 1 mL) and dried *in vacuo*. Yield ^{1}H NMR (400 MHz, C_6D_6) δ 17.74, 17.50, 12.55, 10.26, 8.00, 6.01, 1.96. Evans Method (C_6D_6): μ_B 1.5 ± 0.2. UV-Vis (THF): λ_{max} nm (ε_{max} M^{-1} cm^{-1}) 350 (sh, 1.8 × 10^3), 455 (9.6 x 10^2), 535 (sh, 6.0 x 10^2), 645 (2.3 x 10^2). Anal. Calcd for $C_{48}H_{68}AuB_2FeKO_6P_2$: C, 62.69 H, 7.45. Found: C, 62.42 H, 7.59.

5.4.5) Fe(CO)(B_2P_2) (2).

A solution of **1** (0.200 g, 0.324 mmol) in toluene was subjected to three freeze-pump-thaw cycles prior to adding 1 atm CO. The reaction was stirred 30 minutes during which time it changed brown/black from red/orange. Volatiles were removed *in vacuo* to afford **2** as a brown/black solid. Yield: 0.201 g, 97%. Single-crystals suitable for XRD analysis were grown by slow evaporation of a benzene solution. ^{1}H NMR (400 MHz, C_6D_6) δ 8.07 (d, J = 7.2 Hz, 2H), 7.76 (dd, J = 6.4, 3.2 Hz, 2H), 7.50 (d, J = 6.7 Hz, 2H), 7.48 – 7.41 (m, 2H), 7.37 – 7.31 (m, 2H), 7.31 – 7.29 (m, 2H), 7.12 (dd, J = 6.5, 3.1 Hz, 2H), 6.95 (dd, J = 6.1, 3.2 Hz, 2H),

2.67 – 2.45 (m, 2H), 1.88 (dq, J = 13.4, 6.6 Hz, 2H), 0.93 (dt, J = 13.8, 7.2 Hz, 12H), 0.82 (d, J = 7.1 Hz, 3H), 0.79 (d, J = 7.1 Hz, 3H), 0.46 (d, J = 7.1 Hz, 3H), 0.42 (d, J = 7.1 Hz, 3H). ^{31}P NMR (162 MHz, C_6D_6) δ 64.94 (s). ^{11}B NMR (128 MHz, C_6D_6) δ 28.82. ^{13}C NMR (101 MHz, C_6D_6) δ 222.8 (t, J = 33.9 Hz), 157.9 (br), 149.1 (d, J = 3.5 Hz), 148.7 (d, J = 3.5 Hz), 138.12, 135.6, 132.5, 132.3, 130.2, 129.9 125.8, 125.8, 105.6, 31.8, 29.0, 28.8, 20.7, 19.6 (d, J = 3.1 Hz), 19.5 (d, J = 1.5 Hz), 18.93. FT-IR: ν_{max} cm^{-1} 1901 (C=O). UV-Vis (THF): λ_{max} nm (ε_{max} M^{-1} cm^{-1}) 435 (8.1 × 10^2), 570 (3.7 x 10^2), 930 (1.5 x 10^1).

5.4.6) [Fe(CO)(B_2P_2)][K(18-c-6)] (2^-).

A solution of **2** (0.030 g, 0.047 mmol) in toluene (5 mL) was added KNapth (0.0104 g, 0.051 mm0l) as a solid and stirred 1 hour. A toluene solution (2 mL) of 18-crown-6 (0.008 g, 0.051 mmol) was added prior to removing volatiles *in vacuo*. The brown/black residue was washed with hexanes (5 x 2 mL), dissolved in THF (2 mL), layered with pentane (5 mL) and placed at –15 °C for 10 hours. Black/brown crystals grew over 2 days that were collected by filtration, washed with pentane (2 x 1 mL) and Et_2O (2 x 1 mL) and dried *in vacuo*. Yield: 0.040 g, 85%. Single-crystals suitable for XRD analysis were grown by layering a saturated toluene solution with pentane. ^{1}H NMR (400 MHz, C_6D_6) δ 2.98. Evans Method (C_6D_6): μ_B 1.3 ± 0.2. FT-IR: ν_{max} cm^{-1} 1892 (C=O), 1832 (C=O). UV-Vis (THF): λ_{max} nm (ε_{max} M^{-1} cm^{-1}) 445 (1.8 × 10^3), 630 (4.1 x 10^2), 730 (4.4 x 10^2), 955 (2.1 x 10^2).

5.4.7) $Fe(CO)(B_2P_2)][2{\cdot}K(18\text{-}c\text{-}6)]$ (2^{2-}).

A solution of $\mathbf{2}^-$ (0.026 g, 0.026 mmol) in THF (2 mL) was added KNapth (0.005 g, 1 mol. Eq.) and stirred 30 minutes during which time a black/green solution formed. A THF solution (2 mL) of 18-crown-6 (0.005 g, 0.029 mmol) was added prior to removing volatiles *in vacuo*. The black/green residue was added Et_2O (4 mL) prior to removing volatiles *in vacuo*. The black/green residue was washed with pentane (3 x 1 mL) and Et_2O (2 x 1 mL) before being dissolved in MeCN (0.5 mL) and layered with a solution of Et_2O:pentane (3 mL, 1:1) before being placed at –15 °C for 10 hours. Black/green crystals grew over 1 day that were decanted from the mother liquor prior to washing with Et_2O (1 x 1 mL) and drying *in vacuo*. Yield 0.030 g, 91%. Single-crystals suitable for XRD analysis were grown by slow evaporation of a benzene solution. ^{1}H NMR (600 MHz, THF-d_8) δ 7.87 (br, 2H), 7.37 (br, 4H), 6.97 (br, 2H), 6.77 (br, 4 H), 6.67 (br, 4H), 6.19 (br, 4H), 3.40 (48H), 2.17 (br, 4H), 1.03 (br, 12H), 0.95 (br, 6H), 0.58 (br, 6H). ^{31}P NMR (243 MHz, THF-d_8) δ 82.03 (s). ^{11}B NMR (193 MHz, THF-d_8) δ 3.89 (br). UV-Vis (THF): λ_{max} nm (ε_{max} M^{-1} cm^{-1}) 440 (3.6×10^3), 605 (3.9×10^3). FT-IR: ν_{max} cm^{-1} 1753 (C=O). Anal. Calcd for $C_{61}H_{92}B_2FeK_2O_{13}P_2$: C, 58.57 H, 7.41. Found: C, 58.26 H, 7.13.

5.5) Spectroscopic Data

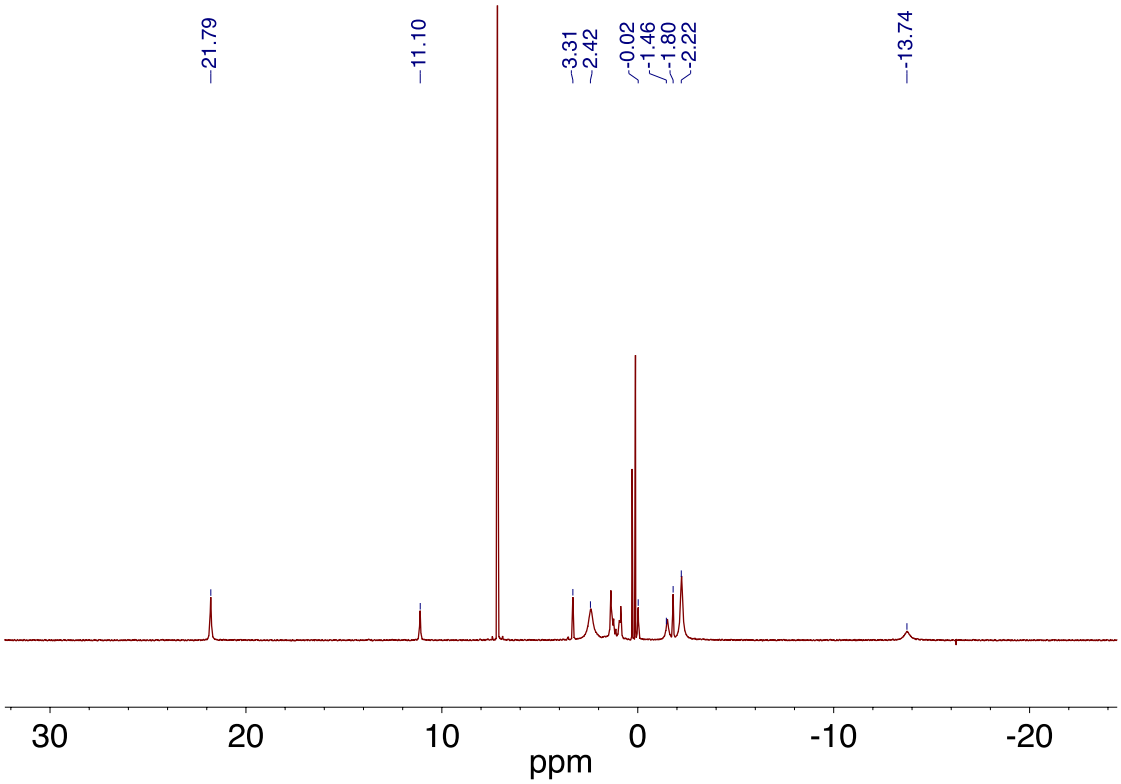

Figure 5.5.1. ^{1}H NMR spectrum of **Fe(B_2P_2)** recorded at 400 MHz in C_6D_6.

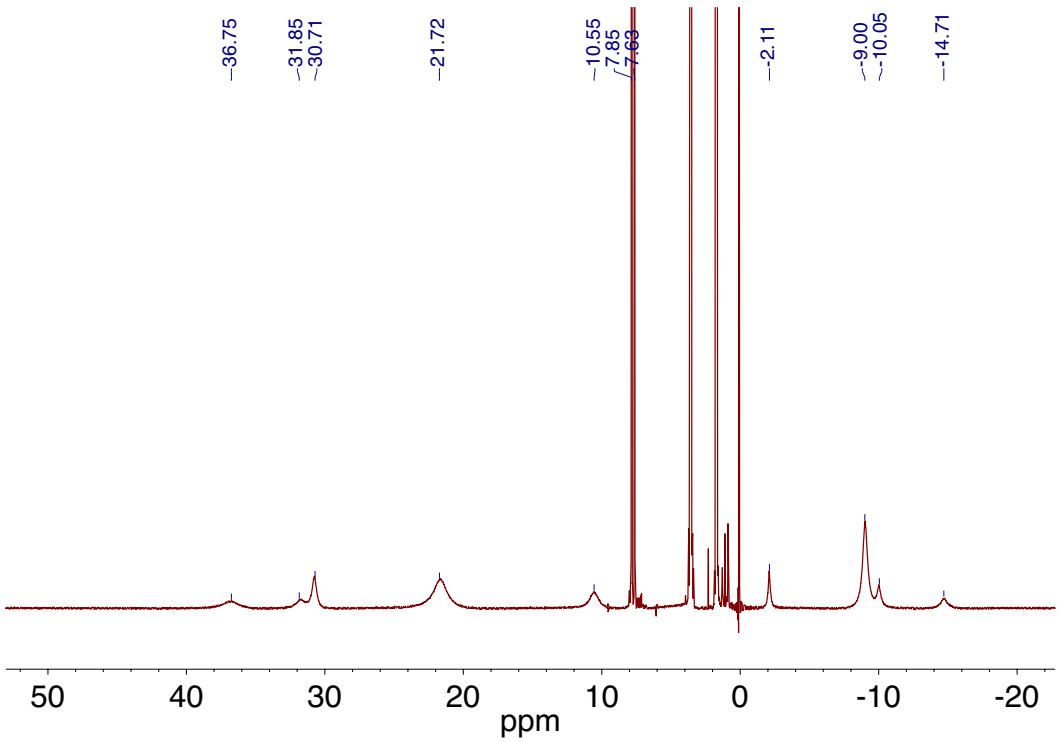

Figure 5.5.2. ^{1}H NMR spectrum of **[Fe(B$_2$P$_2$)][BAr$^{F}_{4}$]** recorded at 400 MHz in THF-d_8.

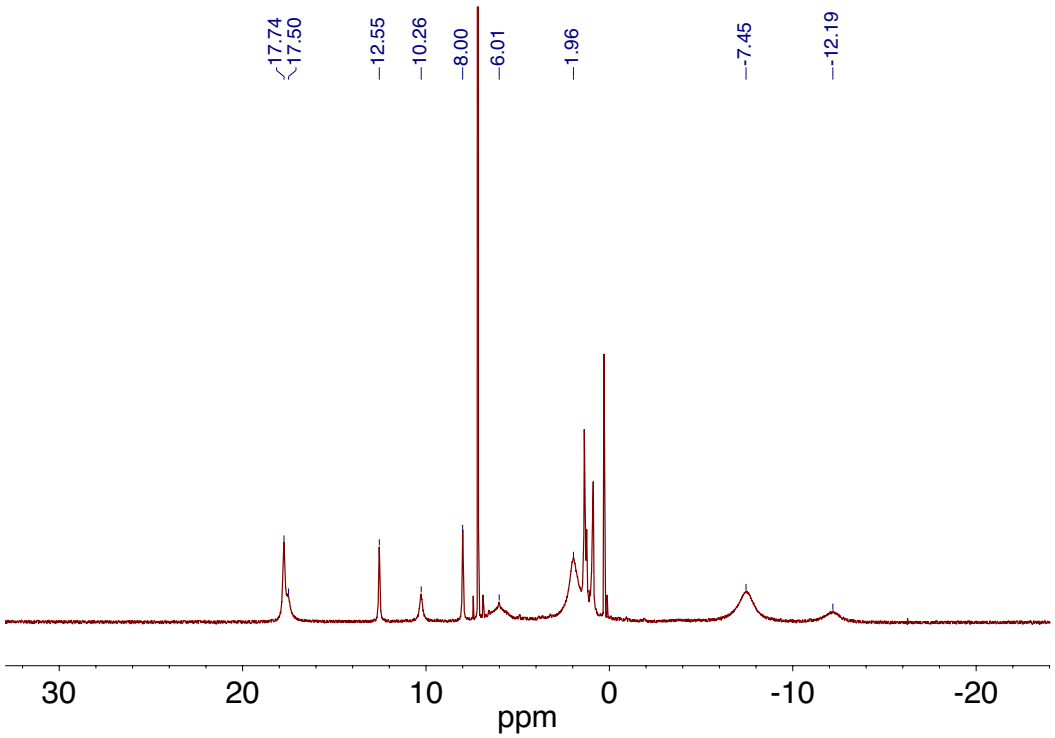

Figure 5.5.3. ^{1}H NMR spectrum of **[Fe(B$_2$P$_2$)][K(18-c-6)]** recorded at 400 MHz in C_6D_6.

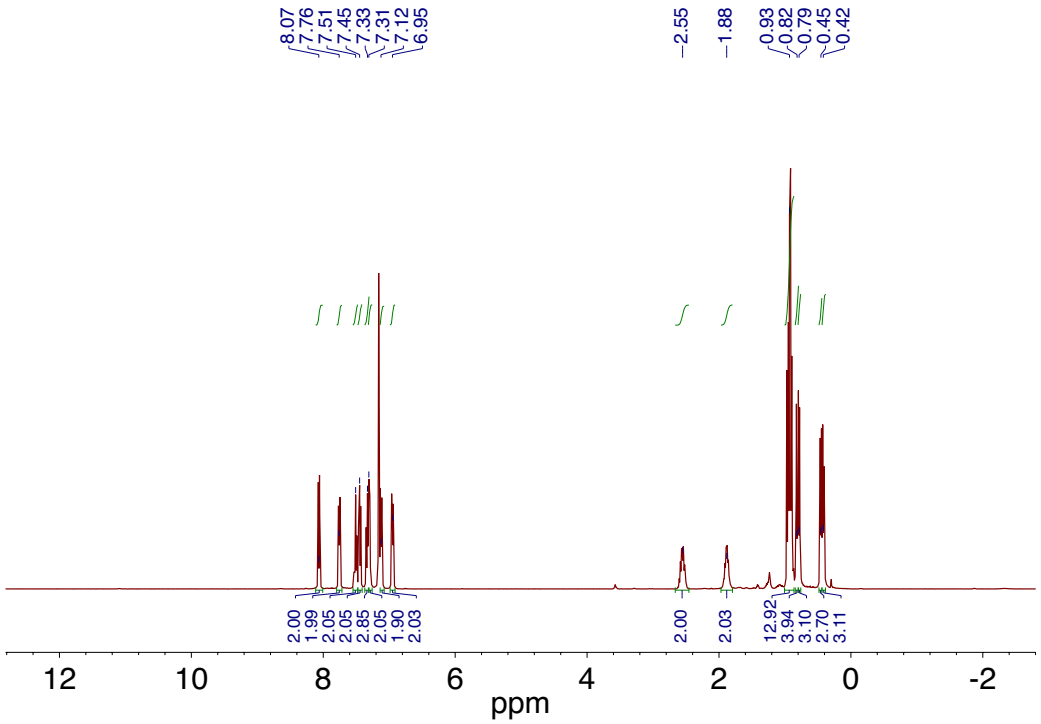

Figure 5.5.4. ^{1}H NMR spectrum of **Fe(CO)(B_2P_2)** recorded at 400 MHz in C_6D_6.

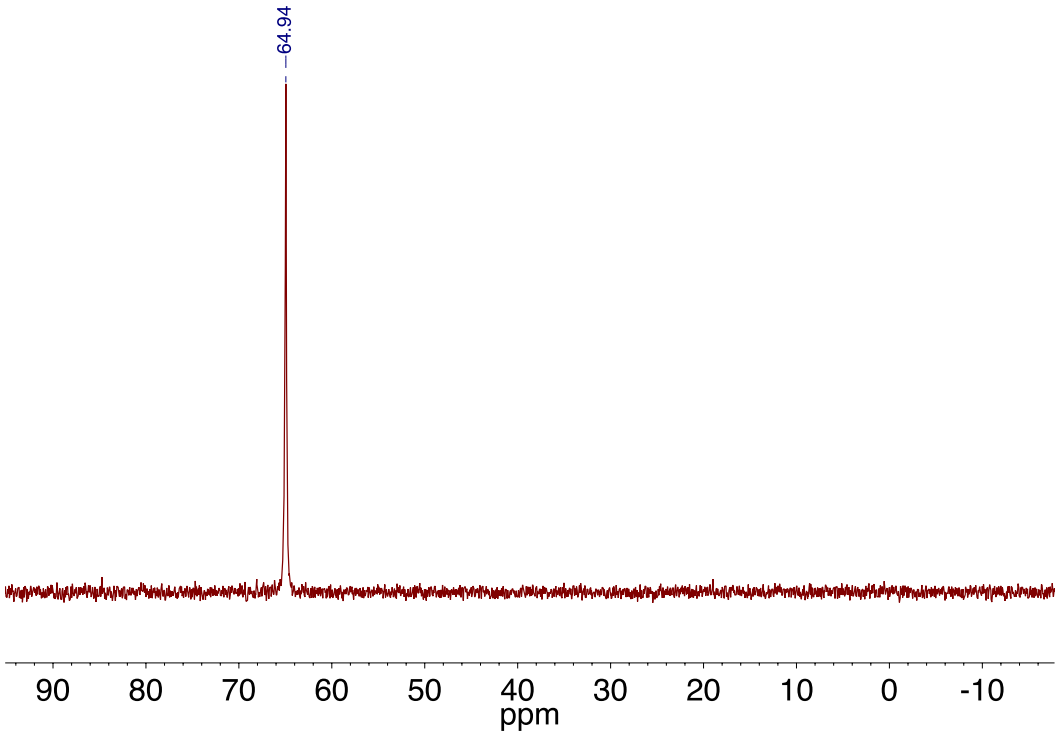

Figure 5.5.5. ^{31}P NMR spectrum of **Fe(CO)(B_2P_2)** recorded at 162 MHz in C_6D_6.

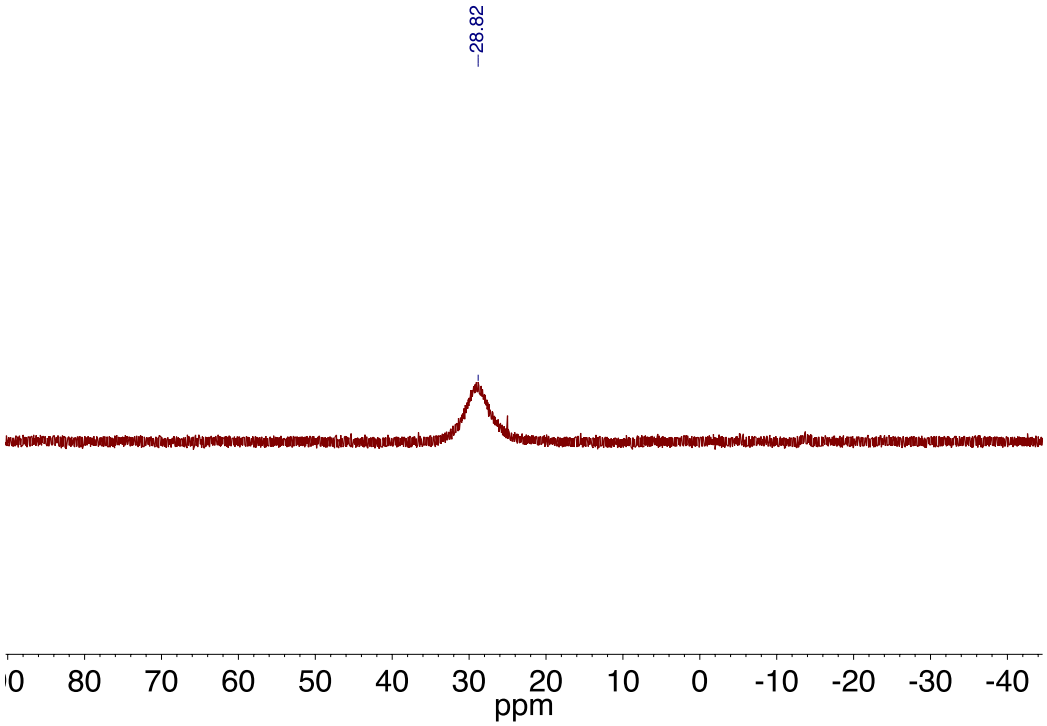

Figure 5.5.6. $^{11}B\{^{1}H\}$ NMR spectrum of **Fe(CO)(B_2P_2)** recorded at 128 MHz in C_6D_6.

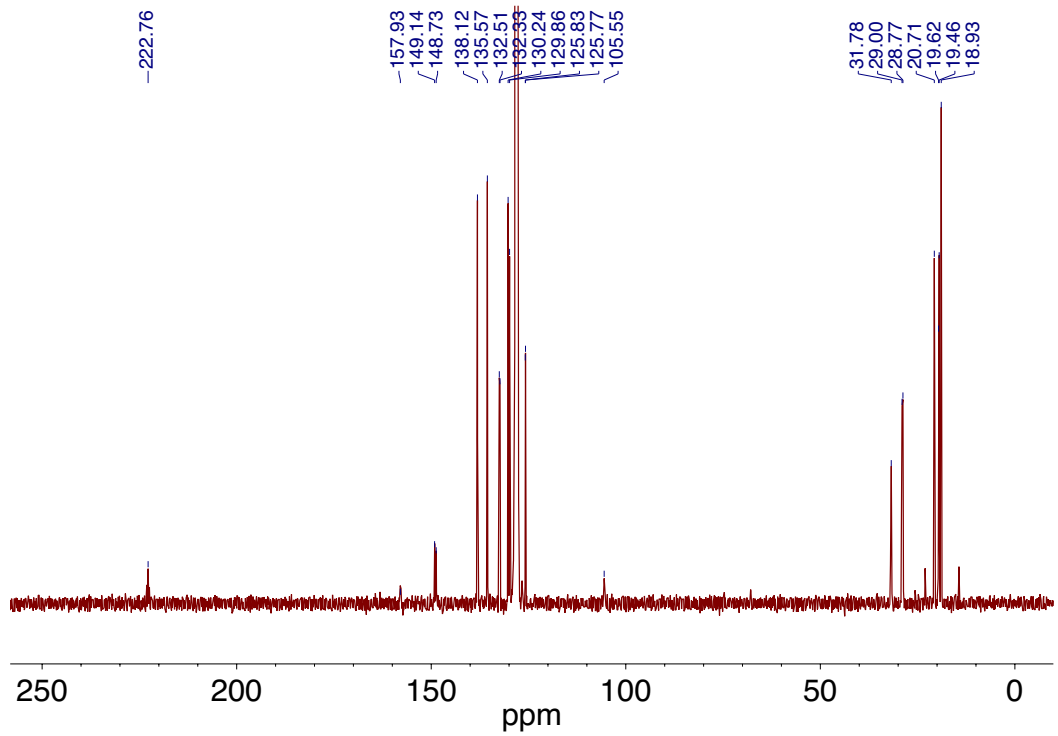

Figure 5.5.7. ^{13}C NMR spectrum of **Fe(CO)(B_2P_2)** recorded at 101 MHz in C_6D_6.

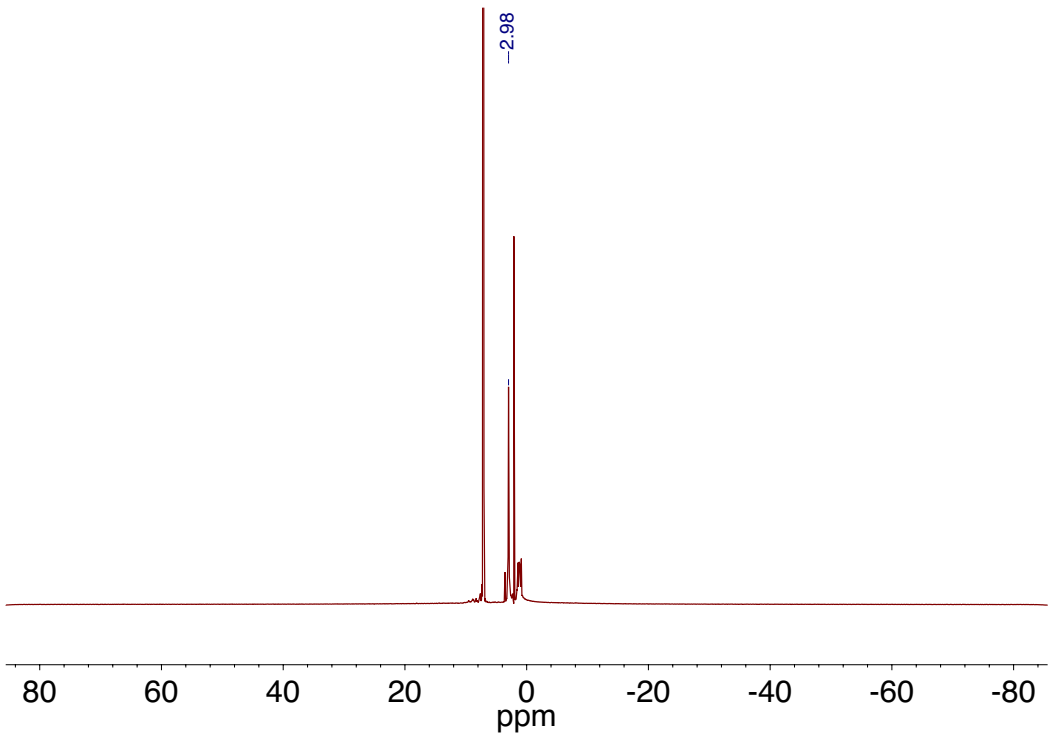

Figure 5.5.8. ^{1}H NMR spectrum of **[Fe(CO)(B_2P_2)][K(18-c-6)]** recorded at 400 MHz in C_6D_6.

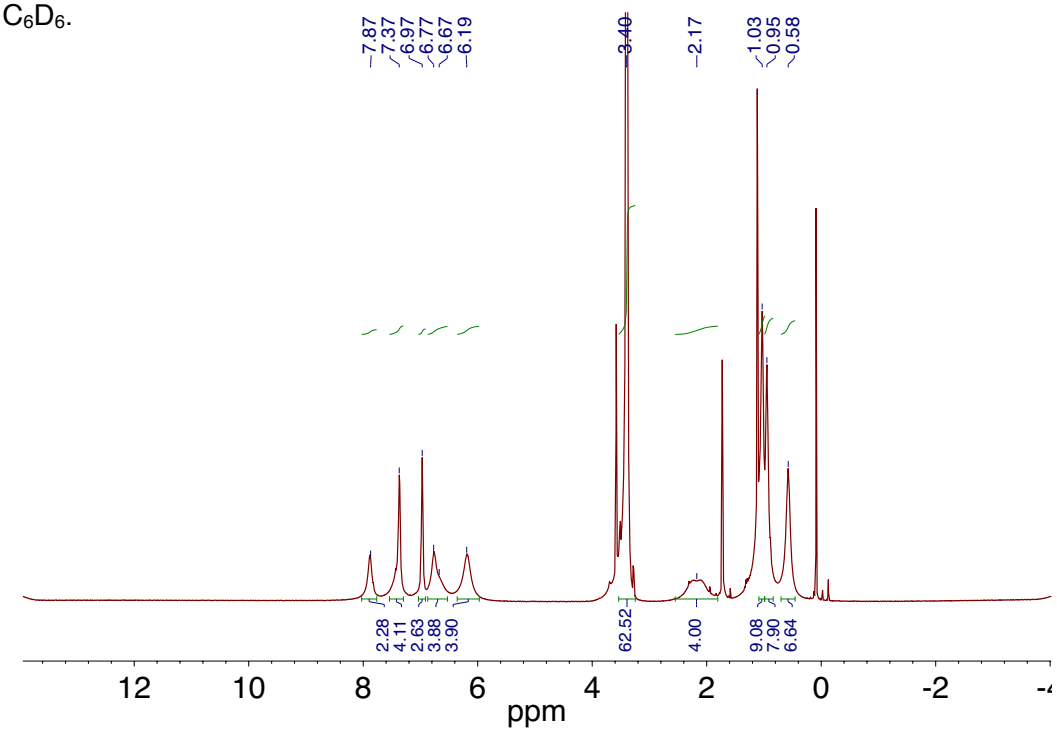

Figure 5.5.9. ^{1}H NMR spectrum of **[Fe(CO)(B_2P_2)][2•K(18-c-6)]** recorded at 600 MHz in THF-d_8.

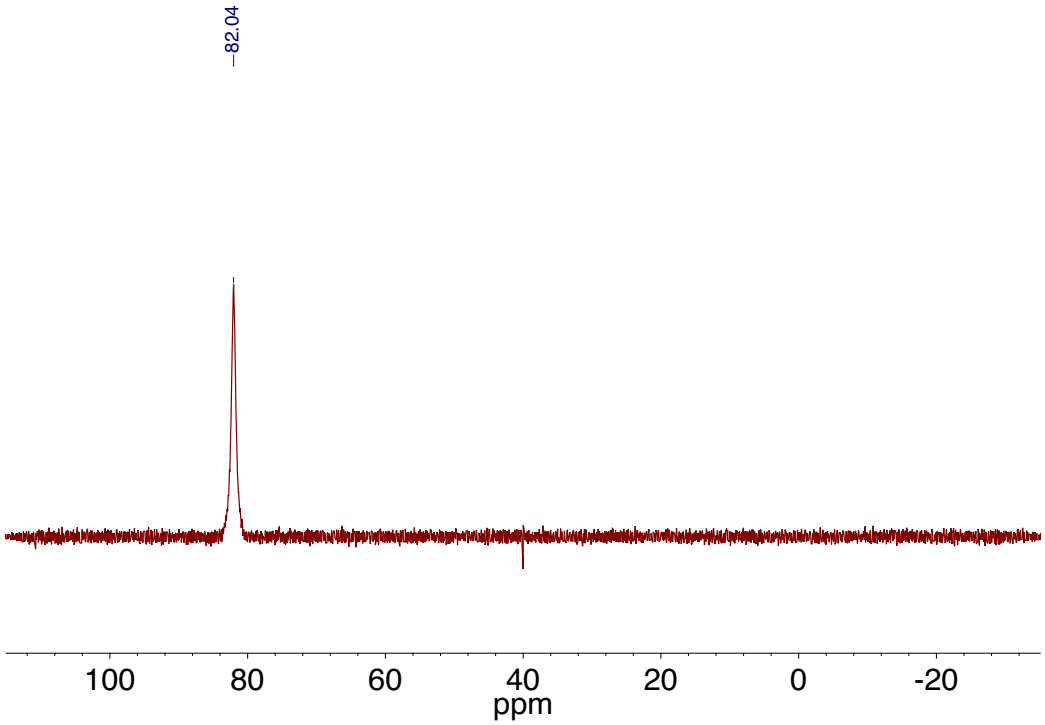

Figure 5.5.10. ^{31}P NMR spectrum of **[Fe(CO)(B_2P_2)][2•K(18-c-6)]** recorded at 243 MHz in THF-d_8.

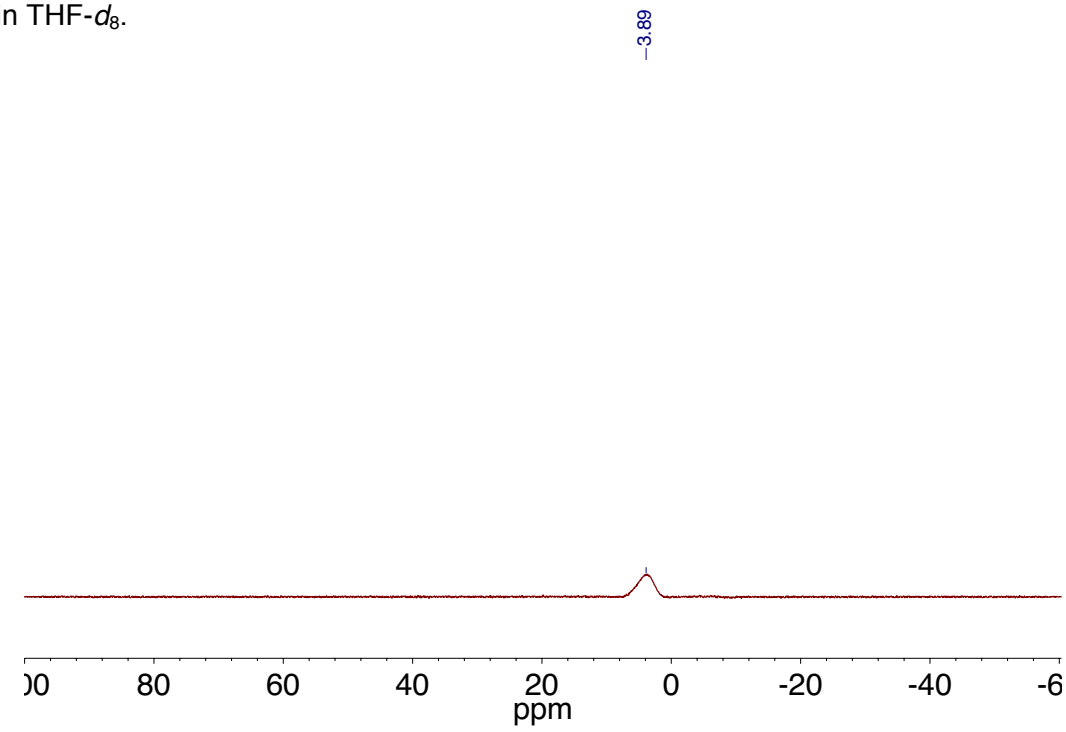

Figure 5.5.11. ^{1}H NMR spectrum of **[Fe(CO)(B_2P_2)][2•K(18-c-6)]** recorded at 193 MHz in THF-d_8.

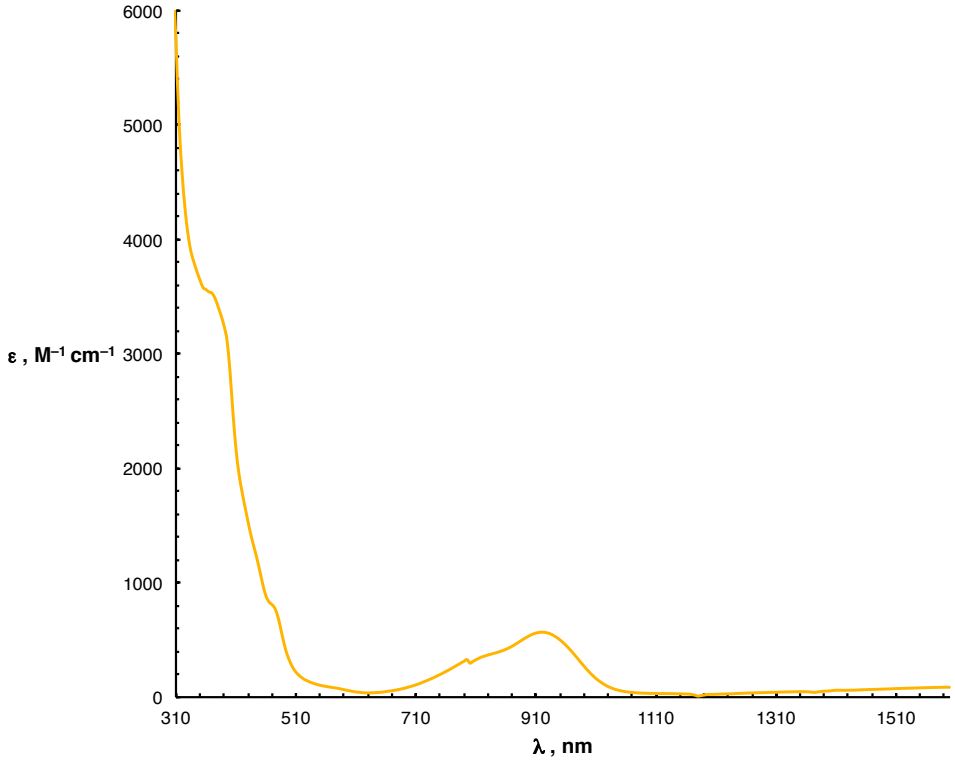

Figure 5.5.12. UV-Vis spectrum of 6.49 x 10^{-4} M **Fe(B_2P_2)** in THF.

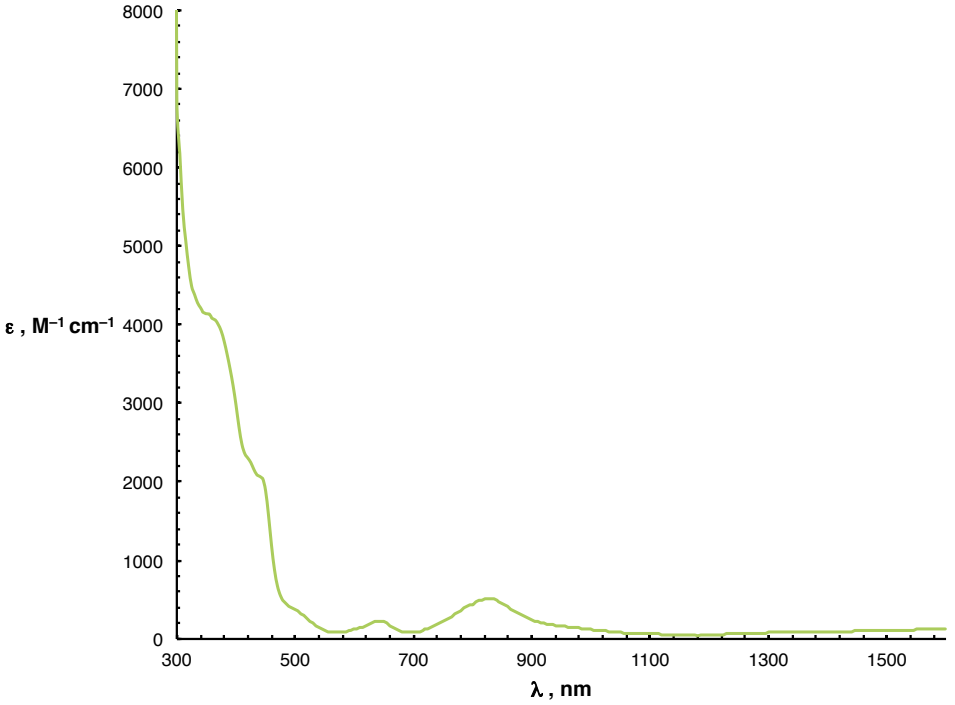

Figure 5.5.13. UV-Vis spectrum of 5.75 x 10^{-4} M **[Fe(B_2P_2)][BAr^F_4]** in THF.

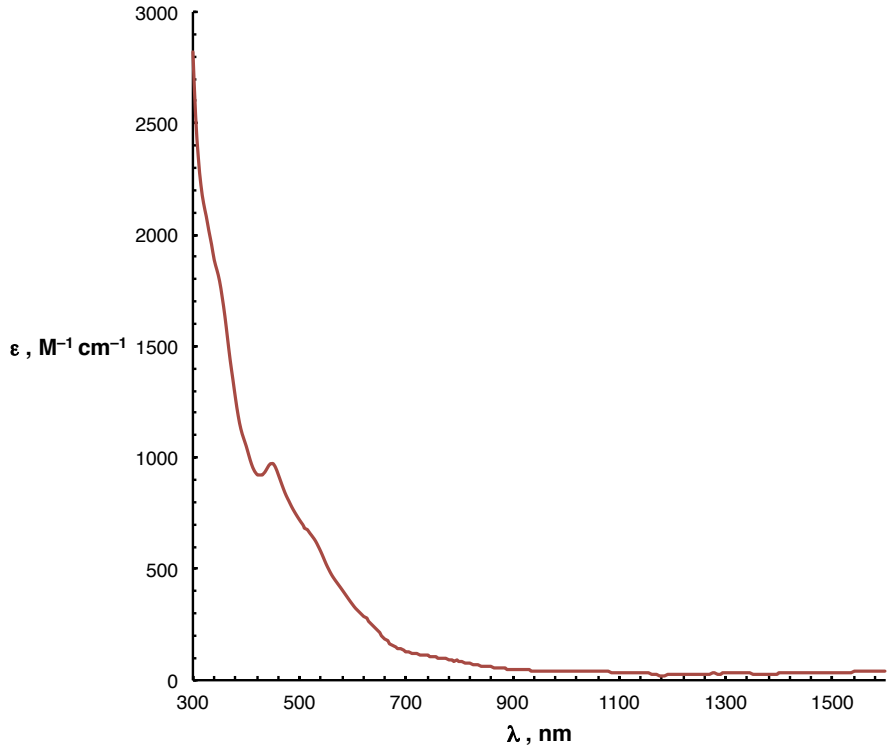

Figure 5.5.14. UV-Vis spectrum of 9.24 x 10^{-4} M **[Fe(B_2P_2)][K(18-c-6)]** in THF.

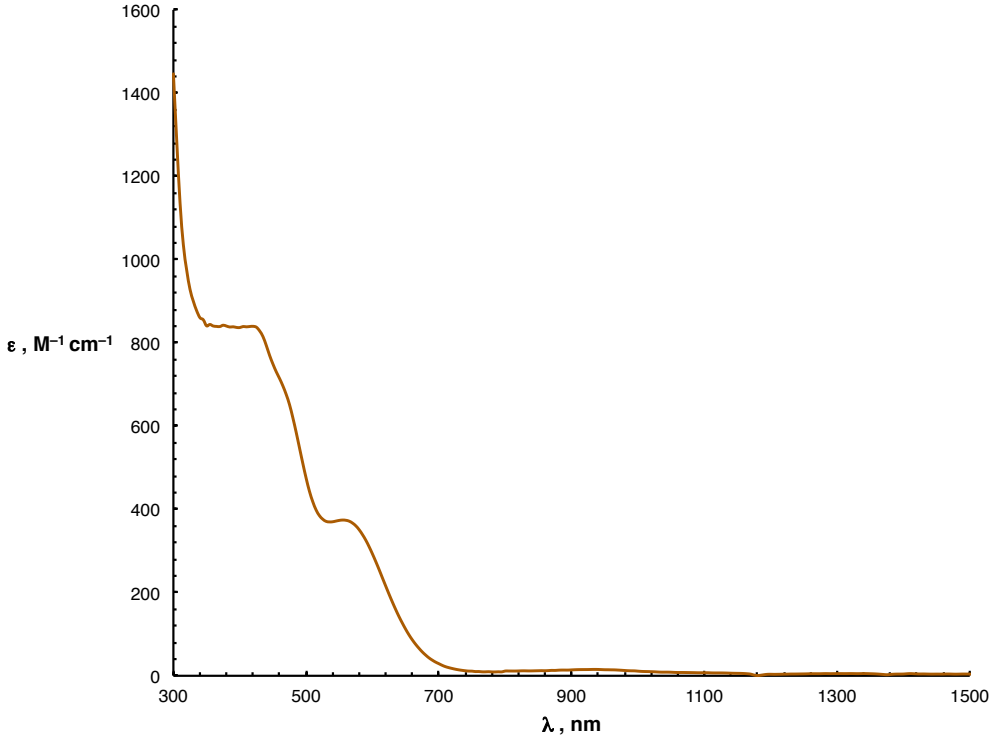

Figure 5.5.15. UV-Vis spectrum of 2.79 x 10^{-3} M **Fe(CO)(B_2P_2)** in THF.

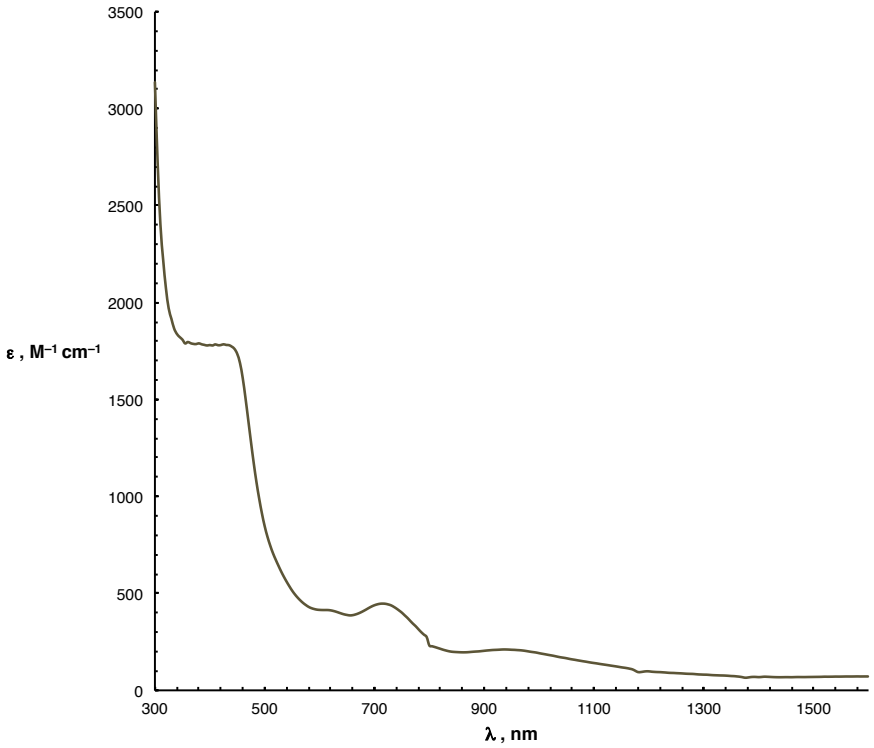

Figure 5.5.16. UV-Vis spectrum of 1.31 x 10^{-3} M **[Fe(CO)(B_2P_2)][K(18-c-6)]** in THF.

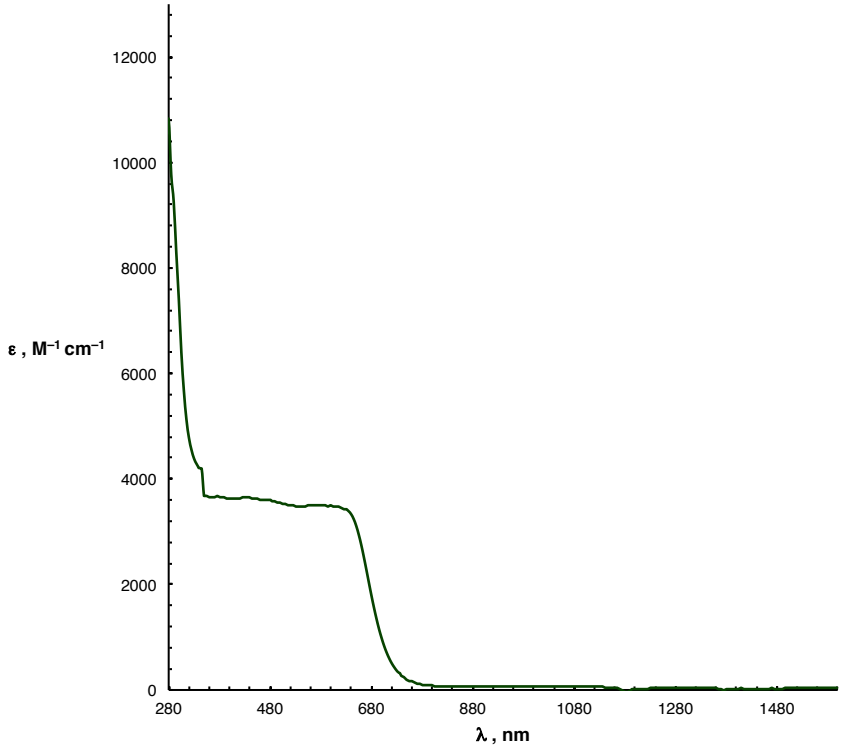

Figure 5.5.17. UV-Vis spectrum of 4.85 x 10^{-4} M **[Fe(CO)(B_2P_2)][2·K(18-c-6)]** in THF.

5.6) Cyclic Voltammetry

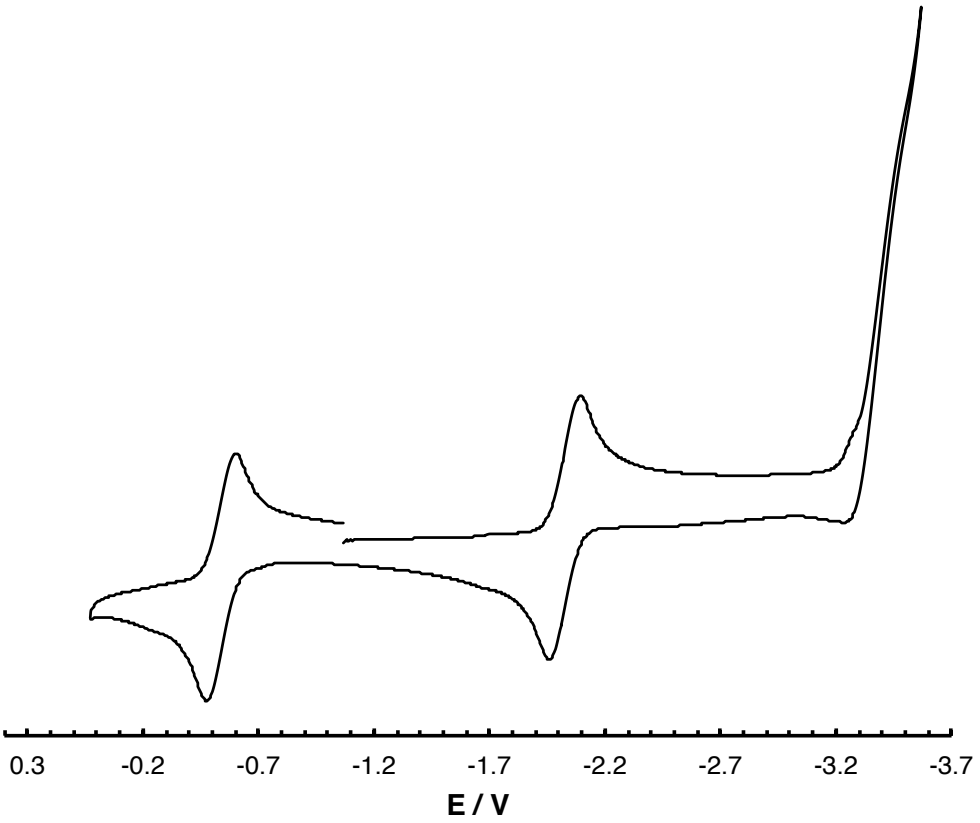

Figure 5.6.1. Cyclic voltammogram of **Fe(B_2P_2)** in THF to –3.6 V. (0.1 M *n*Bu_4NPF_6 as electrolyte, scan rate 100 mV/s, potential vs. Fc^+/Fc).

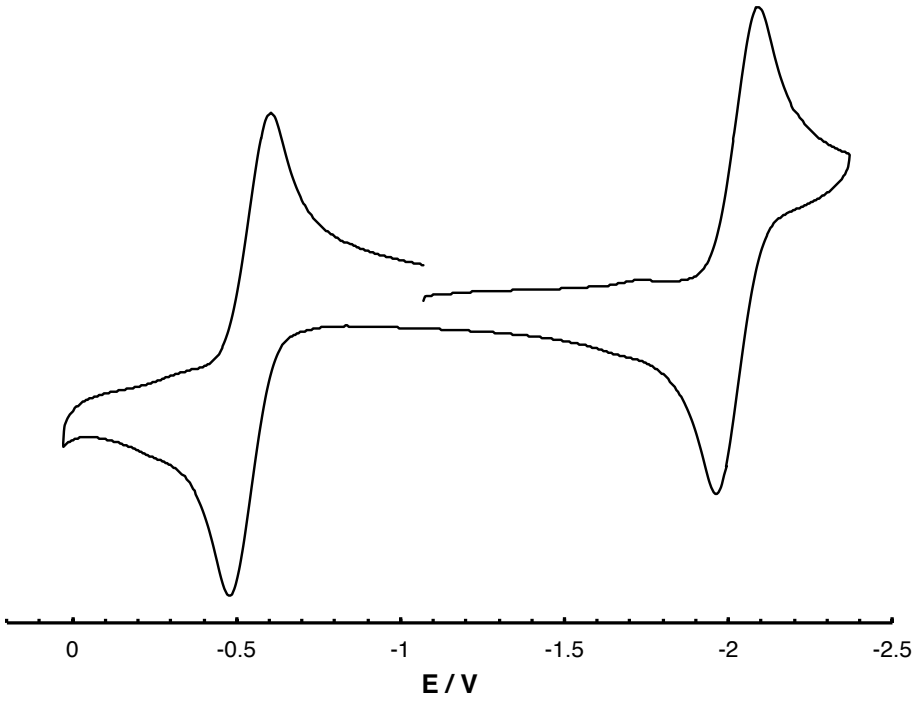

Figure 5.6.2. Cyclic voltammogram of **Fe(B_2P_2)** in THF to –2.4 V. (0.1 M *n*Bu_4NPF_6 as electrolyte, scan rate 100 mV/s, potential vs. Fc^+/Fc).

5.7) X-Ray Crystallography

5.7.1) General Considerations

Single crystals were coated with paratone oil and mounted on cryo-loop glass fibers. X-ray intensity data were collected at 100(2) K on a Bruker APEX2[24] platform-CCD X-ray diffractometer system using fine-focus Mo Kα radiation (λ = 0.71073 Å, 50 kV/30 mA power). The CCD detector was placed at 5.0600 cm from the crystal. Frames were integrated using the Bruker SAINT software package[25] and using a narrow-frame integration algorithm. Absorption corrections were applied to the raw intensity data using the SADABS program.[26] The Bruker SHELXTL software package[27] was used for phase determination and structure refinement.

Atomic coordinates, isotropic and anisotropic displacement parameters of all the non-hydrogen atoms were refined by means of a full matrix least- squares procedure on F^2. The H atoms were included in the refinement in calculated positions riding on the atoms to which they were attached. Relevant details for individual data collections are reported in Tables 5.7.1-5.7.5.

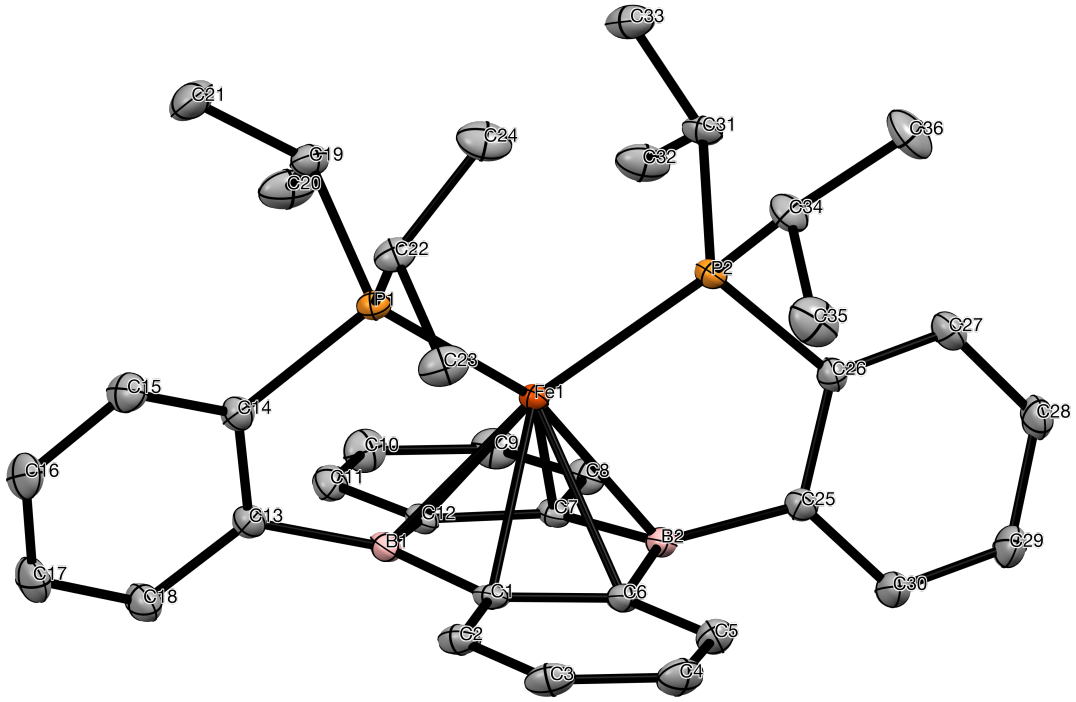

Figure 5.7.1. Labelled thermal ellipsoid plot (50%) for **Fe(B_2P_2)**.

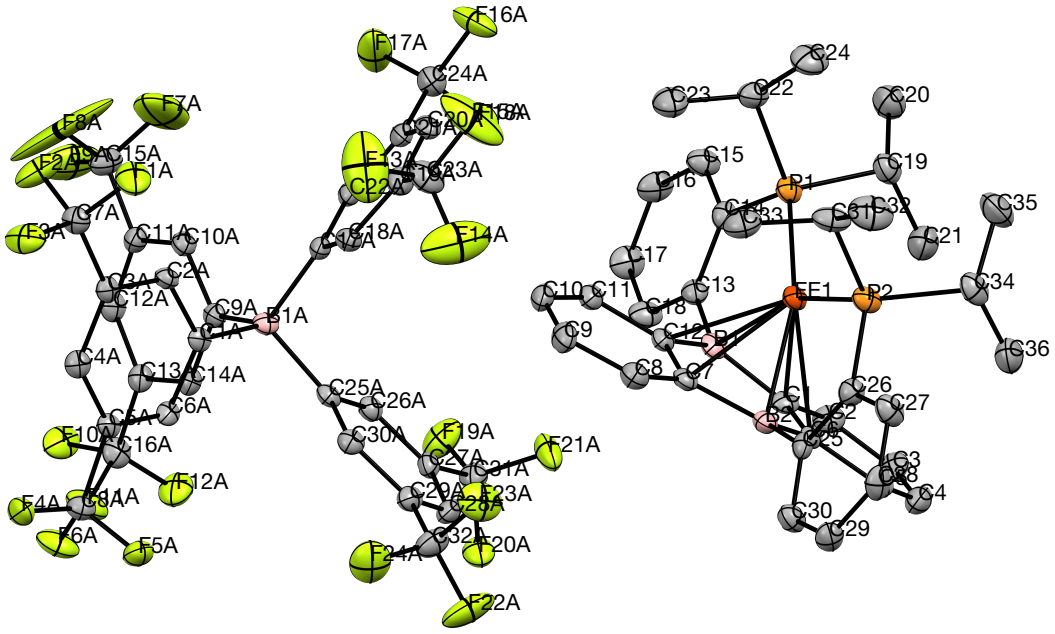

Figure 5.7.2. Labelled thermal ellipsoid plot (50%) for [**Fe(B$_2$P$_2$)][BAr$^{F}_{4}$]**.

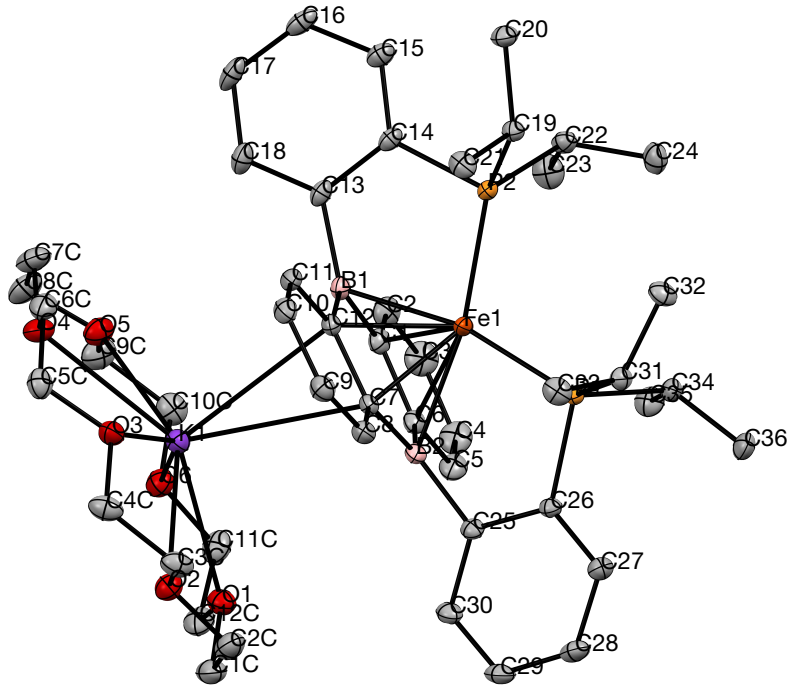

Figure 5.7.3. Labelled thermal ellipsoid plot (50%) for [**Fe(B$_2$P$_2$)][K(18-c-6)]**.

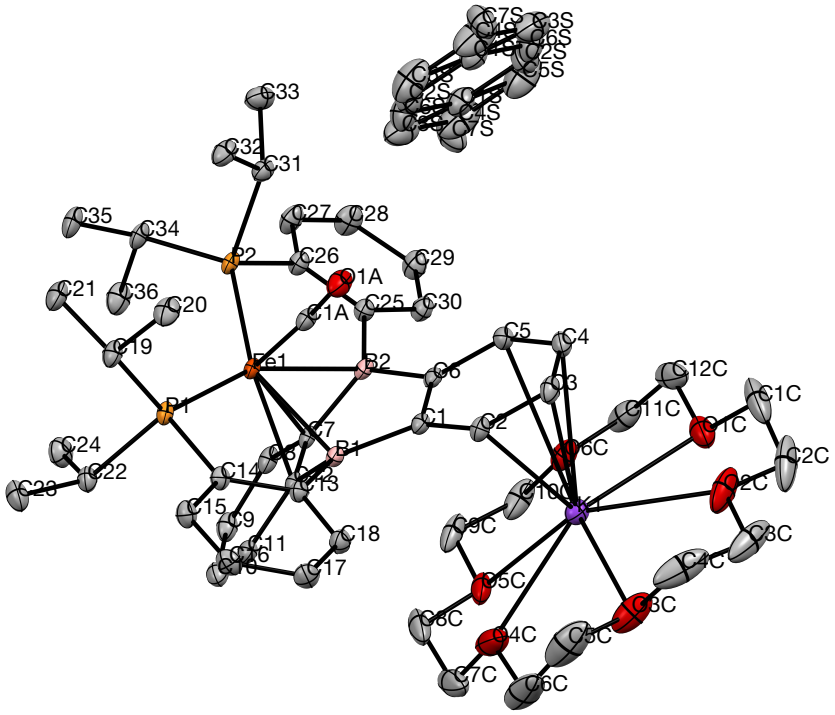

Figure 5.7.4. Labelled thermal ellipsoid plot (50%) for [**Fe(CO)(B_2P_2)][K(18-c-6)]**.

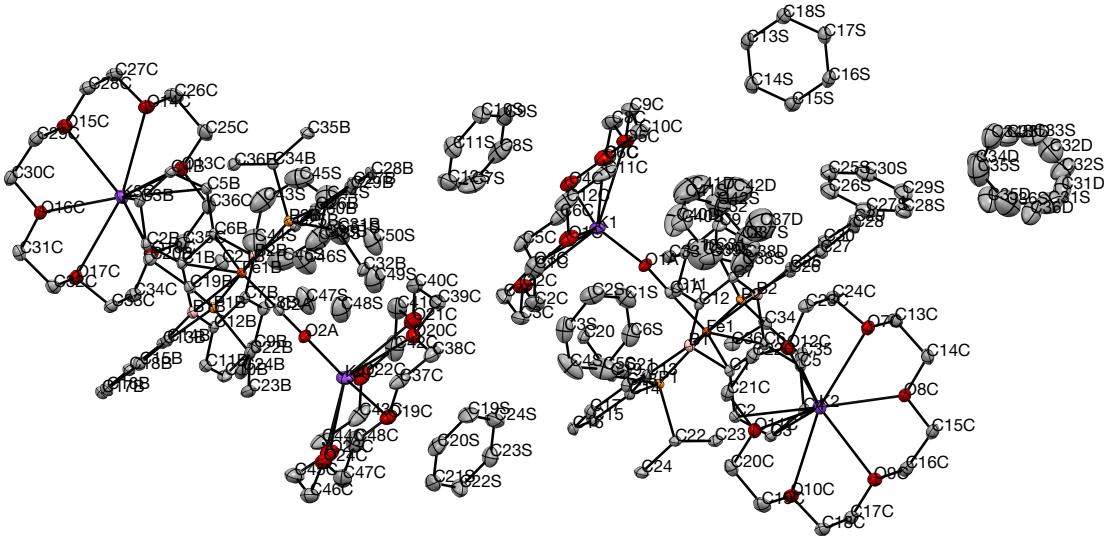

Figure 5.7.5. Labelled thermal ellipsoid plot (50%) for [**Fe(CO)(B_2P_2)][2·K(18-c-6)]**.

Table 5.7.1. Crystal data and structure refinement for **Fe(B_2P_2)**.

Identification code	hh23JT14_0m	
Empirical formula	$C_{36}H_{44}B_2FeP_2$	
Formula weight	616.12 g/mol	
Temperature	100(2) K	
Wavelength	0.71073 Å	
Crystal system	Monoclinic	
Space group	P 21/n (#14)	
Unit cell dimensions	a = 10.4472(5) Å	α= 90°.
	b = 21.6149(10) Å	β= 101.452(1)°.
	c = 14.8016(7) Å	γ = 90°.
Volume	3275.9(3) Å^3	
Z	4	
Density (calculated)	1.249 mg/m^3	
Absorption coefficient	0.582 mm^{-1}	
F(000)	1304	
Crystal size	0.517 x 0.249 x 0.043 mm^3	
θ range for data collection	1.691 to 30.508°.	
Index ranges	–14 ≤ h ≤ 14, –30 ≤ k ≤ 30, –21≤ l ≤ 21	
Reflections collected	78072	
Independent reflections	9990 [R_{int} = 0.0588]	
Completeness to θ = 25.242°	100.0 %	
Absorption correction	Semi-empirical from equivalents	
Refinement method	Full-matrix least-squares on F^2	
Data / restraints / parameters	9990 / 0 / 378	
Goodness-of-fit on F^2	1.027	
Final R indices [$I > 2\sigma_I$]	R_1 = 0.0340, wR_2 = 0.0774	
R indices (all data)	R_1 = 0.0486, wR_2 = 0.0847	
Largest diff. peak and hole	0.508 and -0.291 e/Å^3	

Table 5.7.2. Crystal data and structure refinement for **[Fe(B_2P_2)][BAr^F_4]**.

Identification code	hh98JT45	
Empirical formula	$C_{68}H_{56}B_3F_{24}FeP_2$	
Formula weight	1479.34 g/mol	
Temperature	100(2) K	
Wavelength	0.71073 Å	
Crystal system	Monoclinic	
Space group	$P2_1/c$	
Unit cell dimensions	a = 17.6954(12) Å	α = 90°.
	b = 15.9425(11) Å	β=90.8801(15)°.
	c = 23.6395(17) Å	γ = 90°.
Volume	6668.1(8) $Å^3$	
Z	4	
Density (calculated)	1.474 mg/m^3	
Absorption coefficient	0.383 mm^{-1}	
F(000)	3004	
Crystal size	0.548 x 0.092 x 0.072 mm^3	
θ range for data collection	1.541 to 25.350°	
Index ranges	$-21 \le h \le 21$, $-19 \le k \le 9$, $-28 \le l \le 28$	
Reflections collected	33378	
Independent reflections	11894 [R_{int} = 0.0559]	
Completeness to θ = 25.242°	97.4 %	
Absorption correction	Semi-empirical from equivalents	
Refinement method	Full-matrix least-squares on F^2	
Data / restraints / parameters	11894 / 55 / 930	
Goodness-of-fit on F^2	1.014	
Final R indices [$I > 2\sigma_I$]	R_1 = 0.0476, wR_2 = 0.1076	
R indices (all data, 0.83 Å)	R_1 = 0.0788, wR_2 = 0.1214	
Largest diff. peak and hole	1.166 and –0.494 e/$Å^3$	

Table 5.7.3. Crystal data and structure refinement for **[Fe(B_2P_2)][K(18-c-6)]**.

Identification code	hh30JT18_0m	
Empirical formula	$C_{48}H_{68}B_2FeKO_6P_2$	
Formula weight	919.53 g/mol	
Temperature	100(2) K	
Wavelength	0.71073 Å	
Crystal system	Monoclinic	
Space group	P 21/c (#14)	
Unit cell dimensions	a = 18.2725(7) Å	α = 90°.
	b = 12.6351(5) Å	β = 93.951(1)°.
	c = 20.5816(8) Å	γ = 90°.
Volume	4740.5(3) Å^3	
Z	4	
Density (calculated)	1.288 mg/m^3	
Absorption coefficient	0.520 mm^{-1}	
F(000)	1956	
Crystal size	0.489 x 0.194 x 0.158 mm^3	
θ range for data collection	1.892 to 30.506°.	
Index ranges	$-26 \le h \le 26$, $-18 \le k \le 18$, $-29 \le l \le 29$	
Reflections collected	136396	
Independent reflections	14469 [R_{int} = 0.0386]	
Completeness to θ = 25.242°	100.0 %	
Absorption correction	Semi-empirical from equivalents	
Refinement method	Full-matrix least-squares on F^2	
Data / restraints / parameters	14469 / 0 / 549	
Goodness-of-fit on F^2	1.037	
Final R indices [$I > 2\sigma_I$]	R_1 = 0.0323, wR_2 = 0.0754	
R indices (all data)	R_1 = 0.0430, wR_2 = 0.0803	
Largest diff. peak and hole	0.741 and –1.079 e/Å^3	

Table 5.7.4. Crystal data and structure refinement for **[Fe(CO)(B_2P_2)][K(18-c-6)]**.

Identification code	hh267JT132_0m	
Empirical formula	$C_{52.50}H_{72}B_2FeKO_7P_2$	
Formula weight	993.61 g/mol	
Temperature	100(2) K	
Wavelength	0.71073 Å	
Crystal system	Triclinic	
Space group	P –1	
Unit cell dimensions	a = 10.9125(8) Å	α =88.8577(10)°.
	b = 13.4414(10) Å	β= 84.7961(11)°.
	c = 18.8075(13) Å	γ =67.6877(10)°.
Volume	2541.3(3) Å^3	
Z	2	
Density (calculated)	1.298 mg/m^3	
Absorption coefficient	0.492 mm^{-1}	
F(000)	1056	
Crystal size	0.456 x 0.320 x 0.302 mm^3	
θ range for data collection	1.638 to 28.282°.	
Index ranges	$-14 \le h \le 14$, $-17 \le k \le 17$, $-25 \le l \le 25$	
Reflections collected	75000	
Independent reflections	12593 [R_{int} = 0.0260]	
Completeness to θ = 25.242°	99.9 %	
Absorption correction	Semi-empirical from equivalents	
Refinement method	Full-matrix least-squares on F^2	
Data / restraints / parameters	12593 / 0 / 631	
Goodness-of-fit on F^2	1.035	
Final R indices [$I > 2\sigma_I$]	R_1 = 0.0344, wR_2 = 0.0879	
R indices (all data)	R_1 = 0.0390, wR_2 = 0.0918	
Largest diff. peak and hole	0.875 and –0.436 e/Å^3	

Table 5.7.5. Crystal data and structure refinement for **[Fe(CO)(B_2P_2)][2·K(18-c-6)]**.

Identification code	hh90JT42_0m	
Empirical formula	$C_{83.62}H_{114.62}B_2FeK_2O_{13}P_2$	
Formula weight	1545.45 g/mol	
Temperature	100(2) K	
Wavelength	0.71073 Å	
Crystal system	Triclinic	
Space group	P –1	
Unit cell dimensions	a = 15.4512(5) Å	α = 71.4046(5)°.
	b = 22.6844(7) Å	β = 79.2156(5)°.
	c = 25.3554(8) Å	γ = 83.4671(5)°.
Volume	8260.4(5) Å^3	
Z	4	
Density (calculated)	1.243 mg/m^3	
Absorption coefficient	0.382 mm^{-1}	
F(000)	3297	
Crystal size	0.561 x 0.502 x 0.138 mm^3	
θ range for data collection	1.474 to 27.877°.	
Index ranges	–20 ≤ h ≤ 20, –29 ≤ k ≤ 29, –33 ≤ l ≤ 33	
Reflections collected	262214	
Independent reflections	39381 [R_{int} = 0.0314]	
Completeness to θ = 25.242°	100.0 %	
Absorption correction	Semi-empirical from equivalents	
Refinement method	Full-matrix least-squares on F^2	
Data / restraints / parameters	39381 / 126 / 1955	
Goodness-of-fit on F^2	1.019	
Final R indices [I>2sigma(I)]	R_1 = 0.0304, wR_2 = 0.0755	
R indices (all data)	R_1 = 0.0393, wR_2 = 0.0805	
Largest diff. peak and hole	0.440 and –0.348 e/Å^3	

5.8) References

[1] a) Klein Gebbink R. J. M.; Moret, M-.E. Wiley-VCH: Weinheim, Germany, 2018. b) Fuerstner, A. *Acs Cent. Sci.* **2016**, *2* (11), 778.

[2] a) Chirik, P. J.; Wieghardt, K. *Science* **2010**. b) Luca, O. R.; Crabtree, R. H. *Chem. Soc. Rev.* **2013**, *42* (4), 1440. C) Praneeth, V. K. K.; Ringenberg, M. R.; Ward, T. R. *Angew. Chem. Int. Ed.* **2012**, *51* (41), 10228.

[3] a) Verhoeven, D. G. A.; Moret, M.-E. *Dalton Trans.* **2016**, *45* (40), 15762. b) Bader, A.; Lindner, E. *Coord. Chem. Rev.* **1991**, *108* (1), 27. c) Weng, Z.; Teo, S.; Hor, T. S. A. *Acc. Chem. Res.* **2007**, *40* (8), 676.

[4] van der Vlugt, J. I. *Chem. Ber.* **2012**, *2012* (3), 363.

[5] a) Verhoeven, D. G. A.; van Wiggen, M. A. C.; Kwakernaak, J.; Lutz, M.; Klein Gebbink, R. J. M.; Moret, M.-E. *Chem. Eur. J.* **2018**, *24* (20), 5163. b) Ferreira, R. B.; Murray, L. J. *Acc. Chem. Res.* **2019**, *52* (2), 447. c) Low, C. H.; Rosenberg, J. N.; Lopez, M. A.; Agapie, T. *J. Am. Chem. Soc.* **2018**, *140* (38), 11906.

[6] a) Buss, J. A.; Agapie, T. *Nature* **2016**, *529* (7584), 72. b) Buss, J. A.; Cheng, C.; Agapie, T. *Angew. Chem. Int. Ed.* **2018**, *57* (31), 9670. c) Lin, S.; Day, M. W.; Agapie, T. *J. Am. Chem. Soc.* **2011**, *133* (11), 3828. d) Velian, A.; Lin, S.; Miller, A. J. M.; Day, M. W.; Agapie, T. *J. Am. Chem. Soc.* **2010**, *132* (18), 6296. e) Horak, K. T.; Agapie, T. *J. Am. Chem. Soc.* **2016**, *138* (10), 3443. f) Horak, K. T.; VanderVelde, D. G.; Agapie, T. *Organometallics* **2015**, *34* (19), 4753.

[7] a)Hoffend, C.; Schödel, F.; Bolte, M.; Lerner, H.-W.; Wagner, M. *Chem. Eur. J.* **2012**, *18* (48), 15394. b) Reus, C.; Weidlich, S.; Bolte, M.; Lerner, H.-W.; Wagner, M. *J. Am. Chem. Soc.* **2013**, *135* (34), 12892. c) Kawai, S.; Saito, S.; Osumi, S.; Yamaguchi, S.; Foster, A. S.; Spijker, P.; Meyer, E. *Nat. Commun.* **2015**, *6* (1), 8098. d) Osumi, S.; Saito, S.; Dou, C.; Matsuo, K.; Kume, K.; Yoshikawa, H.; Awaga, K.; Yamaguchi, S. *Chem. Sci.* **2016**, *7* (1), 219. e) Agnoli, S.; Favaro, M. *J. Mater. Chem. A* **2016**, *4* (14), 5002.

[8] A) Lorbach, A.; Bolte, M.; Lerner, H.-W.; Wagner, M. *Organometallics* **2010**, *29* (22), 5762. b) Hoffend, C.; Diefenbach, M.; Januszewski, E.; Bolte, M.; Lerner, H.-W.; Holthausen, M. C.; Wagner, M. *Dalton Trans.* **2013**, *42* (38), 13826. c)

Braunschweig, H.; Dyakonov, V.; Jimenez-Halla, J. O. C.; Kraft, K.; Krummenacher, I.; Radacki, K.; Sperlich, A.; Wahler, J. *Angew. Chem. Int. Ed.* **2012**, *51* (12), 2977.

[9] a) Moret, M.-E.; Zhang, L.; Peters, J. C. *J. Am. Chem. Soc.* **2013**, *135* (10), 3792. b) Braunschweig, H.; Dewhurst, R. D.; Gessner, V. H. *Chem. Soc. Rev.* **2013**, *42* (8), 3197. c) Sircoglou, M.; Bontemps, S.; Bouhadir, G.; Saffon, N.; Miqueu, K.; Gu, W.; Mercy, M.; Chen, C.-H.; Foxman, B. M.; Maron, L.; Ozerov, O. V.; Bourissou, D. *J. Am. Chem. Soc.* **2008**, *130* (49), 16729. d) Crossley, I. R.; Hill, A. F.; Willis, A. C. *Organometallics*, **2006**, *25* (1), 289-299. e) Siebert, W. *Advances in Organometallic Chemistry*; Elsevier, 1980; Vol. 18, pp 301–340.

[10] a) Anderson, J. S.; Rittle, J.; Peters, J. C. *Nature* **2013**, *501* (7465), 84. b) Rittle, J.; Peters, J. C. *Proc. Nat. Acad. of Sci.* **2013**, *110* (40), 15898.

[11] a) Harman, W. H.; Peters, J. C. *J. Am. Chem. Soc.* **2012**, *134* (11), 5080. b) Harman, W. H.; Lin, T.-P.; Peters, J. C. *Angew. Chem. Int. Ed.* **2014**, *53* (4), 1081.

[12] Suess, D. L. M.; Peters, J. C. *J. Am. Chem. Soc.* **2013**, *135* (34), 12580.

[13] a) Essex, L. A.; Taylor, J. W.; Harman, W. H. *Tetrahedron* **2019**, Early View, DOI: 10.1016/j.tet.2019.02.047 b) Taylor, J. W.; McSkimming, A.; Moret, M.-E.; Harman, W. H. *Inorg. Chem.* **2018**, *57* (24), 15406. c) Taylor, J. W.; McSkimming, A.; Moret, M.-E.; Harman, W. H. *Angew. Chem. Int. Ed.* **2017**, *56* (35), 10413.

[14] Grotthuss, von, E.; Diefenbach, M.; Bolte, M.; Lerner, H.-W.; Holthausen, M. C.; Wagner, M. *Angew. Chem. Int. Ed.* **2016**, *55* (45), 14067.

[15] Grotthuss, von, E.; Prey, S. E.; Bolte, M.; Lerner, H.-W.; Wagner, M. *Angew. Chem. Int. Ed.* **2018**.

[16] Grotthuss, von, E.; Nawa, F.; Bolte, M.; Lerner, H.-W.; Wagner, M. *Tetrahedron* **2019**, *75* (1), 26.

[17] Taylor, J. W.; McSkimming, A.; Guzman, C. F.; Harman, W. H. *J. Am. Chem. Soc.* **2017**, *139* (32), jacs.7b06772.

[18] a) Brennessel, W. W.; Ellis, J. E. *Angew. Chem. Int. Ed.* **2007**, *46* (4), 598. b) Brennessel, W. W.; Jilek, R. E.; Ellis, J. E. *Angew. Chem. Int. Ed.* **2007**, *46* (32), 6132.

[19] Müller, P.; Gangnus, B.; Pritzkow, H.; Schulz, H.; Stephan, M.; Siebert, W. *J. Organomet. Chem.* **1995**, *487* (1-2), 235.
[20] Yakelis, N.; Bergman, R. *Organometallics* **2005,** *24*, 3579-3581.

[21] Scott, T.; Ooro, B.; Collins, D.; Shatruk, M.; Yakovenko, A.; Dunbar, K.; Zhou, H.–C. *Chem. Commun.* **2008**, 65-67.

[22] Led, J. J.; Gesmar, H. *Chem. Rev.* **1991**, *91*, 1413-1426.

[23] Stoll, S.; Schweiger, A. *J. Magn. Reson.* **2006**, *178*, 42-55.

[24] APEX 2, version 2014.1-1, Bruker (2014), Bruker AXS Inc., Madison, Wisconsin, USA.

[25] SAINT, version V8.34A, Bruker (2012), Bruker AXS Inc., Madison, Wisconsin, USA.

[26] SADABS, version 2012/1, Bruker (2012), Bruker AXS Inc., Madison, Wisconsin, USA.

[27] SHELXTL, version 2013/4, Bruker (2013), Bruker AXS Inc., Madison, Wisconsin, USA.

Chapter 6) Weak-Field Iron Chemistry with Tris(pyrazolyl)borate Ligands

6.1) Introduction

The biological significance of the MoFe-nitrogenase cofactor (FeMoco) is underscored by the importance of dinitrogen to ammonia conversion for the persistence of life.[1] The performance of MoFe-nitrogenase enzymes is emulated industrially by the Haber-Bosch process that utilizes Fe to perform this reaction on a massive scale.[2] The Haber-Bosch process is perhaps the most important catalytic process for mankind's survival, with roughly 1% of the global energy supply consumed annually carrying it out. Logically, the mechanism by which the FeMoco catalyzes the reduction of nitrogen to ammonia has intrigued and challenged the scientific community for decades.[3] A combination of spectroscopic, biochemical and computational data have pointed at a belt Fe center as the most plausible site for N_2 binding in the active site of the FeMoco

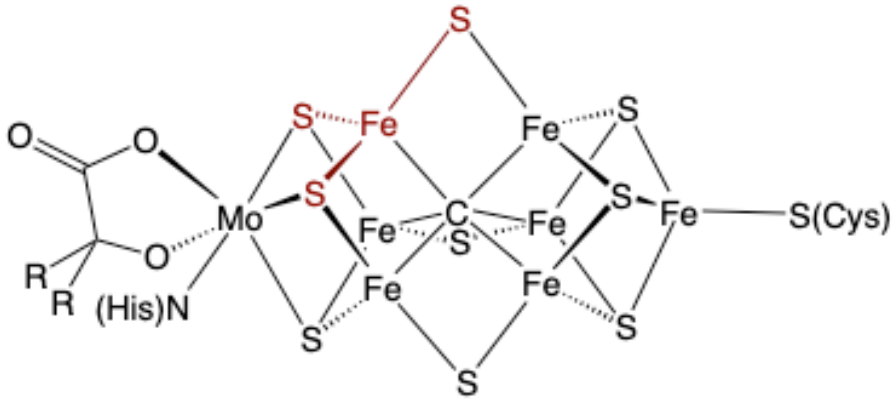

Figure 6.1. The FeMoco active site of nitrogenase with a potential N_2 binding site highlighted in red.

(Figure 6.1.).[4] However, replicating the unique tripodal coordination environment of Fe within the Fe_6C cluster with a sulfurous ligand field has mostly eluded the synthetic community to date.[5] Additionally, the unique weak-field ligands utilized by MoFe-nitrogenase enzymes enforces high-spin Fe centers which offers an additional synthetic challenge.

Model systems are one way to inform these biological systems[6] and, in the case of Fe[7] and Mo,[8] have led to the discovery of synthetic molecular systems capable of catalytically reducing N_2 to NH_3. Since the initial reports of N_2 coordination chemistry with Fe,[9] remarkable progress and insight has been gained through these studies however these systems feature spin states of S = ½ or 1 at Fe and stand in contrast to a hypothetical N_2 adduct of a belt Fe.[10] Amongst the Fe-N_2 complexes that have apparent spin-states greater than S = 1 at Fe are linear bimetallic complexes supported by β-diketiminate (NacNac),[10a] tris(phosphinomethyl)borate (TPB)[10b] or hybrid phosphine/amide ligands.[10c] The bimetallic, linear Fe–(μ-N_2)–Fe nature of many of these systems hinders the assignment of the local ligand field and spin state at Fe. Additionally, the N_2 ligand in these systems, while activated,[11] doesn't feature the expected polarization and spin density expected for a terminal N_2 adduct. As such, the realization of a model-system that features a high-spin Fe center with an N_2 ligand has been hitherto unknown and presents an important area of study.

Previous work in our lab by Dr. Alex McSkimming utilized an adamantyl substituted tris(pyrazoyl)borate ($Tp^{Ad,Me}$) ligand to produce the first terminal, high-spin Fe(I) N_2 complex, $Tp^{Ad,Me}Fe(N_2)$ (**1**).[12] Additionally, through these studies we found without sufficient steric bulk on the Tp ligand (phenyl substituted), the high-spin bimetallic dimer complex, $(Tp^{Ph,Me}Fe)_2(N_2)$ (**2**), was isolated. The synthesis

Scheme 6.1. Synthesis of **1** and **2**.

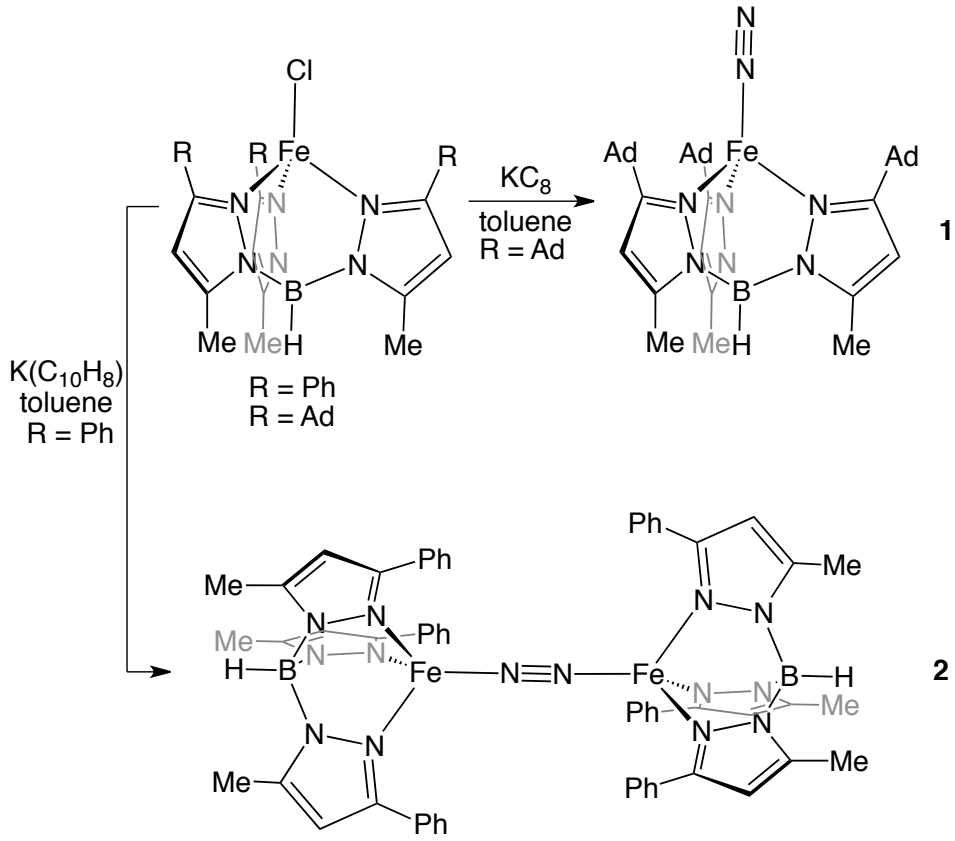

of the $TpFe(N_2)$ complexes, outlined in Scheme 1, lead to the investigation of their electronic structures by EPR, Mössbauer, SQUID magnetometry and DFT. These inquires confirmed that for $Tp^{Ad,Me}Fe(N_2)$ a high-spin, $S = 3/2$ Fe center is bound to the N_2 ligand and that substantial spin-density is located on the N_2

ligand. Following Alex's initial discovery, synthetic efforts to further reduce the TpFe(N_2) complexes in the hopes of functionalization of the N_2 ligand, as well as fundamental ligand displacement studies, were pursued.

Throughout the aforementioned studies, numerous reducing agents were tested to enact the formation of **1** and **2** from $Tp^{Ad,Me}FeCl$ and $Tp^{Ph,Me}FeCl$, respectively. The recent report on the isolation of the benzophenone ketyl radical anion as a crystalline solid,[13] intrigued us as to whether it would result in reduction to the N_2 complex or afford the hypothetical Fe-Ketyl complex. Literature precedent for the formation of an Fe-Ketyl complex is limited[14] as the chemistry of the benzophenone ketyl radical anion has largely remained confined to pairings with alkali and alkaline earth metal salts.[15] A 1999 report of fluorenone-ketyl transfer to Zr was reported by Wakatsuki et. Al,[16] remaining the a rare example of a transition metal ketyl complex until 2014. In 2014, Thomas et.al isolated the related Zr-fluorenone and -*p*-tolybenzophenone ketyl complexes with DFT suggesting a ligand centered radical.[17] Progress towards a structurally characterized benzophenone ketyl complex of a lanthanide was made in 2008 by Meyer et.al. who reported the synthesis of a uranium-ketyl complex and thoroughly investigated its electronic structure with DFT.[18] As such, structurally characterized transition metal benzophenone ketyl complexes are exceedingly rare and thus we pursued the isolation of a Fe-Ketyl complex within the Tp ligand framework. Additionally, the reactivity of the TpFe complexes with CO was

explored as it is isoelectronic with N_2 and offers additional insight into the electronic structure of these systems. The redox chemistry of the TpFe complexes was also explored.

The following chapter is a roughly linear summary of the data I assisted Alex in collecting and he deserves a lion's share of the credit for these discoveries. Additionally, Prof. T. David Harris and his student Jordan DeGayner at Northwestern University are acknowledged for collecting and simulating all of the Mössbauer and SQUID data for the compounds described herein. Our understanding of these molecules would be much less complete without their fantastic help and insights.

6.2) Results and Discussions

The synthesis of the $Tp^{Ph,Me}$Fe-Ketyl (**3**) complex was achieved by addition of crystalline benzophenone radical anion ($K(OCPh_2)$) to $Tp^{Ph,Me}$FeCl in Et_2O. A deep purple solution formed over the course of the reaction and,

Scheme 6.2. Synthesis of **3**

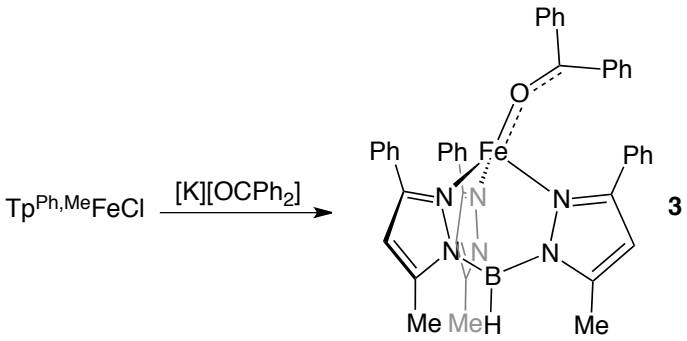

following workup, **3** was isolated in 87% yield. Single-crystal XRD studies of **3**

presented two crystallographically distinct molecules (Figure 6.2.1A). One molecule features a longer Fe-O distance ($d_{Fe\text{-}O}$ = 1.850(1) Å) with accompanying contraction of the ketyl O-C and Fe-N_{Tp} bonds ($d_{O\text{-}C}$ = 1.314(2) Å; $d_{Fe\text{-}N}$ = 2.084 Å). Additionally, the ketyl O atom is canted from the idealized C_3 axis with a B-Fe-O angle of 161.2°. The other distinct molecule is qualitatively opposite,

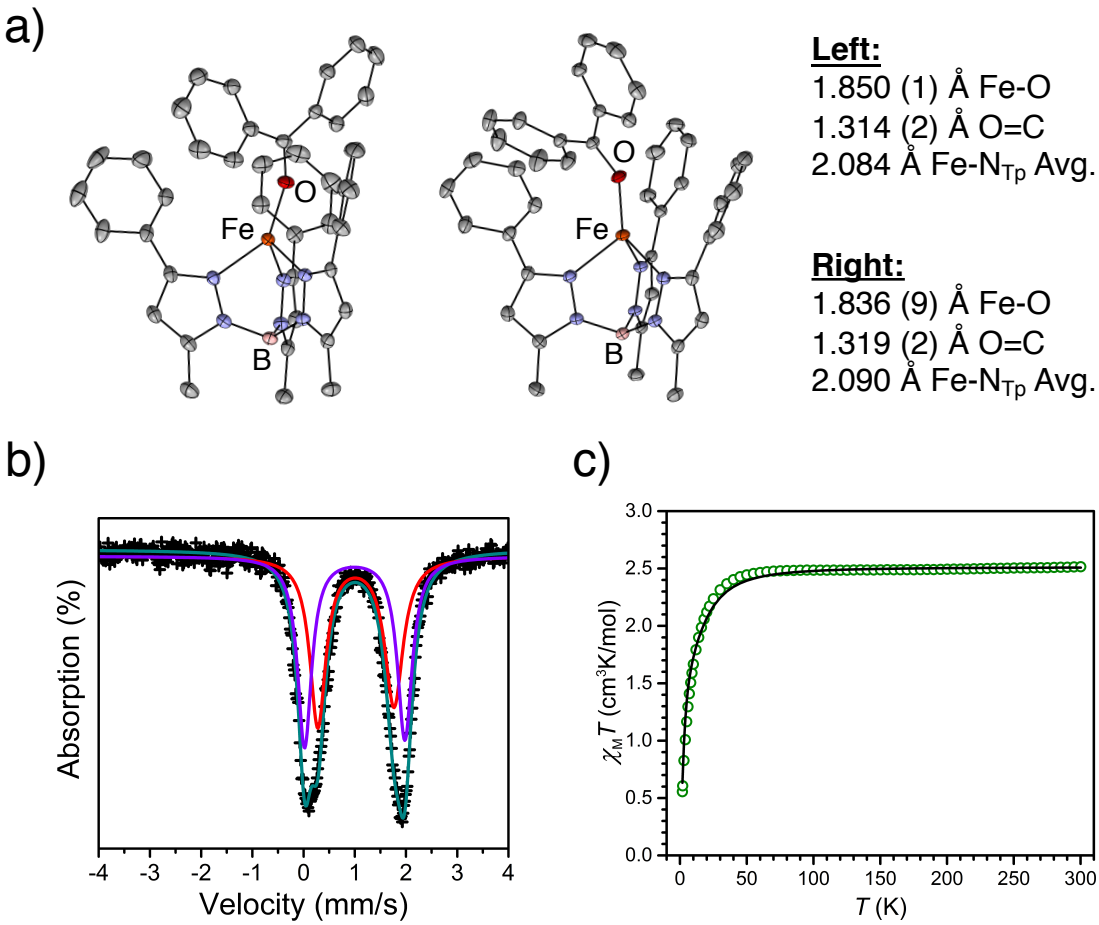

Figure 6.2. a) Thermal ellipsoid plots (50%) of the two crystallographically distinct molecules of **3** with relevant distances inlayed. Unlabeled grey and blue ellipsoids correspond to carbon and nitrogen, respectively. b) Zero-field Mössbauer spectrum of **3** collected at 80 K. The red and purple lines correspond to the two-site fit of the data. c) Variable-temperature dc magnetic susceptibility for **3** collected under an applied magnetic field of 1000 Oe. The black line corresponds to a fit of the data.

featuring a shorter Fe-O distance ($d_{Fe\text{-}O}$ = 1.838(9) Å), longer ketyl O-C and Fe-N_{Tp} bonds ($d_{O\text{-}C}$ = 1.319(2) Å; $d_{Fe\text{-}N}$ = 2.090 Å) and a less canted ketyl O atom (∠B-Fe-O = 175.0°). The sum of the angles about the ketyl carbon in both distinct molecules in the unit cell of **3** are 360°, consistent with sp^2 hybridization being maintained. In support of this, FT-IR spectra of **1** displayed no strong band > 1545 cm^{-1} for a C=O stretch. ^1H NMR data of C_6D_6 solutions of **3** gave spectra consistent with paramagnetism while attempts at collecting EPR spectra of **3** invariably gave no discernable signal down to 100 K. To gain further insight into the electronics of **3**, Mössbauer spectroscopy and SQUID magnetometry data were collected. To our delight, zero-field Mössbauer spectroscopy of **1** revealed a spectrum that was well simulated by modeling two distinct Fe sites with similar isomer shifts (δ = 1.022(4)), 0.999(3) mm s^{-1}) and different quadrupole splitting parameters ($|\Delta E_Q|$ = 1.487(7), 1.959(5) mm s^{-1}), consistent with the two-distinct molecules present in the single-crystal XRD of **3**. SQUID magnetometry data was fit with an μ_{eff} = 2.49 and is suggestive of a high-spin, S = 1 spin state at Fe. Collectively these data support the designation of **3** as a high-spin Fe(II)-ketyl complex.

Interestingly, reaction of **3** with I_2 in THF lead to the formation of a colorless solution that was identified as the $Tp^{Ph,Me}$Fe(I)(THF) (**4**) complex. The single crystal XRD structure of **4** was unremarkable save for the Fe center being in a pseudo-trigonal bipyramidal coordination geometry with I and THF ligands

bound in the solid state. Having expected a compound of the formula $Tp^{Ph,Me}Fe(I)$ given the analogous formula being reported for $Tp^{Ph,Me}Fe(Cl)$,[19] we were shocked to discover the single-crystal XRD structures of the $Tp^{Ph,Me}FeX$ (where X = Cl, Br, I) series have not been reported.[20] Regardless, the formation of **4** suggests that **3** could serve as a synthon for Fe(I) complexes and we further investigated its reactivity.

Scheme 6.3. Synthesis of **4**, **5** and **6**

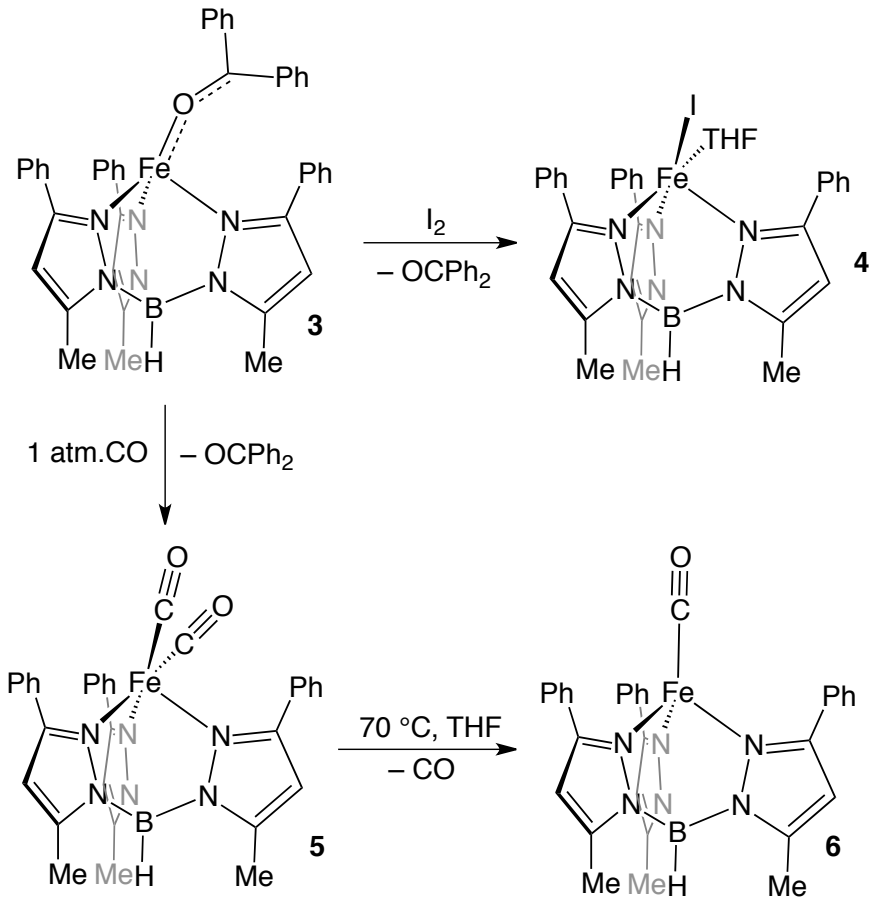

Having discerned the electronic structure of **3**, we were surprised to find that exposure of a solution of **3** to 1 atm. CO lead to the rapid formation of a deep orange solution. Following workup, the dicarbonyl complex, $Tp^{Ph,Me}Fe(CO)_2$ (**5**),

was isolated in 90% yield. Single-crystal XRD data of **5** confirmed it as the dicarbonyl complex with Fe in a pseudo-trigonal bipyramidal coordination geometry. FT-IR spectra of **5** consisted of two bands at 1992 and 1907 cm^{-1} consistent with modest π-backbonding interactions between Fe and the carbonyl ligands. Moreover, addition of 1 atm. of CO to a solution of the dinitrogen dimer **2**

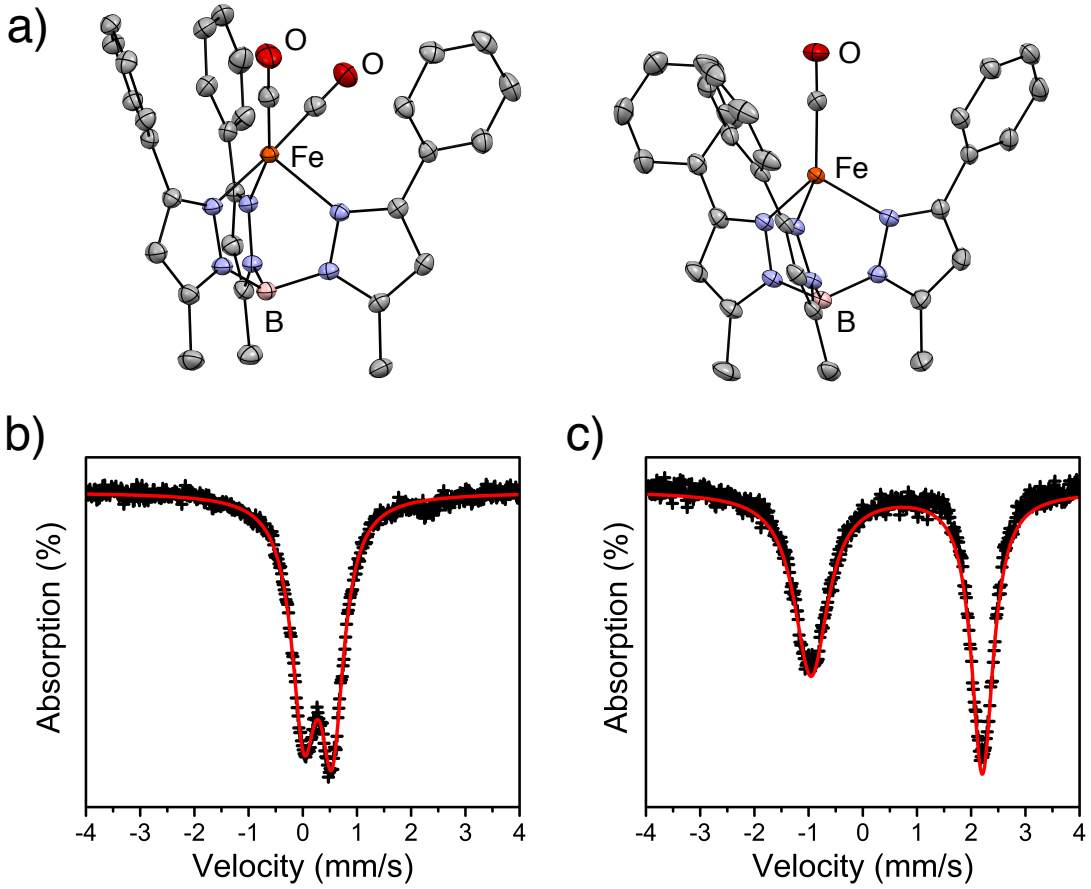

Figure 6.3. a) Thermal ellipsoid plots (50%) of **5** (left) and **6** (right). Unlabeled grey and blue ellipsoids correspond to carbon and nitrogen, respectively. b) Zero-field Mössbauer spectrum of **5** collected at 80 K. The red line corresponds to the fit of the data. c) Zero-field Mössbauer spectrum of **6** collected at 80 K. The red line corresponds to the fit of the data.

resulted in rapid formation of a deep orange solution that matched spectroscopic data of authentic samples of **5**.

Extended exposure of **5** to vacuum (~0.5 mtorr) lead to a small amount of yellow solids that were identified as the mono-CO adduct, $Tp^{Ph,Me}Fe(CO)$ (**6**). Direct synthesis of **6** could be achieved in excellent yields (97%) by refluxing a solution of **5** in THF. The single-crystal XRD data of **5** featured Fe in a tetrahedral coordination geometry with unremarkable distances and angles. FT-IR spectra of **6** featured a prominent band at 1889 cm^{-1} for the CO ligand consistent with increased π-backbonding between Fe and the carbonyl ligand.

The putative assignment of **5** as a $S = 1/2$, d^7 Fe(I) complex and **6** as a $S = 3/2$, d^7 Fe(I) complex by quantitative electron counting practices was explored experimentally by Evan's method measurements, X-band EPR and Mössbauer spectroscopies. Solution ^1H NMR measurements of **5** and **6** gave spectra consistent with paramagnetism with Evan's method measurements producing values of $\mu_{eff} = 1.5 \pm 0.1$ and $\mu_{eff} = 4.4 \pm 0.1$, respectively. X-band EPR measurements of **5** in 2-MeTHF at 109 K gave a rhombic signal with $g_{eff} = 2.107$, 2.044, and 1.966 and well-defined hyperfine coupling. The spectra of **5** was well-simulated by interaction with three equivalent nitrogen nuclei such that $A(^{15}N) =$ [0, 25, 28] MHz. Contrarily, X-band EPR measurements of solid **6** at 102 K gave a spectrum with prominent features at $g_{eff} = 3.8$ and $g_{eff} = 2.0$ consistent with the $m_s \pm ½$ transitions of an axial $S = 3/2$ system. Attempts at collecting

measurements of **6** in 2-MeTHF at 104 K consistently gave rise to a spectra representative of a mixture of **5** and **6** (see Spectroscopic Data). Finally, Mössbauer spectroscopy of **5** and **6** returned isomer shifts (δ = 0.281 (2) and 0.626(3) mm s^{-1}) and quadrupole splitting parameters ($|\Delta E_Q|$ = 0.521(3) and 3.160(5)) mm s^{-1}) that are consistent with a more e^- rich Fe center in **6**. The large asymmetry between the quadrupole doublet for **6** likely stems from slow-magnetic relaxation on the Mössbauer timescale.[21]

The synthesis of **6** represented only the second[22] terminal high-spin, Fe(I) carbonyl complex and we sought to isolate the analogous complex within the $Tp^{Ad,Me}$ ligand framework to gain further electronic insight. Exposure of a solution of $Tp^{Ad,Me}Fe(N_2)$ to 1 atm CO resulted in immediate formation of a yellow-brown solution from which $Tp^{Ad,Me}Fe(CO)$ (**1-CO**) was isolated in 91% yield. In the solid-state, **1-CO** features Fe in a tetrahedral coordination geometry with Fe-CO and FeC-O distances analogous to those in **6**. The lack of formation of a dicarbonyl complex at 1 atm CO is likely the result of steric shielding provided by the adamantyl substituents. ^{1}H NMR solution measurements in C_6D_6 of **1-CO** were consistent with paramagnetism with an Evan's method measurement of μ_{eff} = 4.0 ± 0.3. Additionally, X-band EPR measurements of **1-CO** in 2-MeTHF at 107 K featured prominent features at g_{eff} = 4 and g_{eff} = 2, analogous to those observed for **1** and **6**. Collectively, these results are consistent with a high-spin, S = 3/2 Fe(I) system.

Having isolated and characterized the series of TpFe(I) complexes, we sought to probe the redox chemistry of the terminal N_2 adduct **1**, with the initial goal of functionalizing the N_2. Oxidation of **1** was achieved by addition of silver tetrakis(3,5-bis(trifluoromethyl)phenyl)borate ($AgBAr^F_4$) in DCM to afford the colorless complex, [$Tp^{Ad,Me}Fe(MeCN)$][BAr^F_4] (MeCN = acetonitrile) (**1**$^+$), in 93 %

Scheme 6.4. Synthesis of **1**$^+$ and **1**$^-$**-Li**

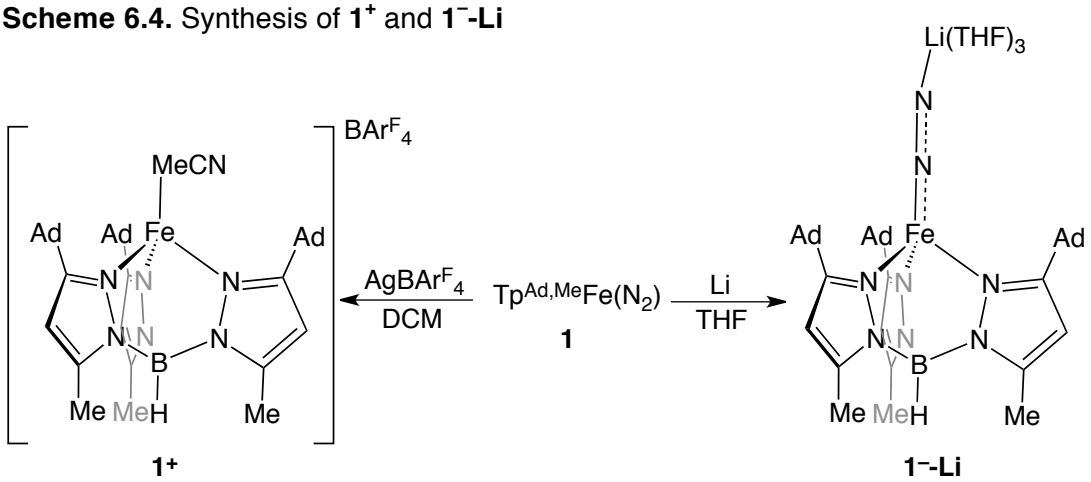

1$^+$ **1**$^-$**-Li**

yield. The single-crystal XRD structure of **1**$^+$ confirmed the formation of a complex salt with an acetonitrile (MeCN) ligand coordinated to the Fe center. Additionally, the Fe-N_{Tp} distances (d_{NFe}Avg = 2.050 Å) were shortened compared to **1** (d_{NFe}Avg = 2.060 Å), consistent with a Fe centered redox process. Synthetic modifications to preclude coordinating solvent to potentially allow the formation of a hypothetical Fe(II)-N_2 complex are being pursued.

In pursuing reduction of **1**, addition of excess Na or Li to THF solutions of $Tp^{Ad,Me}Fe(N_2)$ resulted in the formation of a highly thermally sensitive deep blue solution that decomposed when being left > 1 hour at room temperature.

Nonetheless a careful reduction and crystallization procedure, allowed for the collection of single-crystal XRD data for the Li and Na reduced species. The Li salt, $Tp^{Ad,Me}Fe(N_2)Li(THF)_{3]}$ (**1^--Li**), features a pseudo-tetrahedral Fe center with a very activated N_2 ligand with a N-N distance of 1.184(2) Å. For comparison, the analogous N-N distance in $Tp^{Ad,Me}Fe(N_2)$ is 1.1187 (2) Å and is suggestive of significant activation of the N_2 ligand on reduction. FT-IR spectroscopy reveals a band for the N_2 ligand at 1772 cm^{-1}, nearly 200 cm^{-1} from the band observed for the N_2 ligand in $Tp^{Ad,Me}Fe(N_2)$ (1959 cm^{-1}). The Na salt, $Tp^{Ad,Me}Fe(N_2)Na(THF)_4$ (**1^--Na**), could be prepared in an analogous way as the Li salt however it is significantly more sensitive than its Li counterpart, likely due to stronger ion-pairing interactions with Li than Na.[23] The existence of **1-Li** and **1^--Na** prompted us to conduct an exploratory survey of their reaction chemistry. Unfailingly however, all attempts at addition of electrophiles to THF, toluene or Et_2O solutions of **1^--Li** and **1^--Na** at temperatures ranging from –196 °C to 25 °C lead to oxidation to **1** or decomposition (or both).

Table 6.1. Zero-field Mössbauer parameters, magnetic moment and spin values for select TpFe complexes.

Compound	Isomer Shift, σ mm s^{-1}	Quadrupole Splitting, $\lvert\Delta E_Q\rvert$ mm s^{-1}	μ_{eff}	*S*
$Tp^{Ph,Me}$Fe-Ketyl (**3**)	1.022(4), 0.999(3)	1.487(7), 1.959(5)	4.5	1.5
$Tp^{Ph,Me}$Fe(CO) (**6**)	0.626(3)	3.160(5)	4.4	1.5
$Tp^{Ph,Me}Fe(CO)_2$ (**5**)	0.281(2)	0.521(3)	1.5	0.5
$(Tp^{Ph,Me}Fe)_2(N_2)$ (**2**)	0.941(3)	0.769(4)	6.9	3
$Tp^{Ad,Me}$FeCl	0.961(2)	2.338(3)	5.7	1.5
$Tp^{Ad,Me}Fe(N_2)$ (**1**)	0.915(2)	2.507(3)	3.8	1.5
$Tp^{Ad,Me}Fe(N_2)Li(THF)_3]$ (**1$^-$-Li**)	0.909(2)	0.524(3)	–	–

As **1$^-$-Li** and **1$^-$-Na** represent a rare example of a reduced Fe-N_2 complex in a weak-ligand field we were keen to gain insight into their electronic structure. Mössbauer spectroscopy of **1$^-$-Li** reveals a narrow quadrupole doublet (see Spectrosopic Data) with an isomer shift of δ = 0.909(2) mm s^{-1} and a quadrupole splitting parameter of $\lvert\Delta E_Q\rvert$ = 0.524(3) mm s^{-1}. When comparing these values to our growing library of TpFe Mössbauer data (summarized in Table 6.2.1) the isomer shift is suggestive of little added e^- density at the iron center on going from **1** to **1$^-$-Li**. Additionally, the large quadrupole splitting parameter difference of ~2 mm s^{-1} is consistent with perturbation of the Fe *d*-orbital manifold on reduction. Computational data is being pursued to help discern the nature of the bonding in **1$^-$-Li.**

6.3) Concluding Remarks

In summary, a series of Fe complexes have been prepared with the weak-field $Tp^{Ph,Me}$ and $Tp^{Ad,Me}$ ligands. The reaction of $Tp^{Ph,Me}FeCl$ with the sodium benzophenone radical anion led to the isolation of the ketyl complex, $Tp^{Ph,Me}$Fe-Ketyl, that is best described as d^6, Fe(II) with an electronic ground state of S = 3/2 as determined by SQUID magnetometry. However, the $Tp^{Ph,Me}$Fe-Ketyl complex serves as a synthon for Fe(I) complexes as discerned from its reaction with oxidants to yield the $Tp^{Ph,Me}Fe(I)(THF)$ complex and by its reaction with CO to yield the dicarbonyl complex, $Tp^{Ph,Me}Fe(CO)_2$. The $Tp^{Ph,Me}Fe(CO)_2$ complex features a low-spin, S = 1/2 electronic ground state while loss of a CO ligand by reflux produces the monocarbonyl complex $Tp^{Ph,Me}Fe(CO)$ with a high-spin, S = 3/2 electronic ground state. Synthesis of the analogous monocarbonyl complex, $Tp^{Ad,Me}Fe(CO)$, within the sterically encumbered adamantly ligand framework was achieved and was also identified as having a high-spin, S = 3/2 electronic ground state. Finally, reduction of $Tp^{Ad,Me}Fe(N_2)$ with Li or Na metal lead to anionic complexes. The Li salt was characterized by Mössbauer spectroscopy and is suggestive of significant N_2 based reduction and/or significant Fe-N covalency. The unique ligand field and resulting high-spin nature of the Fe complexes described herein offer a unique window into better understanding biological high-spin Fe(I) chemistry. Further reaction chemistry, electronic

measurement and computational efforts are underway to understand the role of spin-state on N_2 and small molecule binding within the Tp ligand framework.

6.4) Experimental Section

6.4.1) General Considerations

Unless stated otherwise, all compounds were purchased from commercial sources and used without further purification. Solvents were dried and deoxygenated by sparging with argon and passage through activated alumina in a solvent purification system from SG Waters USA, LLC. All manipulations were performed under an N_2 atmosphere either in a glovebox or using standard Schlenk techniques. $K(Ph_2CO)$,[13] $Tp^{Ph,Me}FeCl$,[19] $(Tp^{Ph,Me}Fe)_2(N_2)$, $Tp^{Ad,Me}FeCl$, and $Tp^{Ad,Me}Fe(N_2)$[12] were synthesized according to literature procedures. Elemental analyses were performed by Midwest Microlab, LLC, Indianapolis, IN. Deuterated solvents were purchased from Cambridge Isotope Laboratories Inc., degassed, and dried over activated 4 Å molecular sieves for at least 24 hr prior to use. NMR spectra were recorded on Varian Inova 500 MHz and Bruker Avance 600 MHz spectrometers. ^1H chemical shifts are reported in ppm relative to tetramethylsilane using residual solvent as internal standards. FT-IR spectra were recorded using a Bruker Alpha FT-IR with a universal sampling module collecting at 4 cm^{-1} resolution with 32 scans. EPR X-band spectra were obtained on a Bruker EMX spectrometer controlled by Bruker Win-EPR software suite version 3.0. Simulations were performed using the Easyspin software suite.[24] UV-

Vis spectra were recorded using a Cary Bio 500 spectrometer using a 1 cm path length quartz cuvette with a solvent background subtraction applied. X-ray diffraction studies were performed using a Bruker-AXS diffractometer. Solution phase effective magnetic moments were obtained via the method described by Evans[25] and were performed in triplicate and standard deviations are reported.

6.4.2) $Tp^{Ph,Me}Fe(OCPh_2)$ (3).

To a suspension of $Tp^{Ph,Me}FeCl$ (0.300 g, 0.464 mmol) in Et_2O (10 mL) was added $K(OCPh_2)$ (0.103 g, 1 mol. eq.) as a solid in a single-portion. The mixture was stirred 15 hours before being filtered through celite and rinsed with Et_2O (4 mL). The filtrate was concentrated *in vacuo* to half its volume (ca. 5 mL) before adding hexane (10 mL) whereupon the product began precipitating from solution. The product was collected on a frit, washed with hexane (3 mL) and dried *in vacuo*. An additional crop could be recovered by further concentration of the mother liquor. Yield: 290 mg (87%). Crystals suitable for XRD studies were grown at –35 °C by layering a concentrated THF solution with hexanes. ^1H NMR (500 MHz, C_6D_6) δ 58.68, 43.05, 40.54, 30.84, 8.48, 8.33, 7.08, 6.70, –21.78, –23.60, –67.85. UV-Vis-NIR (THF): λ_{max} (nm) (ε_{max} ($M^{-1}cm^{-1}$)) 807 (sh, 7.8 x 10^2), 544 (5.6 x 10^3), 429 (3.7 x 10^2), 327 (1.6 x 10^4). FT-IR: ν_{max} cm^{-1} 2548 (BH). Calc. for $C_{43}H_{38}BFeN_6O$: C 71.59; H 5.31; N 11.65. Found: C 71.00; H 5.68; N 11.57.

6.4.3) $Tp^{Ph,Me}Fe(I)(THF)$ (4).

A solution of **3** (17 mg, 0.023 mmol) in THF (1 mL) was added iodine (3 mg, 0.5 mol. eq) as a THF solution (1 mL). The reaction was stirred 30 minutes during which time a red/orange solution had developed. Addition of hexanes (5 mL) and concentration *in vacuo* (ca. 2 mL) resulted in ample precipitation of the product as a colorless, crystalline solid that was collected and washed with hexanes (1 mL) before drying *in vacuo*. Yield: 15 mg (87%). Crystals suitable for XRD studies were grown by layering a concentrated THF solution with hexanes. ^1H NMR (500 MHz, C_6D_6) δ 60.69 (s, 1H), 46.11 (s, 0H), 35.57 (s, 3H), 31.80 (s, 0H), 8.91 (s, 2H), 6.79 (s, 2H), 4.20 (s, 2H), 1.87 (s, 2H), -7.75 (s, 2H).

6.4.4) $Tp^{Ph,Me}Fe(CO)_2]$ (5).

A suspension of **1** (50 mg, 0.0452 mmol) in toluene (4 mL) was subjected to three freeze-pump-thaw cycles before adding 1 atm. CO. The reaction was stirred 30 minutes at room temperature during which time the reaction became dark orange. Volatiles were removed *in vacuo* to afford a crude solid that was dissolved in the minimum amount of Et_2O (*ca.* 5 mL), diluted with hexanes (10 mL) and rapidly filtered through celite. This solution was rapidly concentrated *in vacuo* (*ca.* 10 mL) to remove excess Et_2O and placed under a CO atmosphere for 30 minutes where orange crystals of the product immediately separated. Volatiles were removed *in vacuo*, the product washed with hexanes (2 x 2 mL) and dried briefly *in vacuo*. Yield: 48 mg (90%). X-ray quality crystals were grown

by layering a concentrated toluene solution with hexanes. ^{1}H NMR (500 MHz, C_6D_6); under CO: δ 8.35, 7.67, 6.58. Evans Method (C_6D_6): μ_B 1.5 ± 0.1. UV-Vis-NIR (THF): λ_{max} (nm) (ε_{max} ($M^{-1}cm^{-1}$)) 1121 (sh, 2.0 x 10^3), 801 (1.9 x 10^3), 544 (sh, 7.1 x 10^2). FT-IR: ν_{max} cm^{-1} 2546 (BH), 1992, 1907 (CO). Anal. Calc. for $C_{32}H_{28}BFeN_6O_2$: C, 64.57 H, 4.74 N, 14.12. Found: C, 64.37 H, 4.86 N, 14.12.

6.4.5) $Tp^{Ph,Me}Fe(CO)$ (6).

A solution of **5** (97 mg, 0.163 mmol) in THF (3 mL) was refluxed under an atmosphere of N_2 for 4 hours during which time the solution became yellow. The reaction mixture was added three volumes of hexane (9 mL) and concentrated *in vacuo* whereupon the product crystallized. An additional recrystallization from THF/hexanes yielded material suitable for elemental analysis. Yield: 90 mg (97%). X-ray quality crystals were grown by layering a concentrated toluene solution with hexanes. ^{1}H NMR (500 MHz, C_6D_6): δ 38.04, 24.19, 23.66, 10.25, 6.18, –6.36. Evans Method (C_6D_6): μ_B 4.4 ± 0.1. UV-Vis-NIR (THF): λ_{max} (nm) (ε_{max} ($M^{-1}cm^{-1}$)) 463 (6.1 x 10^2), 940 (4.8 x 10^2), 1229 (3.8 x 10^2), 1522 (2.1 x 10^2). FT-IR: ν_{max} cm^{-1} 2545 (BH), 1889 (CO). Anal. Calc. for $C_{31}H_{28}BFeN_6O$ (1 x C_4H_8O): C 65.75; H 5.68; N 13.14. Found: C 65.13; H 5.88; N 13.43.

6.4.6) $Tp^{Ad,Me}Fe(1\text{-}CO)$.

A solution of **1** (35 mg, 0.047 mmol) in toluene (3 mL) was degassed *via* 3 freeze-pump-thaw-cycles and placed under an atmosphere of CO. After stirring for 1 hour volatiles were removed *in vacuo* to afford a yellow-brown crystalline

solid. The product was suspended in ether (3 mL) and collected by filtration. Cooling the mother liquor to –35 °C gave a second crop of crystalline material. Overall yield: 32 mg (91%). An analytical sample was obtained *via* recrystallization from toluene-hexane. ^{1}H NMR (C_6D_6): δ 39.17, 22.79, 16.43, 2.74, 1.29. Evans Method (C_6D_6): μ_B 4.0±0.3. FT-IR: ν_{max} cm^{-1} 1960 (CO), 2547 (BH). UV-Vis-NIR (THF): λ_{max} nm (ε_{max} M^{-1} cm^{-1}) 434 (1.8 × 10^3), 895 (1.1 × 10^3), 1154 (9.6 × 10^2), 1400(sh). Anal. Calc. for $C_{43}H_{58}BFeN_6O$ (0.5 x C_6H_{14}): C: 70.41; H: 8.35; N: 10.71. Found: C: 70.56; H: 8.60; N: 11.08.

6.4.7) [Tp^{Ad,Me}Fe(MeCN)][BAr$^F_4$] (1$^+$).

A solution of Ag[BAr$^F_4$] (0.027 g,0.0280 mmol) in DCM (2 mL) was added to a suspension of [Tp^{Ad,Me}FeCl] (0.020 g, 0.0280 mmol) in DCM (2 mL) containing a drop of MeCN. After stirring for 30 minutes, AgCl was removed *via* filtration and the filtrate diluted with hexane (6 mL). Standing for several hours yielded large colorless needles of the complex that were collected by filtration and washed with several portions of hexane. Yield: 0.041 g, 93%. ^{1}H NMR (CD_2Cl_2): δ 79.48, 69.97, 45.81, 28.00, 8.90, 7.65 (BAr$^F_4$), 7.50 (BAr$^F_4$), 6.48, 1.09, –19.76.

6.4.8) Tp^{Ad,Me}Fe(N$_2$)Li(THF)$_3$ (1$^-$-Li).

A saturated THF solution of **1** (52 mg, 0.070 mmol) was prepared by slow addition of THF (*ca.* 4 mL) to a stirred THF (*ca.* 1 mL) suspension of the complex until all of the solid had dissolved. This solution was filtered through a short pad of celite to ensure complete homogeneity. Freshly cut Li metal (*ca.* 200 mg) was

added rapidly and the solution immediately placed in a –35 °C freezer. After standing un-agitated overnight a dark blue solution was obtained. Two volumes of HMDSO which had been pre-cooled to –35 °C were added and the solution rapidly filtered through a small piece of filter paper. The filtrate was stored at –35 °C for 2 days to afford black prismatic crystals of **1^{-}-Li** which were collected by filtration. Yield: 65 mg (84%). Crystals suitable for XRD studies were grown according to the same method but using a THF-DME (1:1) solvent mixture to dissolve **1**. ^{1}H NMR (THF-d_8, –40 °C, 600 MHz): δ 29.41, 17.57, 14.94, 5.39, -46.15. The complex suffered extensive decomposition to give **1** on compression and so obtaining good IR data was difficult. FT-IR: ν_{max} cm^{-1} 1772 (NN), 2500 (BH). Calc. for $C_{54}H_{82}BFeLiN_8O_3.(THF)_2$: C: 67.14; H: 8.91; N: 10.10. Found: C: 67.29; H: 8.74; N: 10.16.

6.4.9) Tp^{Ad,Me}Fe(N$_2$)Na(THF)$_4$ (1^{-}-Na).

A deep blue-green solution of **1^{-}-Na** in THF could be prepared as per the synthesis of **1^{-}-Li**; however, addition of HMDSO caused an immediate color change to pink and deposition of crystalline **1**. Thus, X-ray quality crystals of **1^{-}-Na** were prepared as follows. A saturated solution of **1** in HMDSO-THF (2:1, *ca.* 2 mL)) was prepared at room temperature and then cooled to –35 °C overnight. The pink crystals of **1** were quickly removed by filtration and the solution cooled back to –35 °C. A roughly 0.5 x 0.5 mm piece of *clean* sodium was added and

the mixture allowed to stand for a week. By this time, plate-like, black crystals of **1^{-}-Na** had grown on the sodium surface which were subjected to XRD studies.

6.5) Spectroscopic Data

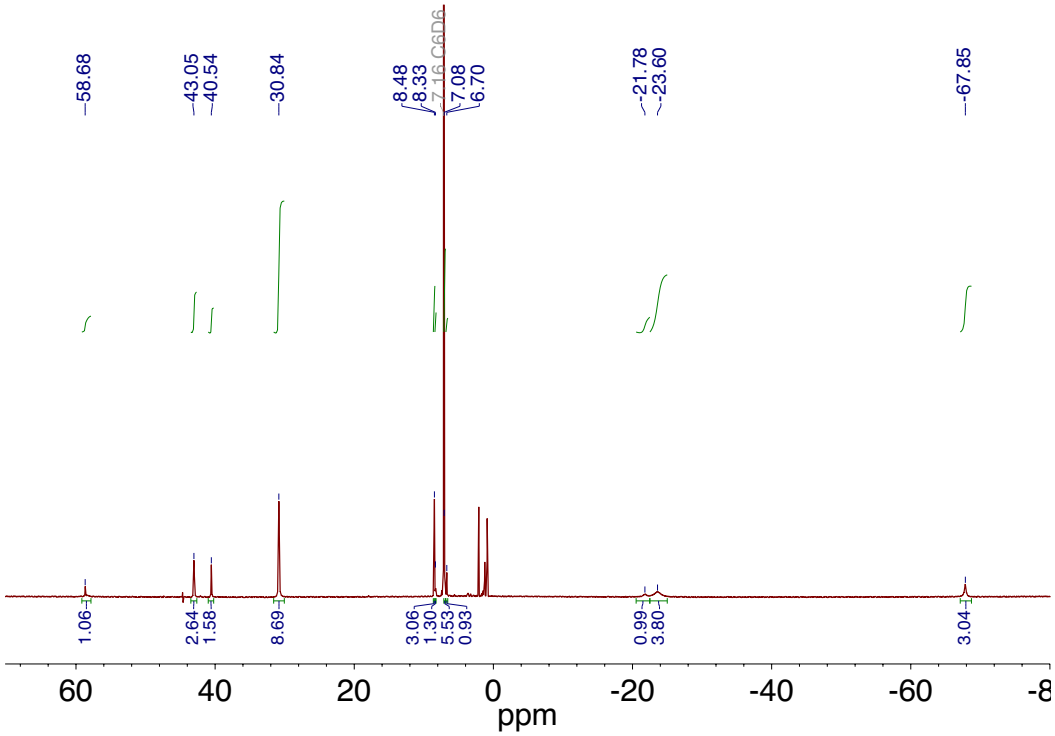

Figure 6.5.1. ^{1}H NMR spectrum of **Tp^{Ph,Me}Fe(Ph$_2$CO)** recorded at 500 MHz in C_6D_6.

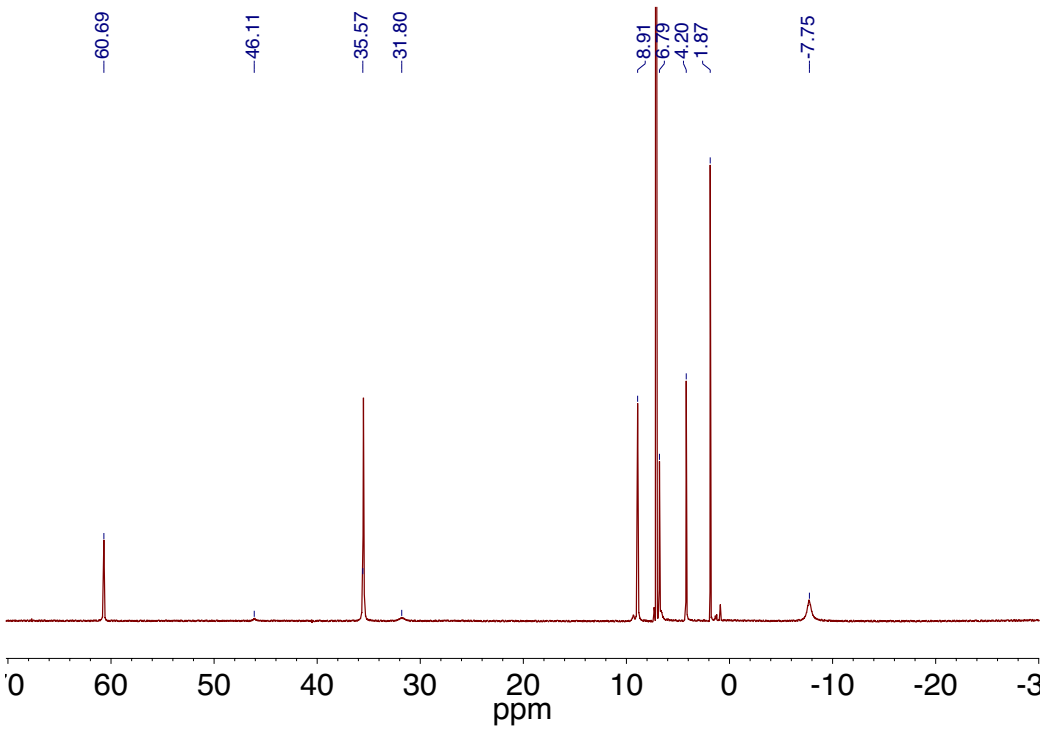

Figure 6.5.2. ^{1}H NMR spectrum of **Tp^{Ph,Me}Fe(I)(THF)** recorded at 500 MHz in C_6D_6.

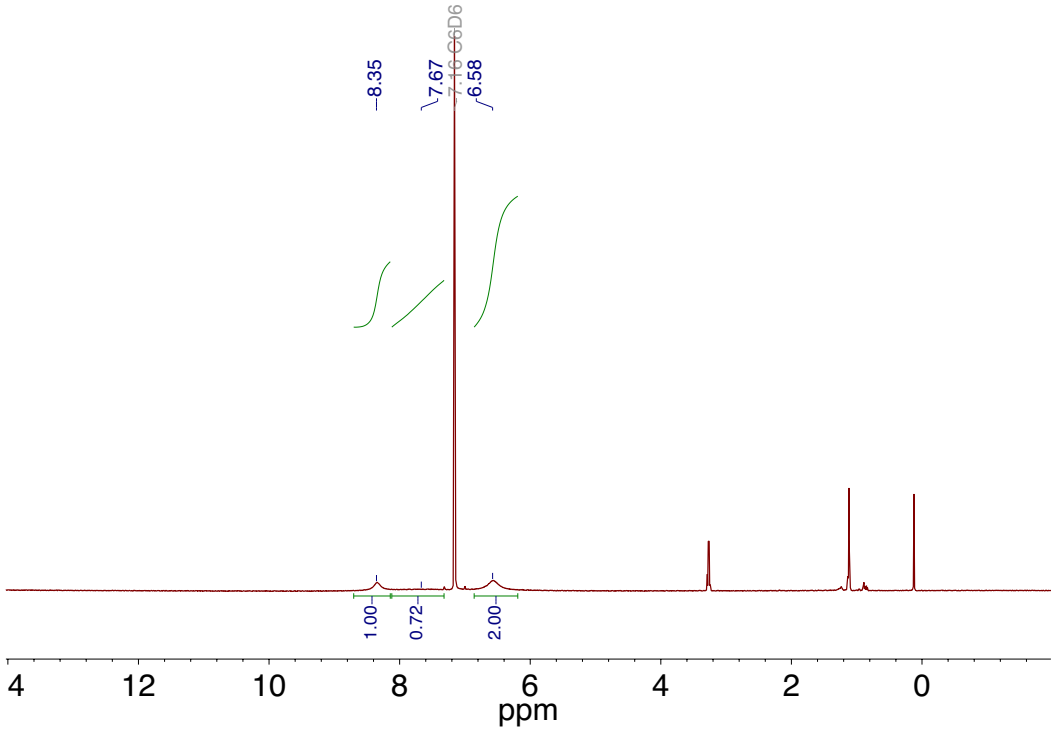

Figure 6.5.3. ^{1}H NMR spectrum of **Tp^{Ph,Me}Fe(CO)$_2$** recorded at 500 MHz in C_6D_6.

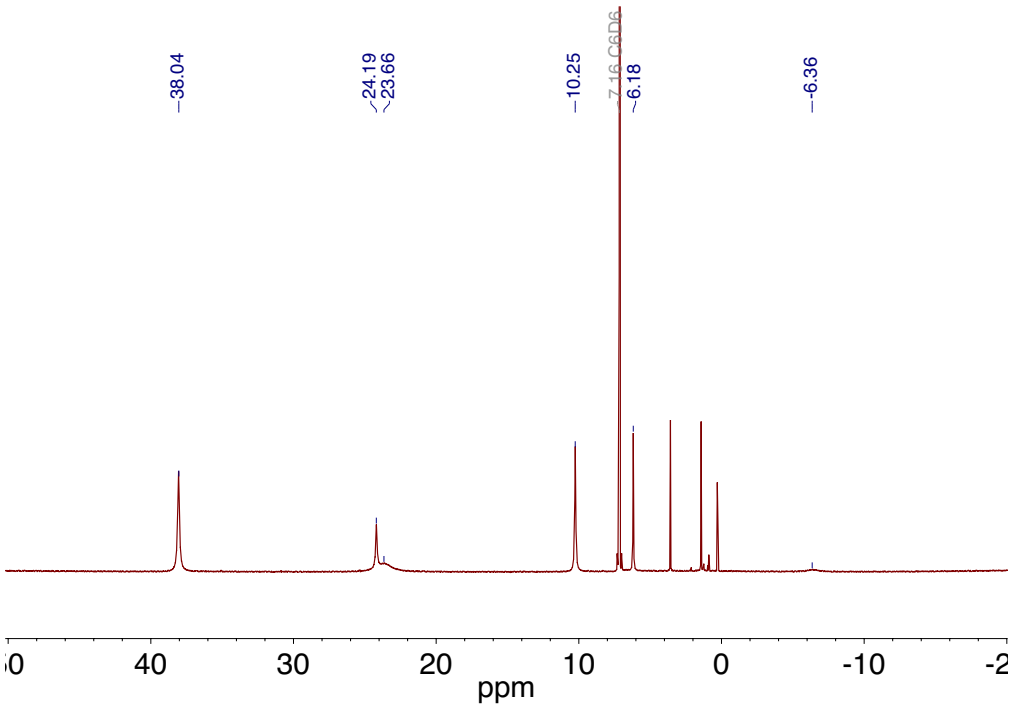

Figure 6.5.4. ^{1}H NMR spectrum of **Tp^{Ph,Me}Fe(CO)** recorded at 500 MHz in C_6D_6.

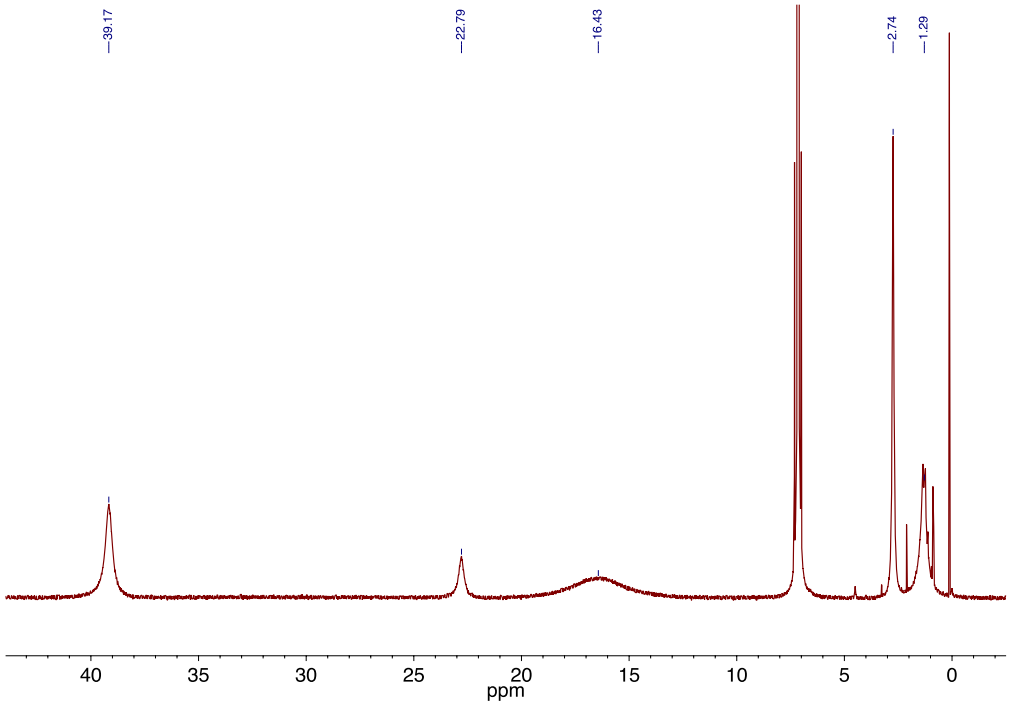

Figure 6.5.5. ^{1}H NMR spectrum of **Tp^{Ad,Me}Fe(CO)** recorded at 500 MHz in C_6D_6.

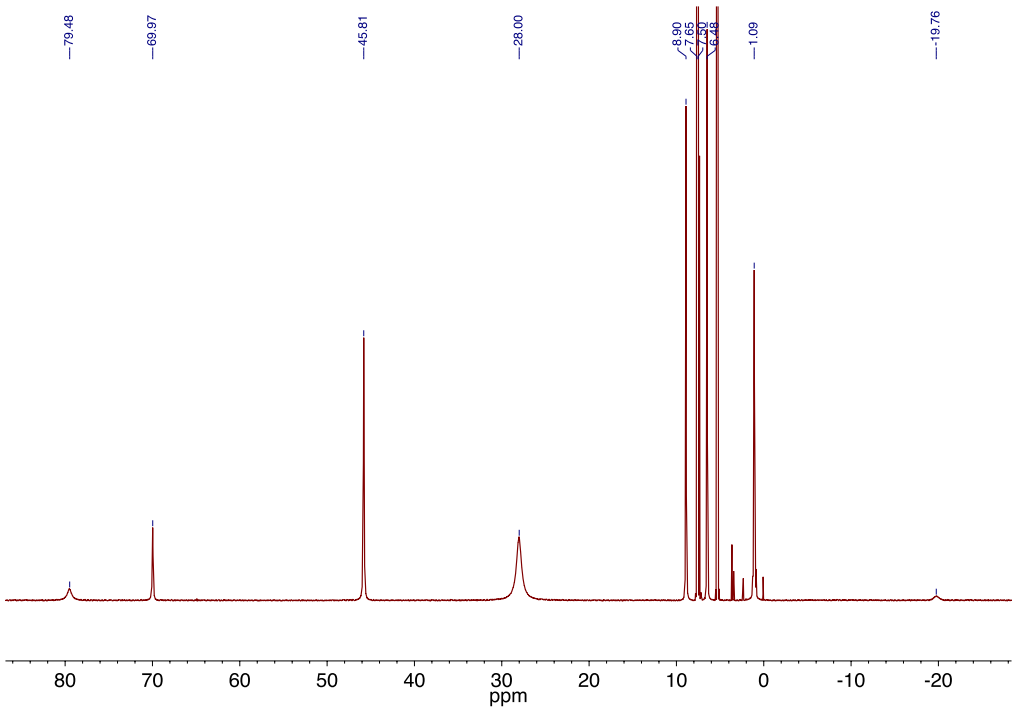

Figure 6.5.6. ^{1}H NMR spectrum of **[Tp^{Ad,Me}Fe(MeCN)][BAr$^{F}_{4}$]** recorded at 500 MHz in CD_2Cl_2.

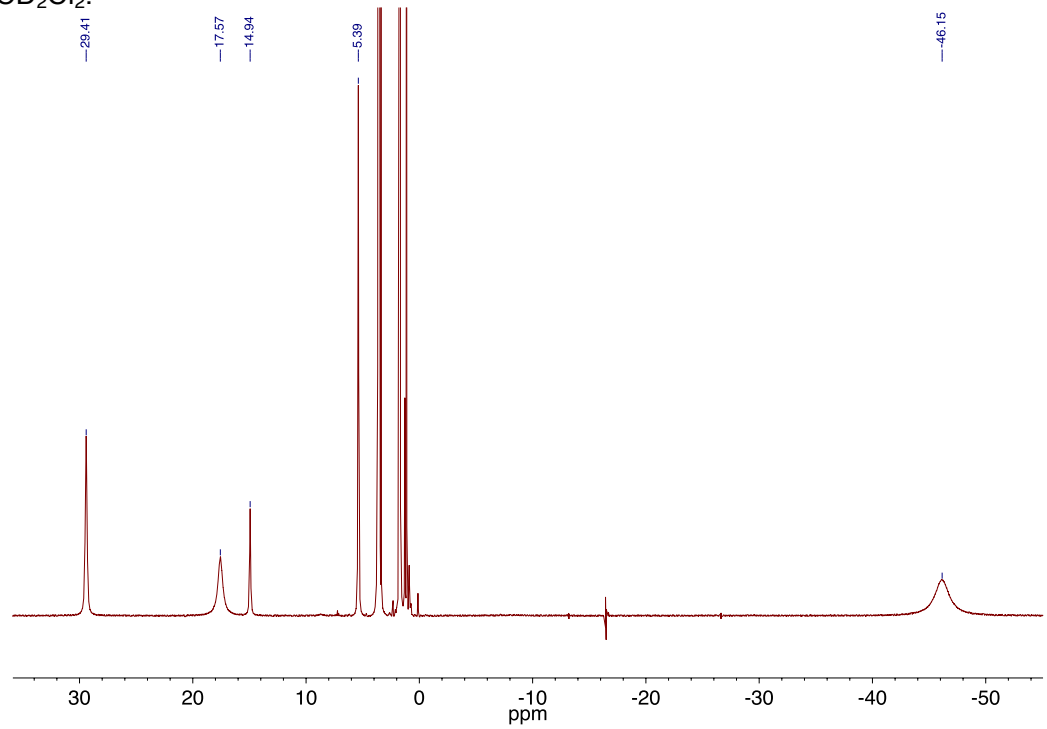

Figure 6.5.7. ^{1}H NMR spectrum of **Tp^{Ad,Me}Fe(N$_2$)Li(THF)$_3$** recorded in THF-d_8 at –40 °C at 600 MHz.

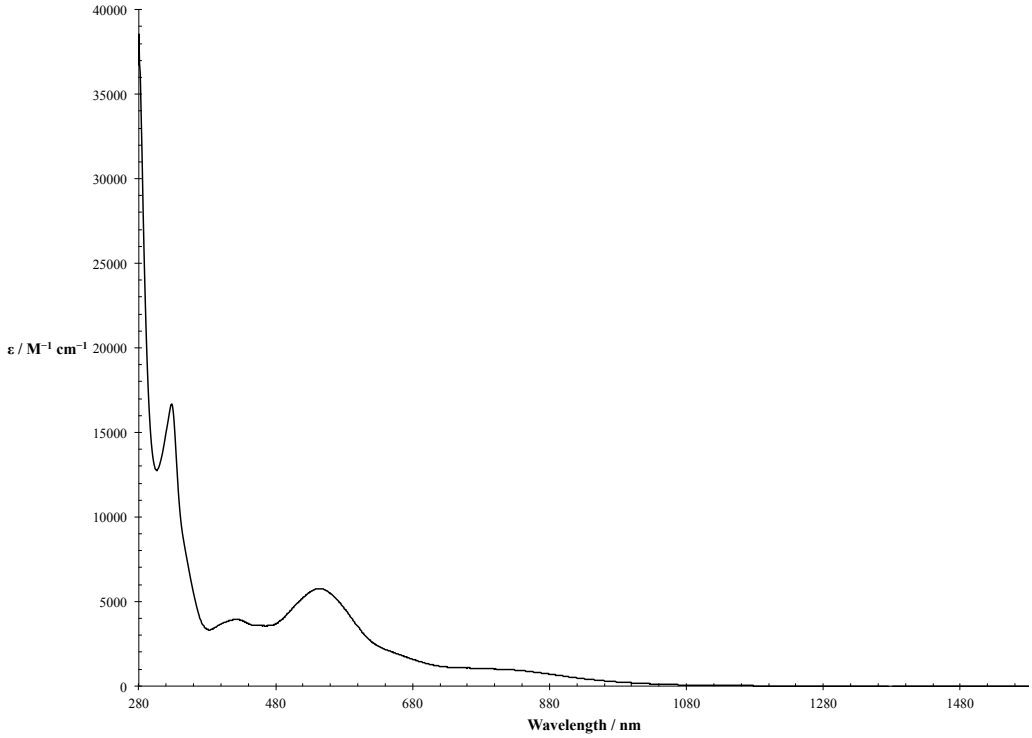

Figure 6.5.8. UV-Vis-NIR spectrum of **$Tp^{Ph,Me}Fe(Ph_2CO)$.**

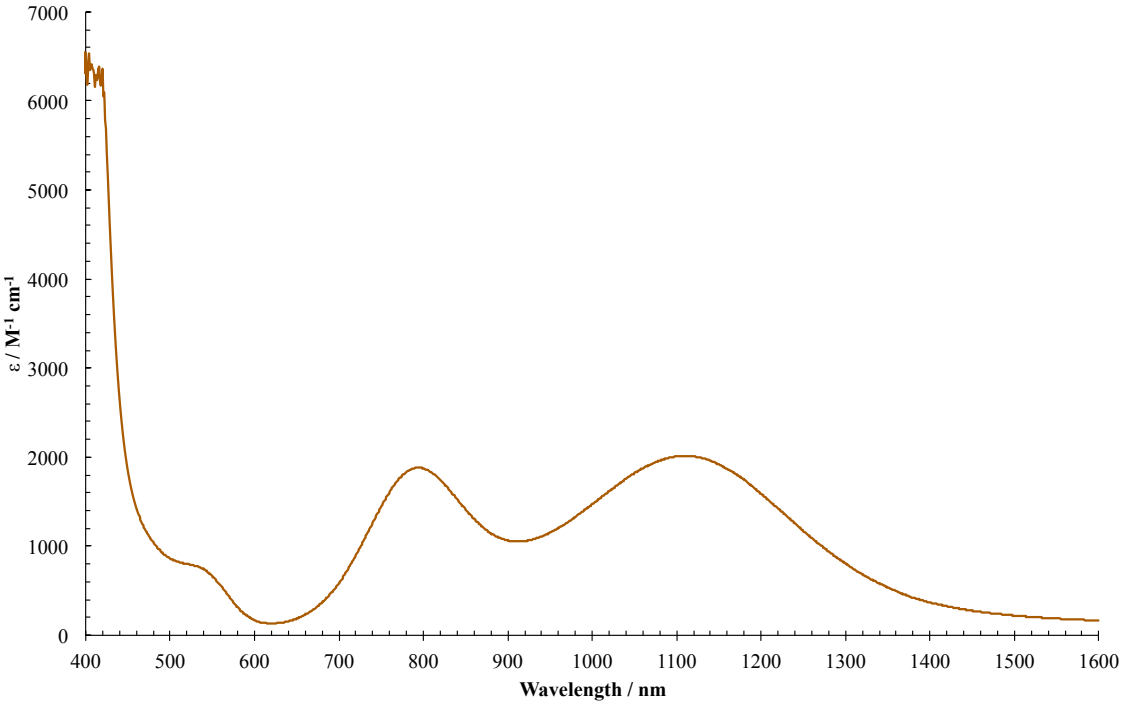

Figure 6.5.9. UV-Vis-NIR spectrum of **$Tp^{Ph,Me}Fe(CO)_2$** in THF.

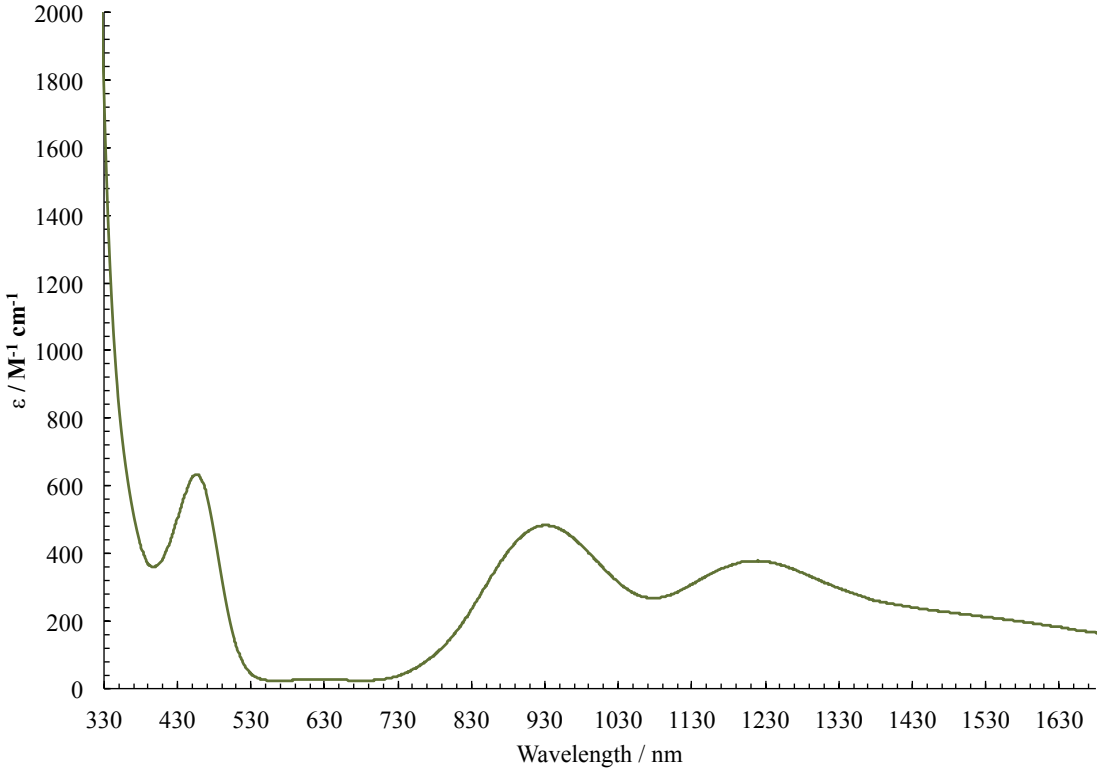

Figure 6.5.10. UV-Vis spectrum of **Tp^{Ph,Me}Fe(CO)** in THF.

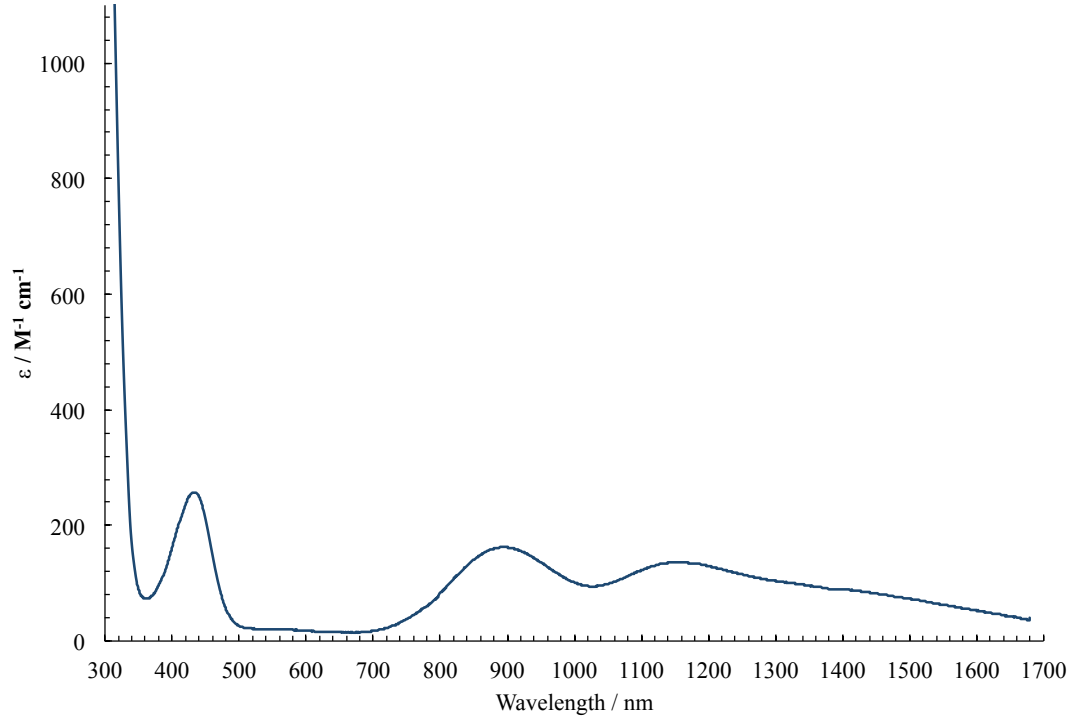

Figure 6.5.11. UV-Vis-NIR spectrum of **Tp^{Ad,Me}Fe(CO)** in THF.

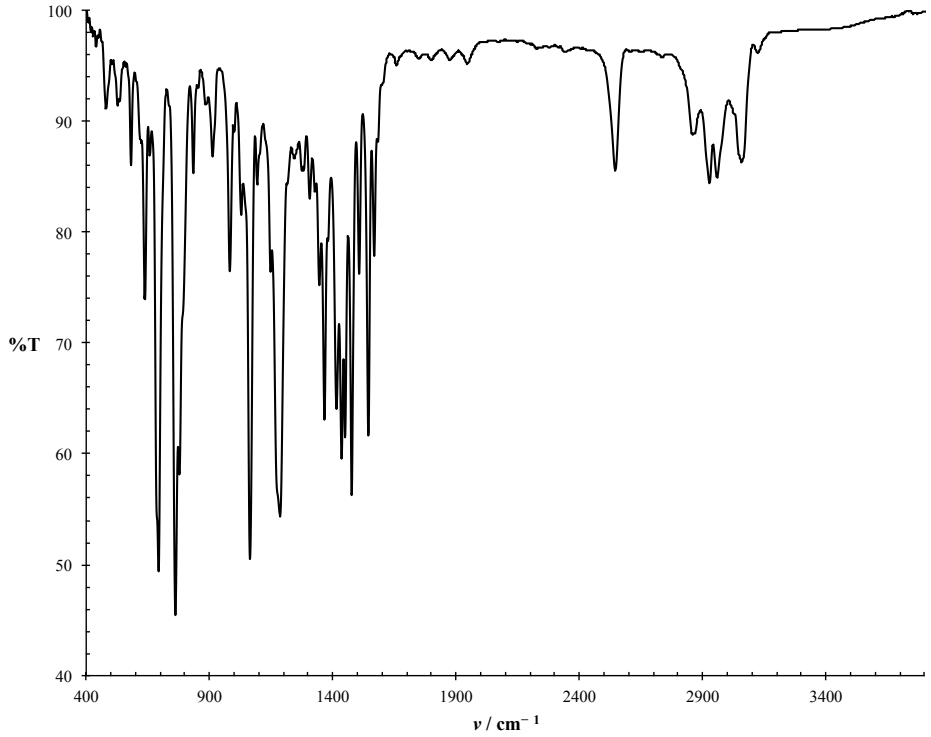

Figure 6.5.12. FT-IR spectrum of **$Tp^{Ph,Me}Fe(Ph_2CO)$.**

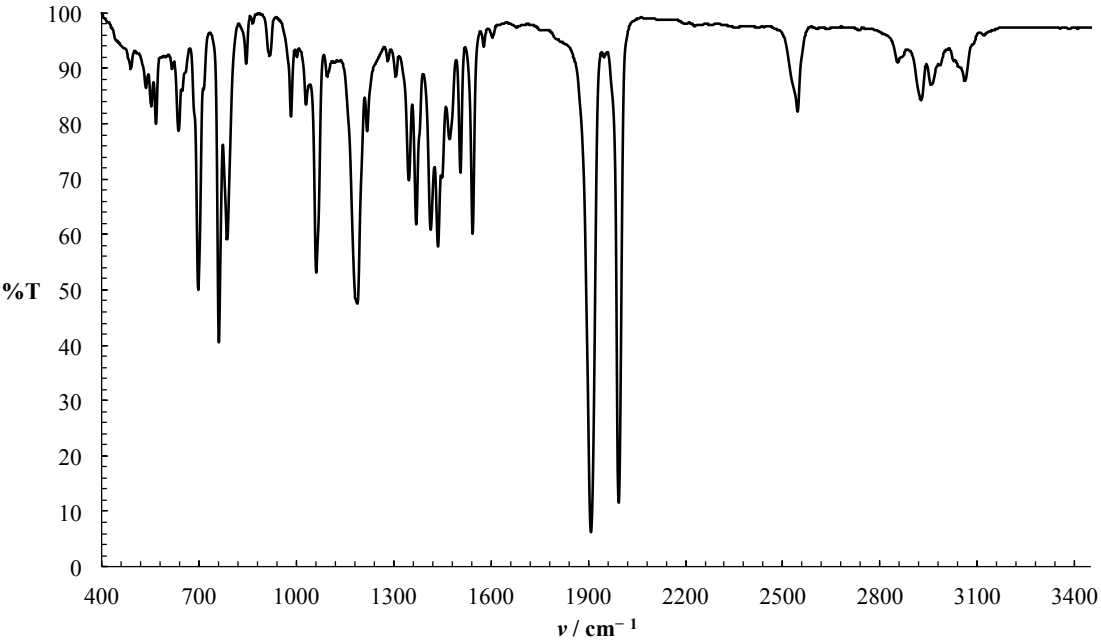

Figure 6.5.13. FT-IR spectrum of **$Tp^{Ph,Me}Fe(CO)_2$.**

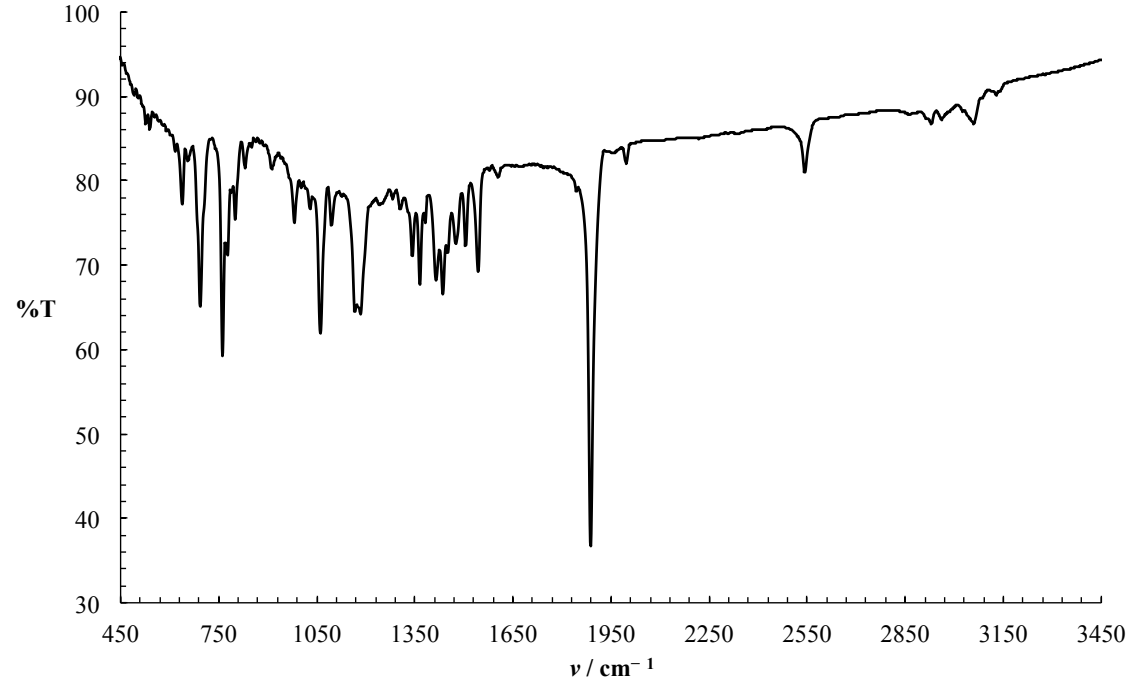

Figure 6.5.14. FT-IR spectrum of **$Tp^{Ph,Me}Fe(CO)$**.

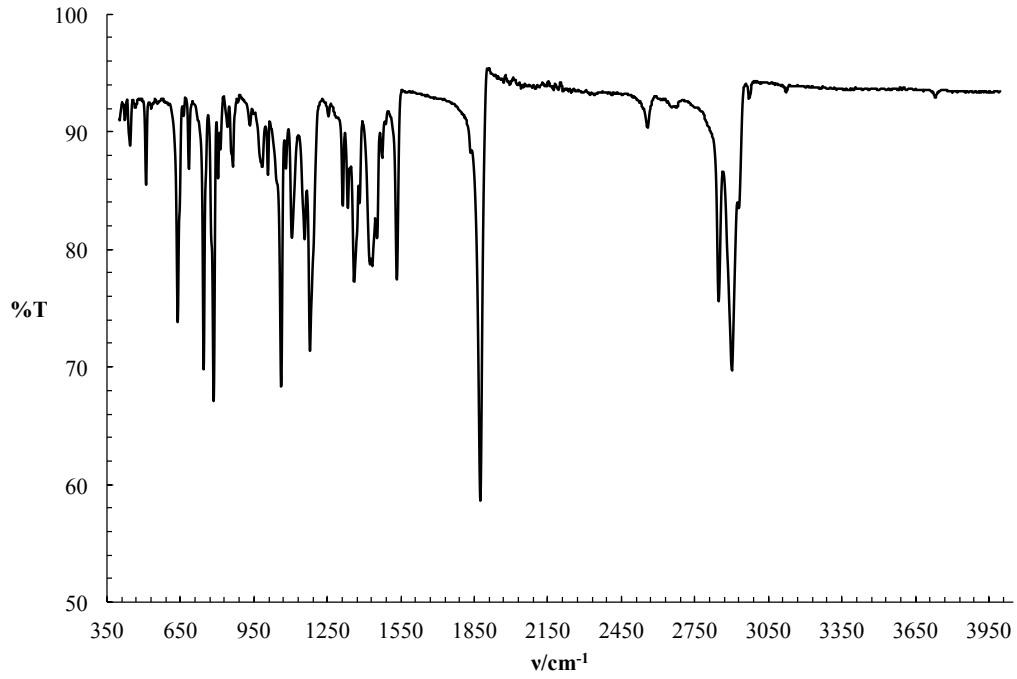

Figure 6.5.15. FT-IR spectrum of **$Tp^{Ad,Me}Fe(CO)$**.

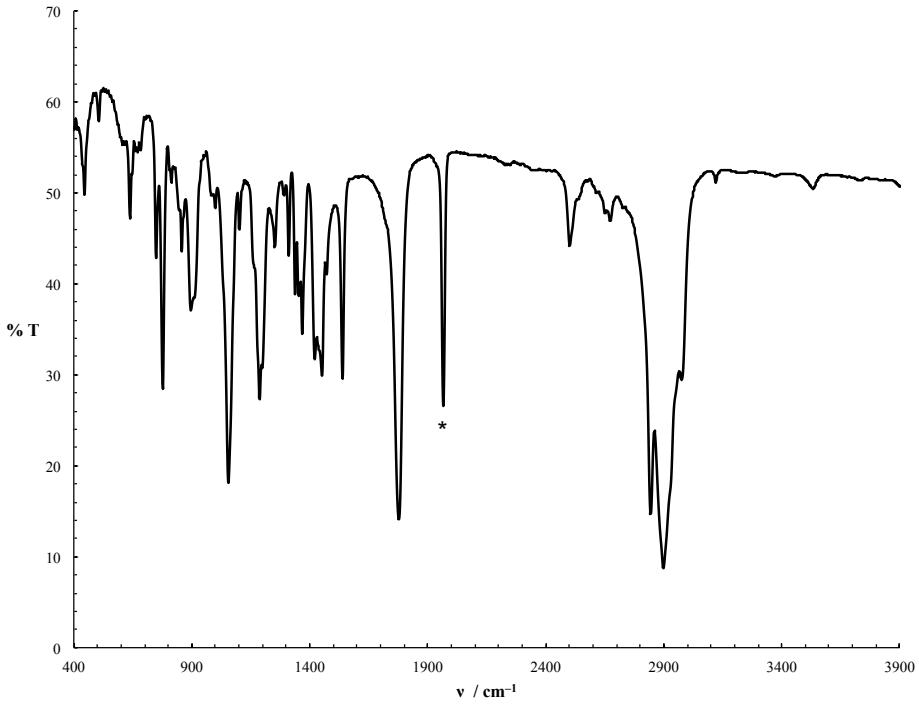

Figure 6.5.16. FT-IR spectrum of $\mathbf{Tp^{Ad,Me}Fe(N_2)Li(THF)_3}$. The peak marked with an asterisk is due to $\mathbf{Tp^{Ad,Me}Fe(N_2)}$.

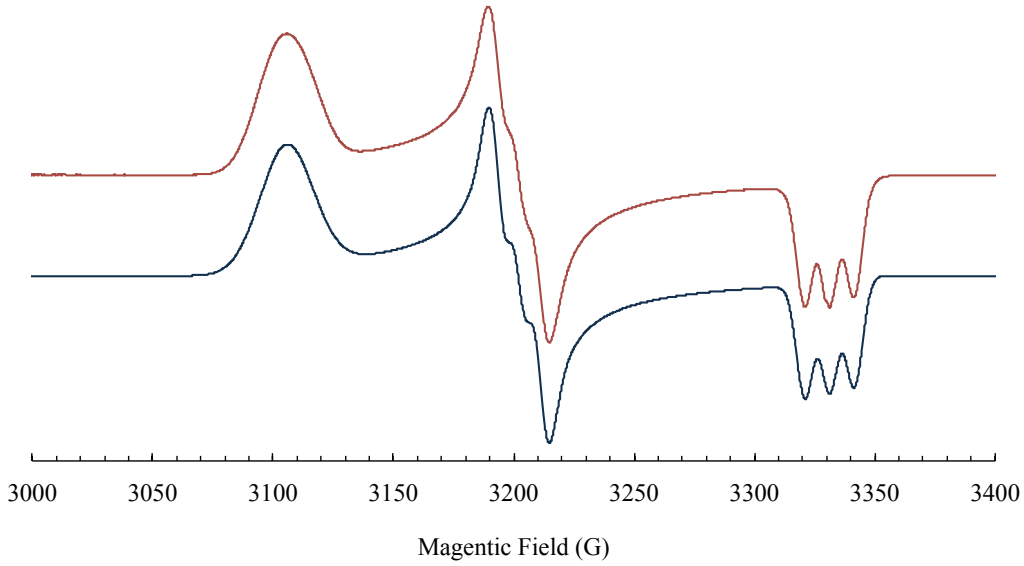

Figure 6.5.17. X-band EPR spectrum (9.323 GHz) of $\mathbf{Tp^{Ph,Me}Fe(CO)_2}$ in 2-MeTHF at 109 K (**red**) and its simulated spectrum (**blue**). Simulation parameters: g_1 = 2.10665, g_2 = 2.04413, g_3 = 1.96622; A_1[N] = 1 MHz, A_2[N] = 25 MHz, A_3[B] = 28 MHz; $HStrain_1$ = 75.9, $HStrain_2$ = 22.0, $HStrain_3$ = 21.4; lw = 0.25.

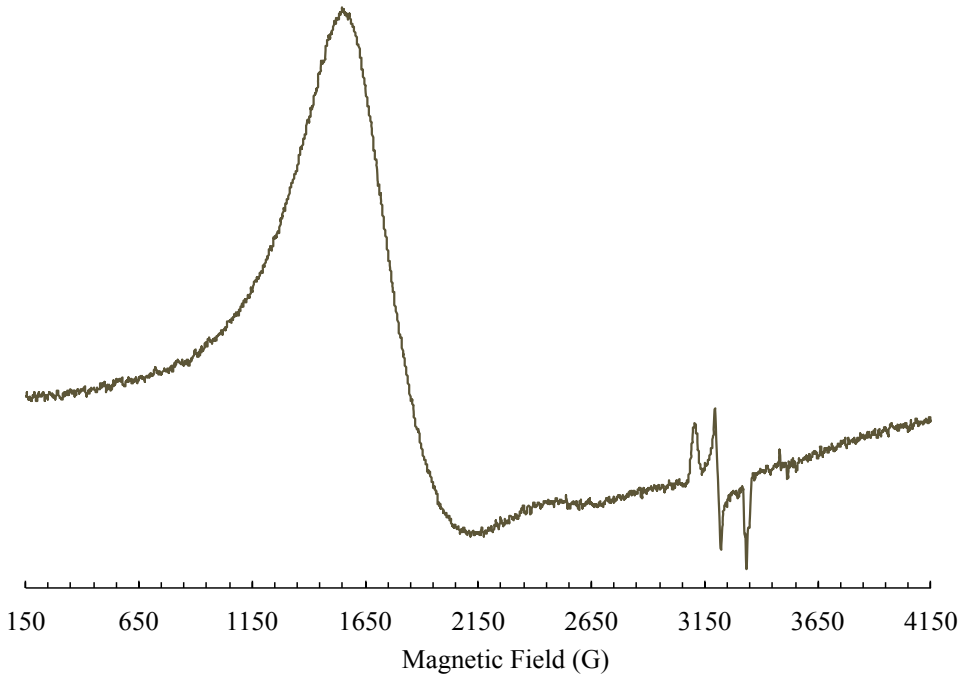

Figure 6.5.18. X-band EPR spectrum (9.326 GHz) of a mixture of **$Tp^{Ph,Me}Fe(CO)$** and **$Tp^{Ph,Me}Fe(CO)_2$** in 2-MeTHF at 104 K (**olive**).

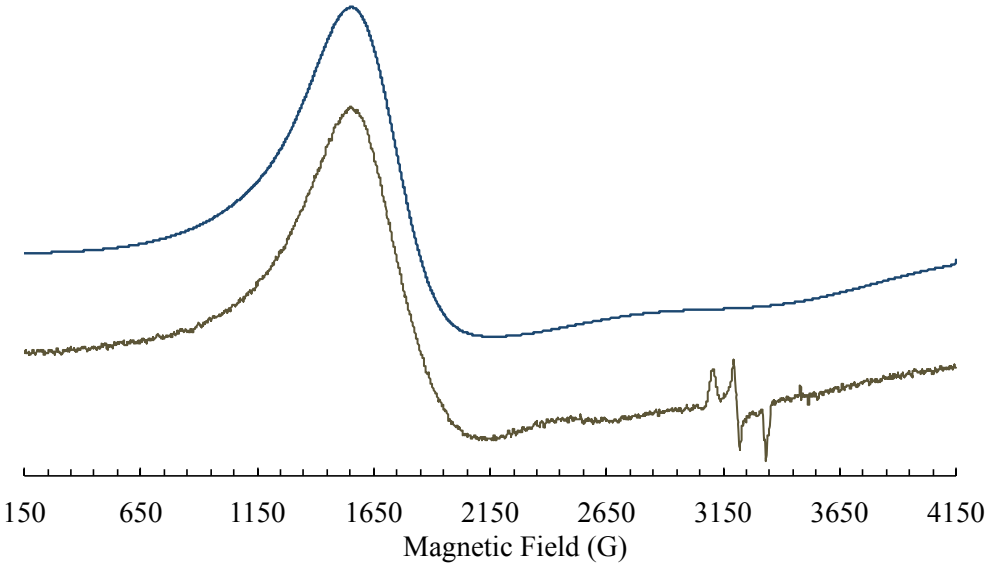

Figure 6.5.19. X-band EPR spectrum (9.326 GHz) of a mixture of **$Tp^{Ph,Me}Fe(CO)$** and **$Tp^{Ph,Me}Fe(CO)_2$** in 2-MeTHF at 104 K (**olive**) and a simulation of the high-spin signal for **$Tp^{Ph,Me}Fe(CO)$** (**blue**). Simulation parameters: g_1 = 3.7707, g_2 = 3.9830, g_3 = 1.9703; $gStrain_1$ = 2.570, $gStrain_2$ = 0.812, $gStrain_3$ = 0.597; lw = 0.2.

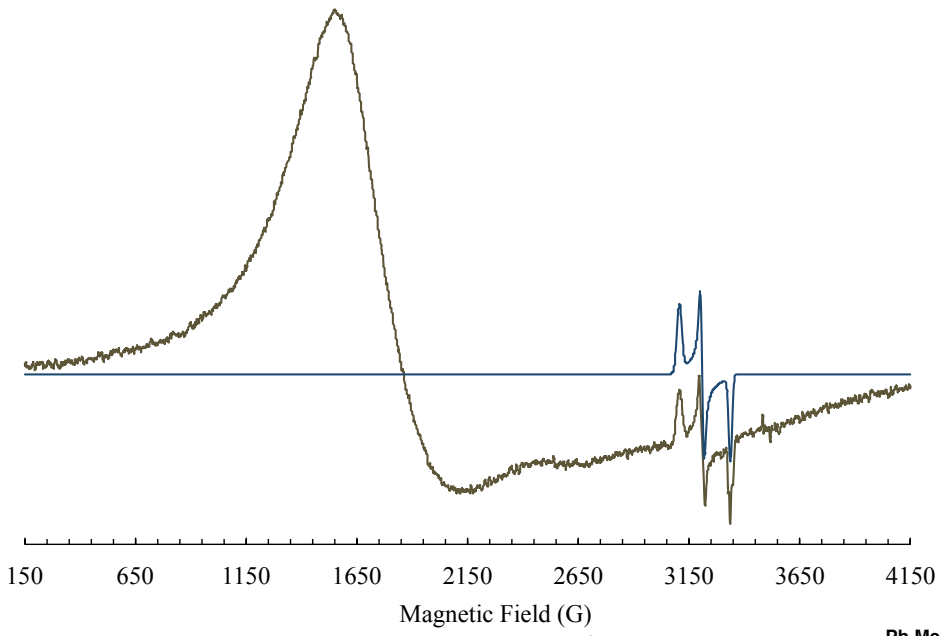

Figure 6.5.20. X-band EPR spectrum (9.326 GHz) of a mixture of **Tp^{Ph,Me}Fe(CO)** and **Tp^{Ph,Me}Fe(CO)$_2$** in 2-MeTHF at 104 K (**olive**) and a simulation of the low-spin signal for **Tp^{Ph,Me}Fe(CO)$_2$** (**blue**). Simulation parameters: g_1 = 2.1460, g_2 = 2.0768, g_3 = 1.9975; A_1[N] = 1 MHz, A_2[B] = 11 MHz, A_3[B] = 28 MHz; HStrain$_1$ = 64.0, HStrain$_2$ = 11.0, HStrain$_3$ = 11.0; lw = 1.50.

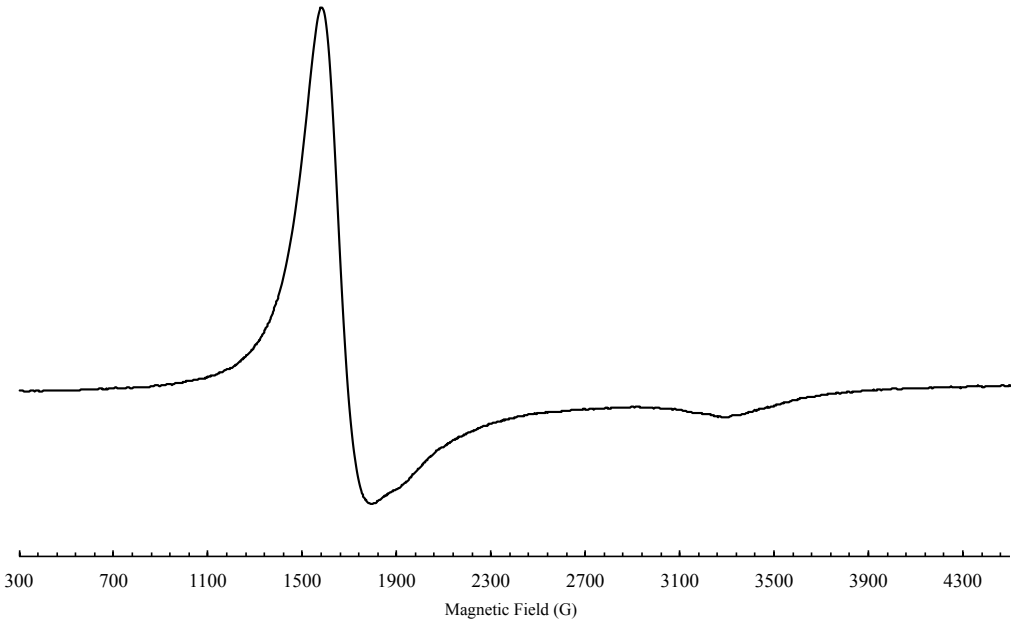

Figure 6.5.21. X-band EPR spectrum (9.312 GHz) of **Tp^{Ad,Me}Fe(CO)** in 2-MeTHF at 107 K.

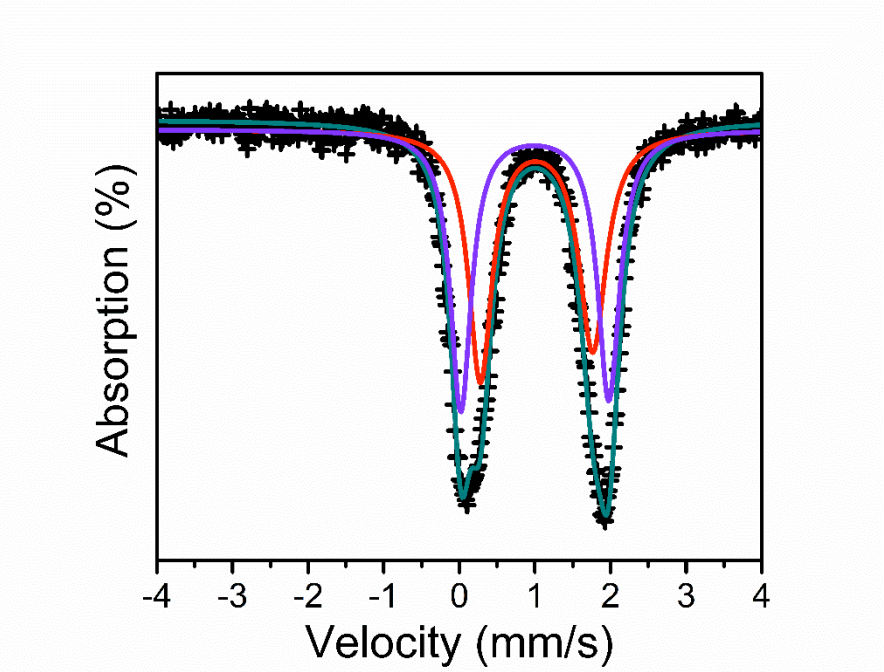

Figure 6.5.22. Zero-field Mössbauer spectrum of **$Tp^{Ph,Me}Fe(Ph_2CO)$** collected at 80 K. Simulation parameters: **Site 1**: δ = 1.022(4) mm/s, Q.S. = 1.487(7) mm/s, Γ_L = 0.38, Γ_R = 0.43; **Site 2**: δ = 0.999(3) mm/s, Q.S. = 1.959(5) mm/s, Γ_L = 0.33, Γ_R = 0.35

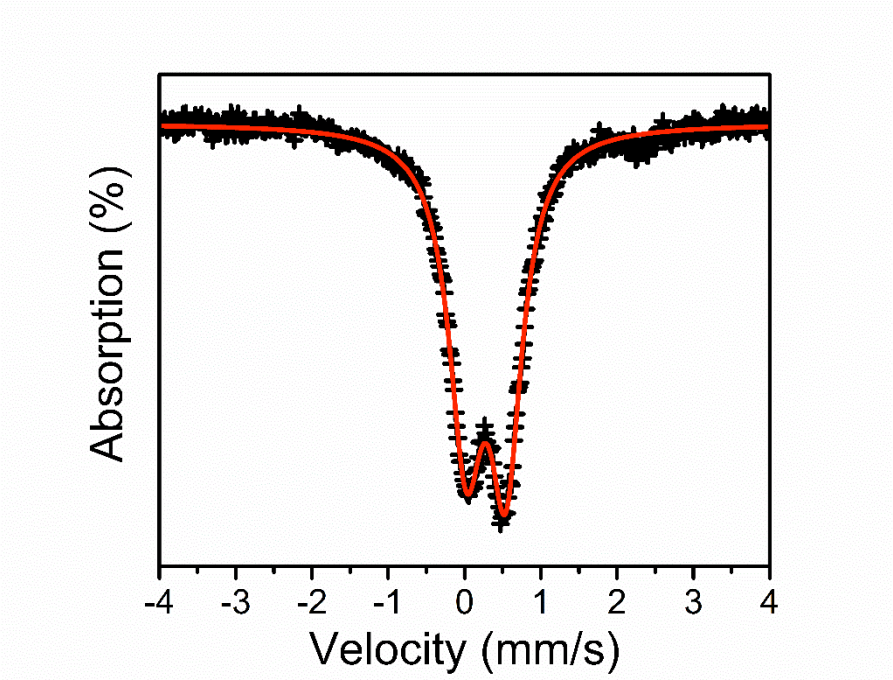

Figure 6.5.23. Zero-field Mössbauer spectrum of **$Tp^{Ph,Me}Fe(CO)_2$** collected at 80 K. Simulation parameters: δ = 0.281(2) mm/s, Q.S. = 0.521(3) mm/s, Γ_L = 0.55, Γ_R = 0.52

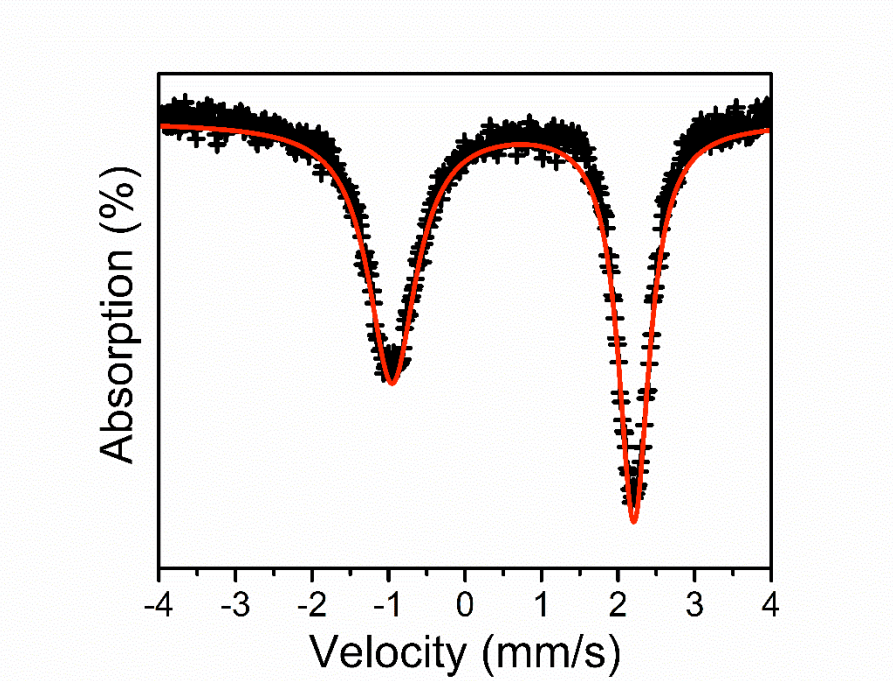

Figure 6.5.24. Zero-field Mössbauer spectrum of **$Tp^{Ph,Me}Fe(CO)$** collected at 80 K. Simulation parameters: δ = 0.626(3) mm/s, Q.S. = 3.160(5) mm/s, Γ_L = 0.76 Γ_R = 0.49

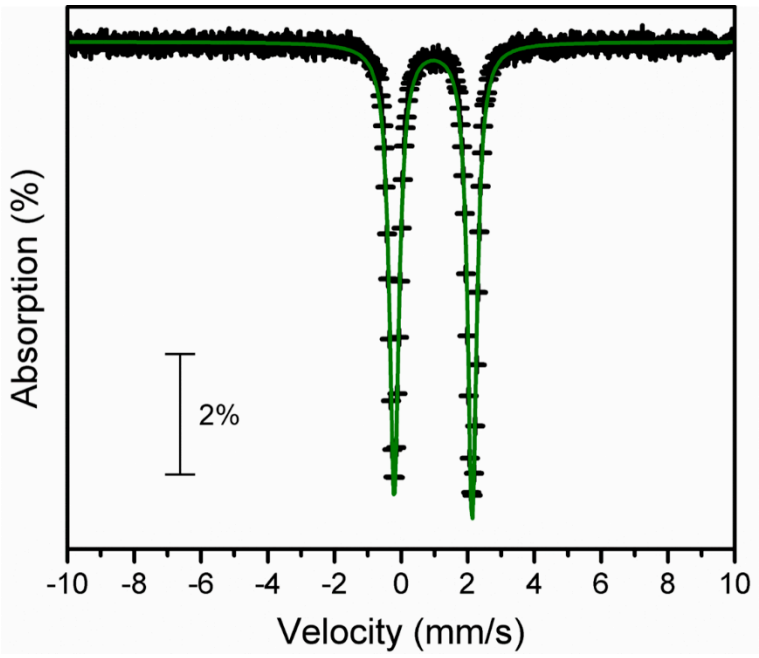

Figure 6.5.25. Zero-field Mössbauer spectrum of **$Tp^{Ad,Me}FeCl$** collected at 80 K. Simulation parameters: δ = 0.961(2) mm/s, Q.S. = 2.338(3) mm/s.

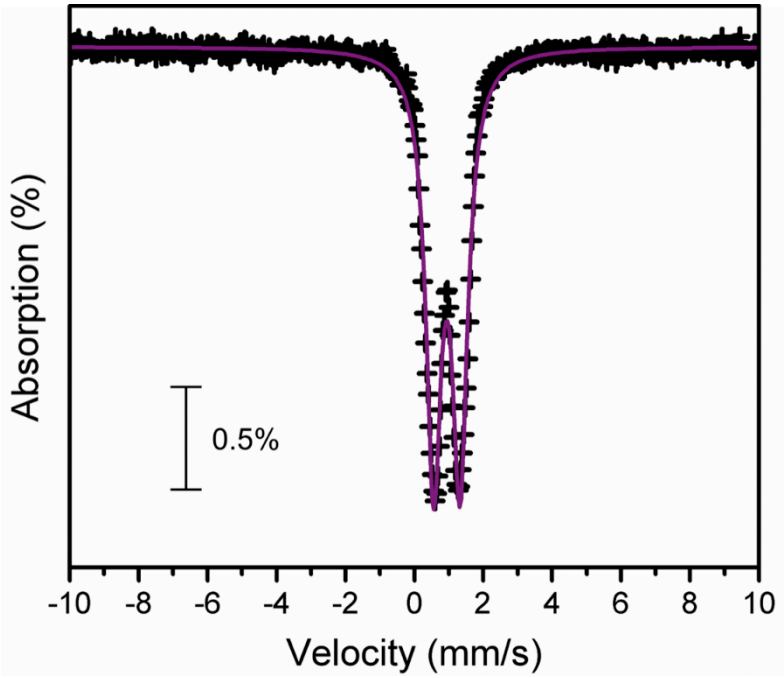

Figure 6.5.26. Zero-field Mössbauer spectrum of **$(Tp^{Ph,Me}Fe)_2(N_2)$** collected at 80 K. Simulation parameters: δ = 0.941(3) mm/s, Q.S. = 0.769(4) mm/s.

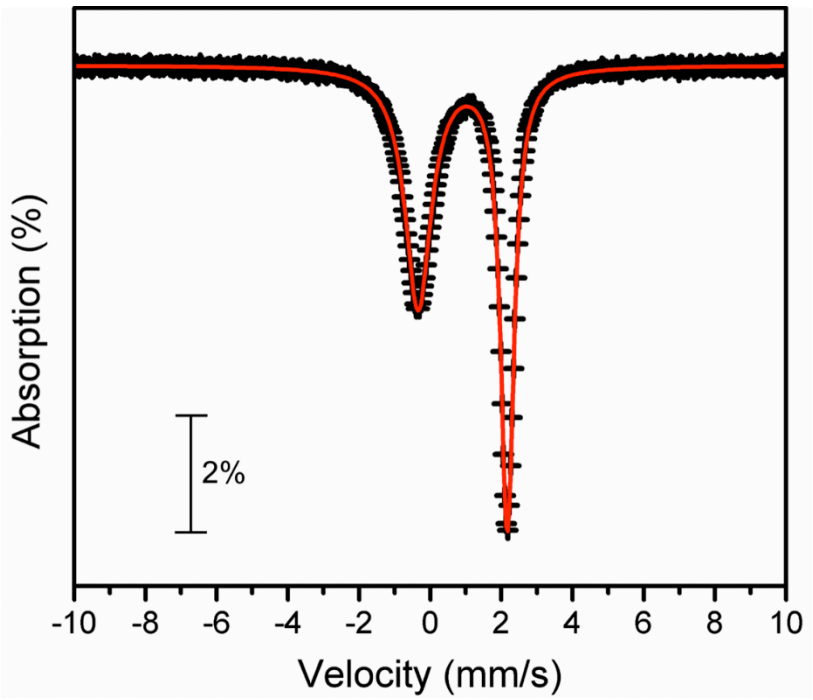

Figure 6.5.27. Zero-field Mössbauer spectrum of **$Tp^{Ad,Me}Fe(N_2)$** collected at 80 K. Simulation parameters: δ = 0.915(2) mm/s, Q.S. = 2.507(3) mm/s, Γ_L = 0.886 (7) Γ_R = 0.460 (3).

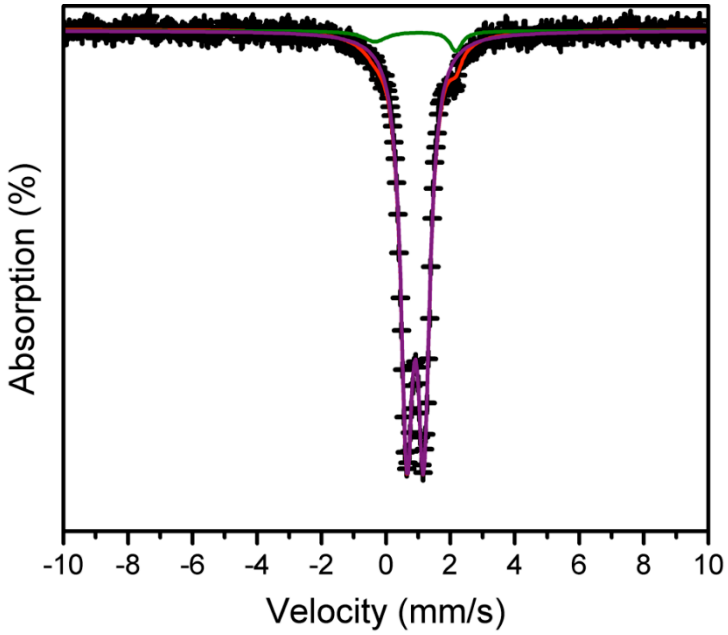

Figure 6.5.28. Zero-field Mössbauer spectrum of **$Tp^{Ad,Me}Fe(N_2)Li(THF)_3$)** collected at 80 K. Simulation parameters: δ = 0.909(2) mm/s, Q.S. = 0.524(3) mm/s, Γ_L = 0.453 Γ_R = 0.455.

6.6) X-Ray Crystallography

6.6.1) General Considerations

Single crystals were coated with paratone oil and mounted on cryo-loop glass fibers. X-ray intensity data were collected at 100(2) K on a Bruker APEX2[26] platform-CCD X-ray diffractometer system using fine-focus Mo Kα radiation (λ = 0.71073 Å, 50 kV/30 mA power). The CCD detector was placed at 5.0600 cm from the crystal. Frames were integrated using the Bruker SAINT software package[27] and using a narrow-frame integration algorithm. Absorption corrections were applied to the raw intensity data using the SADABS program.[28] The Bruker SHELXTL software package[29] was used for phase determination and structure refinement. Atomic coordinates, isotropic and anisotropic displacement parameters of all the non-hydrogen atoms were refined by means of a full matrix least- squares procedure on F^2. The H atoms were included in the refinement in calculated positions riding on the atoms to which they were attached. Relevant details for individual data collections are reported in Tables 6.6.1-6.6.8.

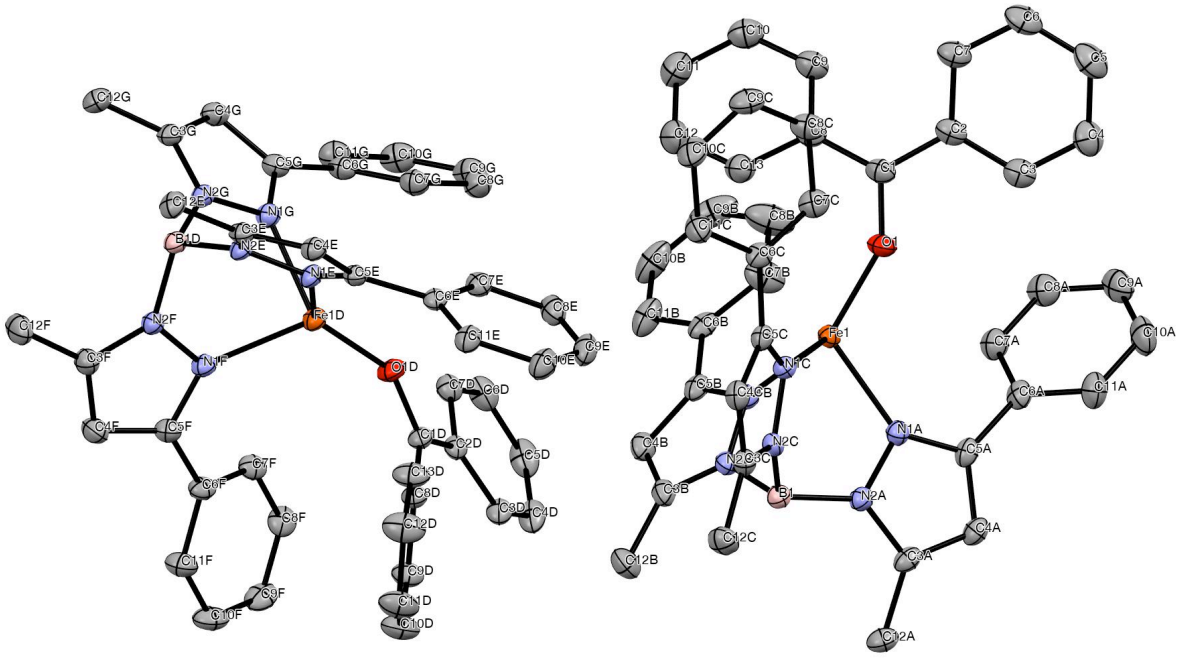

Figure 6.6.1. Labelled thermal ellipsoid plot (50%) for **$Tp^{Ph,Me}Fe(Ph_2CO)$**.

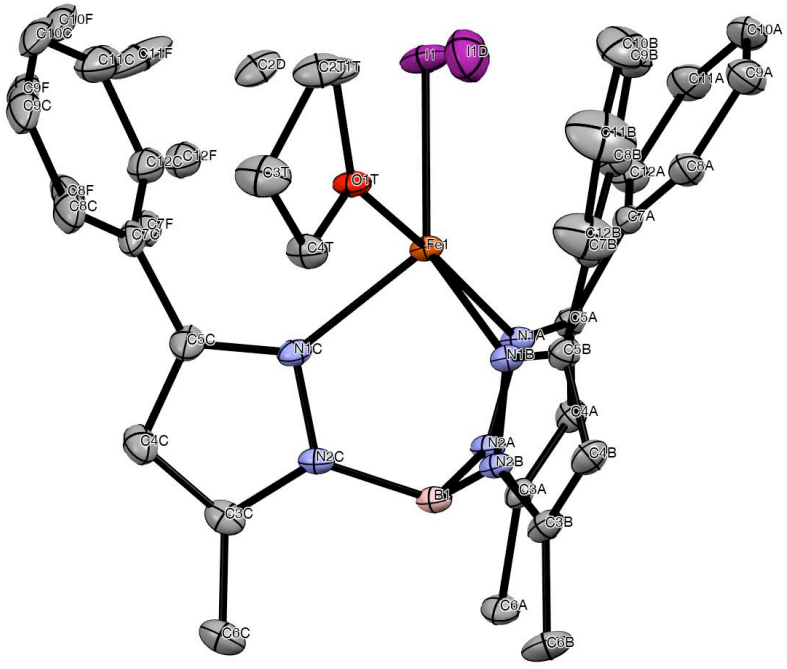

Figure 6.6.2. Labelled thermal ellipsoid plot (50%) for **$Tp^{Ph,Me}Fe(I)(THF)$**.

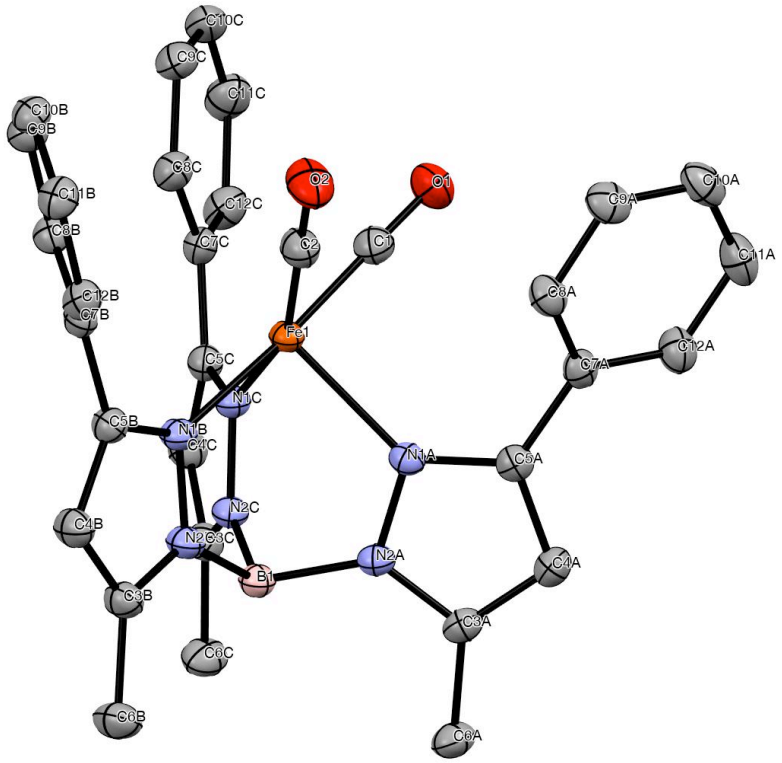

Figure 6.6.3. Labelled thermal ellipsoid plot (50%) for **$Tp^{Ph,Me}Fe(CO)_2$**.

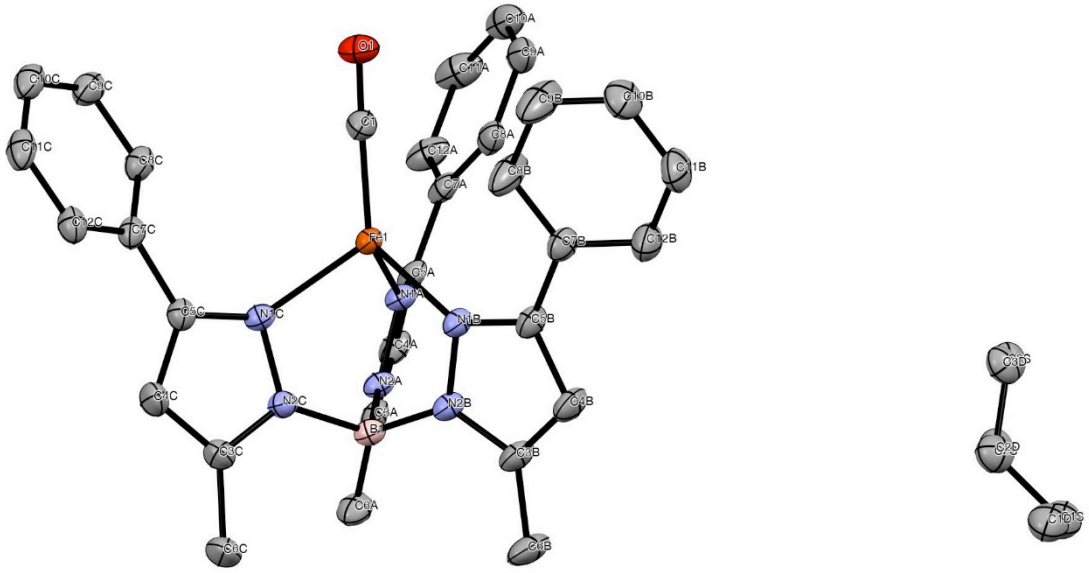

Figure 6.6.4. Labelled thermal ellipsoid plot (50%) for **$Tp^{Ph,Me}Fe(CO)$**.

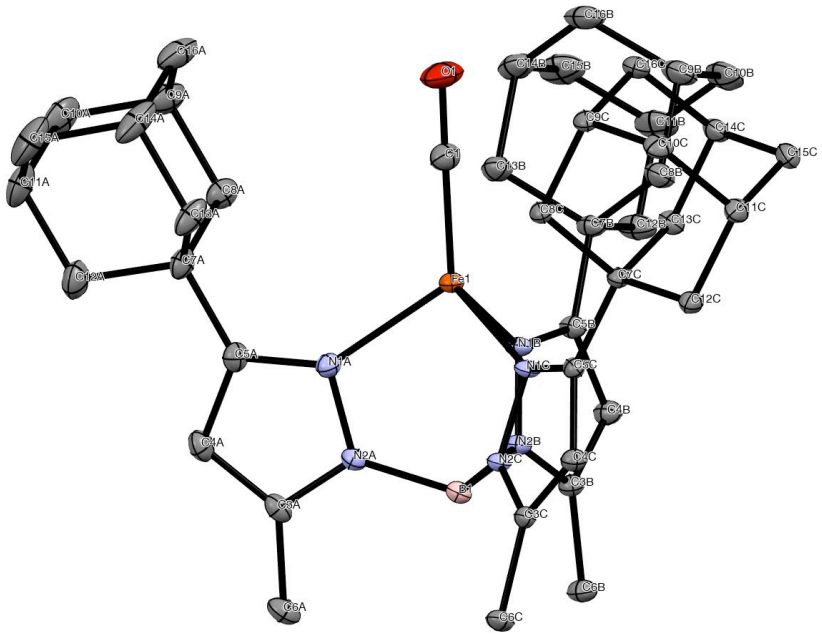

Figure 6.6.5. Labelled thermal ellipsoid plot (50%) for **Tp^{Ad,Me}Fe(CO)**.

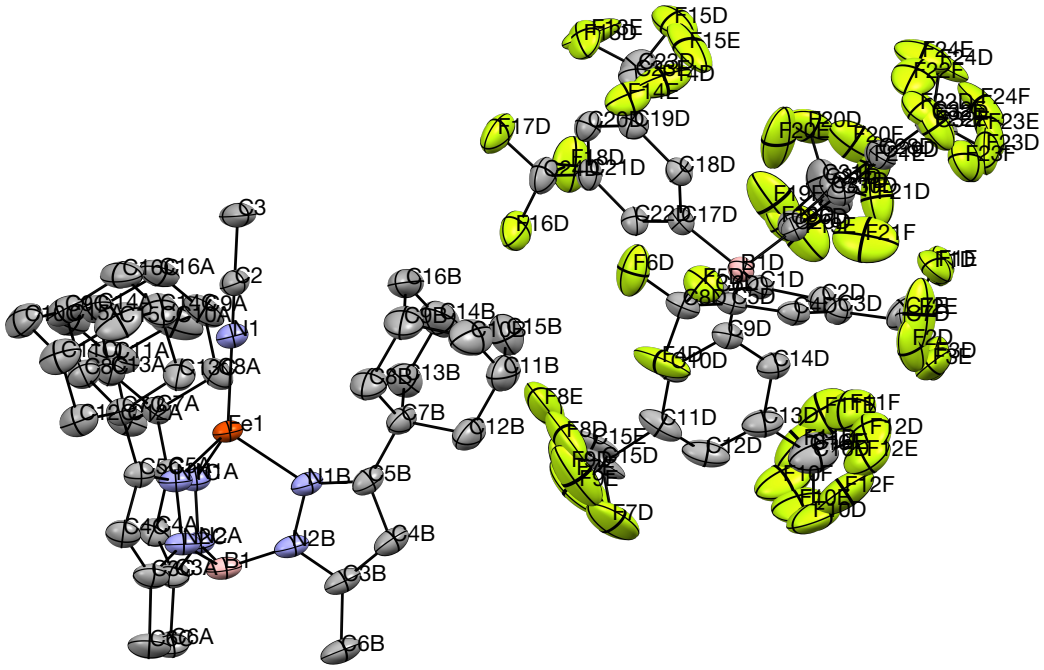

Figure 6.6.6. Labelled thermal ellipsoid plot (50%) for **[Tp^{Ad,Me}Fe(MeCN)][BAr$^{F}_{4}$]**.

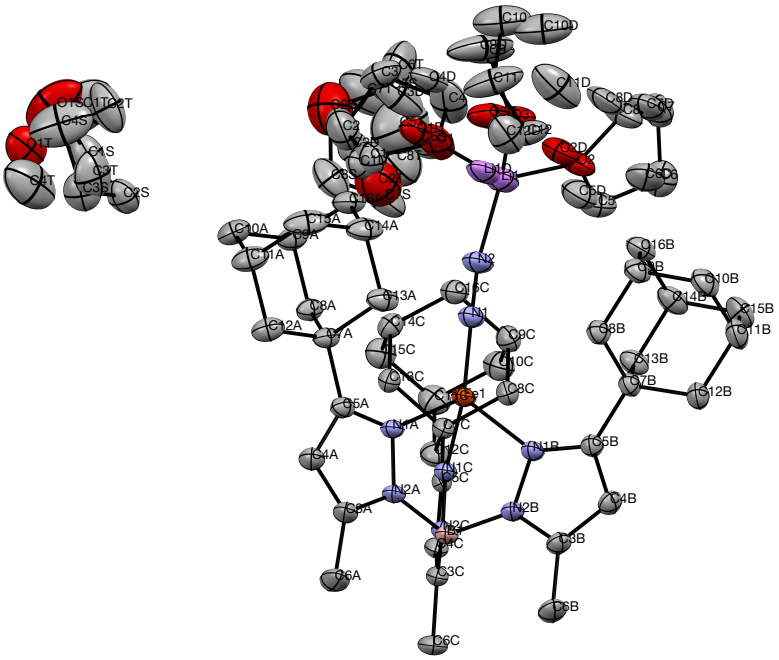

Figure 6.6.7. Labelled thermal ellipsoid plot (50%) for $Tp^{Ad,Me}Fe(N_2)Li(THF)_3$.

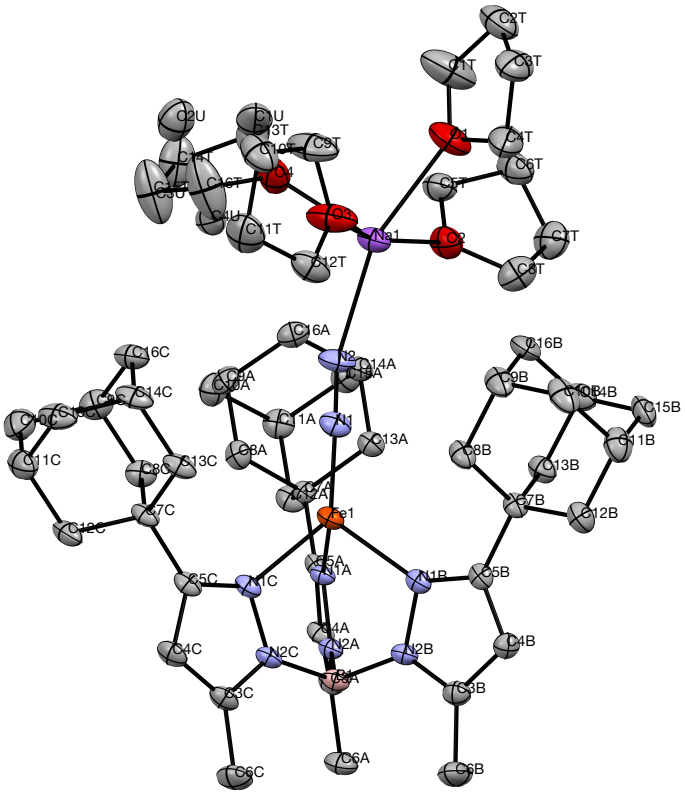

Figure 6.6.8. Labelled thermal ellipsoid plot (50%) for $Tp^{Ad,Me}Fe(N_2)Na(THF)_4$.

Table 6.6.1. Crystal data and structure refinement for **$Tp^{Ph,Me}Fe(Ph_2CO)$**.

Identification code	hh80AM25_0m	
Empirical formula	$C_{43}H_{38}BFeN_6O$	
Formula weight	721.45 g/mol	
Temperature	100(2) K	
Wavelength	0.71073 Å	
Crystal system	Triclinic	
Space group	P –1 (#2)	
Unit cell dimensions	a = 12.0097(4) Å	α = 85.4862(5)°.
	b = 16.0593(5) Å	β = 77.3808(5)°.
	c = 20.0191(7) Å	γ = 79.7749(5)°.
Volume	3704.7(2) $Å^3$	
Z	4	
Density (calculated)	1.293 mg/m^3	
Absorption coefficient	0.450 mm^{-1}	
F(000)	1508	
Crystal size	0.399 x 0.387 x 0.166 mm^3	
θ range for data collection	1.625 to 28.282°.	
Index ranges	$-15 \le h \le 15, -21 \le k \le 21, -26 \le l \le 26$	
Reflections collected	114347	
Independent reflections	18369 [R_{int} = 0.0294]	
Completeness to θ = 25.242°	100.0 %	
Absorption correction	Semi-empirical from equivalents	
Refinement method	Full-matrix least-squares on F^2	
Data / restraints / parameters	18369 / 0 / 949	
Goodness-of-fit on $F2$	1.023	
Final R indices [$I > 2\sigma_I$]	R_1 = 0.0329, wR_2 = 0.0814	
R indices (all data)	R_1 = 0.0408, wR_2 = 0.0861	
Largest diff. peak and hole	0.522 and –0.435 e/$Å^3$	

Table 6.6.2. Crystal data and structure refinement for **$Tp^{Ph,Me}$Fe(I)(THF)**.

Identification code	hh201JT97_0m	
Empirical formula	$C_{34}H_{36}BFeIN_6O$	
Formula weight	738.25 g/mol	
Temperature	100(2) K	
Wavelength	0.71073 Å	
Crystal system	Triclinic	
Space group	P –1	
Unit cell dimensions	a = 11.5216(3) Å	α = 79.3436(5)°.
	b = 11.8482(3) Å	β = 85.0051(5)°.
	c = 12.0474(3) Å	γ = 89.6323(5)°.
Volume	1610.01(7) Å^3	
Z	2	
Density (calculated)	1.523 mg/m^3	
Absorption coefficient	1.465 mm^{-1}	
F(000)	748	
Crystal size	0.346 x 0.208 x 0.115 mm^3	
θ range for data collection	1.727 to 28.282°.	
Index ranges	$-15 \le h \le 15$, $-15 \le k \le 15$, $-16 \le l \le 16$	
Reflections collected	33730	
Independent reflections	7990 [R_{int} = 0.0205]	
Completeness to θ = 25.242°	100.0 %	
Absorption correction	Semi-empirical from equivalents	
Refinement method	Full-matrix least-squares on F^2	
Data / restraints / parameters	7990 / 217 / 448	
Goodness-of-fit on F^2	1.078	
Final R indices [$I > 2\sigma_I$]	R_1 = 0.0285, wR_2 = 0.0717	
R indices (all data)	R_1 = 0.0314, wR_2 = 0.0734	
Largest diff. peak and hole	0.710 and –1.148 e/Å^3	

Table 6.6.3. Crystal data and structure refinement for **$Tp^{Ph,Me}Fe(CO)_2$**.

Identification code	hh147AM53_0m	
Empirical formula	$C_{32}H_{28}BFeN_6O_2$	
Formula weight	595.26 g/mol	
Temperature	100(2) K	
Wavelength	0.71073 Å	
Crystal system	Monoclinic	
Space group	P 21/n	
Unit cell dimensions	a = 9.8312(5) Å	α = 90°.
	b = 17.3613(8) Å	β= 105.9464(8)°.
	c = 17.3922(8) Å	γ = 90°.
Volume	2854.3(2) Å^3	
Z	4	
Density (calculated)	1.385 mg/m^3	
Absorption coefficient	0.570 mm^{-1}	
F(000)	1236	
Crystal size	0.505 x 0.235 x 0.091 mm^3	
θ range for data collection	2.164 to 29.127°.	
Index ranges	$-13 \le h \le 13$, $-13 \le k \le 23$, $-23 \le l \le 23$	
Reflections collected	49230	
Independent reflections	7691 [R_{int} = 0.0286]	
Completeness to θ = 25.242°	99.9 %	
Absorption correction	Semi-empirical from equivalents	
Refinement method	Full-matrix least-squares on F^2	
Data / restraints / parameters	7691 / 0 / 385	
Goodness-of-fit on F^2	1.079	
Final R indices [$I > 2\sigma_I$]	R_1 = 0.0338, wR_2 = 0.0926	
R indices (all data)	R_1 = 0.0413, wR_2 = 0.0961	
Largest diff. peak and hole	0.621 and –0.349 e/Å^3	

Table 6.6.4. Crystal data and structure refinement for **$Tp^{Ph,Me}Fe(CO)$**.

Identification code	hh158AM56_0m	
Empirical formula	$C_{34}H_{35}BFeN_6O$	
Formula weight	610.34 g/mol	
Temperature	100(2) K	
Wavelength	0.71073 Å	
Crystal system	Monoclinic	
Space group	P 21/*c*	
Unit cell dimensions	a = 12.7248(5) Å	α = 90°.
	b = 24.8213(10) Å	β= 114.0709(7)°.
	c = 10.6699(4) Å	γ = 90°.
Volume	3077.0(2) Å^3	
Z	4	
Density (calculated)	1.318 mg/m^3	
Absorption coefficient	0.528 mm^{-1}	
F(000)	1280	
Crystal size	0.384 x 0.267 x 0.027 mm^3	
θ range for data collection	1.641 to 30.506°.	
Index ranges	$-17 \le h \le 18$, $-34 \le k \le 35$, $-15 \le l \le 10$	
Reflections collected	58151	
Independent reflections	9395 [R_{int} = 0.0344]	
Completeness to θ = 25.242°	99.9 %	
Absorption correction	Semi-empirical from equivalents	
Refinement method	Full-matrix least-squares on F^2	
Data / restraints / parameters	9395 / 6 / 418	
Goodness-of-fit on F^2	1.041	
Final R indices [$I > 2\sigma_I$]	R_1 = 0.0346, wR_2 = 0.0869	
R indices (all data)	R_1 = 0.0476, wR_2 = 0.0928	
Largest diff. peak and hole	0.373 and –0.270 e/Å^3	

Table 6.6.5. Crystal data and structure refinement for **$Tp^{Ad,Me}Fe(CO)$**.

Identification code	hh127AM42_0m	
Empirical formula	$C_{43}H_{58}BFeN_6O$	
Formula weight	741.61 g/mol	
Temperature	100(2) K	
Wavelength	0.71073 Å	
Crystal system	Monoclinic	
Space group	P 21/c	
Unit cell dimensions	a = 11.1180(5) Å	α = 90°.
	b = 14.3467(7) Å	β = 98.7075(7)°.
	c = 24.3804(12) Å	γ = 90°.
Volume	3844.0(3) Å^3	
Z	4	
Density (calculated)	1.281 mg/m^3	
Absorption coefficient	0.435 mm^{-1}	
F(000)	1588	
Crystal size	0.557 x 0.501 x 0.341 mm^3	
θ range for data collection	1.652 to 30.508°.	
Index ranges	$-15 \le h \le 15$, $-20 \le k \le 20$, $-34 \le l \le 34$	
Reflections collected	74421	
Independent reflections	11739 [R_{int} = 0.0288]	
Completeness to θ = 25.242°	100.0 %	
Absorption correction	Semi-empirical from equivalents	
Refinement method	Full-matrix least-squares on F^2	
Data / restraints / parameters	11739 / 0 / 475	
Goodness-of-fit on F^2	1.046	
Final R indices [$I > 2\sigma_I$]	R_1 = 0.0307, wR_2 = 0.0799	
R indices (all data)	R_1 = 0.0360, wR_2 = 0.0829	
Largest diff. peak and hole	0.483 and –0.312 e/Å^3	

Table 6.6.6. Crystal data and structure refinement for **[$Tp^{Ad,Me}$Fe(MeCN)][BAr^{F}_{4}]**.

Identification code	hh125AM41-2_0m	
Empirical formula	$C_{76}H_{73}B_2F_{24}FeN_7$	
Formula weight	1617.88 g/mol	
Temperature	197(2) K	
Wavelength	0.71073 Å	
Crystal system	Triclinic	
Space group	P -1	
Unit cell dimensions	a = 14.3742(7) Å	α = 97.1167(8)°.
	b = 15.7977(7) Å	β= 110.2040(7)°.
	c = 18.0438(8) Å	γ = 92.4738(8)°.
Volume	3799.3(3) $Å^3$	
Z	2	
Density (calculated)	1.414 mg/m^3	
Absorption coefficient	0.305 mm^{-1}	
F(000)	1660	
Crystal size	0.569 x 0.478 x 0.317 mm^3	
θ range for data collection	1.572 to 27.103°.	
Index ranges	$-18 \le h \le 18$, $-20 \le k \le 20$, $-23 \le l \le 23$	
Reflections collected	113995	
Independent reflections	16759 [R_{int} = 0.0270]	
Completeness to θ = 25.242°	100.0 %	
Absorption correction	Semi-empirical from equivalents	
Refinement method	Full-matrix least-squares on F^2	
Data / restraints / parameters	16759 / 1213 / 1335	
Goodness-of-fit on F^2	1.027	
Final R indices [$I > 2\sigma_I$]	R_1 = 0.0403, wR_2 = 0.1027	
R indices (all data)	R_1 = 0.0510, wR_2 = 0.1111	
Largest diff. peak and hole	0.527 and –0.461 e/$Å^3$	

Table 6.6.7. Crystal data and structure refinement for $\mathbf{Tp^{Ad,Me}Fe(N_2)Li(THF)_3}$.

Identification code	hh117AM38_0m	
Empirical formula	$C_{62}H_{98}BFeLiN_8O_5$	
Formula weight	1109.08 g/mol	
Temperature	100(2) K	
Wavelength	0.71073 Å	
Crystal system	Monoclinic	
Space group	P 21/n	
Unit cell dimensions	a = 14.7993(5) Å	α = 90°.
	b = 21.0614(8) Å	β= 101.5958(6)°.
	c = 19.4087(7) Å	γ = 90°.
Volume	5926.1(4) Å^3	
Z	4	
Density (calculated)	1.243 mg/m^3	
Absorption coefficient	0.310 mm^{-1}	
F(000)	2400	
Crystal size	0.289 x 0.272 x 0.116 mm^3	
θ range for data collection	1.586 to 30.508°.	
Index ranges	$-21 \le h \le 21$, $-30 \le k \le 30$, $-27 \le l \le 27$	
Reflections collected	173714	
Independent reflections	18088 [R_{int} = 0.0389]	
Completeness to θ = 25.242°	100.0 %	
Absorption correction	Semi-empirical from equivalents	
Refinement method	Full-matrix least-squares on F^2	
Data / restraints / parameters	18088 / 1096 / 934	
Goodness-of-fit on F^2	1.079	
Final R indices [$I > 2\sigma_I$]	R_1 = 0.0621, wR_2 = 0.1732	
R indices (all data)	R_1 = 0.0794, wR_2 = 0.1855	
Largest diff. peak and hole	0.878 and –0.612 e/Å^3	

Table 6.6.8. Crystal data and structure refinement for **$Tp^{Ad,Me}Fe(N_2)Na(THF)_4$**.

Identification code	hh116AM37_0m	
Empirical formula	$C_{62}H_{98}BFeN_8NaO_5$	
Formula weight	1125.13 g/mol	
Temperature	100(2) K	
Wavelength	0.71073 Å	
Crystal system	Orthorhombic	
Space group	P b c a	
Unit cell dimensions	a = 21.7431(9) Å	α = 90°.
	b = 20.6600(9) Å	β = 90°.
	c = 26.0869(11) Å	γ = 90°.
Volume	11718.6(9) Å^3	
Z	8	
Density (calculated)	1.275 mg/m^3	
Absorption coefficient	0.321 mm^{-1}	
F(000)	4864	
Crystal size	0.538 x 0.464 x 0.020 mm^3	
θ range for data collection	1.561 to 25.350°.	
Index ranges	$-26 \le h \le 26$, $-24 \le k \le 24$, $-31 \le l \le 31$	
Reflections collected	231503	
Independent reflections	10718 [R_{int} = 0.1092]	
Completeness to θ = 25.242°	100.0 %	
Absorption correction	Semi-empirical from equivalents	
Refinement method	Full-matrix least-squares on F^2	
Data / restraints / parameters	10718 / 428 / 792	
Goodness-of-fit on F^2	1.037	
Final R indices [$I > 2\sigma_I$]	R_1 = 0.0546, wR_2 = 0.1362	
R indices (all data)	R_1 = 0.0810, wR_2 = 0.1516	
Largest diff. peak and hole	0.744 and –0.654 e/Å^3	

6.7) References

[1] (a) Burgess, B. K.; Lowe, D. J. *Chem. Rev.* **1996**, *96* (7), 2983. (b) Hoffman, B. M.; Dean, D. R.; Seefeldt, L. C. *Acc. Chem. Res.* **2009**, *42* (5), 609. (c) Smil, V. Enriching the Earth; MIT Press: Cambridge, MA, 2001.

[2] (a) Ertl, G. *J. Vac. Sci. & Technol., A* **1983**, *1*, 1247. (b) Appl, M. *Ammonia*, Ullman's Encyclopedia of Industrial Chemistry, 3rd ed.; Weinheim, Germany, 2000; Vol. 22.

[3] Hoffman, B. M.; Lukoyanov, D.; Yang, Z.-Y.; Dean, D. R.; Seefeldt, L. C. *Chem. Rev.* **2014**, *114* (8), 4041.

[4] (a) Kästner, J.; Blöchl, P. E. *J. Am. Chem. Soc.* **2007**, *129* (10), 2998. (b) Hinneman, B.; Nørskov, J. K. *J. Am. Chem. Soc.* **2004**, 126, 3920. (c) Crossland, J. L.; Tyler, D. R. *Coord. Chem. Rev.* **2010**, *254* (17-18), 1883. (d) Holland, P. L. *Can. J. Chem.* **2005**, *83* (4), 296.

[5] Lee, S. C.; Holm, R. H. *Chem. Rev.* **2004**, *104* (2), 1135.

[6] MacKay, B. A.; Fryzuk, M. D. *Chem. Rev.* **2004**, *104* (2), 385.

[7] Anderson, J. S.; Rittle, J.; Peters, J. C. *Nature* **2013**, *501* (7465), 84.

[8] (a) Yandulov, D. V.; Schrock, R. R. *Science* **2003**, *301* (5629), 76. (b) Arashiba, K.; Miyake, Y.; Nishibayashi, Y. *Nat. Chem.* **2010**, *3* (2), 120.

[9] (a) Chatt, J.; Dilworth, J. R.; Richards, R.L. *Chem. Rev.* **1978**, *78*, 589.(b) Ghilardi, C. A.; Midollini, S.; Sacconi, L.; Stoppioni, P *J. Organomet. Chem.* **1981**, *205* (2), 193.

[10] (a) Smith, J. M.; Lachicotte, R. J.; Pittard, K. A.; Cundari, T. R.; Lukat-Rodgers, G.; Rodgers, K. R.; Holland, P. L. *J. Am. Chem. Soc.* **2001**, 123, 9222. (b) Betley, T. A.; Peters, J. C. *J. Am. Chem. Soc.* **2003**, 125, 10782. (c) Chomitz, W. A.; Arnold, J. *Chem. Commun.* **2007**, 4797. (d) Mankad, N. P.; Whited, M. T.; Peters, J. C. *Angew. Chem., Int. Ed.* **2007**, 46, 5768. (e) Scott, J.; Vidyaratne, I.; Korobkov, I.; Gambarotta, S.; Budzelaar, P. H. M. *Inorg. Chem.* **2008**, 47, 896. (f) Rose, R. P.; Jones, C.; Schulten, C.; Aldridge, S.; Stasch, A. *Chem. - Eur. J.* **2008**, 14, 8477. (g) Moret, M.-E.; Peters, J. C. Angew. Chem. Int. Ed. **2011**, 50, 2063. (h) Rudd, P. A.; Liu, S.; Gagliardi, L.; Young, V. G., Jr.; Lu, C. C. *J. Am.*

Chem. Soc. **2011**, 133, 20724. (i) Stieber, S. C. E.; Milsmann, C.; Hoyt, J. M.; Turner, Z. R.; Finkelstein, K. D.; Wieghardt, K.; DeBeer, S.; Chirik, P. J. *Inorg. Chem.* **2012**, 51, 3770. (j) Suess, D. L. M.; Peters, J. C. *J. Am. Chem. Soc.* **2013**, 135, 4938. (k) Creutz, S. E.; Peters, J. C. *J. Am. Chem. Soc.* **2014**, 136, 1105.

[11] (a) MacLeod, K. C.; Holland, P. L. *Nat. Chem.* **2013**, *5* (7), 559.(b) Rodriguez, M. M.; Bill, E.; Brennessel, W. W.; Holland, P. L. *Science* **2011**, *334* (6), 780.

[12] McSkimming, A.; Harman, W. H. *J. Am. Chem. Soc.* **2015**, *137* (28), 8940.

[13] Scott, T. A.; Ooro, B. A.; Collins, D. J.; Shatruk, M.; Yakovenko, A.; Dunbar, K. R.; Zhou, H.-C. *Chem. Commun.* **2009**, 1, 65.

[14] Trovitch, R.J.; Lobkovsky, E.; Eckhard, B.; Chirik, P.J *Organometallics* **2008**, *27*, 1470.

[15] (a) Hou, Z.; Jia, X.; Fujita, A.; Tezuka, H.; Yamazaki, H.; Wakatsuki, Y. *Chem. Eur. J.* **2000**, *6* (16), 2994. (b) Hou, Z.; Jia, X.; Hoshino, M.; Wakatsuki, Y. *Angew. Chem. Int. Ed.* **1997**, *36* (12), 1292. (c) Domingos, A.; Lopes, I.; Waerenborgh, J. C.; Marques, N.; Lin, G. Y.; Zhang, X. W.; Takats, J.; McDonald, R.; Hillier, A.C.; Sella, A.; Elsegood, M.R.J.; Day, V. W. *Inorg. Chem.* **2007**, *46* (22), 9415. (d) Clegg, W.; Izod, K.; O'Shaughnessy, P.; Eaborn, C.; Smith, J. D. *Angew. Chem. Int. Ed.* **1997**, *36* (24), 2815.

[16] Zhaomin Hou; Akira Fujita; Take-aki Koizumi; Hiroshi Yamazaki, A.; Yasuo Wakatsuki. *Organometallics* **1999**, *18* (10), 1979.

[17] Marquard, S. L.; Bezpalko, M. W.; Foxman, B. M.; Thomas, C. M. *Organometallics* **2014**, *33* (8), 2071.

[18] Lam, C. P.; Anthon, C.; Heinemann, F. W.; O'Connor, J. M.; Meyer, K. *J. Am. Chem. Soc.* **2008**, *130* (20), 6567.

[19] Tietz, T.; Limberg, C.; Stößer, R.; Ziemer, B *Chem. Eur. J.* **2011**, *17* (36), 10010.

[20] According to a substructure search performed on 04/8/2019, no $Tp^{Ph,Me}FeX$ (where X = Cl, Br, I) complex could be found in the Cambridge Structural Database (CSD).

[21] Zadrozny, J.M.;Xiao, D.J.; Long, J.R.; Atanasov, M.; Neese, F.; Grandjean, F.; Long, G. J. *Inorg. Chem.* **2013**, *52*, 13123.

[22] Kisko, J. L.; Hascall, T.; Parkin, G. *J. Am. Chem. Soc.* **1998**, 120, 10561.

[23] Msayib, K. J.; Watt, C. *Chem. Soc. Rev.* **1992**, *21* (4), 237.

[24] Stoll, S.; Schweiger, A. *J. Magn. Reson.* **2006**, *178* (1), 42.

[25] Schubert, E. M. *J. Chem. Educ.* **1992**, *69* (1), 62.

[26] APEX 2, version 2014.1-1, Bruker (2014), Bruker AXS Inc., Madison, Wisconsin, USA.

[27] SAINT, version V8.34A, Bruker (2012), Bruker AXS Inc., Madison, Wisconsin, USA.

[28] SADABS, version 2012/1, Bruker (2012), Bruker AXS Inc., Madison, Wisconsin, USA.

[29] SHELXTL, version 2013/4, Bruker (2013), Bruker AXS Inc., Madison, Wisconsin, USA.

Appendix

A1.1) Cobalt Complexes of a Redox-Active Diphosphine-Diboraanthracene Ligand

The cobalt complexes were accessed as the iron complexes previously discussed, through a reductive metalation strategy that proceeds by *in situ* interaction of B_2P_2 with $CoBr_2$ in THF followed by reduction of this intermediate with Rieke Mg in toluene. The neutral $Co(B_2P_2)$ complex was formed in 77% yield as a red/orange powder that was paramagnetic as judged by ^{1}H NMR and Evan's method measurements of $\mu_{eff} = 1.5 \pm 0.1$ The single crystal XRD structure displayed a Co atom bound η^6 to the C_4B_2 core with average Co-C_{DBA} and CoB_{DBA} distances of 2.313 Å and 2.208 Å, respectively. The $Co(B_2P_2)$ complex was investigated by cyclic voltammetry (CV) and featured two reversible redox events at –0.35 and –2.06 V vs. Fc/Fc^+ (THF, 0.1 M nBu$_4$NPF$_6$, 100 mV/s). Oxidation of the $Co(B_2P_2)$ complex was achieved by addition of ferrocenium hexafluorophosphate ($FcPF_6$) to yield the cation, $[Co(B_2P_2)][PF_6]$, as a yellow solid. Single-crystal XRD studies of the cation confirmed its identity as a hexafluorophosphate complex salt with lengthened interactions between Co and the DBA core ($d_{Co\text{-}CDBA}$Avg = 2.415 Å; $d_{Co\text{-}BDBA}$Avg = 2.302 Å). Taken together with the lack of a corresponding oxidation in the CV of B_2P_2 this oxidation is Co centered. Reduction of the $Co(B_2P_2)$ complex was achieved by addition of 1

equivalent of potassium napthalenide to yield the anion, [Co(B_2P_2)][K(18-c-6)], as a dark red solid. Following encapsulation of the K counterion with 18-crown-6 (18-c-6), a single crystal suitable for XRD was obtained. The DBA heterocycle remains flat in the anion with shortened Co-C_{DBA} and Co-B_{DBA} distances of 2.249 Å and 2.169 Å relative to Co(B_2P_2). The [Co(B_2P_2)][K(18-c-6)] complex is diamagnetic, as judged by ^{1}H, ^{31}P and ^{11}B NMR spectroscopies and is consistent with the formulation of it as an 18 e^- complex that is the result of reduction of Co(0) to Co(–1). Additionally, it was found that addition of CO to the [Co(B_2P_2)][K(18-c-6)] complex results in the formation of a diamagnetic, 18 e– complex, [Co(CO)(B_2P_2)][K(18-c-6)], that is the result of ring slippage of Co from a phenylene-DBA ligand to accommodate the CO ligand as judged by single-crystal XRD studies. In the solid-state, the DBA ring bends at the 9,10 vertex to accommodate this change in coordination at Co. The average Co-B_{DBA} distances of 2.255 Å are lengthened relative to [Co(B_2P_2)][K(18-c-6)], likely a result of competitive π-backbonding interaction with the new CO ligand.

A1.2) Experimental Section

A1.2.1) General Considerations

Unless otherwise noted, all manipulations were carried out using standard Schlenk or glovebox techniques under a dinitrogen atmosphere. Solvents were dried and deoxygenated by sparging with argon and passage through activated

alumina in a solvent purification system from SG Waters USA, LLC. Non-halogenated solvents were tested with a standard purple solution of sodium benzophenone ketyl in tetrahydrofuran in order to confirm effective oxygen and moisture removal. 9,10-Bis(2-(diisopropylphosphino)phenyl)-9,10-dihydroboranthrene (B_2P_2), ferrocenium hexafluorophosphate **(**[Fc][PF_6]), and potassium napthalenide ($K(C_{10}H_8)(THF)_{0.5}$) were synthesized according to literature procedures previously mentioned. Deuterated solvents were purchased from Cambridge Isotope Laboratories Inc., degassed, and dried over activated 4 Å molecular sieves for at least 24 hr prior to use. NMR spectra were recorded on Bruker Avance 600 MHz, Bruker NEO 400 MHz, Varian Inova 300 MHz and Varian Inova 500 MHz spectrometers. ^{1}H chemical shifts are reported in ppm relative to tetramethylsilane using residual solvent as internal standards. ^{31}P and ^{11}B chemical shifts are reported in ppm relative to 85% aqueous H_3PO_4 and $BF_3 \cdot Et_2O$, respectively. ^{11}B NMR spectra were manipulated with MestReNova 10.0.2. and had a backwards LP applied to eliminate background signal from the borosilicate NMR tube. EPR X-band spectra were obtained on a Bruker EMX spectrometer controlled by Bruker Win-EPR software suite version 3.0. X-ray diffraction studies were performed using a Bruker-AXS diffractometer. Cyclic Voltammetry (CV) experiments were performed using a Pine AFP1 potentiostat. The cell consisted of a glassy carbon working electrode, a Pt wire auxiliary

electrode and a Pt wire pseudo-reference electrode. All potentials are referenced vs. the Fc/Fc^+ couple measured as an internal standard.

A1.2.2) $Co(B_2P_2)$.

B_2P_2 (0.300 g, 0.535 mmol) was dissolved in THF (8 mL) and added to a THF suspension (2 mL) of $CoBr_2$ (0.118 g, 0.540 mmol). The mixture was stirred 3 hours during which time it became homogenous and deep red. Volatiles were removed *in vacuo* and the residue triterated with Et_2O (5 mL) for 30 minutes prior to removing volatiles *in vacuo*. The residue was extracted with toluene (3 x 3 mL) and filtered through celite. The red filtrate was added Rieke Mg (0.015 g, 0.560 mmol) and vigorously stirred 10 hours. The black/red mixture was filtered through a 1" pad of silica with toluene/Et_2O (1:1) as eluent. Removal of volatiles from the filtrate *in vacuo* yielded the product as a red/orange powder. Yield: 0.256 g, 77%. A single-crystal suitable for XRD was obtained by slow evaporation of a saturated pentane solution. ^1H NMR (500 MHz, C_6D_6) δ 21.28, 13.27, 12.83, 11.79, 9.40, 9.02, 1.83, 1.34, 0.92, –8.68, –10.34. Evans Method (C_6D_6): μ_B 1.5 ± 0.1. MALDI MS: m/z 620.2551; Calcd. For 620.2515.

A1.2.3) $[Co(B_2P_2)][PF_6]$.

$Co(B_2P_2)$ (0.026 g, 0.042 mmol) was dissolved in Et_2O (3 mL) and added to a suspension of ferrocenium hexafluorophosphate (0.010 g, 0.043 mmol) in Et_2O (2 mL). The reaction was stirred 1 hour during which time a yellow crystalline solid had precipitated from a pale red supernatant. The precipitate was collected,

washed with Et_2O (4 x 1 mL) and dried *in vacuo*. Yield: 0.029, 91%. A single-crystal suitable for XRD was obtained by layering a saturated THF solution with toluene.

A1.2.4) Co(B_2P_2)][K(18-c-6)].

Co(B_2P_2) (0.050 g, 0.081 mmol) was dissolved in toluene (3 mL) and added potassium napthalenide (0.017 g, 0.083 mmol) as a solid. The mixture was stirred 1 hour where it became homogenous. The volatiles were removed *in vacuo*, the residue was added pentane (3 mL) and again had its volatiles removed *in vacuo*. The residue was then washed with pentane (4 x 1 mL), redissolved in toluene, added a toluene solution (ca. 1 mL) of 18-crown-6 (0.014 g, 0.081 mmol), layered with pentane (6 mL) and placed at –15 °C for 10 hours. Deep red crystals formed that were decanted from the mother liquor, rinsed with pentane (2 x 1 mL) and dried *in vacuo*. Yield: 0.064 g, 85%. A single-crystal suitable for XRD was obtained by layering a saturated toluene solution with pentane. The ^{1}H NMR (500 MHz, C_6D_6) δ 7.90 (d, J = 6.7 Hz, 2H), 7.52 (t, J = 7.2 Hz, 2H), 7.46 (dd, J = 7.5, 4.7 Hz, 2H), 7.28 (s, 4H), 7.23 (t, J = 7.7 Hz, 2H), 6.63 (s, 4H), 2.12 (dq, J = 14.4, 7.2 Hz, 4H), 0.85 (d, J = 6.9 Hz, 6H), 0.82 (d, J = 7.0 Hz, 6H), 0.72 (d, J = 7.1 Hz, 6H), 0.70 (d, J = 7.2 Hz, 6H). ^{31}P NMR (162 MHz, C_6D_6) δ 64.94 (s).

A1.2.5) [Co(CO)(B_2P_2)][K(18-c-6)].

Co(B_2P_2)][K(18c6)] (0.030 g, 0.033 mmol) was dissolved in THF (3 mL) and subjected to three freeze-pump-thaw cycles prior to adding 1 atm. CO. The reaction was stirred 10 hours prior to removing volatiles *in vacuo* to yield the product as a red solid. Yield: 0.029 g, 94%. A single-crystal suitable for XRD was obtained by layering a saturated toluene solution with pentane. ^{1}H NMR (500 MHz, Benzene-d_6) δ 8.37 (s, 12H), 7.97 (s, 1H), 7.63 (s, 4H), 7.43 (s, 2H), 6.84 (s, 4H), 6.67 (s, 2H), 2.47 (s, 2H), 2.17 (s, 2H), 1.15 (s, 12H), 1.00 (s, 6H), 0.77 (s, 6H). ^{31}P NMR (162 MHz, C_6D_6) δ 65.29 (s).

A1.3) Spectroscopic Data

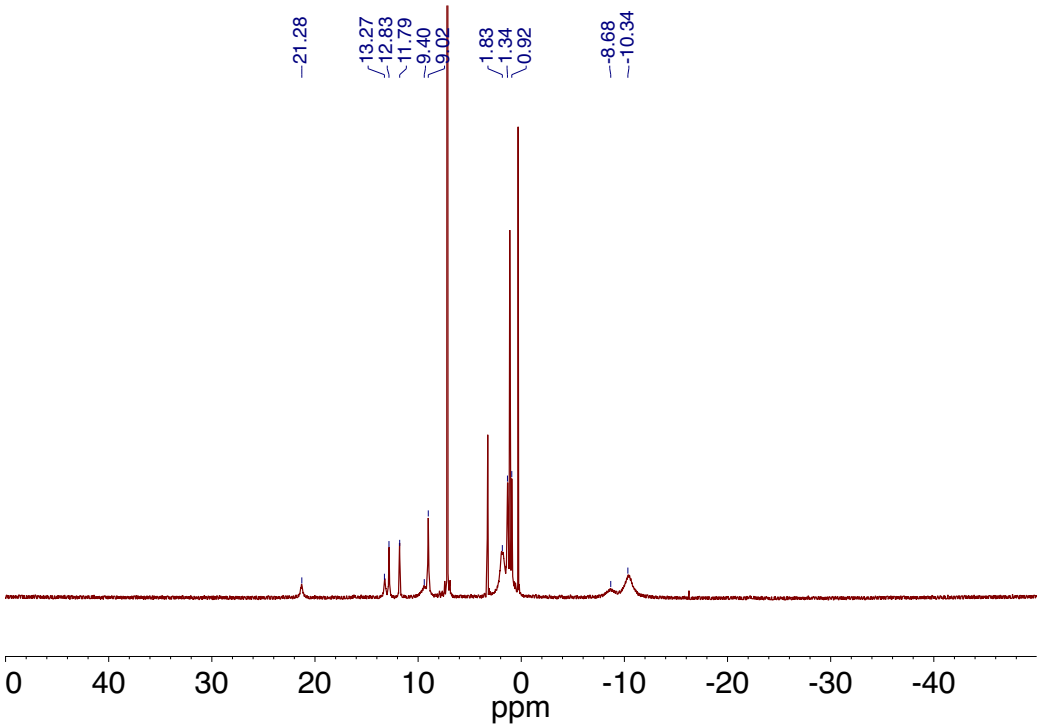

Figure A1.3.1. ^{1}H NMR spectrum of **Co(B_2P_2)** recorded at 500 MHz in C_6D_6.

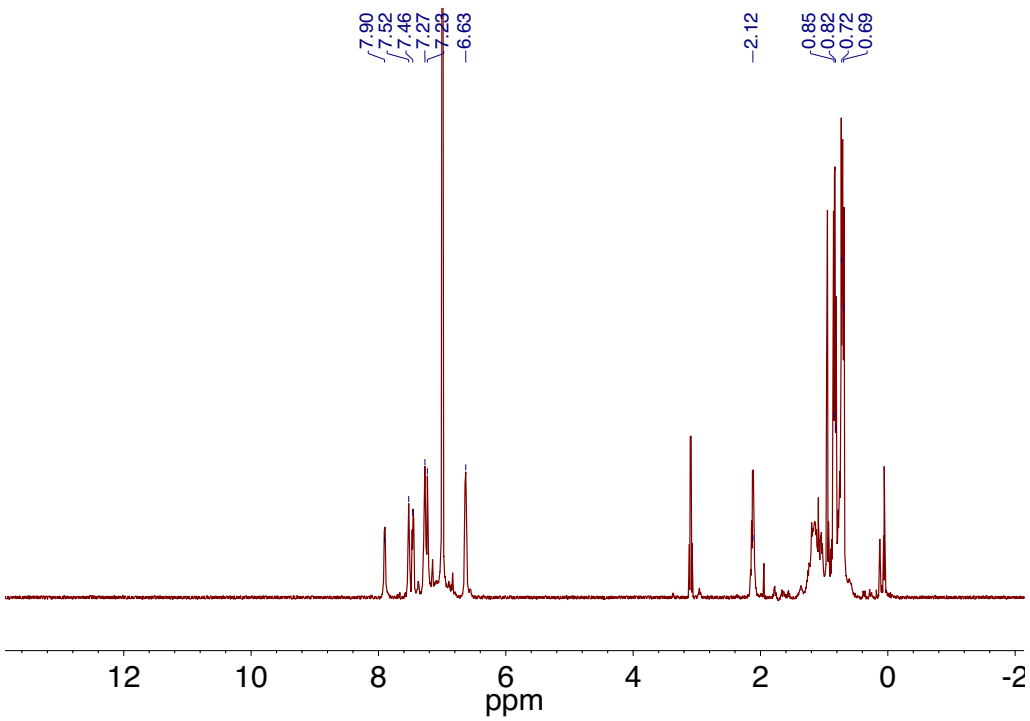

Figure A1.3.2. ^{1}H NMR spectrum of **[Co(B$_2$P$_2$)][K(18-c-6)]** recorded at 400 MHz in C_6D_6

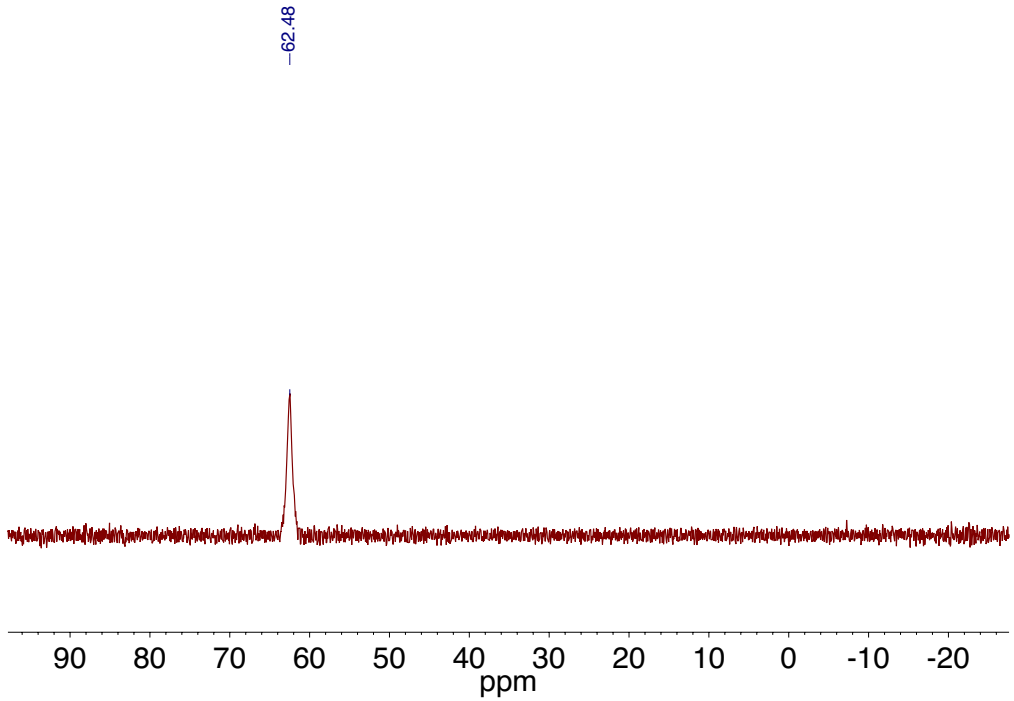

Figure A1.3.3. ^{31}P NMR spectrum of **[Co(B$_2$P$_2$)][K(18-c-6)]** recorded at 194 MHz in C_6D_6.

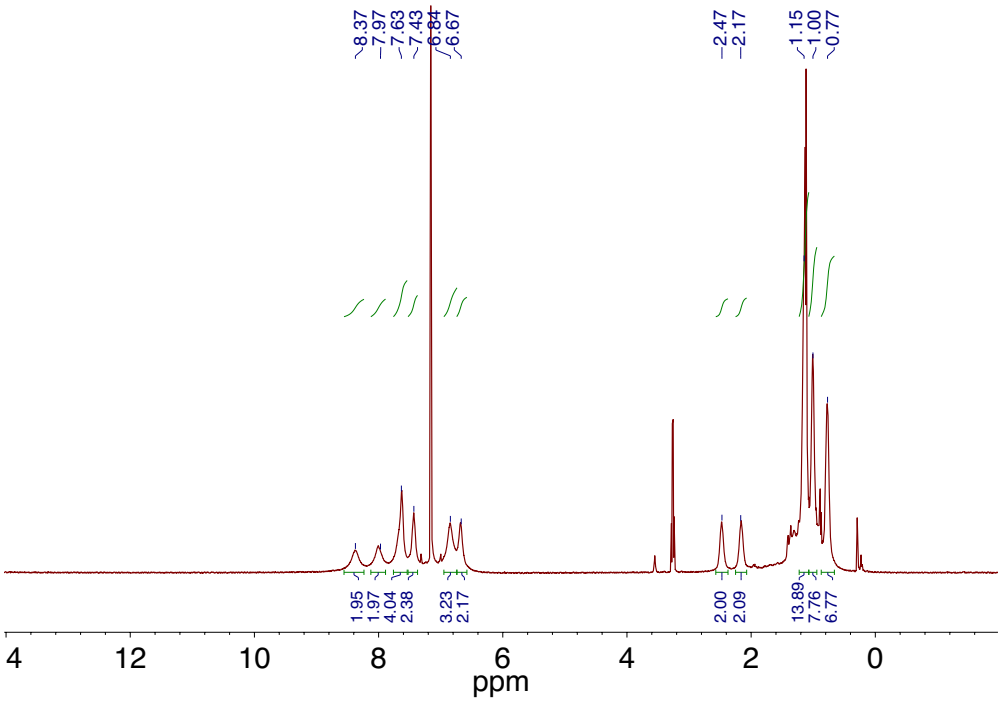

Figure A1.3.4. ^{1}H NMR spectrum of **[Co(CO)(B_2P_2)][K(18-c-6)]** recorded at 400 MHz in C_6D_6.

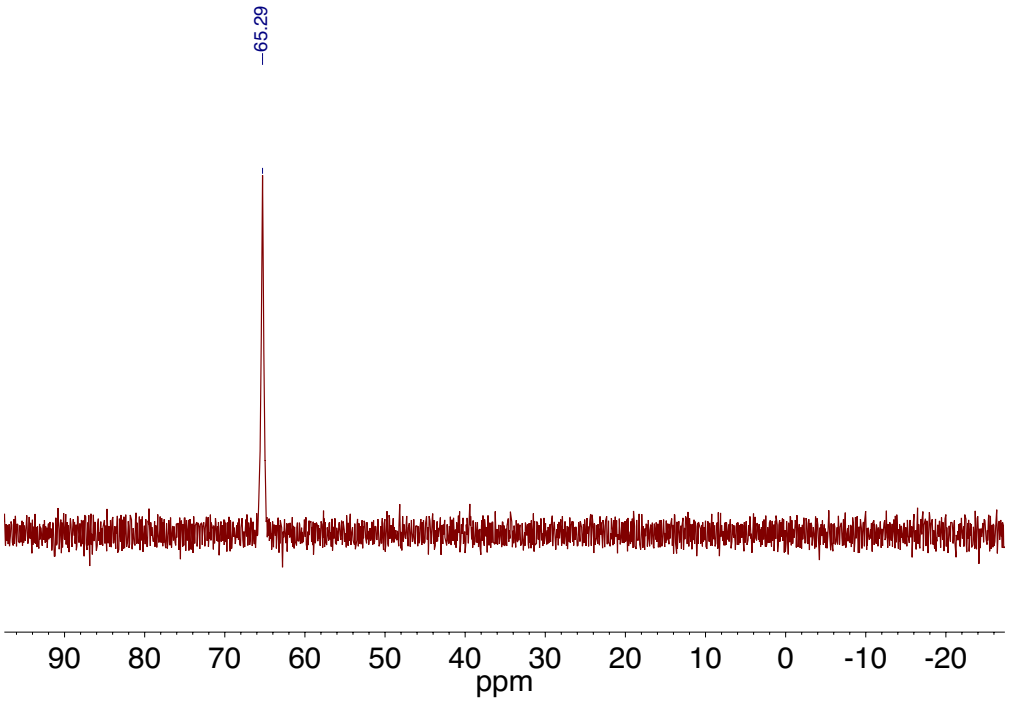

Figure A1.3.5. ^{31}P NMR spectrum of **[Co(CO)(B_2P_2)][K(18-c-6)]** recorded at 162 MHz in C_6D_6.

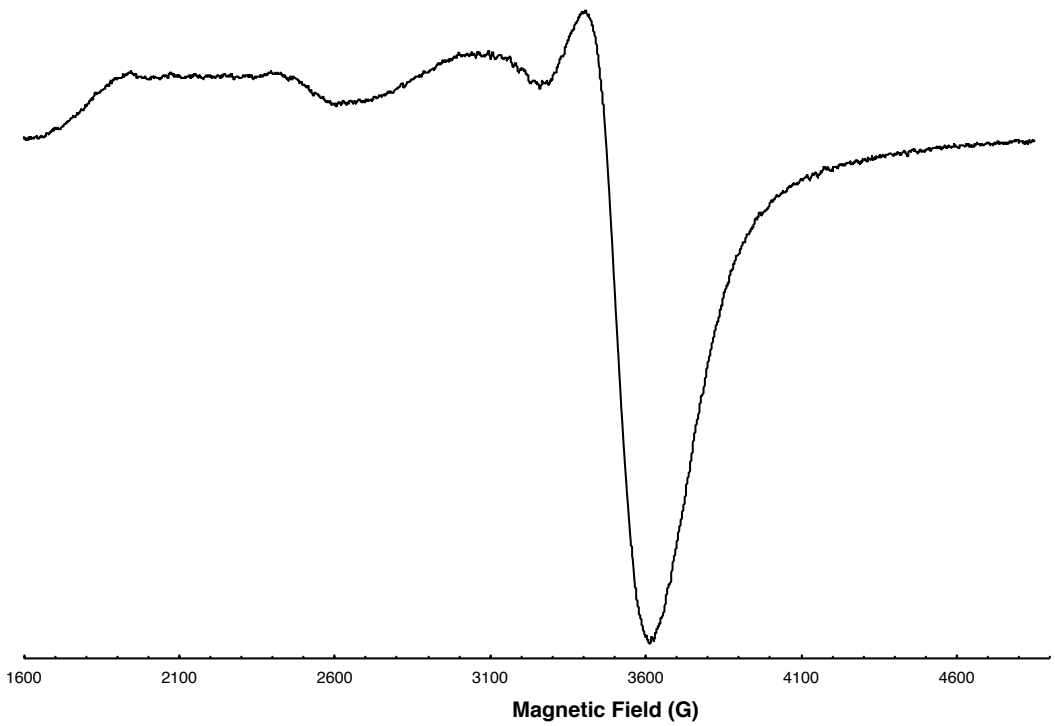

Figure A1.3.6. X-band EPR spectrum (9.133 GHz) of **[Co(B_2P_2)][K(18-c-6)]** recorded as a solid at 108 K.

A1.4) Cyclic Voltammetry

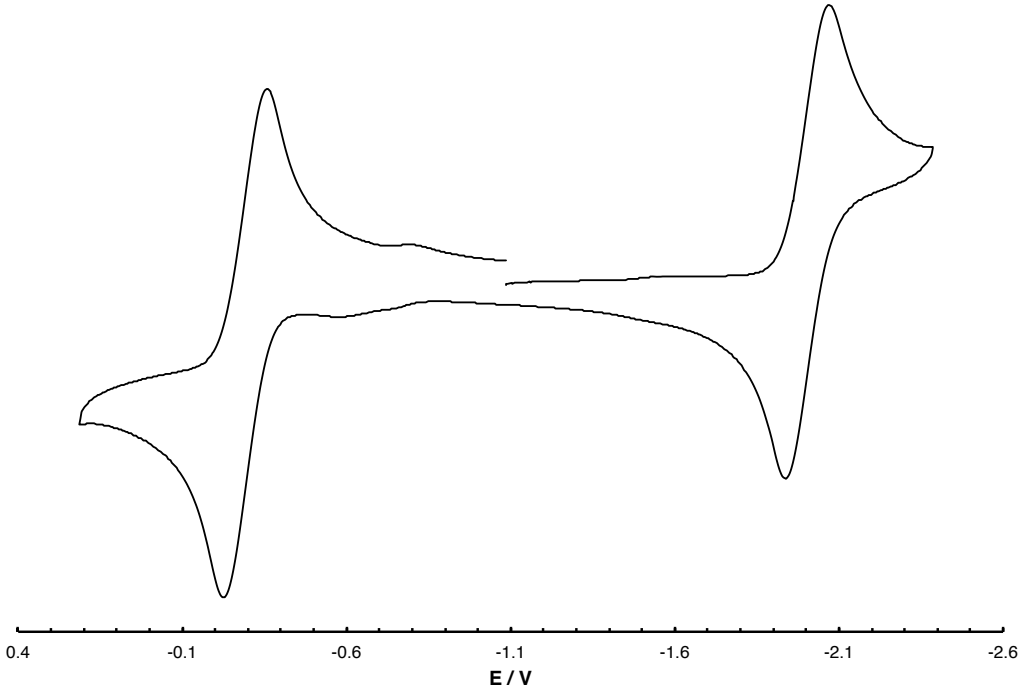

Figure A1.4.1. Cyclic voltammogram of **Co(B_2P_2)** in THF (0.1 M *n*Bu_4NPF_6 as electrolyte, scan rate 100 mV/s, potential vs. Fc^+/Fc).

A1.5) X-Ray Crystallography

A1.5.1) General Considerations

Single crystals were coated with paratone oil and mounted on cryo-loop glass fibers. X-ray intensity data were collected at 100(2) K on a Bruker APEX2[3] platform-CCD X-ray diffractometer system using fine-focus Mo K_α radiation (λ = 0.71073 Å, 50kV/30mA power). The CCD detector was placed at 5.0600 cm from the crystal. Frames were integrated using the Bruker SAINT software package[4] and using a narrow-frame integration algorithm. Absorption corrections were applied to the raw intensity data using the SADABS program.[5] The Bruker SHELXTL software package[6] was used for phase determination and structure refinement. Atomic coordinates, isotropic and anisotropic displacement parameters of all the non-hydrogen atoms were refined by means of a full matrix least-squares procedure on F^2. The H-atoms were included in the refinement in calculated positions riding on the atoms to which they were attached. Relevant details for individual data collections are reported in Tables A1.5.1-A1.5.4.

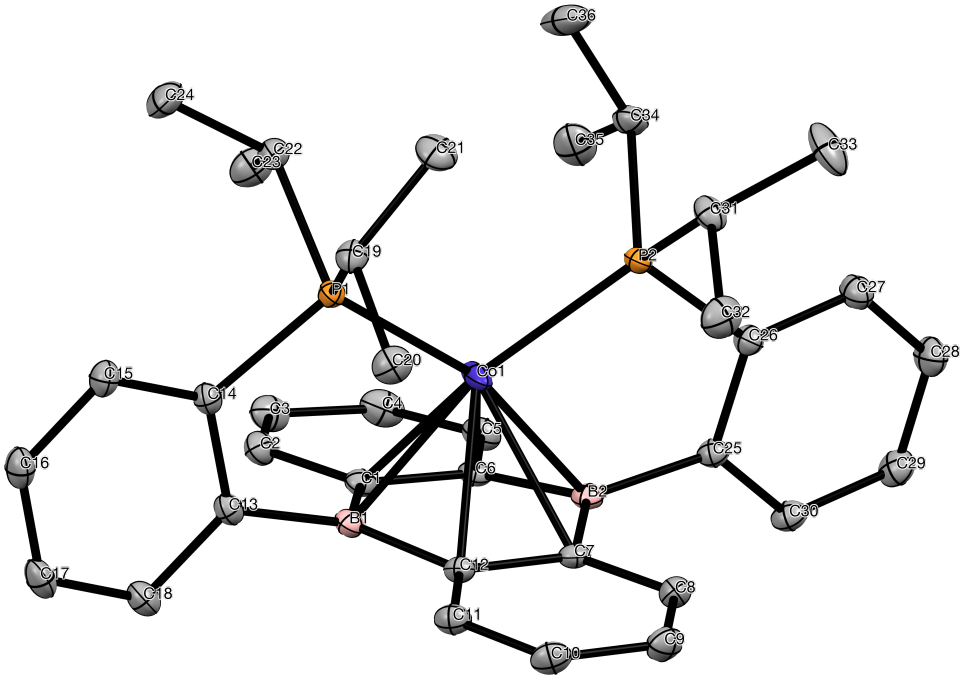

Figure A1.5.1. Labelled thermal ellipsoid plot (50%) for **Co(B_2P_2)**.

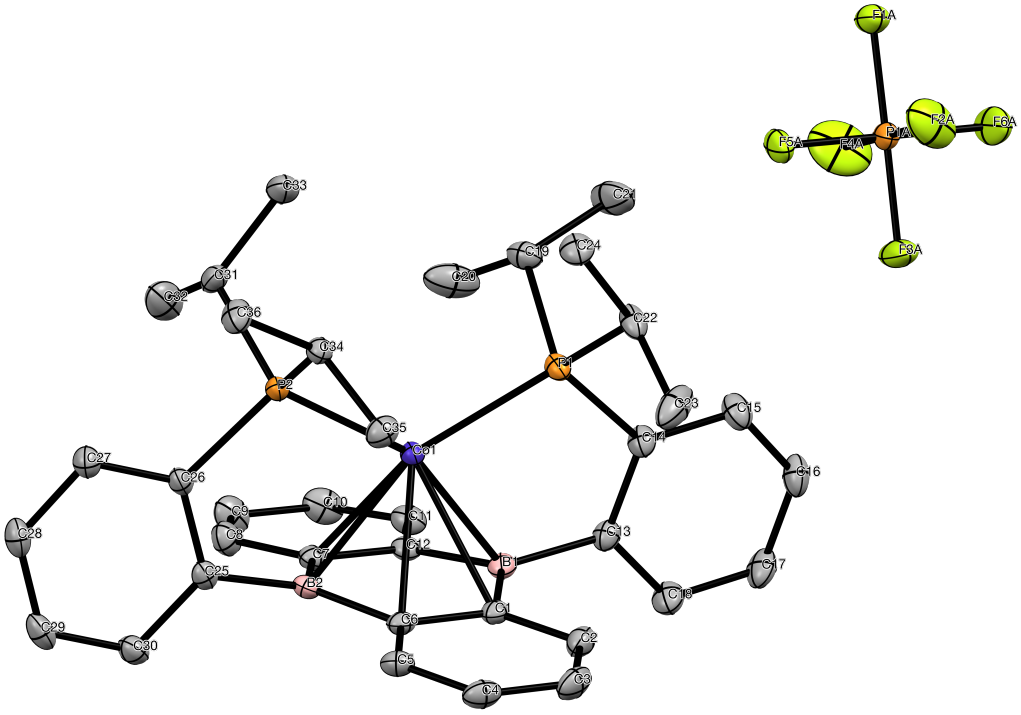

Figure A1.5.2. Labelled thermal ellipsoid plot (50%) for **[Co(B_2P_2)][PF_6].**

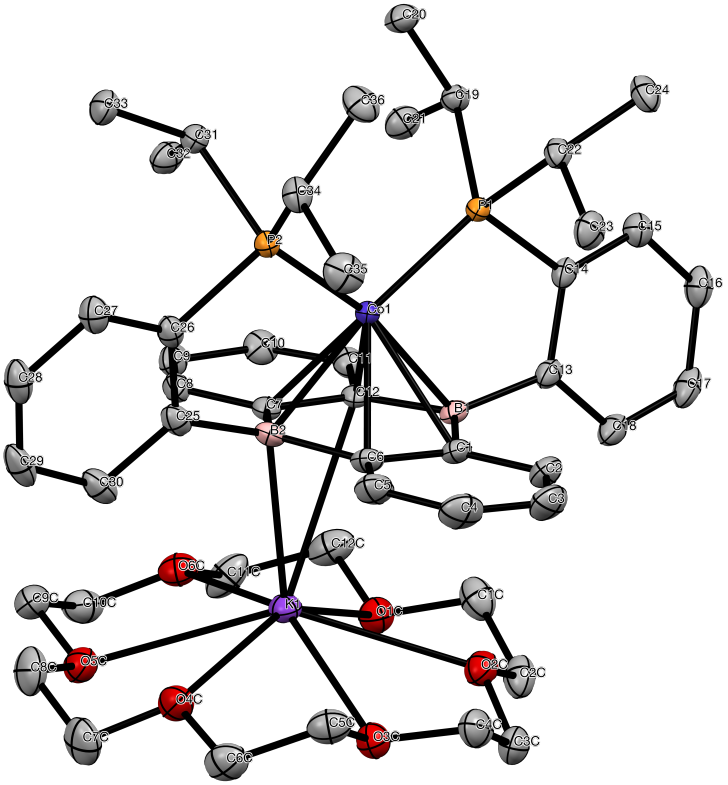

Figure A1.5.3. Labelled thermal ellipsoid plot (50%) for **[Co(B_2P_2)][K(18-c-6)]**.

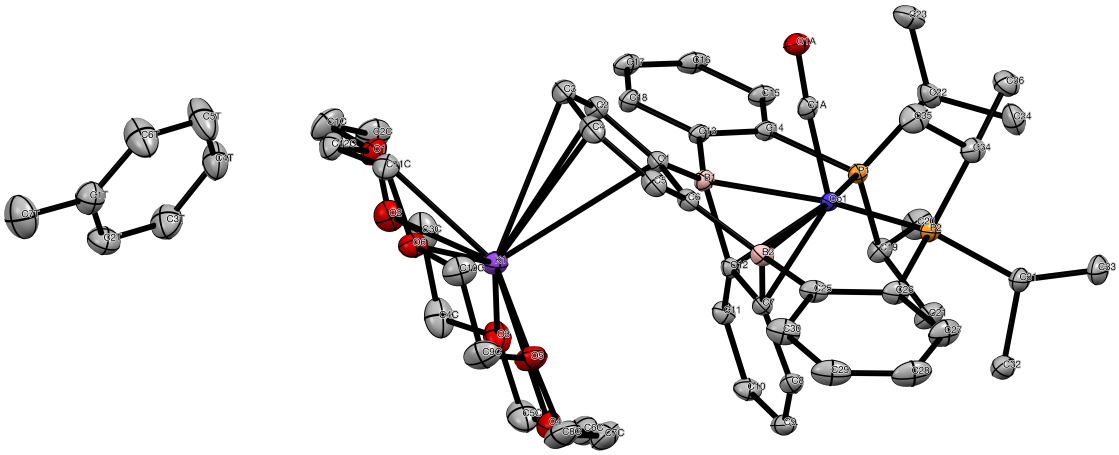

Figure A1.5.4. Labelled thermal ellipsoid plot (50%) for **[Co(CO)(B_2P_2)][K(18-c-6)]**.

Table A1.5.1. Crystal data and structure refinement for **$Co(B_2P_2)$**.

Identification code	hh24JT15_0m	
Empirical formula	$C_{36}H_{44}B_2CoP_2$	
Formula weight	619.20 g/mol	
Temperature	100(2) K	
Wavelength	0.71073 Å	
Crystal system	Orthorhombic	
Space group	P 21 21 21 (#19)	
Unit cell dimensions	a = 9.4943(3) Å	α = 90°.
	b = 15.1991(5) Å	β= 90°.
	c = 22.0856(7) Å	γ = 90°.
Volume	3187.06(18) Å^3	
Z	4	
Density (calculated)	1.290 mg/m^3	
Absorption coefficient	0.663 mm^{-1}	
F(000)	1308	
Crystal size	0.546 x 0.524 x 0.485 mm^3	
θ range for data collection	1.626 to 30.506°.	
Index ranges	$-13 \le h \le 13$, $-21 \le k \le 21$, $-31 \le l \le 31$	
Reflections collected	93738	
Independent reflections	9751 [R_{int} = 0.0249]	
Completeness to θ = 25.242°	99.9 %	
Absorption correction	Semi-empirical from equivalents	
Refinement method	Full-matrix least-squares on F^2	
Data / restraints / parameters	9751 / 0 / 378	
Goodness-of-fit on F^2	1.064	
Final R indices [$I > 2\sigma_I$]	R_1 = 0.0219, wR_2 = 0.0586	
R indices (all data)	R_1 = 0.0226, wR_2 = 0.0590	
Absolute structure parameter	–0.0035(17)	
Largest diff. peak and hole	0.325 and –0.871 e/Å^3	

Table A1.5.2. Crystal data and structure refinement for **[Co(B_2P_2)][PF_6]**.

Identification code	hh38JT24_0m	
Empirical formula	$C_{36}H_{44}B_2CoF_6P_3$	
Formula weight	764.17 g/mol	
Temperature	100(2) K	
Wavelength	0.71073 Å	
Crystal system	Triclinic	
Space group	P –1 (#2)	
Unit cell dimensions	a = 9.8713(4) Å	α = 89.571(1)°.
	b = 12.3688(5) Å	β = 79.129(1)°.
	c = 15.1743(6) Å	γ = 86.494(1)°.
Volume	1816.05(13) $Å^3$	
Z	2	
Density (calculated)	1.397 mg/m^3	
Absorption coefficient	0.661 mm^{-1}	
F(000)	792	
Crystal size	0.433 x 0.292 x 0.122 mm^3	
θ range for data collection	1.649 to 28.281°.	
Index ranges	$-13 \le h \le 13$, $-16 \le k \le 16$, $-20 \le l \le 20$	
Reflections collected	45568	
Independent reflections	8993 [R_{int} = 0.0249]	
Completeness to θ = 25.242°	100.0 %	
Absorption correction	Semi-empirical from equivalents	
Refinement method	Full-matrix least-squares on F^2	
Data / restraints / parameters	8993 / 0 / 441	
Goodness-of-fit on F^2	1.035	
Final R indices [$I > 2\sigma_I$]	$R1$ = 0.0307, $wR2$ = 0.0726	
R indices (all data)	$R1$ = 0.0361, $wR2$ = 0.0755	
Largest diff. peak and hole	0.581 and –0.360 e/A^3	

Table A1.5.3. Crystal data and structure refinement for **[Co(B_2P_2)][K(18-c-6)]**.

Identification code	hh37JT23_0m	
Empirical formula	$C_{48}H_{68}B_2CoKO_6P_2$	
Formula weight	922.61 g/mol	
Temperature	100(2) K	
Wavelength	0.71073 Å	
Crystal system	Monoclinic	
Space group	P 21/c (#14)	
Unit cell dimensions	a = 18.3179(6) Å	α = 90°.
	b = 12.6488(4) Å	β = 94.156(1)°.
	c = 20.4714(6) Å	γ = 90°.
Volume	4730.7(3) Å^3	
Z	4	
Density (calculated)	1.295 mg/m^3	
Absorption coefficient	0.565 mm^{-1}	
F(000)	1960	
Crystal size	0.546 x 0.188 x 0.088 mm^3	
θ range for data collection	1.894 to 28.282°.	
Index ranges	$-24 \le h \le 24$, $-16 \le k \le 16$, $-27 \le l \le 27$	
Reflections collected	113809	
Independent reflections	11753 [R_{int} = 0.0338]	
Completeness to θ = 25.242°	100.0 %	
Absorption correction	Semi-empirical from equivalents	
Refinement method	Full-matrix least-squares on F^2	
Data / restraints / parameters	11753 / 0 / 549	
Goodness-of-fit on F^2	1.062	
Final R indices [$I > 2\sigma_I$]	R_1 = 0.0289, wR_2 = 0.0690	
R indices (all data)	R_1 = 0.0367, wR_2 = 0.0729	
Largest diff. peak and hole	0.409 and –0.219 e/Å^3	

Table A1.5.4. Crystal data and structure refinement for **[Co(CO)(B_2P_2)][K(18-c-6)]**.

Identification code	hh42JT25_0m	
Empirical formula	$C_{56}H_{76}B_2CoKO_7P_2$	
Formula weight	1042.75 g/mol	
Temperature	100(2) K	
Wavelength	0.71073 Å	
Crystal system	Monoclinic	
Space group	P 21/n (#14)	
Unit cell dimensions	a = 12.5740(4) Å	α= 90°.
	b = 28.4895(9) Å	β= 92.4978(5)°.
	c = 15.2343(5) Å	γ = 90°.
Volume	5452.2(3) Å^3	
Z	4	
Density (calculated)	1.270 mg/m^3	
Absorption coefficient	0.500 mm^{-1}	
F(000)	2216	
Crystal size	0.553 x 0.455 x 0.325 mm^3	
θ range for data collection	1.517 to 30.507°.	
Index ranges	$-17 \le h \le 17$, $-40 \le k \le 40$, $-21 \le l \le 21$	
Reflections collected	158312	
Independent reflections	16636 [R_{int} = 0.0278]	
Completeness to θ = 25.242°	100.0 %	
Absorption correction	Semi-empirical from equivalents	
Refinement method	Full-matrix least-squares on F^2	
Data / restraints / parameters	16636 / 0 / 631	
Goodness-of-fit on F^2	1.064	
Final R indices [$I > 2\sigma_I$]	R_1 = 0.0348, wR_2 = 0.0913	
R indices (all data)	R_1 = 0.0392, wR_2 = 0.0941	
Largest diff. peak and hole	1.125 and –0.345 e/Å^3	

A2.1) Nickel Complexes of a Redox-Active Diphosphine-Diboraanthracene Ligand

The nickel complexes of B_2P_2 could be accessed via two different routes. The first, and most straightforward, is achieved by heating B_2P_2 and 1 equivalent of $Ni(PPh_3)_4$ at 50 °C for 10 hours. Alternatively, the aforementioned reductive metalation strategy that was used to access the Fe and Co complexes of B_2P_2 could be utilized by interaction of B_2P_2 with $NiBr_2$ followed by reduction with Rieke Mg. The Ni(B_2P_2) complex was isolated from either method as a red/orange solid that was subjected to single-crystal XRD studies. In the solid-state, the Ni atom was coordinated η^6 to the C_4B_2 core with Ni-C_{DBA} and Ni-B_{DBA} distances of 2.349 Å and 2.916 Å, respectively. The redox chemistry of the Ni(B_2P_2) complex was explored by CV and revealed two, pseudo-reversible redox events at 0.06 V and –2.99 V vs. Fc/Fc^+ (THF, 0.1 M $n$$Bu_4NPF_6$, 100 mV/s). However, the isolation of the redox congeners of the Ni(B_2P_2) complex was not pursued.

A2.2) Experimental Section

A2.2.1) General Considerations

Unless otherwise noted, all manipulations were carried out using standard Schlenk or glovebox techniques under a dinitrogen atmosphere. Solvents were dried and deoxygenated by sparging with argon and passage through activated alumina in a solvent purification system from SG Waters USA, LLC. Non-

halogenated solvents were tested with a standard purple solution of sodium benzophenone ketyl in tetrahydrofuran in order to confirm effective oxygen and moisture removal. 9,10-Bis(2-(diisopropylphosphino)phenyl)-9,10-dihydroboranthrene (B_2P_2) was synthesized according to literature procedures previously mentioned. Elemental analyses were performed by Midwest Microlab, LLC, Indianapolis, IN. Deuterated solvents were purchased from Cambridge Isotope Laboratories Inc., degassed, and dried over activated 4 Å molecular sieves for at least 24 hr prior to use. NMR spectra were recorded on Varian Inova 500 MHz spectrometers. ^{1}H chemical shifts are reported in ppm relative to tetramethylsilane using residual solvent as internal standards. ^{31}P and ^{11}B chemical shifts are reported in ppm relative to 85% aqueous H_3PO_4 and $BF_3 \cdot Et_2O$, respectively. ^{11}B NMR spectra were manipulated with MestReNova 10.0.2. and had a backwards LP applied to eliminate background signal from the borosilicate NMR tube X-ray diffraction studies were performed using a Bruker-AXS diffractometer. Cyclic Voltammetry (CV) experiments were performed using a Pine AFP1 potentiostat. The cell consisted of a glassy carbon working electrode, a Pt wire auxiliary electrode and a Pt wire pseudo-reference electrode. All potentials are referenced vs. the Fc/Fc^{+} couple measured as an internal standard.

A2.2.2) Ni(B_2P_2).

Via $NiBr_2$: A solution of B_2P_2 (0.200 g, 0.357 mmol) in THF (3 mL) was added to a slurry of $NiBr_2$ (0.080 g, 0.366 mmol) in THF (3 mL) and stirred 4 hours. The orange/red mixture had its volatiles removed, was added Et_2O (5 mL) and again had its volatiles removed. The remaining orange/red foam was extracted with toluene (2 x 3 mL) and filtered through celite into a 20 mL vial containing sodium (0.021 g, 0.893 mmol). The solution was stirred 10 hours during which time a deep red solution formed. The mixture was filtered through celite and concentrated to ca. 2 mL before adding Et_2O (5 mL). The mixture was filtered through a 1" pad of silica gel and rinsed with toluene:Et_2O (2:5, 10 mL). Removal of the volatiles gave the product as a red solid. Overall yield: 0.157 g, 71%.

Via $Ni(PPh_3)_4$: A solution of B_2P_2 (0.200 g, 0.357 mmol) in THF (5 mL) was added to $Ni(PPh_3)_4$ (0.395 g, 0.357 mmol) in THF (3 mL) and the mixture stirred at 50 °C for 12 hours. The deep red solution had its volatiles removed *in vacuo* before dissolving the residue in THF:Et_2O (1:9, 10 mL) and passing it through a 1" pad of silica. Removal of the volatiles *in vacuo* gave the product as a red/orange solid. Overall yield: 0.197 g, 89%. X-ray quality crystals were grown by layering a concentrated toluene solution with MeCN. ^{1}H NMR (500 MHz, C_6D_6) δ 8.01 (d, *J* = 7.2 Hz, 2H), 7.62 (dd, *J* = 5.9, 3.4 Hz, 2H), 7.48 (t, *J* = 7.2 Hz, 1H), 7.36 – 7.30 (m, 2H), 7.27 (t, *J* = 7.5 Hz, 2H), 7.11 (dd, *J* = 6, 3.4 Hz, 2H), 2.04 (dp, *J* = 14.2, 7.3 Hz, 2H), 0.74 (d, *J* = 6.9 Hz, 3H), 0.72 (d, *J* = 6.9 Hz, 3H), 0.61 (d, *J* = 7.1 Hz,

3H), 0.58 (d, J = 7.1 Hz, 3H). ^{31}P (202 MHz, C_6D_6) δ 45.6 (s). $^{11}B\{^1H\}$ (160 MHz) δ 27.8 (bs). $^{13}C\{^1H\}$ NMR (126 MHz, C_6D_6) δ 159.3, 143.1-142.9 (m), 135.0, 132.0 – 131.4 (m), 130.6, 130.1, 129.9, 126.9, 125.4, 27.7 (dt, J = 18.3, 8.5 Hz), 20.0, 18.9. UV-vis (THF): λ_{max} (nm) (ε_{max} ($M^{-1}cm^{-1}$)) 318 (sh, 2.5 x 10^4), 372 (1.7 x 10^4), 451 (7.9 x 10^3), 577 (sh, 2.8 x 10^3). Anal. Calcd. for $C_{36}H_{44}B_2NiP_2$ (1 x $C_4H_{10}O$): C, 69.31 H, 7.85. Found: C, 69.98 H, 8.62.

A2.3) Spectroscopic Data

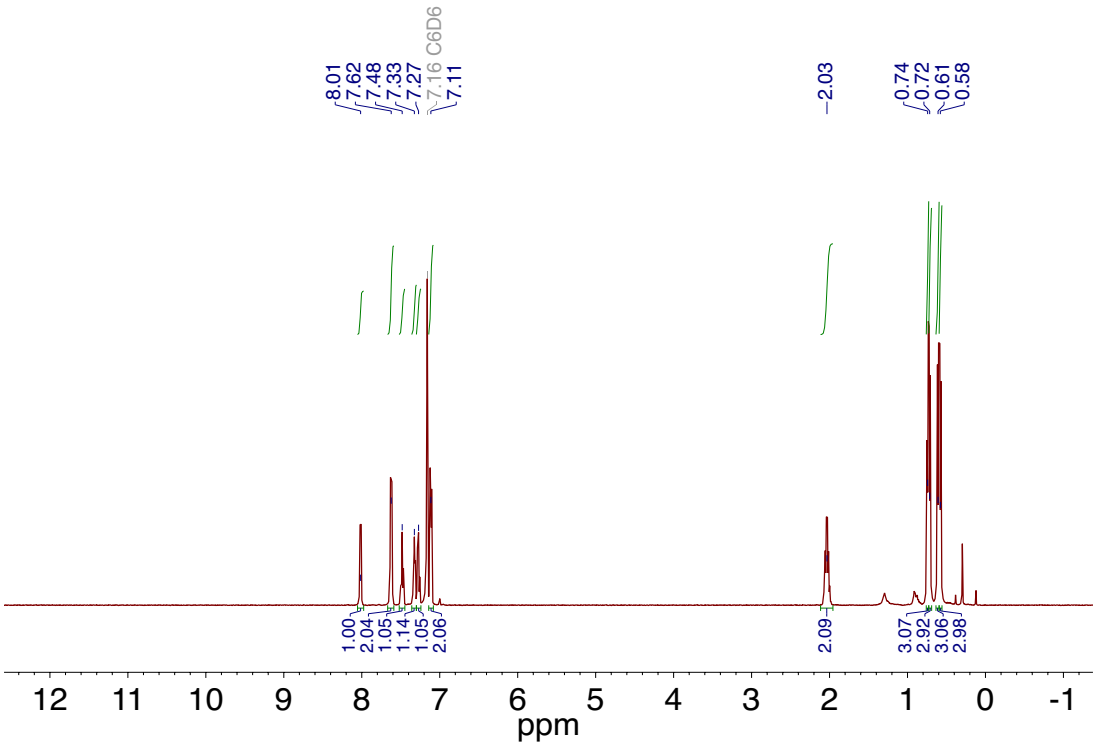

Figure A2.3.1. ^1H NMR spectrum of **Ni(B_2P_2)** recorded at 500 MHz in C_6D_6.

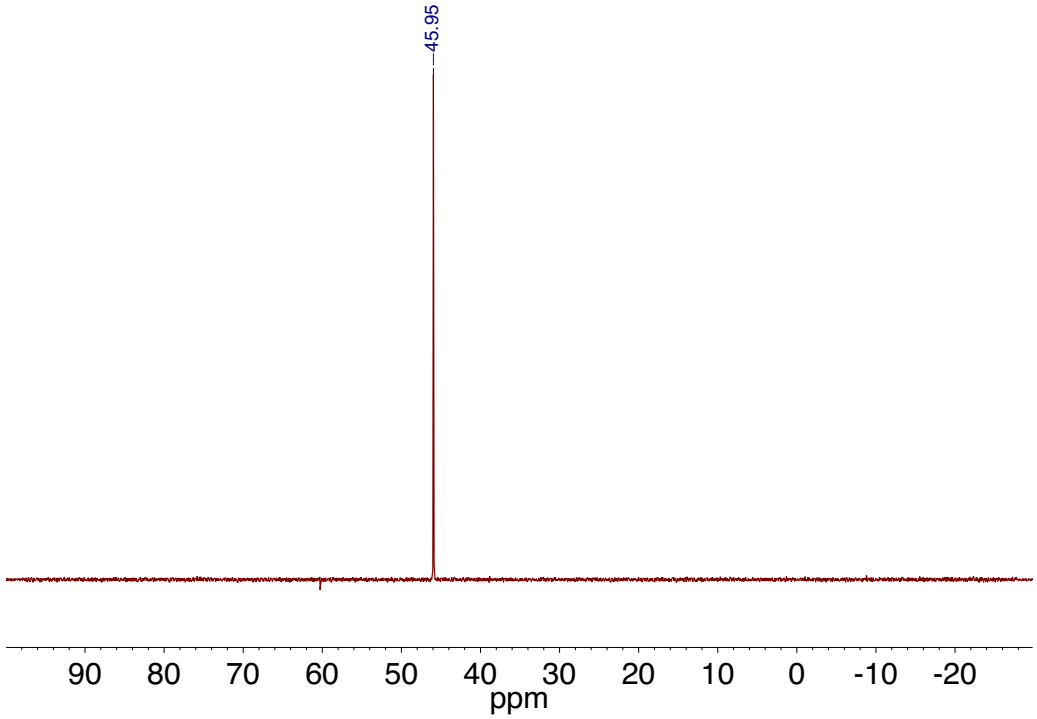

Figure A2.3.2. ^{31}P NMR spectrum of **Ni(B_2P_2)** recorded at 162 MHz in C_6D_6.

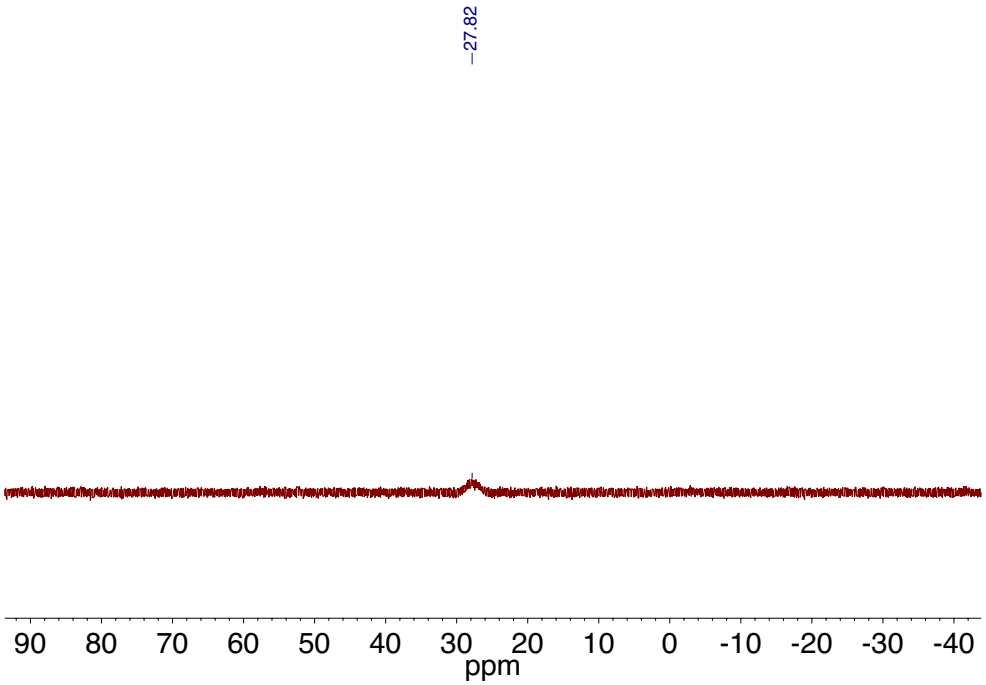

Figure A2.3.3. ^{11}B NMR spectrum of **Ni(B_2P_2)** recorded at 160 MHz in C_6D_6.

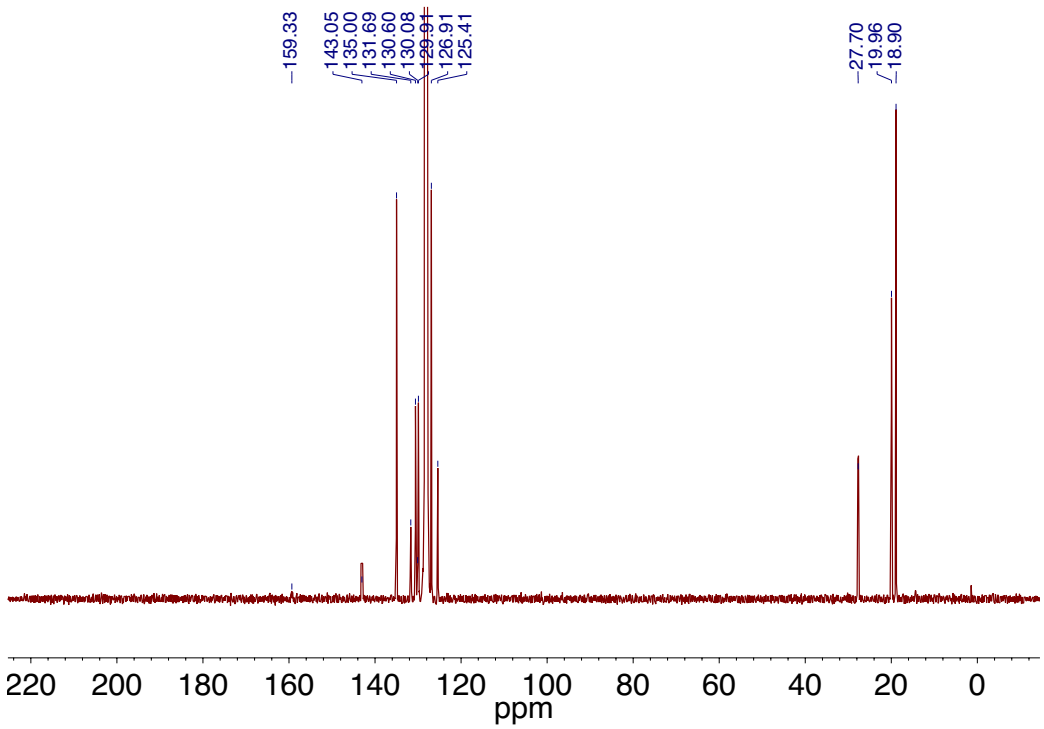

Figure A2.3.4. ^{13}C NMR spectrum of **Ni(B_2P_2)** recorded at 126 MHz in C_6D_6.

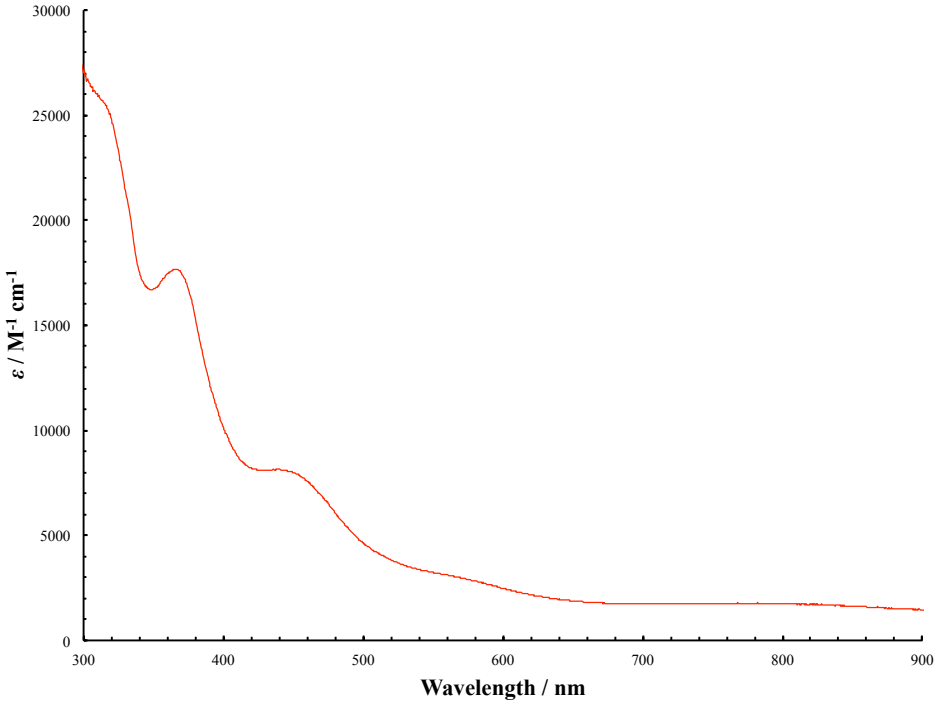

Figure A2.3.5. UV-Vis spectrum of **Ni(B_2P_2)** in THF.

A2.4) Cyclic Volatmmetry

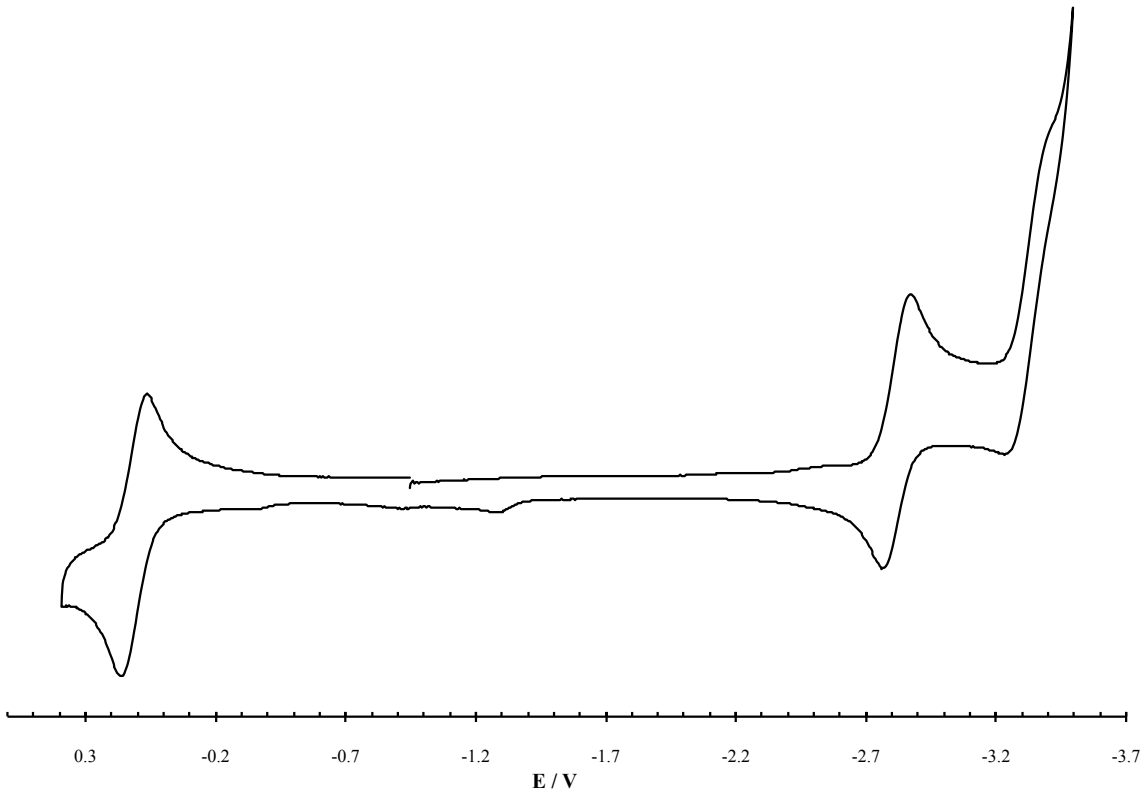

Figure A2.4.1. Cyclic voltammogram of **Ni(B_2P_2)** in THF. (0.1 M nBu$_4$NPF$_6$ as electrolyte, scan rate 100 mV/s).

A2.5) X-Ray Crystallography

A2.5.1) General Considerations

Single crystals were coated with paratone oil and mounted on cryo-loop glass fibers. X-ray intensity data were collected at 100(2) K on a Bruker APEX2[3] platform-CCD X-ray diffractometer system using fine-focus Mo K_α radiation (λ = 0.71073 Å, 50kV/30mA power). The CCD detector was placed at 5.0600 cm from

the crystal. Frames were integrated using the Bruker SAINT software package[4] and using a narrow-frame integration algorithm. Absorption corrections were applied to the raw intensity data using the SADABS program.[5] The Bruker SHELXTL software package[6] was used for phase determination and structure refinement. Atomic coordinates, isotropic and anisotropic displacement parameters of all the non-hydrogen atoms were refined by means of a full matrix least-squares procedure on F^2. The H-atoms were included in the refinement in calculated positions riding on the atoms to which they were attached. Relevant details for individual data collections are reported in Tables A2.5.1.

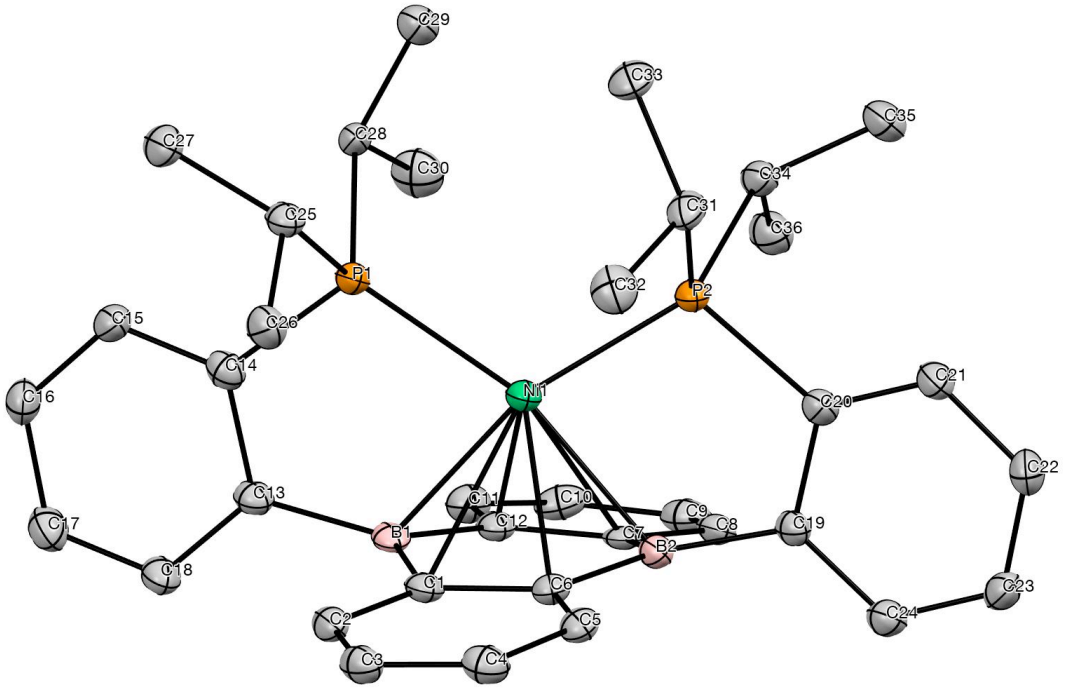

Figure A2.5.1. Labelled thermal ellipsoid plot (50%) for **Ni(B_2P_2)**.

Table A2.5.1. Crystal data and structure refinement for **Ni(B_2P_2)**.

Identification code	hh11JT6	
Empirical formula	$C_{36}H_{44}B_2NiP_2$	
Formula weight	618.98 g/mol	
Temperature	100(2) K	
Wavelength	0.71073 Å	
Crystal system	Monoclinic	
Space group	$P2_1/c$	
Unit cell dimensions	a = 18.6867(17) Å	α = 90°.
	b = 10.9686(10) Å	β= 97.5808(13)°.
	c = 15.4564(14) Å	γ = 90°.
Volume	3140.4(5) Å^3	
Z	4	
Density (calculated)	1.309 mg/m^3	
Absorption coefficient	0.744 mm^{-1}	
F(000)	1312	
Crystal size	0.298 x 0.179 x 0.096 mm^3	
θ range for data collection	2.158 to 29.574°	
Index ranges	$-25 \le h \le 25$, $-15 \le k \le 15$, $-21 \le l \le 21$	
Reflections collected	82323	
Independent reflections	8798 [R_{int} = 0.0833]	
Completeness to θ = 25.242°	100.0 %	
Absorption correction	None	
Refinement method	Full-matrix least-squares on F^2	
Data / restraints / parameters	8798 / 0 / 378	
Goodness-of-fit on F^2	1.070	
Final R indices [$I > 2\sigma_I$]	R_1 = 0.0526, wR_2 = 0.1299	
R indices (all data)	R_1 = 0.0805, wR_2 = 0.1466	
Largest diff. peak and hole	1.379 and –0.483 e/Å^3	

A3.1) N,N-dimethylaniline substituted DBA Molecules

In our efforts to develop DBA molecules that exhibit multi-electron redox chemistry at mild potentials (< –2.0 V), we explored the possibility of utilizing cationic ammonium appendages to modulate the redox chemistry of DBA heterocycles. Additionally, both the 9,10-dihydro-9,10-diboraanthracene and tetrafluorinated, 9,10-dihydro-2,3,7,8-tetrafluoro-9,10-diboraanthracene, heterocycles were investigated. Synthesis of this class of DBA molecule was began by addition of two equivalents of (4-(dimethylamino)-2,6-dimethylphenyl)lithium to 9,10-dibromo-9,10-diboraanthracene or 9,10-dibromo-2,3,7,8-tetrafluoro-9,10-diboraanthracene at –78 °C in toluene. Following workup, a bright red solid, $^{Ar}NMe_2$-DBA, and a bright purple solid, $^{Ar}NMe_2$-^{4F}DBA were isolated excellent yield (88% and 85%, respectively) and characterized by NMR spectroscopies and cyclic voltammetry (CV). CVs of $^{Ar}NMe_2$-DBA revealed two reversible redox couples at –2.02 V and –2.72 V vs Fc/Fc^+ while $^{Ar}NMe_2$-^{4F}DBA featured two reversible redox couples at –1.63 V and –2.56 V vs Fc/Fc^+ (THF, 0.1 M nBu$_4$NPF$_6$, 100 mV/s). As postulated, $^{Ar}NMe_2$-^{4F}DBA featured more positive redox couples than $^{Ar}NMe_2$-DBA, likely as a result of the electron withdrawing nature of the F atoms appended to the DBA heterocycle. Given the promising redox chemistry of $^{Ar}NMe_2$-DBA and $^{Ar}NMe_2$-^{4F}DBA, we sought to alkylate each

C_{Ar}-NMe_2 group to produce ammonium cations that could potentially shift the redox couples even more positive due to increased cationic charge on each molecule. However, attempts at methylation with methyl iodide proved sluggish and ultimately the limited solubility of the products hindered further study. Modification of the aniline substituents to increase the solubility of these derivatives is currently underway in the group.

A3.2) Experimental Section

A3.2.1) General Considerations

Unless otherwise noted, all manipulations were carried out using standard Schlenk or glovebox techniques under a dinitrogen atmosphere. Solvents were dried and deoxygenated by sparging with argon and passage through activated alumina in a solvent purification system from SG Waters USA, LLC. Non-halogenated solvents were tested with a standard purple solution of sodium benzophenone ketyl in tetrahydrofuran in order to confirm effective oxygen and moisture removal. 9,10-dibromo-9,10-diboraanthracene, 9,10-dibromo-2,3,7,8-tetrafluoro-9,10-diboraanthracene and (4-(dimethylamino)-2,6-dimethylphenyl)lithium were synthesized according to literature procedures. Deuterated solvents were purchased from Cambridge Isotope Laboratories Inc., degassed, and dried over activated 4 Å molecular sieves for at least 24 hr prior to use. NMR spectra were recorded on Varian Inova 500 MHz spectrometers. ^{1}H

chemical shifts are reported in ppm relative to tetramethylsilane using residual solvent as internal standards. ^{31}P and ^{11}B chemical shifts are reported in ppm relative to 85% aqueous H_3PO_4 and $BF_3 \cdot Et_2O$, respectively. ^{11}B NMR spectra were manipulated with MestReNova 10.0.2. and had a backwards LP applied to eliminate background signal from the borosilicate NMR tube. Cyclic Voltammetry (CV) experiments were performed using a Pine AFP1 potentiostat. The cell consisted of a glassy carbon working electrode, a Pt wire auxiliary electrode and a Pt wire pseudo-reference electrode. All potentials are referenced vs. the Fc/Fc^+ couple measured as an internal standard.

A3.2.2) 9,10-bis(N,N-3,5-tetramethylaniline)-9,10-diboraanthracene ($^{Ar}NMe_2$-^{4F}DBA).

In the glove box cold well, (4-(dimethylamino)-2,6-dimethylphenyl)lithium (0.097 g, 0.600 mmol) and 9,10-dibromo-9,10-diboraanthracene (0.100 g, 0.299 mmol) were combined at ~ –100 °C prior to adding freshly thawed toluene (5 mL). The reaction mixture was frozen before letting it come to room temperature over 3 hours during which time a deep red solution formed. The reaction was filtered through celite and the volatiles were removed *in vacuo*. The residue was added pentane (4 mL) prior to again removing volatiles *in vacuo*. The residue was then dissolved in THF (3 mL), filtered through celite, added hexanes (8 mL) and concentrated *in vacuo* to cause the product to precipitate as a red, crystalline solid that was collected by filtration and dried *in vacuo*. A second batch could be

recovered by letting a saturated THF/hexane solution stand at –15 °C. Yield: 0.128 g, 91%. ^{1}H NMR (400 MHz, C_6D_6) δ 7.95 (dd, *J* = 5.3, 3.3 Hz, 4H), 7.19 (dd, *J* = 5.4, 3.3 Hz, 4H), 6.63 (s, 4H), 2.74 (s, 12H), 2.21 (s, 12H). ^{11}B NMR (160 MHz, C_6D_6) δ 68.85.

A3.3.3) 9,10-bis(N,N-3,5-tetramethylaniline)-9,10-(2,3,7,8-tetrafluorodiboraanthracene) ($^{Ar}NMe_2$-^{4F}DBA).

In the glove box cold well, (4-(dimethylamino)-2,6-dimethylphenyl)lithium (0.074 g, 0.496 mmol) and 9,10-dibromo-2,3,7,8-tetrafluoro-9,10-diboraanthracene (0.100 g, 0.247 mmol) were combined at ~ –100 °C prior to adding freshly thawed toluene (5 mL). The reaction mixture was frozen before letting it come to room temperature over 3 hours during which time a deep purple solution formed. The reaction was filtered through celite and the volatiles were removed *in vacuo*. The residue was added pentane (4 mL) prior to again removing volatiles *in vacuo*. The residue was then dissolved in THF (3 mL), filtered through celite, added hexanes (8 mL) and concentrated *in vacuo* to cause the product to precipitate as a purple, crystalline solid that was collected by filtration and dried *in vacuo*. A second batch could be recovered by letting a saturated THF/hexane solution stand at –15 °C. Yield: 0.117 g, 87%. ^{1}H NMR (400 MHz, C_6D_6) δ 7.69 (t, *J* = 9.4 Hz, 4H), 6.53 (s, 4H), 2.70 (s, 12H), 2.06 (s, 12H). ^{19}F NMR (376 MHz, C_6D_6) δ -131.97 (t, *J* = 9.5 Hz). ^{11}B NMR (128 MHz, C_6D_6) δ 36.34. ^{13}C NMR

(151 MHz, C_6D_6) δ 155.37 (t, J = 11.3 Hz), 153.65, 153.56, 144.49, 138.96, 111.85, 40.31, 23.42.

A3.3) Spectroscopic Data

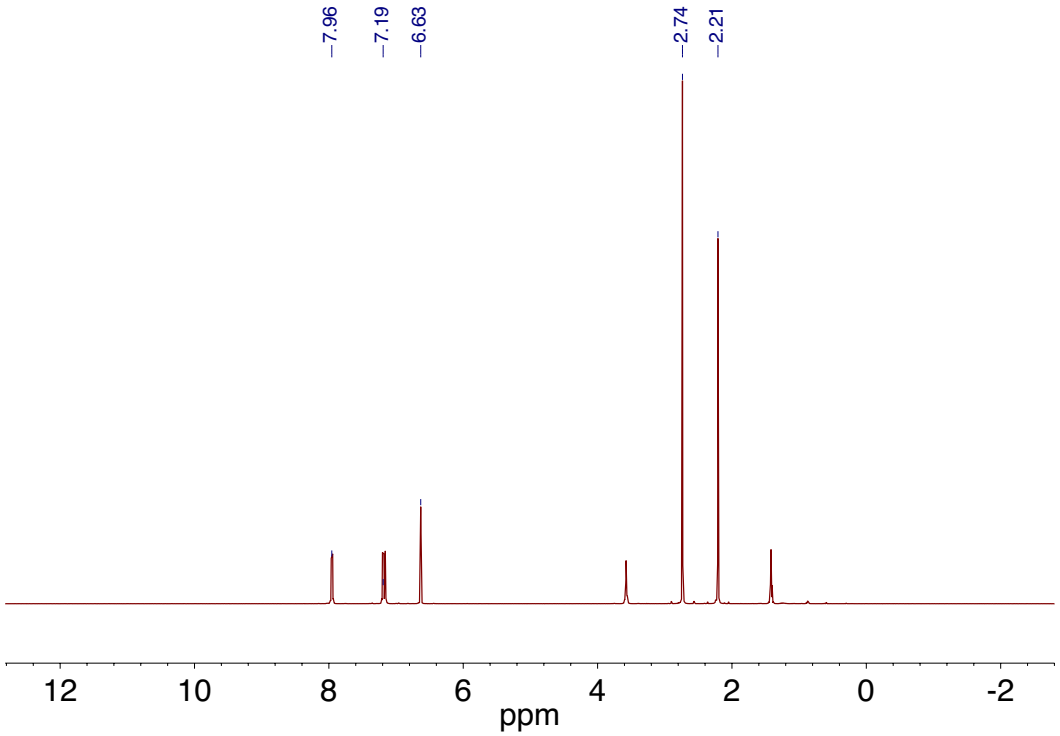

Figure A3.3.1. ^{1}H NMR spectrum of **[^{Ar}NMe$_2$-DBA]** recorded at 500 MHz in C_6D_6.

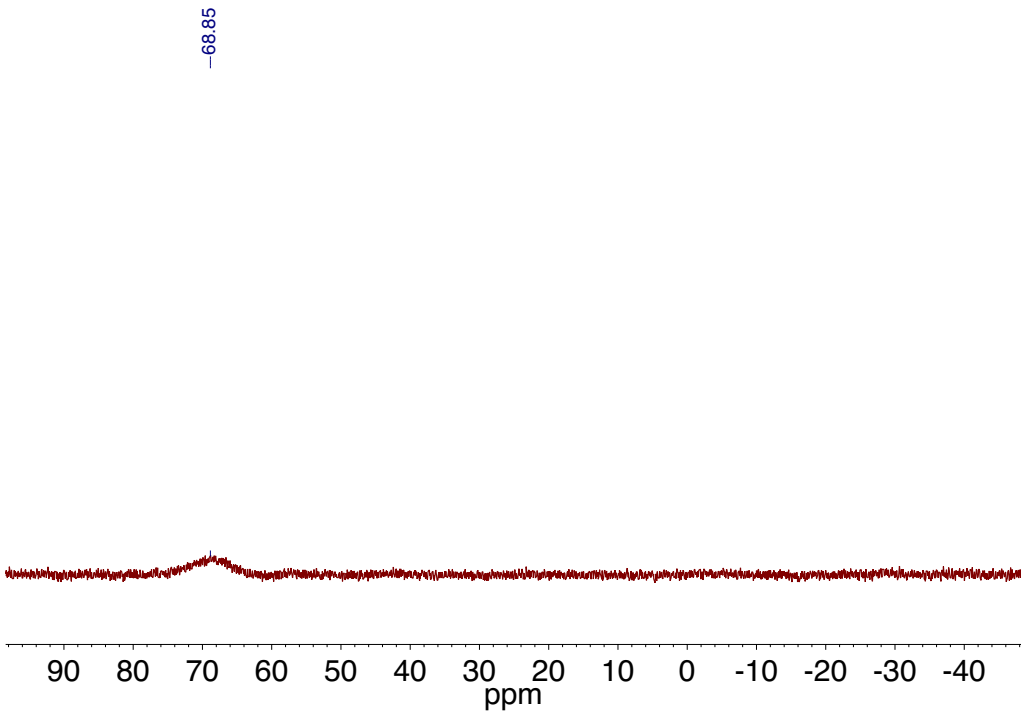

Figure A3.3.2. $^{11}B\{^{1}H\}$ NMR spectrum of **[^{Ar}NMe$_2$-DBA]** recorded at 160 MHz in C_6D_6.

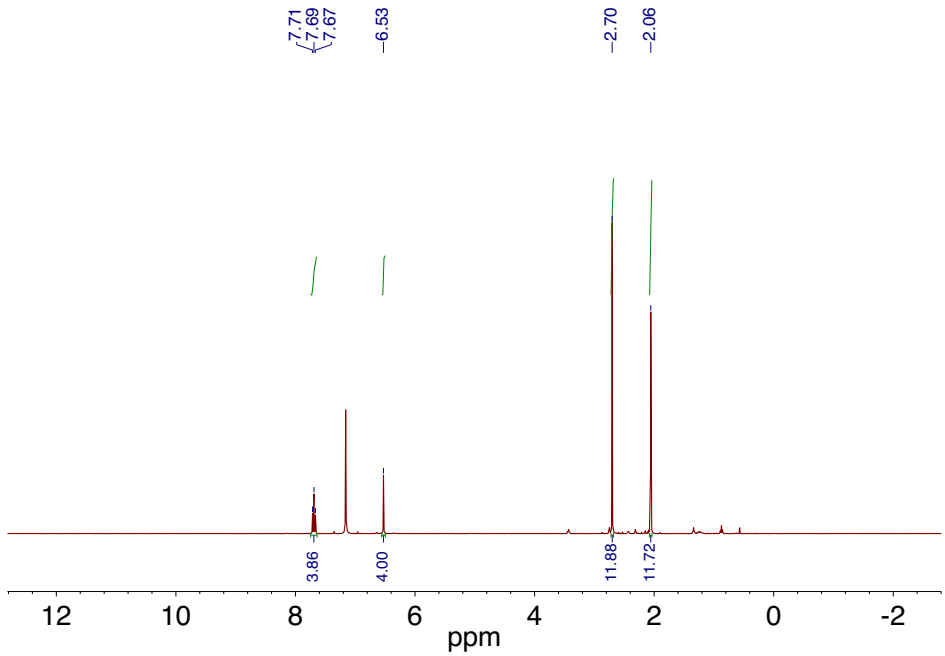

Figure A3.3.3. ^{1}H NMR spectrum of **[^{Ar}NMe$_2$-^{4F}DBA]** recorded at 500 MHz in C_6D_6.

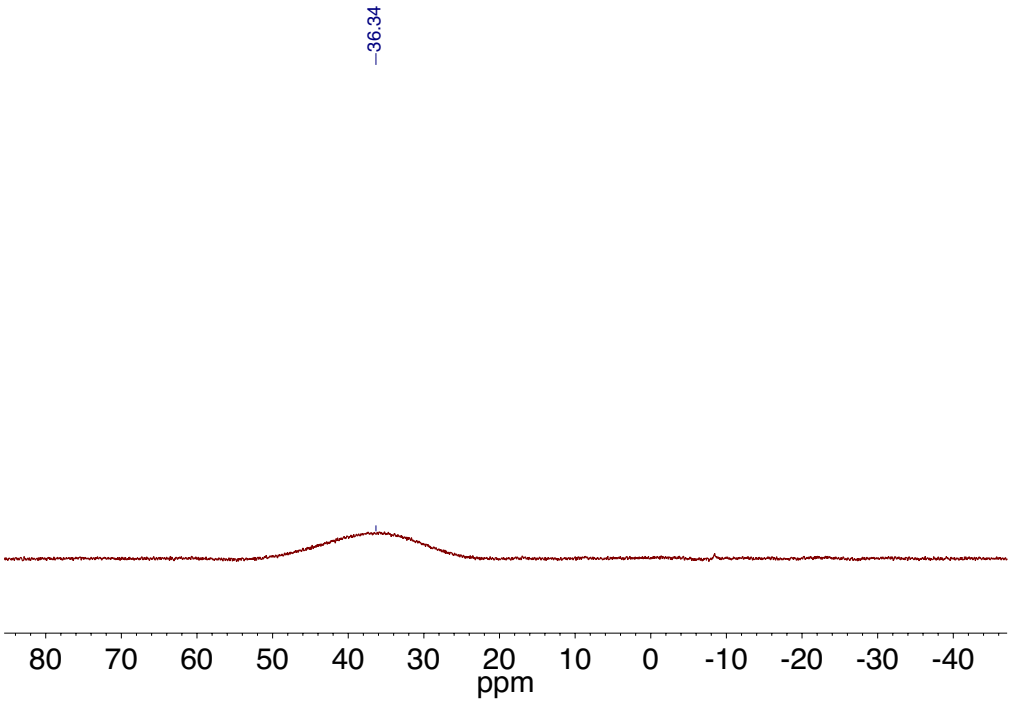

Figure A3.3.4. ^{11}B{^{1}H} NMR spectrum of **[^{Ar}NMe$_2$-^{4F}DBA]** recorded at 160 MHz in C_6D_6.

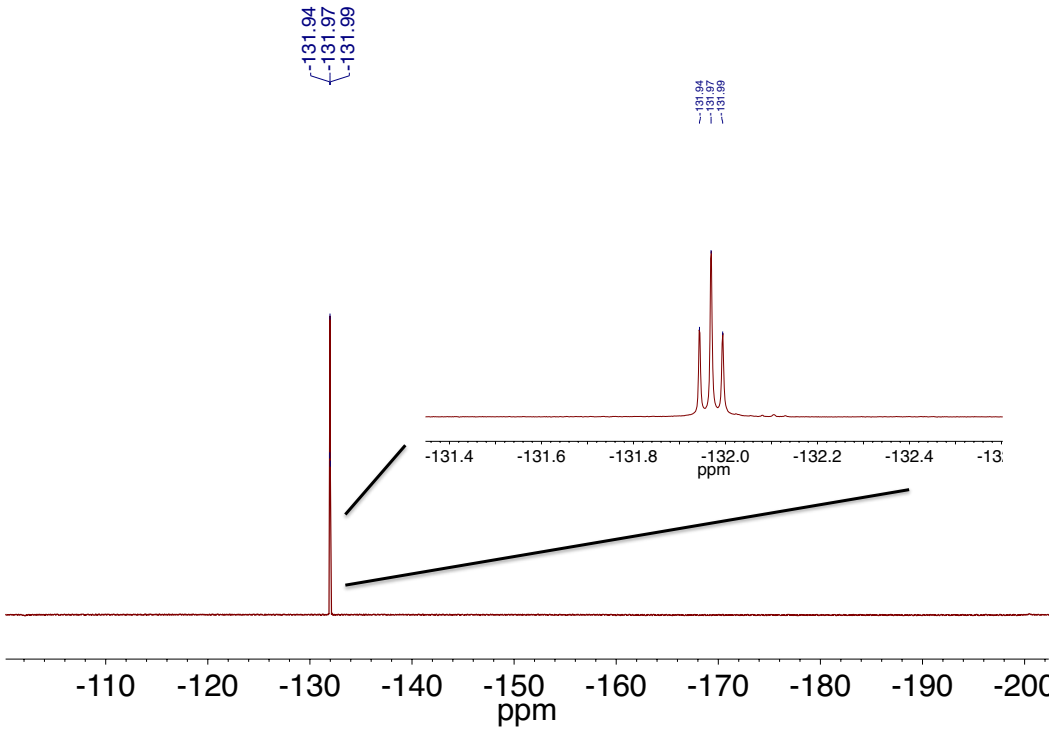

Figure A3.3.5. ^{19}F NMR spectrum of **[^{Ar}NMe$_2$-^{4F}DBA]** recorded at 471 MHz in C_6D_6.

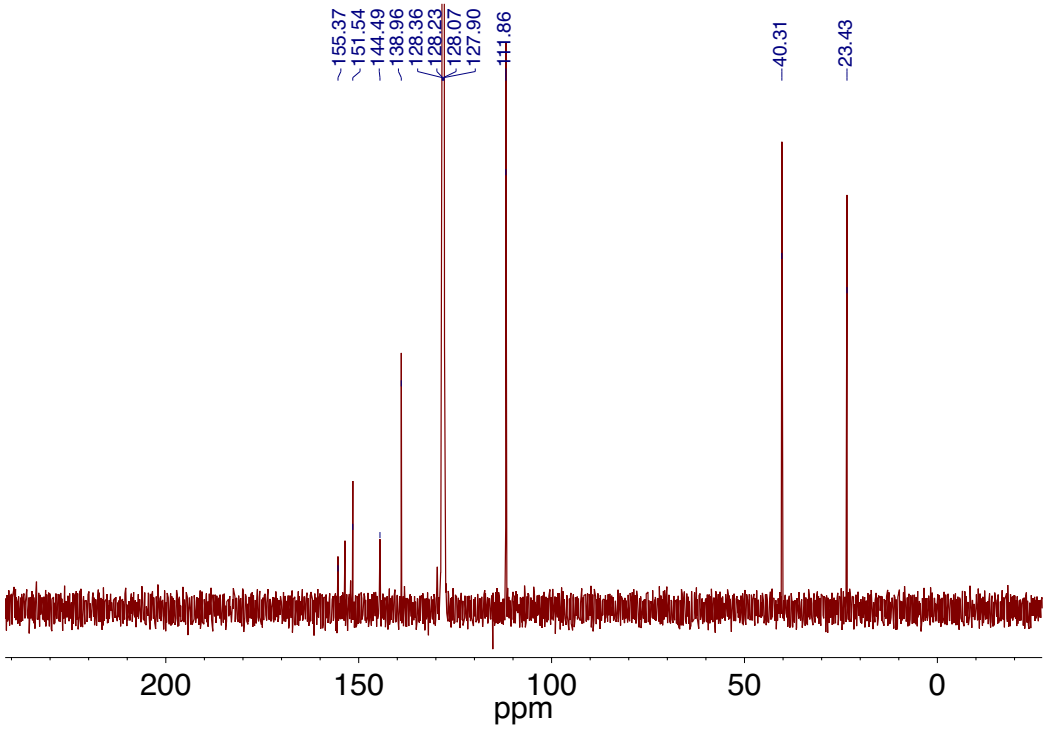

Figure A3.3.6. ^{13}C{^{1}H} NMR spectrum of **^{Ar}NMe$_2$-^{4F}DBA** recorded at 126 MHz in C_6D_6.

A3.4) Cyclic Voltammetry

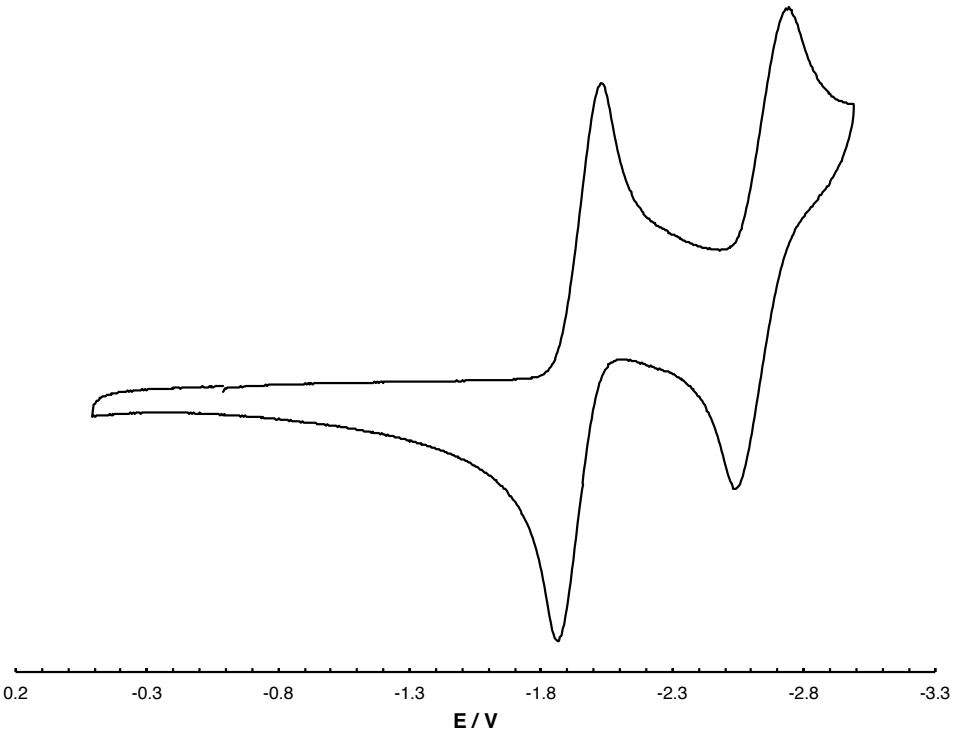

Figure A3.4.1. Cyclic voltammogram of ^{Ar}**NMe$_2$-DBA** in THF (0.1 M *n*Bu$_4$NPF$_6$ as electrolyte, scan rate 100 mV/s, potential vs. Fc$^+$/Fc).

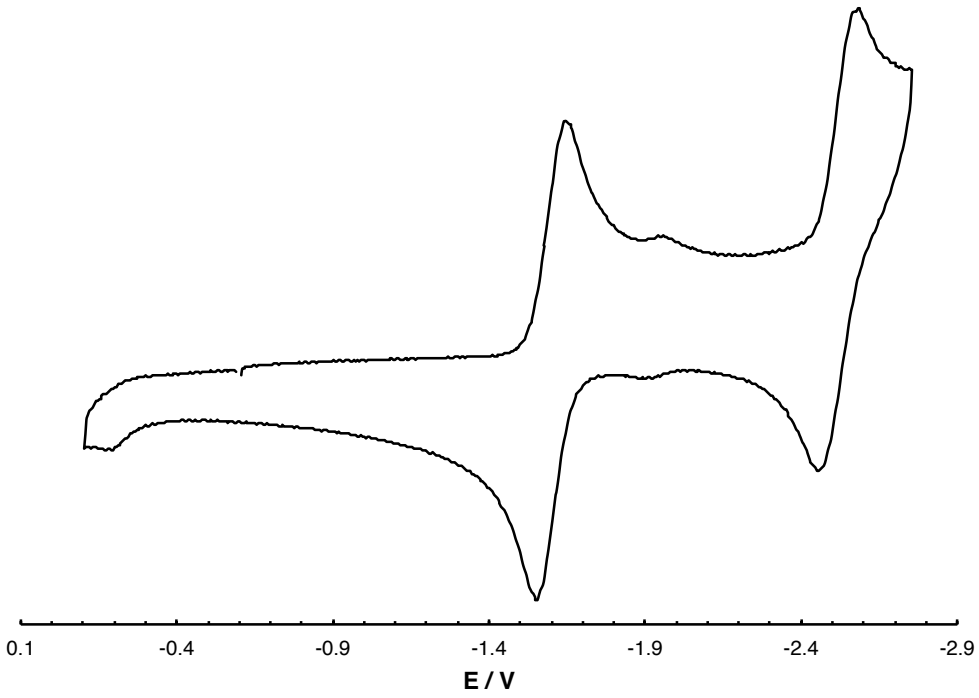

Figure A3.4.2. Cyclic voltammogram of $^{Ar}NMe_2$-^{4F}**DBA** in THF (0.1 M nBu$_4$NPF$_6$ as electrolyte, scan rate 100 mV/s, potential vs. Fc^+/Fc).